STUDIA

UNIVERSITATIS BABEŞ-BOLYAI

Chemia

CLUJ-NAPOCA 2001

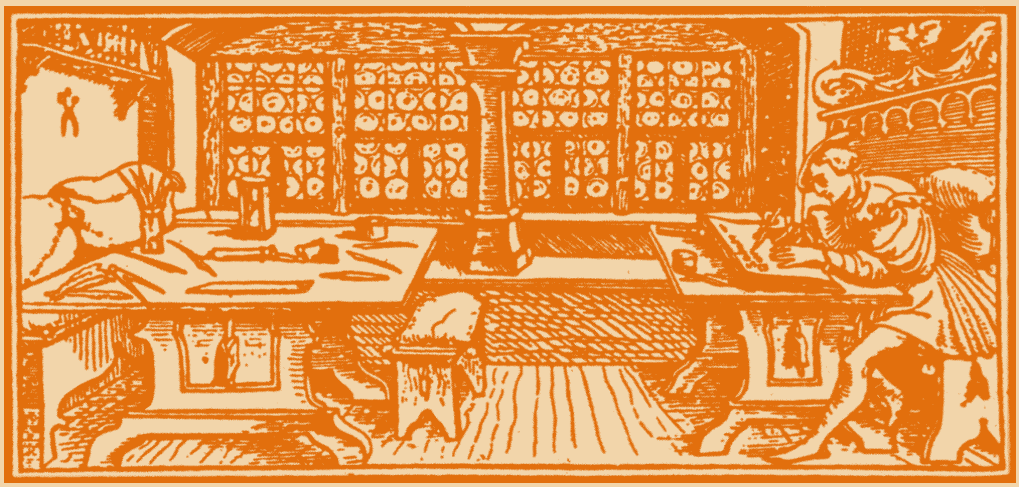

1-2

Anul XLVI **2001**

STUDIA
UNIVERSITATIS BABEŞ-BOLYAI
CHEMIA
1-2

EDITORIAL OFFICE: Gh. Bilaşcu no. 24, 3400 Cluj-Napoca ✦ Phone 064-40.53.52

SUMAR - SOMMAIRE - CONTENTS - INHALT

THE CHEMICAL ENGINEERING SCHOOL OF CLUJ AT THE 30TH ANNIVERSARY

In the days of September 6-8, 2001, at the Faculty of Chemistry and Chemical Engineering of the Cluj-Napoca Babes-Bolyai University were held the proceedings of the anniversary symposium of 30 years from the setting up of the Cluj School of Chemical Engineering.

Organized by the Department of Chemical Engineering and Science of Oxidic Materials together with the Cluj subsidiary of the Society of Chemical Engineering of Romania (SIChR), this symposium succeded in polarizing the interest of the higher education, research, national chemical Projection and industry as well as that of some personalities outside the borders of our country.

The inaugural moment took place in the presence of Romanian Academy's representatives (academician I. Haiduc, chairman of the Cluj subsidiary), of local authorities (Gh. Funar, doctor in economy, mayor of Cluj-Napoca City), of the University (professor dr. N. Bocsan, pro-rector), of the Romanian Chemical Engineering Society (professor dr. engineer L. Literat, chairman of the Cluj subsidiary) of the higher education institutions of Cluj and other university centres.

On this occasion, Mr. Gheorghe Funar, doctor in economy and mayor of Cluj-Napoca City awarded a DIPLOMA of recognition to the Faculty of Chemistry and Chemical Engineering for its special contribution to the Cluj Scientific School's being acknowledged on national and international plane and for having trained the young generation in the spirit of love for the profession they have chosen and for having promoted the vanguard scientific research.

The jubilee ceremony continued with conferences presented in plenum:

1. *The Cluj education of chemical engineering in data and documents of archives* - professor dr. engineer Liviu Literat.

2. *External visibility of Romanian science. A bibliometric study* -academician Ionel Haiduc.

3. *Covalent modifications of graphyte felt electrodes for red-ox catalysis in organic chemistry* -professor dr. Claude Moinet, University of Rennes, France.

The first conference brings forward, on the basis of documents presented for the first time, approaches, actions, events, facts, personages, favourable circumstances and obstacles, periods with light and shadows in the historical itinerary of the Cluj education of chemical engineering. This paper, a documented study of archives, attempts to incline as objectively as possible towards the "chemical engineering in Cluj-Napoca" phenomenon.

The bibliometric study presented by academician I. Haiduc makes a comprehensive synthesis of the Romanian scientific research considered from the angle of the impact in the means of information and diffusion of original research in the international circuit. The study brings to light some not exactly favourable aspects for the Romanian science's image and looks for (objective and subjective) explanations for this state of things. In the hierarchy of scientific production on the world plane some correlations are noticed between the scientific performance of a country and the economic standard, and within the framework of every dependent nation implying priority politics, experience and traditions in research, scientific management etc.

In the last paper, of strict specialty, professor Cl.Moinet discusses about some results in research in the field of organic electrocatalysis performed at the University of Rennes, France. This study makes a punctual analysis of electrode processes and the catalytic act involvement in releasing some modifications in the structure of graphyte felt electrodes, with consequences upon the mechanisms, efficiency and selectivity in red-ox organic catalysis.

The symposium proceedings progressed according to the schedule within the fourth Section, under the form of conferences, papers and posters. A number of 127 papers and 268 authors have been registered and grouped as follows:

In the scientific program also entered: an *international scientific seminar EISEDIMA-RO* having as themes environment legislation, risk and financial administration of disasters, as well as a *Tribune of the young researcher*, meant to stimulate the original and independent research work of students and candidates for a master's degree.

Section	**Confererence**	**Paper**	**Poster**	**Total**
1. Chemical and biochemical engineering, informatics of chemical systems	3	18	15	36
2. Science and engineering of oxidic materials	1	19	6	26
3. Chemistry and protection of the environment	2	12	17	31
4. Chemistry -physics	4	8	22	34
Partial and general total	10	57	60	127

Both actions, having the character of a premiere, proved to be of great interest and consequently are recommended to perpetuate.

The scientific success obtained by the symposium was significant in our opinion, thanks to the value of the papers presented, quality and level of discussions, exchange of information, a more definite knowledge of preoccupations at various schools and collective bodies of research, setting up of new co-operating relationships on national and international planes.

The proceedings of the symposium sections have been recorded on a CD and delivered to participants (CD-ROM, Ed. ACCENT, ISBN 973-99821-8-2,2001). Another part will appear in STUDIA UNIVERSITATIS "BABES-BOLYAI", Chemistry Series No. 1/2001.

Within the framework of the symposium a launching of book took also place (*TECHNICAL CERAMICS. Principles of calculation and projection*), achieved by a teaching staff from the Chair of Chemical Engineering and Science of Oxidic Materials (L. Literat, L. Gagea, F. Goga, E. Mirica, E. Olariu), recently appeared in, the Science Book Publishing House, Cluj-Napoca. It was presented by professor dr. engineer Maria Preda from the Bucharest POLYTECHNIC University, Faculty of Industrial Chemistry, Chair of Science and Engineering of Oxidic Materials.

One cannot disregard the organizers' care for providing agreeable sojourn conditions to participants. We make reference to accomodation in one-room flats pertaining to student hostels, and to the main meal within the faculty (the place destined to the symposium proceedings), at moderate prices, and also to the two free of charge trips and visits organized at Turda Salina (on September 6) and at the Remeti Monastery, Alba Iulia and Aiud (on September 8, 2001).

The splendour and original thrill of Turda Salina's depths, the ad-hoc organized musical audition and cocktails will be, we do hope it, pleasant memories for all participants.

Likewise, the trip on the Geoagiu de Sus valley has revealed other unmistakeable beauties of the Apuseni Mountains which, in the dipper of palms of groove and rock, guard a precious jewel of Romanian architecture, the Remeti Monastery, a symbol of durability, faith and hope.

These moments of delight and, in general, the symposium organization was made possible due to those wanting and being in the position of helping us (S.C. TERAPIA, S.A., S.C. NATEX, S.A., S.C. CEROC S.A., S.C. NAPOLACT S.A., S.C.MUCART S.A. from Cluj- Napoca, S.C. CERASIL S.A. from Oradea, S.C. FAlMAR S.A. from Baia Mare, S.C. SALINA Turda), to whom we address, in this way, our thanks.

We wish that the Cluj school of chemical engineering enjoyed new achievements in its process of being continually appreciated, enjoyed a long and prosperous life, were favoured with success in the scientific competition and in educating series of students and graduates.

MANY HAPPY YEARS!

Professor dr. engineer LIVIU LITERAT

STUDIA UNIVERSITATIS BABEŞ-BOLYAI, CHEMIA, XLVI, 1-2, 2001

AUTOMATIC DEVICE FOR RECORDING AND EXPLORING THE SETTLING CURVES. APPLICATIONS AT THE SYMPTOTIC CLASSIFYING OF POWDERY SYSTEMS

LIVIU LITERAT

Department of Chemical Engineering, Faculty of Chemistry and Chemical Engineering, Babes-Bolyai University,11, Arany Janos, 3400, Cluj-Napoca

SUMMARY. An experimental fitting of original conception, with possible applications to the study of the powdery dispersions depot in liquid media, is presented. The outcoming results are compared to those of other techniques specialized in the same purpose.

The tight correspondence between the data and the results offer credibility to the procedure and recommends it as an accessible constructively and economically alternative.

INTRODUCTION

Considering that the principles of settling analysis methods are already known, we aim at presenting an experimental fitting for the recording of the sedimentation curves. We are also interested in a program that calculates the distribution of fractions in a powdery ensemble dispersed in an immobile liquid [1-3].

The experiment data and the interpretation can be considered as a case study meaning to explicitate the working technique and to underline the performances of the procedure.

EXPERIMENTAL FITTING

The installation is a sequential fitting consisting of a sedimentation vessel (fig.1.), an electronic analytic scales and a computer (PC Pentium) interconnected through an interface RS-232C. A program of data acquisition (LabVIEW, National Instruments Co.) records the variation of the mass (m) in time (t) on the sedimentation scales (1, fig.1.) [4].

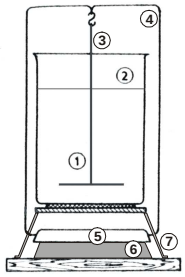

Fig.1. Sedimentation vessel
1. plate to deposit, 2. suspension, 3. hanging wire, 4. frame, 5. scale support, 6. sensor, 7. support of the sedimentation vessel

EXPERIMENTAL DATA. INTERPRETATION. STUDY CASE.

In order to test the performances of the installation, several sedimentation curves for watery suspensions of bentonite and alumina powder in different concentrations (below 1%), have been recorded.

The sample preparation and the recording conditions have been strictly controlled in order to avoid any kind of disturbances.

The sedimentation kinetics is recorded as dependence function

$$m = f(t) \quad (1)$$

The sedimentation curves for bentonite and alumina are presented in figure 2.

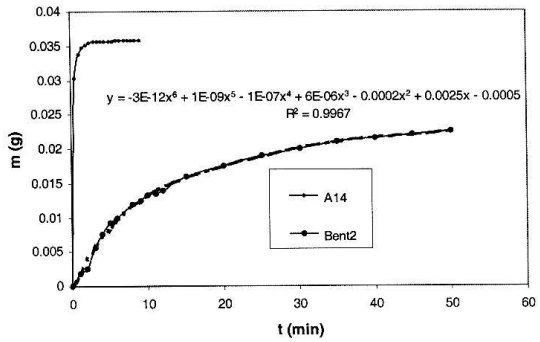

Fig 2. Settling curves: bentonite (•), alumina (•)

Table 1.
The coefficients of the polynomial equations (MATLAB); Alumina A_{14}

Rank	Coefficient	Rank	Coefficient
12	$-3.50*10^{-9}$	5	$7.91*10^{-2}$
11	$2.04*10^{-7}$	4	$-1.76*10^{-1}$
10	$-5.29*10^{-6}$	3	$2.61*10^{-1}$
9	$8.01*10^{-5}$	2	$-2.47*10^{-1}$
8	$-7.87*10^{-4}$	1	$1.36*10^{-1}$
7	$5.26*10^{-3}$	0	$7.2*10^{-7}$
6	$-2.44*10^{-2}$		

In the first one, the most probable curve is traced and the adequate definition function is written in the graph. The sixth degree equation (set in Excel) and the determination coefficient (R^2=0.99967) are eloquent for the accuracy of the recording [6].

For alumina, the graphic corresponds with a twelfth equation, its coefficients being presented in table 1 (MATLAB) [7].

The fashion of the curves underlines the method's capacity to discriminate the behavior of the two powders during the sedimentation process; the bentonite is softly and highly dispersed compared to the alumina, which is much more roughly.

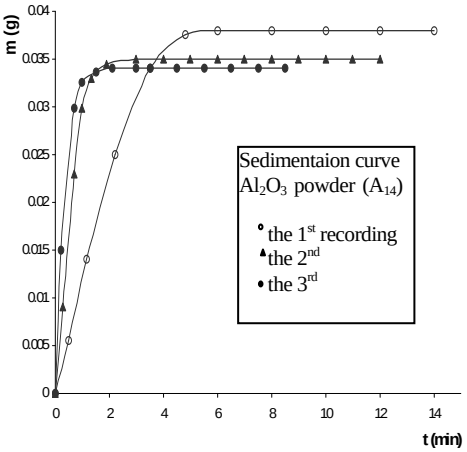

Fig. 3. Sedimentation curves registered after rehomogenisation of the same suspension (alumina)

Another idea that needed checking was to see in what measure, in the same system, after the end of the phase separation process, a remixing of the phases determine the reproduction of the curves at repeat recordings. A problem is faced in situation when rerun of the operation is wanted, and without stopping the recording, after every determination, the dispersion rehomogenizes.

The answer can be found in fig.3. where we can notice in the sedimentation curves a sensitive change of the fashion and laying out, during three successive recordings.

The causes of the changes can be an incomplete mixing of the depot phase, which equals to a modification of the suspension's concentration, a crowding of particles or a solid phase scattering. We attribute the evolution in this case to the first working hypothesis, the final level of the systematically decreasing curves representing proof to this case.

THE EVALUATION OF THE SIZE OF THE PARTICLES.

The sedimentation curves express unmediated correlations between the size (d) and the movement speed (w_0) of the particles during the sedimentation process [2,5].

In the gravitational field (g) the relation w ~ d is [2]

$$w_0 = \left(\frac{4}{3} \frac{d \Delta\rho}{\rho} \frac{g}{\xi} \right)^{\frac{1}{2}} \tag{2}$$

where: $\Delta\rho = \rho_s - \rho$, expresses the difference of the disperse (solid) phase's density (ρ_s) and the dispersing medium (ρ)

$\Delta\rho g$ - represents the driving force of the process

ξ - the strength coefficient (the brake factor of the medium to the movement of the particle) with values dependent on the speed in which the particle moves (the hydrodynamic regime Re) from the shape (Φ) and the roughness of the surface (ε)

$$\xi = f(\mathrm{Re}, \Phi, \varepsilon) \tag{3}$$

The movement regime $\mathrm{Re} = w_0 d \rho / \eta$ (η - the dynamic viscosity of the medium) discriminate 3 hydrodynamic sedimentation domains [2,5,8]

laminar (Stokes)	Re<1	$\xi = 24/\mathrm{Re}$
intermediate (Allen)	1<Re<10^3	$\xi = 18.5/\mathrm{Re}^{0.6}$
turbulent (Newton)	10^3<Re<10^5	$\xi = 0.44$

The speed sedimentation equations corresponding to:

$$w_{0s} = \frac{1}{18} \frac{\Delta\rho}{\eta} g d^2 = k_s d^2 \qquad \text{Stokes domain} \tag{4}$$

$$w_{0A} = 0.15 \frac{(g\Delta\rho)^{0.72}}{\eta^{0.42} \rho^{0.29}} d^{1.14} = k_A d^{1.14} \qquad \text{Allen domain} \tag{5}$$

$$w_{0N} = 1.74 \left(\frac{\Delta\rho}{\rho} g d \right)^{\frac{1}{2}} = k_N d^{\frac{1}{2}} \qquad \text{Newton domain} \tag{6}$$

The equations (4)-(6) rewritten in a more general manner

$$w_0 = kd^x \tag{7}$$

or after logarithmation

$$\ln w_0 = \ln k + x \ln d \tag{8}$$

allow the setting of the sedimentation regime through the values of the x (slope) and k (origin ordinate) parameters from experimental data respectively the selection of the calculus relation $w_o \sim d$ [8].

THE DISTRIBUTION FUNCTION CALCULATION

A distribution function

$$F(d) = \Delta m / \Delta d = f(d) \tag{9}$$

represents the portion (mass) of the particles from a narrow dimension domain (fraction) corresponding to a certain value of the particle size (diameter) d.

In the fig.4. the sedimentation (1) and distribution (9) curves of bentonite are recorded on the same common graph.

For the same bentonite sample, the distribution function are registrated by the Mie method (laser light dispersion) in fig. 5 [1].

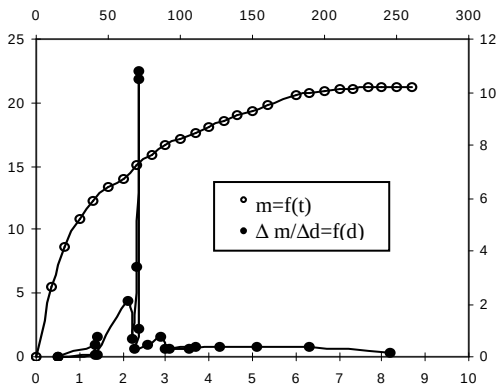

Fig.4. Sedimentation curve and distribution function for bentonite

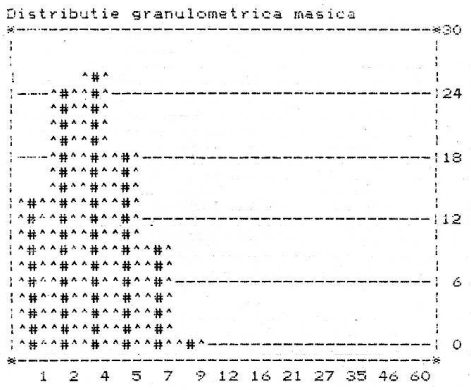

Fig.5. The distribution histogram of fractions in bentonite (laser method)

One can see that the both recording emphasize an unimodal distributin of the powdery fractions with a 2.2 – 2.7 μm median diameter.

As concern the fractions scattering, the Mie (laser) method [1], more sensitive, shows a spread slightly more extended.

RRS DISTRIBUTION CURVE

With the same experimental data, one also calculated the distribution function in accordance with Rosen-Rammler-Sperling (RRS) method [2,3]

$$R/100 = e^{-(d/d')^n} \tag{10}$$

From the graph (fig.6.) in double logarithmic coordinates (11)

$$\ln\ln 100/R = n\ln d - n\ln d' \tag{11}$$

results a straight extended S shaped line [2]. By the intersection of the linear middle zone with the ordinate R=36.8% one can read on the abscissa (projection) the characteristic diameter d' of the granular ensemble and from its inclination (slope), the uniformity factor n or the powder scattering. The obtained values are $d = 2.7\mu m$, and n=1.4 in very good accordance with the other methods applied.

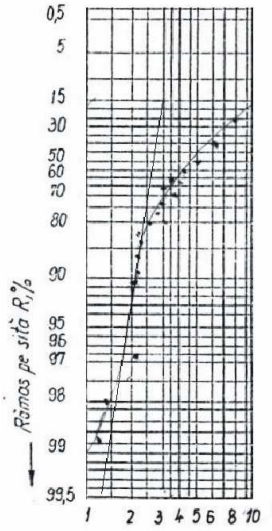

Fig. 6. Rosen-Rammler-Sperling diagram

CONCLUSIONS

The data synthesis underline the following conclusions.

- The suggested proceeding shows performances comparable with other sophisticated and expensive techniques destinated in this domain.
- The recording and calculating fittings are characterized by versatility and allow kinetic studies for different other processes with mass variation.
- The fitting permits, by changing the components (electronic scales) and programming data acquisition, the adapting of sensitivity for different working precisions.
- The constructive and financial accessibility are also important characteristics.

REFERENCES

[1]. I.N. Stanford, Particle size analysis in Pharmaceutics. The Science of dosage form design. Editor M.E. Aulton. Editor Churchill Livingstone, Edinbourgh-London-Melbourne-New York, chap. 33, p. 564-578 , 1988

[2]. L. Literat, Operații şi utilaje in industria materialelor oxidice. Aplicații. Ed. Univ. Babeş-Bolyai, Cluj-Napoca, 1994

[3]. K. Leschonski, Particle characterization. Present State and Possible Future Trends; Preprint, First World Congress Particle technology, Part I, Nurnberg, p.1-16, 1986

[4]. L. Literat, I. Muresan, P. Muresan, Automatic determination of vapours adsorbtion isotherms on porous solids. Acta Technica Napocensis, technical University of Cluj-Napoca, Section CMM, 42 p. 139-146, 1999

[5]. B. Koglin, Untersuchung zur Sedimentationsgeschwindigkeit von Einzelteichen, Freiberg, Forschung sh. A, A 484, p. 35-44, 1971

[6]. G.E. Jones, Excel 5, Editura ALL Educational S.A., Bucureşti, 1995

[7]. Table Curve Program – Jandel Scientific USA

[8]. L. Literat, Rev. chim. 45, nr. 10 p 921, 1994

STUDIA UNIVERSITATIS BABEŞ-BOLYAI, CHEMIA, XLVI, 1-2, 2001

PORE STRUCTURE STABILITY OF ALUMINA BASED MEMBRANES

ANIKO TOTH[1], LIVIU LITERAT[2], LUCIA GAGEA[2]

[1] S.C. PROCEMA S.A. - Cluj-Napoca Branch, str. Beiuşului nr.1
[2] BABEŞ-BOLYAI UNIVERSITY, Faculty of Chemical Engineering, str. Arany Janos nr. 11

ABSTRACT. Certain sintering agent decrease the alumina membranes burning temperature and the other maintain the porosity parameters at stable values, even we increase the burning temperature.

The membranes were prepared from industrial alumina powder, α-$Al(OH)_3$ (Alor-Oradea). The thermally pre-treated powders and the sintering agents, like TiO_2 anatas, Cr_2O_3, La_2O_3 and ceramic binder (Zettlitz kaolin), were mixed in porcelain ball mill for several hours. Before the final thermal treatment, the ball milling powder was compacted by pressing in disks of 30 mm, at 342 daN/cm^2.

The starting materials and the porous ceramics resulted from thermal treatments, were studied by the following methods: X-ray diffraction working with $Cu_{k\alpha}$ radiation, DTA/TG analysis, between 20 and 1000℃, with a rate of 10℃/minute, optical microscopy and Hg porosimetry.

INTRODUCTION

The alumina membranes were used widely in many filtration processes, due to their excellent properties regards to thermal resistance, which affords utilization in separation processes at high temperatures; mechanical strength, which allows their surface to stand high pressure or pressure gradients; chemical inertness, i.e. no corrosion during utilization in acid, basic, and oxido-reducing media. Moreover, there are many possibilities to prepare them in any configuration, according to the separation processes.[1,2]

The alumina based ceramics, sinter at very high temperatures, generally above 1500^0C.[3] In order to reduce the firing temperature, we added to the thermally pre-treated powders the sintering agents mentioned above. The role of these agents was double: first, to reduce the high firing temperature and second, to inhibit the Al_2O_3 crystal growth in the porous ceramic, which lead to the stabilization of the entire membrane texture.[4,5]

EXPERIMENTAL

Obtaining of alumina membranes

The characteristics of alumina powder and some conditions of obtaining membranes by pressing are listed in Table 1 and 2.[6]

The pressing powders were ball milling for seven hours in porcelain mill, with the ratio of 1:1.5:1 for dry powder, balls and water. Rest on the 0056 sieve established the finesse of the milling powders. After milling, the powders

were set to maceration for three days. Before pressing, to powders without ceramic binder, was added organic binder (polyvinyl alcohol) in order to enhance the dry disks mechanical strength. The pressing powders granulometric distributions curves were established by a Fritsch Analysette laser granulometer (fig. 1a, b).

Table 1

Structure of thermally treated alumina powder

Powders		Preliminary thermal treatment		Final thermal treatment
Alumina hydrate	α–$Al(OH)_3$	450℃/60 min	γ-AlO(OH)	1380℃/45 min 1590℃/90 min
Alumina hydrate	α–$Al(OH)_3$	600℃/60 min	γ-Al_2O_3	1380℃/45 min 1590℃/90 min
Alumina hydrate	α–$Al(OH)_3$	1260℃/240 min	α-Al_2O_3	1380℃/45 min 1590℃/90 min

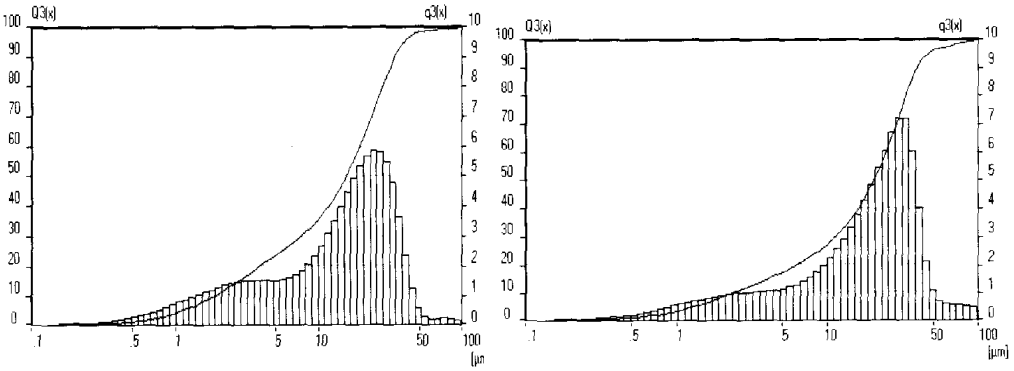

a). sample A *b). sample B*

Fig. 1 The granulometric distribution curves of some pressing powders

The Al_2O_3 crystals are smaller than the granules. The crystals mean diameter established by optical microscopy were between 2-20 µm, depending on the Al_2O_3 powder structure. The granules mean diameter were almost the same, but the porosity parameters of membranes were thoroughly different, depending on the burning temperatures and the sintering agents used.

After drying, the disks were burned at 1260℃, 1380 ℃ and 1590℃ for 4 hours, respectively, 45 and 90 minutes at the final temperatures.

The textural characteristics of alumina membranes

The pore size distribution and total volume of pores were established by a Carlo Erba porosimeter, between 0.2 and 200 atmospheres. The membranes porosity parameters are listed in Table 3.

Table 2

Certain variants of preparing alumina membranes with different sintering agents

Pressing powders	Rest on the 0056 sieve (%)	Granules mean diameter (μm)	Binder	Sintering agents	The structure after final thermal treatment	Symbol of sample
γ-AlO(OH)	0.12	22.80	20% APV	0.5% Cr_2O_3	α-Al_2O_3	A
γ-AlO(OH)	0.12	23.10	20% APV	2% TiO_2	α-Al_2O_3 Al_2TiO_5	B
γ-AlO(OH)	0.10	22.80	20% APV	5% La_2O_3	α-Al_2O_3 $LaAl_{11}O_{18}$	C
γ-Al_2O_3	0.10	22.80	15% kaolin	-	α-Al_2O_3 Al_2SiO_5	D

Table 3

Porosity parameters of the membranes

Symbol	Composition	Firing temperature (^{0}C / min.)	Total volume of pores (mm^3 / g)	Porosity (%)	Pore radius average (μm)	Specific surface area (m^2 / g)
A_1	γ-AlO(OH)/Cr_2O_3	1380/45	395.82	64.439	0.841	3.29
A_2	γ-AlO(OH)/Cr_2O_3	1590/90	222	47.16	1.189	0.92
B	γ-AlO(OH)/TiO_2	1380/45	237.64	27.20	3.35	0.75
C	γ-AlO(OH)/La_2O_3	1590/90	210.69	47.25	0.841	0.84
D_1	γ-Al_2O_3/kaolin	1220/60	426.66	74.40	0.053	8
D_2	γ–Al_2O_3/feldspar/kaolin	1100/120	175.30	21	0.596	0.93
D_3	γ–Al_2O_3/kaolin	1590/90	330	47.85	0.299	0.71

Pore size distribution curves of the samples A, B, C and D, are represented in fig. 2a, b, fig. 3a, b and fig. 4a, b.

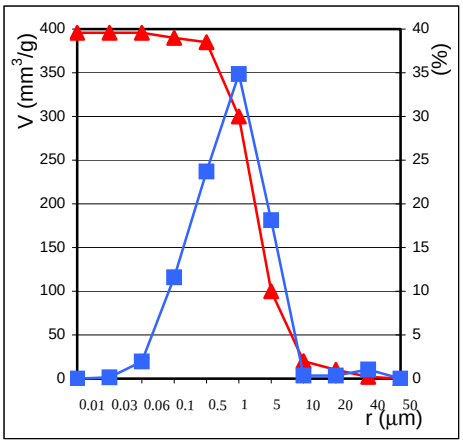

a). sample A_1

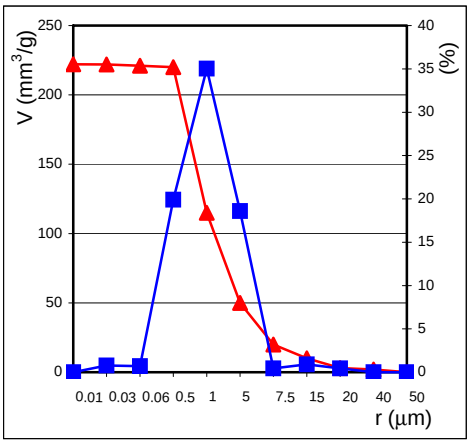

b). sample A_2

Fig. 2 Alumina membranes with Cr_2O_3, burned at different temperatures

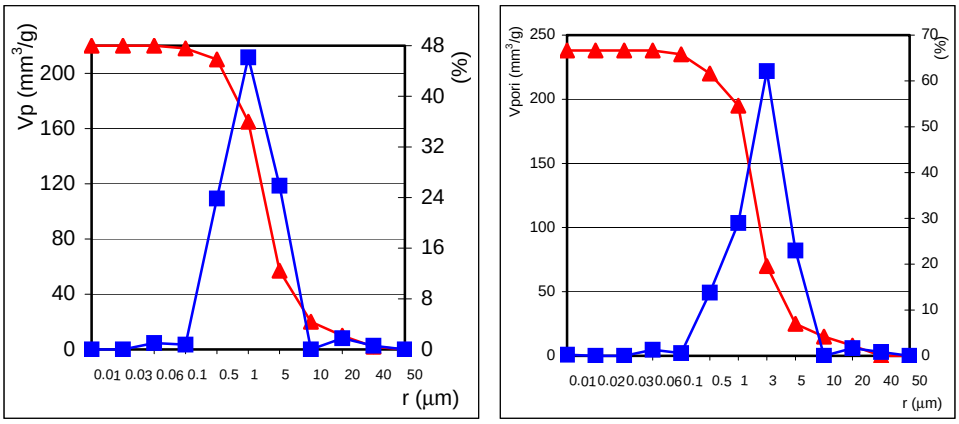

a). sample C *b). sample B*

Fig. 3 Alumina membranes with different sintering agents, burned at different temperatures.

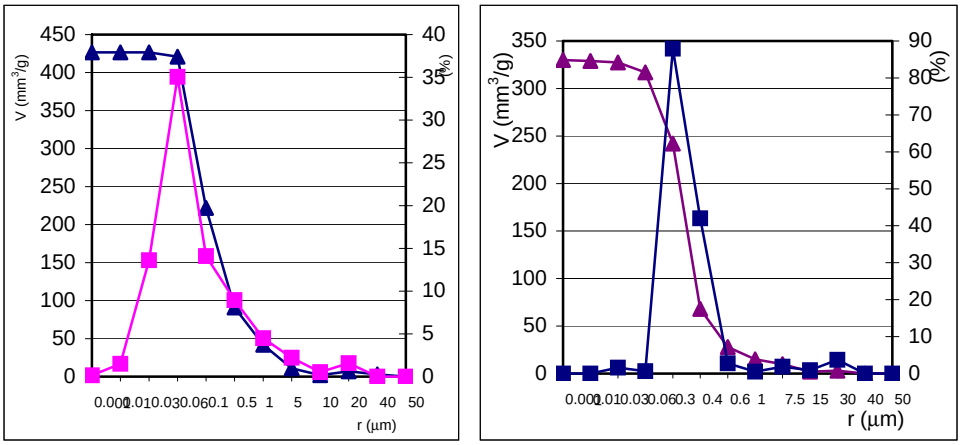

a). sample D_1 *b). sample D_3*

Fig. 4 Alumina membranes with ceramic binder, burned at different temperatures.

RESULTS AND DISCUSSION

The alumina membranes porosity parameters, depended of the powders composition, the sintering agents used and the burning temperatures.

The sample D burned at 1220℃ with ceramic binder (Zettlitz kaolin), have the greatest pore volume, above 426 mm^3/g and the smallest pore radius average, 0.053 μm, but its mechanical strength is the lowest. For this reason, unfortunately, this membrane could not applied in separation processes. Increasing the temperature until 1590℃, the pore radius average

growth to 0.299 μm and the total volume of pores decrease to 330 mm^3/g (fig. 4a, b). At this temperature, alumina reacted with kaolin and result small amounts of SiO_2 from mulit.

We have been tried to decrease the alumina membranes high burning temperature with feldspar adding (sample D_2). But due to melt forming, the porosity decrease to 21%, not enough for filtration processes.

The pore radius average of alumina membranes with Cr_2O_3 (sample A), growing from 0.84 μm to 1.18 μm, as we increasing the burning temperature from 1380℃ to 1590℃ (fig. 2a, b). This means that Cr_2O_3 has inhibiting effect on Al_2O_3 crystal growth. In other words, Cr_2O_3 stabilises the texture and therefore the alumina membrane porosity parameters.

The results obtaining for samples B and C prepared with TiO_2 and La_2O_3 are the most interesting. Some experiments confirmed that TiO_2 anatas decrease the alumina based ceramics burning temperature.[7] We observed that the membranes prepared with TiO_2 anatas, sintered until 1380℃. Unfortunately, this sintering agent has a very undesirable effect, upon the membrane pore structure. So, the anatas enhance the Al_2O_3 crystal growth, followed by the increase of pore size until 3.35 μm and by the decrease of total volume of pores, to 237 mm^3/g.

La_2O_3 has the opposite effect of TiO_2. After burned at 1590℃, the membrane pore radius average is 0.84 μm and the total volume of pores is above 210 mm^3/g, which are very nearest to that of alumina membranes prepared with Cr_2O_3.

The sintering agents, pore structure stabilising effect, result also from the fig.5 represented below.

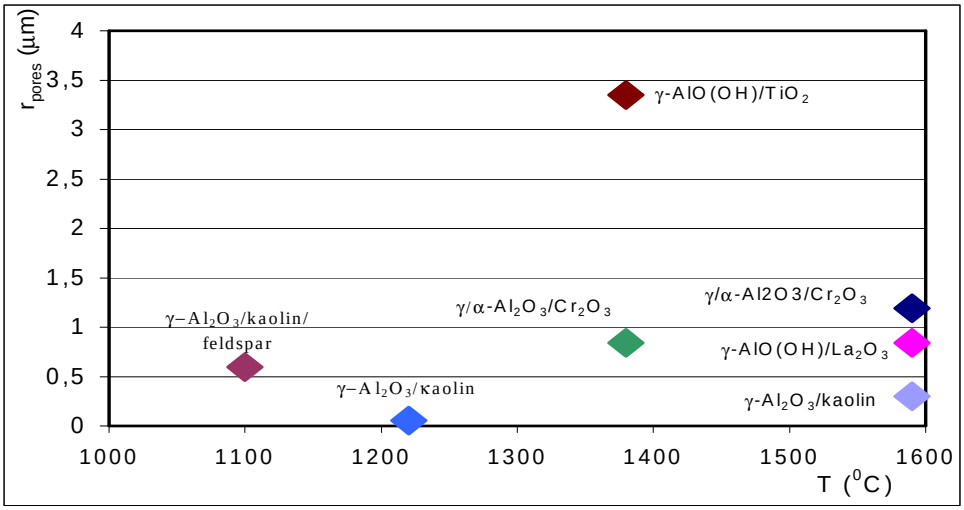

Fig. 5 Pore radius average, depending of temperature and sintering agents.

CONCLUSIONS

The burning temperatures and the sintering agents used, have been influenced the texture and the porosity parameters of alumina membranes. Certain sintering agents decrease the burning temperature of alumina membranes, but unfortunately the textural characteristics alters in a very undesirable manner. Other, maintain the porosity parameters at stable values, even we increasing the burning temperature.

Unfortunately, the TiO_2 sintering agent has a very undesirable effect upon the membrane pore structure. So, at 1380^0C the pore radius average reached 3.35 μm, due to Al_2O_3 crystal growth, what means that pores growing too.

La_2O_3 has the opposite effect of TiO_2. After burned at 1590℃, the membranes pore radius average is 0.84 μm and the total volume of pores is above 210 mm^3/g.

The effect of Cr_2O_3 is near to that of La_2O_3. The pore radius average growing lightly from 0.84 μm to 1.18 μm, as we increasing the burning temperature from 1380℃ to 1590℃.

The ceramic binder enhances the percent of small pores in the membrane texture. For this reason, at 1220^0C, we have been obtained the smallest pore radius average, 0.053 μm and the greatest pore volume, above 426 mm^3/g With increasing the burning temperature to 1590^0C, the pore radius average growing to 0.299 μm and the total volume of pores decrease to 330 mm^3/g.

Utilizing certain sintering agents, like La_2O_3, Cr_2O_3 or even kaolin, we could obtain alumina-based membranes with stabilised pore structure. These membranes are appropriate for use in microfiltration processes, or as supports, for thin, mezoporous films deposition.

REFERENCES

1. K., K., Chan, A., M., Brownstein, (1991), *Bull. of Am. Ceram. Soc.*, 70(40), 703-707.
2. M., Crişan, M., Zaharescu, L., Simionescu, D., Crişan, A., Toth, (1997), *Key Eng. Materials,* 132-136, 1766-1769.
3. L., T., Khan, R., M., McMeeking, F., F., Lange, (1991), *J. of Am. Ceram. Soc.*, 77, 682-685.
4. G., G., Anci, Z., Misirli, V., Gunay, (1996), *Ceramics International*, 22, 23-26.
5. I., I., M., Tijburg, H. de Brun, P., A., Elberse, J., W., Geuse, (1991), *J. of Materials Science*, 5945-5949.
6. A., Toth, L., Gagea, M., Gorea, D., Pop, (1997), *Chimie şi Inginerie Chimică IV*, 296-301.
7. S., Skapin, D., Kalar, D., Savorov, (1993), *J. of Am. Ceram Soc.*, 76(9), 2359-2362.

STUDIA UNIVERSITATIS BABEŞ-BOLYAI, CHEMIA, XLVI, 1-2, 2001

A COMPARATIVE STUDY ON THE OXIDATION OF HYDROXY- AND MERCAPTO- COMPOUNDS BY Cr(VI)

I. BALDEA and D. M. SABOU

Babes-Bolyai Univ. of Cluj, Faculty of Chemistry and Chemical Engineering, Cluj-Napoca 3400, 11 Arany Janos Str., Romania. E-mail: ibaldea@chem.ubbcluj.ro

ABSTRACT. Both, the thiols or mercapto-acids (RSH) and the alcohols or hydroxy-acids (ROH) are easily oxidised by various oxidising agents as Cr(VI), Mn(VII) $Fe(CN)_6^{3-}$, Ce(IV), etc. The importance of such a comparison of the two classes of compounds consists of the resemblance of –OH and –SH functions, as well as the involvement of such oxidation in many biological processes. Our comparative study is based on the literature data as well as our research in the field of oxidation of various thio-compounds as ethane thiol, mercaptoacetic acid, mercaptosuccinic acid, L(+)-cysteine, glutathione, thiophenol benzylmercaptane and alcohols or hydroxy-acids as benzyl alcohol, glycolic acid, lactic acid, malic acid, ascorbic acid by Cr(VI).

Kinetic rate laws are compared and mechanisms are discussed. There is some similar behaviour of two classes of compounds. Using Cr(VI) as oxidising agent, the rate laws, at acidity held constant are of the form:

$$-\frac{d[Cr(VI)]}{dt} = \frac{k'[ROH][Cr(VI)]}{1+K[ROH]} \quad \text{and}$$

$$-\frac{d[Cr(VI)]}{dt} = \frac{k'\{RSH]+k''[RSH]^2}{1+K[RSH]}[Cr(VI)]$$

Many differences were noticed. Generally, the oxidation of hydroxy-compound takes place at the carbon atom bearing the function and carbonyl products were obtained. On the contrary, thiols are oxidised at sulphur atom and disulphide products were obtained. However, the rate laws are similar. Generally, in the Cr(VI) oxidations, intermediate condensed compounds esters or thio-esters have been identified either directly by spectrophotometrical means, or indirectly by the inference on the rate law. With hydroxy-compounds the two-electronic charge transfer prevailed. With thio-compounds both mono- and two-electronic charge transfer takes place, depending on the nature of thiol. The involvement of free radicals has been also proved. Both classes of oxidation are strongly influenced by the acidity of the medium. Other medium effects were noticed.

INTRODUCTION

Oxidations by chromium (VI) have been extensively studied and documented. Some reactions of Cr(VI) include its usage in classical titrimetric analysis in determination of a number of metal ions or reducing agents as well as its usage in preparative organic chemistry [1]. The carcinogenic and mutagenic [2,3] nature of Cr(VI) ion and the fact it is a major industrial pollutant have stimulated intensive research in order to identify substances that effectively reduce Cr(VI) to a less harmful Cr(III) states under mild conditions [4-16]. Among these reducing agents there are alcohols, organic acids or bi-acids, ascorbic acid,

thiol compounds, hydroxy- and mercapto-acids. On the other hand, thiols are considered as the most active groups found in cells and are easily oxidised to less reactive disulphides. The thiol-disulphide interchange reaction is of the great importance in biochemistry [8,17].

That is why we have undertaken the study of oxidation reaction between Cr(VI) and various hydroxy- and thiol- compounds and a comparative discussion on rate laws and mechanisms seems to be quite interesting.

The first difference between the two related organic classes of compounds consists on the fact that when alcohols or hydroxy-acids are oxidised, the carbon atom bearing the function changes its oxidation state [4-7, 15, 16 18], while when thiols are oxidised, the sulphur atom involved in the function is the one to change the oxidation state [8-14, 17].

In order to present some reaction mechanisms, first we have to analyse the valence state of chromium, showed in the following scheme I. It indicates the ways of passing from Cr(VI) to the stable Cr(III) species. It includes one-, two-, or three- equivalent processes.

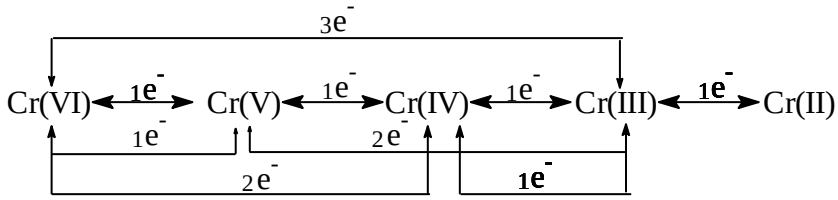

Scheme I

All the ways depicted in the scheme are involved in various oxidation reactions, including co-oxidations and induced reactions [18]. The development of techniques for detecting free radical intermediates or paramagnetic species and techniques of separating product complexes of Cr(III) have given illumination on some mechanistic aspects.

For a one-equivalent reducing agent, a step by step one-equivalent electron transfer reduces Cr(VI) to Cr(III). This route is not the usual one followed with the systems under discussion, with some exceptions. Chromium (VI) is known as a prevalent two-equivalent oxidising agent, and some complications arise, because more reaction routes are now opened. Some three-equivalent reductions of Cr(VI) were also observed, involving concerted action of two substrate molecules.

The variety of species of Cr(VI) in acidic solutions [19, 20] and the presumable passage of chromium through transient unstable species combine to give the system a considerable complexity.

Several groups all over the world dealt and are dealing with kinetic studies of Cr(VI) oxidation [5-18, 21-28] of hydroxyl and thiol compounds. Among them, a group in our laboratory has studied these classes of compounds [29-40].

The reactions under discussion have been found to proceed by inner-sphere mechanisms. It is well known that complexes of chromate of the dichromate, esteric or thioesteric type, stable or transient intermediate species are formed in acidic solutions. The condensation equilibrium of the form:

$$HCrO_4^- + H^+ + X^- \rightleftharpoons XCrO_3^- + H_2O \quad (1)$$

takes place with oxo-anions, halides or pseudo-halides, alcohols, diols, hydroxy-acids, thiols, mercapto-acids.

Table 1.

Equilibrium constants and the position of the charge-transfer ligand-Cr(VI) peak for various condensed compounds of Cr(VI) [33, 40, 42-44]

Compound	λ (nm)	K (M^{-1})
$HOCrO_3^-$	350	-
$O_3SOCrO_3^-$	350	4.1
$HO_2POCrO_3^-$	350	2.9
$CH_3COOCrO_3^-$	347	4.5
$O_2SOCrO_3^-$	350	36
$CH_3OCrO_3^-$	350	4.7
$C_2H_5OCrO_3^-$	358	6.9
$(SCN)OCrO_3^-$	380	9.2
$ClOCrO_3^-$	358	4.2
$O_3S\text{-}SCrO_3^-$	394	1.24×10^4
$Cys\text{-}SCrO_3^-$	426	1.48×10^3
$HOOCCH_2\text{-}SCrO_3^-$	425	1.1×10^3
$HOOCCH_2CH(COOH)\text{-}SCrO_3^-$	412	1.48×10^3
$C_2H_5\text{-}SCrO_3^-$	450	1.2×10^3
$Glu\text{-}SCrO_3^-$	428	1.44×10^3

Within the esteric type complexes, an oxygen atom plays the role of a bridge, and the species exhibits absorption spectra similar to the spectrum of $HCrO_4^-$ [41]. The position of the charge-transfer peak is not shifted significantly as compared to the one exhibited by $HCrO_4^-$. When another atom (Cl, S) is bound to Cr(VI), the charge-transfer peak is shifted towards red. Several data concerning the position of absorption band and formation constant are presented in table 1.

The table reveals that when a sulphur-chromium link is established, the formation constants are three to four orders of magnitude greater than those where an oxygen bridge is involved. On the other hand, the formation kinetics of the esteric or thioesteric type condensed compound has been measured for several cases, and rate laws have been found. The processes are faster than the subsequent redox ones. Therefore, it is undoubtedly established that such

condensed Cr(VI) intermediates are involved in the oxidation of alcohols, hydroxy-acids, thiols and mercapto-acids, they being able to provide low-energy routes for the electron transfer. As usually being the slowest one, electron transfer is rate determining step in most cases. Also, as seen, the complex formation, as well as its further decomposition, can depend on hydrogen ion concentration.

Table 2.

Comparison of the kinetic data on the formation of substrate-chromate complex and redox decomposition at 25°C for various compounds [30]

Substrate	Complex ($XCrO_3^-$)	10^{-3} K M^{-1}	k_f^0 $M^{-1}s^{-1}$	10^{-4} k_f^H $M^{-2}s^{-1}$	k^0 $M^{-1}s^{-1}$	10^{-2} k^H $M^{-2}s^{-1}$
$HCrO_4^-$	$Cr_2O_7^{2-}$	0.098	-	62	-	-
H_2PO_3	$HO_2POCrO_3^-$	0.008	-	50	-	-
$H_2S_2O_3^-$	$O_3SSCrO_3^-$	12.4	-	37	180	185
C_2H_2SH	$C_2H_5SCrO_3^-$	1.2	-	2.3	-	0.15
L-Cysteine	$CysSCrO_3^-$	1.48	2.1	0.014	7.7	0.007
		-	-	0.01	12.0	-
$CH_2(SH)COOH$	$RSCrO_3^-$	1.1	66.3	0.247	11.0	4.33
$HOOCCH_2CH$-(SH)-COOH	$RSCrO_3^-$	1.48	44.1	0.019	23.8	2.03

OXIDATION OF ALCOHOLS AND HYDROXY-ACIDS

The oxidation of alcohols yields aldehydes, ketones or other products when the cleavage of C-C bond takes place, depending on the nature of substrate and the concentration of reacting species [45, 46]. Westheimer reviewed chromate oxidation of alcohols concerning himself chiefly with the reaction mechanism [28, 47, 48]. The mechanism he elaborated for 2-propanol oxidation served as a model for the oxidation of various other substrates, and has been a focus for discussion and research.

$$HCrO_4^- + R_2CHOH \rightleftharpoons R_2CHOCrO_3^- + H_2O \qquad K \qquad (2)$$

$$R_2CHOCrO_3^- \longrightarrow R_2CO + Cr(IV) \qquad \text{r.d.s.} \quad k \qquad (3)$$

The fate of Cr(IV) species is questionable. Several paths are possible, involving subsequent reactions [49].

I. $$Cr(IV) + Cr(VI) \rightleftharpoons 2Cr(V) \qquad (4)$$

$$Cr(V) + R_2CHOH \longrightarrow Cr(III) + R_2C=O \qquad (5)$$

II. $$Cr(IV) + R_2CHOH \longrightarrow Cr(II) + R_2CO \qquad (6)$$

$$Cr(II) + Cr(VI) \longrightarrow Cr(III) + Cr(V) \qquad (7)$$

Mechanism I was favoured by Westheimer. The path II has been dismissed from the very beginning, because Cr(II) is such a powerful reducing agent that it has not been a likely species in the system. However, the interest in it has been recently renewed by some studies like the one on Cr(VI) oxidation of 2(2-hydroxyethyl)pyridine in aqueous acidic media [50].

Chromium (V) behaves like chromate itself and oxidises R_2CHOH in a two-equivalent step [27].

III. $$Cr(IV) + R_2CHOH \longrightarrow Cr(III) + R_2\dot{C}HO \quad (8)$$

$$R_2\dot{C}HO + Cr(VI) \longrightarrow R_2CO + Cr(V) \quad (9)$$

$$Cr(V) + R_2CHOH \longrightarrow Cr(III) + R_2CO \quad (5)$$

The failure to detect free radicals in the early studies had the result that path III has been firstly ruled-out.

However, the oxidation of cyclobutanol [26, 51-54] or even i-propanol made Roček and co-workers to conclude that the organic substrate reduces Cr(IV) in one-equivalent step instead of reacting with Cr(VI) to generate Cr(V). It favours the route III. On the other hand, Wiberg and Mukherjee [55] followed the rate of acetone formation at the oxidation of 2-propanol, relative to the growth and decay of Cr(V) EPR signal in acetic acid solutions, giving support to the route III. In the mechanism I two equivalents of Cr(V) are formed for one acetone molecule, while in the mechanism three, the reciprocal is valid in the early stages of the process. The analysis showed the ratio corresponds to route III. The overall stoichiometry is 1,5 : 1 i-propanol : Cr(VI).

More recently, proofs like the initiation of polymerisation or EPR measurements have undoubtedly proved the existence of free radicals in numerous systems, giving further support to mechanism III. Numerous alcohols or α-hydroxy-acids are reported in the literature to undergo such reaction pathways [15, 36, 56-59].

As we have already mentioned, in some cases Cr(VI) seems to behave different than the usual bi-electronic way towards hydroxylic substrates.

Such an example is the oxidation of ascorbic acid, for which Dixon and co-workers [60] have given a mechanism involving mono-electronic steps only, contrary to those bi-electronic of type III given in previous studies [15, 36]. The conclusion was reached based on the fact that Mn(II) and I^- used to trap the Cr(IV) and Cr(V) intermediates respectively, had no influence either in the mechanism or the stoichiometry. It was confirmed by some theoretical studies [61, 62] using molecular orbital calculations. The rate-determining step is assumed to be the formation of ester intermediate.

Another case is the Oswal and Bakore interpretation of malonic acid oxidation by Cr(VI), either uncatalysed or catalysed by Mn(II) [63]. In this reaction the one-electron decomposition of the intermediate substrate-Cr(VI) complex, giving Cr(V) and free radical, is believed to be rate-determining. Cr(V) reacts further in a bi-electronic path.

A number of Cr(VI) oxidations of alcohols with oxalic acid and α-hydroxy-acids [64-67], as well as oxidations of polyfunctional organic compounds like several α-hydroxy-acids [68-70] or polyhydroxylic compounds like glycerol [71] have been found to proceed by an one-step rate-determining three-electron transfer, leading directly to Cr(III). The free radical formed in the process reduces mono-electronically another Cr(VI) molecule, forming Cr(V). The behaviour of Cr(V) is similar to the usual one of Cr(VI), leading to Cr(III) in a one-step bi-electron transfer.

The suggested mechanism is:

$$Cr(VI) + 2S \longrightarrow CrS_2 \longrightarrow Cr(III) + P + \dot{R} \qquad (10)$$

$$\dot{R} + Cr(VI) \longrightarrow Cr(V) + P \qquad \text{fast} \qquad (11)$$

$$Cr(V) + S \longrightarrow Cr(III) + P \qquad (12)$$

where S stands for substrate, P for product and R• for free radical.

It is believed that at large substrate concentrations, the rate laws second order in substrate (first order in each of the two different substrates in the case of co-oxidations, and first order in polyolic substrates) support the presumption of a one-step three-electron reduction of Cr(VI).

At low substrate concentrations, the reaction order in substrate is only half of the value found at high concentrations (one for one substrate and zero for the second one in co-oxidations). It shows that the process (10) may require two steps: a slow bi-electronic one giving Cr(IV), followed by a fast, mono-electronic one to give Cr(III) and R•. Therefore, the three-electronic mechanism is again reduced to a bi-electronic one of type III.

For the general case of bi-electronic mechanisms, and under the excess concentration of hydroxy-compound (which is the most common setting for experimental measurements), rate laws of the following form:

$$-\frac{d[Cr(VI)]}{dt} = \frac{a[ROH]}{1 + b[ROH]}[Cr(VI)]_t; \qquad (13)$$

$$k_{obs}^{redox} = \frac{a[ROH]}{1 + b[ROH]} \qquad (14)$$

prove themselves to be valid when the redox step is rate determining. A first-order dependence on Cr(VI) total concentration is shown, while the reaction order for the substrate can range between 0 and 1. Depending on the value of parameter b, the zero order is reached when the hydroxy-compound is taken in very large excess. However, under usual experimental conditions a first-order dependence on substrate concentration is also found. The fact is not surprising, Cr(VI) having a strong tendency to behave in a bi-electronic way and hydroxy compounds being well-known as bi-electronic substrates.

There are several situations where not the redox step, but the formation of the intermediate complex is rate determining. For such cases, the global rate law is much simpler:

$$-\frac{d[Cr(VI)]}{dt} = k_1[ROH][Cr(VI)] \quad (15)$$

namely first order in both substrate and oxidant concentrations.

If the substrate is in excess, the observed first-order constant is of the form:

$$k_{obs} = k_1[ROH] \quad (16)$$

The process becomes more complex when the intermediate formation proceeds in more than one step. Such examples are the oxidations of primary alcohols by quinolinium chlorochromate [72], where the redox active form of the intermediate complex is not the linear one initially formed in the equilibrium reaction between ROH and Cr(VI), but the one subsequently formed in a slow, rate determining cyclization step. The cyclic intermediate undergoes a further fast decomposition yielding Cr(IV) and products.

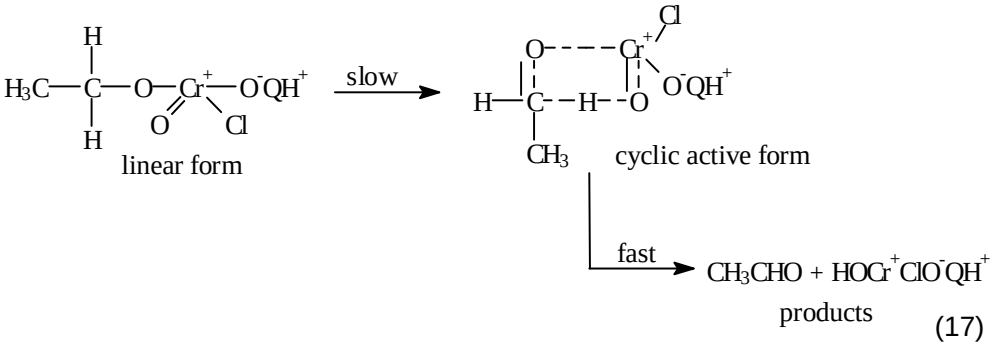

(17)

The cyclic intermediates are a common feature of the inner-sphere oxidation reactions of many hydroxy-compounds. Glycol oxidations proceed, for example, through condensed intermediate species of the form [73]:

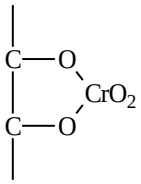

In the case of α-hydroxy-acids, the cyclic intermediates formed can be either hexa- [56] or penta- coordinate [74]; in the first case the carboxylic –OH is involved, while in the second not.

Usually, as discussed, the redox decomposition of the intermediates is the slowest step of the mechanism.

Three-electron oxidations require similar complexes, but involving two substrate molecules [18].

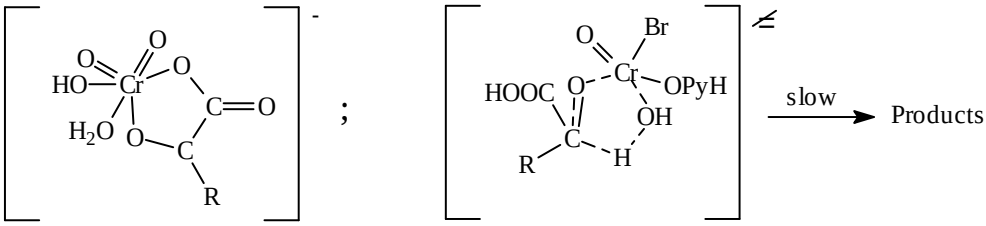

(1) (2)

(1) the intermediate in aqueous media (hexacoordinate)

(2) the intermediate in non-aqueous media (DMSO) (pentacoordinate); the oxidant is pyridin bromochromate

Depending on the lifetime of Cr(V) intermediate in a given system, in certain cases substrate oxidation can proceed through two measurable steps, corresponding to Cr(VI) and Cr(V) reduction respectively. Haight and co-workers found such a situation for lactic acid oxidation [18] under excess of substrate conditions, in acidic medium ($HClO_4$). Cr(V) reduction follows analogous path ways as Cr(VI).

From the assumed mechanism:

$$\mathrm{Cr(VI)} \xrightarrow[k_6]{+\,H_2L} \mathrm{Cr(IV)} \xrightarrow[\text{fast}]{+\,H_2L\ +\,Cr(VI)} \mathrm{Cr(V)} + \mathrm{Cr(III)} + \mathrm{HPy} \xrightarrow[k_5]{+\,H_2L} \mathrm{Cr(III)} + \mathrm{HPy} \tag{18}$$

composed rate laws are obtained:

$$-\frac{d[Cr(VI)]}{dt} = 2k_6[Cr(VI)] \tag{19}$$

$$-\frac{d[Cr(V)]}{dt} = k_5[Cr(V)] - k_6[Cr(VI)] \tag{20}$$

$$\text{where: } [Cr(V)] = \frac{k_6[Cr(VI)]_0}{2k_6 - k_5}(e^{-k_5 t} - e^{-2k_6 t}) \tag{21}$$

Intermediate complexes involving Cr(V) of the similar type with those of Cr(VI) are formed in the process.

In all cases, hydroxy-compounds oxidations with Cr(VI) are subjected to catalysis. Metal ions can play the role of the catalyst in many cases, but the general situation is of acid-base catalysis.

In acidic media, where most of the studies were carried out, both intermediate formation and its decomposition could be hydrogen ion assisted. The rate laws show, therefore, observed rate constants consisting of a sum of zeroth, first and/or second order acid dependent terms:

$$k_{obs} = k^0 + k^I[H^+] + k^{II}[H^+]^2 \quad (22)$$

For each given reaction system, one or another (alternatively more of them) of these terms prevails, depending on the pH value in the reaction mixture and on the nature of the substrate. Under strong acidic conditions, lactic [18, 38] and malic [38] acids exhibit two parallel paths, one first-order and the other one second-order in $[H^+]$. On the contrary, for lactic acid oxidation under weaker acidic conditions, Haight and all [18] found the zeroth-order and second-order in $[H^+]$ paths to be effective.

Ascorbic acid oxidation [36, 60] shows an acid dependence ranging between zeroth and first-order, under mild acidic conditions.

$$k_{obs}^{redox} = \frac{\alpha[ROH]}{1+\beta[ROH]} \quad (14')$$

Under this setting, the cyclic intermediate formation, which would require an extra hydrogen ion, does not take place, accordingly with the fact that second-order dependence in $[H^+]$ is not observed. Alternatively, the non-cyclic chromic ester will undergo a base-assisted two-equivalent electron transfer in the rate determining step:

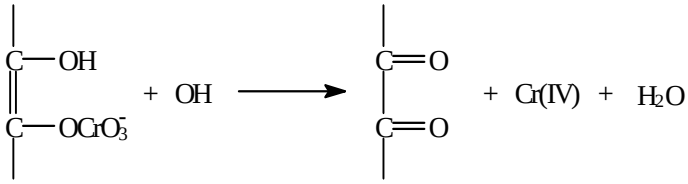

(23)

Few situations were found in which the hydroxy compounds could be oxidised by Cr(VI) by outer-sphere mechanisms. Such ones were assumed for some α-hydroxy-acids (glycolic, lactic and mandelic acids) oxidations with pyridin chlorochromate in acetic acid medium [75] and in absence of catalysts. However, in Ru(III) catalysis, the reaction proceeds *via* an intermediate, showing an inner-sphere process. In the Cr(VI)-Ru-substrate complex, Cr(VI) is linked to Ru(III) by means of the chlorine atom, while between the catalyst and substrate a Ru-O bond is formed.

OXIDATION OF THIOLS AND THIO-ACIDS

The oxidation of thio-compounds yields disulphides, according to the fact that not the carbon atom bearing the –SH group, but the sulphur atom of the thiol function is oxidised.

The processes follow an inner-sphere mechanism as well, consisting of sequences of steps involving first an equilibrium path in which an 1:1 chromate: substrate intermediate complex of thioesteric type is formed (eq. 24) [16, 21-25, 29-34, 43, 76]:

$$HCrO_4^- + RSH \rightleftharpoons RSCrO_3^- + H_2O \qquad k_1, k_{-1}, K_1 \qquad (24)$$

This intermediate reacts by either a bimolecular two-electron transfer redox reaction involving a second substrate molecule and leading to Cr(IV) and disulphide formation (eq. 25):

$$RSCrO_3^- + RSH \longrightarrow Cr(IV) + RSSR \qquad k_2 \qquad (25)$$

or an internal unimolecular one-electron transfer giving Cr(V) and thiyl free radicals (eq. 26) which dimerize to disulphide (eq. 27):

$$RSCrO_3^- \longrightarrow Cr(V) + \dot{R}S \qquad k_3 \qquad (26)$$

$$2\dot{R}S \longrightarrow RSSR \qquad (27)$$

The Cr(IV) and Cr(V) species undergo further fast redox processes yielding Cr(III) products, as in the following sequences:

IV. $$Cr(IV) + RSH \longrightarrow Cr(III) + \dot{R}S \qquad (28)$$

$$2\dot{R}S \longrightarrow RSSR \qquad (27)$$

V. $$Cr(IV) + Cr(VI) \longrightarrow 2Cr(V) \qquad (29)$$

$$Cr(V) + 2RSH \longrightarrow Cr(III) + RSSR \qquad (30)$$

Cr(V) reaction with RSH (eq. 30) is not an elementary process. The behaviour of Cr(V) resembles that of Cr(VI), forming – by similar paths – thio-esters which subsequently also decompose to give Cr(IV) or Cr(III). The overall stoichiometry for all these cases was found 3 : 1 RSH : Cr(VI).

The reaction conditions play an important role on the mechanism. Thus, under the settings of excess concentration of substrate – as the case for most of the studies – the path (30) seems to be less effective, being ultimately dismissed.

Both alternatives described by equations 25 and 26 are of comparable importance on the general picture of thio-compound oxidations. The substrate structure is determining when choosing one or another reaction pathways. Thio-compounds like cysteine [15, 32] and some of its derivatives [15], mercaptoetanol [15], thioglicolate [15], thioglicolic acid [30], thiomalic acid [29], methionine [77] or glutathione [15, 25] where found to follow the route involving the bi-molecular redox process leading to Cr(IV), under both aqueous acidic or neutral-basic conditions. On the other hand, the reactions of other thiol substrates like benzenethiol and α-toluenethiol in acetic acid solutions [39] or unithiol in neutral medium [15] more likely undergo the unimolecular process to form Cr(V). For penicillamine in neutral-slight basic medium [25], both (25) and (26) paths seem to be effective to some extent.

A particular behaviour is found for those dithio-compounds able to form intramolecular S-S bond.

In these cases, another kind of unimolecular internal electron-transfer takes place, involving two electrons and leading to Cr(IV) and the intramolecular disulphide:

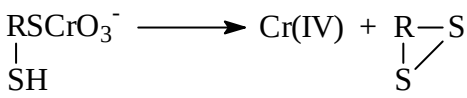

k_4 (31)

Such an example is the oxidation of dithiotreitol in neutral aqueous medium [15]. The overall stoichiometry changes to 1,5 : 1 R-$(SH)_2$: Cr(VI) for these situations.

Although all the papers dealing with the reactions of the type discussed present the bimolecular path as yielding disulphide and Cr(IV), there is an alternative path way, kinetically indistinguishable, in which Cr(V) and a disulphide radical is formed in an one-equivalent process:

$$RSCrO_3^- + RSH \longrightarrow Cr(V) + RS\therefore SR^- \qquad k_5 \qquad (32)$$

Disulphide radical, having a sulphur-sulphur three electron bond, with the third electron in an antibonding orbital, has been identified [78] and characterised for several cases. It was found to be far more stable than the thiyl radical. However, this higher stability allows other interpretations for its appearance.

In neutral or weak acidic solutions, where the thiol substrate could also exist, and therefore react, as deprotonated negative charged species RS^-, the equilibrium reaction between RS^- and thiyl free radicals $R^{\bullet}S$ takes place [17].

$$\overset{\bullet}{R}S + RS^- \rightleftharpoons RSS\overset{\bullet}{R}^- \qquad (33)$$

The thiyl radicals result from one-electron reductions of Cr(V) or Cr(IV) in reactions with other substrate molecules of RS^- form.

All these mechanisms were suggested in accordance with the rate laws.

The equations for both formation and disappearance of the complex can be written. Under excess of thio-compound, pseudo-first-order observed rate constants are dependent only on thiol substrate concentration, as deduced from rate expressions:

$$r_{obs}^{f} = k_1[RSH][Cr(VI)]_t \qquad (34)$$

$$k_{obs}^{f} = k_1[RSH] \qquad (35)$$

$$r_{obs}^{redox} = (k_2[RSH] + k_3)[RSCrO_3^-] = \frac{a[RSH]^2 + b[RSH]}{1 + c[RSH]}[Cr(VI)]_t \qquad (36)$$

$$k_{obs}^{redox} = \frac{a[RSH]^2 + b[RSH]}{1 + c[RSH]} \quad (37)$$

where a, b, c coefficients are certain combinations of the rate constants.

When acidic media are employed, both formation and decay of the thioester can show parallel hydrogen ion assisted path ways. Therefore:

$$k_i = k_i^0 + k_i^I[H^+]; \qquad i \in \{1,2,3\} \quad (38)$$

In most of the cases, the redox decomposition of the intermediate is rate determining.

General rate laws of the form:

$$-\frac{d[Cr(VI)]}{dt} = \frac{(a^0 + a^I[H^+])[RSH]^2 + (b^0 + b^I[H^+])[RSH]}{1 + c[RSH]}[Cr(VI)]_t \quad (39)$$

can be written in acidic media, while the terms first-order in $[H^+]$ can be neglected in neutral-basic media, giving:

$$-\frac{d[Cr(VI)]}{dt} = \frac{a^0[RSH]^2 + b^0[RSH]}{1 + c[RSH]}[Cr(VI)]_t \quad (40)$$

which is a particular case of the more general equation for acidic media.

Depending on the reaction mechanism – as discussed – the term of second or of first order in substrate – corresponding to the bimolecular or monomolecular step respectively – can prevail, leading to two limiting cases, when the secondary process is ruled out.

The ratio formation/decay of the intermediate is a function of the nature of thio-compound. Sometimes, formation is so rapid that stopped-flow technique is necessary to record it. In such situations, the complex formation can be assimilated with either a steady-state – as for cysteine, ethanethiol, thioglicolate, etc. [15] – or pre-equilibrium – like in the glutathione or unithiol oxidations by Cr(VI) [15].

In other cases, where both steps are of comparable speed (the ratio does not exceed the value of 10), a two-stage consecutive process is the theoretical model for approaching the reaction:

$$Cr(VI) \xrightarrow[k_f]{+\,RSH} complex\ Cr(VI):tiol \xrightarrow[k_{redox}]{+\,RSH} Products \quad (41)$$

Some situations were found where the intermediate formation is rate-determining, as being the slower step of the global mechanism.

$$-\frac{d[Cr(VI)]}{dt} = k_1[RSH][Cr(VI)] \quad (42)$$

Penicillamine, thiolactate, thiomalate, dithiothreitol and 2,3 dimercaptosuccinate oxidation in neutral media are such example [15].

DISCUSSIONS AND CONCLUSIONS

The reaction mechanisms for thio-compound oxidations with Cr(VI) show both similarities and differences when compared to those of the analogous hydroxy-compounds.

The fundamental difference between the oxidation reactions of the two classes of substances is – as already noted – that, while for hydroxy-compounds the carbon atom bearing the –OH functional group suffers the oxidation, the thio-compound oxidation takes place at the sulphur atom in the –SH functional group. As a consequence, the reaction products are also of different type.

On the other hand, unlike hydroxy-compounds, which are generally known as bi-equivalent reducing agents, the sulphur atom of thio-compounds provides one electron only. Thus, further consequences on the stoichiometry and reaction mechanism occur. It is known for a fact that the stoichiometric ratios for mono hydroxy-compounds oxidation are generally 1,5 : 1 R–OH : Cr(VI), while ratios of 3 : 1 R–SH : Cr(VI) are valid for oxidations of mono thio-compounds.

Referring to the reaction mechanisms, both classes of compounds undergo inner-sphere processes, *via* analogous intermediate complexes of esteric and thioesteric type respectively (eqs. 2, 24). No or very small difference in the absorption maxima position can be observed for the esteric type intermediates, while the thioesteric intermediates present in most of the cases maxima significantly shifted to the red region. Figure 1 shows the spectrum of Cr(VI)-glutathione mixture [79] in its time evolution, as compared to the spectrum of chromate ion in perchloric acid medium. The intermediate spectrum exhibits a maximum at 428 nm, shifted to the red compared with the $HCrO_4^-$ maximum at 350 nm, as recorded by us using a Jasco 530 spectrophotometer.

The intermediate is formed in an equilibrium step of substitution type; in a limited number of cases its formation is the rate-determining step. Still, for both hydroxy- and thio- compounds, its subsequent redox decomposition is more likely to be rate-determining. This can be done in several ways and here is where new differences appear.

The Cr(VI) preference for bi-electronic reductions combines with the bi-equivalent character of the hydroxy-compounds or the rather mono-equivalent one of thio-compounds. The matching tendency in the case of hydroxy-compounds results in a clear favouring of the bi-electronic route for these substrates. The two-electron donor being already bonded to Cr(VI), the process is a monomolecular internal one, leading to Cr(IV).

In thio-compound oxidations, the bi-electronic route is still important, but requires a second substrate molecule (or at least a second substrate reaction centre – sulphur atom of a –SH group – therefore being a bimolecular

one. For not too bulky thiol substrates, Cr(VI) species and/or solvent molecules, this path way is very likely, taking into account that thiols have good co-ordination properties and therefore easily bound to Cr(VI) centre.

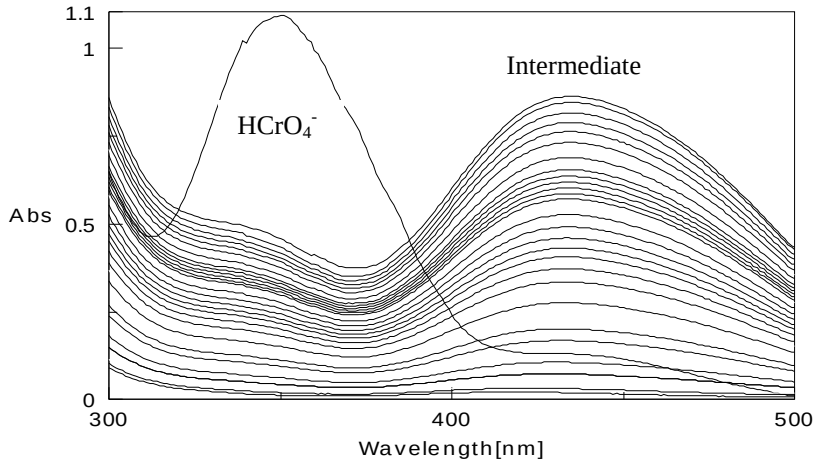

Figure 1. Glutathione : Cr(VI) intermediate complex time-delay spectra in aqueous acidic medium ([GSH]=3.33 x 10^{-3}, [$HCrO_4^-$]=6.67 x 10^{-4}, [$HClO_4$]=3.67 x 10^{-2})

Both thiol substrate mono-electronic character (tendency to form free radicals) and steric impediments contribute to offer an alternate one-electron route for Cr(VI) reduction – this being the unimolecular step in the case under discussion – and leading to Cr(V) formation. The route is of significant importance, being the only available one in some cases or competing with the bi-electronic one in others.

On the contrary, in the case of hydroxy-compounds the mono-electronic reduction of Cr(VI) only occasionally is a viable alternative. A particular manner of combining a two-electron and one-electron redox pathways is through a concerted one-step action, the overall process being assimilated with a three-electron transfer. These situations are also quite rare. For the thio-compound oxidations, three-equivalent processes have not been reported.

The fate of Cr(IV) or Cr(V) species resulted in the above processes is quite similar for both classes. Cr(V) tends to behave bi-electronically, like Cr(VI), yielding Cr(III). Cr(IV) has a number of choices, approximately the same ones regardless the substrate type (alcohol or thiol).

Another common feature of the systems under discussion is the involvement of free radical intermediates.

The rate laws elaborated on the basis of reaction mechanisms are consistent with the above-presented comments. Acidity of the medium strongly influences both classes of oxidations. Still, second-order dependencies, which are likely for hydroxy-compounds due to their need of a second hydrogen ion in the process of the cyclic intermediate formation, were rarely reported for thiocompound oxidation.

REFERENCES

1. M. A v r a m, *Chimie organică*, E. D. P., Bucureşti, **1969;**
   M. I o v u, *Chimie organică*, 2nd eddition, E. D. P., Bucureşti, **1982;**
2. A. S t a n d e v e n, K. W e t t e r h a h n, *J. Am. Coll. Toxicol.*, **1989**, *8*, 125.
3. J. A i y a r, H. B e r k o v i t s, K. E. W e t t e r h a h n, *J. Am. Coll. Toxicol.*, **1990**, *9*, 595.
4. M. M i t e w a, p. B o n t c h e v, *Coord. Chem. Rew.*, **1985**, *61*, 241.
5. S. S i g n o r e l l a, S. G a r c i a, L. S a l a, *Polyhedron*, **1992**, *11*, 1391.
6. S. R a m e s h, S. M a h p a t r o, J. L u i, J. R o č e k, *J. Am. Chem. Soc.*, **1981**, *103*, 5772.
7. V. S r i n i v a s a n, J. R o č e k, *J. Am. Chem. Soc.*, **1978**, *100*, 2789.
8. P. H. C o n n e t t, K. E. W e t t e r h a h n, *Struct. Bonding (Berlin).*, **1983**, *54*, 94.
9. J. F. P e r e z-B e n i t o, C. A r i a s, *Int. J. Chem. Kinet.*, **1993**, *25*, 221.
10. L. Zhang, P. A. Lay, *J. Am. Chem. Soc.*, **1996**, *118*, 12624.
11. M. I t o h, M. N a k a m u r a, T. S u z u k i, K. K a w a i, H. H o r i t s u, K. T a k a m i z a w a, *J. Biochem.*, **1995**, *117*, 780.
12. J. F. P e r e z-B e n i t o, C. A r i a s, *J. Phys. Chem. A*, **1997**, *101*, 4726.
13. J. F. P e r e z-B e n i t o, D. L a m r h a r i, C. A r i a s, *J. Phys. Chem. A*, **1994**, *98*, 12621.
14. P. A. L a y, A. L e v i n a, *Inorg. Chem.*, **1996**, *35*, 7709.
15. P. H. C o n n e t t, K. E. W e t t e r h a h n, *J. Am. Chem. Soc.*, **1985**, *107*, 4282.
16. P. H. C o n n e t t, K. E. W e t t e r h a h n, *J. Am. Chem. Soc.*, **1986**, *108*, 1842.
17. P. A. L a y, A. L e v i n a, *J. Am. Chem. Soc.*, **1998**, *120*, 6704.
18. G. P. H a i g h t, G. M. J u r s i c h, M. T. K e l s o, P. J. M e r r i l l, *Inorg. Chem.*, **1985**, *24*, 2740-2746.
19. I. B a l d e a, *Doctoral Thesis, Cluj*, **1969**.
20. D. S. L e e, R. S t e w a r t, *J. Am. Chem. Soc.*, **1964**, *86*, 3051;
    J. I. T o n g, E. L. K i n g, *J. Am. Chem. Soc.*, **1953**, *75*, 6180.
21. J. P. M c C a n n, A. M c A u l e y, *J. Chem. Soc., Dalton Trans.*, **1975**, 783.
22. A. M c A u l e y, M. A. O l a t u n j i, *Can J. Chem.*, **1977**, *55*, 3328.
23. D. W. K w o n g, D. E. P e n n i n g t o n, *Inorg. Chem.*, **1984**, *23*, 2528.
24. D. A. D i x o n, T. P. D a s g u p t a, N. P. S a d l e r, *Inorg. React. Mech.*, **1998**, *1*, 41.
25. D. A. D i x o n, T. P. D a s g u p t a, N. P. S a d l e r, *J. Chem. Soc., Dalton Trans.*, **1995**, 2267.
26. J. R o č e k, A. E. R a d k o w s k y, *J. Am. Chem. Soc.*, **1973**, *95*, 7123.
27. K. B. W i b e r g, H. S c h ä f e r, *J. Am. Chem. Soc.*, **1969**, *91*, 933.
28. F. H. W e s t h e i m e r, *Chem. Rew.*, **1949**, *45*, 419.
29. I. B a l d e a, *Studia Univ. Babes-Bolyai, Chem.*, **1994**, *39(1-2)*, 138.
30. I. B a l d e a, *Studia Univ. Babes-Bolyai, Chem.*, **1987**, *32(2)*, 42.
31. I. B a l d e a, *Studia Univ. Babes-Bolyai, Chem.*, **1989**, *34(1)*, 80.
32. I. B a l d e a, G. N i a c, *Studia Univ. Babes-Bolyai, Chem.*, **1986**, *31(2)*, 41.

33. G. N i a c, S. S c h ö n, I. B a l d e a, *Studia Univ. Babes-Bolyai, Chem.*, **1986**, *31(2)*, 31.
34. I. B a l d e a, G. N i a c, *Inorg. Chem*., **1970**, *9*, 110.
35. I. B a l d e a, S. S c h ö n, *Studia Univ. Babes-Bolyai, Chem.*, **1973**, *18(1)*, 47.
36. I. B a l d e a, L. M u n t e a n u, *Studia Univ. Babes-Bolyai, Chem.*, **1980**, *25(1)*, 24.
37. I. B a l d e a, M. G i u r g i u, *Studia Univ. Babes-Bolyai, Chem.*, **1992**, *37(1-2)*, 35.
38. I. B a l d e a, C. M u r e s a n u, A. R. C s a v d a r i, *Studia Univ. Babes-Bolyai, Chem.*, **1997**, *42(2)*, 119.
39. I. B a l d e a, D. M. S a b o u, *Rev. Roum. Chim*., **2000**, *45(6)*, 537.
40. G. N i a c, I. B a l d e a, M. L u n g u, *Studia Univ. Babes-Bolyai, Chem.*, **1969**, *14(2)*, 83-87.
41. N. B a i l e y, A. C a r r i n g t o n, K. A. K. L o t t, M. C. R. S y m o n s, *J. Chem. Soc*., **1960**, 240.
42. J. P r e e r, G. P. H a i g h t, J r., *J. Am. Chem. Soc.*, **1965**, *87*, 5256.
43. A. M c A u l e y, M. A. O l a t u n j i, *Can J. Chem*., **1977**, *55*, 3335.
44. G. P. H a i g h t, E. P e r c h o n o c k. P. E m m e n e g g e r, G. G o r d o n, *J. Am. Chem. Soc.*, **1965**, *87*, 3835.
45. K. B. W i b e r g, *Oxidation in Organic Chemistry*, Part A., Acad. Press. New-York, **1965**, p. 69.
46. J. H a m p t o n, A L e o, F. H. W e s t h e i m e r, *J. Am. Chem. Soc.*, **1965**, *87*, 306.
47. A. N o v i c k, F. H. W e s t h e i m e r, *J. Chem. Phys.*, **1973**, *11*, 506.
48. F. H. W e s t h e i m e r, N. N i c o l a i d e s, *J. Am. Chem. Soc.*, **1949**, *71*, 25.
49. W. W a t a n a b e, F. H. W e s t h e i m e r, *J. Chem. Phys.*, **1949**, *17*, 61.
50. E. K i t a, A. P i e t k i e w i c z, *Transit. Met. Chem.*, **2000**, *25*, 126-132.
51. J. R o č e k, A. E. R a d k o w s k y, *J. Amer. Chem. Soc.*, **1968**, *90*, 2986.
52. S. N. M a h a p a t r a, M. K r u m p o l c, J. R o č e k, *J. Amer. Chem. Soc.*, **1980**, *102*, 3799.
53. P. M. N a v e, V. S. T r a h a n o v s k y, *J. Amer. Chem. Soc.*, **1970**, *92*, 1120.
54. V. S. T r a h a n o v s k y, P. M. N a v e, *J. Amer. Chem. Soc.*, **1971**, *93*, 4536.
55. K. B. W i b e r g, S. K. M u k h e r j e e, *J. Amer. Chem. Soc.*, **1970**, *92*, 7599.
56. S. R. S i g n o r e l l a, M. I. S a n t o r o, M. N. M u l e r o, L. F. S a l a, *Can. J. Chem.*, **1984**, *72*, 398.
57. L. F. S a l a, C. P a l o p o l i, S. R. S i g n o r e l l a, *Polyhedron*, **1995**, *14*, 1725.
58. L. F. S a l a, S. R. S i g n o r e l l a, M. R i z o t t o, M. I. F r a s c a r o l i, F. G a n d o l f o, *Can. J. Chem.*, **1992**, *70*, 2046.
59. S. G a r c i a, S. R. S i g n o r e l l a, S. A c e b a l, E. P i a g g i o, L. F. S a l a, *Oxid. Commun.*, **1993**, *16*, 313.
60. D. A. D i x o n, N. P. S a d l e r, T. P. D a s g u p t a, *J. Chem. Soc. Dalton Trans.*, **1993**, *23*, 3489.
61. Y. A b e, H. H o r i i, S. T a n i g u c h i, *Can. J. Chem.*, **1986**, *64*, 360.
62. Y. A b e, S. O k a d a, H. H o r i i, S. T a n i g u c h i, *J. Chem. Soc. Perkin Trans.*, **1987**, *2*, 715.
63. S. L. O s w a l, G. V. B a k o r e, *Ind. J. Chem.*, **1980**, *19A*, 211.
64. F. H a s a n, J. R o č e k, *J. Amer. Chem. Soc.*, **1972**, *94*, 3181.

65. F. H a s a n, J. R o č e k, *J. Amer. Chem. Soc.*, **1972**, *94*, 8946.
66. F. H a s a n, J. R o č e k, *J. Amer. Chem. Soc.*, **1972**, *94*, 9073.
67. F. H a s a n, J. R o č e k, *J. Amer. Chem. Soc.*, **1973**, *95*, 5421.
68. F. H a s a n, J. R o č e k, *J. Amer. Chem. Soc.*, **1975**, *97*, 1444.
69. M. K r u m p o l c, J. R o č e k, *J. Amer. Chem. Soc.*, **1977**, *99*, 137.
70. D. I p, J. R o č e k, *J. Amer. Chem. Soc.*, **1979**, *101*, 6311.
71. P. M. R e d d y, V. J a g a n n a d h a m, B. S e t h u r a m, T. N. R a o, *Ind. J. Chem.*, **1982**, *21A*, 608.
72. A. J a m e e l, *J. Ind. Chem. Soc.*, **1999**, *76*, 263.
73. R. F. J a m e s o n, N. J. B l a c k b u r n, *J. Inorg. Nucl. Chem*., **1985**, *37*, 809.
74. A. A p a r n a, S. K o t h a r i, K. K. B a n e r j i, *J. Chem. Res. (S*), **1994**, 367.
75. K. K u m a r, P. S a r o j a, S. K a n d l i k a r, *Trans. Met. Chem.*, **1994**, 355.
76. J. F. P e r e z-B e n i t o, C. A r i a s, D. L a m r h a r i, *Int. J. Chem. Kinet*., **1994**, *26*, 587.
77. A. P e t r i, I. B a l d e a, *Studia Univ. Babes-Bolyai, Chem.*, **1975**, *20(2)*, 67.
78. Z. M. H o f f m a n, E. H a y s o n, *J. Am. Chem. Soc.*, **1972**, *94*, 7950.
79. I. B a l d e a, D. M. S a b o u, *to be published*.

STUDIA UNIVERSITATIS BABEŞ–BOLYAI, CHEMIA, XLV, 1-2, 2000

THE OXIDATION OF TOLUENE BY POTASSIUM PERMANGANATE IN PERCHLORIC ACID MEDIUM

CLAUDIA MUREŞANU[1], IOAN BÂLDEA[2]

Department of Physical Chemistry, Faculty of Chemistry and Chemical Engineering, "Babes-Bolyai" University of Cluj - Napoca, 11 Arany Janos Str., 3400-Romania.

ABSTRACT. The reaction of potassium permanganate with toluene, catalyzed by Mn^{2+}, was studied spectrophotometrically. Permanganate ion is consumed mainly by two reaction routes: one is the direct oxidation of toluene and the other the reduction by the manganous ion. Both pathways exhibit a first - order dependence with respect to permanganate ion. Our kinetic study includes also the influence of toluene, hydrogen ion and manganous ion concentration upon reaction rate. The rate laws for the two reaction routes and for the global reaction were established. Several possible reaction mechanisms are discussed for C – H bond breaking in the case of direct oxidation of toluene by permanganate and for Mn^{3+} generation by reduction of MnO_4^- with Mn^{2+}.

KEYWORDS: toluene, potassium permanganate, catalysis, redox reactions, kinetics.

Potassium permanganate is a well-known oxidant for various organic compounds, in acidic and basic media. We mention here only a few examples, like the oxidation of olefins[1], oxalic[2 - 4] and formic acid[5], 2,6-dinitrophenols[6], toluene[7], substituted toluenes[8] and ethylbenzene[9].

Related to the subject of our paper are the earlier works of Cullis and Ladbury[7-9]. They studied the oxidation of aromatic hydrocarbons with potassium permanganate, in a 50% aqueous acetic acid medium, by means of an iodometrical method. The main product was the corresponding aldehyde, for toluene and substituted toluenes oxidation and acetophenone in the case of ethylbenzene oxidation, when a stoichometric ratio of initial concentrations of reactants was used. Besides side chain oxidation aromatic ring disruption was also observed, especially for the oxidation of xylenes. The results of the kinetic studies about the oxidation of aromatic hydrocarbons mentioned above[7-9] revealed that, all reactions are first-order with respect to MnO_4^- concentration. Toluene, chlorotoluene and ethylbenzene oxidations are first order with respect to the organic compound, while for m- and p-xylene this order was less than one. A clear autocatalytic effect of Mn(II), involving the Mn(III) intermediate, could not be proved. It seemed rather that the mechanism of these reactions has two pathways, one in which Mn(III) is implied and one independent of this species[7-9]. The recent papers of Gardner and Kuehnert deal with the oxidation of alkylbenzenes in aqueous buffer[10] and in neat toluene[11]. They developed a hydride transfer mechanism for toluene oxidation in aqueous buffer and a radical mechanism if the reaction was performed in organic solvent. Benzyl alcohol[12-14] and benzaldehyde[15-17] oxidation with MnO_4^- were studied in acid medium while for toluene oxidation no recent kinetic are available in

[1]*muresanu@chem.ubbcluj.ro;* [2]*ibaldea@chem.ubbcluj.ro*

this medium. That is why we considered it interesting to devote this paper to a more detailed investigation of toluene oxidation by potassium permanganate in perchloric acid medium.

EXPERIMENTAL

The chemicals used in this study were of reagent grade purity and were acquired from commercial sources (Reactivul Bucuresti and Merck).

Kinetic measurements were performed by means of a Zeiss Spekol spectrophotometer, provided with a temperature jacket surrounding the cell holder. The jacket was connected to a Wobser U-10 recirculatory water bath. Reaction mixtures were prepared directly into the spectrophotometer glass cell, of 5-cm path length. The reaction was started by adding a measured amount of $KMnO_4$ stock solution over the mixture of toluene, $HClO_4$, $MnSO_4$, $NaClO_4$ in twice distilled water. Absorbance was measured at 520 nm, where $KMnO_4$ UV/VIS spectrum exhibits a maximum.

RESULTS AND DISCUSSIONS

Kinetic runs were performed in the presence of toluene and Mn(II) excess. Absorbance readings were processed according to the integrated form of a first-order rate law:

$$\ln(A - A_\infty) = \ln(A_0 - A_\infty) - k_{obsd} \cdot t \qquad (1)$$

where: A_0, A_∞ and A are the measured values of absorbance at the beginning, the end and at different time moments of the reaction;
k_{obsd} is the observed first-order rate constant.

Semilogarithimic plots $\ln(A - A_\infty)$ *versus* t, at several excess concentrations of toluene were linear (***Fig.1***) up to 90 % of completion, so that it is obvious that reaction order with respect to MnO_4^- is one. If the reaction was approaching its end a slight downward curvature was noticed.

Observed rate constants were determined from the slopes of linear plots, of eq. (1), using a least square method. Two to four replicate kinetic runs were carried out for each set of conditions.

It is considered that the depletion of MnO_4^-, in the presence of Mn^{2+}, occurs by two pathways:

Pathway 1, which means the direct oxidation of toluene by permanganate;

Pathway 2, which is the autocatalytic, first order reduction of MnO_4^- by the manganous ion.

Our results, summarized in ***Table 1***, revealed that enlarged concentrations of toluene lead to increased values of first-order rate constants according to:

$$k_{obsd} = (2.4 \pm 0.5) \cdot 10^{-4} + (0.34 \pm 0.04) \cdot [\text{Toluene}]_0 \qquad \text{at } 45^0\text{C} \qquad (2)$$

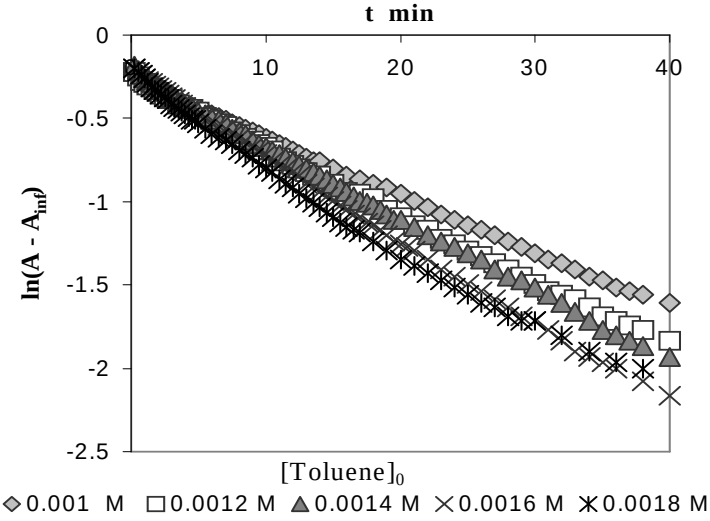

Fig.1 First order semilogarithmic plots at several excess concentrations of toluene; $[MnO_4^-] = 7\cdot10^{-5}$; $[HClO_4] = 1.4$; $[MnSO_4] = 10^{-2}$ mol·dm^{-3} and $\mu = 1.5$ mol·dm^{-3} at 45^{0}C.

where the term of zero-order with respect to toluene represents the consumption of MnO_4^- due to the reaction:

$$MnO_4^- + 4Mn^{2+} + 8H^+ \rightarrow 5Mn^{3+} + 4H_2O \qquad (3)$$

The rate constant determined in the absence of toluene, $k_0 = 3.9\pm0.2$ s^{-1}at $[H^+] = 1.4$, $\mu = 1.5$ mol·dm^{-3} and 45^{0}C, is a close value to the intercept of eq.(3).

Table 1.

The dependence of first-order rate constants for toluene oxidation on the excess concentration of toluene; $[MnO_4^-] = 7\cdot10^{-5}$; $[HClO_4] = 1.4$; $[MnSO_4] = 10^{-2}$ mol·dm^{-3} and $\mu = 1.5$ mol·dm^{-3} at 45^{0}C.

$10^3\cdot[Toluene]_0$ (mol·dm^{-3})	1.0	1.2	1.4	1.6	1.8
$10^4\cdot\overline{k}_{obsd}$ (s^{-1})	5.8±0.6	6.5±0.3	7.2±0.2	7.9±0.3	8.6±0.2
$10^4\cdot\overline{k}^*_{obsd}$ (s^{-1})	3.4±0.4	4.1±0.3	4.8±0.3	5.5±0.2	6.4±0.3

The values of first – order rate constants corrected for reduction of permanganate by manganous ion, $k^*_{obsd} = k_{obsd} - 2.4\cdot10^{-4}$, exhibited a first – order influence with respect to toluene concentration:

$$k^*_{obsd} = (1.5\pm0.5)\cdot10^{-6} + (0.34\pm0.04)[Toluene]_0 \qquad \text{at } 45^0C \qquad (4)$$
$$k^*_{obsd} \approx (0.34\pm0.04)[Toluene]_0$$

The influence exerted by hydrogen ion concentration was investigated in the limits of 1 to 1.5 mol·dm^{-3} at constant toluene and Mn(II) concentration. The results presented in **Table 2** prove a linear dependence of the rate constant on the [H^+], of the form:

$$k_{obsd} = (2.7\pm0.8)\cdot10^{-4} + (2.7\pm0.2)\cdot10^{-4}\cdot[H^+] \qquad \text{at } 45^0C \qquad (5)$$

A similar correction procedure, as for the influence of organic substrate, was used also in this case: $k^*_{obsd} = k_{obsd} - k_{0,}$ where k_0 are the rate constants of pathway 2 obtained from kinetic runs in the absence of toluene (**Table *2***).

$$k_0 = (2.7\pm1.1)\cdot10^{-5}+(1.7\pm0.1)\cdot10^{-4}\cdot[H^+] \qquad \text{at } 45^0C \qquad (6)$$
$$k^*_{obsd} = (2.4\pm0.1)\cdot10^{-4}+(9.34\pm0.6)\cdot10^{-5}\cdot[H^+] \qquad \text{at } 45^0C \qquad (7)$$

This relationship is valid in strong acid media. At low acid concentration it is to expect a downward curvature of the $k_{obsd} = f(t)$ dependence, tending to a constant value, like that obtained by Cullis and Ladbury[7], because $KMnO_4$ keeps it oxidizing effect upon organic substrates also in low acidic, neutral media and alkaline media.

Table 2.

The dependence of first-order rate constants for toluene oxidation on [H^+]; [Toluene]$_0$=1.2·10^{-3}; [MnO_4^-] = 7·10^{-5}; [$MnSO_4$] = 10^{-2} mol·dm^{-3} and μ = 1.5 mol·dm^{-3} at 45^{0}C.

[H^+] (mol·dm^{-3})	1	1.1	1.2	1.3	1.4	1.5
$10^4\cdot\bar{k}_{obsd}$ (s^{-1})	5.4±0.1	5.7±0.1	6.0±0.2	6.2±0.2	6.5±0.1	6.8±0.1
$10^4\cdot\bar{k}_0$ (s^{-1})	2.0±0.1	2.2±0.2	2.4±0.1	2.5±0.2	2.7±0.1	2.9±0.2
$10^4\cdot\bar{k}^*_{obsd}$ (s^{-1})	3.4±0.1	3.6±0.1	3.8±0.2	3.8±0.2	3.4±0.1	3.9±0.2

Because several autocatalytic oxidations of organic compounds by $KMnO_4$ are mentioned in literature[2-6], we have studied the influence of Mn(II) upon the reaction rate. But, as it can be seen (***Fig.2***) no sigmoid curve was obtained for the change of absorbance with time, in the absence of Mn(II). Although we couldn't identify any autocatalytic effect, the reaction evolves much faster in the presence of Mn(II), proving the catalytic influence of manganous ion. A similar situation has been observed by other authors[7-9] in the case of toluene, xylenes, chlorotoluene and ethylbenzene.

The first-order rate constant exhibits a second - order dependence on manganous ion concentration, with a small intercept:

$$k_{obsd} = (3.2\pm0.3)\cdot10^{-4} + (3.08\pm0.13)\cdot[Mn(II)]^2 \qquad \text{at } 45^0C \qquad (8)$$

where the first term corresponds to the rate constant of toluene oxidation in the absence of Mn(II).

A similar dependence is obtained by processing data from kinetic runs in the absence of toluene:

$$k_0 = (6.65\pm0.06)\cdot10^{-5} + (3.23\pm0.11)\cdot[Mn^{2+}]^2 \qquad 45^0C \qquad (9)$$

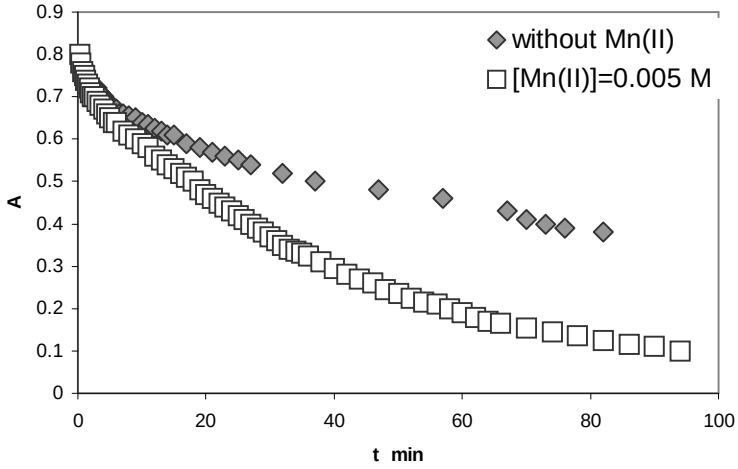

Fig. 2 The variation of absorbance with time in the absence and in the presence of Mn(II) catalyst $[Toluene]_0=1.2\cdot10^{-3}$; $[MnO_4^-] = 7\cdot10^{-5}$; $[HClO_4] = 1.4$ mol·dm^{-3} and $\mu = 1.5$ mol·dm^{-3} at 45^0C.

where the intercept represents the rate constant for solvent oxidation by permanganate ion. The manganous ion influences only the second pathway, this is why the dependence of the rate constants eq. (6) and (7) exhibits approximately the same slope.

Table 3.

The dependence of first-order rate constants for toluene oxidation on $[Mn^{2+}]$; $[Toluene]_0=1.2\cdot10^{-3}$; $[MnO_4^-] = 7\cdot10^{-5}$; $[H^+] = 1.4$ and $\mu = 1.5$ mol·dm^{-3} at 45^0C.

$10^2\cdot[Mn^{2+}]$ (mol·dm^{-3})	0.5	1	1.5	2
$10^4\cdot\bar{k}_{obsd}$ (s^{-1})	3.5±0.7	6.4±0.1	10.4±0.1	15.5±0.4
$10^4\cdot\bar{k}_0$ (s^{-1})	1.4±0.1	3.9±0.2	7.9±0.1	13.6±0.2

The rate law represents the sum of the rates for the two pathways:

$$r = -\frac{d[MnO_4^-]}{dt} = (k_0\cdot[Mn(II)^2] + k\cdot[Toluen]_0)[H^+][MnO_4^-] \qquad (10)$$

CONCLUSIONS

The oxidation of toluene by Mn(VII) yields benzaldehyde and benzoic acid, for reactions performed in aqueous acetic acid[7], aqueous buffer[10] and in neat toluene[11].

Therefore it is reasonable to consider the formation of same products if the reaction takes place in aqueous $HClO_4$ solution.

Many kinetic studies underline the large isotopic effect observed for the oxidation of organic compounds, like toluene, benzyl alcohol, tolylvaleric acids and for substituted mandelate ions[10, 13, 18, 19, 20] with permanganate. Such a behavior indicates the C – H bond cleavage is the rate determining step. The oxidation of the C – H bond by $KMnO_4$ may proceed by: **A.** proton transfer abstraction[11,12]; **B.** hydrogen atom abstraction[20]; **C**. hydride abstraction[10]; **D**. a [2 + 2] addition of a reactive C – H bond[18, 19] to an Mn = O bond ; **D.** formation of a manganese ester[17, 21].

Literature information, together with the experimental rate law, eq. (10) are to be accommodate by the reaction mechanism. In our opinion these requests are satisfied by three of the above mentioned reaction mechanisms, considering that oxidation proceeds by permanganate ion (pathway 1).

❖ A [2+2] addition of a C – H bond to the Mn = O bond, continued by homolytic or heterolytic bond cleavage in the rate determining step and subsequent reaction of the intermediate with the solvent.

$$MnO_4^- + H^+ \rightleftharpoons HMnO_4 \qquad K, \text{ fast} \qquad (11)$$

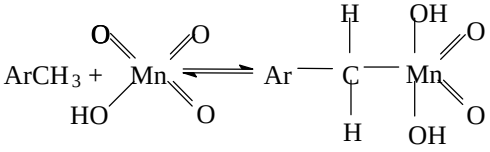

K_1, fast (12)

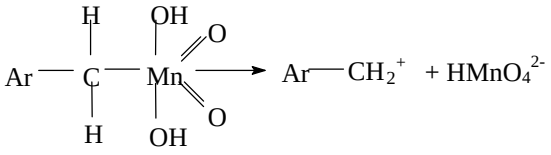

k_2, slow (13)

$$Ar{-}CH_2^+ + H_2O \longrightarrow Ar{-}CH_2OH + H^+ \qquad k_3 \qquad (14)$$

A free radical intermediate was excluded because experiments undertaken with toluene and benzylic alcohol in aqueous medium ruled out this possibility[10, 13]. The resulting rate law will depend on permanganate, reductant and hydrogen ion concentration according to:

$$r = k_2K_1K[ArCH_3][MnO_4^-][H^+] \qquad (15)$$

❖ Hydride abstraction which in this case occurs similar to a SN_2 mechanism: With the rate law:

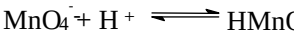

K (16)

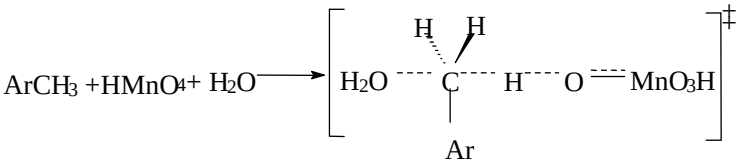

fast, K1 (17)

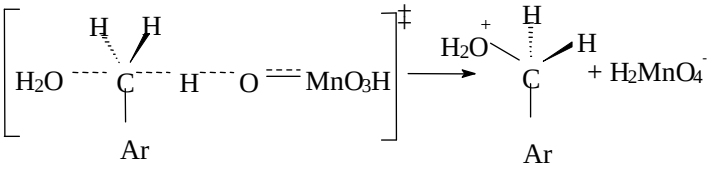

slow, k (18)

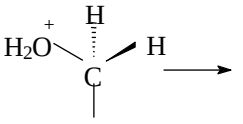

fast (19)

$$r = kKK_1[ArCH_3][H^+][H_2O][MnO_4^-] \quad (20)$$

Although the association constant for $HMnO_4$ is very low[17] ($K = 2.99 \cdot 10^{-3}$) there are cases for which a greater reactivity of $HMnO_4$ compared to MnO_4^- is mentioned[22, 23]

- The formation of an ester between permanganate ion and toluene, followed by the acid catalyzed hydrolysis of the ester.

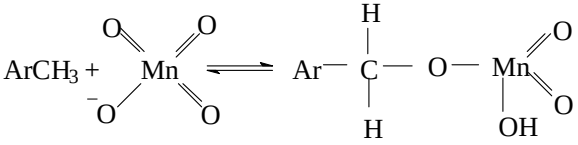

fast, K*1 (21)

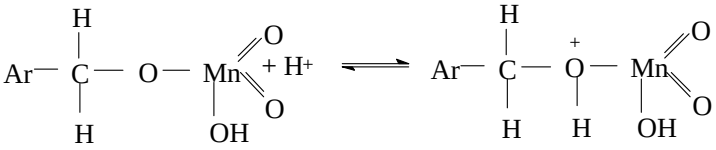

fast, K*2 (22)

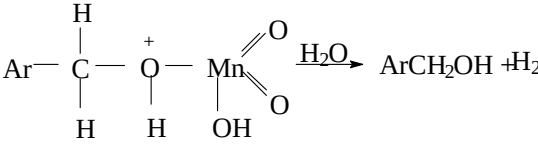

slow, k3 (23)

This mechanism will lead to a rate law similar to that deduced above:

$$r_1 = k_3 K^*_1 K^*_2 [ArCH_3][MnO_4^-][H^+][H_2O] \quad (24)$$

All these three mechanisms lead to a rate law of first order with respect to MnO_4^-, H^+ and toluene, similar to that obtained by us for the first pathway.

In high acidic medium several redox and dismutation reactions between manganese species might occur, which explains why no MnO_2 formation was observed:

$$5H_2MnO_4 + 8H^+ \longrightarrow 4MnO_4^- + Mn^{2+} + 4H_2O \quad (25)$$

$$2H_3MnO_4 + 4H^+ \longrightarrow H_2MnO_4 + MnO_2 + 2H_2O \quad (26)$$

$$MnO_2 + 4\,Mn^{2+} + 4H^+ \longrightarrow 2Mn^{3+} + 2H_2O \quad (27)$$

Hydrogen ion abstraction will be the rate determining step[24, 25. 26-28], when Mn^{3+} is the oxidizing species (pathway 2), followed by other reactions of the formed intermediate:

$$ArCH_3 + Mn^{3+} \xrightarrow{k} ArCH_2^{\bullet} + H^+ + Mn^{2+} \quad \text{slow} \quad (28)$$

$$ArCH_2^{\bullet} + Mn^{3+} \longrightarrow ArCH_2^{+} + Mn^{2+} \quad \text{fast} \quad (29)$$

$$ArCH_2^{+} + H_2O \longrightarrow ArCH_2OH + H^+ \quad \text{fast} \quad (30)$$

Recent literature on this subject, suggests for the generation of the Mn^{3+} intermediate, the formation of a monomeric and a dimeric Mn^{2+} complex (I), with a bridging ligand[4], or the formation of a dinuclear complex between MnO_4^- and Mn^{2+} with oxo bridge[22], followed by the reduction of the complex by Mn^{2+} to Mn^{3+}. Our reaction mixtures contained only ClO_4^- and SO_4^{2-} anions, which are weak in complexing Mn^{2+}, that is why we considered the formation of the MnO_4^- - Mn^{2+} complex:

$$Mn^{2+} + MnO_4^- \rightleftharpoons I \qquad K_c \quad (31)$$

$$I + Mn^{2+} \longrightarrow 2Mn^{3+} + H_2O \qquad k_0 \quad (32)$$

The influence of hydrogen ion may be explained in two ways: if it is considered that the permanganic acid forms the binuclear complex with Mn^{2+}, or if it is considered that the hydrogen ion is involved in reduction of the complex. The formation of Mn^{3+} was considered as the rate-determining step, and the deduced rate law came to the form:

$$r_2 = k_0[MnO_4^-][Mn^{2+}]^2[H^+] \quad (33)$$

Although the rate law is quite similar to our experimental rate law eq.(10), we will continue the experimental investigations to come to a better understanding of the overall mechanism.

REFERENCES

1. L e e D. G. and C h e n T. : *J. Am. Chem. Soc*., **1989**,*111*, 7534-7538.
2. W a w r e z e n c z i c E. M. and V r o n s k a M. : *Z. Phys. Chem. (Leipzig)*, **1980**, *261(2)*, 306-312.
3. P o w e l l R. T. O s k i n, T. and G a n a p a t s h u b r a m a n i a n N. : *J. Phys. Chem*., **1989**, *93*, 2718-2721.
4. P i m i e n t a V. , L a v a b r e D. , L e v y G. and M i c h e a u J. C. : *J. Phys. Chem*., **1994,** *98*, 13294-13299.
5. M a n n D. R. and T o m p k i n s F. C. : *Trans. Faraday Soc*., **1941,** *37*, 201-209.
6. A l e x a n d e r E. A. and T o m p k i n s F. C. : *Trans. Faraday Soc*., **1939,** *35*, 1156-1165.
7. C u l l i s C. F. and L a d b u r y J. W. : *J. Chem. Soc*., **1955**, 555-560.
8. C u l l i s C. F. and L a d b u r y J. W. : *J. Chem. Soc*., **1955**, 1407-1412.
9. C u l l i s C. F. and L a d b u r y J. W. : *J. Chem. Soc*., **1955**, 2851-2854.
10. G a r d n e r K. A. and M a y e r J. M. : *Science*, **1995**, *269*, 1849 – 1851.
11. G a r d n e r K. A. , K u e h n e r t L. L. and M a y e r J. M. : *Inorg. Chem*., **1997**, *36*, 2069 – 2078.
12. C o r m a A. , L a m b i e s V. , M e l o F. V. and P a l o u J. : *Anal. Quim*., **1980**, *76*, 304-310.
13. B a n e r j i K. K. : *J.C.S. Perkin 2*, **1973**, 435 – 437.
14. M a t h u r S. , G u p t a A. and B a n e r j i K. : *Ind. J. Chem.*, **1988**, *27A*, 581 – 583.
15. T o m p k i n s F. C. : *Trans. Faraday Soc*., **1943**, *39*, 280 – 287.
16. W i b e r g K. B. and S t e w a r t R. : *J. Am. Chem. Soc*., **1955**, *77*, 1786 – 1795.
17. S e n G u p t a K. K. , S e n P. K. and M u k h o p a d h y a y G. : *Trans. Met. Chem.*, **1993**, *18*, 369 – 371.
18. L e e D. G. and C h e n T. : *J. Org. Chem.*, **1991**, *56*, 5341 – 5345.
19. L e e D. G. and C h e n T. : *J. Am. Chem. Soc.,* **1993**, *115*, 11231 – 11236.
20. B r a u m a n n J. I. and P a n d e l l A. J. : *J. Am. Chem. Soc.*, **1970**, *92*, 329 – 335.
21. W i b e r g K. and F o x A. S. : *J. Am. Chem. Soc*., **1963**, *85*, 3487 – 3491.
22. S i m o y i R. H. , D e K e p p e r P. , E p s t e i n I. R. and K u s t i n K. :*Inorg. Chem*., **1986**, *25*, 538 – 542.
23. B h a t i a I., B a n e r j i K. K : *J.C.S. Perkin Trans. 2*, **1983**, 1577 – 1580.
24. V e n k a t a c h a l a p a t h y M. S. , R a m a s w a m y R. and U d u p a H. V .K. : *Bull. Acad. Pol. Scien. (Ser. Chim.)*, **1959**, *7*, 629 – 631.
25. V e n k a t a c h a l a p a t h y M. S. , R a m a s w a m y R. and U d u p a H. V .K : *Bull. Acad. Pol. Scien. (Ser. Chim.)*, **1958**, *6*, 487 – 489

26. H e i b a E. I. , D e s s a u R. M. and K o e h l W. J. :*J. Am. Chem. Soc.*, **1969**, *91*, 138 – 145.
27. H a n o t i e r J. , H a n o t i e r – B r i d o u x M. and R a d z e t z k y P. :*J.C.S. Perkin 2*, **1973**, *4*, 381 – 386.
28. A n d r u l i s P. ,. D e w a e r M. J. S , D i e t z R. and. H u n t R. L : *J. Am. Chem. Soc*., **1966**, *88*, 5473 – 5478

STUDIA UNIVERSITATIS BABEŞ-BOLYAI, CHEMIA, XLVI, 1-2, 2001

OPTIMAL CONTROL OF BRINE ELECTROLYSIS IN ION EXCHANGE MEMBRANE REACTORS

IMRE-LUCACI Á.

University "Babeş-Bolyai" of Cluj-Napoca, Faculty of Chemistry and Chemical Engineering, Department of Chemical Engineering, Arany János 11, 3400 Cluj-Napoca, Romania, email: aimre@chem.ubbcluj.ro

ABSTRACT. In an earlier work an optimal management of brine electrolysis plan was presented to minimize the electric energy costs by taking into account the different electric energy costs between day and night[1]. This is maintained by the national electric energy suppliers to compensate the different consumption demanding in the electric network system between day and night period of the day. For the brine electrolysis industry it is important to use this situation in its one advantage. The main way to do this is by varying the current load of the reactors between day/night time period in order to minimize the cost of electric energy.

In this paper, based on simulations using a mathematical model of an IEM (Ion Exchange Membrane) reactor, the optimal control of a brine electrolysis plant is presented, taking into account these possibilities.

By simulation, it is proved that Model Predictive Control (MPC) of the electrochemical reactors can be used to apply the results obtained by the optimization algorithm.

It is possible to estimate that the electric energy cost savings obtained by this way can be between 5 to 20%, depending by the ratio between day/night energy costs and the ratio between the current daily production and the nominal daily capacity of the plant.

INTRODUCTION

In an earlier work[1] the minimization of electric energy costs for a brine electrolysis plan equipped with ion exchange membrane (IEM) reactors was presented.

The main issue was to maintain the production level of the plant but operating at different current load thus to benefit as much it is possible by the different electric energy costs between day and night.

The optimization results (figure 1 and 2) showed us that a saving between 5-20% in electric energy costs could be obtained without diminishing the production level of the plant. This result could be implemented by using an efficient control system in order to maintain the quality of the products which could lead to a total annual saving of about 1 million $.

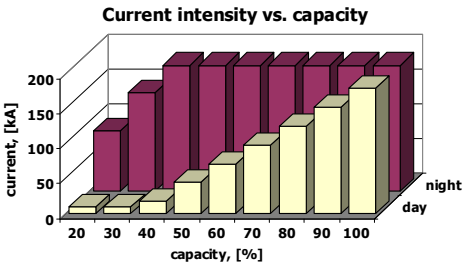

Figure 1. The results of the optimization.

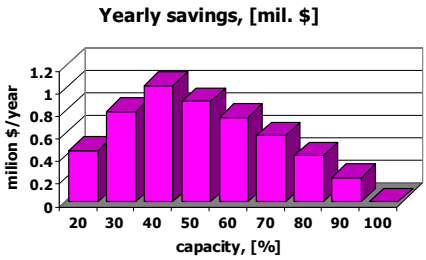

Figure 2. Yearly savings.

OPTIMAL CONTROL

The goal of optimal control of the IEM plant, minimizing the electric energy costs involved in the process can be reached by using an efficient control system in order to minimize the perturbing effect of a steep change in the cells current load.

The structure of the optimal control system of the IEM (Ion Exchange Membrane) plant includes two levels (figure 3):

- optimization level;
- control level.

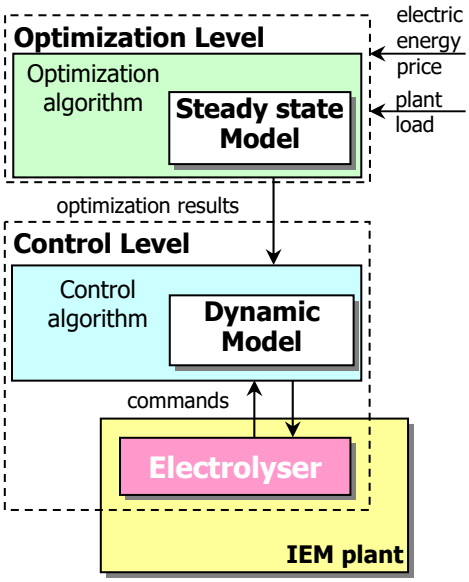

Figure 3. Optimal control system structure of the IEM plant.

The optimization level of the optimal control system includes the elements presented at the optimization section of this paper.

The goal of the control level of the optimal control system is to maintain the quality of the products between the specifications. By this we understand to preserve de NaOH concentration and the brine concentration at the outlet of the cell at their nominal values.

A minimal control structure in which we have 2 controlled variables (brine and NaOH concentration at cell outlet) and two manipulated variables (brine and caustic soda flow at cell inlet) can be selected [2, 3, 4].

This control structure can be performed by two main ways:

- SISO (Single input/Single Output) control structures using two PID controllers;
- MIMO (Multiple Inputs/Multiple Outputs) control structure based on Model Predictive Control (MPC).

For the SISO control structure the following control loops were selected:

loop 1: controlled variable: brine concentration at cell outlet
manipulated variable: brine inlet flow
loop 2: controlled variable: caustic soda concentration at cell outlet
manipulated variable: caustic soda inlet flow

Two PI controllers were used for these two loops. Controller tuning was made by simulation using the Ziegler-Nichols method. Parameters for these controllers are presented in table 1.

Table 1.
Controller parameters

Controller	Type	K_r	T_I [s]
1	PI	15	4500
2	PI	30	5200

For the MIMO control structure, using MPC, a dynamic model of the IEM reactor was used. This model is an analytical model and includes 14 differential and more than 65 nonlinear algebraic equations [2].

In the case of MPC of the membrane cell, the same controlled variables and manipulated variables were used and the optimal values for the internal parameters of the controller were determined by simulation as follows [10, 11]:

- model horizon $T = 14400$;
- control horizon $U = 2$;
- prediction horizon $V = 10$;
- weighting matrix for predicted errors $W_1 = [0.05\ 0.05]$;
- weighting matrix for control moves $W_2 = [1\ 1]$;
- sampling period $\Delta t = 1$ s.

The controlled variables were subject to the following constrain:

$$y_{min} \leq y(k+l|k) \leq y_{max}$$

where:

$y_{min} = 0$, [m^3/s]

$y_{max} = 2 \cdot y_{nom}$

y_{nom} - nominal flow for brine/caustic soda, [m^3/s].

For a comparison of the performances of the SISO and the MIMO control structures in the case of the optimal control of an IEM plant, simulations were used. The simulations were made in Matlab and SIMULINK computational environment (figure 4).

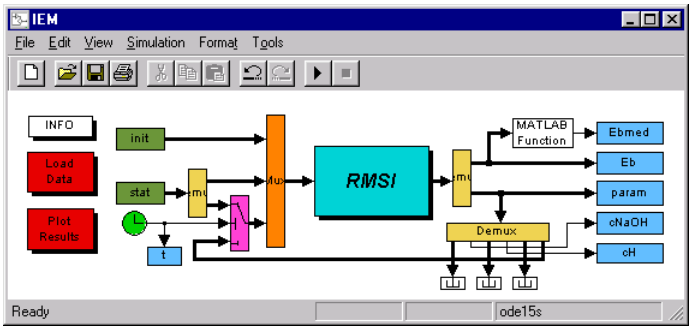

Figure 4. SIMULINK program for IEM reactor.

The simulations test how the control systems are working when the current load of the electrolyser suffers a steep change (according to the results obtained in the optimization level of the optimal control system).

The following results were obtained for a change in current load corresponding to a modification in the plant capacity from 70% to 50% from the nominal capacity of the plant.

In figure 5 we can observe that in the case of the SISO control structure the control is inefficient because the current load modification induces a perturbation which cannot been eliminated after a quite long period of time (more than 1 hour).

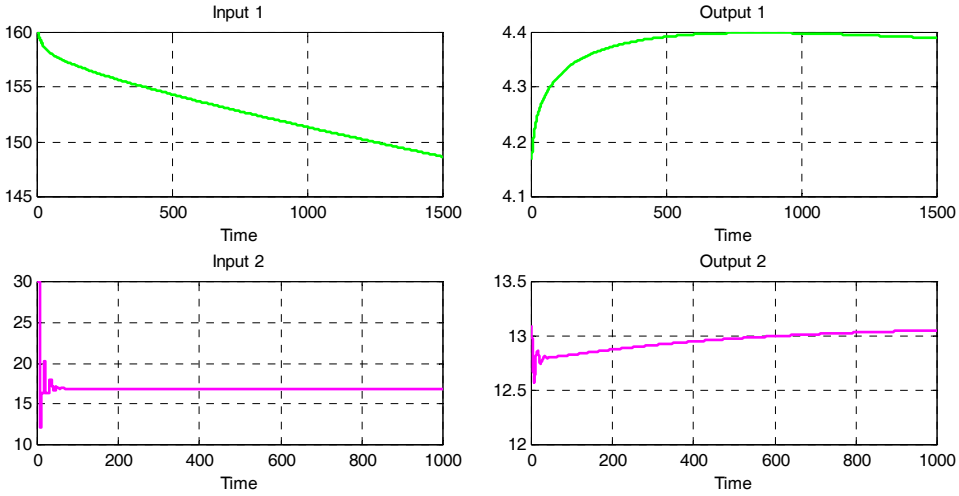

Figure 5. SISO control structure – simulated behavior.
Input 1 brine flow at the inlet of the cell, in [l/h]
Input 2 caustic soda flow at the inlet of the cell, in [l/h]
Output 1 brine concentration at the outlet of the cell, in [kmol/m^3]
Output 2 NaOH concentration at the outlet of the cell, in [kmol/m^3]

From the results presented in figure 6 we can observe that the MIMO structure has a much better performance than the SISO control structure. In less than 20-25 minutes the controlled variables return to their initial values.

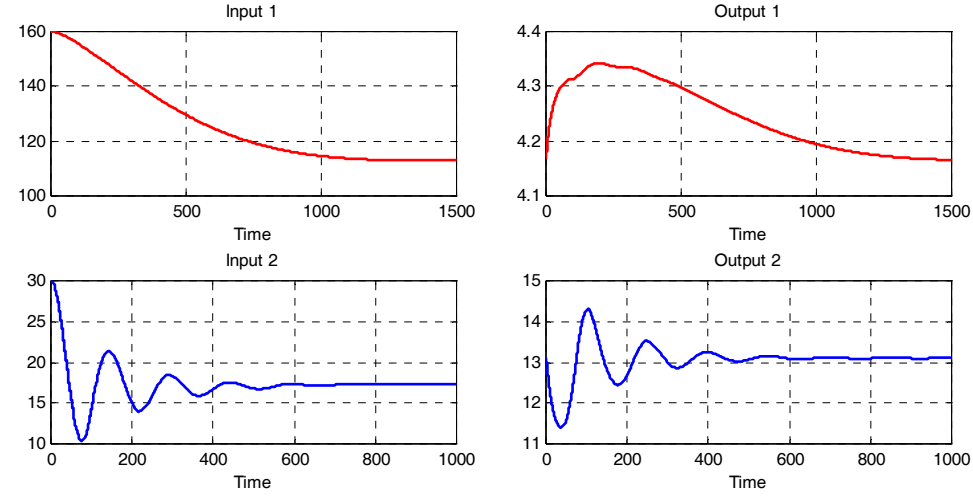

Figure 6. MIMO control structure – simulated behavior.
Input 1 brine flow at the inlet of the cell, in [l/h]
Input 2 caustic soda flow at the inlet of the cell, in [l/h]
Output 1 brine concentration at the outlet of the cell, in [kmol/m^3]
Output 2 NaOH concentration at the outlet of the cell, in [kmol/m^3]

CONCLUSIONS

The optimal control problem of an IEM plant was studied in the case of electric energy consumption costs minimization.

Taking into account that the price of electric energy is differentiated by the moment of the day, it is possible to use this to obtain important cost savings.

The results of the optimization proves that it is possible to obtain 5-20% electric energy cost savings, depending on the relative capacity at which the plant is operated at a given moment.

For the implementation of the optimization results two simple control structures were tested: the SISO and the MIMO control structures.

By means of simulation it was proved that a MIMO control structure could be more effective.

NOMENCLATURE

k, l	step index
T	model horizon in MPC
U	control horizon in MPC
V	prediction horizon in MPC
y	controlled variables
y_{max}	maximal value of the controlled variable
y_{min}	minimal value of the controlled variable
y_{nom}	nominal value of the controlled variable
W_1	weighting matrix for predicted errors in MPC
W_2	weighting matrix for control moves in MPC
Δt	sampling period in MPC

REFERENCES

1. A. Imre-Lucaci, Electric power consumption cost minimization in brine electrolysis by ion exchange membrane reactors, *Studia Universitatis Babes-Bolyai, Chemia*, 2001, 51-56
2. A. Imre-Lucaci, Modeling and control of brine electrolysis processes in amalgam cathode reactors and ion exchange membrane reactors, *PhD Thesis*, Univ. “Babes-Bolyai” Cluj-Napoca, Romania, 1999
3. Ş. Agachi, A. Imre-Lucaci, Control Strategies for Brine Electrolysis by Ion Exchange Membrane Cell Process, *Computer Aided Chemical Engineering*, **8**, Elsevier, 2000, 289-294
4. Ş. Agachi, A. Imre-Lucaci, Model predictive control of brine electrolysis by ion exchange membrane reactors, *14-th International Conference of Chemical and Process Engineering*, CHISA’2000, Praga, 2000

STUDIA UNIVERSITATIS BABEŞ-BOLYAI, CHEMIA, XLVI, 1-2, 2001

ELECTRIC POWER CONSUMPTION COST MINIMIZATION IN BRINE ELECTROLYSIS BY ION EXCHANGE MEMBRANE REACTORS

IMRE-LUCACI Á.

University "Babeş-Bolyai" of Cluj-Napoca, Faculty of Chemistry and Chemical Engineering, Department of Chemical Engineering, Arany János 11, 3400 Cluj-Napoca, Romania, email: aimre@chem.ubbcluj.ro

ABSTRACT. The brine electrolysis is one of the highest energy consuming industrial electrochemical process, especially electric energy. In many countries are different electric energy costs between day and night to compensate the different consumption demanding in the electric network system. For the brine electrolysis industry it is important to use this situation in its one advantage. There are two main ways to do this:

- by a different current load of the reactors between day/night time period;
- by using a different number of reactors in the day/night time period.

Each variant has positive and negative aspects.

In this paper, based on simulations using a mathematical model of an IEM (Ion Exchange Membrane) reactor, the optimization of a brine electrolysis plant is presented, taking into account both possibilities.

For this purpose, an earlier presented mathematical model of the IEM reactor was further developed to simulate an entire plant. The objective function of the optimization is the minimization of the electric current costs used in the electrochemical reactors and, in the same time, to preserve the level of daily capacity of products (chlorine, caustic soda, and hydrogen).

INTRODUCTION

Energy consumption, especially electric energy, is one of the most important parts of the costs implied in electrolysis processes [1,2].

In the ion exchange membrane process, beside the electrolysers, electric power is used also by the pumps and compressors to pipe the fluids in the process and by the agitators of the vessels and reactors [2].

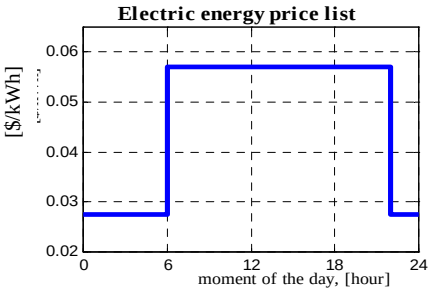

Figure 1. Electric energy price, (Romania, 2001).

Minimization of the electric power cost is worthwhile taking into account that the price of the electric energy is depending by the moment of the day (see figure 1). Thus during the day (from 6AM to 10PM) the price is high and during the night (from 10PM to 6AM) is low.

To initiate the optimization, in this case to minimize the electric power cost, we need to select the decision variables, to express the objective function and to select and set the constraints.

The optimization is considered taking into account two different approaches:

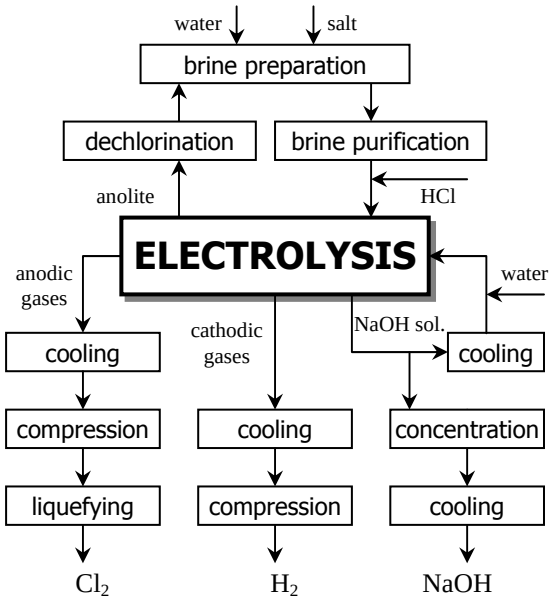

Figure 2. Block diagram of the IEM process.

plant is 150,000 t of NaOH.

The mathematical model of the electrolyser was presented in previous works [3, 4] and is based on mass, energy and voltage balance equations written for each cell [5-9]. This model includes more than 89 nonlinear algebraic equations. The plant model was developed using ChemCAD process simulation software [10].

This mathematical model was used to show the electric energy consumption taking into account the total current load of the plant and for the second approach, depending on the number of reactor rows in operation at a given time.

The electrical circuit structure for electric energy supply of the electrolysers is a combination of serial and parallel connections, depending by the power supply characteristics. In the case of the considered plant we have the following electrical

A. varying the current intensity at which the electrolysers are operated;
B. varying the number of electrolysers operated at a time.

The constraint considered in both cases is an equality constraint in which we fix the production of the plant, expressed in NaOH [t/day].

In both cases we need to express the electric power consumption in the plant depending on the production, current intensity and number of electrolysers. For this, we need to develop a mathematical model of the whole installation in which all fluid streams are included. The block diagram of the entire installation is presented in figure 2. The annual capacity of the

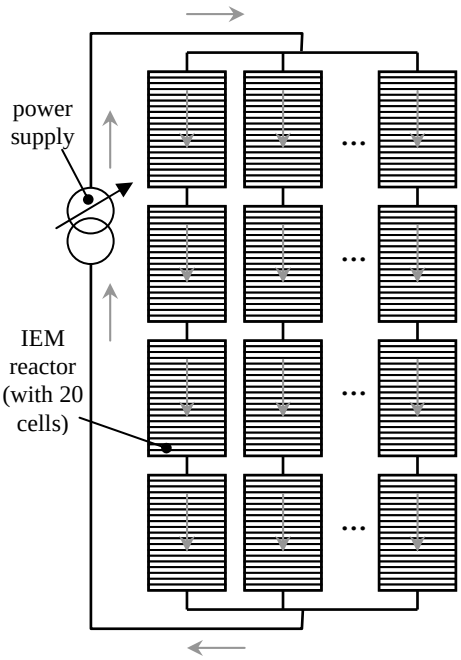

Figure 3. Electric circuit of the plant.

circuits (see figure 3). The power supply can provide electric energy at 240V and 180 KA. For the total capacity we have 80 electrolysers, each with 20 cells, structured in 20 rows (on which electrolysers are coupled in parallel) and with 4 electrolysers in each row (electrolysers coupled in a series).

OPTIMIZATION

To optimize the process, we need to describe through mathematical expressions the costs of electric energy consumed in the entire plant.

For the estimation of the electric energy consumed in the plant (excepting the electric energy consumed in the electrolysers) by pumps, compressors and other electrical operated installations, large sets of simulations in ChemCAD[10] were made. The obtained results were used, by means of regressions, to formulate the dependency expression depending on the capacity at which the whole plant is operated. The estimation of the electric energy consumed in the electrolysis phase was made by simulation based on the mathematical model of the electrolysers. Also, the simulations allow us to compute the voltage at which the electrochemical process takes place.

Case A

In this case the total current intensities at which the plant is operated during the day/night periods were considered as independent variables.

The objective function has the following mathematical expression:

$$\min_{I_{day},I_{night}} \quad f_{ob} = c_{day}\left(I_{day}\right)p_{day}t_{day} + c_{night}\left(I_{night}\right)p_{night}t_{night} \tag{1}$$

subject to the following constraint:

$$P_{h,day}t_{day} + P_{h,night}t_{night} = P_D \tag{2}$$

Case B

In this second case the numbers of reactor rows operated at a given time in the day/night period were considered independent variables.

The objective function is:

$$\min_{N_{day},N_{night}} \quad f_{ob} = c_{day}\left(N_{day}\right)p_{day}t_{day} + c_{night}\left(N_{night}\right)p_{night}t_{night} \tag{3}$$

subject to the same constraint (equation 2).

After all these considerations an optimization problem with two independent variables and with an equality constraint was obtained in both cases.

RESULTS

To solve the optimization problems, the Matlab function fmincon from Optimization Toolbox was used.

For case A, the searching domain of the solutions was

$$I_{day}, I_{night} \in [0.1\ldots1]\cdot I_{nom} \tag{4}$$

and for case B

$$N_{day}, N_{night} \in [5 \ldots N_{total}] \quad (5)$$

The optimization problem was solved for different values of operating capacities of the plant, starting from 20% of the nominal capacity (150,000 t/year of NaOH) till the nominal capacity. The obtained results were represented in the figures 4 and 5.

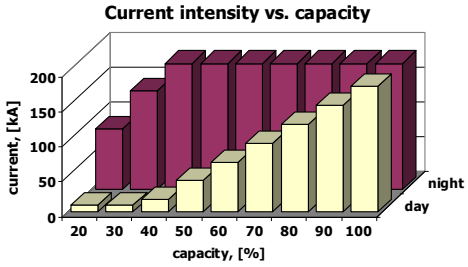

Figure 4. The results of the optimization for case A.

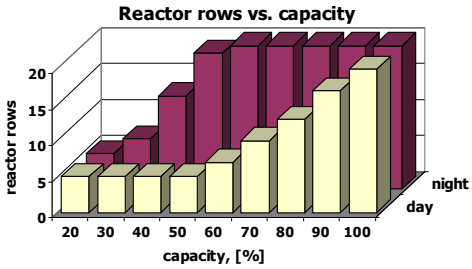

Figure 5. The results of the optimization for case B.

According to these results, the theoretical savings that we could achieve relative to normal operation (without taking into account the differentiated costs of the electric energy) can be observed from figures 6 and 7. The total savings (figure 8 and 9), in [$/year] show us that this problem can have an important economic impact.

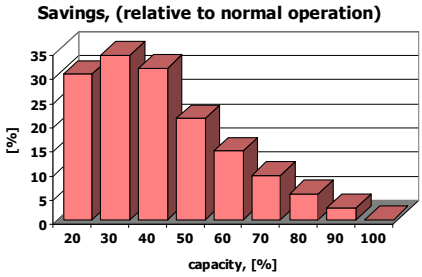

Figure 6. Relative savings in the case A.

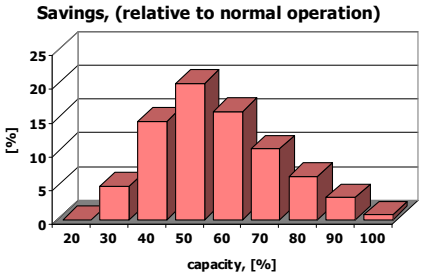

Figure 7. Relative savings in the case B.

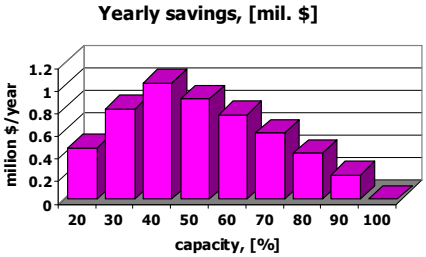

Figure 8. Yearly savings in the case A.

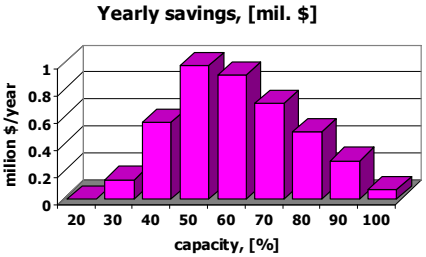

Figure 9. Yearly savings in the case B.

To benefit as much as possible from these economical advantages, we need to have an efficient control system of the electrolysers. This is important in both cases but especially in case A.

CONCLUSIONS

The optimization of an IEM plant was studied in the case of electric energy consumption costs minimization. Taking into account that the price of electric energy is differentiated by the moment of the day, it is possible to use this to obtain important cost savings. The results of the optimization proves that it is possible to obtain 5-20% electric energy cost savings, depending on the relative capacity at which runs the plant at a given moment. Also, the importance of an effective control system is emphasized to preserve the quality of the product during the practical implementation of the optimization results.

NOMENCLATURE

c_{day}	plant capacity during the day
c_{night}	plant capacity during the night
I_{day}	current intensity during the day, [A]
I_{night}	current intensity during the night, [A]
I_{nom}	nominal current intensity, [A]
$P_{h,day}$	production of NaOH during the day, [t/h]
$P_{h,night}$	production of NaOH during the night, [t/h]
P_D	production of NaOH, [t/day]
p_{day}	electric energy price during the day, p_{day}=0.058 [$/kWh]
p_{night}	electric energy price during the night, p_{night}=0.028 [$/kWh]
N_{day}	reactor rows operated during the day
N_{night}	reactor rows operated during the night
N_{total}	total number of reactor rows, N_{total}=20

REFERENCES

1. Delmas, F., Production of sodium hydroxide and chlorine by membrane electrolysis, *Rev. Electr. Electron.*, **3**, 1995, 21-24
2. A. Szép, F. Bandrabur, I. Mânea, Brine electrolysis by ion exchange membrane process, *Editura CERMI*, Iaşi, Romania, 1998
3. A. Imre, I. Bunea, Ş. Agachi, Using neural networks in modeling and optimization of the ion exchange membrane electrolyzers, Part I – Analitical model, *Stud. Univ. "Babeş-Bolyai"*, *Chem.*, **39**(1-2), 1994, 28-35

4. Ş. Agachi, I. Bunea, A. Imre, Using neural networks in modeling and optimization of the ion exchange membrane electrolyzers, Part II – Neural network model, *Stud. Univ. "Babeş-Bolyai"*, *Chem.*, **39**(1-2), 1994, 36-44
5. R.R. Chandran, D.T. Chin, Reactor analysis of a chlor-alkali membrane cell, *Electrochim. Acta*, **31**, 1986, 39-50
6. Pokhozhaev, S.J., Mathematical model of electrolysis, *Dokl. Akad. Nauk*, **332**(6), 1993, 690
7. H.S. Burney, Membrane Chlor-Alkali Process, in *Modern Aspects of Electrochemistry*, **24**, Plenum Press, New-York, 1993
8. Noaki, Y., Shiroki, H., Design and optimization of advanced membrane chlor-alkali electrolyzer, *Proc. Electrochem. Soc.*, **14**, 1999, 124-135
9. A. Imre-Lucaci, Modeling and control of brine electrolysis processes in amalgam cathode reactors and ion exchange membrane reactors, *PhD Thesis*, Univ. "Babeş-Bolyai" Cluj-Napoca, Romania, 1999
10. * * *, User Guide for ChemCAD 5, *Chemstations Inc*., 2001

STUDIA UNIVERSITATIS BABEŞ-BOLYAI, CHEMIA, XLVI, 1-2, 2001

ADSORPTION STUDIES OF CADMIUM FROM DILUTED SOLUTIONS

A.DUTA, I. BENGA, C. IOSIF, R. TICA

Transilvania University of Brasov, Chemistry Dept. I. Maniu 50, 2200 Brasov

ABSTRACT. The paper presents some results of the adsorption tests of cadmium from aqueous solutions on three different substrates. The optimised conditions of the process are identified and the adsorption parameters are calculated from the Langmuir plots. Considerations about the mechanism and efficiency of the process are done.

KEYWORDS: adsorption, ion exchange, cadmium, wastewater treatment.

1. INTRODUCTION

Ionic cadmium occurs in natural waters coming from wastewater insufficiently treated. Cadmium has a chemical structure closely the one of zinc and can replace it in the enzymes, leading to a decrease in their effect as catalysts. This is the reason why cadmium is considered toxic for living organisms, including humans. The first cadmium disease was registered in 1970 in Japan under the name “Itai-Itai”. Cadmium is a cumulative poison: at birth the concentration is null and by ageing the ions deposit in leaver and kidneys leading to disturbances in the calcium metabolism and to a weak bones structure, [1,2].

Normally, cadmium appears in very low concentrations (less than 1μg/L) but industrial pollution can increase this value. The toxic dose is considered by the Romanian standard at 5μg/L and by WHO at 3 μg/L, [3].

Water treatment for cadmium removal can be easily done – as for the other metal cations, [4, 5] – using the ion exchange process. This process is effective at medium concentrations but it must be carefully developed when very low ion concentrations are involved.

Considering the concentration at which cadmium is dangerous, the ion exchange process must be optimise for obtaining high efficiency. The paper studies the adsorption of cadmium ions on two different cation exchangers and one substrate of modified anion exchanger; the optimised adsorption conditions and the isotherms that allowed to make assumptions on the mechanism of the processes are presented.

2. EXPERIMENTAL

1. *Solutions*

- Solutions of cadmium nitrate with the concentration 10^{-3}….10^{-1} Eg/L were prepared using $Cd(NO_3)_2 \cdot 4H_2O$, 99.7% (Reactivul Romania) and bi- distilled water.
- Solutions of Ethylenediaminotetraacetic acid Disodium salt Dihydrate, $C_{10}H_{14}N_2Na_2O_8 \cdot 2H_2O$), Complexon III (Reanal Budapest, Hungary), as reactive for cadmium concentration identification.

- Solid solution of NaCl - Eriochrome Black T (Chemapol, Chech Rep.) as indicator.
- Buffer solution $NH_4OH – NH_4Cl$ (pH=9).

2. *adsorption substrates*:

Table 1.

Characteristics of the adsorption substrate

Name	Type	Exchange capacity [mE/g]	Prorsity	Manufacturer
C-100	Sulfonic cation exchanger, R-SO_3Na	2.5	Micro	VIROLITE Or. Victoria, Romania
CC-21	Carboxilate cation exchanger, R-COONa	10	Medium	
AT- VP	Surface modified anion exchanger*)	-		Laboratory

*) on the surface of the anion exchanger AT-14 there was adsorbed pyrocatechol violet (PV) from a 1% water solution, [6].

3. *Adsorption tests*

Experiments were done in a flask, by bringing in direct contact the metal solution and the substrate, at room temperature, under stirring. Concentration was evaluated before and after the process and the values were used for further calculations.

3. RESULTS AND DISCUSSIONS

Laboratory tests were done in order to optimise the adsorption conditions.

Previous studies, [7,8] proved that an adequate ratio: weight of substrate: volume of solution is 1: 10 considering the efficiency but also the technological parameters. In the same studies a contact time of 5 minutes was sufficient for the adsorption process of any transitional metal. This time was evaluated from the curve adsorption efficiency vs. contact time, at the point where any significant increase was no longer registered. In the case of cadmium, after 5 minutes of adsorption, the efficiency was higher than 90%, both for a 0.05 Eg/L and for a 0.005 Eg/L solution, on each of the ion exchangers that were investigated. Table 2 shows these results:

Table 2

Optimization of the adsorption time

No.	$C_I \times 10^3$[Eg/L]	$C_F \times 10^3$[Eg/L]	Time [min]	Efficiency [%]
1	49	2.4	1	95.1
		2.2	3	95.5
		0.48	5	99.02
2	4.98	0.153	1	96.93
		0.11	3	97.99
		0.064	5	98.71

Of course, in industrial conditions, of continuos flow, contact times lower than one minute are of no use, therefor our decision regarding 5 minute for the contact time is more the result of a technological approach.

Adsorption tests were done and, based on the results, the adsorption isotherms are plot as molar adsorption coefficient vs. equilibrium concentration, Fig. 1 and Fig.2.

The ion exchange process is a special type of chemical adsorption that is well described by the Langmuir equation, [9]. Still, Fig. 1 one doesn't revel the accurate shape of the Langmuir isotherm at the very low concentration when the process is under diffusion control.

The adsorption on AT-VP occurs as a reaction of forming the Cd - PV complex and is also a chemosorption. In this case, as in the previous, the adsorption conditions were well chosen and the saturation of the substrate was not reached.

Considering that in all cases the Langmuir equation describes well the process, the parameters χ_{max} and A were evaluated by representing the linear form of the isotherm:

$$\frac{c}{\chi} = \frac{1}{\chi_{max} A} + \frac{1}{\chi_{max}} c \qquad (1)$$

Based on the A value, the adsorption heat was evaluated:

$$\Delta H^{ads} = -RT \ln A \qquad (2)$$

Cadmium exists in water as cadmium hexa-hydrate, $[Cd(H_2O)_6]^{2+}$ which is an ion with high volume. The ion exchangers have a high number of adsorption points and the values of the maximum adsorption coefficients are consequently high. In the case of AT-VP, the much lower value could be a consequence of the distribution of the active centres on a reduced surface. One may drop this conclusion considering that PV has also a large volume but only one active end for complexation so that its adsorption could actually reduce the number of active centres on the surface.

Table 3

Adsorption characteristics of the cadmium ion on the investigated substrates

Substrate	C-100	CC-21	AT-VP
X_{max} [mg/g]	390.6	299.4	8.59
ΔH^{ads} [cal/moles]	-203.43	-363.13	-2445.12

The data presented in Table 3 indicate that the adsorption products are more stable in the case of the Cd-VP complexes and this may be considered a drawback if the regeneration of the substrate must also be consider.

The adsorption efficiency of the cadmium ion on the ion exchange substrates is very high over a wide equilibrium concentration range. However, at very low concentrations, the At-VP substrate proved to be more efficient. Changing the adsorption technological conditions (i.e. the ration substrate volume: solution volume and/or contact time) this substrate will increase its efficiency.

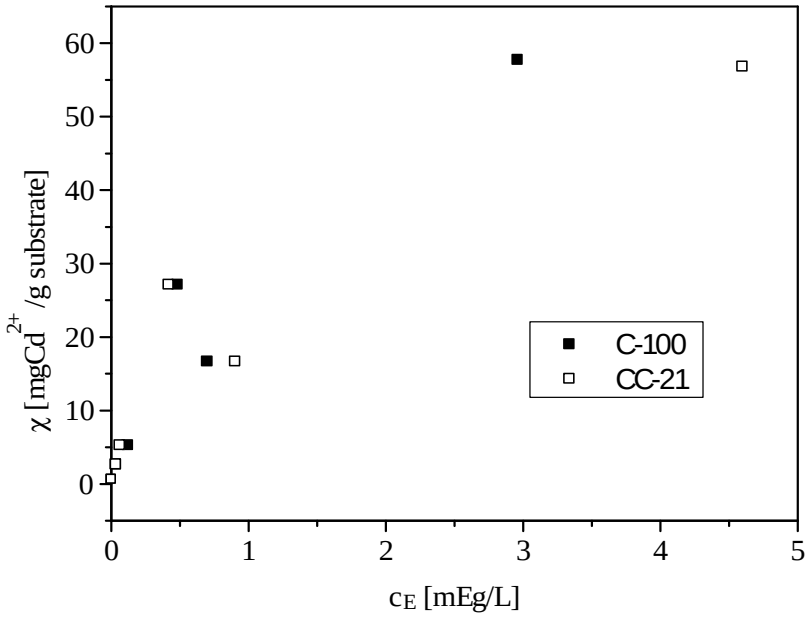

Fig. 1 Adsorption isotherms of the cadmium on ion exchangers

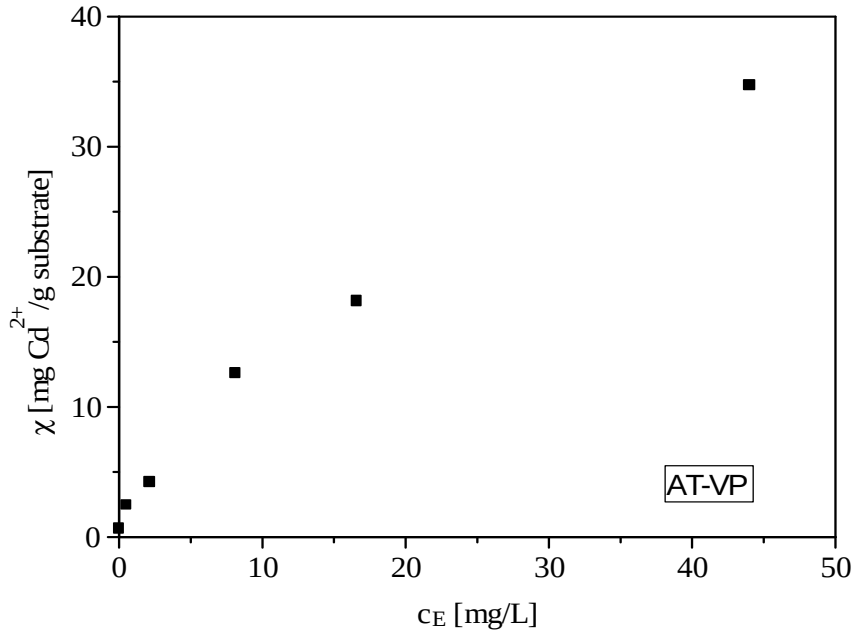

Fig. 2 Adsorption isotherm of the Cd^{2+} on the modified anionite

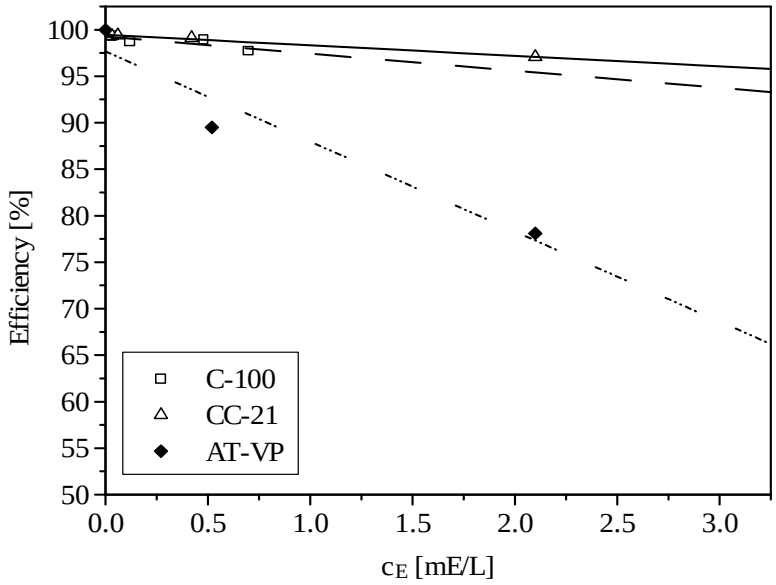

Fig. 3 Adsorption efficiency of cadmium ion

Previous studies were done using this adsorbent for advanced adsorption of other heavy metals. A comparative view is given in Table 4:

Table 4

Adsorption efficiency on AT-VP

C_i [Eg/L]	Efficiency [%]		
	Zn^{2+}	Cu^{2+}	Cd^{2+}
0.0001	39	72	-
0.001	36	18	100
0.01	7	12	78.1
0.1	3.5	5	58.5
Environment's pH	natural	natural	8-10

4. CONCLUSIONS

Ionic cadmium adsorption was tested on three substrates: two cation exchangers macro- respectively medium porous and a modified anion exchanger PV adsorbed onto its surface.

The adsorption isotherms, corresponding to the Langmuir equation described well the process, according to the theoretical premises of the chemosorption. The hydrated cadmium ion has a quite large volume and the adsorption on AT-VP was less efficient at medium concentrations but proved to be the most effective in very dilute solutions.

REFERENCES

1. Singhal, M., Maerali, H., Cadmium Toxicology, Marcel Dekker&Inc., New York, 1979
2. Paasivirta, J., Environmental Polutants, Analysis and toxicity, Lewis Publishers, Chelsea, 1991
3. Haiduc, I., Chimia Mediului Ambiant – Controlul Calității Apelor, Ed. Universității Babes-Bolyai, Cluj Napoca, 1996
4. Roques, H., Chemical Water Treatment, VCH Publishers Inc., New York, USA, 1996
5. Water Quality Association, Water Treatment Fundamentals, A Study Guide, USA, 1996
6. Duta, A., Tica, R., Perniu, D., Nanu, D., Coman, G., Modified Ion Exchanger Used in Advanced Adsorption of Transitional Cations, Fundamentals of Adsorption, Giens, France, Mai 1998
7. Tica, R., Costea, C., Duta, A., Draghici , C., Waste Water Treatment in Copper Metallurgy, Bul. Univ. "TRANSILVANIA"; Vol. XXXV (ISSN 1220 - 9414), 1993, pg. 91-96
8. Bucur, C., Dalbea, V., Giubelean, M., Duta, A., Investigații asupra substraturilor cu capacitate de reținere a ionilor de zinc din ape reziduale, Bul. Ştiințific al Acad. de Aviație "H. Coandă" (ISSN 1453 - 0139),Vol 5, 1996, pg. 65 –69
9. Myers, D., Surface, Interface and Colloids, VCH, New York ,1994

STUDIA UNIVERSITATIS BABEŞ-BOLYAI, CHEMIA, XLVI, 1-2, 2001

ALKYLATION OF TOLUENE WITH METHANOL OVER MCM-22 AND MCM-36

E. DUMITRIU[*], IOANA FECHETE[*], P. CAULLET[**], H. KESSLER[**], V. HULEA[*], X. BOURDON[**]

[*] *Laboratory of Catalysis, Technical University of Iasi, 71 D.Mangeron, Iasi-6600, Romania*
[**] *Laboratoire de Materiaux Mineraux, ENSCMu-UHA, Mulhouse, France*
Ioana Fechete – corresponding author. tel: +40-32-278-683;
fax: +40-32-271-311; e-mail: ifechete@ch.tuiasi.ro

ABSTRACT. MCM-36 materials were prepared by swelling the layered MCM-22 precursors with large organic molecules and then pillaring the resulting material with polymeric silica. The BET surface area of MCM-36 was 2.5 to 3 times higher than that of MCM-22. The catalytic activity and selectivity of both MCM-36 and MCM-22 were investigated in the gas-phase alkylation of toluene with methanol at reaction temperatures ranging from 498 to 673K. The methylation of toluene produces a mixture of xylenes as main products. The influence of reaction temperature, pulse number, and toluene/ methanol ratio upon the conversion of toluene and selectivities of the products were investigated. The superior catalytic performance of MCM-36 compared with MCM-22 for this reaction indicates that the open mesoporous structure can be successfully utilized to make acid sites of the layers accessible to large molecules.

1. Introduction

The gas phase alkylation of toluene with methanol over zeolite catalysts to xylenes was reported by Venuto in the early sixties [1]. This reaction could be of great interest to industry as a potential source of p- and o-xylene provided that the loss of methanol in side reactions, clearly seen from the literature data [2], is eliminated or, at least, greatly suppressed.

Various zeolites, such as ZSM-5, REY, SAPOs were tested as catalysts in the alkylation of toluene with methanol [3-5]. It now accepted that the alkylation reaction proceeds through a Rideal-mechanism [6], where the Bronsted acid sites are the active centers and the reaction intermediates are carbenium ions [1].

The previous studies showed that the selectivity in this reaction is strongly influenced by the acidity strength and the pore size of the catalyst. Thus, medium pore zeolites such as M-ZSM-5 (M = B, Cr, Fe), which possess only weak and medium acid sites, are very selective towards p-xylene in the alkylation of toluene with methanol [7].

In our study two new zeolites, MCM-22 and MCM-36, have been tested as catalysts in gas phase alkylation of toluene with methanol. Zeolite MCM-22 combines the properties of 10 MR (membered rings) and 12 MR porosity [8]. The narrow acces to the 12 MR channels through the 10 MR openings, seriously hampering the diffusion of bulky molecules. To avoid this limitation, the pillared

zeolite MCM-36 has been developed [9-10]. This material combines the benefits of microporous, crystalline zeolite layers with those of the pillared mesoporous structures. Due to this doubly porous structure, an increased accessibility of parts of the crystalline surface, a high thermal stability, and a large sorption capacity, these materials are promising catalysts for the conversion of hydrocarbons, especially in reactions involving larger, bulkier molecules [11].

2. Experimental

MCM-22 and MCM-36 were synthesised according the methode reported elsewhere [12]. The materials were characterized by various methods: XRD (Philips PW 1800 diffractometer and STOE STADI-P,CuK_{α}), nitrogen adsorption (Micromeritics ASAP 2100, sample activation at 523K for 18h), scanning electron microscopy (SEM, PHILIPS XL,30).

The catalytic reactions using toluene and methanol (high purity reagents) were run in a pulse type microreactor containing 30 mg of catalyst with particle size 0.25-0.43 mm. The microreactor consisted in a stainless steel tube (o.d. 6 mm, i.d. 3.5 mm and length 80 mm) with catalyst particles packed between quartz plugs. Prior to reaction, the catalyst was activated under airflow at 500°C for 3h, followed by cooling to the reaction temperature under nitrogen flow (26 ml/min, 140 kPa). Samples of 1.0 μl of the reagents were injected at constant temperature and the reaction products were analyzed using an on-line GC equipped with FI detector.

3. Results and discussion

3.1. Characterization of the catalysts. The first data concerning the synthesis of MCM-22 have been reported by the scientists from Mobil in 1990 [13]. The structure of MCM-22 has been shown to consist of layers linked together along the *c*-axis by oxygen bridges and contains two independent pore systems [14-15]. Within the layers are two-dimensional sinusoidal 10-M ring channels, and between two adjacent layers are 12-M ring supercages (~ 0.71 x 0.71 x 1.82 nm) communicating with each other through 10-M ring apertures.

The unusual structure of zeolite MCM-22 is formed from a layered precursor designated as an MCM-22(P) [13], which is able to condensate the silanol groups present on the layer surfaces by calcination, and leading to the formation of the 3D structure shown in Figure 1.

The pillared zeolite MCM-36 can be prepared from the same MCM-22(P) starting materials, using large molecules, such as cethyltrimethylammonium chloride (CTMAC) and polymeric silica (Figure 1).

We have synthesized a MCM-22(P) samples with SiO_2/Al_2O_3 ratio of 100. The diffraction pattern of this material agrees well with those previously reported [16](Figure 2a). The calcined sample gives sharper reflections than as-synthesized samples, as shown in Figure 2b, and the (001) reflection characteristic to the layered structure of MCM-22(P) disappears. The high crystallinity and phase purity of the MCM-22 zeolite could be considered as prove for the quality of its precursor.

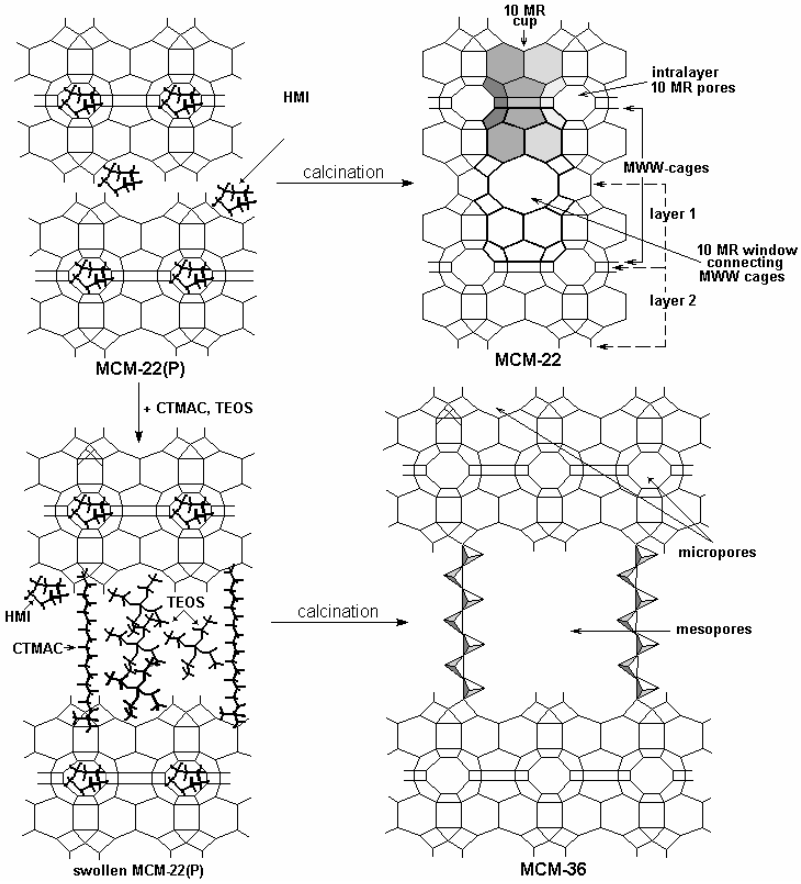

Figure 1. Schematic representation of MCM-22(P), MCM-22 and MCM-36 structures.

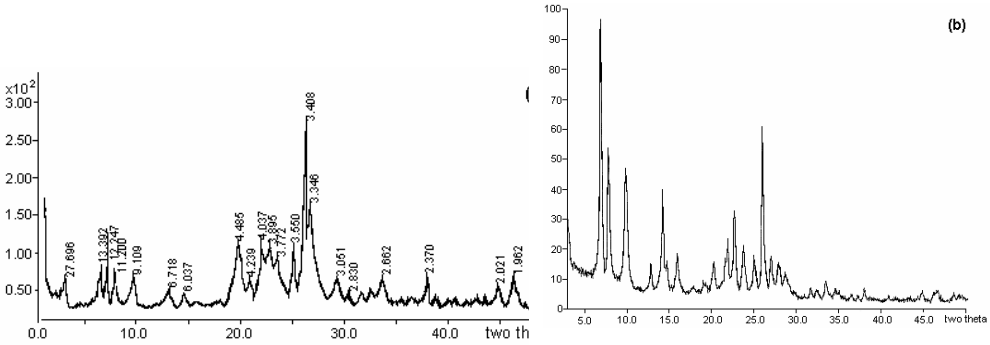

Figure 2. Powder XRD patterns of the (a) MCM-22(P) sample and (b) the calcined sample (MCM-22) synthesized from the mixture with SiO_2/Al_2O_3 molar ratio of 100.

MCM-36 material was prepared by swelling the layered MCM-22 precursor with large molecules of CTMAC and then pillaring the resulting material with polymeric silica. As known, in the MCM-36 phase, the polymeric silica as pillars is formed during the hydrolysis and condensation of silicates from tetraethylorthosilicate. The hydrolysis reaction replaces the ethoxy groups with hydroxyl groups. In the next stage, the condensation reactions involving the silanol groups produce siloxane bonds, leading initially to oligomeric and polymeric structures.

Depending on the conditions, the final structures of the polymeric SiO_2 can be formed as nearly linear polymeric structures or three-dimensional branched structures.

The XRD pattern of the MCM-36 sample is shown in Figure 3. All peaks observed correspond perfectly to those of the MCM-36 material reported previously [12].

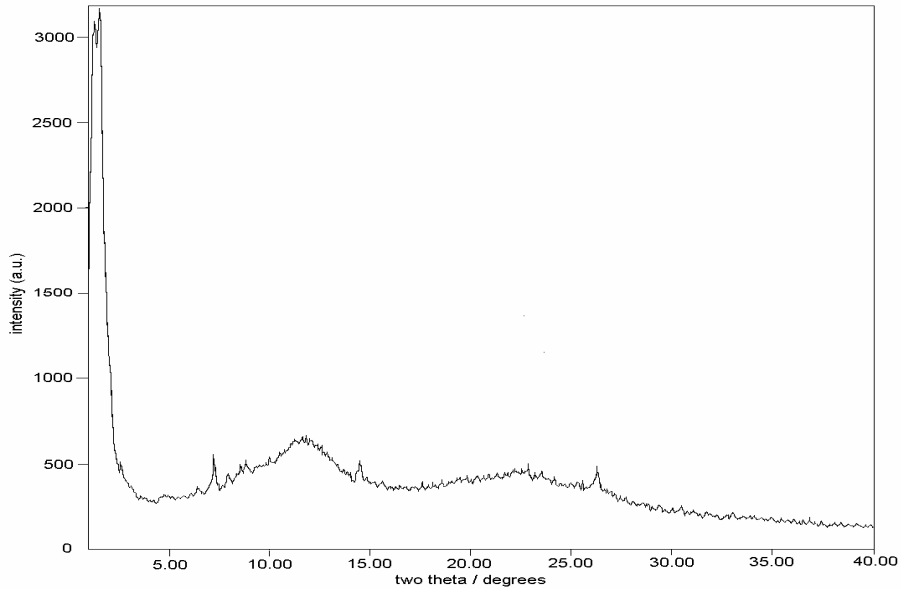

Figure 3. Powder X-ray diffraction pattern of MCM-36.

Compared with the pattern of MCM-22(P) in Figure 2, the characteristic 002 plane reflection at $2\theta \sim 6.6°$ disappears upon pillaring. On the other hand, an intense low-angle reflection appears at 2θ between 1 and 2°, which corresponds to a *d*-spacing of 5.9 nm. This represents the new *c*-parameter of the unit cell. The *d*-value includes both the *c*-parameter of the unit cell of MCM-22 and the spacing distance between the layers of MCM-36. Therefore, the distance between two layers in MCM-36 can be calculated by subtracting the thickness of the layer (*c*-parameter of MCM-22 is equal to 2.51 nm [14]. The values for the sample obtained suggest an average interlayer distance of 3.4 nm.

The morphologies of crystals, determined by SEM, are mostly platelets of approximately 2μm diameter and 0.1-0.2 thickness bunched into 4-5 μm particles.

The textural properties of the calcined MCM-22 and MCM-36 samples were measured by nitrogen adsorption. The pure MCM-22 sample gives a specific surface area (S_t) of 465 $m^2\ g^{-1}$ and a total pore volume of 0.28 cm^3g^{-1} which are typical for this type of zeolite [17]. The higher specific area of MCM-36 (807 m^2g^{-1}) sample than that of MCM-22 (465 $m^2\ g^{-1}$), approximately twice, without doubt demonstrates that MCM-36 does not have pore system as MCM-22.

The external surface areas were estimated by using *t*-plots. Therefore, for MCM-22 zeolite resulted that the micropores are dominant (V_{micro} = 0.12 cm^3g^{-1}), while for the pillared structure of MCM-36 the mesopores are dominant (V_{meso} = 0.497 cm^3g^{-1}). The external surface area, S_{ext}, in the larger mesopores was estimated at about 76 m^2g^{-1}. From a tubular model as $4V_{meso}/(S_t-S_{ext})$, the average mesopore size of approximately 3nm was estimated, and this value satisfactorily agrees with XRD data.

3.2. Alkylation of toluene with methanol. During the alkylation reaction of toluene with methanol on acid catalysts, para- and ortho-xylene are mainly formed, especially at low levels of conversion. Moreover, besides the primary alkylation, consecutive reactions, such as xylenes isomerization and toluene polyalkylation giving trimethylbenzenes (TMB) and tetramethylbenzenes (TeMB) can also occur. In the case of zeolites, the competition between these reactions and the selectivity of the alkylation process depends of both reaction conditions (temperature, contact time, pressure, etc) and textural properties of catalyst (shape and size of pores, external surface area, etc).

3.2.1. Effect of reaction temperature. Table 1 summarizes the main results of the alkylation reaction between toluene and methanol over MCM-22 and MCM-36, obtained in the range temperature of 498-673K, with a toluene/methanol molar ratio = 1.

Table 1.

The main results of the alkylation of toluene with methanol

	MCM-22			MCM-36		
Reaction temperature, K	498	548	673	498	548	673
Toluene conversion, %mol	22.4	32.5	46.5	7.9	19.1	35.7
Alkylated products, %mol						
Xylenes	18.13	22.49	30.3	7.35	13.42	24.06
Trimethylbenzenes	4.24	9.67	14.57	0.58	3.87	9.36
Tetramethylbenzenes	1.03	5.23	8.56	0.43	1.87	6.45
Xylenes selectivity, %						
p-xylene	72.14	52.69	30.39	28.29	29.95	29.42
m-xylene	16.76	26.76	50.51	17.55	22.20	43.51
o-xylene	11.08	20.54	19.09	54.14	47.83	27.01
TMBs selectivity, %						
1,3,5-TMB	0	6.10	20.59	0	0	19.01
1,2,4-TMB	97.40	86.24	66.98	55.17	59.68	69.01
1,2,3-TMB	2.60	7.65	12.42	44.83	40.32	11.96

These data lead to the following remarks:

(i) As expected, the conversion of toluene increases with the reaction temperature. Compared to MCM-22, MCM-36 showed a lower toluene conversion for all temperatures.

(ii) A high selectivity for the ring alkylation of toluene towards xylenes was obtained under our reaction conditions. However, over both zeolites, the amount of polyalkylated products, such as TMB and TeMB, increases when the reaction temperature increases.

(iii) The reaction temperature affects the distribution of xylene isomers. But, this distribution also depends on the catalyst type. Thus, at low temperature, MCM-22 catalyst showed a high para-selectivity (more than 70% p-xylene in the mixture of xylenes), while MCM-36 leads to o-xylene as major isomer (about 55%). An important amount of p-xylene (amount 30%) was also obtained over MCM-36.It is known that the para- and ortho-isomers are the primary products of the electrophile substitution reactions.

The difference in behavior of MCM-22 and MCM-36 can be explained taking into account their porosity. The selectivity seems to be a consequence of product shape selectivity. Thus, in the case of MCM-22, the 10 MR windows of about 0.52 nm in diameter cause great hindrances in the diffusion of o-xylene isomer, while p-xylene, a "linear" molecule, can easily passed through these windows. On the contrary, the difusion of products is not influenced by the mesopores of MCM-36, and the xylene isomer composition is similar to those of non-shape-selective catalysts. The ortho-rich product distribution is obtained as required by the principles of aromatic electrophilic substitution [18].

As can be seen from table 1 data, the increase in the reaction temperature leads to a decrease of both o- and p-xylene, while m-xylene increases and at 673K the xylene distribution becomes close to the thermodynamic equilibrium (50% m-xylene, 25% p-xylene and 25% o-xylene). At a high reaction temperature, the primary products p- and o-xylene are involved into the rearrangement reaction towards m-xylene, the highest thermodynamic stable dimethylbenzene isomer.

3.2.2. Effect of the toluene/methanol ratio. Some catalytic tests were performed over MCM-22 and MCM-36 at 498K, using three toluene/methanol initial ratio. It can be seen from Table 2 that with increase in toluene/methanol ratio, the selectivity to xylene increases too. An equimolar reagent ratio leads to the highest conversion of toluene.

Table 2.

The effect of toluene/methanol ratio on the catalysts behavior

	MCM-22			MCM-36		
Toluene/methanol, molar ratio	0.5	1	2	0.5	1	2
Toluene conversion, %mol	22.6	30.2	13.7	10.7	12.1	7.3
Xylene selectivity, %	67.4	77.5	81.1	86.7	90.0	90.3
TMB selectivity, %	32.6	22.5	18.9	13.3	10.0	90.7

3.2.3. Effect of time on stream. Generally, the activity and selectivity of zeolites change during the reactions of organic compounds, because of progressive blocking of acid sites and pores by coke. The rate of the coke formation strongly depends on the strength of acid sites and the pore size of catalyst. As can be seen from Figure 4, the catalytic activity of medium pore MCM-22, expressed in term of toluene conversion progressively decreases when the number of pulses increases. The selectivity to xylene decreases too. On the contrary, large pore MCM-36 shows a very high stability to coking. Thus, toluene conversion, xylenes and TMBs selectivities remain almost unchanged after 40 pulses (Figure 4).

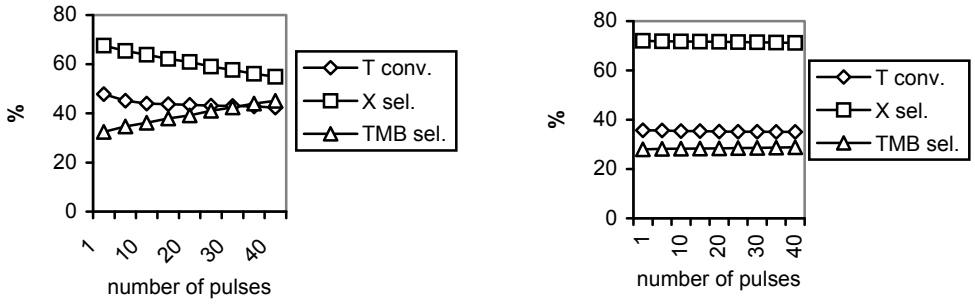

Figure 4. Variation of toluene conversion (T cov.), xylene selectivity (X sel.) and TMB selectivity (TMB sel.) as function of the number of pulses for MCM-22 and MCM-36, at 673K.

4. Conclusion

As stated before, both MCM-22 and MCM-36 zeolites are active catalysts in the gas phase alkylation of toluene with methanol. At a low reaction temperature, the selectivity to p- and o-xylene, the primary alkylation products, was very high over tested catalysts. Large pore MCM-36 is more stable to coking that medium pore MCM-22.

REFERENCES

1. P.B. Venuto, L.A. Hamilton, P.S. Landis and J.J. Wise, *J. Catal.,* 5,1966,484
2. W.W. Kaeding, C. Chu, L.B. Young, B. Weinstein and S.A. Butter, *J.Catal.,* 67,1981,159
3. N.Y. Chen, *J. Catal.,* 114,1988,17
4. E. Dumitriu, S. Oprea and K.Yousef, *Rev. Chim. (Bucuresti*), 35,1984,906
5. A.M. Prakash, S.V.V. Chilukuri, R.P. Bagwe, S. Ashtekar and D.K. Chakrabarty, *Microp. Mater*., 6,1996,89
6. F.M. Bautista, J.M. Campelo, A. Garcia, D. Luna, J.M. Marina and A.A. Romero, *React. Kinet. Catal. Lett.,* 57(1),1996,61

7. R.B. Borade, A.B. Halgeri and T.S.P. Prasada Rao, *7-th Int.Zeolites Conf.,* Tokyo, 1986, p.851
8. M. Leonowicz, J.A. Lawton, S.L. Lawton and M.K. Rubin, *Science,* 264A,1994,1910
9. C.T.-W Chu, C.T. Kresge, W.J. Roth, K.G. Simmons and J.C. Vartuli, *US Patent* 5 292 698, 1994
10. C.T. Kresge, W.J. Roth, K.G. Simmons and J.C. Vartuli, *US Patent* 5 229 341,1993
11. C.T. Chu, H. Altaf, A.M.J. Huss, C.T. Kresge and W.J. Roth, *US Patent* No.5 258 569,1993
12 Y.J. He, G.S. Nivarthy, F. Eder, K. Seshan and J.A. Lercher, *Microp. Mesop. Mat*., 25,1998, 207
13. M.K . Rubin and P. Chu*, US Patent,* 4 954 325, 1990
14. M.E. Leonowicz, J.A. Lawton, S.L. Lawton and M.K. Rubin, *Science*, 264,1994,1910
S.L. Lawton, M.E. Leonowicz, R.D. Partidge, P. Chu, M.K. Rubin, *Microp. Mesop*. *Mat.* 23,1998,109
S.L. Lawton, A.S. Fung, G.J. Kennedy, L.B. Alemany, C.D. Chang, G. Hatzikos, D.N. Lissy, M.K. Rubin, H.K.C. Timken, S. Steurnagel and D.E. Wossner, *J.Phys. Chem*., 100, 1996,3788
17. P. Wu, T. Komatsu and T. Yashima, *Microp. Mesop. Mat*., 22,1998,343
18. J. Kaspi, D. D.Montogmeri and G.A. Olah, *J.Org.Chem*., 43,1978,3137

STUDIA UNIVERSITATIS BABEŞ-BOLYAI, CHEMIA, XLVI, 1-2, 2001

SYNTHESIS OF NEW ALKYLANTS WITH ESTERS OF N-(m-AMINOBENZOYL)-L-ASPARAGIC ACID SUPPORT

CRISTINA BĂSU[1], V. ŞUNEL[2], M. POPA[3], LĂCRĂMIOARA BĂLĂIȚĂ-RUSU[3] and DOINA SÎRBU[2]

1. *S.C. Antibiotice S.A., Research & Development Department, 1 Valea Lupului Street, 6600 Iaşi, Romania*
2. *University "Al. I. Cuza" Iaşi, Faculty of Chemistry, Departament of Organic Chemistry, Bd. Carol I, 6600 Iaşi, Romania*
3. *"Ghe. Asachi" Technical University Iaşi, Bd. D. Mangeron, 71 A, 6600 Iaşi, Romania*

ABSTRACT. In order to obtain new antitumoural compounds acting as alkylating agents, some esters were synthesized, to the α- and β-carboxylic group of the N-(m-aminobenzoyl)-L-asparagic acid. These esters were then converted into di-(β-hydroxyethyl)-amino compounds by condensation with ethylene oxide in a diluted acetic acid medium. By substituting the chlorine for the hydroxylic groups the corresponding di-(β-chloroethyl)-amino compounds were obtained.

INTRODUCTION

Among the chemotherapics used for treatment of some malign tumors the N-mustards are particularly important. Their cytostatic activity is exerted by an alkylating effect of blocking some components participating to the anarchical growth of cancerous cells.

The great disadvantage of treating some cancerous forms with N-mustards consists in their high toxicity due to the low selectivity toward the neoplastic cells, the normal cells, especially those with a higher rate of growth, being also affected.

In some extent disadvantage may be overcome by grafting the bis-(β-chloroethyl)-amino group on certain compounds characteristics of the organism. By means of such derivatives the transport of N-mustards till the cell level is facilitated, the toxicity lowered and the cytostatic action improved by their either antagonistic or antimetabolitic effects.

Several investigators [1-4] have synthesized N-mustards of such structure some of that are already used in the cancer chemotherapy.

In previous paper [5-14] a series of new N-mustards containing the active group grafted on derivatives of N-(m-nitrobenzoyl)-DL-asparagine N-(m-aminobenzoyl)-DL-asparagic acid and on N-(m-aminobenzoyl)-DL-asparagine were synthesized.

EXPERIMENTAL

a) N-(m-aminobenzoyl)-L-asparagic acid (II)

10 g (3.035 mole) of N-(m-nitrobenzoyl)-L-asparagic acid Was solved in ammonia. The obtained solution was introduced in a reaction vessel provided with a reflux refrigerator, through which penetrate a glass tube till bottom of the vessel. Through the glass tube was introduced a sulphuretted hydrogen current for 1 hour,

heating the flask for 10 minutes at intervals of 3 hours. In last half of hour, the introduction of sulphuretted hydrogen was made to a continuous heating. After cooling, one part of sulphur obtain from reaction was removed by filtration. The filtrate was shake twice in a separator with 60 ml carbon sulphide for removing the sulphur remained in a reaction mixture. After removing the carbon sulphide, the aqueous level was treated in a flask, under stirring, with a concentrated HCl solution, to pH 2.5-3, when a yellowish precipitate was separated. It was filtered off, dried and recrystallized from boiling water. The solid product melting at 156-158^{o}C was thus obtained in a 70 % yield.

Analyses for $C_{11}H_{12}N_2O_5$:

	C, %	H,%	N,%
Calculated:	52.38	4.76	11.11
Found:	52.99	4.12	11.37

IR (KBr): 2800-3200 $cm^{-1}\nu_{NH\ amidic}$, 1660 $cm^{-1}\nu_{C=O}$, 1540v $cm^{-1}\nu_{\ amide\ -II\ band}$ and 860 cm^{-1} disubstituted aromatic ring.

b) Dimethylic ester of N-(m-aminobenzoyl)-L-asparagic acid (III)

5 g of m-aminobenzoyl-L-asparagic acid was treated with 40 ml methylic alcohol previously saturated with gaseous hydrogen chloride at 0 ^{o}C. The obtained mixture was allowed to stay at the room temperature till the whole quantity of m-aminobenzoyl-L-aspa-ragic acid passed into solution. The hydrogen chloride and the excess of methylic alcohol was removed by evaporation at low temperature of 40-45 ^{o}C. The remaining residue was diluted with water till a volume of 250 ml and then neutralized at pH 8 with a concentrated ammonia solution. The dimethylic ester of m-aminobenzoyl-L-asparagic acid was thus precipitated quantitatively. After filtration, drying and recrystallization from ethylic alcohol the pure compound was obtained as needle crystals melting at 124-126 ^{o}C.

Analyses for $C_{13}H_{16}N_2O_5$:

	C, %	H,%	N,%
Calculated:	55.71	5.71	10.00
Found:	56.08	5.25	9.77

IR (KBr): 2800-3300 $cm^{-1}\nu_{NH\ amidic}$, 1640 $cm^{-1}\nu_{C=O}$, 1240 $cm^{-1}\nu_{\ C-O-C}$ and 840 cm^{-1} disubstituted aromatic ring.

c) Diethylic ester of N-(m-aminobenzoyl)-L-asparagic acid (IV)

It was prepared similarly (*vide supra*) from 5 g (0.02 mole) of I and 40 ml ethylic alcohol 96 % previously saturated with gaseous hydrogen cloride at 0 ^{o}C, recrystallized from ethanol. The pure product was obtained as a white powder, yield 62.4%, m.p. 144-146^{o}C.

Analyses for $C_{15}H_{20}N_2O_5$:

	C, %	H,%	N,%
Calculated:	58.44	6.50	9.09
Found:	58.61	7.01	9.57

IR (KBr): 2950-3300 $cm^{-1}\nu_{NH\ amidic}$, 1645 $cm^{-1}\nu_{C=O}$, 1235 $cm^{-1}\nu_{\ C\text{-}O\text{-}C}$ and 830 cm^{-1} disubstituted aromatic ring.

d) Dimethylic ester of m-[bis-(β-hydroxyethyl)-amino]-benzoyl-L-asparagic acid (V)

To a suspension of 2,27 g III in 50 ml water amd 40 ml glacial acetic acid, 5,5 ml ethylene oxide were added. After maintaining for 24 hours at the room temperature the obtained mixture was neutralized with sodium bicarbonate. An oil product thus separates which was extracted in ethyl acetate and washed with water in a separating funnel. The obtained product was dried on anhydrous sodium sulphate, filtered and the excess of ethyl acetate distilled under vacuum. Cooling separated a light yellow solid product. After repeated washings with anhydrous ethylic ether and drying it was melted at 66-68 ^{o}C.

Analyses for $C_{17}H_{27}N_2O_7$:

	C, %	H,%	N,%
Calculated:	54.98	7.28	7.55
Found:	55.22	7.11	7.87

IR (KBr): 3000-3400 $cm^{-1}\nu_{OH}$, 1705 $cm^{-1}\nu_{C=O}$, 1300 $cm^{-1}\nu_{\ C\text{-}N}$,1230 $cm^{-1}\nu_{\ C\text{-}O\text{-}C}$, 1050 $cm^{-1}\nu_{\ C\text{-}OH}$ and 825 cm^{-1} disubstituted aromatic ring.

e) Diethylic ester of m-[bis-(β-hydroxyethyl)-amino]-benzoyl-L-asparagic acid (VI)

It was obtained from 2,5 g IV and 7,5 ml ethylene oxide in 50 ml water and 40 ml glacial acetic acid according to a procedure described upper.

The final product that melts at 72-74 ^{0}C is light yellow. Yield 57.8 %.

Analyses for $C_{19}H_{29}N_2O_7$:

	C, %	H,%	N,%
Calculated:	57.43	7.30	7.05
Found:	57.83	7.02	7.66

IR (KBr): 2800-3400 $cm^{-1}\nu_{OH}$, 1730 $cm^{-1}\nu_{C=O}$, 1335 $cm^{-1}\nu_{\ C\text{-}N}$,1205 $cm^{-1}\nu_{\ C\text{-}O\text{-}C}$, 1070 $cm^{-1}\nu_{\ C\text{-}OH}$ and 835 cm^{-1} disubstituted aromatic ring.

f) Dimethylic ester of m-[bis-(β-chloroethyl)-amino]-benzoyl-L-asparagic acid (VII)

A suspension of 2,3 g compound V in 25 ml anhydrous chloroform was treated with 10 g thionyl chloride. After refluxing the obtained mixture on a bath for 3 hours a homogeneous solution was formed. The solvent as well as the excess of thionyl chloride were removed by vacuum distillation and the remained resinous product was solved in anhydrous benzene. After drying on anhydrous sodium sulphate, filtration and benzene distillation under vacuum a colorless crystalline product melting at 35-37 ^{o}C was obtained.

Analyses for $C_{17}H_{25}Cl_2N_2O_5$:

	C, %	H, %	Cl, %	N, %
Calculated:	50.00	6.13	17.40	6.86
Found:	50.23	6.54	17.91	6.32

IR (KBr): 3300 $cm^{-1}\nu_{NH}$, 1720 $cm^{-1}\nu_{C=O}$, 1540 $cm^{-1}\nu_{\ amide\ -II\ band,}$ 1330 $cm^{-1}\nu_{\ C\text{-}N}$, 1210 $cm^{-1}\nu_{\ C\text{-}O\text{-}C}$, 750 $cm^{-1}\nu_{\ C\text{-}Cl}$ and 830 cm^{-1} disubstituted aromatic ring.

g) Diethylic ester of m-[bis-(β-chloroethyl)-amino]-benzoyl-L-asparagic acid (VIII)

I was prepared similarly started from 2,5 g compound VI and 10 g thionyl chloride in 30 ml anhydrous chloroform. The final product was melted at 37-40 ^{o}C.

Analyses for $C_{19}H_{27}Cl_2N_2O_5$:

	C, %	H, %	Cl, %	N, %
Calculated:	52.53	6.22	16.85	6.45
Found:	52.05	6.69	17.10	6.22

IR (KBr): 3330 cm$^{-1}\nu_{NH}$, 1735 cm$^{-1}\nu_{C=O}$, 1535 cm$^{-1}\nu_{\text{amide –II band}}$,1340 cm$^{-1}\nu_{\text{C-N}}$, 1205 cm$^{-1}\nu_{\text{C-O-C}}$, 720 cm$^{-1}\nu_{\text{C-Cl}}$ and 840 cm^{-1} disubstituted aromatic ring.

RESULTS AND DISCUSSION

In the present paper two N-mustards with di-(β-chloroethyl)-amino group grafted on a dipeptide, namely on the dimethylic ester of m-aminobenzoyl-L-asparagic acid or diethylic ester of m-aminobenzoyl-L-asparagic acid, respectively, were synthesized.

Firstly, N-(m-aminobenzoyl)-L-asparagic acid (II) was synthesized by reducing the N-(m-nitrobenzoyl)-L-asparagic acid (I) with sulphuretted hydrogen current:

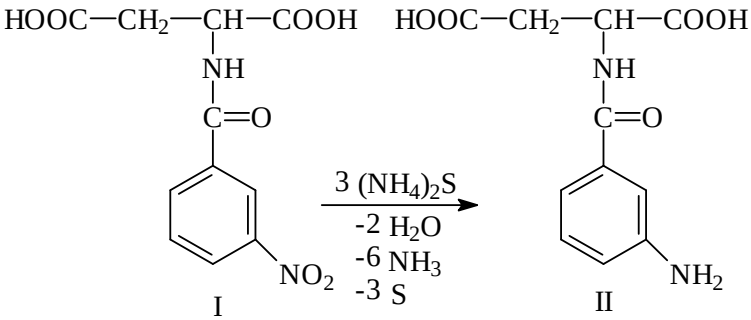

I II

The esters (III,IV) were obtained by treating the acid (II) with excess of alcohol saturated previously with gaseous hydrogen chloride:

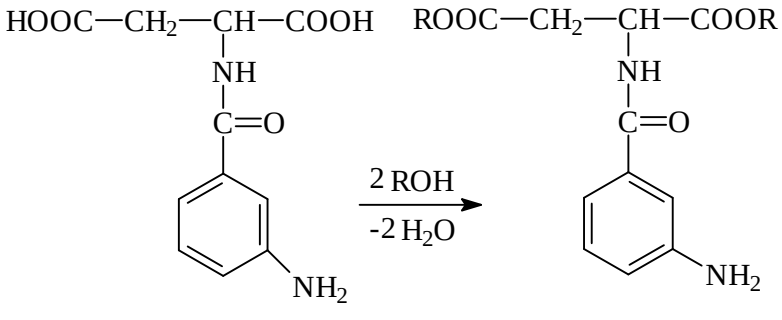

II III,IV

In order to transform the amino into bis-(β-chloroethyl)-amino group, the corresponding bis-(β-hydroxyethyl)-amino intermediates (V,VI) were prepared by treating the amino compounds (III,IV) with ethylene oxide in diluted acetic acid medium:

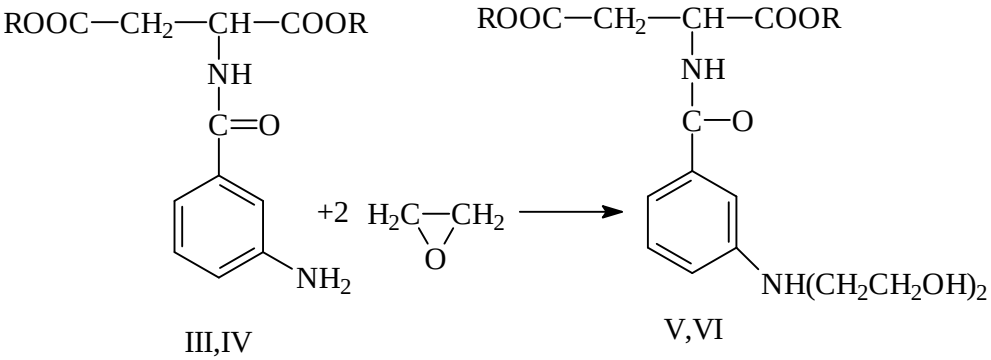

III,IV V,VI

By substituting the chlorine for hydroxylic group in the bis-(β-hydroxyethylic)-amino compounds the corresponding bis-(β-chloroethylic)-amino compounds were obtained. In this connection, the chlorination of the esters of m-[bis-(β-hydroxyethylic)-amino]-benzoyl-L-asparagic acid (V,VI) was carried out by means of thionyl chloride.

By treating the compounds (V,VI) with an excess of thionyl chloride in chloroformic solution, followed by refluxing on a water bath for 3 hours, solving in anhydrous benzene and removing the excess of the benzene, the final products (VII,VIII) were obtained:

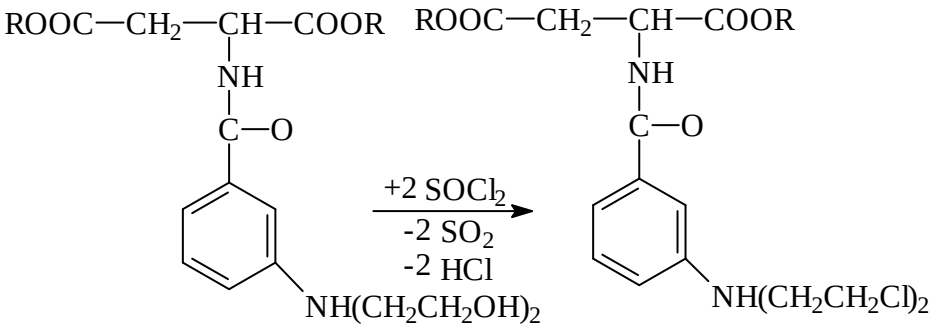

V,VI VII,VIII

CONCLUZII

Two new N-mustards, derivatives of the m-aminobenzoyl-L-asparagic acid were synthesized by chlorinating the m-[bis-(β-hydroxyethyl)-amino]-benzoyl-L-asparagic acid with thionyl chloride.

Most of the bands occurring in the spectra of the synthesized compounds were explained, the molecular structures determined by chemical methods being thus confirmed.

REFERENCES

1. Friedlos, F., Denny, W.A., Palmer, B.D., Springer, C.J., J. Med. Chem., **40**, 1997, p. 1270
2. Lee, M., Garbiras, B.J., Synth. Commun., **24**, 1994, p. 3129
3. Lyttle, M., Satyam, A., Bauer, K., Caldwell, C., J. Med. Chem., **40**, 1997, p.1134
4. Roux, Ch., Modro, A.M., Modro, T.A., J. Chem. Res. Synop., **3**, 1997, p.100
5. Şunel,V., Apostolescu, M., Budeanu, C.H., Dăneț, D., Rev. Chimie (Bucureşti), **33**, nr. 12, 1982, p. 1099
6. Şunel, V., Ciugureanu, C., Budeanu, C.H., Antohe, N., Popoa, M., Rev. Chimie (Bucureşti), **39**, nr. 7, 1988, p. 577
7. Şunel, V., Cecal, A., Şoldea, C., Asandei, N., Rev. Roumaine de Chimie, **40**, nr. 7-8, 1995, p. 763
8. Şunel, V., Cecal, A., Bull. Inst. Polit. Iaşi, s.II c., **36**, nr. 3-4, 1990, p. 57
9. Şunel, V., Ciugureanu, C., Ungureanu, M., Rev. Medico-Chirurgicală (Iaşi), **97**, nr. 2, 1993, p. 273
10. Şunel, V., Băsu, C., Şoldea, C., Sîrbu, D., An. Şt. Univ. "Al. I. Cuza" (Iaşi), s. I c, **6**, 1998, p. 35
11. Şunel, V., Băsu, C., An. Şt. Univ. "Al. I. Cuza" (Iaşi), s. I c, **7**, 1999, p. 111
12. Şoldea, C., Şunel,V., Comp. Rend. Acad. Bulg. Sci., **48**, nr. 9, 1995, p. 67
13. Şunel, V., Ciovică, S., Asandei, N., Cellulose Chem. Technol., **29**, nr.4,1995, p.411
14. Şunel, V., Popa, M., Popa, A., Şoldea, C., Cellulose Chem. Technol., **34**, nr. 2, 2000, p.216

STUDIA UNIVERSITATIS BABEŞ-BOLYAI, CHEMIA, XLVI, 1-2, 2001

THE SYNTHESIS OF ALLYLIC SPIRODIOLS USING ORGANOCERIUM REAGENTS

DOINA SIRBU[1]*, VALERIU SUNEL[1], MARCEL POPA[2], CRISTINA BASU[3]

[1]Chemistry Department, "Al.I.Cuza" University of Iasi,
Bd. Carol I, 11, 6600 Iasi, Romania;
[2]The "Ghe. Asachi" Technical University, Iasi;
[3]S.C. Antibiotice S.A., Iasi, Romania;
**tel: + 47 032 201278, e-mail: dsirbu@uaic.ro*

ABSTRACT. The organocerium reagents were successfully used to perform the 1,2-addition reactions to carbonyl groups of the α,β-unsaturated spirodiketones. Thus, using phenylcerium (II) chloride and thienylcerium (II) chloride, we have prepared the allylic diols 1,6-dithienylspiro[4,4]nona-2,7-diene-1,6-diol (**3**) and 1,6-diphenylspiro[4,4]nona-2,7-diene-1,6-diol (**4**) in yield 85% and 45% respectively. In addition, we have obtained 6-hydroxy-6-phenylspiro[4,4]nona-2,7-dien-1-one (**5**) in 25% yield.

INTRODUCTION

The stereochemical features and chiroptical properties of substituted spirane systems have been the focus of several studies. In this context, successful chiral resolutions of those systems have been reported[1-6]. The use of the rigid framework of spiranes for stereocontrol of pharmacophoric groups in bioorganic molecules, or the use of appropriately substituted spiranes as chiral auxiliaries, have received little attention. The enantiomers of *cis/cis*-spiro[4,4]nonan-1,6-diols, however, have been investigated for their ability to induce stereoselectivity in metal hydride reductions of phenyl alkyl ketones[7], and in the hydroformilation of styrene[8]. Simple symmetrical systems such as the spiro[4,4]nonane system have been studied in connection with their C_2-symmetry and chiroptical properties[1,3,6,9].

RESULTS AND DISCUSSIONS

We have initiated work on the preparation and palladium mediated transformations of cyclospiranes. In a previous paper[10], we reported results from studies on substitutions and stereoselectivities in reactions in the spiro[4,4]nona-2,7-diene-1,6-dione[11]. We have extended our investigations on the substitutions in the same spirane, being primarily interested in substitutions next to the spirocenter, in the α,α'-positions. This is a difficult task, due to the stereohindrance created by the spirocenter.

A very good approach for preparation of α,α'-substituted spiranes was to use organo-cerium reagents. It is known that using organolitium reagents and cerium (III) halides we can prepare organocerium reagents.[12] The last ones have been found to be extremely useful in organic synthesis, reacting with α,β-unsaturated carbonyl compounds to give 1,2-addition products (allylic alcohols) in good to high yields.

We used initially a simple organolithium compound, BuLi, to find the reaction conditions for preparation of $BuCeCl_2$ and for the 1,2-addition to the spiro[4,4]nona-2,7-diene-1,6-dione (**1**) (Scheme 1). The first step was to carefully dry $CeCl_3$ heptahydrate, and then to prepare the organocerium reagent. The reaction of $BuCeCl_2$ with the spirodiketone (**1**) took place in 1 h and we obtained, after purification, 85% of 1,6-dibutyl-spiro[4,4]nona-2,7-diene-1,6-diol (**2**). The structural assignment of the signals of the product was made using the ^1H and ^{13}C NMR spectra.

Scheme 1:

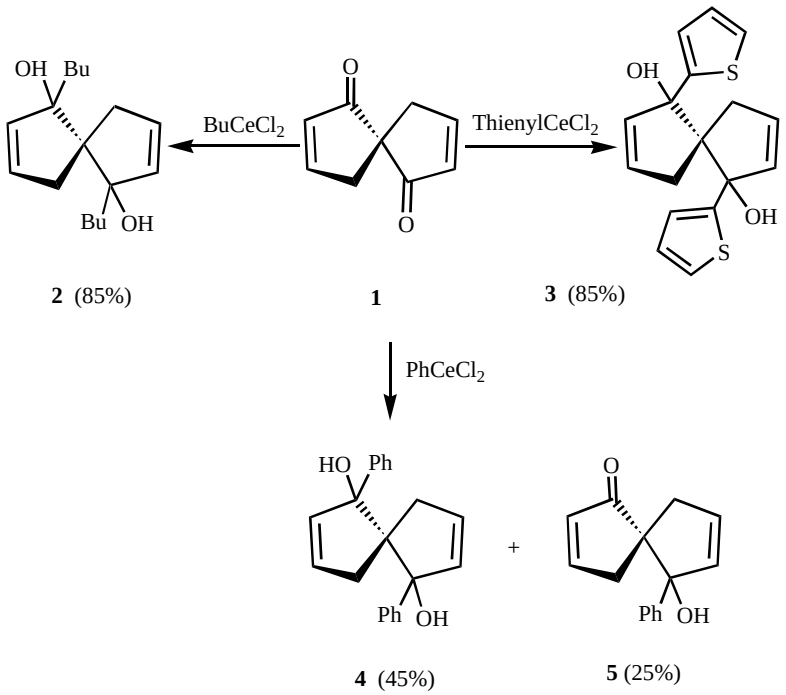

2 (85%) **1** **3** (85%)

4 (45%) **5** (25%)

Our goal was to introduce in the α,α'-positions thienyl and phenyl substituents. Our target molecules were 1,6-bis(thienyl)-spiro[4,4]nona-2,7-diene-1,6-diol (**3**) and 1,6-diphenyl-spiro[4,4]nona-2,7-diene-1,6-diol (**4**) (Scheme 1). Following the same procedure and reactions conditions similar with the ones we used for our test reaction, we have obtained the products **3** and **4** in yield 85% and 45% respectively. In the case of phenylceriumchloride we have obtained also 25% of the mono-addition product: 6-hydroxy-6-phenylspiro[4,4]nona-2,7-dien-1-one (**5**). This result showed that the reaction with phenylceriumchloride occures slower and the stereohindrance at the α-carbon is bigger, when we have already introduced a phenyl substituent. The correct assignment of the signals of the products was made using ^1H and ^{13}C NMR spectroscopy. We have also used IR, elemental analysis and HRMS, and they were all in accordance with the structures presented for the products **2-5**.

CONCLUSIONS

We have successfully used organocerium derivatives to perform the 1,2-addition to the carbonyl groups from the α,β-unsaturated spirodiketones. The procedure was relatively simple and the reactions time was short. The new products 1,6-bis(thienyl)-spiro[4,4]nona-2,7-diene-1,6-diol (**3**) and 1,6-diphenyl-spiro[4,4]nona-2,7-diene-1,6-diol (**4**) were obtained in in yield 85% and 45% respectively. In addition, we have obtained 6-hydroxy-6-phenylspiro[4,4]nona-2,7-dien-1-one (**5**) in 25% yield. The structures of all the products were in accordance with the NMR, IR and HRMS spectra.

EXPERIMENTAL

^{1}H NMR spectra were recorded in $CDCl_3$ at 200 MHz with Bruker DPX 200. The ^{13}C spectra were recorded in $CDCl_3$ at 50 MHz. Chemical shifts are reported in ppm using residual $CHCl_3$ (7.24 ppm) and $CDCl_3$ (77.00 ppm) as references. The mass spectra under electron impact conditions (EI) were recorded at 70 eV ionizing potential; methane was used for chemical ionization (CI). The spectra are presented as *m/z* (% rel. int.).

General procedure for preparation of organocerium reagents: Cerium (III) chloride heptahydrate (*ca*. 20 g) was placed in a round-bottomed flask connected to a dry ice-trap. The flask was evacuated and heated to 100 °C for 2 h. The resulting opaque solid was then heated *in vacuo,* at 140 °C for 4-5 h. While the flask was still hot, argon gas was introduced, after which the flask was cooled in an ice bath. THF (10 ml / g $CeCl_3$) was added with vigorous stirring. The ice bath was removed and the suspension was stirred well for 2 h or more (o.n.) under argon at room temperature. The flask was cooled to -78 °C and an organolithium compound (1.5 eqv.) was added with a syringe. Stirring for 0.5-2 h at the same temperature, or a somewhat higher temperature (-40 to -20 °C), results in the formation of a yellow or red suspension, which was ready for use.

1,6-Dibutylspiro[4,4]nona-2,7-diene-1,6-diol (2): With the method described above, we have prepared $BuCeCl_2$. To the suspension of this organocerium reagent, cooled at –78 °C, a solution of spirodiketone **1** (0.5 g, 3.37 mmol) in dry THF was added. After 1 h at the same temperature, the reaction was completed (follow TLC). Concentrated aq. ammonium chloride was added to the reaction mixture and the resulting solution was filtered through Celite. The filtrate was extracted with ethyl acetate (2x) and the resulting organic layers were dried over $MgSO_4$. The solvent was removed *in vacuo*, and the product was purified by flash chromatography, using hexane: ethyl acetate, 6 : 1 as eluent. We have obtained 0.75 g (85%) of pure product as a white solid, having m.p. 72 °C (from EtOAc/hexane). Found: C, 77.49; H, 10.84. Calc. for $C_{17}H_{28}O_2$: C, 77.27, H, 10.60. HRMS: *M* 264.2077. Calc. for $C_{17}H_{28}O_2$: 264.2089. ^{1}H NMR (200 MHz): δ 0.9 (t, 6H,

CH_3), 1.25 (m, 6H, CH_2), 1.55 (m, 4H, CH_2), 1.85 (m, 4H, CH_2), 2.75 (d, 2H, CH_2), 3.2 (s, 2H, OH), 5.9 (m, 4H, CH=). ^{13}C NMR δ 14 (CH_2), 24 (CH_2), 27 (CH_2), 38 (CH_2), 42 (CH_2), 61 (C), 88 (CHOH), 133 (CH=), 137 (CH=). IR (film) ν cm^{-1}: 3450 (br.), 3000, 1350. MS(EI): *m/z* 264 (M^+, 6), 246 (100), 228 (10), 203 (26), 189 (60), 161 (62), 133 (29), 117 (26), 105 (25), 91 (34), 85 (28), 57 (39), 41 (32).

1.6-Dithienylspiro[4,4]nona-2,7-diene-1,6-diol (3): The thienyllitium reagent was prepared by adding BuLi (10.11 ml sol 1.6 M in hexane, 16.2 mmol) to a solution of thiophene (1.77 ml, 21.6 mmol) in dry THF (10 ml), cooled to 0 °C. The mixture was allowed to warm up to room temperature and stirred for another 0.5 h. Then, the flask was cooled at -78 °C and the solution containing thienyllitium was added over the $CeCl_3$ suspension in THF, precooled at -78 °C. The resulting mixture, containing the thienylcerium reagent was stirred at this temperature for 1 h, before the spiro[4,4]nona-2,7-diene-1,6-dione (**1**) (1 g, 6.75 mmol) in dry THF (10 ml) was added. The resulting brown mixture was stirred for another hour at -78 °C, when TLC monitoring showed the reaction to be completed. Concentrated aq. ammonium chloride was added to the reaction mixture and the resulting solution was filtered through Celite. The filtrate was extracted with ethyl acetate (2x), the resulting organic layers were dried ($MgSO_4$), the solvent was removed *in vacuo* and the product was purified by flash chromatography, using hexane: ethyl acetate 4 : 1 as eluent. 1.7 g (80%) of an yellow oil was obtained. HRMS: *M* 316.0599. Calc. for $C_{17}H_{16}O_2S_2$: 316.0597. ^{1}H NMR (200 MHz): δ 2.05 (d, 1H, CH_2), 2.3 (d, 1H, CH_2), 2.55 (d, 1H, CH_2), 2.8 (s, 1H, OH), 3.6 (d, 1H, CH_2), 3.8 (s, 1H, OH), 5.8 (m, 2H, CH=), 5.95 (s, 1H, CH=), 6.1 (d, 1H, CH=), 6.2 (m, 1H, CH=), 6.75 (t, 1H, CH=), 6.9 (m, 2H, CH=), 7.05 (d, 1H, CHS), 7.2 (d, 1H, CHS). ^{13}C NMR δ 43 (CH_2), 44 (CH_2), 60 (C), 81 (d, CHOH), 123, 123.5, 124, 125.5, 125.8, 126, 130, 136, 137, 139 (CH=), 153, 154 (CS). IR (film) ν cm^{-1}: 3450, 3000, 2940, 1420. MS(EI): *m/z* 316 (M^+, 3), 299 (20), 298 (100), 280 (18), 247 (6), 187 (91), 172 (21), 153 (28), 147 (25), 111 (65), 97 (9), 77 (9), 45 (9), 39 (16).

1,6-Diphenylspiro[4,4]nona-2,7-diene-1,6-diol (4) was prepared using the procedure described above for compound **3**. 3.2 g (8.6 mmol) of $CeCl_3{\cdot}7H_2O$ were dried, dissolved in THF (30 ml), then phenyllithium (5.37 ml sol 1.6 M in THF, 8.6 mmol) was added. To the $PhCeCl_2$ suspension, cooled at -78 °C, a solution of diketone **1** (424 mg, 2.86 mmol) dissolved in THF (5 ml) was added. The reaction mixture was stirred at the same temperature for 1 h. After work up, the product was purified by flash chromatography, eluting with hexane : EtOAc, 4 : 1. The pure product was a yellow crystalline solid having m.p. 126-128 °C (CH_2Cl_2); yield 392 mg (45%). Found: C, 83.07; H, 6.78. Calc. for $C_{21}H_{20}O_2$: C, 82.89; H, 6.57. HRMS *M*: 304.1482. Calc. for $C_{21}H_{20}O_2$: 304.1485. ^{1}H NMR (200 MHz): δ 1.95 (d, *J* 17 Hz, 2 H, CH_2), 2.50 (d, *J* 17 Hz, 2 H, CH_2), 4.25 (s, 2 H, OH), 5.79-5.85 (m, 2 H, CH=), 5.89-5.96 (m, 2 H, CH=), 7.25-7.45 (m, 8 H, Ph), 7.65 (d, *J* 9 Hz, 2 H, Ph). ^{13}C NMR δ 44.8 (CH_2), 63.0 (C), 90.8 (CHOH), 127.0, 127.6, 129.5, 143.5 (Ph), 133.9, 137.5 (CH=). IR (film) ν cm^{-1}: 3460, 2980, 2900, 1450. MS(EI): *m/z* 304 (M^+, 1), 287 (24), 286 (100), 268 (10), 181 (87), 166 (23), 141 (14), 115 (16), 105 (62), 77 (28).

6-Hydroxy-6-phenylspiro[4,4]nona-2,7-dien-1-one (5) was obtained together with product **4** and the products were separated by flash chromatography. Pale yellow crystalline material with m.p. 120-122 °C ($CDCl_3$); yield 162 mg (25%). Found: C, 79.89; H, 6.34. Calc. for $C_{15}H_{14}O_2$: C, 79.64; H, 6.19. HRMS: *M* 226.0988. Calc. for $C_{15}H_{14}O_2$: 226.0993. ^{1}H NMR (200 MHz): δ 2.15-2.28 (doublet of multiplets, 1 H, CH_2), 2.35-2.46 (doublet of multiplets, 2 H, CH_2), 2.89-2.98 (doublet of multiplets, 1 H, CH_2), 4.40 (s, 1 H, OH), 5.91-5.99 (m, 1 H, CH=), 6.10-6.15 (m, 1 H, CH=), 6.19-6.24 (m, 1 H, CH=), 7.22-7.39 (m, 5 H, Ph), 7.46-7.51 (m, 1 H, CH=). ^{13}C NMR δ 42.9 (CH_2), 44.5 (CH_2), 60.0 (C), 89.4 (CPh), 125.7, 127.4, 128.1, 142.5 (Ph), 132.45, 132.48, 137.4, 164.5 (CH=), 213.2 (CO). IR (film) ν cm^{-1}: 3400, 2900, 1680. MS(EI): *m/z* 226 (M^+, 62), 208 (13), 179 (13), 165 (11), 144 (11), 128 (14), 121 (100), 105 (72), 77 (18), 55 (26), 51 (28), 39 (22), 28 (20).

REFERENCES

1. Gerlach, H., Muller W., *Helv. Chim. Acta*, **1972**, *55*, 2277.
2. Gerlach, H., *Helv. Chim. Acta*, **1968**, *51*, 1587.
3. Cram, D.J., Van Duuren, B.L., *J. Am. Chem. Soc.*, **1955**, *77*, 3576.
4. Hardegger, E., Maeder, E., Semarne, H.M., Cram, D.J., *J. Am. Chem. Soc.*, **1959**, *81*, 2729.
5. Harada, N., Ai, T., Uda, H., *J. Chem. Soc., Chem. Commun*., **1982**, 232.
6. Sumiyoshi, M., Kuritani, H., Shingu, K., *J. Chem. Soc., Chem. Commun*., **1977**, 812.
7. Srivastava, N., Mital, A., Kumar., *J. Chem. Soc., Chem. Commun*., **1992**, 493.
8. Jiang, Y., Xue, S., Li, Z., Deng, J., Mi, A., Chan, A.C., *Tetrahedron: Asymmetry*, **1998**, *9*, 3185.
9. Nieman, J.A., Parvez, M., Keay, B.A., *Tetrahedron: Asymmetry*, **1993**, *4*, 1973.
10. Sirbu, D., Falk-Pedersen, M-L., Romming, C., Undheim, K., *Tetrahedron*, **1999**, *55*, 6703.
11. Semmelhack, M.F., Foss, J.C., Katz, S., *J. Am. Chem. Soc.*, **1973**, *95*, 7325.
12. Imamoto, T., Sugiura, Y., *J. Phys. Org. Chem*., **1989**, *2*, 93.

STUDIA UNIVERSITATIS BABEŞ-BOLYAI, CHEMIA, XLVI, 1-2, 2001

THE RECOVERY OF THE ZINC AND NICKEL IONS BY IONIC EXCHANGE FROM ELECTROPLATING WASTEWATERS

IGOR CREŢESCU[*], GABRIELA ŞOREANU[*], MARIA PETRUC[**], GABRIELA CÂRJE[*], MATEI MACOVEANU[*]

[*] *Technical University "Gh. Asachi", Iasi, Industrial Chemistry Faculty*
71 A, D. Mangeron, 6600-IAŞI, ROMÂNIA
[**]*Environmental Agency,10 bis, Văscăuţeanu, 6600-IAŞI, ROMÂNIA*

ABSTRACT. This paper presents the possibility of recovering the ions of heavy metals (such as zinc or nickel that usually appear in acid galvanic wastewaters) after they were retained on a chelate resin of the Purolite S 930 type. By eluting them with a regenerative solution based on different mineral acid, the metals may be selective recovered from the resin.

Introduction

The traditional technology used in the course of time by the majority of electroplating enterprises, meant to prevent the pollution of effluents, consists in the precipitation and dilution of the noxious solutions down to concentrations, which would not affect the quality of the environment. However, due to a dramatic exhaustion of the water resources, modern waste water treatments have been promoted recently, with a view to aligning our country up with the environment, the saving of water and raw material resources.

Made the various ways of purifying galvanic wastewaters, mention could be mach of [1]: precipitation, reverse osmosis, electrodialysis, evaporation, electrolysis and ionic exchange.

From the point of view of the effectiveness in removing the heavy metals out of galvanic wastewaters, ionic exchange is the most attractive method. This becomes attractive especially due to the purification of wastewaters, with the possibility to recover the valuable components (heavy metal ions) retained during the exhaustion stage. The ionic exchange method is simple and economical (economy of water, raw materials and reagents) and this explains why it is preferred to the other water purification methods. This method has been applied lately in our country, too, as a result of the appearance on the market of new types of exchangers, produced by PUROLITE/VIROLITE Company (USA); due to their higher quality, these exchangers have replaced the domestically produced ones.

The paper presents a comparative study on the possibility of recovering, out of the galvanic rinse waters, the ions of zinc and nickel respectively, after they had been retained on the Purolite S930 chelate exchanger.

Since the efficiency of the resin regeneration process depends on a multitude of factors [1-3], the paper focuses on certain aspects regarding the resin operation during regeneration stage, under certain operating conditions, with a view to increasing the efficiency of valuable component recovery. The purpose was thus to determine the influence of the following factors on the regeneration of the Purolite S930 type of resin: flow rate, concentration, temperature and type of regeneration agent.

Experimental Part

The experimental installation and the influence of the certain factors on the loading of the resin with zinc and respectively, nickel ions for the recuperative purification of galvanic wastewaters were minutely described in some prior studies [4-5]. Using synthetic waters, the characteristics of the rinse wastewaters were simulated. These characteristics correspond to the acid sulphate type of electroplating baths. The experiment, under dynamic operating conditions, using a chelate exchanger resin (Purolite S930 type), whose main characteristics were presented in technical bulletin [6].

In order to study the influence of certain factors on the process of regeneration with a view to recovering the zinc and respectively, the nickel ions, the loading of the resin with metallic ions was performed each time under the same conditions; the flow rate of the processed solution at passage down through the column was F_v = 5 mL/min, the initial concentration of solution c_0 = 0.5 g/L Me(II); pH of zinc solution pH_{Zn} = 5.5, pH of nickel solution pH_{Ni} = 5.6; the experiment was made at room temperature (t = 18 °C); the quantity of dry resin used was a = 2.83 ± 0.02 g. The analyse of the metallic ions was performed complexonometrically [4-5].

The regeneration was performed in equicurrent, by eluting the zinc and respectively, nickel ions from the exhausted resin with mineral acid solutions (HCl, H_2SO_4), under certain experimental conditions.

The operating flow rate ranged between 2-5 mL/min. Corresponding to the flow rate of 2 mL/min, the average speed rate of the regeneration solution through the column was of $0.18 \cdot 10^{-3}$ m/s. The temperature range under study was between 18-30 °C. The concentration of the regenerative solutions ranged between 2-5 % H_2SO_4 and 10% HCl respectively. Their representative concentrations were selected, taking into account the maximum allow able concentration of acids for which the resin structure would not be affected due to oxidising effects [1].

Results and Discussions

The Influence of the Regenerative Agent

Figure 1 – a, b presents the elution curves of Zn(II) and respectively, Ni(II) ions retained on the chelate resin when the following regeneration agents are used: 5% H_2SO_4, 10% HCl. Due to the mineral acids, the resin is brought under the H^+ form; the sulphuric acid is preferred to the hydrochloric acid, because, by using the former, we obtain a zinc or nickel sulphate as eluted substance. These

solutions after adjusted the composition, might be recycled eventually in the electroplating bath of the sulphate type. As can be see in Figure 1 – a, b, the elution of the Zn(II) ions takes place faster in the presence of the H_2SO_4 solution, while the Ni(II) ions are more easily eluted when using the HCl solution. The average concentration of the eluted substance at the end of the regeneration process of the resin with mineral acids is of 4.54 g Zn(II)/L and 1.2 g Ni(II)/L, respectively – when using a 5% H_2SO_4 solution - and of 1.51 g Zn(II)/L and 3.59 g Ni(II)/L, respectively – when using a 10% HCl solution. Higher concentrations of the metallic ions from the eluted solution may be obtained through an incomplete regeneration of the resin, i.e. by stopping the process at certain time intervals, corresponding to the appearance of traces of metal in the effluent (eluted solution). The results obtained indicate the possibility of performing a selective elution in case the nickel and zinc ions are mixed in the solution, by successively using H_2SO_4 and HCl solutions of various concentrations, so that the ions might be extracted in turn, thus obtaining high purity eluted substance in effluents.

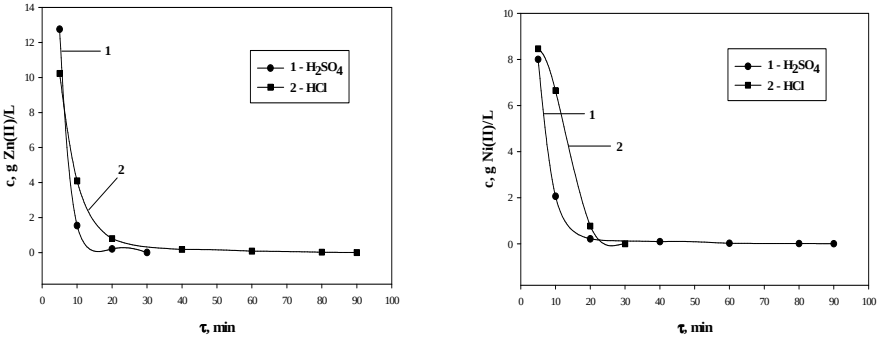

a b

Fig. 1. Time - dependent variation of the concentration of Zn(II) - a, respectively, Ni(II) - b, ions from the eluted solution during the regeneration process of the S 930 type of resin, with various regeneration agents: 1 – 5% H_2SO_4; 2-10% HCl. a = 2.83 ± 0.02 g dry resin; F_v = 2 mL/min; t = 18 °C.

The discussions will focus on the regeneration of the resin when using H_2SO_4 solution, because in this case the resulting eluted solution contains $ZnSO_4$ and respectively, $NiSO_4$, both of which are main components of the electroplating baths of the sulphate type.

The Flow Rate of the Regenerative Solution

Figure 2 - a, b presents the time – dependent variation of the concentration of the metallic ions from the eluted solutions for different flow rate of the regenerative solution.

The higher the flow rate, the lower the regeneration time span. However, this induces an increase in the volume of the eluted solution and thus a decrease in the concentration of the metallic ions.

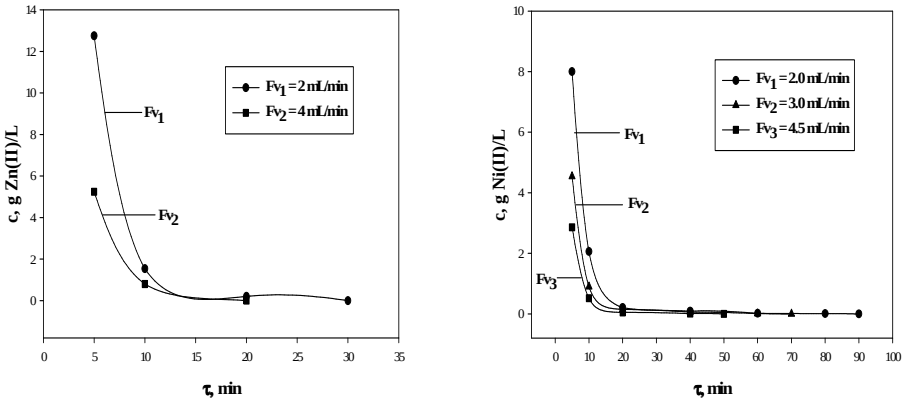

a b

Fig. 2. Time-dependent variation of the concentration of Zn(II) – a , respectively Ni(II) – b, ions from the eluted substance during the regeneration process of the S 930 type of resin. a = 2.83 ± 0.02 g dry resin; t = 18 °C; c_{H2SO4} = 5%.

The Concentration of Regenerative Solution

The use of higher concentration of regenerative solutions favours the displacement of the ionic exchange equilibrium to the left. Hence, appears the possibility to obtain, in a shorter period, eluted solutions with a higher concentration of metallic ions; for low concentrations, the regeneration process is slowed down and the concentration of the eluted solutions becomes lawyer.

The Temperature of the Regenerative Solution

As it has already been shown [4-6], the direct ionic exchange reaction is endothermic, while the reverse reaction is exothermic. In conformity with what has been stated, the temperature increase will favour only the direct reaction and the equilibrium will be displaced far off, to the right. However, the experimental data pointed to a slightly beneficial influence of temperature on the regeneration process (the reverse reaction), which is better evinced in the initial moments of the process. This could be the result of the intensification of the mass transfer and of the difference between the solvation energies of the ions in the solution and those of the ions in the resin. Another explanation may be found while taking into account the beneficial influence of temperature on the reaction rate, especially if the system under study is far from the state of equilibrium as a result of the hydrodynamic operating conditions. It can be noticed that, towards the end of the regeneration process, the influence of temperature becomes less and less significant.

Conclusions

- On the basis of the kinetic curves, it can be stated that the Zn(II) ions are more easily eluted with sulphuric acid, whole the Ni(II) ions are more easily eluted with hydrochloric acid, which might enable one to perform a selective separation of the two from the mixture;
- The use of high flow rate of the regenerative solution leads to a shortening of the regeneration time, but also to a decrease in the concentration of the metallic ions from the eluted solution;
- A highly concentrated eluted solutions may be obtained when the concentration of the regenerative solution increases; in this case the regeneration time reduces dramatically;
- The influence of temperature on the regeneration process is made manifest at the beginning of the process, when due to the intensification of the mass transfer under the impact of heat, a slightly higher concentration of the eluted solutions is obtained; at the same time, the regeneration time span is reduced when higher temperatures are used for the regenerative agent;

BIBLIOGRAPHY

1. Gergely, A., Bay, E., Dumitrescu, M., *Tratarea apelor reziduale şi recuperarea electroliților în galvanotehnică,* Editura Tehnică, Bucureşti, 1992, 260p;
2. Şoreanu, G., Crețescu, I., Macoveanu, M., Chirica, M., *Revista de Chimie*, vol.51, nr.10, 2000, p.807-810;
3. Ivanov, V.A., *Progress in Ion Exchange. Advances and Applications,* Ed. A. Dyer, M.J.Hudson, P.A.Williams, The Royal Soc. Chem, Cambridge, 1997, 498p
4. Crețescu, I., Şoreanu, G., Macoveanu, M., *Journal of Balkan Ecology*, vol.3, nr.4, 2000, p. 96-101;
5. Crețescu, I., Şoreanu, G., Macoveanu, M., Chirica, M, *Revista de Chimie*, vol. 52, nr. 3, 2001, p.146-150;
6. ****Purolite Ion Exchangers Bulletin, Technical Caracteristics*, Hamilton-Rio Design, Epson, UK, 1996.

STUDIA UNIVERSITATIS BABEŞ-BOLYAI, CHEMIA, XLVI, 1-2, 2001

OPTIMIZATION OF SOME WATER TREATMENT CONTAINING ORGANIC DYES (BROWN VOPSIDER DNRL 101) BY OXIDATION WITH HYDROGEN PEROXIDE ASSOCIATED WITH UV IRRADIATION

CARMEN ZAHARIA, MIOARA SURPĂȚEANU and M. MACOVEANU

"Gh. Asachi" Technical University of Iaşi, Faculty of Industrial Chemistry
Department of Environmental Engineering

ABSTRACT. It was studied the photooxidation with hydrogen peroxide of some waters containing the organic dye – Brown Vopsider DNRL 101 – in different conditions of operation. It was proposed a mathematical model of the studied process having two independent variables: pH and irradiation time. Also, there were determined the best operational conditions and the optimum value of the decolouring degree. The dye destruction was appreciated through the removal of samples colour expressed through the decolouring degree.

1. INTRODUCTION

From the preliminary studies concerning the decolouring of some aqueous solutions of dyes by oxidation with hydrogen peroxide (H_2O_2) associated with UV irradiation [1], it seems that under the principal factors with high influence on the photooxidation with hydrogen peroxide are the pH and irradiation time. This two factors can be the variables of an wastewater treatment containing the Brown Vopsider DNRL 101.

Into the decolouring processes are difficult to establish the best operational conditions for a satisfactory reduction of colour until a reasonable level for the evacuation into different emissaries.

That is way, it was used a programme of experimental data calculation during the photooxidation with hydrogen peroxide in the presence of a Fe^{2+} cathalyst for some waters containing Brown Vopsider DNRL 101 dye. This programme can be easely applied and adapted for the operational conditions and for other types of waters with different dyes.

To establish the mathematical model of such a decolouring process, it was used the experimental compositive rotative planning of two level (2^2 type) [2].

2. Materials and methods

2.1. Reagents and apparatus

- Brown Vopsider DNRL 101, aqueous solution of 0.1 g/l;
- Hydrogen peroxide, 30 % solution;
- Sulphuric acid, solution 4 N;
- Sodium hydroxide, solution 2 N;
- Iron sulphate, aqueous solution of 10 mg/l Fe^{2+};
- DRELL 2000 Spectrophotometer, HACH company;

- Photooxidation reactor. It was used a tubular reactor [3], with a capacity of ~ 500 cm^3 and 45 cm in height, having a casing for the keeping of a constant temperature. The UV light source of the reactor is a lamp with mercury vapours of medium pressure having 12 cm in length, 20 mm in diameter. It is an alternating curent lamp. The lamp emits UV radiations with a large UV range (180 - 400 nm), representing 30 % of the torch power. The rest represents the contribution of visible radiations (15 %), thermal radiations (35 %) şi the heat losses conduction on the electrodes (20 %).
- PC Computer.

2.2. Analysis methods

The study on the destruction of aqueous dyes solutions by oxidation with hydrogen peroxide associated with UV light was based on the variation vs time of decolouring degree. Under the UV light action, the hydrogen peroxide forms $HO\cdot$ radicals according to reaction [4],[5]:

$$H_2O_2 + h\nu \rightarrow 2HO\cdot$$

and the $HO\cdot$ radicals initiate a chain of radicalic reactions that lead to the destruction of organic matter, respectively to the samples decolouring.

In the presence of iron salts, the formation of $HO\cdot$ radicals:

$$Fe^{2+} + H_2O_2 \rightarrow Fe^{3+} + HO^- + HO\cdot$$

is accelerated and an acidic medium facilitates the decolouring process.

The study of destruction expressed by the variation of decolouring degree was required the determination of samples colour before and during the oxidation process.

The colour determination was spectrophotometrically done by measurement of absorbance at 456 nm, the blank was the distillated water. The colour was expressed in Hazen units (UH) according to the fact that an absorbance of 0.069 at 456 nm corresponds to 50 UH [5].

The appreciation of decolouring degree (DD) was done according with the relation:

$$DD\% = \frac{C_i - C_t}{C_i} \cdot 100$$

where: C_i - the initial intensity of colour [UH];

C_t - The intensity of colour at *t* time of the photooxidation [UH];

The Brown Vopsider DNRL 101 dye is an unitary compound having the following structure:

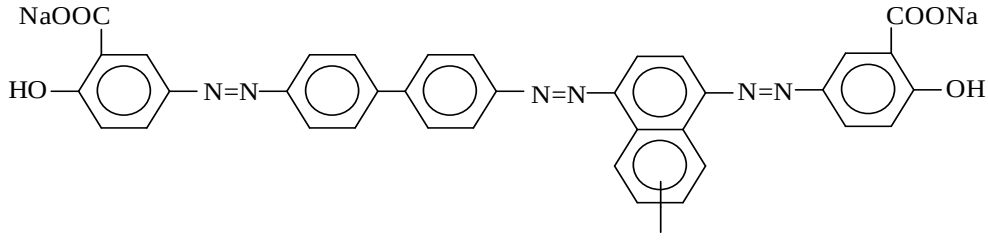

Brown Vopsider DNRL 101

Because of the great number of aromatic nucleus, this dye is integrated into the class of nonbiodegradable compounds.

The standard working sample was prepared from 250 ml dye solution with the addition of hydrogen peroxide (2.5 ml), catalyst (5 ml of Fe^{2+} solution) and sulphuric acid or sodium hydroxide according to the followed target. The pH adjustment was done with NaOH 2N or H_2SO_4 4N and directly reading at a HACH pH-meter.

On this standard sample, there were comparatively done kinetic studies concerning the influence of pH and irradiation time on the decolouring process by photooxidation with hydrogen peroxide.

In the case of UV irradiation, the samples was introduced into the photooxidation reactor (Fig.1), and the samples destined for the absorbance measurements were sampling from reactor at intervals of 10 minutes.

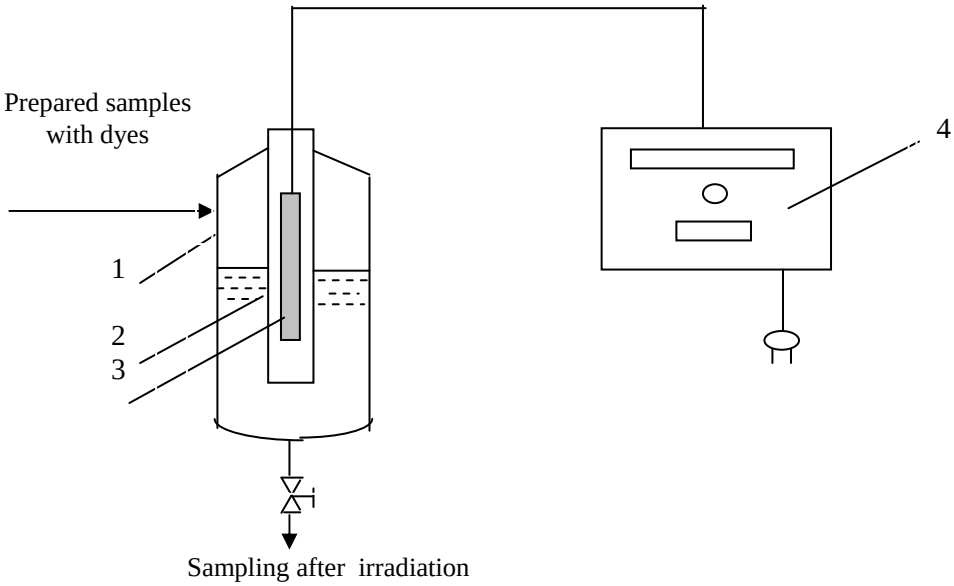

Fig.1. Photooxidation reactor
1 - photooxidation reactor; 2 - quartz tube; 3 - UV lamp; 4 - UV adapter.

The central planning has the advantage of no excessive experiments in comparison with the number of coefficients to be determined.

Into the admisible field of independent variables, for each variable – z_i (pH or irradiation time) – is established a basic value – z_{io} – and a variation step - Δz_{io} of each variables. Adding the variation step at the basic value is obtained the superior and subtraction of the step value leads to the inferior level of variable. The codification value of z_i variable named X_i is determined with the relation [8]: $\mathbf{x_i = \frac{z_i - z_{i0}}{\Delta z_{i0}}}$

So, the superior level is coded *+1*, inferior level *–1* and the basic level *0*. There are possible other values of the variable level (α_t) [7],[8].

Into this experimental cental compositive planning, the codificated variables will have the next values: -1.414, -1, 0, +1, +1.414 into a specific order.

As an optimization criterion was chosen the decolouring degree. The experimental results during the photooxidation with hydrogen peroxide for the establised values of the two independent variables, are synthetized into the experimental matrix.

After that, it was applied the Fisher test to determine the F value with the relation [9]:

$$F = \frac{(n-1)\cdot\sum_{i=1}^{n}(Y_{ei}-\overline{Y}_e)^2}{(k-1)\cdot\sum_{i=1}^{k}(Y_{eki}-\overline{Y}_{ek})^2}$$

where:

Y_{ei} – the experimental values of the dependent variable (decolouring degree, %);

$\overline{Y}_e$ - the average value of the dependent variable;

Y_{eki} – the experimental values of dependent variable into the centre of the programme;

$\overline{Y}_{ek}$ - the average value of the experimental values into the centre of the programme;

n - the total number of experiments from the experimental matrix;

k - the number of experiments into the centre of the programme.

If $F > F_{tab,}$ (F_{tab} is the value of F test from the statistical tables) [8], it can be said that the deviation of the experimental data from the average value it is not the result of experimental errors, but it is determined by the influence of independent variables (pH and irradiation time) on the decolouring degree.

To establish the relation between the dependent variable (Y - decolouring degree, %) and the two independent variables as a whole, it will be determined the multiple correlation coefficient in accordance with the relation [9].

$$R_{Y_{x1x2}} = \sqrt{1-\frac{\sum_{i=1}^{n}(Y_{ei}-Y_{ci})^2}{\sum_{i=1}^{n}(Y_{ei}-\overline{Y}_e)2}}$$

If the R_{Yx1x2} value is close to one, the independent variables have a significant importance on the dependent variable.

2.3. The central compositive rotative planning of 2^2 type

There were chosen the principal factors that influence the decolouring process of some waters charged with Brown Vopsider DNRL 101 as a result of oxidation with hydrogen peroxide associated with UV irradiation (preliminary

experiments). The pH and irradiation time factors were considered as independent variables in this treatment with high influence on the decolouring degree.

The computational programme of the experimental data on the decolouring process by photooxidation with H_2O_2 must be easily applied into good operational conditions.

The experimental central compositive rotative planning of 2^2 type proposes a mathematical model [7]:

$$Y = b_0 + \sum_{i=1}^{2} b_i \cdot X_i + \sum_{i=1}^{2} b_{ii} \cdot X_i^2 + b_{12} \cdot X_1 \cdot X_2$$

The model coefficients are determined using the following relations (Table 1) [7].

Table 1.

Relations for the calculation of the model coefficients.

$b_0 = 0{,}2 \cdot \sum_{i=1}^{13} Y_{ei} - 0{,}1 \cdot (\sum_{i=1}^{13} x_1^2 \cdot Y_{ei} + \sum_{i=1}^{13} x_2^2 \cdot Y_{ei})$
$b_1 = 0{,}125 \cdot \sum_{i=1}^{13} X_1 . Y_{ei}$
$b_2 = 0{,}125 \cdot \sum_{i=1}^{13} x_2 \cdot Y_{ei}$
$b_{11} = 0{,}125 \cdot \sum_{i=1}^{13} x_1^2 \cdot Y_{ei} + 0{,}01875 \cdot (\sum_{i=1}^{13} x_1^2 \cdot Y_{ei} + \sum_{i=1}^{13} x_2^2 \cdot Y_{ei}) - 0{,}1 \cdot \sum_{i=1}^{13} Y_{ei}$
$b_{22} = 0{,}125 \cdot \sum_{i=1}^{13} x_2^2 \cdot Y_{ei} + 0{,}01875 \cdot (\sum_{i=1}^{13} x_1^2 \cdot Y_{ei} + \sum_{i=1}^{13} x_2^2 \cdot Y_{ei}) - 0{,}1 \cdot \sum_{i=1}^{13} Y_{ei}$
$b_{12} = 0{,}25 \cdot \sum_{i=1}^{13} x_1 \cdot x_2 \cdot Y_{ei}$

To verify the significance of the multiple correlation coefficient it is used the Fisher test [9]: $F_c = \frac{n-b-1}{b} \cdot \frac{R^2_{Y_{x_1x_2x_3}}}{1-R^2_{Y_{x_1x_2x_3}}}$

where: b – the number of independent variables.

If the Fisher constant for the free degree ν_1= n-k-1=10 and ν_2= k=2 is higher than the value from the statistical table /4/, F_{tab}=4.14, it is considered that the independent variables have a significant importance on the dependent variable.

After that there are tested the model coefficients using the Student test [9].

To verify the model correctness, respectively, its ability to mathematically expressed the decolouring process by photooxidation with hydrogen peroxide, there are compared the experimental data with the values calculated with the proposed model and calculated the deviation *A* using the next relation [2],[7]:

$$A = \frac{Y_{ci} - Y_{ei}}{Y_{ci}} \cdot 100 \cdot$$

3. Results and discussion

The mathematical model is representative for all the similary experiment on some samples of 250 ml synthetic waters initially having a colour coresponding to an absorbance at 456 nm of 2.382 and 1890.476 UH and a COD (carbon organic demand) of 2.6 mg O_2/l (determined using the spectrophotometric method with $K_2Cr_2O_7$ in high acidic medium and COD cathalyst).

The codification of the independent variables for the decolouring process of the synthetic waters containing the Brown Vopsider DNRL 101 dye is presented into the next table (Tabel 2).

Tabel 2.

The Codification of the Independent Variables.

Variable/Value	Real variable	Codificated variable	Real basic value, z_{01}	Variation step, Δz_i
pH	Z_1	X_1	8	2
Irradiation time, min	Z_2	X_2	20	10

The experimental matrix of the decolouring process with UV irradiation and hydrogen peroxide is presented into the Table 3 (Y is the decolouring degree, %).

Table 3.

The Experimental Matrix of the Decolouring Process.

Exp.no.	Z_1	Z_2	X_1	X_2	Y [%]
1	6	10	-1	-1	46.07
2	6	30	-1	+1	78.75
3	10	10	+1	-1	27.2
4	10	30	+1	+1	43.42
5	5.172	20	-1.414	0	72.29
6	13.656	20	1.414	0	49.41
7	8	5.86	0	-1.414	23.12
8	8	34.14	0	1.414	93.34
9	8	20	0	0	69.89
10	8	20	0	0	71.13
11	8	20	0	0	70.64
12	8	20	0	0	70.21
13	8	20	0	0	70.87

The value from the statistical table of the Fisher test is $\mathbf{F_{tab}}(\alpha=99, \nu_1=n-1=12, \nu_2=\kappa-1=1)= 4.75$ and the calculated value is **F** = **155856.35** for the **Y** function.

Because $F > F_{tab,}$ it can be said that the deviation of the experimental values from the average value is not the result of experimental errors, but is determined by the influence of the independent variables. After that, it can be determined the mathematical expression of the dependent variable (Y).

The expression of the mathematical model of Y is:

$$Y = 70.548 - 10.819X_1 + 18.524X_2 - 7.519X_1^2 - 8.829X_2^2 - 4.115X_1 \cdot X_2$$

To establish the relation between the dependent variable and the all independent variables as a whole, it is determined the multiple correlation coefficient.

His value is R_{Yx1x2} =0.939726, value close to unit. This fact demonstrates the important influence of the independent variables on the dependent variable.

The Fisher constant for the free degree ν_1= n-k-1=10 and ν_2= k=2 is F_{tab}=4.14 and F_{calc}= 37.766075, value higher than the value from the statistical table. This fact demonstrates that the independent variables have a significant influence on the dependent variable (Table 4).

Table 4.

The Verifying of the Mathematical Model

No.exp	X_1	X_2	Y [%]	Y_c [%]	Deviation [%]
1	-1	-1	46.07	42.38	-8.707
2	-1	+1	78.75	86.658	9.125
3	+1	-1	27.2	28.972	6.116
4	+1	+1	43.42	47.79	9.54
5	-1.414	0	72.29	70.812	-2.086
6	1.414	0	49.41	46.216	6.91
7	0	-1.414	23.12	26.702	13.415
8	0	1.414	93.34	89.088	4.77
9	0	0	69.89	70.548	0.933
10	0	0	71.13	70.548	-0.825
11	0	0	70.64	70.548	-0.1304
12	0	0	70.21	70.548	0.479
13	0	0	70.87	70.548	-0.456

The testing of the model coefficient using Student test establishes that all the coefficients are significant.

The application of the classic optimization methods lead to the conclussion that this function – Y - presents a distinct maximum for:

X_1 = -1.07506, X_2 = +1.29957 for a value of dependent variable: Y_{opt} = 88.4 %.

Transposing in real values, these values correspond to a pH of 5.85 and an irradiation time of 32.957 minutes.

To verify the correctness of the mathematical model, there are compared the experimental values with the values calculated with the model and calculated the deviation *A.* The average deviation value is of 3.086 %, each of this individual value being into the interval of ± 10 %. This fact indicates a good agreement of the experimental values with the values calculated with the mathematical model.

The interpretation of the proposed mathematical model for the decolouring process of the waters containing Brown Vopsider DNRL 101 dye by photooxidation with hydrogen peroxide

Analysing the expression of the Y function. It can be said that the most important influence on the decolouring degree of the waters containing the Brown Vopsider DNRL 101 has the X_2 variable (irradiation time, min), emphasized by the higher value of the X_2 coefficient, as well of the X_2^2 coefficient. Nevertheless, important is also the influence of pH, demonstrated by the relatively higher value of X_1 and X_1^2 coefficients. The pH decreasing leads to an increasing of the decolouring degree, demonstrated by the negative coefficient of X_1X_2. The influence of X_2 variable is almost of 1.7 degree higher than of X_1 variable and their effect is opposite.

Into the next figures are presented the dependences of the decolouring degree (%) of the two independent variables, pH and irradiation time (Fig.2), as well as the dependence of the decolouring degree of each variable, in the conditions of a constant keeping of the other variable at the codificated value of 0 (Fig.3).

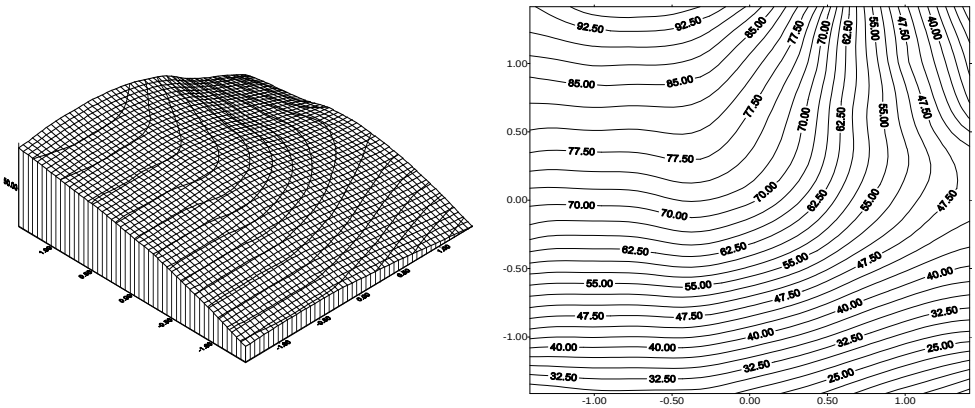

Fig.2. The dependence of Y vs the two variables

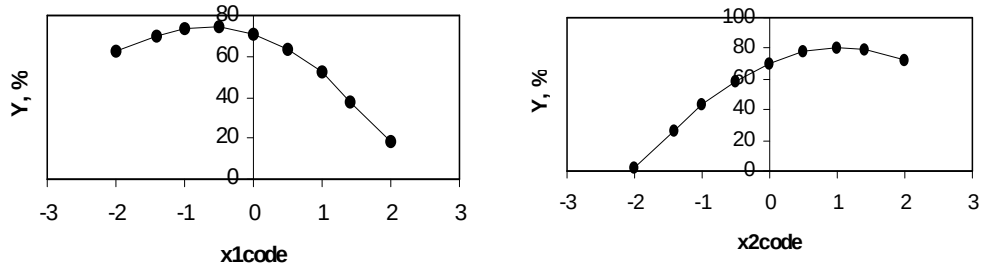

a: $Y=Y(x_1,0)$ b: $Y=Y(0,X_2)$

Fig.3. The dependence of Y vs each variable.

In figure 3a is represented the dependence of decolouring degree versus the X_1 (pH); it seems that exists a maximum (x_1= -0.7194) that corresponds to a pH of 6.5612, for a constant value of the irradiation time (20 minute, the basic value).

In figure 3b, it seems that exists into the experimental field a maximum of the decolouring degree vs the X_2 variable (irradiation time) for a value of +1.049 for X_2 which corresponds to an irradiation time of 30.49 minutes, in the conditions of a constant value of pH (pH=8).

CONCLUSSIONS

1. The photooxidation with hydrogen peroxide in the presence of Fe^{2+} catalyst leads to high decolouring degree for relatively low irradiation time and acidic value of pH.
2. It was established a mathematical expression of the decolouring process by oxidation of some waters containing Brown Vopsider DNRL 101 dye by oxidation with hydrogen peroxide associated with UV irradiation and Fe^{2+} cathalyst. The mathematical model is elaborated considering as optimization criterion – the dependent variable - the decolouring degree and as independent variables - the pH and irradiation time.
3. There were determined the optimum values of the independent variables that correspond to a pH of 5.85 and an irradiation time of 32.957 minutes.
4. It seems that there are obtained high values of the decolouring degree (88.4 %) at the specific optimum values of pH and irradiation time.
5. It was verified the mathematical model and it seems that this model is adequate, the average deviation having the value of 3.086 % being into the admisible limits of deviation (± 10 %).
6. There were represented the dependences of the decolouring degree vs the variation of the independent variables, as well as individually of each independent variable in the conditions of a constant value of the other (the basic value). It seems that exists a maximum for the considered values of independent variables corresponding to a pH of 6.512 and, respectively, to an irradiation time of 30.49 minutes.

REFERENCES

1. Ph.D thesis of Mr. eng. Bertea Andrei-Petru, "Possibilities of Reduction the Pollutants from the Wastewaters Generated into the the Chemical Finishing of Textiles" (1997).
2. Macoveanu M., Nicu V., Curievici I., "Basis of chemical technology. The methodology of mathematical model elaboration into the chemical industry", vol.IV, Rotaprint Press, Iaşi, 1987.
3. Teodosiu Carmen, Macoveanu M. and Duca Gh., "Advanced treatment of wastewaters containing non-biodegradable compounds", Ed."Gh.Asachi", Iasi, 1997.

4. Carey J.H., *Water Poll.Res.J. Canada*, vol 27, no 1, 1992.
5. Golimowski J., Golimiwska K., *Analytica Chemica Acta*, 325, 3, 11-133, 1996.
6. Leeuwen J., Schell H., Berger M., Drikas M., Bursill D., Chow C., Closen J., *J. Water SRT - Aqua*, vol 46, no.5,261-273, 1997.
7. Cojocaru N., Clocotici V., Dobra D., "Statistical methods applied into the textile industry", Ed.Tehnică, Bucureşti, 1986.
8. Taloi I., "Process optimization from metallurgy", Ed.Tehnica, Bucuresti, 1987.
9. Gluck A., "Mathematical methods into the chemical industry. Elements of optimization", Ed.Tehnică, Bucureşti, 1971.

STUDIA UNIVERSITATIS BABEŞ-BOLYAI, CHEMIA, XLVI, 1-2, 2001

SELECTIVE SEPARATION OF DICARBOXYLIC ACIDS BY REACTIVE EXTRACTION

DAN CASCAVAL, CORNELIU ONISCU*, ANCA-IRINA GALACTION**

** Technical University "Gh. Asachi" Iasi, Faculty of Industrial Chemistry, D. Mangeron 71 , 6600, Iasi*

*** University of Medicine and Pharmacy "Gr.T. Popa" Iasi, Faculty of Medical Bioengineering, University 16, 6600, Iasi*

ABSTRACT. In this paper the studies on separation of some dicarboxylic acids (oxalic acid, malonic acid, succinic acid and adipic acid) by reactive extraction with Amberlite LA-2 in butyl acetate were continued. Thus, the conditions for a selective extraction were settled. The individual selective extraction is not possible because of the comparable values of acidic constants for oxalic and malonic acids, on the one hand, and for succinic and adipic acids, on the other hand. In this case, only selective extraction of oxalic and malonic acids can be achieved.

For a high selectivity, both a molar ratio of 0.9 - 1 between the strong dicarboxylic acids (oxalic and malonic acids) and the extractant and a concentration of Amberlite LA - 1 lower than the stoichiometric value for all acids extraction are required.

INTRODUCTION

Since 1970 the advantages offered by the reactive extraction determined the extension of the applications area towards the separation of organic compounds. In present, the conditions for reactive extraction of some derivatives, namely : carboxylic acids, amino acids, phenolic derivatives, alcohols, antibiotics, are intensively studied with the purpose of industrial scale application [1].

In the previous works the mechanism, the limiting steps and the kinetic of the reactive extraction of some dicarboxylic acids (oxalic, malonic, succinic and adipic acids) by Amberlite LA-2 in butyl acetate have been settled [2].The aim of this paper is to study the possibility of selective separation of these acids by extraction. The technique which was used is dissociative extraction, based on the difference between their acidity. This technique has been used on selective separation of some isomer organic bases having different basic capacities by reactive extraction with a strong mineral acid [3, 4].

EXPERIMENTAL PART

The experimental studies have been carried out in two separate stages. The first one consists of the preliminary study on selective extraction of oxalic, malonic, succinic and adipic acids. The laboratory equipment used includes a modified extraction cell of the Lewis type described in the pervious papers [2]. The studies were carried out in a continuous system, the aqueous phase and the organic phase being separately fed and mixed by means of two perforated blade stirrers with variable rotation speed (0 - 1000 rpm). The two phases throughputs were: 1.6 l/h for aqueous phase and 2.15 l/h for solvent phase. The initial concentrations of dicarboxylic acids in aqueous solution were : oxalic acid 1.53 and 4.83 g/l, malonic acid 1.50 and 4.77 g/l, succinic acid 1.57 and 5.07 g/l, adipic acid 1.53 and 4.73 g/l.

Stamps prelevation has been carried out from the aqueous phase evacuation tract.

The second stage represents the study on these organic acids extraction in a glass column provided with a vibratory mixer [5, 6]. In this case, a very high interfacial area and a high mass transfer rate have been obtained. The volume ratio between the aqueous phase and solvent phase was 1, each phase volume being of 50 cm^3. The acids initial concentrations in aqueous solution were : oxalic acid 0.92 - 4.60 g/l, malonic acid 1.06 - 5.30 g/l, succinic acid 1.10 - 5.51 g/l, adipid acid 1.00 - 5.02 g/l.

After the mixing of the two phases for 1 minute, the resulting emulsion was separated in a centrifugal separator at 5000 rpm.

In both experiments the organic phase was butyl acetate with a content of 20 g/l Amberlite LA-2 .

The extraction process development has been followed by pH - metric titration of initial aqueous solution and raffinate with a sodium hydroxide solution of $1.74.10^{-2}$ N and 3.10^{-2} N respectively, and by analyzing the obtained curves.

RESULTS AND DISCUSSIONS

As a function of their acidity the dicarboxylic acids studied can be grouped in two categories: oxalic and malonic acids, on the one hand, and succinic and adipic acids, on the other hand, as can it be observed from the Table 1 [7]. The possibility of the individual selective extraction is repressed by the presence of this difference between the two groups and by the comparable acidity values for the organic acids existed in the same group, determining the selective extraction of oxalic and malonic acids. Although this phenomena represents the main characteristic of this extraction system, the separation selectivity has been strongly depended by the acids overall concentration in the initial aqueous solution, or by dicarboxylic acids and Amberlite LA-2 molar ratio, respectively.

The variation of the specific mass flow for oxalic and malonic acids and for succinic and adipic acids, as well as the variation of the selectivity factor, calculated as the ratio of these two specific mass flows, with the rotation speed have been followed in the preliminary studies.

Table 1.

Values of the acidic constants for the extracted dicarboxylic acids.

Dicarboxylic acid	k_1	k_2
Oxalic acid	$6.5\ 10^{-2}$	$6.1\ 10^{-5}$
Malonic acid	$1.4\ 10^{-2}$	$8.7\ 10^{-7}$
Succinic acid	$6.9\ 10^{-5}$	$2.8\ 10^{-6}$
Adipic acid	$3.7\ 10^{-5}$	$3.9\ 10^{-6}$

For low initial concentrations of dicarboxylic acids in aqueous solution an increase of the specific mass flows can be observed, the increase being significantly for the strong acids, especially (Figure 1).

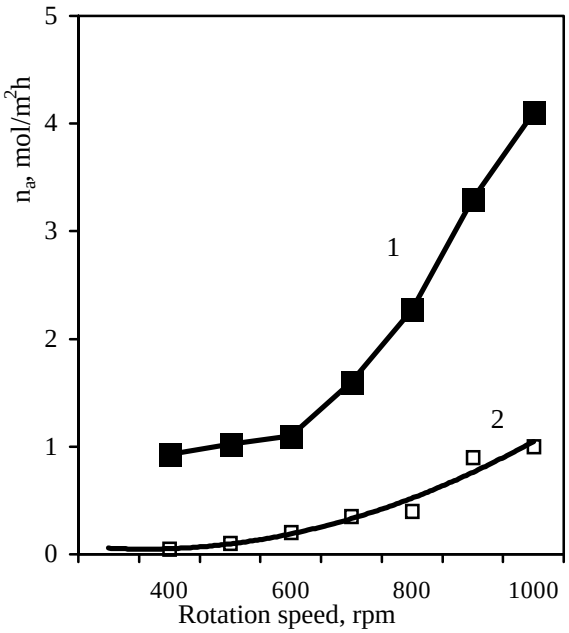

Figure 1. Specific mass flow, n_a, *versus* rotation speed (1 - oxalic and malonic acids, 2 - succinic and adipic acids; initial concentrations: 1.53 g/l oxalic acid, 1.50 g/l malonic acid; 1.57 g/l succinic acid, 1.53 g/l adipic acid).

The weak acids, succinic acid and adipic acid, cannot be extracted for rotation speeds below 400 rpm. In this case, the selectivity factor has an infinite value and than decreases to a value of 3.14 corresponding to a rotation speed of 1000 rpm (Figure 2, curve 1).

Increasing the initial acids concentration a change in extraction process evolution has been observed, namely the increase in the specific mass flow for oxalic and malonic acids. In the same time, it was observed that a constant value of the specific mass flow for succinic and adipic acids was obtained, disregarding the increase of rotation speed (Figure 3).

The difference in extraction system behaviour is the result of the change in reactive extraction mechanism by changing the acids initial concentration combined with the influence of the diffusion towards the contacting interface.

The reactive extraction mechanism can be expressed by following interface equilibrium :

$$m\ R(COOH)_{2\,(aq)} + p\ A_{(o)} \quad \equiv \quad [R(COOH)_2]_m.A_{p\,(o)}$$

where $R(COOH)_2$ is the dicarboxylic acid and A is the extractant of Amberlite LA-2 type.

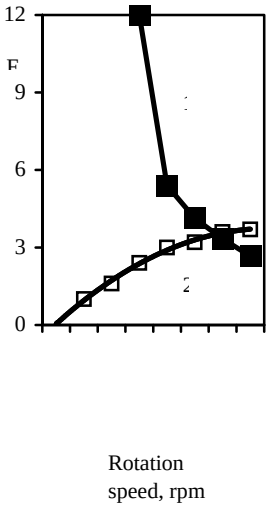

Figure 2. Variation of selectivity factor, F, with rotation speed.

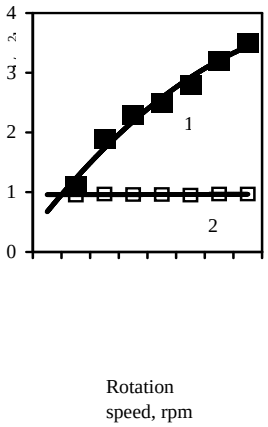

Figure 3. Specific mass flow, n_a, *versus* rotation speed (1 - oxalic and malonic acids, 2 - succinic and adipic acids; initial concentrations: 4.83 g/l oxalic acid, 4.77 g/l malonic acid, 5.07 g/l succinic acid, 4.73 g/l adipic acid)*.*

For a constant value of the extractant concentration, the structure of the formed complex is determined by the level of the organic acid concentration, as follows :

a. for a molar ratio between

b. for a molar ratio nearly 1, the extraction system components react in a equimolecular proportion forming : $R(COOH)_2.A$;

c. at high initial concentration of the organic acids, a third phase of high complex concentration can appeared in non - polar diluents (butyl acetate, for example). In this case, the structure of the complex is $[R(COOH)_2]_m.A_p$ [8]. For a molar ratio greater than 1 this complex can be formed, too.

In the first series of experimental studies the extraction mechanism was **a.**, owing to the molar ratio between dicarboxylic acids and extractant of 0.8. For a diffusional regime, at low rotation speed, the interfacial concentration of the extractant is low, below the stoichiometric necessity, thus reacting with the strong acids especially. By increasing the rotation speed the extractant concentration at the interface is increased, becoming greater than the requirement for oxalic and malonic extraction only. The results consists in the increase in mass flow of weak acids, succinic acid and adipic acid.

At the initial concentration of the acids greater than former, for a molar ratio between dicarboxylic acids and Amberlite LA-2 of 3.3, the formation of complexes of **c.** type is possible, even at very low rotation speed level. The rotation

speed increase, respectively the diffusion rate increase, determines the increase in interfacial concentration of the extraction system components. According as the strong acids reach the interface the extractant will preferential react with them.

From these data the following conclusion can be drawn : the extractant concentration in organic phase must be lower than the stoichiometric necessity for all dicarboxylic acids extraction and the value of the molar ratio between strong acids (oxalic and malonic acids) and Amberlite LA-2 must be nearly 1 for a high selectivity of reactive extraction process.

The results obtained in extraction column with vibratory mixer have been confirmed the earlier conclusions. By increasing the overall acids concentration in aqueous solution, respectively by increasing the molar ratio value between the acids and the extractant from 0.68 to 3.43, the decrease of the reactive extraction yield for oxalic and malonic acids from 100 % to 53.05 % has been observed. The reactive extraction yield for succinic and adipic acids decreases to a minimum value of 26.77 %, then increasing to 35.33 %. The overall extraction yield has been linearly reduced by increasing the acids concentration (Figure 4).

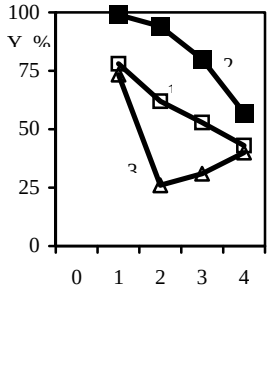

Figure 4. Influence of molar ratio M between dicarboxylic acids and extractant on reactive extraction yield, Y (1 - overall extraction yield, 2 - oxalic and malonic acids extraction yield, 3 - succinic and adipic acids extraction yield).

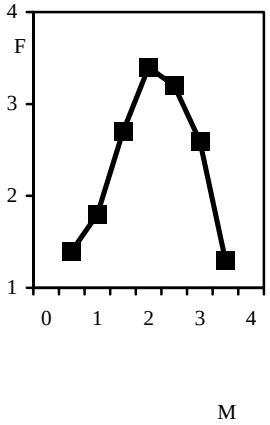

Figure 5. Variation of selectivity factor, F, with molar ratio, M.

The selectivity factor, calculated as ratio of the extraction degrees of the two acid groups, had a particularly evolution, reaching a maximum of 3.45 for a value of ratio between the total acids moles and extractant moles of 1.71, and for a molar ratio between strong acids and extractant of 0.95, as can be seen from Figure 5.

The selectivity factor maximum value corresponds to the extraction degree minimum value for the weak acids.

CONCLUSIONS

The obtained data indicate the possibility of the oxalic and malonic acids selective separation by dissociative extraction with Amberlite LA-2 in butyl acetate by means of the difference on acidic constants. However, the individual selective extraction cannot be achieved because of the small differences between the acidity of each acid group components.

Using a molar ratio between the strong acids and Amberlite LA-2 of 0.9 - 1, concomitant with an extractant concentration less than the requirement for total acids extraction, a high selectivity value can be reached.

REFERENCES

1. M. H. I. Baird - Can. J. Chem. Eng. 1991, 69(12), 1287.
2. D. Cascaval, R. Tudose, C. Oniscu - South. Braz. J. Chem. 1997, 5(5), 97.
3. M. M. Anwar, C. Hanson, A.N. Patel, M. W. T Pratt. - Trans. Instit. Chem. Eng. 1971, 49(2), 95.
4. M. M. Anwar, C. Hanson, A.N. Patel, M. W. T. Pratt - Trans. Instit. Chem. Eng. 1973, 51(2), 151.
5. C. Oniscu, R. Tudose, D. Cascaval - Rev. Roum. Chim. 1994, 39(11), 1343.
6. D. Cascaval, C. Oniscu, R. Tudose - Buletin I. P. I. 1996, 42(1-2), 73.
7. C.D. Nenitescu – “Chimie organica”, vol.1, E.D.P., Bucharest, pp. 756, 1980.
8. H.J. Rehm, G. Reed, A. Puhler, P. Stadler (Eds) – “Biotechnology”, vol 3, VCH Weinheim, pp. 569, 1993.

STUDIA UNIVERSITATIS BABEŞ-BOLYAI, CHEMIA, XLVI, 1-2, 2001

SOME TYPICAL CYCLIC VOLTAMOGRAMS OBTAINED FOR DENTAL ALLOYS IN SIMULATED HUMAN BODY FLUIDS

N. AELENEI, GH. NEMTOI[*], D. MARECI, DELIA AELENEI, CARMEN CHIPER[**], R. CHELARIU[***]

"Gh. Asachi" Technical University, Physical Chemistry Department, 6600 Iasi
**) "Al.I.Cuza" University, Physical and theoretical Chemistry Department, 6600-Iasi*
***) "Gr.T.Popa" University of Medicine and Pharmacy, 6600-Iasi, Romania*
****) "Gh. Asachi" University, Faculty of Material Science and Engineering, 6600-Iasi*

ABSTRACT. The existence of various classes of implant materials and metallic alloys used in dentistry, as well as the complex compositions of natural or simulated human body fluids, make possible to appear a very contrasting and complicated chemical and electrochemical behaviour. Among the experimental methods for studying the corrosion performances in simulated human body fluids, the potentiodynamic tests take up a special place, being very rapid and providing many informations about the electrochemical processes involved.

A few cyclic voltamograms are presented and discussed, analyzing the main processes which characterize the electrochemical behaviour of the studied materials in various solutions, as: passivation by anodic oxidation (titanium and titanium alloys in acidic media and in Ringer type solutions), "pitting" type corrosion (Cu-Al-Fe and Ni-Cr-Fe alloys in artificial saliva), secondary anodic processes as insoluble salt formation (Cu-Al-Fe alloy in a complex sulfuric medium and allied titanium in Ringer solution).

KEY WORDS: titanium alloys, gaudent, cyclic voltamograms, corrosion, pitting corrosion

INTRODUCTION

The corrosion of metals and metallic alloys in aqueous environments of body fluids is one of the major processes that cause problems when these materials are used as implants in the human body [1]. The corrosion resistance of various metal alloys is evaluated usually by such techniques as immersion tests or vapor contact tests, which nevertheless are subjective and time consuming. On the other hand, as a guide for optimum corrosion resistance, American Dental Association prescribes some composition limits of alloy [2], but it has been demonstrated that composition limits are not always a guarantee of satisfactory corrosion resistance [3].

Because corrosion in an aqueous medium of the sort provided by body fluids is an electrochemical process [1], [4], many electrochemical methods can be used for characterizing the corrosion processes, these being very quick tests for screening of alloys from the corrosion stand point. The electrochemical measurements include zero-current tests (open circuit potential-time curves), impedance tests, potentiostatic tests, linear polarization curves and cyclic polarization curves. By far, the most common electrochemical test for corrosion resistance is cyclic polarization, where the working electrode, realized on the basis of the

studied alloy, is polarized in a positive direction (potential increases) until localized or generalized corrosion initiates, as indicated by a large increase of the corrosion current, followed by a cathodic polarization (a polarization in a negative direction) until a pre-established potential, when the current have a negative value. These potential curves evidences many electrochemical processes which are involved in the corrosion or passivation of metallic alloys.

This paper presents a few typical cyclic voltamograms, evidencing different electrochemical processes characteristic for metallic biomaterials.

EXPERIMENTAL

The corrosion behaviour of the investigated alloys was studied by cyclic polarization curves obtained on a VoltaLab 32 electrochemical system (Radiometer Copenhagen) consisting from a potentiostat, an electrochemical interface and a computer equipped with the acquisition and processing data software Voltamaster 2. The three-electrode electrochemical cell used was equipped with a thermostatic system and a stirring and bubbling of inert gas system. Working cylinder electrodes were mounted in a teflon support to enable the connecting to rotating electrode of electrochemical system. A 0.02 cm^2 cross-area of working electrode was used. Each specimen was polished with SiC paper down up 2500 grit specification, washed in distilled water, degreased with acetone, washed and maintained in double-distilled water until the immersion of specimen within the electrochemical cell. A saturated calomel electrode (SCE) was used as a reference and a platinum electrode as a counter. The electrolytes were maintained at 36.5 ^oC throughout the tests. In some tests the electrolytes were de-aerated with pure nitrogen gas at a flow rate of 150 cm^3/min for 60 min before and 15 min after the immersion of the work electrodes.

From a test to another the testing conditions were modified, namely: potential range, scan rate of potential (dE/dt), resolution time t_r and corrosion medium.

The compositions of the used electrolytes are presenten in Table 1.

Table 1

The compositions of the corrosion media

Nr.	Electrolyte	Composition
1	SALIVA 1 (Fusayama [5]) pH = 6.18	NaCl - 0.400 g/L, KCl - 0.400 g/L, $NaH_2PO_4.H_2O$ - 0.690 g/L, $Na_2S.\ 9H_2O$ - 0.005 g/L, Urea - 1.000 g/L, $CaCl_2.2H_2O$ - 0.795 g/L
2	SALIVA 2 (Rondelli, [6]) pH = 7.75	KCl - 1.47 g/L, $NaHCO_3$ - 1.25 g/L, KSCN - 0.52 g/L, $KH_2PO_4.H_2O$ - 0.19 g/L
3	RINGER 1 PH = 6.3	NaCl /8.6 g/l , KCl - 0.3 g/l , $CaCl_2$- 0.33 g/l H_2O , HCl 0.1N – 1mL
4	RINGER 2 [7] pH = 7.3	NaCl /8.6 g/l , KCl - 0.3 g/l , $CaCl_2$- 0.33 g/l H_2O , HCl 0.1N – 1mL
5	ACIDIC SOLUTION 3 pH = 2.64	Lactic acid - 4.5 g/l, NaCl - 2.9 g/l
6	ACIDIC SOLUTION 4 pH = 1.35	H_2SO_4 /- 9.8 g/l , NaCl - 4.3 g/l
7	HCl, 1N	37.5 gHCl/l
8	H_2SO_4, 1N	49 g H_2SO_4/l

The studied alloys have the composition presented in Table 2.

Table 2

The compositions of the studied alloys

Nr .crt.	ALLOY	MAIN COMPOSITION
1	GAUDENT S	Cu-82.0 %, Al-9.97 %, Ni – 4.35 %, Fe – 1.32 %, Mn – 2.04 %
2	Ti6Al4V	Ti – 90 %, Al – 6%, V – 4 %
3	Ti5Al2.5Fe	Ti – 92.5 %, Al – 5%, Fe –2.5 %
4	V – ALLOY	Ni-72%, Cr-20%, Fe-6%
5	N - ALLOY	Ni-63%, Cr-25%, Mo-10%
6	C - ALLOY	Co-65%, Cr-29%, Mo-6%
7	VITTALIUM 2000	Co-63.8%, Cr-28.5%, Mo-6%

RESULTS AND DISCUSSION

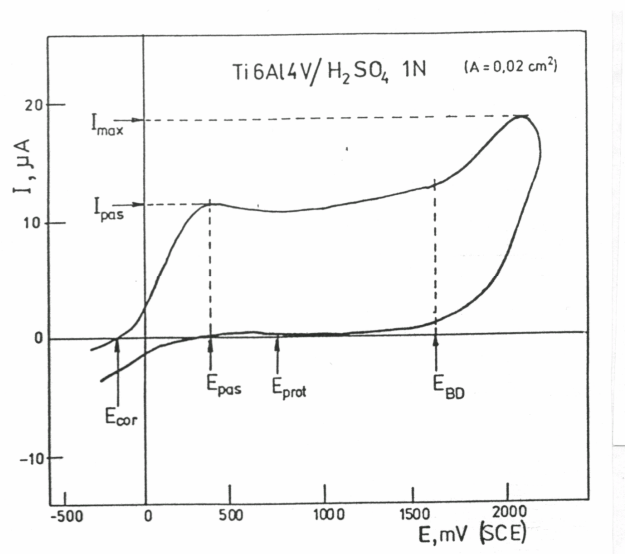

Fig. 1. Cyclic voltamogram for Ti6Al4V alloy 1N H_2SO_4 at 36.5^{0}C, dE/dt=20 mV/s, t_r=0.8s

In Fig 1 is presented the cyclic voltamogram for Ti6Al4V alloy in 1N sulfuric acid. This curve is characteristic for materials which in an adequate medium presents an anodic oxidation process, in this case $Ti \rightarrow Ti^{4+}$ and the formed TiO_2 is a protecting film which prevent the corrosion. This process takes place in the potential domain E_{pass} – E_{BD} and is characterized by the passivation current, I_{pass}. At potentials higher than E_{BD} the anodic corrosion or oxygen formation take place.

When the reverse branch of the voltamogram passes by zero current value, $E = E_{prot}$, one considers that the respective material is protected against corrosion.

Fig.2 presents, comparatively, the cyclic votamograms for Ti6Al4V alloy in acid media (1N H_2SO_4), in weak acid and weak basic simulated human fluids on Ringer type. These point out that, as different on the electrochemical behavior in sulfuric acid, in more complex media other anodic processes, as salt formation and deposition on the metal surface disturb the passivation process. Moreover, in these

media the degradation processes are more pronounced, as indicate by fact that the corrosion current at potentials higher than break down potential is much more than that for pure acid medium.

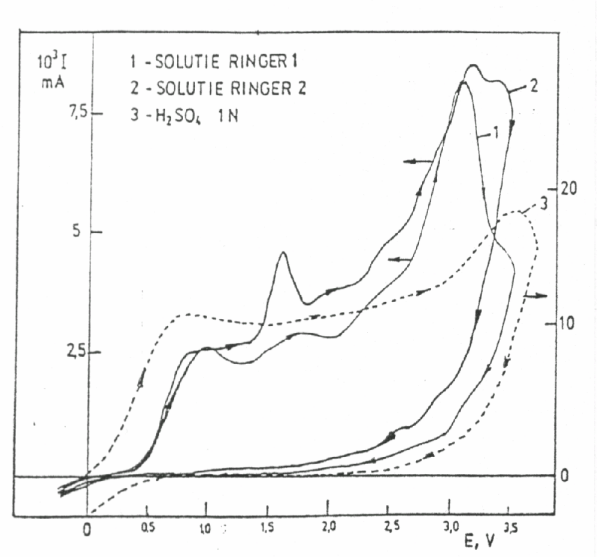

Cyclic voltamograms for Ti5Al2.5Fe in sulfuric acid and in Ringer solutions emphasize a similar behavior (Fig 3 and 4). In sulfuric acid the oxidation/ passivation process is non-disturbed and the formed TiO_2 film is stable, while in Ringer solutions the disturbing processes is more pronounced than those found in the case of Ti6Al4V alloy. This is due to the Fe from alloy composition.

Fig. 2. Cyclic voltamogram for Ti6Al4V in H_2SO_4 and Ringer solutions at 36.5^{0}C, dE/dt=20 mV/s

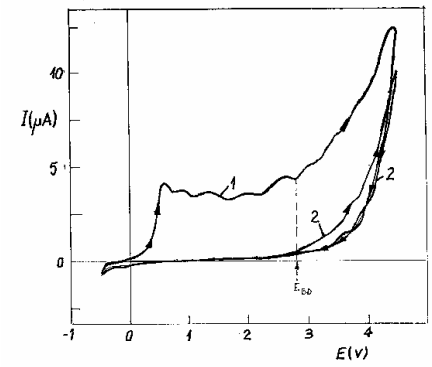

Fig 3. Cyclic voltamograms for Ti5Al2.5Fe In H_2SO_4 1N – (1) – fresh cleaned surface (2)- electrochemical passived surface

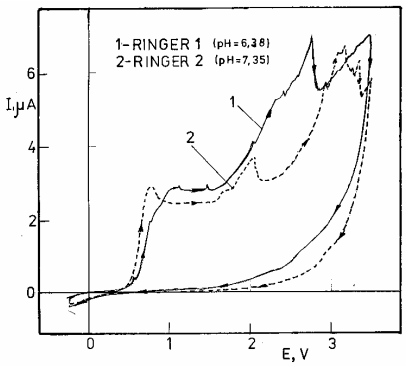

Fig. 4. Cyclic voltamograms for Ti5Al2.5Fe in Ringer solutions(1) ; pH =6.38; (2) **-** Ringer 2 soluttion; pH = 7.35

The anodic passivation process is not present in the case of the alloys without titanium as in the case of the non-noble Ni-Cr or Co-Cr alloys.

In Fig. 5 are presented some cyclic voltamograms obtained for V-alloy (Ni-Cr-Fe) obtained in deaerated SALIVA 2 (Rondelli) working with, fresh surface, old surface or cathodic polarized surfaces of the studied electrode:

- curve 1 - fresh surface;
- curves 2 and 3 - old surface (after first and second cyclic polarization
- curve 4 - registered after 10 s cathodic polarization at –500 mV;

- curve 5 – registered after 30 s cathodic polarization at –500 mV;
- curve 6 - registered after 120 s of cathodic polarization at –500 mV.

As can be seen these curves point out a "pitting" corrosion, irrespective of metal surface preparing. This behaviour is due only to presence of the iron in the alloy.

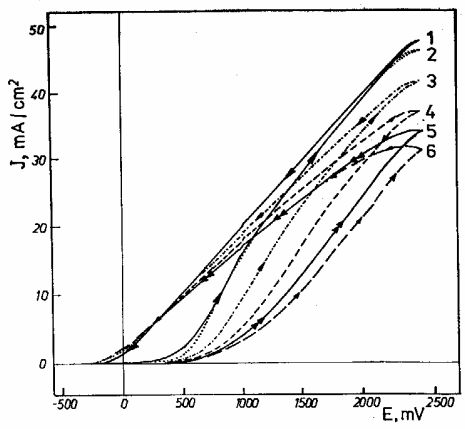

Fig. 5. Cyclic potentiodynamic curves for V-alloy in SALIVA 2, at 36.5 °C; dE/dt=50 mV/s t_r = 0.8 s

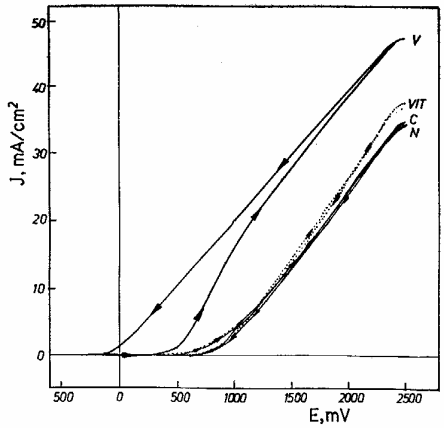

Fig. 6. Cyclic potentiodynamic curves for non-noble alloys in SALIVA 2, at 36.5 °C dE/dt=50 mV/s , t_r = 0.8 s

The cyclic potentiodynamic curves for the other three non-noble dental alloys (N, C and Vitallium 2000), by comparison with those obtained in same condition for V-alloy, are presented in Fig. 6. While the Ni-Cr-Fe alloy exhibit a typical curve for pitting corrosion, appearing at a relative little electrode potential, the alloys without iron in composition exhibit a generalized corrosion, taking place at a much more potential, the same for the three samples. This generalized corrosion is due perhaps to the oxidizing dissolution of Cr. Relative high values of the break down potential can be associated wit the presence of molybdenum in alloy, this element playing a distinctive role for the passivation rate decrease and provide an efficient resistance to pitting (quite different from the Fe-containing alloys).

The behavior of the Gaudent alloy in various corrosion media are presented in Fig. 7, 8.

It can be seen the essential role of the corrosion medium. Thus, in Fusayama 's solution (SALIVA 1) the alloy exhibit a pitting type corrosion, with a relative large potential domain of repassivation. In Rondelli solution (SALIVA 2) also a pitting corrosion is prresent, but the repassivation interval is considerable reduced; the break down potential and the repassivation potential coincides [8]

In the saline organic solution (acidic solution 3) the current densities are two time higher than those obtained in the other two solutions and no pitting corrosion is observed. In this case a typical dissolution process being perhaps the most probable process, but a hysterezis loop appears.

In sulfuric acid solution (acidic solution 4) the cyclic voltamogram is quite complexe, indicating a very complicated corrosion process, where the dissolution of CuO or Cu_2O fim is accompanied by formation of some insoluble saline deposits or soluble salts.

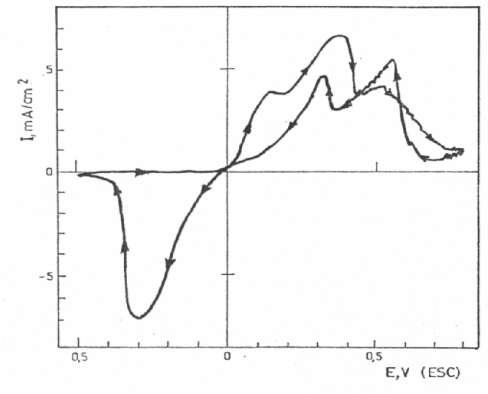

Fig. 7. Cyclic voltamograms for Gaudent S in SALIVA 1, SALIVA 2 and acidic solution 3 dE/dt = 50 mV/s, t_r = 0.8 s

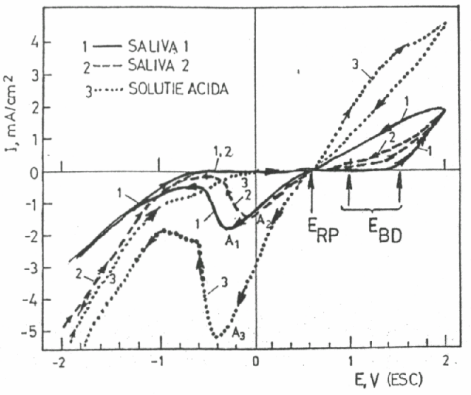

Fig. 8. Cyclic voltamogran for Gaudent S in acidic solution 4 ; dE/dt = 50 mV/s t_r = 0.8 s

In all solutions, the cyclic polarization curves for Gaudent S alloy exhibit a pronounced cathodic peak associated with any electro-reduction processes of the corrosion products [9].

CONCLUSIONS

The cyclic polarization curves have very different shapes depending on nature and composition of the studied alloy, on composition of the corrosion media, on pH, and so on.

Cyclic polarisation curves offer many informations concerning the passivation/corrosion processes taking place in various alloy/corrosion media systems under action of an electrode potential.

REFERENCES

1. Syrett B.C. and Acharya A eds., “Corrosion and degradation of implant materials”, ASTM, Phyladelphia, Pa, 1979, Special Technical Publication - 684
2. *** “Guide to Dental Material and Devices”, 7th Ed, American Dental Association, Chicago, 1975
3. 3.Burse A.B., Swartz M.L., Phillips R.W., Dykema R.V., *J. Biomed. Mat. Res.,* **6**, 1972, 267
4. Pourbaix M.:Electrochemical Corrosion of Metallic Biomaterials. *Biomaterials,* 1984, nr. 3, 122-134.
5. Fusayama T. Katazori T. Nomoto S.: Corrosion of gold and amalgam placed in contact with each other -*J. Dental Res.,* 1963, vol. 42, 1183-1197.
6. Rondelli G.: Corrosion Resistance Tests on NiTi Shape memory alloy - *Biomaterials*, 1996, vol. 17, 2003-2008.
7. Rondelli G., Vicentini B., Cigada A. - The corrosion behaviour of Ni- titanium shape memory alloys*. Corr. Sci*., 1990, vol. 30, 805-812;
8. N. Forna, V. Burlui, Gh. Nemtoi, N. Aelenei, Anca Indrei, Delia Aelenei, S. Martu; Some aspects concerning the electrochemical corrosion of the Gaudent S alloy, *Rev.Med.Chir.,* 2001*,* **105** (1), 151-156;
9. N. Forna, V. Burlui, D. Budae, Carmen Chiper, Delia Aelenei, I. Gradinaru, R. Chelariu, Coroziunea aliajului dentar Gaudent S in prezenta ionilor SO_4^{2-} si Cl^-., *Medicina stomatologica,* 2001, **5** (1), 344-347.

STUDIA UNIVERSITATIS BABEŞ-BOLYAI, CHEMIA, XLVI, 1-2, 2001

GAS HOLDUP AND LIQUID VELOCITY IN A TRIPHASIC EXTERNAL-LOOP AIRLIFT REACTOR

MARIA GAVRILESCU, FLORINA UNGUREANU

Technical University "Gh. Asachi" Iasi, Faculty of Industrial Chemistry, Mangeron Blvd. 71, 6600-IASI, Romania

ABSTRACT. Airlift reactors are heterogeneous contactors suitable for processes in which a close contact between phases and a good mixing are required. Airlift reactors are attractive for research and industry due to their particular hydrodynamic characteristics, which can be easily modified by the selection of a set of geometrical and operating parameters. Under these concerns, experiments were conducted to discern the relationship between the hydrodynamics of a solid-suspended external-loop airlift reactor of laboratory scale, and the operating conditions such as the gas velocity, the solids loading and density. The air flow rate, solids loading and solids density significantly affect the hydrodynamic characteristics of the investigated external-loop airlift reactor. Empirical correlation for gas holdup and liquid circulation velocity were proposed and found to be functions on the above-mentioned operating parameters. A reasonable agreement is found between the predicted and the measured values.

1. Introduction

Airlift reactors are heterogeneous contactors suitable for processes in which a close contact between phases and a good mixing are required. They are attractive for research and industry due to their particular hydrodynamic characteristics, which can be easily modified by the selection of a set of geometrical and operating parameters.

Airlift reactors are largely applied in biotechnology and environmental engineering, so that they appear to be one of the must important bioreactor configurations. They are most particularly employed in cultivation of plant and animal cells, as well as for waste water treatment, where combine a high treatment capacity with a low ground area occupied [1-3].

Airlift reactors are column reactors divided into two sections [4-6]:

- the riser, where the gas is injected;
- the downcomer.

They are classified according to the way in which the loop for circulating liquid is arranged, as follows:

- the internal-loop airlift reactors, which contain the riser and the downcomer in the same column;
- the external-loop airlift reactors, where the riser and the downcomer are separated tubes, side-by-side and connected at the top and the bottom by pipes.

External-loop airlift bioreactors have been frequently used in laboratory investigations, as well as in bench-scale and pilot-plant systems, because of the more-defined conditions and characteristic properties:

- a complete degassing of the liquid at the top which prevent the accumulation of gases produced during biological processes, which can reduce the mass transfer driving force;

- no zones of irregular flow at top and bottom of the bioreactor;
- easy removal of heat from the device;
- easy measurement and control of liquid circulation rate in the downcomer without complications arising from the gas content.

External-loop airlift reactors have also been used as gas-liquid (-solid) contacting devices in biological processes, preferentially at large scale, due mainly to their high controllable liquid circulation rates, a key design/operating parameter [7].

Some of the hydrodynamic parameters of interest in reactor design are the gas holdup, the magnitude of induced liquid circulation, and the liquid phase dispersion coefficient in various regions of the reactor. The gas holdup impacts upon reactor design because the total volume of the reactor for any range of operating costs and conditions depends on the maximum holdup that must be accommodated. The gas holdup also determines the residence time of the gas and liquid and, in combination with the bubble size, it influences the gas-liquid interfacial area available for mass transfer. The liquid circulation originates from the difference in the bulk densities of the fluids in the riser and downcomer [2,4,6,8-10].

The investigation is simpler when a two-phase system is involved. The complexity increases when a third phase (solid) is present into the system. The fermentation processes, as well as the biological waste treatment are characterized by the presence of a solid phase, slightly denser than water and where dynamic solid concentrations and density may occur. Usually, these investigations are performed at laboratory or pilot scales.

The main problem encountered when passing from laboratory to a larger scale is the changes of the fluid dynamics in the system. In environmental biological remediation processes, the microorganisms used for removal of polluting compounds can be immobilized as biofilm on solid particles of 1-2 mm diameter (sand, beads, charcoal), which are entrained by the liquid circulation flow. Because particle density changes as the biofilm grows, it is important to investigate the effect of solid loading and density on the airlift behavior. Therefore, mathematical models that should quantify these influences are valuable.

Several authors investigated the effect of the solid phase presence in airlift reactors on the hydrodynamic behavior [4,11-15]. Working with a low-density solid phase and with high amounts of solids, Freitas and Teixeira [11] found that liquid velocity in an external-loop reactor was drastically reduced by the presence of high-density solid particles. Kochbeck et al. [12] stressed that the liquid velocity in an external-loop airlift reactor was affected by the solid presence. Freitas et al. [13] found that solid loading and density had a considerable influence on gas holdup, liquid velocity and mixing time of an internal-loop airlift reactor with an enlarged degassing zone.

The flow and pathway complexity of these mixtures make difficult the hydrodynamic modeling of the airlift reactors. This problem becomes complicate when the solid density is variable, as in the biofilm processes [2,16]. Also, the influence of the solids on hydrodynamics is significant and hard to be predicted, because it can be in a continuous dynamic:

- changing quantity
- changing density
- changing size.

Only few of the models in literature describe the hydrodynamic of three-phase airlift reactors [2,4,13].

In this work, the behavior of a laboratory three-phase external-loop reactor was investigated. The objective of this study was to examine the hydrodynamic behavior when the hydrodynamic parameters are affected by the operating parameters. Therefore, the effect of gas superficial velocity, solid loading and solid density on gas holdup and liquid velocity were determined experimentally. Also, mathematical correlation between the gas holdup as well as the liquid velocity, and the specified parameters, respectively were developed and validated.

2. Experimental

Experiments were performed in an external-loop airlift reactor of laboratory scale, made of glass, with a working volume of 1.8 L, schematically depicted in Fig.1. The main geometrical parameters are presented in Table 1.

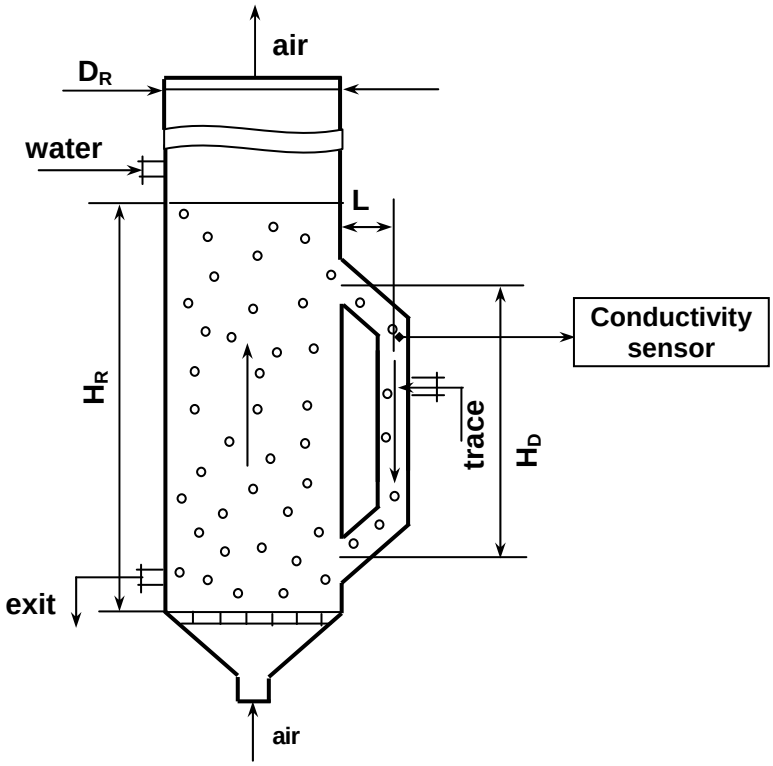

Fig. 1. Experimental setup

The downcomer joins the riser 0.20 m above the distributing plate. Air was used as gas phase, injected through a porous plate (G1 type). The superficial gas velocity ranged initially between v_{SGR} = 0.006 – 0.11 m/s. The superficial gas velocities are based on the riser cross sectional area, at normal conditions (10^5 Pa, 20^0C). Tap water was used as liquid phase. The particles used as solid phase were polypropylene (d_s = 2.3 ± 0.125 mm) and glass (d_s = 2.5 ± 0.150 mm) beads, respectively. The density values were as follows: ρ = 1200 kg/m^3, for the polypropylene beads and ρ = 3200 kg/m^3 for the glass beads. The solid fraction ranged between ε_S = 0 – 20 %.

The experiments were performed at room temperature (20 ± 2^oC) in batch mode. The average volumetric riser gas hold-up (ε_{GR}) was determined from the manometric measurements of the hydrostatic pressure in the riser [4,9]. The sensor was connected to the reference via a differential manometer. Air bubbles in the manometer line were removed by frequent bleeding of the system; pressure oscillations were dampened out by the insertion of capillary sections in the line. It was assumed that the separation of the gas from the liquid phase is complete at the top of the reactor and the liquid flowing in the downcomer was bubble-free.

A tracer method was employed for liquid circulation measurement. The liquid velocity in downcomer was measured with a conductivity probe, as follows: for each set of experimental conditions, a pulse of saturated NaCl solution was injected into the downcomer entrance [4,8,10]. The response was determined by the conductivity probe placed under the injection point at a distance of 0,8 m. The data acquisition was stopped once a constant conductivity value was achieved. Three replicates were made for each set of experimental conditions, with a mean error of 5%.

Table 1.

Geometric characteristics of the laboratory external-loop airlift reactor

Characteristic	***Symbol***	***Units***	***Value***
Riser height	H_R	m	1.16
Downcomer height	H_D	m	0.55
Connecting pipes length	L	m	0.05
Riser cross sectional area	A_R	m^2	0.22
Riser diameter	D_R	m	0.06
Downcomer diameter	D_D	m	0.025
Downcomer cross sectional area	A_D	m^2	0.031
Downcomer to riser cross sectional areas ratio	A_D/A_R	-	0.14
Liquid volume	V_L	m^3	0.0018

The downcomer linear velocity, v_{LD} was determined from the length of the liquid path and the period between two adjacent conductivity maxima of the pulse propagation, using the following relation:

$$v_{LD} = \frac{x}{\Delta t} \qquad (1)$$

where x is the distance between the injection point and the probe, Δt is the time required by the tracer to travel from the injection point to the probe (the first peak of the response curve).

3. Results and Discussion

The need to work with triphasic dispersions is common seen in chemical engineering and biotechnology. Information on the behavior of suspensions and the gas and liquid flow required to attain the fully suspended state is essential for design and operation, knowing that airlift reactors are better to suspending solids than bubble columns [1, 17,18].

Preliminary experiments made with the two categories of beads showed that the solid distribution in the airlift device generally tend to be uniform for gas superficial velocities higher than v_{SGR} = 0.01 m/s, although the lower limit for v_{SGR} was 0.006 m/s in biphasic systems. Information on minimum fluidization velocity, concentration of solids in riser and downcomer, and solid segregation in solid mixtures will be published in a future work.

No experiments were made with different sparger configurations. There are data in literature on the influence of the gas sparger on hydrodynamics in airlift contactors. Most of them show that the gas sparger has little influence on the hydrodynamic parameters in airlift reactors, as long as the entire cross-section of the riser is uniformly sparged [4,19,20]. Merchuk [20] found that there is no difference in the gas holdup and liquid velocity for different distributing plates, in gas-liquid systems circulating in an external-loop airlift reactor. Chisti [3,4] showed that the sparger had a little effect on gas holdup in tall airlift reactors, when plates were properly designed. Contrary reports showed that this influence exists. Freitas et al. [13] reported that a distributing plate of 0.5 mm orifices has shown a different gas holdups when compared with those having 1.0; 1.6 mm hole diameters. Similar results were reported by Snape et al. [21]. Also, transition between homogeneous to heterogeneous regime differs when plates with different hole diameters were used [11,13], the transition being most pronounced for the smallest orifices. For triphasic gas-liquid solid systems it was reported that the solid content supress the differences between initial bubble size generated by different types of plates, enhanced by the influence of liquid circulation. This makes also the difference between the airlift and bubble column bioreactors [3-6].

Gas holdup

For different experimental conditions, gas hold-up measured in the riser was found dependent on the riser gas superficial velocity, solid loading and solid density (Fig. 2).

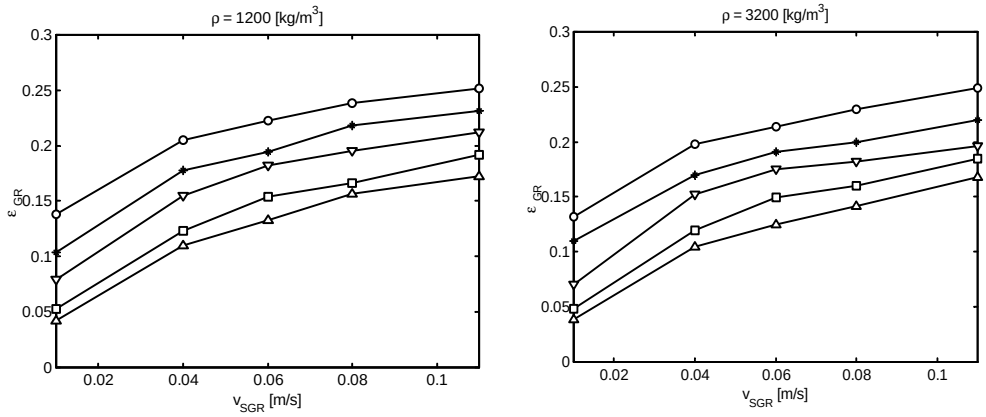

Fig. 2. Dependence of the gas holdup in the riser on the gas superficial velocity (a - ρ = 1200 kg/m^3; b - ρ = 3200 kg/m^3; ε_S: --o-- 0%; --∗--5%; -- —10%; --x-- 15%; --Δ-- 20%).

Gas holdup increases rapidly with gas superficial velocity up to a certain value of v_{SGR} and then changes the slope of the dependence. This can be ascribed to the change of bubbling flow in the riser to transition ($v_{SGR} \cong 0.04$ m/s) and turbulent ($v_{SGR} \cong 0.08$ m/s) flow respectively. This behavior was reported in literature often comparative to that in a bubble column where the transition is less smoother than in the airlift reactors, because the superimposed liquid circulation reduces the influence of sparger configuration on bubbling regime [4,13-15].

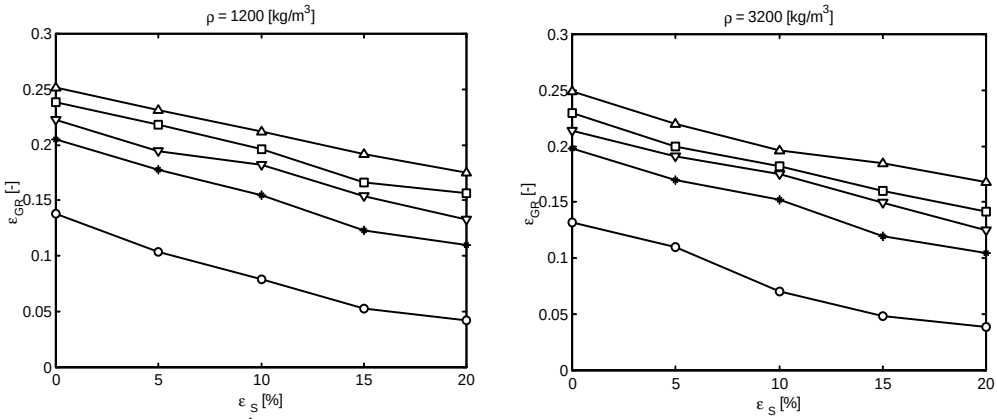

Fig. 3. Effect of solid loading on gas holdup (a - ρ = 1200 kg/m^3; b - ρ = 3200 kg/m^3; v_{SGR}: --o—0.01 m/s; --∗--0.04 m/s -- — 0.06 m/s; --x—0.08 m/s; --Δ-- 0.11 m/s).

The effect of solid loading is marked: the progressive solid loading in the system results in a significant decrease in riser gas holdup (Fig. 3). This behaviour can be considered as the result of reduced flow area of gas and liquid phase and coalescence development and increasing. Also, it seems that solid density has a

comparable influence on riser holdup with that solid loading. It can be also seen in Fig. 4 the combined effect of gas superficial velocity and solid loading on gas holdup for the particles with different densities.

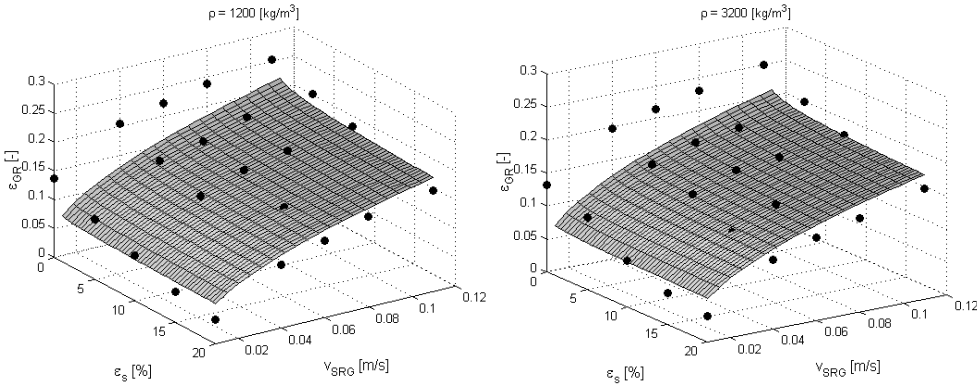

a) b)

Fig.4. Influence of solids loading and riser superficial gas velocity on the riser gas holdup for two densities of the solid particles (a - ρ = 1200 kg/m^3; b - ρ = 3200 kg/m^3).

For lower air flow rates, riser gas holdup is a strong function of the riser superficial gas velocity, increasing with the increase of the air flow rate. For higher air flow rates, gas holdup dependence on gas superficial velocity becomes smaller. The effect of solid loading is clear, once the progressive introduction of solids in the system results in gas holdup decreasing, as a result of diminishing in flow area and as a consequence of coalescence intensification. Also from Fig. 4 (a,b) it seems that solid density has little influence on riser gas holdup, being observed a small decreases of ε_{GR} with the increase of solid density.

Liquid velocity

As was expected, downcomer liquid velocity increases with any increasing in riser gas superficial velocity (Fig.5).

At small gas flow rates, the riser gas holdup increases considerably more with increasing gas velocity than that in the downcomer [26]. Thus, the resulting large driving force leads to a larger increase of liquid velocity for low superficial gas velocity, whereas at larger gas throughputs, the liquid velocity tends to level [11-13]. As can be seen from Fig. 6, the dependence of downcomer liquid velocity becomes less marked with increasing solid loading. Also, the effect of solid density on downcomer linear liquid velocity consists in an increasing of v_{SLD} with density increase, probably because of the inertial effects. Also, the solid particles cause frictional loss as a consequence of the reduction of the flow area of gas and liquid phases. Similar results were reported by Freitas et al. [13], Lu et al. [27]. Downcomer liquid velocity on gas superficial velocity in the riser decreases with solid loading, mainly as a consequence of circulation driving force diminishing, reflected by the decrease of riser holdup because of bubble coalescence development.

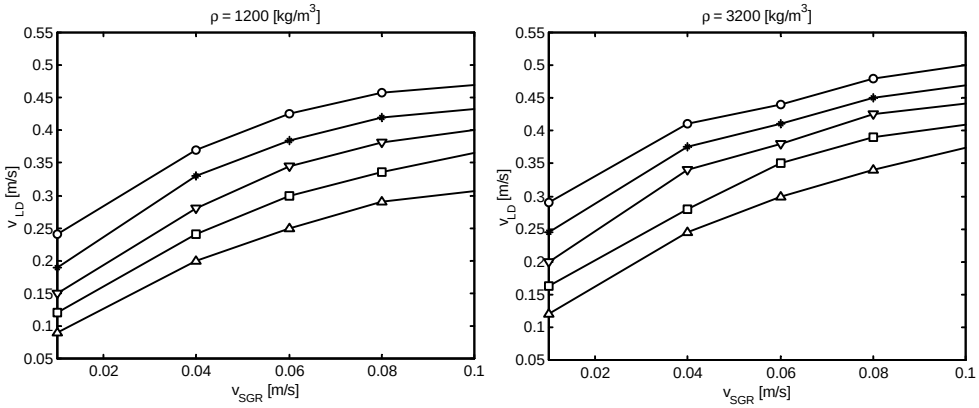

Fig. 5. Variation of the downcomer liquid velocity with the superficial gas velocity in the riser (signification of symbols as in Fig.2).

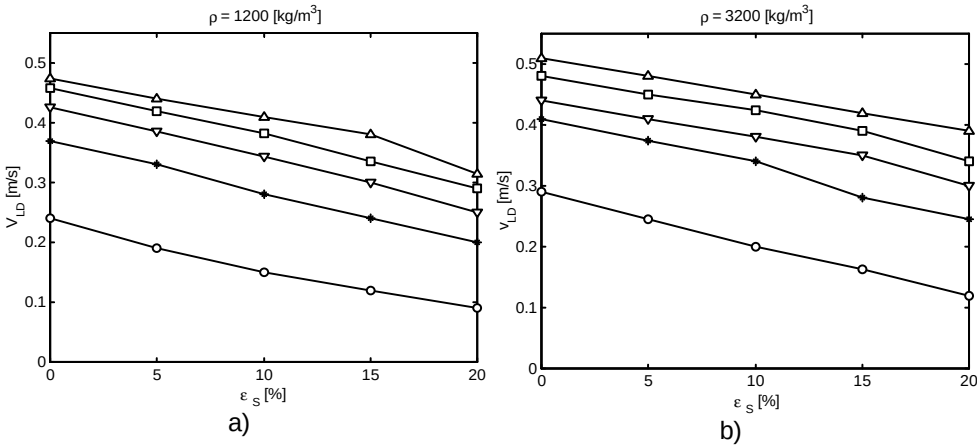

Fig. 6. Effect of solid loading on downcomer liquid velocity (signification of symbols as in Fig.3).

The influence of solid loading and gas superficial velocity on the downcomer liquid velocity is represented tridimensionally in Fig. 7. The increase of solid loadings produces a decrease of the liquid velocity, due to the decrease of driving force for circulation, and riser holdup is also reduced by the introduction of solids (Figs 3,4). Figs. 7a and 7b compares the downcomer liquid velocity for low and high density solids, allowing for the conclusion that, generally, solid density produces a small increase in v_{LD}.

Correlation of data

The hydrodynamic variables ε_{GR} and v_{LD} were correlated to the main operating parameter v_{SGR} and the solid loading and density using non-linear regression. The following equations resulted:

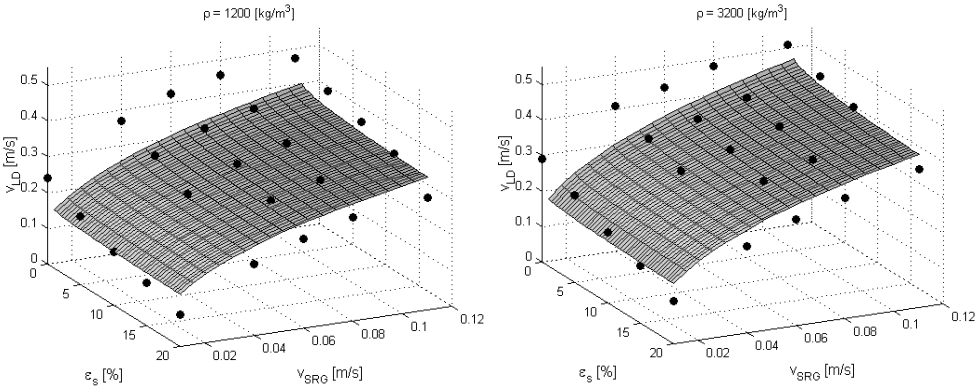

a) b)

Fig. 7. Influence of riser superficial velocity and solid loading on downcomer linear liquid velocity, for two densities of solid particles (a - ρ = 1200 kg/m^3; b - ρ = 3200 kg/m^3).

$$\varepsilon_{GR} = 0.835\, v_{SGR}^{0.45}\, \varepsilon_S^{-0.055}\, \rho^{-0.043} \qquad (2)$$

$$r = 0.900,\ s^2 = 6.59 \cdot 10^{-4}$$

$$v_{LD} = 0.28\, v_{SGR}^{0.39}\, \varepsilon_S^{-0.042}\, \rho^{0.175} \qquad (3)$$

$$r = 0.923,\ s^2 = 2{,}06 \cdot 10^{-3}$$

Comparison of the calculated and measured ε_{GR} and v_{LD} values are given in Figs. 8 and 9. ε_{GR} predictions based on eq. 2 generally are in good agreement with the experimental data, with an average error of 6%. The comparison between experimental v_{LD} data and those calculated with eq. (3) shows a good concordance, the average error being 5%.

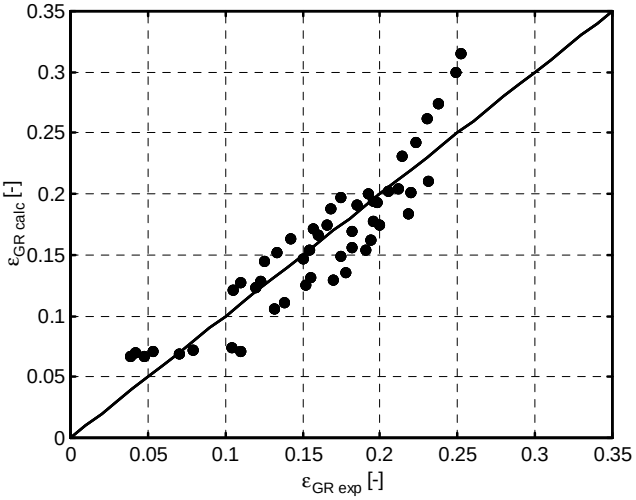

Fig. 8. Correlation of the calculated (with eq. 2) and experiemntal ε_{GR} data.

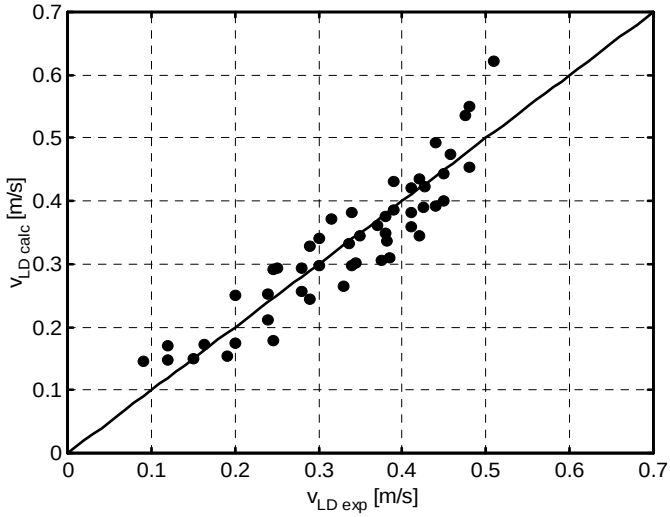

Fig. 9. Correlation of the calculated (with eq. 3) and experiemntal v_{LD} data

4. Conclusions

Gas holdup and liquid velocity were measured in a laboratory external-loop airlift reactor with gas-liquid-solid dispersions. Experiments were performed to investigate the effect of the operating parameters, the riser gas superficial velocity, the solid loading and density on the riser gas holdup and the downcomer liquid velocity. No experiments were conducted to found the effect of the distributor on hydrodynamics.

Both hydrodynamic parameters investigated were found to vary with the gas superficial velocity and solid loading, dependent on the particle density.

Airflow rate and solid loading have a great effect on riser gas holdup and downcomer liquid velocity. The increase in riser air velocity leads to an increase in riser gas holdup and liquid velocity. In opposition, the introduction of solids generates a tendency of decreasing of the gas holdup and liquid velocity. The solid density increase affect gas holdup and liquid velocity.

The present investigation clearly evidenced that the presence of the third phase (solid) in an airlift reactor can have a strong influence on performance of these contactors.

In terms of these adjustable parameters, it is possible to predict ε_{GR} and v_{LD} with the correlation developed by non-linear regression. Therefore, knowledge of the hydrodynamic behavior of the triphasic airlift reactors and the factors that influence it is necessary for design, modeling and operation, being of particular importance during the process of scaleup from laboratory to industrial scale.

Additional investigations have to be performed in large-scale external-loop airlifts to verify the proposed correlation between parameters.

REFERENCES

1 P.D. Gaspillo, S. Goto, J. Chem. Eng. Japan 24 (1991) 680-682.

2 J.B. Snape, I.J. Dunn, J. Ingham, J.E. Prenosil, *Dynamics of Environmental Bioprocesses. Modelling and Simulation,* Weinheim, VCH Verlagsgesellschaft, 1995.

3 Y. Chisti, Appl. Mech. Rev., 51 (1998) 33-112.

4 Y. Chisti, *Airlift Bioreactors*, Elsevier, London-New York, 1989.

5 M. Gavrilescu, *Pneumatic Bioreactors*, Dosoftei Press, Iasi-Romania, 1997.

6 U. Onken, P. Weiland, *Advances in Biotechnological Processes*, Vol 1, New York, Alan R. Liss, pp.67-95.

7 K. Akita, O. Nakanishi, K. Tsuchiya, Chem. Eng. Sci. 49 (1994) 2521-2533.

8 M. Gavrilescu, R.Z. Tudose, Chemical Engineering Communications, 156 (1996) 89-113.

9 M. Gavrilescu, R.Z. Tudose, Bioprocess Engineering, 18 (1998) 17-26.

10 M. Gavrilescu, R.Z. Tudose, Bioprocess Engineering, 18 (1998) 83-89.

11 C. Freitas, J.T. Teixeira, Bioprocess Eng. 18 (1997) 267-279.

12 B. Kochbeck, M. Lindert, D.C. Hempel, Chem. Eng. Sci. 40 (1992) 1301-1310.

13 C. Freitas, M. Fialova, J. Zahradnik, J.A. Teixeira, Chem. Eng. Sci. 55 (2000) 4961-4972

14 S.J. Hwang, Y.L. Cheng, Chem. Eng. Sci. 52 (1997) 3949-3960.

15 W.A.J. van Benthum, R.G.J.M. van der Lans, M.C.M. van Loosdrecht, J.J. Heijnen, Chem. Eng. Sci. 55 (2000) 699-711.

16 M. Gavrilescu, M., Macoveanu, Bioprocess Eng. 23 (2000) 95-106.

17 S. Goto, Y. Matsumoto, P. Gaspillo, Chemical Engineering Communications, 85 (1989) 181-191.

18 M. Immich, U. Onken, Chemical Engineering Science, 47 (1992) 3379-3386.

19 U. Onken, P. Weiland, European Journal of Applied Microbiology and Biotechnology, 10 (1980) 31-40.

20 J.C. Merchuk, Chemical Engineering Science, 41 (1986) 11-16.

21 J.B. Snape, M. Fialova, M. Zahradnik, N.H. Thomas, Chemical Engineering Science 47 (1992) 3387-3394.

22 M.A. Young, R.G. Carbonell, D.F. Ollis, AIChEJ, 37 (1991) 403-428.

23 M. Gavrilescu, R.Z. Tudose, Chem. Eng. J., 69 (1998) 85-91.

24 M. Chisti, B. Halard, M. Moo-Young, Chem. Eng. Sci. 43 (1988) 451-457.

25 M. Gavrilescu, R.Z. Tudose, Chem. Eng. J., 66 (1997) 96-104.

26 M. Gavrilescu, *Study of heterogeneous systems flow in airlift reactors, Thesis*, Technical University of Iasi, 1997.

27 W-J. Lu, S.J. Hwang, C.M. Chang, Chem. Eng. Sci., 40 (1995) 1301-1310.

STUDIA UNIVERSITATIS BABEŞ-BOLYAI, CHEMIA, XLVI, 1-2, 2001

STUDIES OF STEEL CORROSION IN CHLORIDE ENVIRONMENT

CRISTINA IOSIF, ANCA DUȚĂ, RODICA ȚICĂ

Transilvania University, Chemistry Dept., I. Maniu 50, 2200 Brasov

ABSTRACT. The corrosion processes were studied on steel samples in different solutions, which contain Cl^- and H^+ ions.

The tests were done on a galvanostatic installation and the experimental results were used to obtain the Tafel plots. Then, the kinetic and thermodynamic parameters were calculated (the density of corrosion current, the mass index, the penetration index and the corrosion potential). Also the influence of $K_2Cr_2O_7$ addition in the corrosion environment was discussed.

KEYWORDS: corrosion sintered steel, corrosion inhibitor.

1. INTRODUCTION

Corrosion is an undesired and spontaneous process, which affects all the metallic surfaces or alloys in the presence of the corrosion agents from the environment.

The process consists in the oxidation of a metal and a reduction of one of the species from the environment.

The characteristics of this process depend on three types of factors:

a) the nature of the metal surface;
b) the nature of the corrosion agent;
c) the corrosion conditions.

The modification of one of them could produce a modification of the corrosion parameters. Thus by alloying the metallic surface the potential usually increases and passivation may occur.

For example by alloying iron with chromium, the corrosion potential increases from the value – 440 mV to + 180 mV, [9]. The final value of the corrosion potential depends of the chromium percent, [3].

This paper describes the corrosion process of a steel with low carbon content in HCl and $CaCl_2$ solutions. The chloride ion is one of the most aggressive corrosion agents and in combination with dissolved O_2 is able to form oxy-chlorides which are also soluble compounds, responsible of the corrosion, [10].

The aggressive action of the environment is reduced by adding a corrosion inhibitor as sulfate, chromate, phosphate. In this purpose we tests also the influence of $K_2Cr_2O_7$ on the corrosion process.

2. EXPERIMENTAL

The analyzed steel, OLC 45 is an iron alloy with the composition: 0.45 % C, 0.2%Mn, 0.17 % Si, 0.04 %S, and 0.04 % P, [4].

Tests were done on uncovered samples and samples covered with a protective chromium layer. A copper layer was first deposit on the steel sample, then the protective layer was done by galvanic covering.

Before testing, the samples were mechanically polished degreased and washed in acetone.

As corrosion agent there were used the following solutions:

HCl 0.1N

$CaCl_2$ 0.1N

HCl 0.1N +$CaCl_2$ 0.1N

The influence of $K_2Cr_2O_7$ was studied using HCl + $K_2Cr_2O_7$ solutions with concentration between 10^{-1}–10^{-3} moles/L.

Tests were done at room temperature using a galvanostatic installation, previously presented [5,6] and current-potential data were used to obtain the Tafel plots. Measurements started by evaluating the static equilibrium potential, then the intensity was stepwise modified and the potential was measured, both on the sample and on the platinum counter-electrode (S=1cm$^{2)}$) using a saturated calomel electrode as reference:

$(Hg/HgCl_2/Cl^-_{SAT}$ E_{SCE} = 0.2422 V)

The electrode was polarized first catodically then anodically.

3. RESULTS AND DISCUSSIONS

Using the experimental data the polarization curves were plot in the Tafel co-ordinates: lgI = F(E). (Fig. 1, and Fig. 2). Based on these plots the corrosion current I_{CORR} and potential E_{CORR} are evaluated. Same types of plots are used also for the data in the corrosion environments containing $K_2Cr_2O_7$ at different concentrations.

The corrosion potential is the thermodynamic measure of the reactivity of a metallic material in reaction with aggressive agent. This value gives information about the superficial modification of the metal which lead to a lower or a higher activity than the standard value, which is for iron: E^0_{Fe} = - 0.440 V.

The kinetic parameters of the corrosion are: the density of the corrosion current, the corrosion rate, K_g, and the penetration index, P_{mm}.

For a sample with surface aria, A sample density of the corrosion current is given in relation (1):

$$j_{corr} = \frac{I_{corr}}{A_{sample}} \tag{1}$$

The corrosion rate, K_g and the penetration index, P_{mm} can be calculated for a metallic material with the molecular weight, M_{metal} , and the density,ρ as follows :

$$K_g = \frac{M_{metal}}{ZF} j_{corr} \text{ [g / m}^2\text{ h]} \tag{2}$$

$$P_{mm} = \frac{K_g 8760}{\rho} \text{ [mm / year]} \tag{3}$$

were F= 96489 A·s, is the Faraday number and Z is the number of electrons lost by the metallic material during the oxidation process.

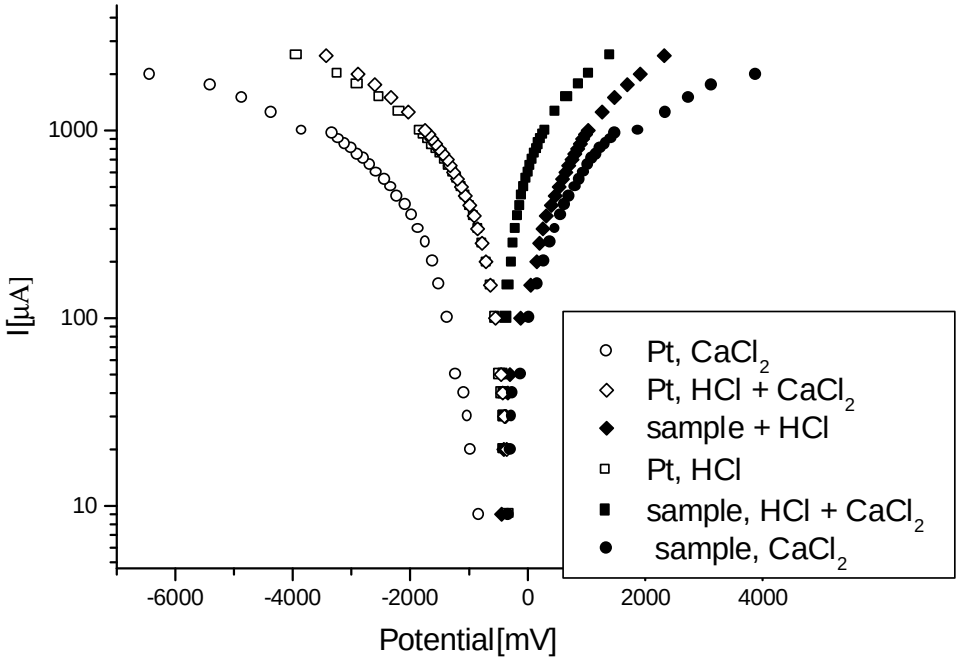

Fig. 1 Corrosion of OLC 45/Cu/Cr in different chloride solution

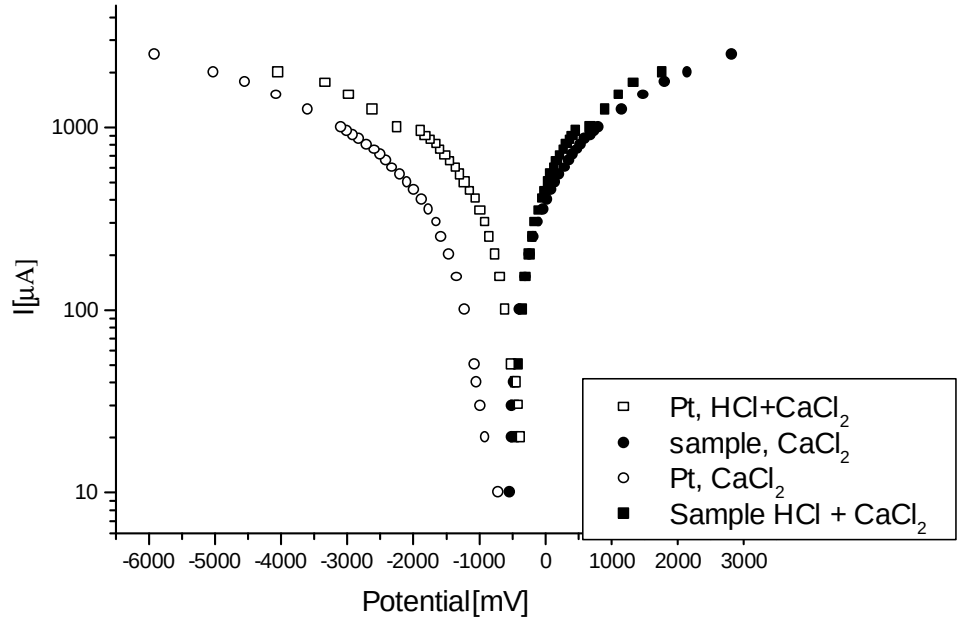

Fig. 2 Corrosion of OLC45 in different chloride solutions

Kinetic parameters

Table 1 and 2 present the kinetic parameters calculated using relations (1) –(3)

Table 1

Kinetic parameters in the absence of $K_2Cr_2O_7$:

Sample	Corrosion agent	K_g [g / m^2 h]	P_{mm} [g / m^2 h]	E_{CORR} [mV]	E_{METAL}^0 [mV]
OLC 45	HCl 0.1 n	1.68	1.87	-400	-440
OLC 45/Cu/Cr		0.91	1.1	-380	-720
OlC 45	$CaCl_2$ 0.1 n	0.38	0.42	-550	-440
OlC 45 /Cu/Cr		0.0.21	0.25	-550	-720
OlC 45	HCl + $CaCl_2$ 0.1 n	2.27	2.52	-400	-440
OlC 45/Cu/Cr		0.93	1.13	-450	-720

Table 2

Influence of adding $K_2Cr_2O_7$ on the corrosion rate of OLC45:

Sample	Corrosion agent	K_g [g / m^2 h]	P_{mm} [g / m^2 h]	E_{CORR} [mV]	E_{METAL}^0 [mV]
OLC 45	HCl 0.1 n	1.68	1.87	-400	-440
OLC 45 /Cu/Cr		0.91	1.1	-380	-720
OlC 45	HCl 0.1 n+ $K_2Cr_2O_7$ 0.1m	13.52	15.07	+120	-440
OlC 45/Cu/Cr		2.05	2.49	+515	-720
OlC 45	HCl 0.1 n + $K_2Cr_2O_7$ 0.01 m	10.56	11.56	-135	-440
OlC 45/Cu/Cr		4.37	5.31	+180	-720
OlC 45	HCl 0.1n + $K_2Cr_2O_7$ 0.001m	11.49	4.76	-125	-440
OlC 45/Cu/Cr		4.76	5.79	+125	-720

The results allow the next observations:

- For both samples the values for index penetration is:
- $(P_{mm})_{CaCl2} < (P_{mm})_{HCl} < (P_{mm})_{HCL + CaCl2}$
- A reduction of index penetration and corrosion rate for the samples covered with chromium, appears in every testing corrosion agent. So, chromium covering increases samples resistance at corrosion.
- The results obtain in $CaCl_2$ corrosion agent confirm the inhibitor action of this in a non-acid environment, [8]. In the presence of HCl and $CaCl_2$ environment the samples exhibit a cumulate effect of the chlorine ions, Cl^-, from HCl and from $CaCl_2$. Thus, the values obtain for the kinetic parameters in the presence of HCl and $CaCl_2$ environment are comparable with the values obtain by summarizing the results obtained separately in the two agents.

- Comparatively, the kinetic parameters values present a considerable increase by adding $K_2Cr_2O_7$. The chromate ions are known as anodic inhibitors, [7] but only in an non-acid environment. In a very acidic solution anodic inhibitors act like corrosion accelerators. Also, is very important to use the correct concentration of chromate: a small quantity can produce an increase of the intensity corrosion process in the already existent reaction points. The presence of the Cl^- ions may produce the pitting corrosion apparition, [2]. In this case higher quantities of inhibitor are of help only for protected samples. Fig 3 presents synthetically all theses observations.

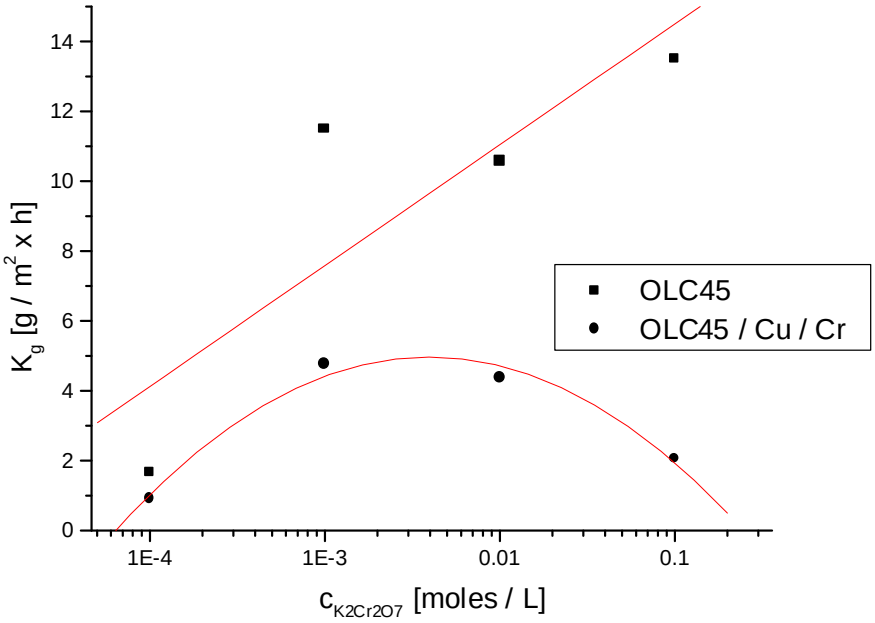

Fig. 3 Mass index of OLC 45 in HCl 0.1N + $K_2Cr_2O_7$

Thermodynamic studies

As it is know the corrosion potential value, $E_{CORR,}$ gives information about the likelihood of the processes between the metal substrate and the corrosion agent. Thus we can discussed the corrosion thermodynamic aspects.

Table 1 and table 2 give these values; In the activator absence the value of the corrosion potentials of both samples confirm the classical corrosion reaction of iron in H^+ as corrosion agent, [1]:

$$Fe^0 \rightarrow Fe^{2+} + 2e^- \qquad (4)$$

For this reaction the electrical potential was compared with the standard value of the oxidation-reduction couple Cr^{3+} / Cr : $E^0_{Cr3+/Cr}$ = - 720 mV.

By using the activator two oxidation-reduction couples are formed: Fe^0/Fe^{2+} and Cr^{6+}/Cr^{3+}. For the last couple, the corresponding reduction equation is:

$$Cr_2O_7^{2-} + 6\,e^- + 14\,H^+ \rightarrow 2Cr^{3+} + 7\,H_2O \quad (5)$$

The theoretical value of the oxidation-reduction potential is [9]:

$$E^0_{Cr6+/Cr3+} = +660 \text{ mV}.$$

This value is comparable with the experimental results (Table 2).

Thus, the dominating process confirms the formation of chromium soluble compounds, responsible for the corrosion process.

4. CONCLUSION

The corrosion process was investigated in different chloride environments using a galvanostatic installation and the corrosion parameters were calculated. It was tested rough and protected steel samples with low carbon content. The steel samples protected with a copper/chromium layer have registered higher corrosion resistance than the unprotected samples due to the more inert chromium oxide layer, which increase the oxidation-reduction potential of iron, [3].

The rate of corrosion in every case was:

$$(P_{mm})_{CaCl2} < (P_{mm})_{HCl} < (P_{mm})_{HCl + CaCl2}$$

It was studied also the effect of adding $K_2Cr_2O_7$ in the environment.

For the uncovered samples the results confirm an activator effect of $K_2Cr_2O_7$ for the all range of the tested concentration. By covering with a chromium protective layer the corrosion resistance increases and $K_2Cr_2O_7$ may turn into an inhibitor in the higher concentrations domain.

REFERENCES

1. Ament, P.C.H., Corrosion Fatigue of Structural Steel in SeaWater, Delft University Press, Delft, 1998.
2. Jansen, L., Pitting Corrosion of Stainless Steels - The Role of Inclusions and the Effect of Surface Deformation, Proefschrift Tehnische Universitet, Delft, 1993.
3. Oniciu, L., Coroziunea metalelor, Editura Ştiințifică şi Enciclopedică, Bucureşti, 1986.
4. Gădea, S., Metalurgia şi studiul materialelor, Editura didactică şi pedagogică, Bucureşti,1987.
5. Duță, A., Dinescu,I., Țică, R., Electron Microscop Investigation on Coroded Steels Cluj-Napoca, 2000.
6. Duță, A., Ursuțiu, D., Țică, R., Nanu, D., Dinescu, I., Corrosion of Sintered Steel in NaCl Solutions, Iaşi 2000.
7. Constantinescu, M., Badea, T., Coroziune şi protecție anticorozovă, Editura didactică şi pedagogică, Bucureşti,1978.
8. Zamfir, S., Vidu, R., Brănzoi, V., Coroziunea materialelor metalice, Editura didactică şi pedagogică, Bucureşti, 1994.
9. Niac, G., Voiculescu, V., Băldea, M., Formule, tabele, probleme de chimie fizică, Editura Dacia, Cluj- Napoca,1984

STUDIA UNIVERSITATIS BABEŞ-BOLYAI, CHEMIA, XLVI, 1-2, 2001

THE INDIVIDUAL MASS TRANSFER IN THE ETEROGEN LIQUID-LIQUID SYSTEMS

GABRIELA APREOTESEI LISA, RADU Z. TUDOSE*

Technical University "Gh.Asachi'' Iasi, Faculty of Industrial Chemistry, Department of Physical Chemistry (gapreot@ch.tuiasi.ro)
[*]Department of Chemical Engineering, B-dul D. Mangeron, no. 71A, Iasi 6600, Romania

ABSTRACT. The improved Lewis cell was used as an efficient device to determine the mass transfer coefficient for any ternary multi-component systems. In this paper the individual mass transfer coefficients were determined for the ternary systems: water-acetone-carbon tetrachloride, using a Lewis cell, operating continuous and batch regime, with a constant stirring rate.

1. INTRODUCTION

The mass transfer intensity can be quantified using the individual mass transfer coefficients for each phase. For the liquid-liquid extraction, the determination of these coefficients is a difficult task that was approached by lots of researchers, using two different ways (Colburn and Welch, 1942; Pratt, 1983).

In one of these ways, two partially miscible liquids were used. One of them is saturated with the other, whose saturation degree is monitored when they are contacted. This method is not very precise and can be applied in a limited number of situations.

In another way, ternary systems are used, having different values of the partition coefficients that are also different from 1. In this case, it may be considered that the mass transfer resistance is located in the phase with the lower equilibrium concentration. This hypothesis involves a great degree of uncertainty (Apreotesei and Tudose, 1998) and the method cannot be applied to any system.

In the both methods shortly described above, one of the contacted phases is dispersed as drops into the other, so that the interfacial area is difficult to determine, because the drops are deformable and the mixing intensity between the two phases is variable (Atagunduz et al., 1968; McManamey, 1961; Harikrishnan et al. 1994).

In this paper, these disadvantages are overcome by using an improved Lewis cell, which operates continuously. The experimental set-up and the operating procedure allow to determine the interfacial areas (contact surface between phases) precisely, while the mixing can be well controlled for every phase.

The Lewis cell (Lewis, 1954) with several improvements remains the most efficient method to determine the mass transfer coefficients for any ternary or for systems with more components, as the G.L. Standard stated. Numerous researchers conceived such modified cells, especially for reactive extraction study (Pratt, 1983).

The Lewis cell presented in this work was used to determine the individual mass transfer coefficients for the ternary system water acetone-carbon tetrachloride (Tudose and Apreotesei, 2000).

To asses the behaviour of the mean residence times in the cell compartments, the extraction of the acetone from carbon tetrachloride, during continuous and batch operation modes, respectively, for the same stirring intensity (850 rot/min) and solute initial concentration (7% weight).

2. EXPERIMENTAL TECHNIQUE

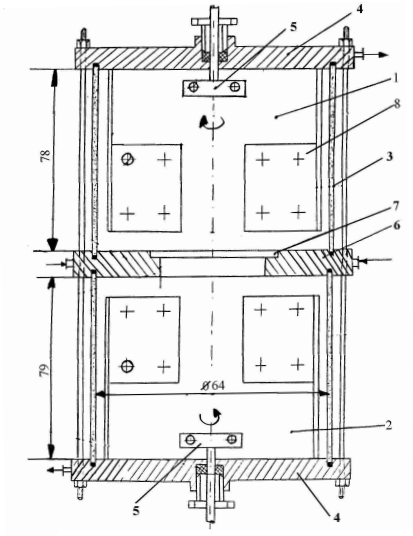

Fig. 1 Extraction cell

The cell used for the study of the mass transfer in continuous and batch operation mode was made out of Cr-Ni stainless steel and glass (Fig. 1). The compartments (1) and (2), where the aqueous and organic phases are introduced have the side walls made out of glass (3). The two edges are equipped with metallic seals (4), which support the bearings of the blade mixer (5), driven by separate engines, with changeable speed, between 80÷1200 rpm. The compartments are separated by a metallic plate (6), which has a central hole with the diameter of 30 mm, where the interface between the two liquids is located (7). The hole diameter can be modified using several rings.

Several orifices were also made in the central plate to assure the feed of the compartments with liquids.

To avoid the interface deformation by the turbulence, three baffles were placed inside each compartment. Each baffle has four holes of a 4 mm diameter. Similar holes were made on the agitator blade surfaces.

The experiments were performed using the following ternary system water-acetone-carbon tetrachloride in continuous and batch operation mode. Both liquids, water and carbon tetrachloride were purified previously by distillation, considering that carbon tetrachloride forms an azeotrope with acetone.

The feed flow rates in continuous operation mode ranged between 1,5÷6,6 kg/h organic phase and 0,87÷3,5 kg/h aqueous phase. In the batch operating mode, we studied the behaviour of the concentrations at mean residence time values ranged between 11÷90 min.

The acetone concentrations at the entrance and exit for both phases were determined using the refractometric method. Acetone balance was used to verify the measuring accuracy.

To establish the dominant resistance, the experiments occurred in the following conditions:

- mixing of the aqueous phase only;
- mixing of the organic phase only;
- mixing of both phases.

Experiments were performed using stirrer speeds of 850 rpm, when a uniform distribution of solute concentration in the liquid bulk of each compartment results and the specific transferred flux becomes independent on stirrer speed.

3. RESULTS AND DISCUSSIONS

The cell used for experimentation has a very small specific surface (namely 1.4 m^2/m^3) calculated as a ratio of the interface area between phases to the volume of both compartments of the cell. This type of specific surface calculation applies for industrial extraction columns, as well. In these conditions it is expected that the specific flux of the transferred solute is small and dependent of the cell compartments. (Tudose and Apreotesei 2000).

The dependence between the phase concentrations and the mean residence time was assessed in both discontinuous and continuous operation modes. The experiences were performed using a solution of acetone in carbon tetrachloride (7% weight) and distilled water. The concentrations were determined in mixing and non-mixing conditions of a single or both phases, at the same mixing intensity (850 rpm), when the transferred flux do not depend on the stirrer speed.

Figures 2 and 3 evidence the changes in the both phases exit concentrations as functions on the mean residence time in the cell compartments.

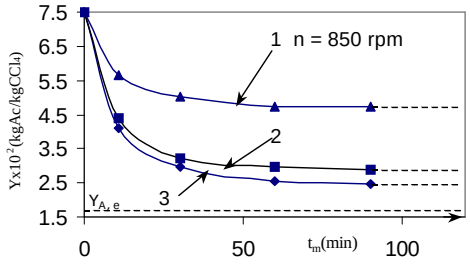

Fig. 2 The variation of the acetone concentration in the organic phase with the mean residence time in the cell in batch operating mode: 1- organic phase agitated, aqueus phase non-agitated, 2- aqueous phase agitated, organic phase neagitated, 3- both phases agitated

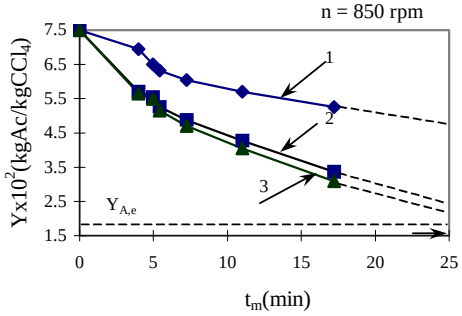

Fig. 3 Variation of acetone concentration in organic phase with the mean residence time in the cell, in the continuous operation mode

First of all, it was observed that the concentration s tends slowly to the equilibrium state owing to the small specific areas.

Second, when only one of the phases -the organic one- was mixed, the diminishing of the exit concentration is very slowly, this fact sugesting that it exists a dominant resistance in the non-agitated phase. When the aqueous phase was stirred, the concentration diminishes more rapidly ouring to a higher transfer resistance and a lower value of the molecular diffusion coefficient of this phase, comparative with the organic phase.

As was expected, the mixing of the both phases leads to an increased mass transfer intensity and the exit concentration tends to the equilibrium value.

From figs. 2 and 3 it results that the equilibrium state was reached wery slowlyouring to a very small specific area, so that it can be concluded that the mean distribution times could be chosen at very different values in the continuous operation mode.

The equilibrium data for the system water -acetone-carbon tetrachloride are presented in fig.4 (curve LF). Any point P on the ordinate represents the initial concentration of the solute in the organic phase, considering the hypothesis that the solvent (water) is pure ($Y_{A,i}$). The equilibrium solute concentration ($Y_{A,e}$) is represented by the point Q. The line PQ is the operation curve for the solute transfer from organic phase to aqueous one. The concentration of the phases at the cell exit will be done by the point M, on the line PQ.

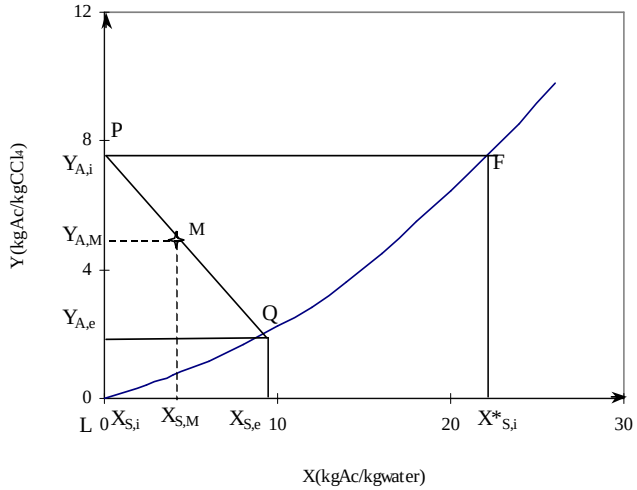

Fig.4 The operating and equilibrium curves

For this situation, the equations for the specific flux of the transferred solute will be the following:

$$n_{B,YX} = k_{X,YX} \cdot \left(X_{S,e} - X_{S,i}\right) = k_{Y,YX} \cdot \left(Y_{A,i} - Y_{A,e}\right) \quad (1)$$

They were calculated based on the rafinat and extract concentration at the exit of the cell, knowing the contact surface between phases. The individual coefficients were obtained from eqs.1.

The variation of the individual mass transfer coefficients with the residence time in the cell, in the continuous separation mode is represented in fig. 5.

The values of the coefficient decrease slowly with the cell residence time, ouring to a more rapidly decrease of the specific flux of the transferred solute, compared to the driving force. Higher individual coefficient values in the organic phase were obtained when a single phase was stirred (fig. 5a, curve 1), while these values were smaller when only the aqueous phase was stirred (curve 2).

The process intensity is diminished when the phase were the transfer resistance is predominant was not stirred, and this fact explains the small values of the transfer coefficients, when the organic phase was not agitated.

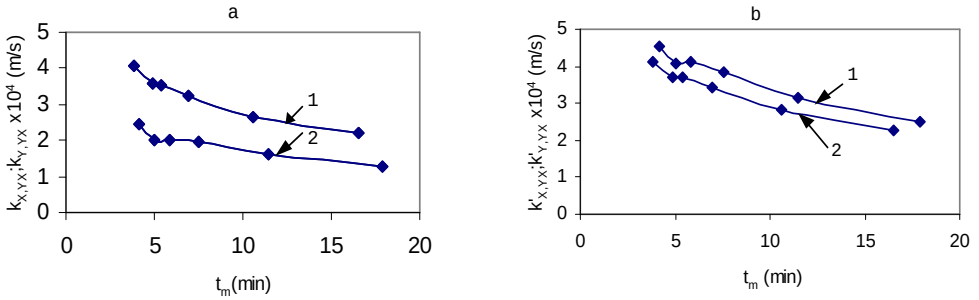

Fig. 5 The variation of the individual mass transfer coefficients with the residence time in the cell

a - a single phase stirred
1- $k_{Y,YX}$, only the organic phase stirred
2- $k_{X,YX}$, only the aqueous phase stirred

b - both phase stirred
1- $k'_{Y,YX}$
2- $k'_{X,YX}$

When both phases are agitated, the specific phases are agitated the specific flux of the transferred solute becomes independent on the stirrer speed and the individual coefficient values phases are different in the two phases.

For the system water-acetone carbon tetrachloride (fig. 5b) presented in this paper, the mass transfer coefficients in the phase were the equilibrium concentration of the solute is smaller (organic phase) are smaller than those in the adjacent phase.

This conclusion apparently contradicts the considerations of other authors (Harishnan et al., 1994). The individual coefficients were calculated from relations 1, were the driving forces were used, expressed through the difference between the feed concentration and the equilibrium value. For higher mixing intensity in both cell compartments, the solute is uniform distributed and the concentration. In this situation, the true driving forces are represented by the differences in the concentration values in cell compartments (point M, fig. 4) and an equilibrium values: ($X_{S,e}$-$X_{S,M}$) şi ($Y_{A,M}$-$Y_{A,e}$).

Table 1 presents the individual coefficient values in the two phases calculated using the true driving forces, when both phase are agitated intensely.

Table 1.

The individual mass transfer coefficients calculated using the true driving forces

t_m(min)	3.99	4.96	5.62	7.25	11.01	17.21
$k_{X,YX}$ (m/s)	$10.37x10^{-4}$	$7.94x10^{-4}$	$7.39x10^{-4}$	$7.00x10^{-4}$	$6.8x10^{-4}$	$6.41x10^{-4}$
$k_{Y,YX}$ (m/s)	$9.70 x10^{-4}$	$7.13x10^{-4}$	$6.72x10^{-4}$	$6.30x10^{-4}$	$6.0x10^{-4}$	$5.57x10^{-4}$

The individual coefficients in the organic phase, were the solute concentration is lower, have smaller values than those in the aqueous phase. The results are in concordance with those obtained by other authors.

The experiments performed in botch operation mode, for mean residence time values in the cell ranged between 11÷90 min allowed the calculation of the individual coefficients using the relationship (2), proposed by Lewis (Lewis 1954).

$$k_{X,Y} = \frac{V}{a \cdot t_m} \ln\left(c^*_{X,Y} - c_{X,Y}\right) \tag{2}$$

When the residence time is increased up to 30 min, the individual coefficients in the aqueous phase as well as those in the organic phase decrease significantly (figs. 6, 7). For longer residence times, the decreasing is insignificant as a result of the diminishing of the transferred solute flux.

As in the continuous operation mode, the experiments in the batch operation mode were performed with a single or both phases stirring.

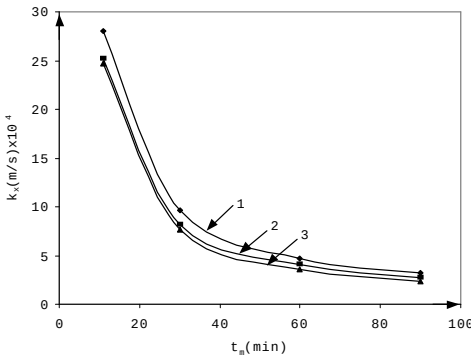

Fig. 6 The variation of the individual mass transfer coefficients in the aqueous phase with the residence time in the cell: 1- organic phase agitated, aqueus phase non-agitated, 2- aqueous phase agitated, organic phase neagitated, 3- both phases agitated

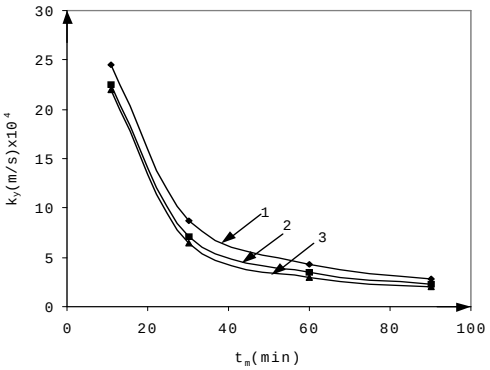

Fig. 7 The variation of the individual mass transfer coefficients in the organic phase with the residence time in the cell

The highest values of the individual mass transfer coefficient in the batch operation mode were obtained when the organic phase was mixed, because in the determinatt resistance to mass transfer is located in that phase.

The individual mass transfer coefficients obtained in this situation were a little higher than those presented in literature, in both operation modes (continuous and batch). Other authors have chosen such systems were the dominant resistance to the mass transfer was located in a single phase. In fact they determined the overall mass transfer coefficient, which was considered equal with the individual coefficient. In this way, the resulted values are a litle lower than the true value of the individual coefficients obtained in this paper. McManamey obtained in 1961 a

value of the individual mass transfer coefficient of $k_x=0.233x10^{-4}$m/s using the method Colburn and Welsh in a batch Lewis cell, with the system i-butanol-water. This value has the same order as that determined in this paper, were the value of the coefficients are dependent on the mean resistance time in the cell.

4. CONCLUSIONS

- The improved Lewis cell represents one of the most efficient method for determination of the mass transfer coefficients, in any ternary system;
- The mass transfer area is strictly measurable and can be modified under certain limits.
- The cell allowed the operation is bach and continuous mode.
- The individual mass transfer coefficient for acetone extracted from CCl_4 and water were calculated both in continuous and batch operation mode.
- The results were compared with those from literature. It was evidenced that the individual mass transfer coefficients presented in this paper are sensibly higher than those reported in literature, for binary systems, obtained using a aproximate method, that can be applied for a limited number of situations.

NOTATIONS

a- mass transfer surface, m^2;
Ac- acetone;
B- notation for solute;
c- acetone concentration (kg/m^2);
$c^{'}$- acetone equilibrium concentration (kg/m^2);
k- individual mass transfers coefficient when only one phase is stirred, m/s;
$k^{'}$- individual mass transfer coefficient when both phases are stirred, m/s;
n- stirrer speed, rpm;
n_B- the specific flux of the transferred solute, $kgAc/m^2s$;
S- notation for solvent;
t_m- mean residence times in the cell compartments (s);
X- acetone concentration in the aqueous phase, kgAc/kgwater;
Y- acetone concentration in the organic phase, kgAc/kgS;

SUBSCRIPT

ag- agitation;
A- initial solution;
B- solute;
e- equilibrium;
s- solution;
S- solvent;
X- aqueous phase;
Y- organic phase;
YX- the transfer direction is from organic to aqueous phase

REFERENCES

1. Apreotesei G. and Tudose R.Z., *SICHEM'98, International Chemistry Show*, 20-23 octombrie, 48, 1998.
2. Atagunduz G., Austin L.J. and Sawistowski H., *Chemie-Ing.-Techn*., 40, 922, 1968.
3. Colburn A.P. and Welsh D.G., *Trans. Amer. Inst. Chem. Engrs*., 38, 179, 1942.
4. Davies J.T. and Rideal E.K., "Interfacial Phenomena", Academic Press, New York, 1961.
5. Harikrishnan T.L., Probahavathy N.K. şi Varna Y.B.C., *Chem. Eng. Journal*, 15, 7, 1994.
6. Lewis J. B., *Chem. Eng. Sci.*, 3, 248, 1954.
7. McManamey W.J., *Chem. Eng. Sci*., 15, 251, 1961.
8. Pratt H.R.C., Handbook of solvent extraction, T. Wihlley – Interscience Publication, New-York, 1983.
9. Tudose R.Z. and Apreotesei G., *Chem. Eng. Processing*, accepted for publication, 2000.

STUDIA UNIVERSITATIS BABEŞ-BOLYAI, CHEMIA, XLVI, 1-2, 2001

VAPOUR-LIQUID EQUILIBRIA IN AQUEOUS SOLUTIONS OF AMMONIA AND CARBON DIOXIDE USING NEURAL NETWORKS

GABOR S. SZASZ, ZOLTAN K. NAGY, SERBAN P. AGACHI

Babes-Bolyai University of Cluj-Napoca, Faculty of Chemistry and Chemical Engineering, Arany Janos 11, 3400, Cluj-Napoca

ABSTRACT. Aqueous electrolyte solutions are common in industrial processes. For ecological and economical reasons, aqueous liquids from chemical and petrochemical plants, containing weak electrolytes, have to be treated before they can be released into natural waters.

The physical interaction and chemical interactions in the liquid phase govern the equilibrium. Thus the mathematical model of the vapor-liquid equilibrium is a highly nonlinear algebraic equation system.

As an alternative to the classical model, burdened by many assumptions and crude estimations, the use of neural networks is proposed.

Introduction

Phase equilibrium in aqueous electrolyte solutions containing volatile substances like ammonia and sour gases, is an important issue from the point of view of process engineering. Typical examples are the cleaning of raw gases in power stations, the Solvay process for the production of sodium carbonate or applications on the field of environmental protection.

Due to chemical reactions in the liquid phase and strong deviations from ideality the NH_3-CO_2 –H_2O has complex behavior. Edwards et al. [1,2] developed a mathematical model, based on Pitzer equation [3] and the virial equation of state, for prediction of the system behavior at different concentrations and temperatures.

The model was further extended and developed by Kurz et al.[4] and Krop [5] in order to enlarge the temperature and concentration domain.

Experimental information on phase equilibrium in the system NH_3-CO_2 – H_2O are now available over a wide range of temperatures and concentrations. Thus this paper propose the use of ANN as an alternative modeling.

Modeling

Components involved in the NH_3-CO_2 –H_2O system are present not only in neutral form, but also in ionic form, due to chemical reactions in the liquid phase. These reactions are the following:

$$NH_3 + H_2O \rightleftharpoons NH_4^+ + OH^- \quad \text{(I)}$$

$$CO_2 + H_2O \rightleftharpoons HCO_3^- + H^+ \quad \text{(II)}$$

$$HCO_3^- \rightleftharpoons CO_3^= + H^+ \quad \text{(III)}$$

$$NH_3 + HCO_3^- \rightleftharpoons NH_2COO^- + H_2O \quad \text{(IV)}$$

$$H_2O \rightleftharpoons H^+ + OH^- \quad \text{(V)}$$

Thus in the liquid phase are present nine species with concentrations depending on the chemical equilibrium. Due to these five reactions and interactions between species the difference between the real concentration and total concentration of ammonia and carbon dioxide is significant with direct influence on vapor phase.

To calculate the true concentrations in the liquid phase the condition for chemical equilibrium is applied for reactions I-V:

$$K_{I-V}(T) = \prod_i (m_i \cdot \gamma_i)^{\nu_{i(I-V)}} \quad (1)$$

The balance equations for the ammonia and carbon dioxide and water are:

$$m_{NH_3,tot} = m_{NH_3} + m_{NH_4^+} + m_{NH_2COO^-} \quad (2)$$

$$m_{CO_2,tot} = m_{CO_2} + m_{HCO_3^-} + m_{CO_3^=} + m_{NH_2COO^-} \quad (3)$$

$$x_w = \frac{\frac{1000}{M_w}}{\frac{1000}{M_w} + \sum_{i \neq w} m_i} \quad (4)$$

The last equation to take in to account is the charge balance

$$m_{NH_4^+} + m_{H^+} = m_{OH^-} + m_{HCO_3^-} + 2 \cdot m_{CO_3^=} + m_{NH_2COO^-} \quad (5)$$

This set of equation has to be solved using an iterative procedure. The calculation requires: temperature dependent equilibrium constants $K_1 – K_5$ [7], activity coefficients of all species present in the liquid phase, Henry's constants [7,8] for ammonia and carbon dioxide in pure water as well as information on the vapor phase nonideality and the partial molar volumes of the dissolved gases [2].

The total pressure and the composition of the vapor phase can be calculated from:

$$p \cdot y_w \cdot \varphi_w^v = p_w^s \cdot \varphi_w^s \cdot a_w \cdot e^{\frac{v_w \cdot (p - p_w^s)}{R \cdot T}} \quad (6)$$

$$p \cdot y_i \cdot \varphi_i^v = H_{i,w}(T) \cdot \gamma_i \cdot m_i \cdot e^{\frac{v_{i,w}^{\infty}(p - p_w^s)}{R \cdot T}} \quad (7)$$

where i = NH_3, CO_2

Neural Networks

A neural network is a computer program architecture for nonlinear computations, which is composed of many, highly interconnected, simple elements operating in parallel. These elements (neuron) are inspired by biological nervous systems. An individual processing element (neuron) can have any number

of inputs, but only one output that is generally related to the inputs by a transfer function. The most frequently used transfer functions are: sigmoid function, hyperbolic tangent function, sine function, linear and saturated linear transfer function. The argument of the transfer function is the sum of the input elements of the corresponding neuron, each input being multiplied by the associated weight which shows the strength of the connection between two neurons.

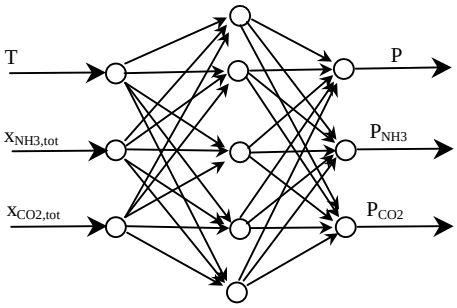

Figure 1. Structure of a Neural Network

A simple neural network is presented in figure 1, such a structure can be more complex with a number a hidden layers and variable number of neurons in each layer. The number of layers and neurons in each layer are very important configuration information determined by trial.

Results and Discussion

The calculations were made in Matlab 5.3 modeling environment using the Neural Network toolbox v3.0 provided with this software. The neural network used in this work was a feed forward network with three neurons in the input ($m_{NH3,\ tot}$, $m_{CO2,\ tot}$ and T) and output layers (p_{NH3} , p_{CO2} and p). Further the network had 2 hidden layers with 23 and 11 neurons each. The transfer function used was a hyperbolic tangent sigmoid.

Tabel 1.

Vapor-liquid equilibrium results at 353.15K

$m_{NH3,tot}$	$m_{CO3,tot}$	Experimental			ANN		
		p_{NH3} [MPa]	p_{CO2} [MPa]	p [MPa]	p_{NH3} [MPa]	p_{CO2} [Mpa]	p [MPa]
5.93	3.326	0.0173	0.171	0.2274	0.0171	0.1686	0.2306
9.03	5.304	0.022	0.291	0.3507	0.0215	0.2929	0.3604
12.17	7.736	0.0203	0.649	0.7033	0.0211	0.6399	0.7082

The vapor-liquid experimental data used (more then 300 points) for training and testing the network were taken from literature [2,4,9]. The available data was used to create two data sets, a bigger one for training of the network and a smaller for testing purpose. The network was trained using a backpropagation algorithm with Bayesian regularization.

The results are presented in tables 1 to 4, all were taken from the testing set. As can be seen, the calculated values are in good agreement with the measurements. Calculation made by the analytical model also showed good agreement with the measurements, but the results are more parameter dependent and the model needs considerably more development effort.

Further, the computational time for the analytical model is considerable higher around 1s while the neural network model execution time is only 0.04s.

Table 2

Vapor-liquid equilibrium results at 360.15K

$m_{NH3,tot}$	$m_{CO3,tot}$	Experimental			ANN		
		p_{NH3} [MPa]	p_{CO2} [MPa]	p [MPa]	p_{NH3} [MPa]	p_{CO2} [MPa]	p [MPa]
1.638	0.954	0.0053	0.157	0.2181	0.0051	0.1607	0.2223
3.406	2.423	0.0044	0.591	0.6542	0.0041	0.5938	0.6507
4.78	3.335	0.0055	0.724	0.7851	0.006	0.7297	0.7849
6.54	2.831	0.0388	0.0936	0.1869	0.0391	0.0918	0.1837
7.759	4.329	0.0213	0.299	0.3736	0.0217	0.3062	0.3753
9.812	4.28	0.0588	0.1	0.2119	0.0698	0.0873	0.2146
12.35	9.285	0.0114	3.581	3.663	0.0136	3.5537	3.6372
12.48	7.062	0.0275	0.448	0.5184	0.0267	0.4439	0.5189
14.07	7.323	0.0448	0.284	0.3746	0.0449	0.2767	0.3728

Tabel 3

Vapor-liquid equilibrium results at 373.15K

$m_{NH3,tot}$	$m_{CO3,tot}$	Experimental			ANN		
		p_{NH3} [MPa]	p_{CO2} [MPa]	p [MPa]	p_{NH3} [MPa]	p_{CO2} [MPa]	p [MPa]
0.95	0.438	0.007	0.124	0.2294	0.0074	0.1455	0.2493
1.078	0.94	0.001	0.905	0.9938	0.0007	1.039	1.1359
3.964	1.848	0.0311	0.245	0.374	0.0307	0.2375	0.3572
7.858	3.327	0.0736	0.205	0.3559	0.0736	0.2073	0.3525
8.08	4.436	0.033	0.663	0.7836	0.0304	0.6574	0.7485
11.17	4.016	0.168	0.114	0.377	0.1509	0.1244	0.3557

Table 4

Vapor-liquid equilibrium results at 393.15K

$m_{NH3,tot}$	$m_{CO3,tot}$	Experimental			ANN		
		p_{NH3} [MPa]	p_{CO2} [MPa]	p [MPa]	p_{NH3} [MPa]	p_{CO2} [MPa]	p [MPa]
0.703	0.419	0.0044	0.539	0.7403	0.0048	0.5638	0.7586
3.821	1.06	0.0943	0.184	0.4719	0.1056	0.2187	0.4979
5.822	2.284	0.0923	0.531	0.7823	0.0787	0.5334	0.7815
7.99	4.748	0.0363	2.795	2.9705	0.0359	2.9734	3.1614
11.95	7.174	0.0468	3.972	4.1609	0.0513	3.9561	4.1238

The prediction error of the neural model varies between 0.1% and 20%. This shows that the experimental data were insufficient and not very well distributed. In future when new measurements would be available the neural model can be trained with the new data making the model more precisely in predictions

Conclusions

The use of Artificial Neural Networks was proposed for vapor-liquid equilibrium modeling of NH_3-CO_2-H_2O system. It was showed that the results obtained with the neural network were in good agreement with the measurements. Additionally the Neural Network model presented considerably smaller execution times making it suitable for process modeling.

LIST OF SYMBOLS

H – Henry's constant
$K_{l\text{-}V}$ – reaction equlibrium constant
m_i – molality of component i
p - total pressure
p_i – partial pressure of component I
p_w^s – partial pressure of water at saturation
R – universal gas constant
T - temperature
v_m – partial molar volume
y_i – component mole fraction

Greek Letters
γ – activity coefficient
φ – fugacity coefficient
ν - stoichiometric coefficient of component i.

REFERENCES

1. T J Edwards, J Newman , J M Prausnitz, *AIChE Journal*, 21(2), 1975, 248-259.
2. T J Edwards, G Maurer, J Newman, J M Prausnitz, *AIChE J.*, 24(6), 1978, 966-976.
3. K S Pitzer, *The Journal of Physical Chemistry,* 77(2), 1973, 268-277.
4. F Kurz, B Rumpf, G Maurer, *Fluid Phase Equilibria, 104*, 1995, 261-275.
5. Jadwiga Krop, *Fluid Phase Equilibria, 163*, 1999, 209-229.

6. K Thomsen, P Rasmussen, *Chemical Engineering Science*, 54, 1999, 1787-1802
7. V Bieling, B Rumpf, F Strepp, G Maurer, *Fluid Phase Equilibria,* 53, 1989, 251-259.
8. K Kawazuishi, J M Prausnitz, *Ind.Eng. Chem.Res.,* 26, 1987, 1485-1488.
9. U Gopert, G Maurer, *Fluid Phase Equilibria, 41*, 1988, 153-185.
10. Ellen M Pawlikowski, J Newman, J M Prausnitz, *Ind. Eng. Chem. Process Des. Dev*., 21, 1982, 764-770.

STUDIA UNIVERSITATIS BABEŞ-BOLYAI, CHEMIA, XLVI, 1-2, 2001

NANOSTRUCTURED CdS FILMS OBTAINED BY SPRAY PYROLYSIS. I. THE INFLUENCE OF DEPOSITION PARAMETERS ON THE FILM QUALITY

VIOLETA POPESCU, HOREA IUSTIN NAŞCU

ABSTRACT. A study regarding conditions for spray pyrolysis deposition of CdS nanostructured films on glass substrates, using aqueous solution containing $CdCl_2$, thiourea and surfactants, is presented. Dry air was used as carrier gas. Deposition parameters such as: substrate temperature, solution composition, gas and solution flow rates, deposition time, layer number, and distance between spraying nozzle and substrate were studied. The optimal conditions for obtaining compact, adherent, and optically clear, with good esthetical looking, thermoreflecting films were established. The film thickness was in the range 20-80 nm. The mechanism of CdS film deposition on glass substrates take places by thermal decomposition of the complexes $[Cd(H_2O)(SCN_2H_4)]Cl_2$ and $[Cd(SCN_2H_4)_2]Cl_2$. These films can be applied for solar control coatings.

Introduction. Progress in development, characterisation, and utilisation of advanced materials has been spectacular [1]. The preparation of nanostructured materials, by physical or chemical methods, [2] has become an important branch of advanced materials.

A reduction in particle size to the nanometer scale results in quantum size effects, at dimensions comparable to the length of the de Broglie electron.

Band-gape engineering by size and dimension quantization is important since it leads to mechanical, chemical, electrical, optical, magnetic, electro-optical properties, which are substantially different from those, observed for bulk material [1].

The study of metallic sulfide films deposited on transparent substrates was stimulated by their possible application to the manufacture of solar control coatings. Optical properties of PbS thin films chemical bath deposited have been studied comparatively with those of thin Au and Ni layers [3]. VIS transmission and near-IR reflection are comparable with those of metallic films. CuS [4] and PbS [5] films deposited on glass by spray pyrolysis are also suitable, for solar control coatings.

Spray pyrolysis was successfully used for CdS deposition on different substrates [6,7,8], on different conditions.

The studies of reaction between cadmium salts and thiourea, with forming of CdS films by this method were performed by IR spectroscopy [9-12].

Two possible mechanism for CdS film formation were proposed: hydrolytic [13] and by thermal decomposition of Cd (II)·thiourea complexes [10].

Hydrolysis mechanism could be explained after Bursuc at al by the following reactions [13]:

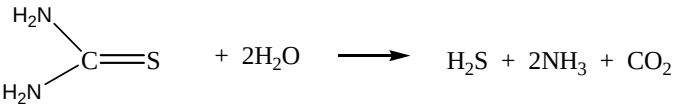

(1)

$$CdCl_2 + H_2S \longrightarrow CdS + 2HCl \qquad (2)$$

and after Semenov et al [10]:

The second proposed mechanism consists of thermal decomposition of complexes:$[Cd(SCN_2H_4)_2]Cl_2$; $CdCl_2 \cdot [Cd(SCN_2H_4)]Cl_2$ and $Cd(H_2O)(SCN_2H_4)]Cl_2$ [11].

By fast heating at a temperature higher than 210°C, $[Cd(SCN_2H_4)_2]Cl_2$ decomposes after the following reaction:

$$[Cd(SCN_2H_4)_2]Cl_2 \xrightarrow{3O_2} CdS + 2NH_4Cl + 2CO_2 + SO_2 + N_2 \quad (5)$$

The aim of this paper is to establish the best condition for spray pyrolysis

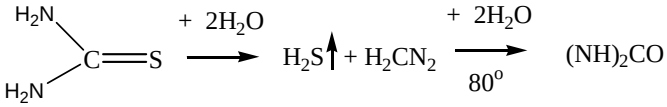

(3)

$$Cd^{2+} + S^{2-} \longrightarrow CdS \quad (4)$$

deposition of adherent, optically clear, homogenous, thermoreflective CdS nanostructured films from solutions containing $CdCl_2$, thiourea in the presence of ether sulfate 12-14 (ES) as surfactant. The later dramatically influences the film quality, limiting the grain growth. For the first time CdS nanostructured films were obtained in the presence of surfactant.

Experimental. The experimental set-up for spray pyrolysis deposition used by us also for CuS [4] and PbS [5], nanometric films consists of a reaction chamber foreseen to its lower part with a plate heated by electrical resistance. On the plate, the substrate is placed. Substrate temperature is measured with a thermocouple. Above the substrate at variable distances (10-30 cm) the glass-spraying nozzle is fixed. The solution is sprayed (from a reservoir) by means of the carrier gas, incidently to the substrate. Standard commercial glass slides, ($75x25x1mm^3$), were used as substrates. The spraying solution consists of an aqueous solution of 0,01–0,1 M $CdCl_2$ and 0,01–0,1 M thiourea and ES. The reagents were analytical grade, except ES which is a technical anionic surfactant (made by "Intreprinderea de Detergenți" Timişoara Romania). The substrate temperature was 200-500^{o}C, the gas (dry air used as carrier gas) flow rate 40-70 ml/s. The spraying time vary between 10-30 seconds and the layer number between 1-5. The thickness of the film was determined by microweighting and spectrophotometrically with a photocolorimeter FEK-M (USSR).

Results and discussion. The quality of the films depends on many factors such as: substrate temperature, distance between spraying nozzle and substrate, deposition time, number of deposited layers, reagent concentration, and the liquid flow rate. After some preliminary studies regarding deposition condition, working with aqueous solution containing $Cd(CH_3COO)_2$ or $CdCl_2$ in the presence of thiourea, in the same conditions of concentration, $CdCl_2$ was selected as cadmium salt taking into consideration the uniformity of obtained film.

Using spraying solutions containing, 0,1 M $CdCl_2$ and 0,1M thiourea, ***the influence of the deposition time*** on the thickness and the quality of the obtained film was studied. The thickness of the film increases linearly with the deposition time (fig. 1). Increasing the deposition time to 30 seconds the quality of the film worsen. The film presents spots and thickness variation. During the deposition process, the substrate temperature decreases, the reaction isn't complete. Secondary reaction products are trapped in to the film.

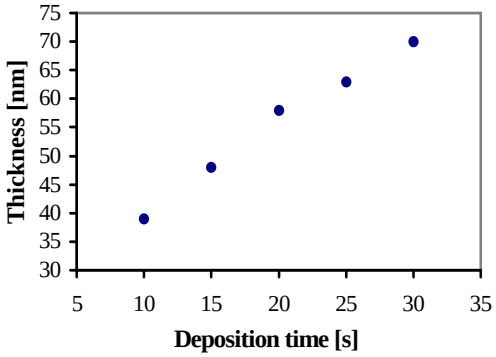

Fig. 1. Influence of the deposition time on the thickness of the film

The thickness of the films has been determined through the spectrometrical method using an FEK-M spectrometer with blue filter. The calibration curve (fig.2) has been obtained on samples with known thickness, micrograviметrically determined. For thickness determination the following relationship have been established: $h=k \cdot A$ [nm] where $k = 10^2$ is a constant, and A is the absorbance.

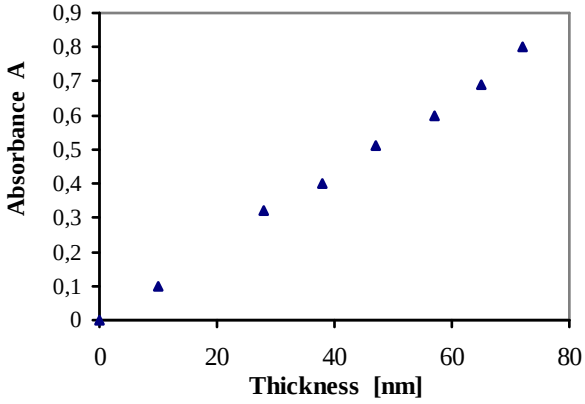

Fig 2. Calibration curve on the spectrophotometric determination of CdS nanometric film

Deposition ***temperature*** influence was studied for the range 150-500°C. The best results (the most uniform films) were obtained at 450°C.

The influence of the reagent concentration was studied using solutions containing $CdCl_2$, and thiourea in equimolar ratio in the range 0,01 - 0,1 M and $3x10^{-3}$ % ES 12-14. Three layers were deposited, 10 seconds for each layer, solution-spraying flow rate 20 ml/s, the distance nozzle-substrate 20 cm and substrate temperature 450^0C. Yellow, uniform, adherent, optically clear films, which thickness was between 15-54 nm were obtained.

Variation of film thickness as a function of the concentration of the spraying solution is presented in fig.3 and 4. For equimolar ratio of reagents when $[Cd(SCN_2H_4)_2]Cl_2$ are formed (fig.3) a linear increases of the film thickness with the reagent concentration take places.

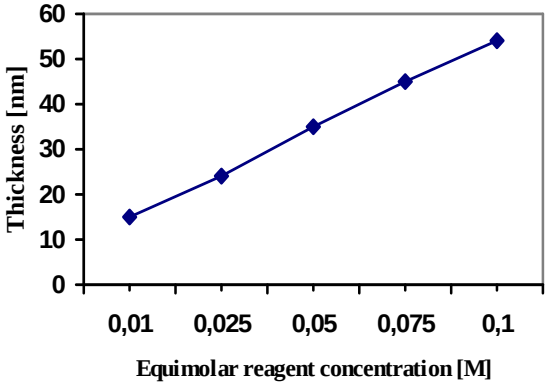

Fig. 3. Variation of CdS film thickness as a function of equimolar reagent concentration

For equimolar reagent concentration the best results were obtained for solution concentration less than 0,025 M $CdCl_2$ and thiourea. The films are uniform and perfectly clear when the thickness is less than 54 nm. All of the films was good optical properties. Using diluted solutions the deposition of more than 3 layers were necessary.

Varying thiourea concentration, at constant content of $CdCl_2$ (0,025 M) the conditions for $Cd(SCN_2H_4)_2]Cl_2$ complex formation was created (fig. 4. Curve 1). By spraying aqueous solutions on heated substrate, in the first stage, the deposition of a thin solid film of this complex take places [10,14]. In the second stage, complexes decompose with the formation of CdS film (relationship 5). The CdS film thickness increases linearly with the increasing of thiourea concentration.

Keeping thiourea concentration constant (0,1 M) and varying $CdCl_2$ concentration (fig. 4. Curve 2), film thickness increases till thiourea concentration reach 0,05 M, (thiourea: $CdCl_2$ 2:1 molar ratio) when formation of $[Cd(SCN_2H_4)_2]Cl_2$ complex take places, and than when that ratio Cd(II):thiourea decreases the thickness remain unchanged. That means the reaction rate remains constant because the concentration of the complexes is constant.

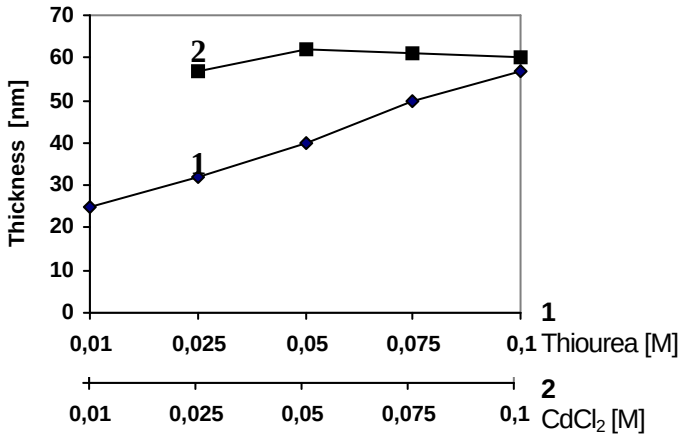

Fig. 4. Variation of CdS film thickness as a function of reagent concentration

For obtaining optically clear, uniform films with proper thickness multi-layered (2-5 layer) films were deposited from equimolar ratio $CdCl_2$-thiourea 0,025 M solutions, when $[Cd(H_2O)(SCN_2H_4)]Cl_2$ is the intermediate reaction product. Good uniform films were obtained also with solutions containing 0,05 M $CdCl_2$, 0,1 M thiourea from $[Cd(SCN_2H_4)_2]Cl_2$. The best results were obtained for 3 layered film.

Conclusions. A study regarding conditions for spray pyrolysis deposition of CdS nanostructured films on glass substrates using aqueous solution containing $CdCl_2$, thiourea and ES as surfactant was presented. The thickness of the film increases linearly with the deposition time in the range 10-30 s. A relationship between absorbance value and thickness has been established. Regarding deposition temperature, the most uniform films were obtained at 450°C. Solution concentration influences the film formation and the quality of the film. The best results were obtained for solution containing less than 0,025 M $CdCl_2$ and thiourea in equimolar ratio, in the presence of $3 \cdot 10^{-3}$ ES, when solution-spraying rate was 20 ml/min, the distance nozzle-substrate 20 cm. Uniform optically clear multi-layered films were obtained also using solutions containing 0,05 M $CdCl_2$, 0,1 M thiourea in the presence of ES. In the both cases the films are uniform and perfectly clear, when the thickness is less than 54 nm. All of the obtained films have good optical properties. Using diluted solutions the deposition of more than 3 layers were necessary. The film thickness was in the range 20-80 nm. These films can be applied to the manufacture of solar control coatings.

The mechanism of CdS film deposition on glass substrates take places by thermal decomposition of the complexes $[Cd(H_2O)(SCN_2H_4)]Cl_2$ and $[Cd(SCN_2H_4)_2]Cl_2$.

REFERENCES

1. J.H., Fendler, F.C., Meldrum, *Adv. Mater.* **7** (7), 607, (1995).
2. G.A. Ozin, *Adv. Mater.,* **4**, 607, (1992).
3. I. Pop, V. Ionescu (Popescu), C. Nascu, V. Vomir, R. Grecu, E. Indrea, *Thin Solid Films,* **307** (119), 240 (1997).
4. C. Naşcu, I. Pop, V. Ionescu (Popescu), E Indrea, I. Bratu, *Materials Letters*, **32** (73), 73 (1997).
5. H. Naşcu, V. Popescu and C. Naşcu, BRAMAT *Intl. Conf. on Mater. Sci. and Engineering, Braşov, Proceedings*, vol. IV, 31, (2001).
6. R.R. Chamberlin, J.S. Skarman, *J. Electrochem. Soc.,***113**(1), 86, (1966).
7. Ya A. Ugai, O.B. Iaţenko, V.N. Semenov, E.M. Averbach, *Izvest. Akad. Nauk. SSSR, Neorg. Mater.,***9**(11), 2055, (1973).
8. K.Z. Hefme, H.A. Jessem, *Acta, Physica Hungarion,***73**(1), 29, (1993).
9. Y. Ma Yale, R.H. Bube, *J. Electrochem. Soc.,* **124**(9), 1430, (1977).
10. V.N. Semenov, E.M. Averbach, L.A. Mihaleva, *Zhur. Neorg. Khim.,* **24** (4), 911, (1979).
11. M. I. Krunsk, E. Ya. Mellikov, E.E. Sork, *Zhur. Neorg. Khim.,* **30** (6), 911, (1985).
12. Ya. A. Ugai, V.N. Semenov, E.M. Averbach, *Zhur. Prikl. Khim.,* **50**(11), 2409, (1988).
13. I. Bursuc, Gh.Zet, M. Gherghel, I. Roşca, E. Gherasimescu, I. Mihai, *Bul. Inst. Politehnic Iaşi,* **XXIX** (XXXIII) (1-4), secţia I Mecanică, 79, (1983).
14. V.N. Semenov, K. Kisnadat, *Zhur. Prikl. Khim.,* **63**(1), 31 (1990).

STUDIA UNIVERSITATIS BABEŞ-BOLYAI, CHEMIA, XLVI, 1-2, 2001

NANOMETRIC CdS FILMS OBTAINED BY SPRAY PYROLYSIS. II. OPTICAL PROPERTIES

VIOLETA POPESCU[1], RODICA GRECU[2], ELENA MARIA PICĂ[1]

ABSTRACT. The paper presents the results concerning optical properties of nanometric CdS (20-80 nm) films obtained by spray pyrolysis on glass substrate from aqueous solution containing $CdCl_2$, thiourea and ether sulfate 12-14 (ES). Transmission and absorption spectra in Vis range wavelength were presented. Near-IR reflection was also determined. The film thickness was determined microgravimetrically and spectrometrically. The vis transmittance varies between 45-60% and the NIR reflectance is 15-32%. The obtained results lead to the conclusion that CdS nanostructured films could be applied as solar control coatings.

Introduction. CdS thin films are well known because of the applications in achievement of solar cells. Metal sulphides such as lead sulphides [1], cooper sulphides [2-4] and cadmium sulphides [5], have good solar control properties, because of those good transmission for visible range radiation (λ=400-700 nm) higher than 10-80 % and near IR reflection of 20-45%. Those properties limit the unwanted increasing of temperature inside the building and cars, providing good lighting properties. Yellow CdS films has one more advantage in the esthetical looks. The visible transmittance is higher than stainless steel, Ni or Au layers [6].

Thin CdS films were obtained successfully on different substrates by spray pyrolysis [7-9] using cadmium salts and thiourea., at 120-450°C. Chemical bath deposition was also a successfully method for nanostructured film preparation [10-12].

Temperature is an important parameter, which influence the properties of the film. Even if CdS films were obtained at temperatures smaller than 200°, optical properties were not good enough [13]. The purity of the film was low, because of the secondary products of reaction trapped into the film. Complexes formed between Cd salts and thiourea were not completely decomposed. Film deposition does not take places at constant temperature. Because of the temperature gradients the grain growth is limited to sizes below 1 μm [14].

In order to increase the film purity, the films were subjected to thermal treatment [15]. Photoelectrical properties were improved, but optical properties vary insignificantly.

We obtained adherent, optically clear, homogenous, thermoreflective CdS nanostructured films from solutions containing $CdCl_2$, thiourea in the presence of ether sulfate 12-14 (ES) as surfactant, by spray pyrolysis deposition [16].

The aim of this paper is to present optical properties of CdS obtained films.

Technical University of Cluj-Napoca

Experimental details. The experimental set-up for spray pyrolysis deposition used by us also for CuS [2] and PbS [1] was described elsewhere. On the heated substrate at 300-500°C the solution containing $CdCl_2$, thiourea (TU) and ether sulfate 12-14 (ES) is sprayed. Dry air was used as carrier gas. A multi-layered film was deposited. The flow rate of the solution varies between 40-70 ml/sec.

The thickness of the film was determined spectrophotometrically with a photocolorimeter FEK-M [16]. The transmittance and absorbance using neutral and/or blue filter respectively were determined with a photocolorimeter FEK-M.

The VIS transmission and absorption spectra have been recorded with a SPECORD UV-VIS spectrometer and those of the NIR reflection with a UR-20 Carl Zeiss Jena spectrophotometer. NIR extension of UR-20 spectrophotometer was made by a calibration with known standards, using the LiF prisma.

Results and discussion. The obtained films are light yellows, having a good adherence to the glass substrate.

The thickness and the optical properties of the films depend on many factors such as: reagent concentration, substrate temperature, number of deposited layers, distance between spraying nozzle and substrate and the solution flow rate [16].

Optical properties, for CdS monolayers films, deposited from aqueous solution containing equimolar $CdCl_2$ and thiourea (air flow rate - 66.66 ml/sec, substrate temperature - 450^0C, the distance from substrate to the spraying nozzle 25 cm) are presented in table 1.

Table 1

Optical properties of CdS monolayers films deposited by spray pyrolysis from aqueous solution containing equimolar 0.1 M $CdCl_2$ and thiourea; (T [%] –transmittance)

Sample	Deposition time [seconds]	T [%]		Thickness [nm]	Observations
		Neutral filter	Blue filter		
1	10	59.8	56.20	39	Yellow adherent, optically clear film, uniform thickness
2	15	58.1	54.5	48.5	Relatively optically clear uniform film
3	20	51.6	48.8	61.0	Yellow adherent, transparent, optically clear film, with spots
4	25	50.0	47	63.0	Ununiform film with spots

For increasing the uniformity of the film, 3 layers were deposited in the presence of (ES) from equimolar solution varying the concentration of the solutions (table 2). The deposition time for each layer was 10 seconds, airflow rate - 66.66 ml/sec, substrate temperature - 450^0C. Visible transmittance for samples presented in table 2 are presented in fig. 1.

Nanostructured CdS films presented in fig. 1 have a good transmission for wavelength bigger than 550 nm.

Visible transmission spectra for another series of samples obtained from solution with different concentration of reagents were recorded and presented in Fig. 2. Obtaining conditions for films are presented in table 3.

Table 2

Condition for CdS films formation by spray pyrolysis from aqueous solution containing $CdCl_2$ and thiourea in the presence of ES $3 \cdot 10^{-3}$ %

Sample	Solution composition $CdCl_2$:TU	h [nm]	Observations
5	0.1:0.1	54	Adherent, relatively optically clear film
6	0.05:0.05	35	Adherent, optically clear film
7	0.025:0.025	24	Transparent optically clear film
8	0.01:0.01	15	Optically clear film

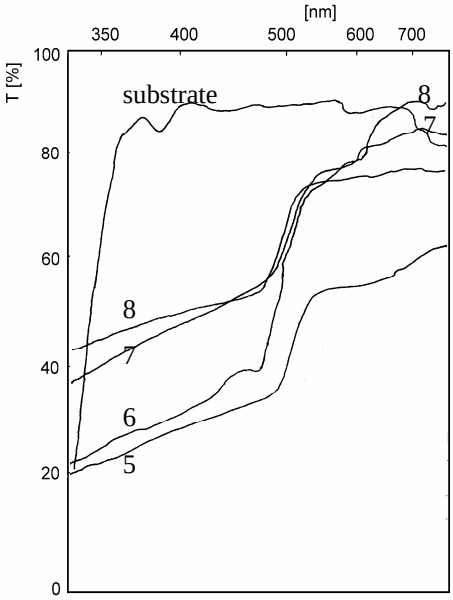

Fig. 1. Visible transmission spectra of glass slides as thick as 1 mm, coated with CdS films deposited from equimolar ratio solution containing $CdCl_2$, thiourea and ES.

From Fig.2. can be seen that in the range (350-700 nm) the transmittance of the films are increasing, starting from very low values (T<10 %), and having a maximum between 550 and 700 nm value. The thickest films have the lowest transmittance. Between 500-700 nm the transmittance varies from 65% for sample 11 (72 nm) to 92% for sample 9 (34 nm).

Table 3

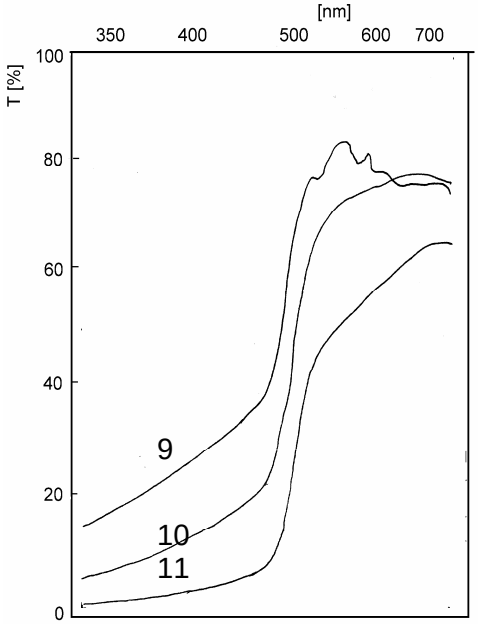

Fig. 2. Visible transmission spectra of glass slides as thick as 1 mm, coated with CdS films different thickness

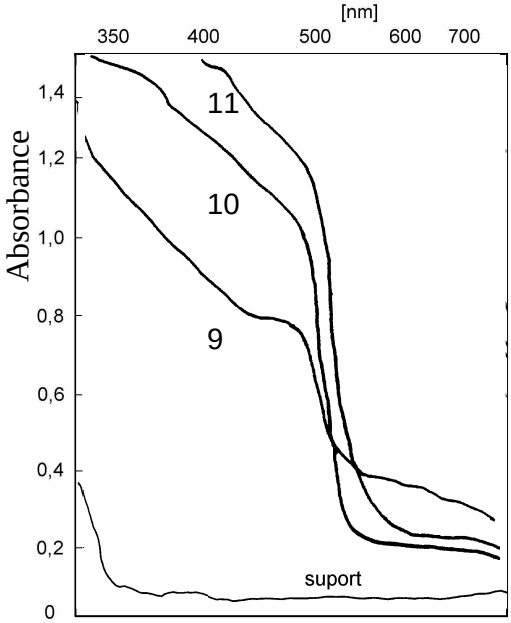

Fig. 3. Absorption spectra of glass slides as thick as 1 mm, coated with CdS films different thickness

Condition for CdS films formation by spray pyrolysis from aqueous solution containing $CdCl_2$ and thiourea, as well as thickness h (air flow rate - 66.66 ml/sec, substrate temperature - 450^{0}C, 3 layers were deposited each layer for 10 seconds)

Sample	Solution composition	h [nm]
9	0.025 M $CdCl_2$; 0.1 M thiourea; $3x10^{-3}$ % ES	34
10	0.05 M $CdCl_2$; 0.1 M thiourea; $3x10^{-3}$ % ES	62
11	0.075 M $CdCl_2$; 0.1 M thiourea; $3x10^{-3}$ % ES	72

For the same samples (presented in Fig.2) the absorption spectra were recorded (Fig.3.). Absorption decreases linearly in the range 330-500 nm, than a suddenly decrees take places for about 500 nm. This behaviour made possible the spectrophotometrical method for thickness determination.

For samples presented in Fig.3. NIR reflection spectra have been recorded (Fig. 4). All the samples present a maximum for reflectance at approximately 1.2 μm. CdS nanostructured films deposited by spray pyrolysis have maximum NIR reflectance of about 30%. Those properties provide good solar control properties.

Fig. 4. Near IR reflection spectra for Cd S films deposited by spray pyrolysis

Conclusions. CdS nanometric films as thick as 34-72 nm, having the visible transmittance between 45-80 % and the near –IR reflectance of about 15-32 % were obtained by spray pyrolysis. The deposition conditions influence the thickness and the optical properties. Controlling the film thickness film with known optical properties could be preparated. The obtained results lead to the conclusion that CdS nanostructured films have solar control properties.

REFERENCES

1. H. Naşcu, V. Popescu and C. Naşcu, BRAMAT *Intl. Conf. on Mater. Sci. and Engineering, Braşov, Proceedings*, vol. IV, 31, (2001).
2. C. Naşcu, I. Pop, V. Ionescu (Popescu), E Indrea, I. Bratu, *Materials Letters*, **32** (73), 73 (1997).
3. C. Naşcu, V. Popescu, H. Naşcu, *RoPM, Cluj-Napoca Romania Second international Conference on Powder Metallurgy, 6-8 July,* 779, (2000).
4. C. Naşcu, V. Popescu, H. Naşcu, *RoPM, Cluj-Napoca Romania Second international Conference on Powder Metallurgy, 6-8 July*, 615, (2000).
5. V. Popescu, E. M. Pică, I. Pop, R. Grecu, *Thin Solid Films,* **349**, 67, (1997).
6. I. Pop, V. Ionescu (Popescu), C. Nascu, V. Vomir, R. Grecu, E. Indrea, *Thin Solid Films,* **307** (119), 240 (1997).
7. R. R. Chamberlin, J. S. Skarman, *J. Electrochem. Soc.,***113**(1), 86, (1966).
8. Ya A. Ugai, O. B. Iaţenko, V. N. Semenov, E. M. Averbach, *Izvest. Akad. Nauk. SSSR, Neorg. Mater.,***9**(11), 2055, (1973).
9. K .Z. Hefme, H. A. Jessem, *Acta, Physica Hungarion,***73**(1), 29, (1993).
10. M. T. S. Nair, P. K. Nair, R.A. Zingaro, *J. Phys. D. Appl. Phys.,* **75,** 1557, (1994).
11. J. M. Dona, J. Herrero, *J. Electrochem. Soc.,* **144,** 4081, (1997).
12. J. M. Dona, J. Herrero, *J. Electrochem. Soc.,* **144,** 4091, (1997).

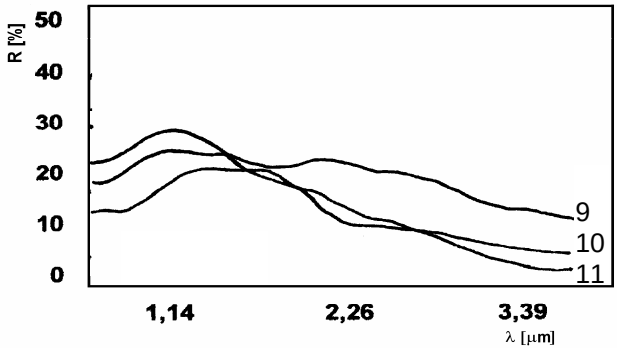

13. M. Krunks, E. Mellikov, E. I. Lork, M. B. Vidrievich, *Tr. Tallin. Politekn. Inst.,* **587,** 211, (1984).
14. M. Lo Savio, M. E. Oliveri, *Nuovo Cimento Soc. Ital. Fis.,* **44**(4)**,** 249, (1985).
15.M. Escosura, E. Garcia-Camarero, F. Arjona, F. Rueda, *Sol. Cells,* **11**(3)**,** 211, (1984).
16. V. Popescu, H. I. Naşcu, Simpozionul "*30 de Ani de Învățământ Superior de Inginerie Chimică la Cluj-Napoca*" (in press).

Acknowledgements.

This work was supported by a grant from CNCSIS - Roumanian National Council of Scientific Research (12, code 244), Financial support offered by the Romanian Ministry of Education and Research

The author whishes to thank to dr. I. Bratu from Institute of Isotopic and Molecular Technology, Cluj-Napoca, Romania for near-IR reflectance spectra recording

STUDIA UNIVERSITATIS BABEŞ-BOLYAI, CHEMIA, XLVI, 1-2, 2001

A CHITOSAN/CARBOXYMETHYLCELLULOSE COMPLEX USED FOR THE pH-CONTROLLED DELIVERY OF CEFTRIAXONE

N. AELENEI, M. CHIRITA*, I.M. POPA, DELIA AELENEI*, DANIELA ANDREI, GABRIELA CARJA

"Gh. Asachi" Technical University Iasi, Physical Chemistry Department, r/6600 Iasi
"Gr. T. Popa" University of Medicine and Pharmacy, Medical Bioengineering University, Iasi, 6600

ABSTRACT. Ceftriaxone is a parenteral third generation cephalosporin antibiotic owing a typical "zwitterion" molecule, containing both basic and acidic radicals. Due to the specific structure this drug forms stable complexes with both polyanionic macromolecular compounds - as carboxymethylcellulose (CMC) and polycationic macromolecular compounds - as chitosan. Consequently, a chitosan/CMC/ceftriaxone complex can be obtained and used for the controlled release of the drug, the release rate being strongly influenced on the pH.. The optimal chitosan/CMC combination ratio was determined spectrophotomrtrically. An insoluble chitosan/CMC/Ceftriaxone complex, containing 17% ceftriaxone, was prepared. The kinetic of ceftriaxone release was analyzed as a function of the elution medium pH. The experimental data point out that the maximum quantities of the released ceftriaxone are obtained after 200 min at pH=1.95 and pH=11.75, and after 1600 min at pH=4.68, pH=5.74, pH=6.54 and pH=7.34. The maximum quantity of drug released from the complex is strongly dependent on the pH, being closed by 100% in strong acidic and basic solutions, while it becomes only approximately 5% at pH = 6.54. This behaviour was explained by the intricate structure of the complex.

KEY WORDS: chitosan/carboxymethylcellulose/ceftriaxone complex, controlled-release

INTRODUCTION

Controlled-release drug delivery combines reproductible dosage from design with clinical pharmacology, particularly steady-state pharmacology. Controlled release drug delivery currently involves control of either the time course or location of drug delivery. Control of time course of drug is the more classical approach, while site specific or targeted delivery – which involves drug delivery to a specific organ, a class of cells or a physiological compartment – is mostly in the research stage.

Delivery rates from temporal controlled systems may be characterized in terms of their kinetics and physical processes. Of particular interest are zero-order systems - for which the released drug quantity is constant with time. These systems can allow foe selection of precise efficacious plasmatic levels after titration for inter-individual variation or its may be important to select plasma levels that avoid adverse drug reactions [1]. A second potential advantage of zero-order dosage forms is improved efficiency of delivery of the drug; steady-state delivery of the drug may be more efficient when the distribution of the drug into the receptor compartment is much slower than elimination from the receptor compartment.

The variety routes available for drug delivery corresponds to the biological membranes in human body: oral, nasal or vaginal mucous, gastrointestinal tract, eye or skin. Oral drug delivery is the most common route, the drug being absorbed through the various membranes along the gastrointestinal tract and the controlled release device traverses a whole domain of pH, from 1...2 in stomach, 4 ... 5.5 in duodenum and 5.5 ... 7.5 in jejunum. Transit through the ileum is more regular (pH = 7...7.5) and entrance in the colon may be accompanied by a 0.5 to 1.0 units increase in pH [2], [3]. The total gastrointestinal transit time is highly variable, varying from less than a day to several days [3], [4]. Oral delivery of drugs seems to offer a combination of advantages of transdermal and oral delivery. A bucal device is both a sublingual tablet and a sub-gingival pellet - used in periodontal treatments. The sub-lingual device has the advantage of a very easy application and removal, and permitting to obtain a rapid increase in the local concentration of the drug, for a long period of time. However, a very limited domain of pH, comprised between 5.5 and 7.5 restricts the bucal administration, this fact entails the choice of an adequate delivery device, with very high delivery rate - in sublingual administration and with very slow release rate in sub-gingival application.

Ceftriaxone is a parenteral third generation cephalosporin antibiotic owing a typical “zwitterion” molecule, containing both basic and acid radicals (Fig. 1,a).

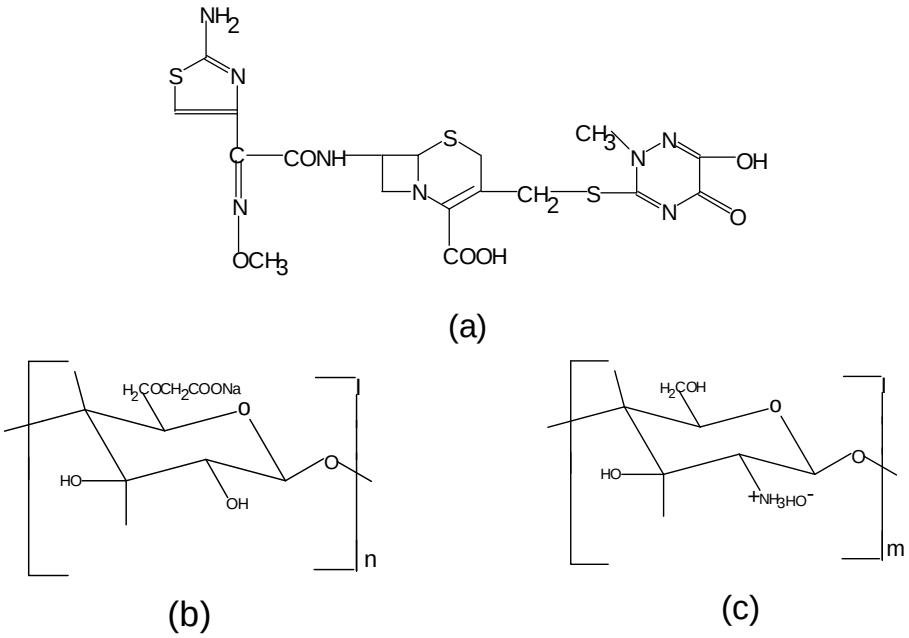

Fig. 1 – Structure of ceftriaxone (a), Carboxymethylcellulose (b) and Chitosan (c)

In vitro, this antibiotic exerts a pronounced activity against a wide range of gram negative and gram positive microorganisms. Dou to the specific structure this drug is able to form stable complexes with both polyanionic macromolecular compounds - as carboxymethylcellulose (CMC) (Fig.1,b) and polycationic macromolecular compounds /- as Chitosan (Fig. 1,c).

Simultaneous complexation of ceftriaxone with CMC and chitosan leads to a very pH-sensitive complex, which can be used for controlled delivery of ceftriaxone.

EXPERIMENTAL

Chitosan sample, having a molecular weight of 150,000 g mol^{-1} and a 12% acetylation degree was obtained from the Genetical Chemical Department of Sherbrooke University, Canada. Carboxymethylcellulose was supplied by Austranal Co. and has an esterification degree of 81 %.

The optimal Chitosan/CMC was determined spectrophometrically, measuring the absorbency of the supernatant phase separated from a series of dilute solutions with various CMC/chitosan ratios (Fig. 2.). From these data, the optimal gravimetric ratio was found to be m (CMC)/ m (Chitosan)= 1.2.

The quantitative determinations of ceftriaxone, both for analysis and kinetically studies, were performed by spectrophotometric measurement [5] using an UV-VIS spectrophotometer of VSU-2P type.

The Chitosan/CMC/Ceftriaxone complex was obtained, at ordinary temperature, solving an excess of ceftriaxone into a 0.4 % CMC solution (pH = 5.8) and pouring this solution, drop by drop, under energetically stirring for three hours, into 0.4 % Chitosan solution (pH = 5.8). The gravimetric ratios between the three components in the final mixture was m (Chitosan)/ m (CMC)/ m (Ceftriaxone)= 1:1.5:1.45.

The insoluble complex was separated through centrifugation at 3500 rpm, for 15 min, washed with water and acetone and dried in vacuum at room temperature. This complex contain 17.3 % Ceftriaxone.

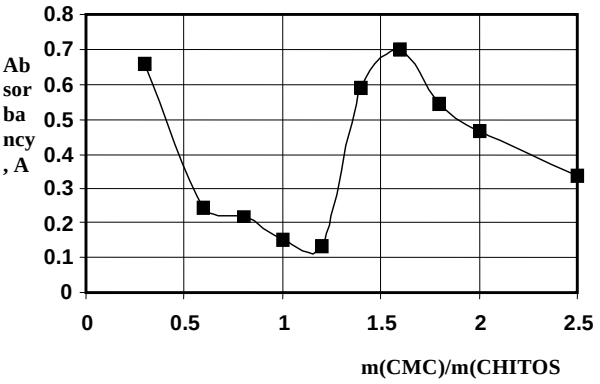

Fig. 2. The supernatant absorbancy versus CMC/CHITOSAN ratio

For kinetic studies the dry complex was compressed, at 5 kg/cm^2 for three minutes, in platelike cylindrical form of 13 mm diameter and 1.1 ... 1.4 mm thickness.

The weights of the complex samples were comprised between 0.13 and 0.2 g for an eluent volume of 100 cm^3.

The study of Ceftriaxone release from the complex was carried out by an elution technique in aqueous medium

of different pH values, at 37 ^{o}C, The solution samples of 1mL were extracted at different time intervals and analyzed spectrophotometrically, determining the quantity of released ceftriaxone (m_t).

The maximum quantities of ceftriaxone present in the solid samples, m_f, were determined by measuring the solution absorbency 72 hours after the initiation of the release.

RESULTS AND DISCUSSIONS

The kinetic curves obtained by elution in different buffer solutions are presented in Fig. 3.

From these curves it can be see that in very strong acid solutions (pH=1.95) or in very basic solutions (pH=11.73) the release rate is very great achieving maximum release after eight hours of elution, but the drug shows a weak; the degradation rate being of 0.7 % in acidic media and 0.4 % in basic media.

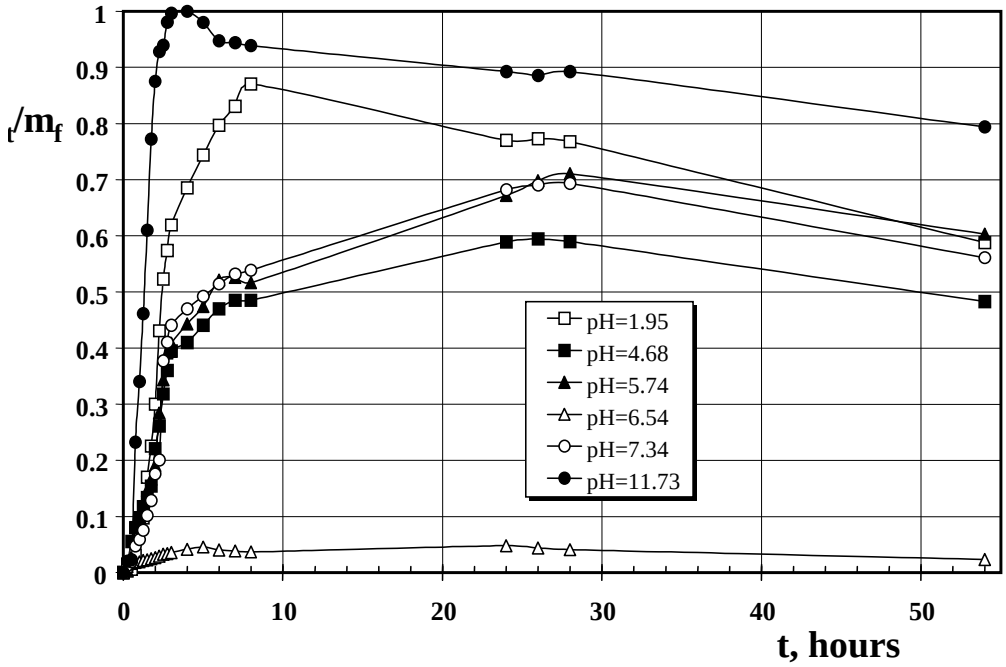

Fig. 3 - Ceftriaxon release from the CHITOSAN/CMC/CEFTRIAXON complex , as of pH and time

At moderate pH values (pH = 4.69; 5.74 and 7.34) the release rate is also moderate and degradation process is at the same time present, excepting for pH = 5.74.

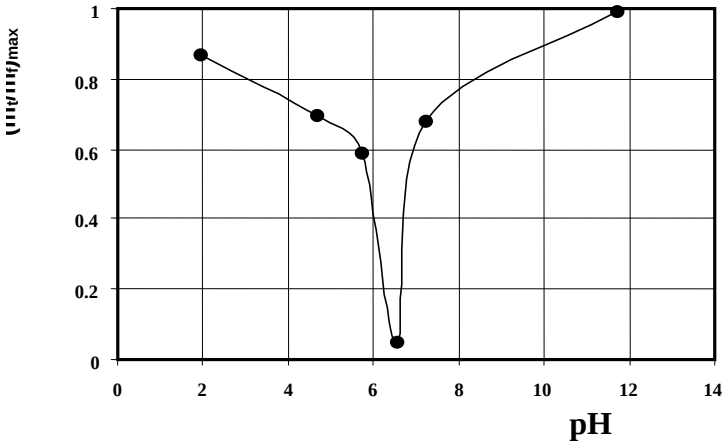

Fig. 4 Dependence on pH of the maximum relative quantity released after 50 hours of elution

The sample mentained in water (pH = 6.54) through was scattered like a powder after 90 min, release a very small quantity of drug (~ 5 %) and the degradation process is very reduced.

The maximum quantity of the released drug from complex is strongly dependent on pH; being closed by 100 % in strong acidic and basic solutions and becoming equal with only 5 % at pH = 6.54. This behaviour is due to the intricate structure of the studied complex, which presents an isoelectric point in the weak acidic domain, and to "zwitterion" structure of the drug, this being characterized by pK_a=3 for COO^-, pK_b= 3.2 for NH_3^+ and pK_{OH} (enolic) = 4.1

CONCLUSIONS

The Ceftriaxone, a parenteral third generation cephalosporine antibiotic, can be used as long-time local application in treatment of some severe periodontal infections. This utilization is assigned by the very lower rate of ceftriaxone release from the Chitosan/CMC/Ceftriaxone complex in the neutral pH media (pH=6.54 – which is in the same time the isoelectric point of the drug.

The higher release rates obtained in both strongly acid and strongly basic media is due to the increasing solubility of the drug as a result of the ionization of the acidic or basic groups.

REFERENCES

1. Berner B., Dinh S. "Fundamental concepts in controlled Release", in Treatise on Controlled Drug Delivery, A. Kydonieus Ed., Marcel Dekker Inc., N.Y, 1989
2. R. J. Mrsny, Controlled Drug Delivery – Challenges and Strategies, Kinam Park, Ed., ACS Professional Refference Book, Whasington, 1997.

3. L. Long, A.S. Hoffman & P. Sadurny, Ph Sensitive Hydrogels, Based on Thermally Reverseble Gels for Enteric Drug Delivery, Proc. Int. Symp. Control. Rel. Bioact. Mater, 1989, p. 95.
4. H. W. Davenport, "Phy Biology of Digestivo Tract", Year Book Medical Publishers, Chicago, 1982.
5. N. Aelenei, I. M. Popa, D. Andrei, Delia Aelenei, A. Mărculescu. *Farmacia*, vol. XLVII, nr. 6, 2000, p. 43 – 49

STUDIA UNIVERSITATIS BABEŞ-BOLYAI, CHEMIA, XLVI, 1-2, 2001

ASPECTS CONCERNING FIXED FILM BIOLOGICAL WASTEWATER TREATMENT

RODICA ELENA CECLAN*, OCTAVIAN FLOAREA*, MIHAIL CECLAN**

Universitatea Politehnica din Bucureşti
**Catedra Inginerie Chimică, Tel.: 092 170662,*
Fax: 211 6798, E-mail: r_ceclan@chim.upb.ro
***Catedra Echipament Termomecanic Clasic şi Nuclear*

ABSTRACT. The biological wastewater treatment is a very actual problem taking into account the necessity of aligning the Romanian laws to the European standards. As an interdisciplinary science the chemical engineering plays an important role in achieving this kind of wastewater treatment.

The fixed film treatment technology are extremely important in public health control and in environmental protection, being based on the natural mechanism of biological water cleaning.

The paper presents the state of the art in the field of biological treatment of municipal wastewater using the fixed film technique (biofilm).

The principal causes, water pollution sources and wastewater contaminants are shown; some analytical methods for the water pollution control are also presented.

The classification of methods for biological wastewater treatment is accompanied by the issue of the essential functional element of every such equipment, the biofilm issue.

After its definition and its approach as ecosystem, information concerning the biofilm composition, structure and formation mechanism are systemized.

Physical and mathematical models of the wastewater treatment process are systemized.

1. INTRODUCTION

The biological treatment of municipal wastewater is used as an economical possibility in order to remove the biodegradable organic pollutants and to obtain a water quality in accordance with international environmental standards.

Utilization of biological fixed-film processes (biofilm) presents the advantages of an enhanced biomass accumulation in biofilm systems by its attachment to a fixed medium, and of short liquid retention times that are possible without washout of the microbial population or loss of treatment efficiency.

The main equipment is a fixed film bioreactor containing a packing of plastic materials which offers a large surface for the growth of microbial film and can then be exposed to wastewater and oxygen, in order to effect organic substrate consumption by the biofilm.

The use of plastic packing in biofilters has become current practice, because of its large specific surface area and favorable voidage. The plastic media can be well ventilated and allow the operation of a biofilter with large hydraulic and organic loads. Random plastic modules, vertical (semi) corrugated bundles or cross-flow media are used.

The biofilter is a three-phase system characterized by extremely complex physical, chemical and biological processes. Because of its great complexity, it is difficult to elucidate experimentally the influence of different parameters and of their interactions on the performance of the process.

Simulation of processes that take place in a biofilter by using mathematical models illustrating as well as possible the biophysical reality allows exploring different biofilter operation strategies, in order to improve the bioprocess performance and to establish the optimal plant design methods.

The wastewater aerobic purifying processes occurs by elementary processes as transport of organic substrate and of oxygen through the wastewater film to the interface with the biofilm and biochemical reaction at the interface. The purifying process can be described by mass and momentum balance equations and by its biochemical kinetics, which are characteristic for living systems.

The paper presents shortly a conference concerning a review of fixed film biological wastewater treatment state of the art.

2. WASTEWATER CHARACTERISTICS AND EFFLUENT QUALITY PARAMETERS

In many arid and semi-arid countries water is becoming an increasingly scarce resource and planners are forced to consider any sources of water which might be used economically and effectively to promote further development.

Expansion of urban populations and increased coverage of domestic water supply and sewerage give rise to greater quantities of municipal wastewater.

Properly planned use of municipal wastewater alleviates surface water pollution problems and not only conserves valuable water. The nitrogen and phosphorus content of wastewater might reduce or eliminate the requirements for commercial fertilizers.

Municipal wastewater is mainly comprised of water (99.9%) together with relatively small concentrations of suspended and dissolved organic and inorganic solids. Among the organic substances present in sewage are carbohydrates, lignin, fats, soaps, synthetic detergents, proteins and their decomposition products, as well as various natural and synthetic organic chemicals from the process industries. Table 1 shows the levels of the major constituents of strong, medium and weak domestic wastewaters

Table 1:

MAJOR CONSTITUENTS OF TYPICAL DOMESTIC WASTEWATER

Constituent	**Concentration, [mg/l]**		
	Strong	**Medium**	**Weak**
Total solids	1200	700	350
Dissolved solids (TDS)	850	500	250
Suspended solids	350	200	100

Constituent	**Concentration, [mg/l]**		
	Strong	**Medium**	**Weak**
Nitrogen (as N)	85	40	20
Phosphorus (as P)	20	10	6
Chloride	100	50	30
Alkalinity (as $CaCO_3$)	200	100	50
Grease	150	100	50
BOD_5	300	200	100

Municipal wastewater also contains a variety of inorganic substances from domestic and industrial sources, including a number of potentially toxic elements such as arsenic, cadmium, chromium, copper, lead, mercury, zinc, etc.

Contaminants of greatest concern are the pathogenic micro- and macro-organisms.

Pathogenic viruses, bacteria, protozoa and helminthes may be present in raw municipal wastewater and will survive in the environment for long periods (Table 2).

Table 2:

POSSIBLE LEVELS OF PATHOGENS IN WASTEWATER

Type of pathogen		**Survival times, [days]** (Figures in brackets show the usual survival time)		
		Faeces and sludge	**Fresh water and sewage**	**Soil**
Viruses:	*Enteroviruses*	<100 (<20)	<120 (<50)	<100 (<20)
Bacteria:	*Escherichia coli*	<90 (<50)	<60 (<30)	<70 (<20)
	Salmonella spp.	<60 (<30)	<60 (<30)	<70 (<20)
	Shigella spp.	<30 (<10)	<30 (<10)	-
	Vibrio cholerae	<30 (<5)	<30 (<10)	<20 (<10)
Protozoa:	*Entamoeba histolytica*	<30 (<15)	<30 (<15)	<20 (<10)
Helminthes:	*Ascaris Lumbricoides*	Months*	Months*	Months*
*eggs	Hookworms: *Anglostoma duedenale*; *Necator americanus*	Months*	Months*	Months*
	Schistosoma mansoni	Months*	Months*	Months*
	Taenia saginata	Months*	Months*	Months*
	Trichuris trichiura	Months*	Months*	Months*

3. WASTEWATER TREATMENT SYSTEMS

The principal objective of wastewater treatment is generally to allow human and industrial effluents to be disposed of without danger to human health or unacceptable damage to the natural environment. The design of wastewater treatment plants is usually based on the need to reduce organic and suspended solids loads to limit pollution of the environment

Conventional wastewater treatment consists of a combination of physical, chemical, and biological processes and operations to remove solids, organic matter and, sometimes, nutrients from wastewater. General terms used to describe different degrees of treatment, in order of increasing treatment level, are preliminary, primary, secondary, and tertiary and/or advanced wastewater treatment. Disinfection to remove pathogens follows sometimes the last treatment step.

The step involving the use of biological systems follows after preliminary and primary treatment, where removal of coarse solids and other large materials often found in raw wastewater and of settleable organic and inorganic solids by sedimentation was performed, is the secondary treatment.

The ***secondary treatment*** objective of is the further treatment of the effluent from primary treatment, to remove the residual organics and suspended solids. In most cases, secondary treatment follows primary treatment and involves the removal of *biodegradable* dissolved and colloidal organic matter using *aerobic biological treatment processes*. Aerobic biological treatment is performed in the presence of oxygen by aerobic microorganisms (principally bacteria) that metabolize the organic matter in the wastewater, thereby producing more microorganisms and inorganic end-products (principally CO_2, NH_3, and H_2O). The microorganisms must be separated from the treated wastewater by sedimentation to produce clarified secondary effluent. The biological solids removed during secondary sedimentation, called secondary or biological sludge, are normally combined with primary sludge for sludge processing.

Common high-rate biological processes, characterized by relatively small reactor volumes and high concentrations of microorganisms, include the activated sludge processes, trickling filters or biofilters, oxidation ditches, and rotating biological contactors (RBC). A combination of two of these processes in series (e.g., biofilter followed by activated sludge) is sometimes used to treat municipal wastewater containing a high concentration of organic material from industrial sources.

In the *activated sludge process*, the dispersed-growth reactor is an aeration tank or basin containing a suspension of the wastewater and microorganisms, the mixed liquor. The contents of the aeration tank are mixed vigorously by aeration devices, which also supply oxygen to the biological suspension. Hydraulic retention time in the aeration tanks usually ranges from 3 to 8 hours but can be higher with high BOD_5 wastewaters. Following the aeration step, the microorganisms are separated from the liquid by sedimentation and the clarified liquid is secondary effluent. A portion of the biological sludge is recycled to the aeration basin to maintain a high mixed-liquor suspended solids (MLSS) level. The remainder is removed from the process and sent to sludge processing to maintain a relatively constant concentration of microorganisms in the system. Several variations of the basic activated sludge process, such as extended aeration and oxidation ditches, are in common use, but the principles are similar.

A *trickling filter* or *biofilter* consists of a basin or tower filled with support media such as stones, plastic shapes, or wooden slats. Wastewater is applied intermittently, or sometimes continuously, over the media. Microorganisms become attached to the media and form a *biological layer* or *fixed film*. Organic matter in the wastewater diffuses into the film, where it is metabolized. Oxygen is normally supplied to the film by the natural flow of air either up or down through the media, depending on the relative temperatures of the wastewater and ambient air. Blowers can also supply forced air but this is rarely necessary. The thickness of the biofilm increases as new organisms grow. Periodically, portions of the film 'slough off the media. The sloughed material is separated from the liquid in a secondary clarifier and discharged to sludge processing. Clarified liquid from the secondary clarifier is the secondary effluent and a portion is often recycled to the biofilter to improve hydraulic distribution of the wastewater over the filter.

Rotating biological contactors (RBCs) are *fixed-film* reactors similar to biofilters in that organisms are attached to support media. In the case of the RBC, the support media are slowly rotating discs that are partially submerged in flowing wastewater in the reactor. Oxygen is supplied to the attached biofilm from the air when the film is out of the water and from the liquid when submerged, since oxygen is transferred to the wastewater by surface turbulence created by the discs' rotation. Sloughed pieces of biofilm are removed in the same manner described for biofilters.

Biofilms present a range of unique opportunities for application in environmental tech-nologies for cleanup and containment of hazardous wastes. They may be found on essentially any environmental surface in which sufficient moisture is present. Their development is most rapid in flowing systems where adequate nutrients are available.

Biological treatment systems rely on the metabolic versatility of mixed microbial populations for their efficiency.

Biofilms are composed of populations or communities of microorganisms adhering to environmental surfaces. These microorganisms are usually encased in an extracellular polysaccharide (glycocalyx) that they themselves synthesize.

The formation of a biofilm follows a course the nature of which can be predicted and recorded (figure 1).

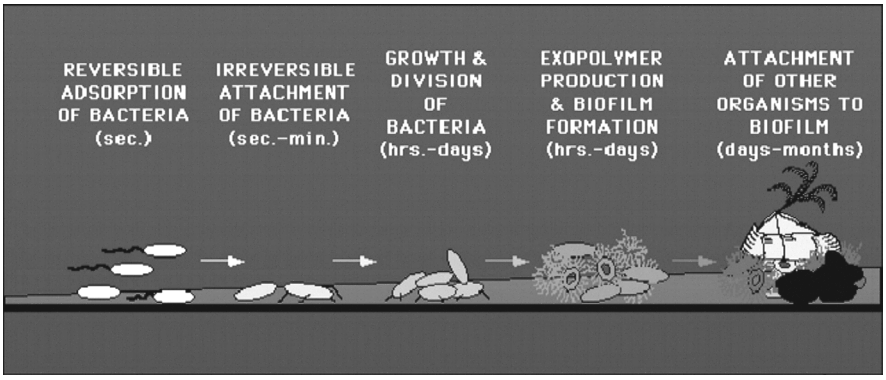

Figure 1: Biofilm formation

4. MODELING OF FIXED FILM BIOLOGICAL

A physical model of the biological fixed film wastewater treatment process is shown in figure 2.

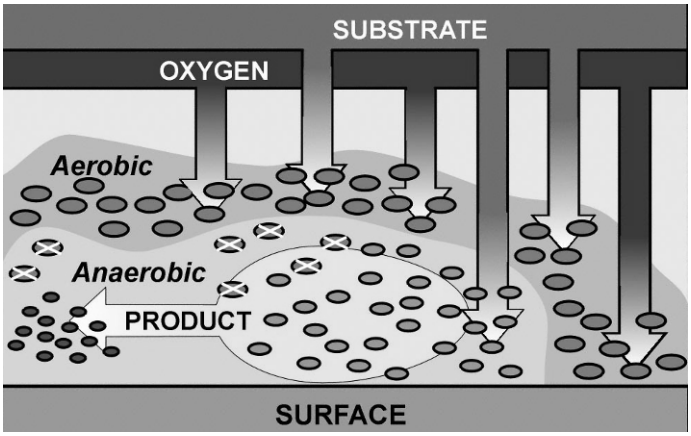

Figure 2: Physical model of fixed film wastewater treatment process

The wastewater aerobic purifying processes occurs by elementary processes as transport of organic substrate and of oxygen through the wastewater film to the interface with the biofilm and biochemical reaction at the interface. The purifying process can be described by mass and momentum balance equations and by its biochemical kinetics, which are characteristic for living systems.

Three kind of mathematical models are used:

- an “old generation” of mathematical models, represented by empirical (NRC, Ten States, British Manual, etc) and semiempirical models. Semiempirical models assume biofilters are pseudohomogeneous systems, with a flat organic contaminant concentration profile through the cross section of the biofilter. The mass conservation of organic substrate in a differential volume of a biofilter, where the rate determining stage of process is taken to be the first-order biochemical reaction occurring at the biofilm-wastewater interface is used for obtaining this kind of model.
- an “intermediate generation” of mathematical models considers the biofilter as a heterogeneous system and appears from the need to quantify substrate utilization rate and biofilm growth rate.
- the “new generation” of mathematical models was initiated by B.E.Logan, who takes into account both substrate/oxygen diffusional transport through the wastewater film and the first-order biochemical reaction occurring at the biofilm - wastewater interface.

5. CONCLUSION

The paper shows that the fixed film treatment technology is important in public health control and in environmental protection, being based on the natural mechanism of biological water cleaning.

The biological treatment of municipal wastewater is used as an economical possibility in order to remove the biodegradable organic pollutants and to obtain a water quality in accordance with international environmental standards.

The step involving the use of biological systems follows after preliminary and primary treatment, where removal of coarse solids and other large materials often found in raw wastewater and of settleable organic and inorganic solids by sedimentation was performed, is the secondary treatment.

The paper shows some physical and mathematical models of the wastewater treatment process, based on three kind of mathematical models, in order to demonstrate the efficiency of the biological treatment of municipal wastewater.

REFERENCES

1. Ceclan, R. E.; Floarea, O.; Bercia, R.; Ceclan, M., *Science and Technology of Environmental Protection*, Bucharest-Romania, **7(1)**, 11 – 17, 2000
2. Ceclan, R. E.; Floarea, O.; Bercia, R.; Ceclan, M., *Science and Technology of Environmental Protection*, Bucharest-Romania, **7(2)**, 20-28, 2000
3. Ceclan, R.E., Editura Printech, Bucureşti, 2001, ISBN: 973-652-315-2
4. Katzbauer, B., Narodoslawski, M., Moser, A., *Bioprocess Engng.***12**, 173-179, 1995
5. Logan, B.E., Hermanowicz, S.W., Parker, D.S., *Journal WPCF*, **59** (12), 1029-1042, 1987
6. Logan, B.E., Hermanowicz, S.W., Parker, D.S., *Journal WPCF*, **59** (12), 1017-1028, 1987
7. Logan, B.E., *J.of Environmental Engng*.**119** (6), 1059-1076,1993
8. Moser, A., *Bioprocess Technology*, Springer Vela, N.Y.-Wien, 1988
9. *** *Design of Municipal Wastewater treatment Plant***,** WEF Manual of Practice nr.8, N.Y.,1992
10. ****Wastewater Engineering*, Metcalf&Eddy, Inc., McGrawHill, Inc., 1991

STUDIA UNIVERSITATIS BABEŞ-BOLYAI, CHEMIA, XLVI, 1-2, 2001

POTENTIOMETRIC ANALYSIS OF ANIONIC SURFACTANTS BY ION-SELECTIVE ELECTRODE CONTAINING METHYLTRICAPRYLAMMONIUM CHLORIDE

CRISTINA MIHALI*, ELENA HOPÎRTEAN, GABRIELA OPREA*

**Universitatea de Nord Baia Mare, str. Dr. V. Babeş nr. 62/A, 4800 Baia Mare*

ABSTRACT. Surfactants are very important in modern society, but they are also important pollutants. They have a negative impact on the environment especially on water.

Anionic surfactants are the most widespread among the surfactants class. They comprise approximately 70% of all the surfactants manufactured; therefore they are often subject of environmental monitoring. The determination of anionic surfactants with surfactants-selective electrodes is an alternative method to the standard methylene blue-method and the two-phase titration method.

We realised a polymeric membrane electrode selective to anionic surfactant based on methyltricaprylammonium chloride and plasticized with tricresylphosphate. This electrode gives a linear response for sodium dodecylsulphate between $5x10^{-6}$ and $5x10^{-3}$ with a nearnernstian slope.

INTRODUCTION

Surfactants are organic compounds which, when added to a mixed system such as water and air, induced a reduction of the air-water interfacial tension. Nowadays surfactants are widely produced and consumed industrially and domestically. Anionic surfactant have the largest extent with the approximately 70% of all the surfactant manufactured [1]. The anionic surfactant concentration is usually monitored in the environment, in cleaning processes and during the fabrication of raw materials and formulated detergent products. The most frequently used method for the analysis of the anionic surfactant is two-phase titration. In the last years many others methods were developed: extractive-spectophotometric methods [2-6], chromatographic techniques [7-10], and electrochemical methods.

Recently an overview of the electroanalytical method devoted to surfactant analysis was published [11]. Among the electrochemical methods, the potentiometric methods are well represented because they are simple, fast and cheap. There are many anionic surfactant sensible electrodes described in the literature [12-30]. The first surfactant sensible electrodes were liquid membrane electrodes but polymeric membrane electrodes, which are more robust and stable, replaced them.

Basically, the electroactive substance of a membrane for a surfactant-sensitive electrode consists of an association of an ion-pair ($C^+ A^-$), where A^- is an anionic surfactant and C^+ is a positively charged counter ion, as a cationic surfactant, a cationic dye or a cationic metal-complex. But, the preparation of the ionic pair compound is difficult enough because a high purity of this compound is required.

Also, the ion-pair compound may be unsuitable with the system PVC-solvent and plasticizer. That why we try to prepare a membrane electrode sensitive to anionic surfactant based just on a cationic compound.

Metyltricaprylammonium chloride (Aliquat 336S) is recommended as electrodic component for the potentiometric determination of some inorganic anions as Cl^- and NO_3^- [31].

We prepared and tested a polymeric-membrane electrode sensible to anionic surfactant with metyltricaprylammonium chloride as electroactive substance.

EXPERIMENTAL

Reagents

All reagents and solvents used to prepare the working solutions and the membranes were of analytical reagent grade. The solutions were prepared using doubly distilled water.

The plasticizer used was tricresylphosphate supplied by BDH Chemicals.

The standard anionic surfactants used was sodium dodecylsulphate (SDS) from Merck. Metyltricaprylammonium chloride (Aliquat 336 S) was from Fluka.

Membrane preparation

The sensing membrane was prepared with the following proportions (w/w): 33% polymer (high molecular mass PVC), 66% plasticiser (tricresylphosphate) and 1% metyltricaprylammonium chloride. The components of the membrane were dissolved in tetrahydrofuran (8ml for 1g membrane composition). The composition was poured to the end of an electrodic body on a copper pill that takes the membrane-electrode potential and obeyed to a slowly evaporation of tetrahidrofuran.

The electrode was conditioned by soaking in 10^{-3}M solution of sodium dodecylsulfate for at least one hour before measurement.

The experiments were realised at room temperature (21ºC –22ºC) and the analyte solutions were magnetically stirred during measurements.

The calibration solutions were prepared by successive dilutions, adding the necessary volume of concentrated Na_2SO_4 solution in order to obtain a constant ionic force corresponding to 0,01 M Na_2SO_4 solutions.

Apparatus

All the calibration measurements were carried out with a digital milivoltmeter E0302 (10^9 Ω input impedance).

The refernce electrode was calomel saturated electrode (Senzorom).

RESULTS AND DISCUSSIONS

Electrode calibration

According the literature [29] a 0,01 M Na_2SO_4 supporting electrolyte is used. The calibration curve is realised between $1x10^{-7}$ M and $1x10^{-2}$ M solutions of sodium dodecylsulfate. The membrane electrode exhibits a nearnernstian response between $5x10^{-6}$ and $5x10^{-3}$ M SDS. Above $5x10^{-3}$ M, SDS forms micelles, this reduces the amount of free surfactant and a decrease in the potential of the electrode is observed: this concentration corresponds to the critical micellar concentration (CMC). The CMC value determined for SDS ($5x10^{-3}$M) is closed to

the value reported in the literature ($8x10^{-3}$ M) [32]. A smaller value can be explained as follow: the calibration was performed in solution containing also inorganic salts added to mentain a constant ionic force, but this conduces to a smaller activity of the surfactant and as consequence a smaller value for the CMC.

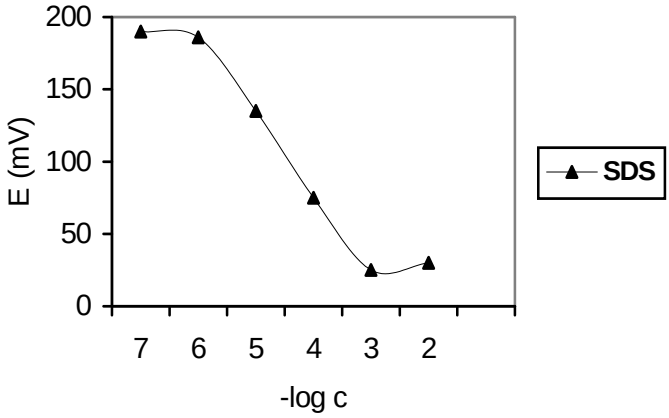

Figure 1 Calibration curve E= f (pC_{SDS}) of the surfactant electrode in aqueous solutions containing Na_2SO_4 (0,01M)

pH effect

The effect of pH on the potential of the Aliquat electrode is determined by adding few microliters of concentrated sodium hydroxide or sulfuric acid to an aqueous solution containing 10^{-4}M SDS. The potential/pH dependence for the surfactant electrode is shown in figure 2.

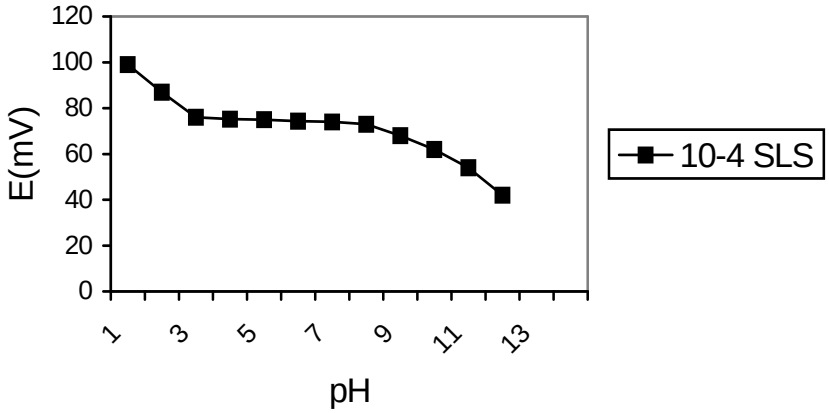

Figure 2 pH influence on the potentiometric response of the Aliquat 336 electrode sensible to SLS in the presence of 10^{-4}M SLS

The potential of the electrode is only slightly influenced by a pH variation in the range 3-8.

CONCLUSIONS

An polymeric membrane electrode based on metyltricaprylammonium chloride (Aliquat 336 S) as electroactive substance has been prepared.

The electrode was tested against sodium dodecylsulfate and a nearnernstian slope was founded in the range $5x10^{-6}$ and $5x10^{-3}$M.

pH influence was determined finding that the electrode potential is stable in the range of pH 3-8.

REFERENCES

1. Sanchez, J., Beltran, A., Alonso, J., Jimenez, C., del Valle, M., Anal. Chim. Acta, **382**, 1999, p. 157.
2. Yamamoto, K., Motomizu, S., Analyst, **112**, 1987, p. 1405.
3. del Valle, M., Alonso, J., Bartroli, J., Marti, I., Analyst, **113**, 1988, p. 1677.
4. Kubota, H., Idei, M., Motomizu, S., Analyst, **115**, 1990, p. 1109.
5. Fytianos, K., Vasilakakis, Raikos, N., J. Environ. Sci, **A32**, 1997, p. 953.
6. Chen, Y., Wang, S., Wu, R., Qi, D., Zhou, T., Anal. Lett., **31**, 1998, p. 691.
7. Nakae, A., Tsuji, K., Yamanaka, M., Anal.Chem., **53**, 1981, p. 1818.
8. Field, J.A., Miller, D. J., Field, T. M., Hawthorne, S.B., Giger, W., Anal. Chem, **64**, 1992, p. 3161.
9. Popenoe, D. D., Morris, S. J., Horn, P. S., Norwood, K. T., Anal. Chem., **66**, 1994, p. 1620.
10. Di Corcia, A., Samperi, R., Environ. Sci. Technol., **28**, 1994, p. 850.
11. Gerlache, M., Kauffmann, J. M., Quarin, G., Vire, J. C., Bryant, G. A., Talbot, J. M., Talanta, **43**, 1996, p. 507.
12. Gavach, C., Bertrand, C., Anal. Chim. Acta, **55**, 1971, p. 385.
13. Birch, B. J., Clarke, D. E., Anal. Chim. Acta, **61**, 1972, p. 159.
14. Birch, B. J., Clarke, D. E., Anal. Chim. Acta, **67**, 1973, p. 387.
15. Fujinaga, T., Okazaki, S., Freiser, H., Anal. Chem., **46**, 1974, p.1842.
16. Ciocan, N., Anghel, D., Tenside Detergents, **13**, 1976, p. 188.
17. Cutler, S. G., Mears, P., Hall, D. G., J. Electroanal. Chem., **85**, 1977, p. 85.
18. Ciocan, N., Anghel, D.,Fresenius Z. anal. Chem., **290**, 1978, p. 237.
19. Hoke,H. S., Collins, A. G., Reynolds, C. A., Anal. Chem. , **51**, 1979, p. 859.
20. Vytřas, K., Dajdova, M., Mach, V., Anal. Chim. Acta, **127**, 1981, p. 165.
21. Anghel, D., Popescu, G., Löwy, D., Rev. Chim., **34**, 1983, p. 1106.
22. Dowle, C. J., Cooksey, B. G., Ottaway, J. M., Campbell, W. C., Analyst, **112**, 1987, p. 1299.
23. Campanella, L., Mazzei, F.,Tomassetti, M., Sbrilli, R., Analyst, **113**, 1988 p.325.
24. Szczepaniak, W., Analyst, **115**, 1990, p. 1451.
25. Löwy, D., Pătruț, A., Anghel, D., Óvári, F.,Walter, M., Magy. Kem. Foly, **97**, 1991, p.460.

26. Makowezkaja, L. J., Majslina, I. J., Wolosowitzsch, S. P., Seifen-Öle-Fette-Wachse, **117**, 1991, p. 565.
27. Baró-Romà, J., Sánchez, J., Del Valle, M., Alonso, J., Bartroli, J., Sensors and Actuators B, **15-16**, 1993, p. 179.
28. Campanella, L., Battilotti, M., Borraccino, A., Colapicchioni, C., Tomassetti, M., Visco, G., Sensors and Actuators B, **18-19**, 1994, p. 321.
29. Gerlache, M., Sentürk, Z., Viré, J. C., Kauffmann, J. M., Anal. Chim. Acta, **349**, 1997, p. 59.
30. Sànchez, J., Beltran, A., Alonso, C., Jiménez, C., del Valle, M., Anal. Chim. Acta, **382**, 1998, p. 157.
31. Veselý, J., Wiess, D., Štulik, K., Analysis with ion-selective electrodes, Ellis Horwood Limited Publishers, John Wiley & Sons NewYork.
32. Chifu, E., Chimia coloizilor şi a interfețelor, Presa Universitară Clujeană, Cluj-Napoca, 2000.

STUDIA UNIVERSITATIS BABEŞ-BOLYAI, CHEMIA, XLVI, 1-2, 2001

THE COPPER, LEAD AND ZINC RECOVERY OF THE MINERALS PARTIAL OXIDATED WITH CHELATANT ACTION REAGENTS

GABRIELA OPREA, CRISTINA MIHALI

Universitatea de Nord Baia Mare, str. Dr. V. Babe¿ nr. 62/A, 4800 Baia Mare

ABSTRACT. The flotation of copper minerals with salicylaldoxyne shows a good selectivity of the reagent. 8-hydroxyquinoline (oxyne) is less selective because part of calcite floates and decreases the copper content of the concentrate. In this case is demonstrated the utility of the flotation in two steps when the recovery percentage of the copper increases in the concentrate and decrease in the sterile.

The flotation of the lead and zinc minerals partial oxidated with oxyne shows an increase in the recovery of lead and zinc when the flotation in two stages is replaced by the flotation in three stages, better then the replacing of one stage with two stages flotation.

For copper, lead and zinc partial oxidated minerals the results obtained using oxyne are net superior to those obtained by preliminary sulphating of the surface.By using of the oxyne the recoveries increases as well as the metal content.

INTRODUCTION

The chelating action reagents are used to for ores separation by flotation [1-6], because if it was proved that it is specific for certain ions in solution, they would keep their selectivity even in the case of the adsorption to the surface of the minerals which contain these metallic ions [7-13].

Considering that the ores which follow to be studied contained the Cu (II), Pb(II), Zn(II) ions, we studied some chelating action reagents which form, in solution, stable chelatant compounds with these ions. We used a microflotation device [4-6]. Salicylaldoxyme and 8-hydroxyquinoline (oxyne), which gave the best results, were used for the ores containing oxidized minerals because, with common collectors, a satisfying recovery (couldn't be) is not attained and even when it is realized, a selective separation from the sterile is not achieved.

EXPERIMENTAL

For the experimental determinations we used a Wedag microflotation cell.

The two reagents with chelatant action salicylaldoxyme and oxyne, were tested in order to study their behaviour relating the natural minerals (the ones partially oxidised) containing copper, lead and zinc which contains quartz and calcite and have a grading in the range 45-250 μ.

When salicylaldoxyme is used, the experimental took place in the following way: 200 g ore are introduced in 1l cuve, 800 cm^3 water are added, pH is fixed at 8, the reagent's solution is introduced, and after 5 minutes of conditioning it is floated 2-5 minutes (till the foams is exhausted), with a rotor speed of 1200 rotation /minute. 150 g/t foaming agent are introduced one minute before the end of the conditioning.

For the oxyne, a different procedure is adopted, because its solution in oil forms an emulsion with the water. The reagent's solution was 3 minutes emulsified with 200 cm^3 water in the flotation cell, the pH was mentained at 7,5-8, the conditioning time was 10 minutes and during the flotation an air stream was introduced for 5 minutes.

The concentrate and the sterile obtained after the flotation are filtered, dried, weighted and analysed to determinate copper, zinc or lead.

The experimental followed the influence of the reagent's concentration (salicylaldoxyme or oxyne) on the copper, zinc or lead content and also the recovery percent of these metals in the partially oxidised ores studied.

RESULTS AND DISCUSSIONS

In a series of determinations salicylaldoxyme was used for the copper recovery from the ore composed by malachite and calcite containing 0,92% Cu.

It was worked at different salicylaldoxyme concentrations ranging 140 g/t - 1500 g/t. The copper content (% Cu) in the concentrates and steriles obtained were calculated.

In figures 1 and 2 can be noticed a good selectivity of the salicylaldoxyme, which at 750 g/t concentration leads to a concentrate containing 45,8% Cu.

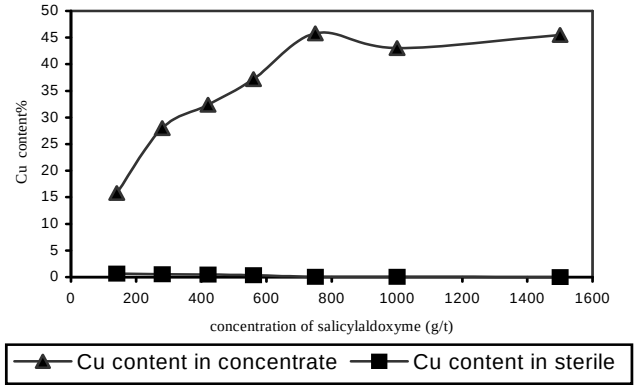

Figure 1 The variation of copper's content in concentrate and in sterile depending on the concentration of salicylaldoxime for a copper ore

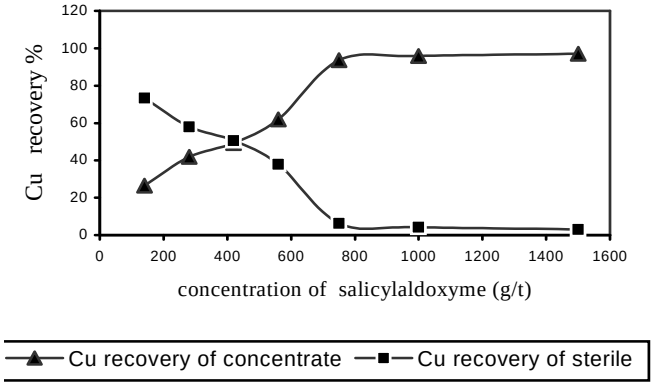

Figure 2 The variation of the copper's recovery in concentrate and in sterile depending on the salicylaldoxyme concentration for a copper ore

In these conditions a 93,6% recovery is attained and copper's content in the sterile is 0,06%. For 1500 g/t reagent, the recovery increases at 97%, the copper content in the concentrate decreases at 45.5% and in the sterile decreases significant till 0,028%.

Another series of determinations were realised using the 8-hydroxyquinoline (oxyne) for copper, lead and zinc recovery for three sorts of ores: copper, lead-zinc and copper-lead-zinc ore.

Malachite and calcite with 0,67% content of Cu constitute the sample of copper ore.

It was worked at different oxyne's concentrations ranging between 500 g/t and 2500 g/t.

In figures 3 and 4, the variation of Cu content and Cu recovery in the concentrate and in the sterile depending on the oxyne concentration can be followed.

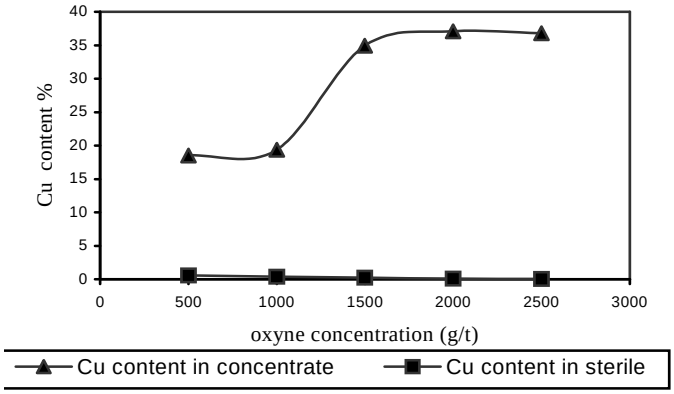

Figure 3 The variation of copper's content in concentrate and in sterile depending on the oxyne's concentration for a copper ore

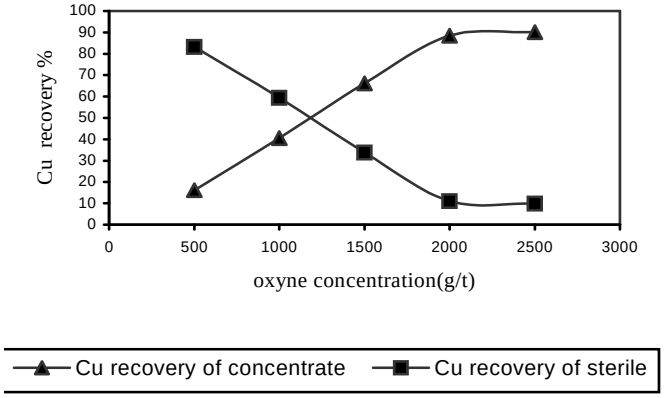

Figure 4 The variation of the copper's recovery in concentrate and in sterile depending on the oxyne concentration for a copper ore

It can be noticed that good copper recovery from the concentrate (88,5% respectively 90,14% is realised only at high oxyne's concentration, 2000g/t respectively 2500 g/t. In these conditions, the copper recovery from sterile decreases at 11,5% respectively 9,86% (greater values then in the case of the salicylaldoxyme). The copper content in the concentrate is 37,1% respectively 36,8%, smaller then in the case of salicylaldoxyme. This event demonstrates that a fraction of calcite floats and so the oxyne is less selective then salicylaldoxyme.

The influence of the reagent's addition in stages was followed using the same ore. For 2500 g/t reagent we realised a two stages flotation using 1500 g/t respectively 1000 g/t oxyne in every stage therefore two concentrates and a sterile were obtained. A cumulative concentrate is calculated from the two concentrates. It is noticed a recovery of 97,5% Cu of the concentrate and 2,5% Cu of the sterile and a 36,56% Cu content that demonstrates the utility of the two stages flotation for the increase of the util metal's recovery.

In the same time, by passing from one at two stages flotation the copper content in the sterile decreases from 0,067% to 0,017%.

The sample of lead-zinc ore was constituted by sulphuric lead and zinc and oxidised ores (galene, blende, lead and zinc sulphates, lead and zinc oxydes, cerusite and smithsonite) and also calcite. From the total zinc, which represents 2,98% almost 30% is oxidised and from the total lead which represents 1,25 % in proportion of 48% is oxidised. We made a flotation in one, two and three stages using the same total amount of reagent 3000 g/t, but splited into steps of 2000 g/t and 1000 g/t respectively 1500 g/t, 1000 g/t and 500 g/t.

The experimental results are presented in Figures 5 and 6. At the three stages flotation (comparing with two stages flotation) we noticed a better growing of the util metal recovery from 89,8% to 98,34 % for zinc and from 83,4 % to 92,5 % for lead related to the passing from one stage to two stages (Figure 6).

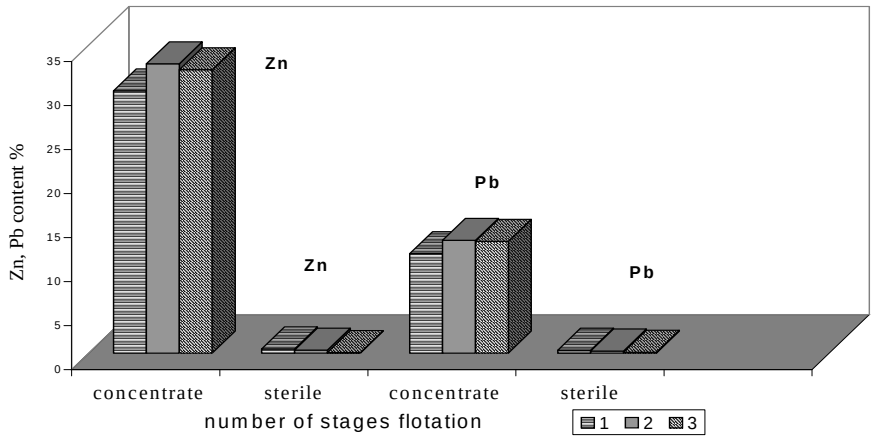

Figure 5 Zn or Pb content in concentrate and in sterile for one, two and three stages flotation

The lead and zinc content of the concentrate grows more when is passed from one to two stages flotation: from 29,8% to 32,87 % for zinc and from 11,80% to 12,80 % for lead and is mentained then almost constant for three stages flotation. The lead and zinc content in the flotation sterile is low in all the cases for example for zinc is 0,33% in two stages and 0,054 % in three stages flotation.

The sample of copper-lead-zinc ore contained: lead as carbonate, sulphate, pyromorfite and vanadite in proportion of 35 %, the difference being galene; copper as sulphate, carbonate (29%) and the remainder percent was as sulphide and calcopyrite; zinc as sulphate, carbonate (20%) and the difference being blende, quartz and calcite.

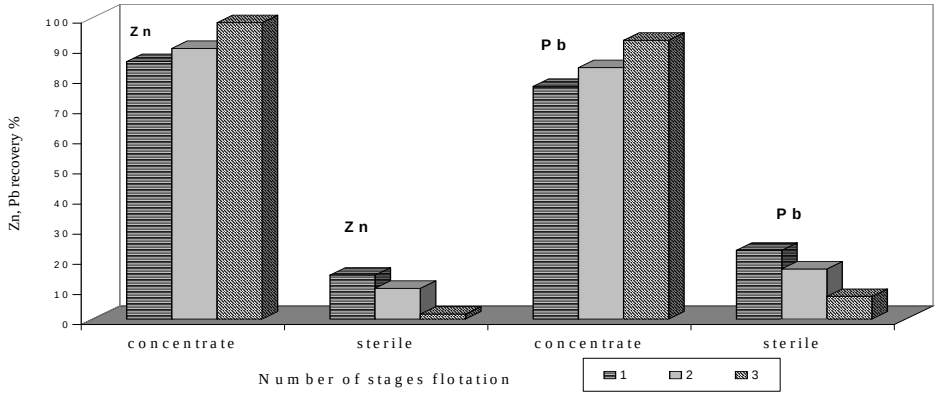

Figure 6 Zn or Pb recovery in concentrate and in sterile for one, two and three stages flotation

We performed a three-stages flotation, when we measured 1500 g/t, 1000 g/t and 500 g/t in every stage. We also performed a two stages flotation with 2000 g/t and 1000 g/t reagent in every stage.

The experimental results are included and are shown in Figures 7 and 8. An increasing of the recovery can be noticed at the passing from two to three stages flotation: for copper from 84,65% to 92,8%, for lead from 83,2 to 91,5% and for zinc from 90,74 % to 98,9%.

When the reagent 8-hydroxyqinoline is used, the results obtained are superior related at the flotation with amyl xanthate after a preliminary sulphating of the ore's surface. Therefore can be noticed an important increasing of the recovery especially for lead from 78,65% to 91,5% and for copper from 83,34% to 92,8%. For zinc the increasing realised was from 94,06% to 98,9%. The metal content in the concentrate enlarged from 1,01% to 2,18% for copper, from 5,28% to 12% for lead and from 10,41% to 21,2% for zinc. It is very important the fact that the metal content in the sterile decreased from 0,12% to 0,02% for zinc, from 0,27% to 0,097% for lead and from 0,037% to 0,015% for copper.

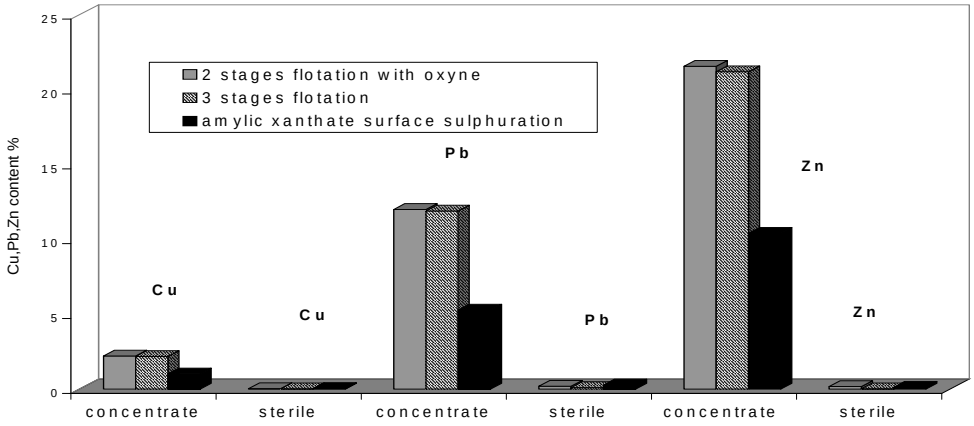

Figure 7 Cu, Zn and Pb content in concentrate and in sterile for two and three stages flotation and for amylic xanthate sulphuration of the surface

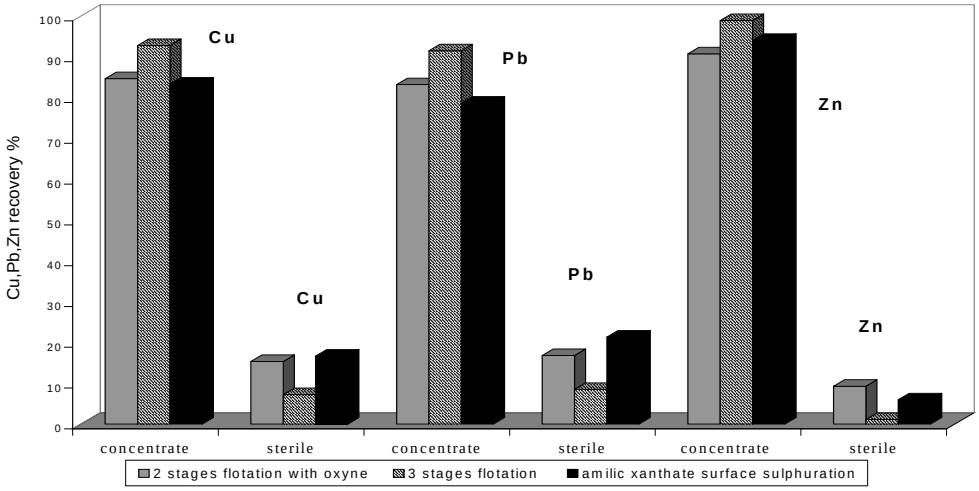

Figure 8 Cu, Zn and Pb recovery in concentrate and in sterile for two and three stages flotation and for amylic xanthate sulphuration of the surface

CONCLUSIONS

1. For the copper ore flotation with salicylaldoxyme can be noticed a good reagent selectivity that leads, for a concentration of 750 g/t reagent, to a concentrate containing 45,8% Cu.
2. A maximum recovery of the copper (97%) with 1500 g/t reagent when is realised the copper in the sterile is the least (0,028%).
3. With the oxyne (8-hydroxyquinoline), also used for copper's ores are realised goods copper recoveries (90,14%) at a concentration of 2500 g/t. This reagent is less selective then the salicylaldoxyme as it was demonstrated by the copper

content in the concentrate which has been maxim 37,1%. We demonstrated in this case that the two-stages flotation is very advantageous because the copper recovery increases at 97,5% and the copper content in the sterile decreases at 0,017% this being very important.

4. In the case of the partially oxidised lead-zinc ores the recovery are greater for the three stages flotation respectively 98,34% for zinc and 92,5 for lead when the oxyne is used.
5. For the partially oxidised copper-lead-zinc ores the obtained results using the oxyne are clearly better then those obtained by the amyl xanthate flotation after a preliminary sulphating of the ore's surface. So the recoveries increase for lead from 78,65% to 91,5%, for copper from 83,34 % to 92,8% and for zinc from 94,06 to 98,9%. The metal's content increases in the concentrate and decreases in the sterile.
6. Using the reagent with chelatant action, salicylaldoxyme and oxyne, is eliminated the difference between the oxidised and sulphured ores concerning the recovery of the util metal.

REFERENCES

1. G. Rinelli, A. M. Marabini, *International Minerala Processing Congress*, London (1978)
2. J.L. Cecille, M. J. Cruz, G. Barbery, J. J. Fripiat, *J. Colloid and Interface Science,* (1980)
3. G. Oprea, *Scientific Symposium with International Participation: Technologies for processing of refractory raw materials and for environment protection in areas with extractive industry*, vol. I, p. 127-135, Baia Mare (1995).
4. G. Oprea, C. Mihali – *Studia Univ. Babes Bolya*, *Ser. Chemia*, XLIII, 1-2, pag. 116-125 (1998)
5. G. Oprea, C. Mihali – *Analele Universitatii din Oradea, Fascicola Chimie*, IV, p. 111-118, ISSN, 1224-7626 (1998)
6. G. Oprea, C. Mihali – *Studia Univ. Babes Bolyai, Ser. Chemia* Cluj Napoca, XLV, in press (2000)
7. V. M. Lovel, L. A. Goold, N. P. Finkelstein, *Internat. J. Mineral Process*., vol 1, p. 183 (1974)
8. R. G. Grendler, *J. Phys. Chem*.; vol. 66, p. 879 (1962)
9. J. Mielczarski, P. Novak, J. W. Strojek, A. Pomianowski, *International Minerala Processing Congress,* Varszawa, p. 61 (1979)
10. S. Raghavan, D. W. Fuerstenau, *J. Colloid Interface Sci*. ; Vol. 50**,** p. 319-330 (1975)
11. G. Oprea, *The Conference of Chemistry and Chemical Engineering*, vol. III, part I, p.115-121, Bucuresti (1995)
12. G. Oprea, E. Chifu – *Stud. Univ. Babes Bolyai, 5 Chemia* 2/1986, p. 65-68, Cluj Napoca (1986)
13. G. Oprea, *Proceedings of International seventh Beijing Conference and Exhibition on Instrumental Analysis*, *C. Spectroscopy BCEIA*, Shanghai, China p. 149-150 (1997)

STUDIA UNIVERSITATIS BABEŞ-BOLYAI, CHEMIA, XLVI, 1-2, 2001

COPPER SOLVENT EXTRACTION FROM ACID SOLUTIONS OBTAINED BY ORES SOLUBILIZATION

CAMELIA LUMINITA VARGA

Department of Chemistry, North University of Baia Mare, 4800 Baia Mare, Romania

ABSTRACT. Solvent extraction is the separation technique used, in this case, for purification and concentration of acid solutions obtained by low-grade copper ores leaching. The acid solution contents, beside copper, considerable amounts of zinc, lead and iron, which are undesirable components. To separate the copper from this unwished elements, copper was extracted by chelatable extractant (α-benzoin oxime, named cupron). To increased the extraction efficiency, two contacting methods, between aqueous and organic phase, were investigated. When one organic phase was contacted successionally with three loaded aqueous phases, it was obtained an increase of copper concentration in organic phase, relate to the case in which one aqueous phase was contacted sequential with three unloaded organic phase.

INTRODUCTION

The solutions obtained by acid solubilization of low-grade complexes ores contents, beside copper, considerable amounts of zinc, lead and iron. In the most hydrometallurgical processes of copper winning, the final step is electrowinning (electrolysis). The presence of zinc, lead and iron in leaching solution disturbs the electrowinning process. Therefore, is necessary to separate copper from undesirable components and, in the same time, to concentrate copper in the solution, by solvent extraction.

The purpose of this paper is to test two method of contact between aqueous and organic phase, with a view to obtain a higher copper concentration in organic phase. Therefore, the aqueous and organic phase were submitted to a three-stapes extraction succession, either using only one aqueous phase and three unloaded organic phases, or using only one organic phase and three loaded aqueous phases.

EXPERIMENTAL

The extraction solvent

As extraction solvent, α-benzoin oxime in benzol was used. The extracting agent (structure I), named cuprous [1], forms a chelate compound (structure II) by azote (N) and hydroxylic oxygen (OH) atoms with cupric ion [2-3].

The aqueous phase

The aqueous phase subjected to solvent extraction, was obtained at Cavnic Mine ore solubilization [4-7], under following experimental conditions:

- ratio solid/liquid: 1/7.5
- solubilization agent: H_2SO_4 8 N;

- oxidizing agents: $Fe_2(SO_4)_3$ 30 g/l and air bubbling at 200 l/hour in a volume of 210 ml leaching agent;
- solubilization temperature: 60°C;
- solubilization time: 24 hours;
- fraction of ore: -160+100 μm.

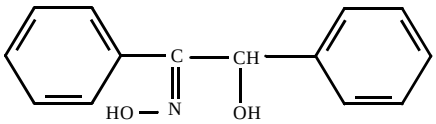

(I)

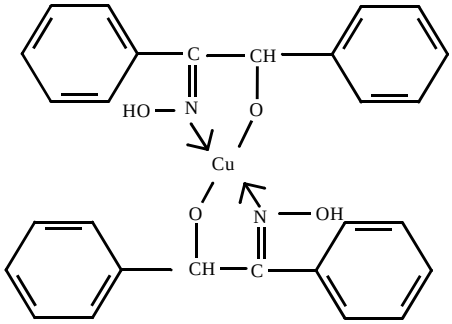

(II)

The chemical and mineralogical composition of the low-grade chalcocite-covellite-chalcopyrite ore is given in table 1.

Table 1.

The chemical and mineralogical composition of low-grade ore.

Element	%	Element	Compounds	%
Cu	0.37	Cu	sulphates	0.003
Pb	1.50		carbonates and oxides	0.013
Zn	2.00		chalcocite and covellite	0.144
Au	0.38*		chalcopyrite	0.212
Ag	45.7*	Pb	sulphates	0.140
Fe	7.52		carbonates	0.110
As	0.00		sulphides	1.010
S	7.92		oxidic compounds	0.240
SiO_2	53.4	Zn	sulphates	0.005
* g/t			carbonates and oxides	0.065
			silicates	0.080
			sulphides	1.855

The copper and iron content of aqueous phase obtained by acid solubilization, in presence of oxidizing agents, is presented in table 2.

Table 2.

The copper and iron content of aqueous phase.

$C_{Cu^{2+}}$ (g/l)	$C_{Fe_{total}}$ (g/l)	$C_{Fe^{2+}}$ (g/l)
0.26	6.85	5.10

The solvent extraction experimental conditions

The copper extraction from aqueous phase was carried out by a three-stapes extraction succession, which is showed schematically in figure 1.

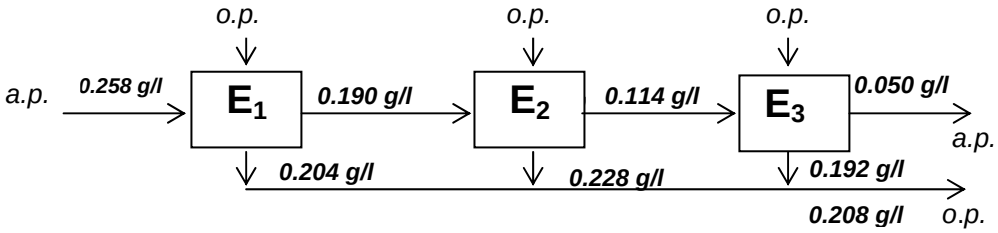

Figure 1. The diagram of modifications in aqueous (a.p.) and organic phases (o.p.) copper content.

In this case, the experimental conditions were the following:

- aqueous phase volume: 15 ml;
- organic phase volume: 5 ml;
- α-benzoin oxime concentration in benzol: 0.5 moles/l;
- phases contact time: 20 minutes/step.

The phases separation was made with separating funnel and the copper concentration in solution was analysed by spectrophotometrical method, using cuprizon (oxalic acid bis(cyclohexylidenhidrazide)) as complexing agent.

In the second method of aqueous and organic phase contact, schematically showed in figure 2, the copper extraction was realized by a three steps extraction succession, using only one organic phase, under the following conditions:

- aqueous phase volume: 15 ml;
- organic phase volume: 15 ml;
- α-benzoin oxime concentration in benzol: 0.5 moles/l;
- phases contact time: 20 minutes/step.

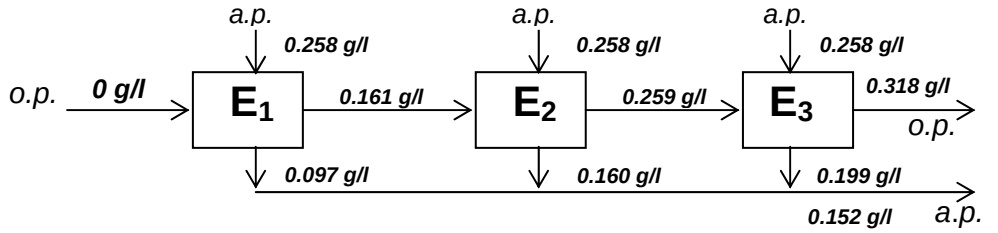

Figure 2. The diagram of modifications in organic (o.p.) and aqueous phases (a.p.) copper content.

RESULTS AND DISCUSSIONS

The values of extracted by first method copper percent, for each step of extraction (E_1, E_2 and E_3), for first and second steps of extraction (E_{1-2}) and for all three steps of extraction (E_{1-3}) are presented in figure 3.

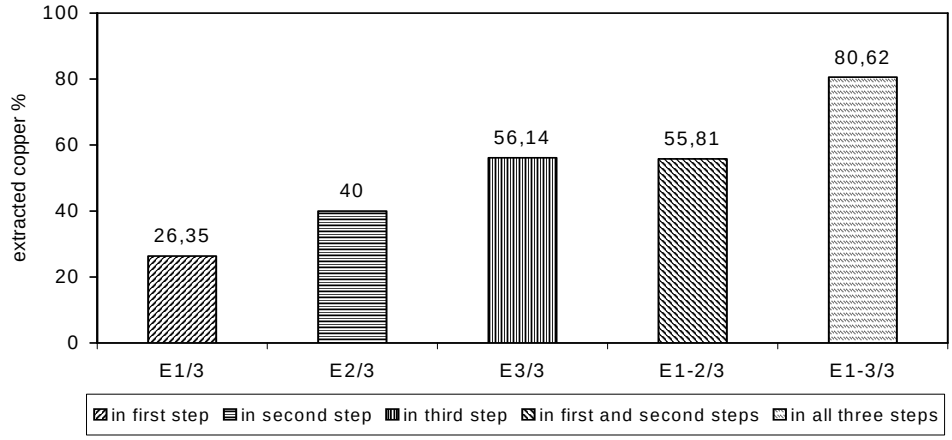

Figure 3. The extracted by first method copper percents in: first, second, third, first and second, and all three steps.

In figure 4 are presented the values of extracted by second method copper percent, for each step of extraction (E_1, E_2 and E_3), for first and second steps of extraction (E_{1-2}) and for all three steps of extraction (E_{1-3}).

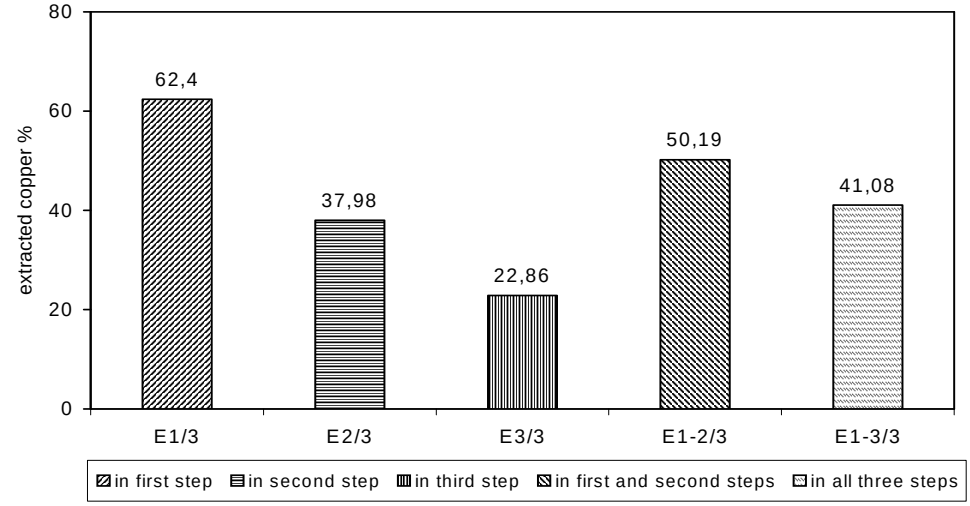

Figure 4. The extracted by second method copper percents in: first, second, third, first and second, and all three steps.

To increase moreover the extracted copper percent and the copper concentration in organic phase, the partial unloaded aqueous phase obtained by second extraction method was submitted, in the same experimental conditions, to another three-stage extraction succession.

In this case, the diagram of modification in aqueous and organic phases copper content is presented in figure 5.

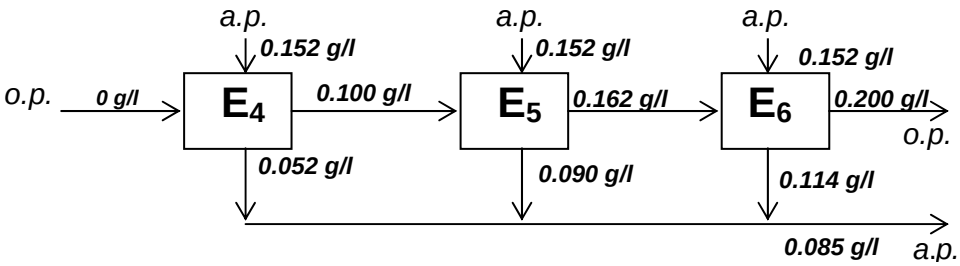

Figure 5. The diagram of modifications in organic (o.p.) and aqueous phases (a.p.) copper content.

The values of extracted copper percent, in this case, are presented in figure 6.

In table 3 are contained the initial and final copper concentrations of aqueous and organic phases for each of steps, the extracted copper percents according to steps and the total extracted copper percent after six steps of extractions.

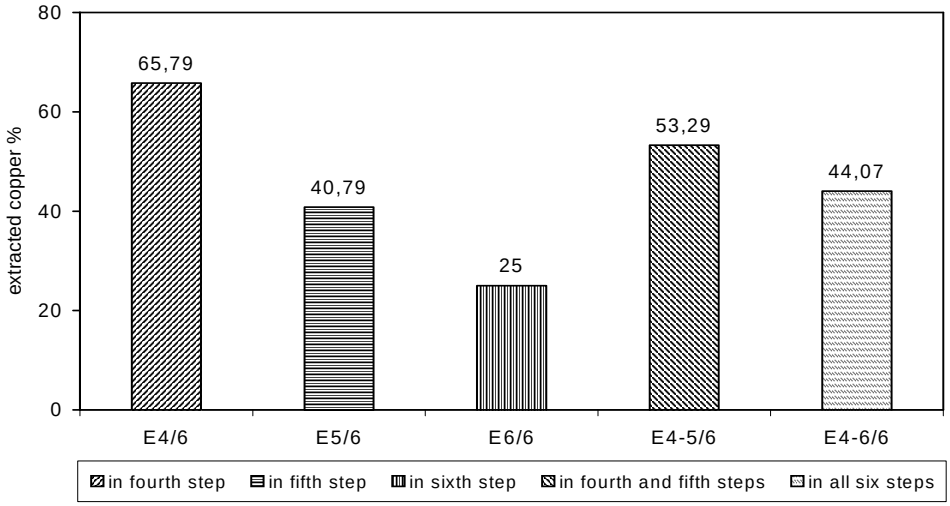

Figure 6. The extracted by second method copper percents in: fourth, fifth, sixth, fourth and fifth, and all six steps.

Table 3.

The initial and final copper concentrations of aqueous and organic phases, and the extracted copper percents.

Step	Aquouse phase		Organic phase		Extracted copper %			
	$c_{initial}$ (g/l)	c_{final} (g/l)	$c_{initial}$ (g/l)	c_{final} (g/l)				
E_1	0.258	0.097	0.000	0.161	62.40	50.19	41.08	67.05
E_2	0.258	0.160	0.161	0.259	37.98			
E_3	0.258	0.199	0.259	0.318	22.86			
E_4	0.152	0.052	0.000	0.100	65.79	53.29	44.07	
E_5	0.152	0.090	0.100	0.162	40.79			
E_6	0.152	0.114	0.162	0.200	25.00			

CONCLUSIONS

The examination of the extracted copper percent obtained values leads to the following conclusions:

(a) the extracted by first method (when is used only one aqueous phase and three unloaded organic phases) copper percent amounts to 80.62% after three-stages extraction succession; although the extracted copper percent is raised enough, the copper concentration in organic phase is mealy 0.208 g/l;
(b) when the second extraction method is used (three loaded aqueous phases and only one organic phase) the extracted copper percent amounts to 41.08% after three-stages extraction succession; in this case, the copper content in organic phase is higher (0.318 g/l) than the copper concentration in organic phase (0.208 g/l) obtained by first method, though the extracted copper percent after all three extraction steps (41.08%) is lower than the extracted by first method copper percent (80.62%);
(c) the increase of extraction steps number until six, leads to an extracted copper percent of 67.05%.

REFERENCES

[1]. Balanescu, G., Dictionar de chimie, Ed. Tehn., Bucharest, **1964**;
[2]. Perescu, N., Chimia extractiei cu solventi si aplicatii, cap. 2, 3, 6, Ed. Academiei, Bucharest, **1985**;
[3]. Hudson, M.J., *Hydrometallurgy*, **1982**, *9*, 149;
[4]. Varga, C.L., Oniciu, L., *Studia Univ. Babeş-Bolyai, Chem.,* **1999**, *44*(1-2), 193;
[5]. Varga, C.L., Oniciu, L., Bâldea, I., *Studia Univ. Babeş-Bolyai, Chem.,* **1999**, *44*(1-2), 249;
[6]. Varga, C.L., *Ph. D. Thesis*, Babes-Bolyai University of Cluj-Napoca, **2000**;
[7]. Varga, C.L., *Bull. Sci. of North University of Baia Mare, Chem.-Bio.*, **2001**, *14*, accepted.

STUDIA UNIVERSITATIS BABEŞ-BOLYAI, CHEMIA, XLVI, 1-2, 2001

COMPARISON OF PID TUNING ALGORITHMS FOR PROCESSES WITH TIME DELAY

FLORINA UNGUREANU

Technical University of Iasi, Faculty of Industrial Chemistry, Bd. D. Mangeron, 71, 6000, Iasi, Romania

ABSTRACT. The purpose of this paper is to study by simulation some PID tuning methods for process with time delay. The ZIGLER-NICHOLS (ZN), ALESSANDRO BRAMBILLA (AB) and INTERNAL MODEL CONTROL (IMC) methods are considered. The performances of the close-loop are studied, for 1st and 2nd order plus time delay processes, in the cases of step set point and load disturbance.

1. INTRODUCTION

The main characteristics of the dynamic behaviour of the chemical processes (especially heat and mass transfer units) are the time delay and the long settling time that depends on the inputs and dimensions of the equipment. Usually, the models used are the 1st and 2nd order with time delay. These mathematical models describe the real processes with uncertainty due to the approximations considered or to the parameters variation in time. Despite the availability of advanced algorithms, conventional controllers (PI and PID type) are still widely used in process industry due to their versatility, effectiveness and easy to use them. Another quality of PID control algorithms is that they are known to be robust, i.e. the performances of the closed-loop do not deteriorate significantly with changing process conditions. But, the popular tuning methods ZIGLER and NICHOLS (ZN) or COHEN and COON (CC) give a too oscillating response of the closed-loop, with long settling time and require continuous plant cycling. Also, it is well known that ZN and CC tuning rules don't lead to good performances of the close-loop in the case of processes with large time delay – the loop becomes unstable if time delay increases.

As a consequence, the subject of tuning conventional controllers has received great attention, with the goal to give tuning algorithms to achieve better performance that from ZN and CC rules, especially for processes with large time delay. A. BRAMBILLA developed a simple method (AB) that obtains a single tuning parameter enabling PID controllers to give a desired response rivalling more advanced algorithms [2].

M. MORARI and E. ZAFIRIOU used Internal Model Control design procedure to derive PID controller parameters for a large variety of models commonly used in the process industry [3]. The IMC tuning method uses also a single adjustable parameter that corresponds approximately to the closed-loop time constant and it is selected by the designer to achieve the appropriate compromise between performance and robustness.

This paper evaluates AB and IMC tuning methods and compares them to ZN rule.

2. DESCRIPTION OF THE TUNING METHODS

For a large variety of processes from chemical industry, the models commonly used are:

- the first order plus time delay, with the transfer functions given by eq. (1)

$$G_p(s) = \frac{k_p \cdot e^{-s \cdot T_d}}{T_p \cdot s + 1}, \tag{1}$$

where k_p is the process steady state gain, T_p is the time constant and T_d is the time delay (dead time);

- the second order plus time delay, with the transfer functions given by eq. (2)

$$G_p(s) = \frac{k_p \cdot e^{-s \cdot T_d}}{(T_{p1} \cdot s + 1) \cdot (T_{p2} \cdot s + 1)}, \tag{2}$$

where k_p is the process steady state gain, T_{p1} and T_{p2} are the time constants and T_d is the time delay (dead time).

In the case of AB tuning method, the dynamic parameters of a PI or PID controller (k_C, T_I and T_D) are functions of the process parameters, presented in *Table 1* for different process transfer functions.

Table 1.

The parameters of a PID controller for AB tuning method

Process model	k_C	T_I	T_D
first order plus time delay	$\frac{1}{k_P} \cdot \frac{T_P + T_d/2}{T_d(c+1)}$	$T_P + T_d/2$	$\frac{T_P \cdot T_d}{2T_P + T_d}$
second order plus time delay	$\frac{1}{k_P} \cdot \frac{T_{p1} + T_{P2} + T_d/2}{T_d(2c+1)}$	$T_{P1} + T_{P2} + T_d/2$	$\frac{T_{P1} \cdot T_{P2} + (T_{P1} + T_{P2}) \cdot T_d}{T_{P1} + T_{P2} + T_d}$

The only tuning parameter is **c**, appearing in the gain of the controller and affecting the speed of response. It can be noted that controller parameters k_C and T_I have the same expressions for PI and PID but the tuning parameter **c** has different values in the two cases as widely presented in [2]. Parameter **c** depends on the ratio T_d/T_p (first order process) or $T_d/(T_{p1}+T_{p2})$ (second order process).

Because Internal Model Control (IMC) is very general and powerful M. MORARI and E. ZAFIRIOU explored the relationships between IMC, PI and PID in order to gain insight into the tuning of these simpler controllers, their performance, robustness and limitations. First of all, for a process with time delay, the pure delay ($e^{-T_d \cdot s}$) is rationalised by a Padé polynomial of zeroth or first order (eq. 3):

First order Padé approximation

$$e^{-T_d \cdot s} \approx 1 \qquad (3)$$

Second order Padé approximation

$$e^{-T_m s} = \frac{1 - T_m / 2 \cdot s}{1 + T_m / 2 \cdot s}.$$

In this maner it is obtained a nominal model $\tilde{G}_p(s)$ for the real proces. It was found that for virtualy all nominal models common in industrial practice, IMC leads to PID controllers for which the parameters are calculated with expresions from *Table 2*. This problem is discussed in more details in [3]. In *Table 2*, λ is the single adjustable parameter that corresponds approximately to the closed-loop time constant and it is selected to achieve the appropriate compromise between robustness and performances. There are practical recommendations for choosing the value of λ. For a PID controller the ratio $\lambda/T_d>0.25$ and for a PI controller $\lambda/T_d>1.7$. For some nominal models, the PID controller is augmented by a first order filter with time constant T_F.

Table 2.

IMC controllers for nominal models, interpreted as PID controllers with filter

Type	Nominal model $\tilde{G}_P$	$k_C k_p$	T_I	T_D	T_F
A	$\frac{k_p}{T_p s+1}$	$\frac{T_p}{\lambda}$	T_p	-	-
B	$\frac{k_p}{(T_{p_1} s+1)(T_{p_2} s+1)}$	$\frac{T_{p_1}+T_{p_2}}{\lambda}$	$T_{p_1}+T_{p_2}$	$\frac{T_{p_1} T_{p_2}}{T_{p_1}+T_{p_2}}$	-
C	$\frac{k_p}{T_p^2 s^2+2\zeta T_p s+1}$	$\frac{2\zeta T_p}{\lambda}$	$2\zeta T_p$	$\frac{T_p}{2\zeta}$	-
D	$k_p \frac{-\beta s+1}{T_p^2 s^2+2\zeta T_p s+1}$	$\frac{2\zeta T_p}{2\beta+\lambda}$	$2\zeta T_p$	$\frac{T_p}{2\zeta}$	$\frac{\beta\lambda}{2\beta+\lambda}$
E	$\frac{k_p}{s(T_p s+1)}$	$\frac{2\lambda+T_p}{\lambda^2}$	$2\lambda+T_p$	$\frac{2\lambda T_p}{2\lambda+T_p}$	-
F	$k_p \frac{-\beta s+1}{s(T_p s+1)}$	$\frac{1}{2\beta+\lambda}$	-	T_p	$\frac{\beta\lambda}{2\beta+\lambda}$

3. SIMULATION

First order with time delay process

It is considered a 1st order plus time delay process described by equation (1) with the following nominal values of the parameters: k_p= 0.08, T_d =2.5 min and T_p=9 min.

ZN tuning rule leads to the following controller parameters: k_C =60.24, T_I=5.7 and T_D=0.95.

By using AB tuning method, the controller parameters obtained are: k_C =38.825, T_I=10.25 and T_D=0.56 with adjustable parameter **c**=0.32

For the process considered, a first-order Padé approximations for the time delay yields the following transfer function for the nominal process:

$$\tilde{G}_p(s) = \frac{-0.1s + 0.08}{11.25s^2 + 10.25s + 1} \quad . \tag{4}$$

This nominal process has the general form corresponding to case D from *Table 2* and the PID controller parameters for IMC tuning rule have the values k_C =41,T_I=10.25 and T_D=1.09. A first-order filter with time constant T_F augments the PID controller. For λ=0.7 the transfer function of the filter is

$$G_f(s) = \frac{1}{0.25s + 1} \quad . \tag{5}$$

As it can be observed, the controller parameters for AB and IMC are very different from those of ZN, especially k_C and T_I.

All the simulation work in this paper was performed using the package SIMULINK from MATLAB 5.0.

The performances of the three methods are compared in *Figs.1-4*. The variations in time of the controlled variable (y), for the nominal values of the process parameters, are plotted in *Fig. 1*. As it was expected, the time responses of the closed loop are much better for AB and IMC methods. This fact is also pointed out by the IAE criteria presented in *Fig. 3*. In *Fig. 2* there are shown the time responses for a +40% error in time delay. This figure illustrates the robustness of AB and IMC methods. ZN method is at the instability limit.

Fig. 4 shows the responses of the three tuning methods to a unit step in load disturbance, for the nominal value of the time delay. AB and IMC methods produce satisfactory tuning, while ZN rule is too oscillatory. In the case of load disturbance, for all the tuning rules considered, the settling time is longer than in the case of step set point.

Second order with time dalay process

It is considered a 2^{nd} order plus time delay process described by equation (2) with the following nominal values of the parameters: k_p= 1, T_d =2 min, T_{p1}=1 min and T_{p2}=2 min.

For ZN tuning rule the controller parameters are: k_C =1.92, T_I=4.8 and T_D=0.8.

If AB tuning rule is used, the controller parameters are k_C =1.1, T_I=4 and T_D=1.25 with adjustable parameter **c**=0.4.

For IMC tuning of the process considered, a zeroth order Padé approximations for the time delay yields the following transfer function for the nominal process:

$$\tilde{G}_p(s) = \frac{1}{(s+1)\cdot(2s+1)} \quad . \tag{6}$$

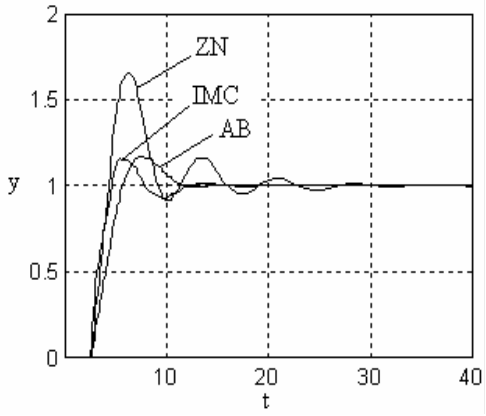

Fig.1. Time responses for T_d=2.5 min, in the case of step set point

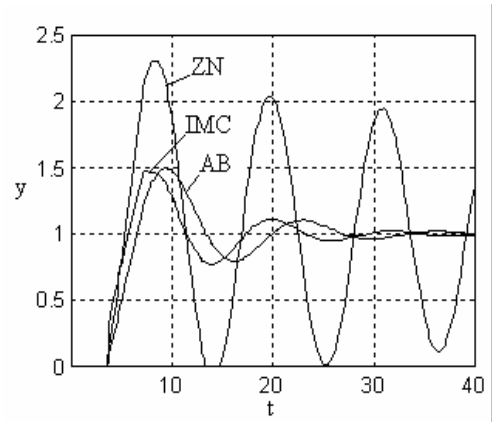

Fig.2. Time responses for T_d=3.5 min, in the case of step set point

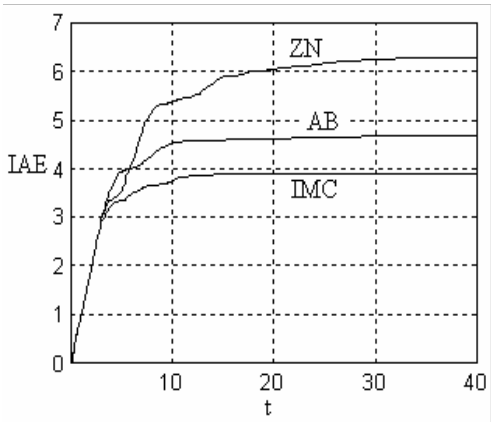

Fig.3. IAE criterion in the case of step set point

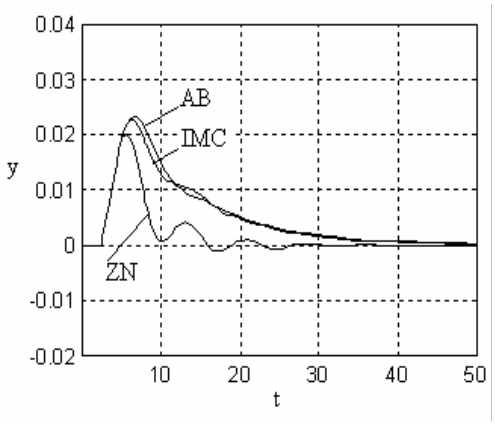

Fig.4. Time responses for T_d=2.5 min, in the case of load disturbance

This nominal process corresponds to the case B from *Table 2* and the PID controller parameters for IMC tuning method have the values k_C =1,T_I=3 and T_D=0.66 for λ=3.

In *Figs. 5-8* there are presented the results of simulations, leading to the same conclusions like those obtained in the case of a 1st order process with time delay. For ZN algorithm, the settling time is too long and the open loop becomes unstable for a +50% variation of the time delay (*Fig. 6*). For the process considered the IMC algorithm leads to better controller settings than AB algorithm: the overshoot is smaller (*Fig.5*), the robustness is greater (*Fig.6*) and the IAE value is less (*Fig.7*)

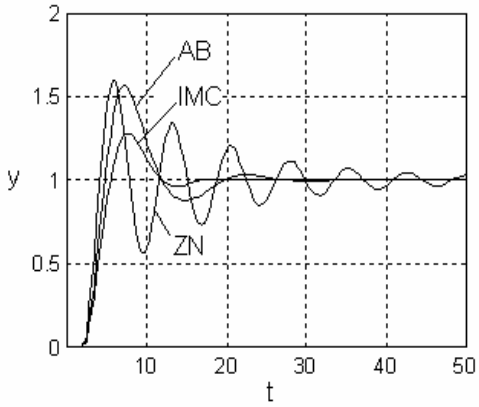

Fig.5. Time responses for T_d=2 min, in the case of step set point

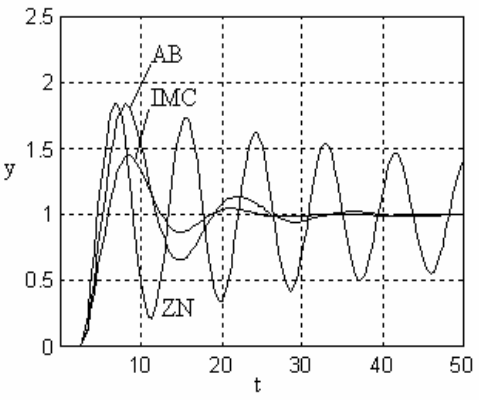

Fig.6. Time responses for T_d=3 min, in the case of step set point

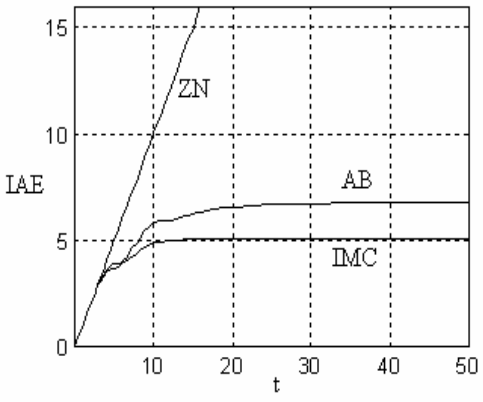

Fig.7. IAE criterion in the case of step set point

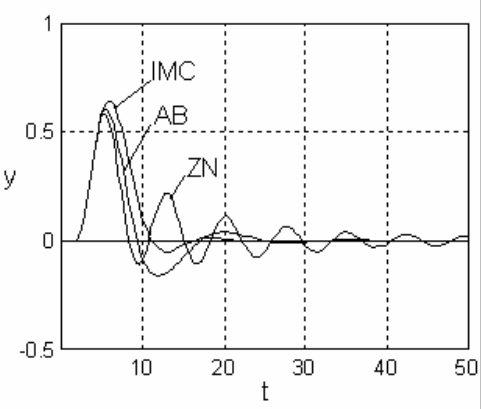

Fig.8. Time responses for T_d=2 min, in the case of load disturbance

4. CONCLUSIONS

This paper studied the performances of the closed loop for PID controllers tuned with ZN, AB and IMC algorithms. The simulations have shown that AB and IMC tuning methods lead to better controller settings than ZN method, both for 1st and 2nd order process with time delay, in the case of set point changes and disturbance. The IAE criteria pointed out this fact. Both IMC and AB methods are very robust in comparison with ZN method which is very sensitive to time delay changes. For ZN method, the close loop becomes unstable if a variation of +30-50% in time delay occurs.

The performances of AB and IMC are very close. These two methods require good knowledge about the process model (steady state gain, time constants and dead time) and this seams to be a disadvantage. But, due to their high robustness, the closed loop performances are not significantly affected by model uncertainty or by process conditions changes.

REFERENCES

1. ABBAS, A., Hung. J. Ind. Chem., 1995, **23**, 189-194.
2. BRAMBILLA A., CHEN S., SCALI C., Hydrocarbon Processing, 1990, **69**(11), 53-58.
3. MORARI M., ZAFIRIOU E., *Robust Process Control*, Prentice Hall, New Jersey, pp. 113-140, 1989.

STUDIA UNIVERSITATIS BABEŞ-BOLYAI, CHEMIA, XLVI, 1-2, 2001

SAFETY ANALYSIS OF CHEMICAL REACTORS

ATTILA MOLNÁR, JOZEF MARKOŠ, ĽUDOVÍT JELEMENSKÝ

Dep. of Chemical and Biochemical Engineering, Faculty of Chemical Technology, Slovak Technical University, Radlinského 9, Bratislava, Slovakia.
E-mail: attila@chtf.stuba.sk, markos@cvt.stuba.sk, jelemen@chtf.stuba.sk

Key words: multiple reactions, CSTR, multiple steady states, safety analysis, HYSYS

1. INTRODUCTION

Modern trends in reactor design or reactor parameter revision make use of software tools primarily designated for simulation. A proper engineering tool for design and simulation studies is HYSYS. The safety analyses provided by these tools are mostly insufficient.

From the view of the operation safety, the attention should be focused on chemical reactors. In many reactors highly exothermic reactions are running. Therefore, the rate of heat generation and cooling possibilities are the most significant criterions of design. The number of reactors where the main specification is the safe operation is low. Many reactors were designed by “scale-up” method and were run without safety analysis.

Chemical production in which chemical reactions take place at extreme conditions (high temperature and pressure), require a detailed analysis of possible danger situations, which may lead to industry accidents with menace of lives and health not only of workers, but also of civilians. The Directive 96/82/EC on the control of major-accident hazards determines the duties of the operators of chemical productions to identify the potential danger that may result from their activities. Individual accent lays on the analysis of danger that may result from chemical reactions performed not only at standard conditions, but also at undesirable situations. The accident in Seveso, Italy in 1976, showed the implications, which may result from darkness about the existence and conditions of subsidiary reactions. [Lees, 1996].

Safety criterions of modern design of equipment are not evaluated during the whole design process, but only within specific decision steps. Identification of risky states during design process can significantly reduce or completely remove its occurrence. About 25% of accidents in chemical industry took place due to mistakes in design and at least 30% of mentioned accidents were evincible [Lees, 1996].

1.1. Historical review

The study of multiple steady states of a stirred tank reactor in which a single reaction occurs has been the subject of much research of many authors[1]. The existence of more than one chemical reaction makes the system complicated, thus the analytical solution of this system is becoming very complex.

[1] System of equations is relatively simple and therefore the information can be obtained easily.

The first mention of the existence of multiple steady states and the associated stability phenomena was made by [Liljenroth, 1918]. A paper on autothermic reactors contains an argument for stability from the slopes of the heat generation and removal curves [Heerden, 1953]. For the first time [Bilous and Amundson, 1955] treated the reactor as a dynamical system, and by using Ljapunovov's method of linearization, a pair of algebraic conditions for local stability was given. They had touched a topic of a consecutive reaction scheme A → B → C and had shown that up to five steady states might be expected under some conditions.

Mathematical methods for solving complex systems of equations were developed [Kubíček, 1976, Kubíček, 1983, Holodniok and Kubíček, 1984, Holodniok and Kubíček, 1984, Holodniok, Klíč, et. al., 1986, Marek and Schreiber, 1991]. The study of multiple steady states, stability and dynamics of reactive distillation are the topics of the recent years.

2. PROGRAM HYSYS

Process modeling that cannot be simply calculated, often consumes a lot of time. Especially in that cases when the model requires new calculations with various initial conditions that must be entered manually. Using an integrated engineering package like HYSYS, all the required applications work within common integrated environment. The true integrated environment has a number of advantages [Pongo and Poras, 1996]:

1. All information are shared, rather than transferred among applications,
2. All applications use common thermodynamic models,
3. All applications use common flow sheet topology,
4. User only need to learn one interface
5. User can switch between modeling applications at any time, gaining the most complete understanding of the process

The integrated environment is a combination of all models with data and therefore it is simply to design a steady state model, perform optimization, carry out some sizing and costing calculations, to do some dynamic modeling to determine appropriate control strategies. Finally, we might perform some on-line modeling using actual plant data for "what-if" studies.

2.1. Safety analysis by HYSYS

From some points of view, the utilization of HYSYS for safety analysis of continuous stirred reactor is not suitable. The identification of multiple steady states with HYSYS is not sufficient, even though this is the primary step when identifying the possible dangerous states of a reactor [Purdeková, 1999, Kvinta, 2000]. The program can identify only some of the steady states of the reactor, but neither the stability nor the number of steady states [Kvinta, 2000]. The advantages of the program are in dynamic regime, which is suitable for on-line simulations of properties not visible in steady state. Benefits are in monitoring the jumps between steady states, but there are some limitations in the starting conditions of reactor startup [Purdeková, 1999].

3. MATHEMATICAL MODELING OF CSTR

3.1. Material balance

Suppose we have R chemical reactions taking place between S species in a continuous flow stirred tank reactor. Let ν_{ij} be the stoichiometric coefficient[2] of the j-th species in the i-th reaction. Let r_i be the rate of the i-th reaction[3] defined so that $\nu_{ij}.r_i$ gives the rate of production of the j-th species in the i-th reaction.

Assuming that the reactor is ideally mixed and the volume flow of feed is constant[4], the material balance which describe the system is in form

$$\tau\frac{dc_j}{dt} = c_{j0} - c_j + \tau\sum_{i=1}^{R}\nu_{ij}.r_i(c_1,\ldots,c_S,T), \qquad j = 1\ldots S$$

$$t = 0: \quad c_j = c_j^0 \quad T = T^0 \tag{1}$$

The startup of reactor depends on choice of initial conditions of concentrations and temperature [Purdeková, 1999].

3.2. Enthalpy balance

A curve of generated heat and a line of cooling are using the same simplifications as the enthalpy balance. We can omit the enthalpy balance of cooling fluid.

$$\tau.\sum_{j=1}^{S}c_j.c_{pj}.\frac{dT}{dt} = \sum_{j=1}^{S}c_{j0}.c_{pj}.(T_0 - T) + \frac{U.A}{V}.(T_c - T) + \tau.\sum_{i=1}^{R}(-\Delta_r H_i).r_i \tag{2}$$

The right hand side of equation (2) represents the heat exchange and the heat of chemical reactions. The heat of reactions copies the curve of heat generation. The heat exchange copies the cooling line. We can consider that the parameters of heat exchange are constants and in this case, the heat exchange copies the cooling line [Westerterp, Swaaij, et. al., 1984, Fogler, 1992].

Neglecting the dependence of some coefficients on temperature or composition may markedly touch the precision of the calculated steady state and consequently the calculated steady state moves. On the other hand, sometimes this is the only way to get approximative results.

3.3. Multiple steady states

The points of intersection of the curve of heat generation and the cooling line give us the temperature at which the reactor can be operated at steady state. Depending on selected parameters the cooling line and the heating curve may intersect in one or more points. In case of more reactions, the number of steady states is increasing [Carberry and Varma, 1987].

---

[2] By convention, the stoichiometric coefficients are taken to be positive for products, negative for reactants, and zero for inert.

[3] Dependence of reaction velocity on temperature is described by Arrhenius equation.

[4] We need another equation to desctribe the change of volume of the reaction mixture.

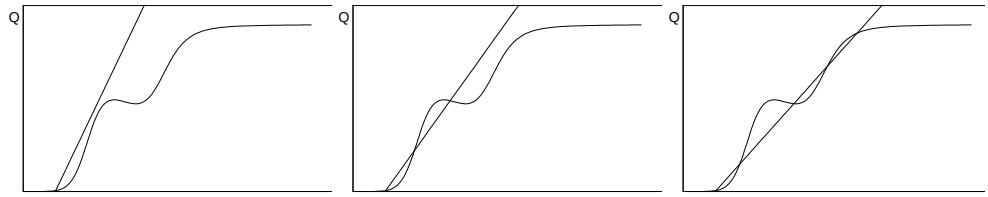

Fig. 1: Variations of steady states in case of two paralell reactions in the following form: A → B → C and A → D. The changing parameter is the overal coefficient of heat exchange.

Appropriate changes of these parameters can change the number and position of steady states (Figure 1). The existence of multiple steady states is a characteristic phenomenon for continuous stirred reactors and involves serious danger mostly for exothermic reactions that must be operated in some of lower steady state [Horák and Pašek, 1980, Westerterp, Swaaij, et at., 1984].

3.3.1. The number of steady states

For systems with a simple reaction scheme there is a possibility of analytical solution [Schneider, Aris, et. al., 1973, Cohen and Keener, 1976, Farr and Aris, 1986]. In these days, the existing computation power allows us to study the problem from different point of view and search the multiple steady states numerically. The simplest method is the mapping of the desired interval of parameters. There are also some other methods that allow us to predict intervals where multiple steady states can occur [Hlaváček and Rompay, 1981, Kubíček, 1983, Holodniok and Kubíček, 1984, Holodniok, Klíč, et at., 1986].

3.3.2. Stability of steady states

The common usage of the words multiplicity, stability and sensitivity in the literature is according to the following definitions [Schmitz, 1974]: the multiplicity of steady states is the number of different sets of state variables at which the time rate of change of all state variables is identically zero for a fixed set of conditions or parameters. A steady state is stable if perturbations within an arbitrary small neighborhood surrounding the state die away to zero. If even the smallest of such perturbations grows, the steady state is unstable. Even though the steady state is stable, we don't have any information about the way of getting steady, even if it reaches the steady state.

Very simple definition of stability was mentioned [Heerden, 1953]. The stability can be determined by comparing the slopes of the cooling line and the tangent of the heat-generating curve at the point of steady state.

The region of asymptotic stability surrounding the potential steady state is defined as a set of initial conditions, from which the system of trajectories are asymptotically approaching the steady state [Sabo and Dranoff, 1970]. In common, in the case of more steady states, each steady state is surrounded by such region. The imaginary border called separatrix then surrounds the largest area of asymptotic stability [Berger and Perlmutter, 1965].

The stability of steady states can be obtained from analyzes of differential equations of material and enthalpy balances. For nonlinear systems the stability of solution is characterized by eigenvalues $\lambda_1..\lambda_n$ of the linearized matrix of differential equations. Some characterization of stability condition is in table 1, more about possible odds in [Holodniok, Klíč, et at., 1986].

Tab. 1

Characterization of the stability of steady states by eigenvalues

	$Re(\lambda_i)<0$	$Re(\lambda_i)>0$	$Re(\lambda_i)=0$
$Im(\lambda_i) = 0$	Stable node	Unstable node	
$Im(\lambda_i) \neq 0$	Stable oscillating focus	Unstable oscillating focus	Hopf bifurcation

3.4. Dependence of solution on parameters

A region with one steady state qualitativelly differs from the region with more steady states. A suitable algorithm for evalution of the dependence of the solution of a system of equations on the parameter α can draw single solutions into braches. Each branch ends in a branching point, where the system qualitativelly changes with the change of parameter α. Qualitative changes like these are real bifurcations (fig. 2).

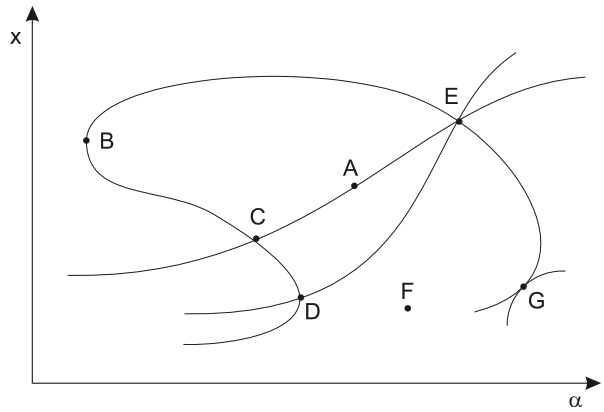

Fig. 2: Branches and types of bifurcation points: A – regular point, B – limit point, C – double bifurkation point, D – limit bifurcation point, E – triple bifurcation, F – isolated point, H – cusp.

A parameterization with respect to the arc length of the solution locus seems to be a powerful technique which overcomes the dificulties with branching points [Kubíček, 1976, Kubíček, 1983, Holodniok and Kubíček, 1984, Holodniok and Kubíček, 1984, Holodniok, Klíč, et at., 1986, Marek and Schreiber, 1991]

The algorithm can be simply extended by another parameter β to draw a bifurcation diagram in the space of these two parameters. We can calculate all the limit and bifurcation points for each chosen value of parameters α and β. Then, we can assume that these points are dependent on parameter β and draw the branches in the parametric space α-β. Each region is characterized with the same number of solutions. Crossing the branch line, the number of solution changes with

two (Fig. 8). We can use the same way to construct the curve of bifurcation points to obtain information about the stability of branching points.

3.5. Dynamic regime

At the reactor startup, it is very important to know the initial conditions and the way the reactor reaches the steady state [Purdeková, 1999]. For example, a significant overshot in temperature may cause a reactant or product to degrade or the overshot may be unacceptable for safe operation [Westerterp, Swaaij, et at., 1984, Fogler, 1992]. If either case were to occur, we would say that the system exceeded the practical stability limit (Fig. 6).

The time dependence of concentration or temperature, or the concentration-temperature phase diagram is used to determine the trajectory manifesting how the reactor reaches the steady state. Following figures shows some basic characteristic signs like monotonous fixing (Fig. 3), oscillatory behavior of concentrations or temperature (Fig. 4), or a limit cycle (Fig. 5).

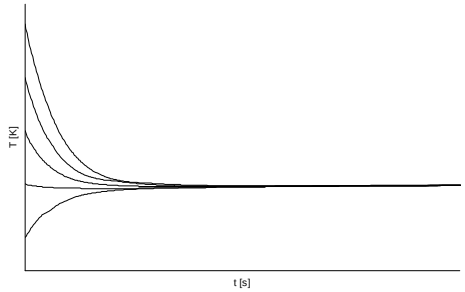

Fig. 3: Approach to steady state. Steady state is a node.

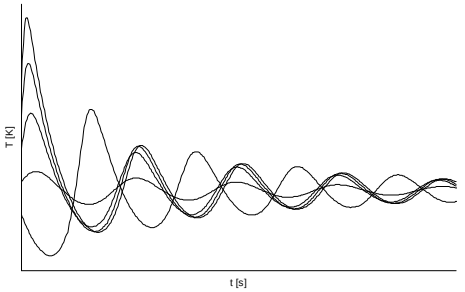

Fig. 4: Approach to steady state. Steady state is focus with damped oscilations.

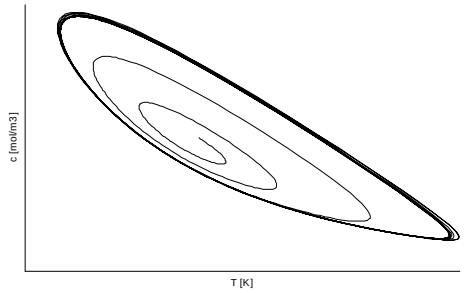

Fig. 5: Phase diagram of limit cycle approaching from inside (the steady state will be never reached). This state is characterized by twisting the trajectory around the steady state.

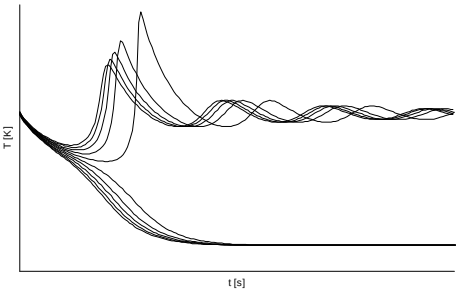

Fig. 6: Approaching various steady states and exceeding the practical stability limit. All the trajectories start withing close interval. Trajectories ending in uppers steady states are crossing a maximum and ends in focus. Lower steady state is a node.

4. CONCLUSION

The safety analysis of chemical reactors is necessary. Most of the software engineering tools do not provide a deeper safety analysis of the designed units. This problem is mostly solved by transfer of achieved information into another application, which is capable to perform these analyses. As available literature has shown, many authors were concerning with dynamic behavior of continuous stirred tank reactors with one single chemical reaction. In real conditions, there are reactors with various parallel and consecutive reactions with various heat generation. Some of them may become significant during unacceptable conditions (fails in technological regime, significant changes of inlet variables, etc.). With the respect to complexity of safety analysis (information sources of physical and chemical properties of reacting mixtures, equilibrium, etc.), our goal is to create an interface that would allow us to work with professional engineering software like HYSYS.

A narrow analysis of HYSYS showed some possibilities to enhance the provided information with extended safety analysis by using the large HYSYS database. Within the integrated simulation environment a new client program should utilize large databases of the hosting program and perform safety analysis of stirred tank reactor at various conditions, like startup, shutdown, influence of changes in input variables on the reactor regime (ignition, blowout, runaway etc). The safety analysis should contain steps of identifying the steady states and their stability, causes and ways of switching between steady states and parametric sensitivity.

5. LIST OF USED SYMBOLS

Symbols of Latin alphabet

A	Area	m^2
c	Molar concentration	$mol.m^{-3}$
c_p	Molar heat capacity	$J.mol^{-1}.K^{-1}$
E	Activation energy	$J.mol^{-1}$
$\Delta_r H$	Heat of reaction	$J.mol^{-1}$
k	Homogenous reaction velocity, dimension depends on kinetics	
k_∞	Pre-exponential factor in the Arrhenius equation for homogenous reaction; the dimension depending on kinetics	
Q	Heat flow	$J.s^{-1}$
r	Molar rate of production	$mol.m^{-3}.s^{-1}$
R	Gas constant	$J.mol^{-1}.K^{-1}$
t	Time	s
T	Temperature	K
U	Overall heat transfer coefficient	$W.m^{-2}.K^{-1}$
V_r	Volume of reactor/reaction mixture	m^3
V	Volume flow	$m^3.s^{-1}$

Greek symbols

α	Parameter	
β	Parameter	
ν	Stoichiometric coefficient	
τ	Space time	s

Subscript

0	Inlet variables (T, c)
c	Coolant (T)
i	Index of reactions (r, R)
j	Index of compounds (c, c_0)

Superscript

0	Initial conditions

BIBLIOGRAPHY

1. Berger, J. S. and D. D. Perlmutter, Chemical engineering science, 1965, **20**, 147-156
2. Bilous, O. and N. R. Amundson, AIChE, 1955, **1**, 513-521
3. Carberry, J. J. and A. Varma, Marcel Dekker, Inc., New York, 1987
4. Cohen, D. S. and J. P. Keener, A->B->C, Chemical engineering science, 1976, **31**, (115-122),
5. Farr, W. W. and R. Aris, Chemical Engineering Science, 1986, **41**, (6), 1385-1402
6. Fogler, H. S., Elements of chemical reaction engineering. Prentice Hall, Inc., London, 1992
7. Heerden, C. v., Ind. Engng Chem., 1953, **45**, 1242-1247
8. Hlaváček, V. and P. v. Rompay, Chemical engineering science, 1981, **36**, (10), 1587-1597
9. Holodniok, M., A. Klíč, et al., Metody analýzy nelineárních dynamických modelů. Academia, Praha, 1986
10. Holodniok, M. and M. Kubíček, Journal of Computational Physics, 1984, **55**, 254-267
11. Holodniok, M. and M. Kubíček, Applied mathematics and computation, 1984, **15**, 261-274
12. Horák, J. and J. Pašek, Design of industrial chemical reactors by the aid of laboratory data. SNTL, Praha, 1980
13. Kubíček, M., ACM Transactions on Mathematical Software, 1976, **2**, (1), 98-107
14. Kubíček, M., Numerical algorithms for the solution of chemical-engineering problems. SNTL/Alfa, Praha, 1983
15. Kvinta, F., Assesment of the feasibility of the application of the HYSYS program in planing of accidents (In Slovak), KCHBI CHTF, Bratislava, STU, 2000,
16. Lees, F. P., Loss Prevention in the Process Industries. Hazard identification, assessment and control. Reed Educational and Professional Publishing, England, 1996
17. Liljenroth, F. G., Chem. Metall. Eng., 1918, **19**, 287

18. Marek, M. and I. Schreiber, Chaotic Behavior of Deterministic Dissipative Systems. Academia, Praha, 1991
19. Pongo, J. and W. Poras, HYSYS Reference. Hyprotech Ltd., 1996
20. Purdeková, M., Feasibility of the application of the HYSYS program in the safety analysis of a stirred flow tank reactor (In Slovak), KCHBI CHTF, Bratislava, STU, 1999,
21. Sabo, D. S. and J. S. Dranoff, Stability analysis of a Continous Flow Stirred Tank Reactor with Consecutive Reactions, AIChE, 1970,
22. Schmitz, R. A., Advances in chemistry series, 1974, **148**,
23. Schneider, D. R., R. Aris, et al., Chemical engineering science, 1973, **28**, 885-896
24. Westerterp, K. R., W. P. M. v. Swaaij, et al., Chemical Reactor Design and Operation. Netherlands University Press, Amsterdam, 1984

STUDIA UNIVERSITATIS BABEŞ-BOLYAI, CHEMIA, XLVI, 1-2, 2001

THE INFLUENCE OF THE REINFORCING MATERIALS ON THE PROPERTIES OF THE DENTAL COMPOSITES

MARIOARA MOLDOVAN[1], CRISTINA PREJMEREAN[1], VIOLETA POPESCU[2], MARIA BRIE[1], GABRIEL FÜRTOŞ[1]

ABSTRACT. The influence of inorganic reinforcing materials and their mixtures on the strength, hardness, and color shade of composite materials was studied. Variation of grain size distribution and specific area on composite surface appearance and on tensile and compressive strength was also studied. The size and the shape of the particles were investigated with a TESLA BS-500 electronic microscope. The particles have irregular shapes. Grain size distribution was determined with a COULTER-COUDLTER instrument, and specific area corresponding to each grain size was determined by the BET method. Compressive and tensile strength were determined with an INSTRON device. The best results regarding compressive strength were obtained using powders with specific area of 2.1 m^2/g. Abrasion tests were made after maintaining the samples at 37°C in water for a week. Rate of wear was also investigated. The rate of wear increases as the specific area increasing from 1.9 to 2.9 m^2/g. The obtained results are between imposed limits for dental materials.

INTRODUCTION

The literature offers a series of examples of inorganic reinforcing materials used as reinforcing materials for dental composites: silicates, lithium aluminosilicates[1-4], hidroxylapatita[6,8], glasses[5,7,8], quartz[1,-5,7], silica[1-9], ceramics[5,10] and oxides (Al_2O_3, TiO_2)[11]. From those materials, silica and quartz have been successfully used for composites used in dentistry[4-9]. It is important that those materials to be *chemical inert* for ensuring the resistance of the composite at the action of the agents from the mouth cavity. The coefficient of thermal expansion of the composite mast be as close as possible to those of hard dental tissue (α=10-11·10^{-6}/°C). The refractive index closed to the one of the enamel offers to the composite esthetical properties. Good mechanical strength for improving the mechanical properties of the composite must be close to those of the hard dental tissue. Taking into account those facts the composites with quartz and colloidal silica[5,7] are suitable for this kind of applications.

The aim of this paper is the characterization of the inorganic reinforcing materials used for obtaining of dental composite, as well as their influence on the mechanical proprieties of those.

EXPERIMENTAL DETAILS

Materials and methods. The technical characteristics of quartz and silica were studied in comparison to the ones of the inorganic phases from enamel and dentine.

Quartz powder. Quartz powders of different grain size were obtained by ball milling, obtaining grain sizes between 0.3-0.6 mm, (purity degree of 99.5 %). For smaller particles of quartz the grinding was performed in wet medium containing water and ethanol 1:1 ratio. The ratio material:balls:liquid was 1:1.5:0.4, the speed of rotation was (55 rotation/minutes). The size and shape of the particles were analyzed on a TESLA – 500 electronic microscope.

The grain size distribution was determined at the COULTER-COUNTER machine and the specific areas that correspond to each granulation were determined through the BET method.

Colloidal silica powders. In order to study the influence of the micro reinforcing grains upon the composites' proprieties, we used the imported colloidal silica (Degusso) with the grain size between 0.05 – 0.2 μm and the specific area of 180 m^2/g.

With all these powders we formed a series of liquid-powder composites determining after polymerization the compressive strength and abrasion resistance. The strength tests were performed on cylindrical bars having the diameter of 4 mm and the height of 8 mm, after keeping its for a week at 37^0C in water. We mention that the strength tests were made on 10 bars for each sample.

The powder-liquid composites consists of:

- Monomer mixture: 2.2-bis[4-(2-methacryloyloxypropoxy)-phenyl] propane (Bis-GMA) 65% (obtained in our laboratory) and triethyleneglycol dimethacrylate (DMTEG) 35% (Sigma Aldrich Chemia Grubh, Steinheim – Germany), where the polymeric accelerator was dissolved, N,N-bis (2-hydroxyethyl)-p-toluidine;
- Initiating system made out of: polymerization initiator POB – benzoil peroxide 0.3% de and polymerization accelerator DHEPT – N.N-(2-hydroxyethyl-p-toluidine) 1%;
- Different reinforcing systems: quartz, colloidal silica, quartz + colloidal silica.

The abrasion resistance tests of the composite were executed on bars with the same sizes as for the compressive strength test. The influence of the specific area of the powder on the wear abrasion resistance was studied, by rotating the bars on the surface of the abrasive paper No. 400 at constant pressure and rotating speed. The length of each distance followed by each sample on the surface of new abrasive paper was kept constant for each bar (15 cm). The wear degree was calculated by the loss of volume of the cylindrical bar after erosion taking into consideration the initial and the final sizes (diameter and height) of the bar.

RESULTS AND DISCUSSIONS

Technical characteristics of used quartz and silica in comparison to the ones of the inorganic phase from the enamel and dentine are presented in table 1. From the table 1 one can se that the hardness, tensile and compressive strength, and the elasticity modulus for quartz and silica are higher than the one of the enamel and dentine. The coefficient of thermal expansion has close

values for enamel, dentine and colloidal silica, but for quartz is higher. Refractive index is also close enough for all the tested materials.

Grain size distribution is a function of the specific area of the powder. The data for quartz are presented in fig. 1. In what concerned the grain size distribution of the powders with specific area between 1.45 m^2/g and 3.3 m^2/g, one can observe the existence of a wide field, in which the diameter of the particles was between 1μ and 50μ. Between those limits the amount of the powder with smaller particles or larger ones is different from a powder to another. When the specific area increases, the amount of the powder with particles with diameters under 10 μ increases to, while the amount of powder with diameters bigger than 10 μ gets smaller.

Table 1

Technical characteristics of quartz and silica in comparison to the ones of the inorganic phase from the dentine

Material	**Enamel**	**Dentine**	**Quartz**		**Colloidal Silica**
Chemical composition [% wt]	Ca 7.8 P 17.7 Mg 0.45 CO_2 2.5	Ca 35.5 P 16.7 Mg 1.80 CO_2 3.9	SiO_2 99.56 Al_2O_3 0.08 CaO 0.03 MgO 0.02 Na_2O 0.04 Fe_2O_3 0.025 K_2O 0.01	Si 4 6.53 Al 0.042 Ca 0.021 Mg 0.012 Na 0.033 Fe 0.017 K 0.008	SiO_2 99.999
Density [g/cm^3]	2.9	2.9	2.65		2.24
Knoop Hardness	320 – 343	65 - 70	710 – 790		500
S_t [kgf / cm^2]	103	500 – 525	900		800
S_C [kgf / cm^2]	980 – 3940	2100 – 3500	12300		10000
$\alpha\ 10^{-6}$	10 – 11	10 – 11	26.4		11.5
E [kgf / cm^2]	97 – 830	76 – 193	800 – 1400		700
Refractive index n_D	1.60	1.56	1.553		1.691
S_t is tensile strength; S_c is compressive strength; α is the coefficient of thermal expansion; E is elasticity modulus					

The influence of quartz specific area on the appearance of the dental composite material is presented in table 2. Surface of the composite materials get smoother with increasing of quartz specific area (the amount of particles smaller than 5 μm (45.2 % - sample 7 with specific area of 3.2 m^2/g in comparison with 13 % - sample 1 with specific area of 1.45 m_2/g).

Table 2

The influence of quartz specific area on the appearance of the dental composite material

Sample	**I**	**II**	**III**	**IV**	**V**	**VI**	**VII**
Specific area [m^2/g]	1.45	1.9	2.1	2.2	2.5	2.9	3.2
Surface appearance of the composite	coarse	coarse	slightly smooth	slightly smooth	smooth	smooth	fine

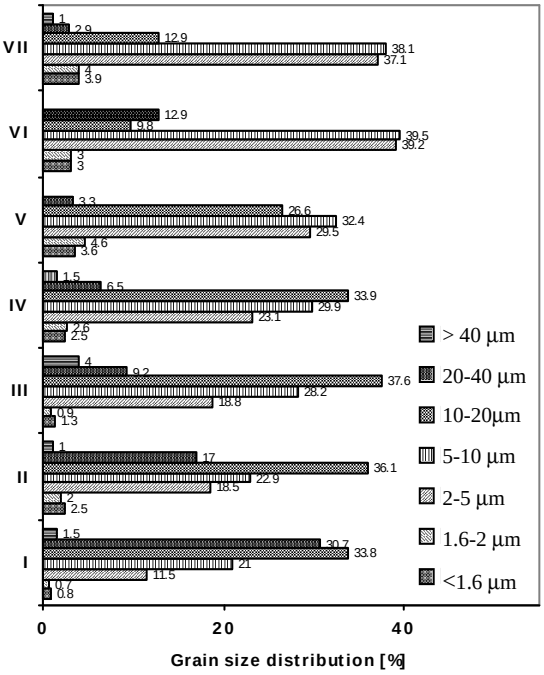

Fig. 1. Grain size distribution as a function of specific area for quartz samples presented in table 2.

In table 3 the specific area, and powder concentration of reinforcing materials for dental use composites is presented.

The compressive strength values for composites reinforced with quartz, colloidal silica and quartz/silica mixture (table 3) is presented in fig. 2.

From fig.2 can be seen that the highest value of the compressive strength was registered in the case of the composite obtained with the powder containing quartz having the specific area 2.1 m^2/g. The value of the compressive strength for the composite with reinforcing material of colloidal silica is below the average level of the one of the composites having quartz as reinforcing material (for charging of 47.3%). Because of the small sizes of the silica particles in the case of this system composite powder-liquid, it was not possible to achieve a good homogeneity of the two phases. By mixing the materials, more and more air is inserted into the composite. Air inclusion leads to smaller values for compressive strength. In the cases of the composites with quartz and silica a decreases of the value of compressive strength can be observed. The highest value can corresponding to the composite with the charging degree of 77%. Remarkable is the fact that at a small variation of the filling's charging degree, do not cause significant difference from a composite to another as we expected. Compressive strength varies between 2358-2536 kgf/cm^2.

Table 3

Specific area and powder concentration of reinforcing materials for dental use composite

Material	Specific area [m^2/g]	Powder [% wt]
Quartz I	2.1	75
Quartz II	2.5	75
Quartz III	2.9	75
colloidal silica	180	47.3
Quartz + 2% silica		77
Quartz + 10% silica		75
Quartz + 20% silica		73.7

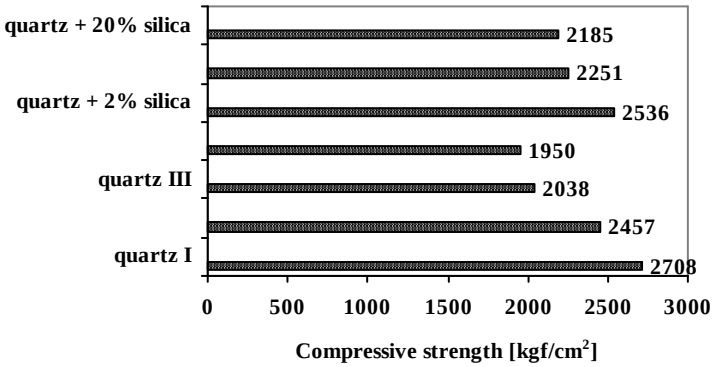

Fig. 2. The compressive strength values for composites reinforced with quart, colloidal silica and quart with silica mixture

The values calculated for the abrasion resistance is given in table 4.

Table 4

Abrasion resistance as a function of specific area for quartz

Material	Specific area [m^2/g]	h_o [mm]	D [mm]	Δh [mm]	Average h loss [mm]	V loss [mm^3]	V loss [%]
Quartz	1.9	8.21 8.30	4.50 4.82	0.66 0.66	0.66	11.251	8
	2.1	8.36 8.22	3.88 3.88	1.02 1.00	1.01	11.936	12
	2.5	8.22 8.40	3.88 3.88	1.24 1.26	1.25	14.772	15
	2.9	8.20 8.22	3.90 3.82	1.50 1.32	1.41	17	16.491
h_o is initial bar height; d is bar diameter; Δh is height loss; V is bar volume							

It can be observed an increasing of the loss of volume as far as the specific area of the quartz powder grows from 1.9 to 2.9 m^2/g. The smallest abrasive wear was observed at the composite which contains as reinforcing material quartz powder with specific area of 1.9 m^2/g.

The electron photographic images presented in fig. 3 a representing the colloidal silica powders, the fluffy appearance can be observed as well as the agglomerates of the particles that couldn't be separated between them. Fig. 3 b showed the irregular shapes of the quartz particles.

CONCLUSIONS

The studied quartz powders take part in the class of the macro fillings, presenting values of the composites' mechanical strength that are between the limits previewed for this type of materials.

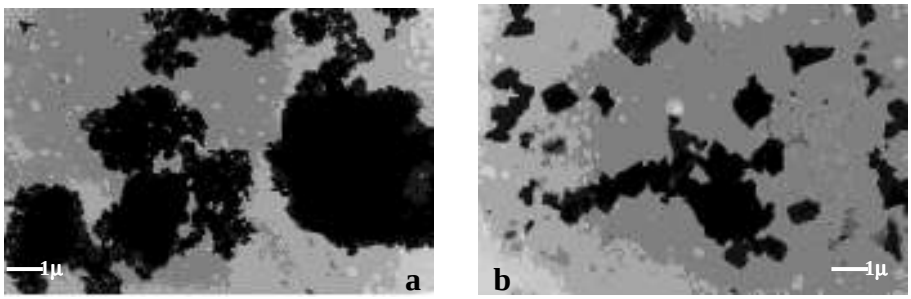

Fig. 3. Micrographs powder: a) Colloidal silica *b*) Quartz powder

The influence of inorganic reinforcing materials and their mixtures on the strength, hardness, of composite materials was studied. Variation of grain size distribution and specific area on composite surface appearance and on tensile and compressive strength was also studied. The size and the shape of the particles were investigated. The particles have irregular shapes. Grain size distribution was determined, and specific area corresponding to each grain size was determined. Compressive and tensile strength were determined. The best results regarding compressive strength were obtained using powders with specific area of 2.1 m^2/g. The rate of wear increases with increasing of the specific area from 1.9 to 2.9 m^2/g. The obtained results are between imposed limits for dental materials.

REFERENCES

1. R. L. Bowen, *American Dent Assoc*, 69, 481, (1964).
2. D. Bratu, L. Mikuluk, D. Munteanu, *Tehnici adezive in stomatologie*, Editura Facla, Timisoara, 122, (1982).
3. P. Lamgrechts, M. Bream, G. Vanherle, *International Symposium on Posterior Composite Resin Dental, Restorative Materials*, July, 1985.
4. D. C. Smith, *International Symposium on Posterior Composite Resin Dental, Restorative Materials*, July, 1985.
5. R. G. Craig, E. R. Dootz, *J. of Oral Rehabilitation*, 23, 751, (1996).
6. W. Suchanek, M. Yoshimura, *J. Mater. Res*, 13, 94, (1998).
7. J. L. Ferracane, *Crit Rev Oral Biol Med*, 6, 302, (1995).
8. S. Imazato, H.Tarumi, N.Ebi, S.Ebisu*, J of Dentistry,* 28, 61, (2000).
9. M. Kobayashi, M. Neo, S. Shinzato, M.Matsushita, T.Nakamura, *J. Biomed. Mater. Res.*, 49, 106, (2000).
10. Y. Kitasako, M.F. Burrow, T. Nikaido, J. Tagami, *Dent. Mater., 16,* 1, (2000).
11. M. Miyazaki, B. K. Moore, H. Onose, *Eur. J. Oral Sci*.,104, 600, (1996)**.**

STUDIA UNIVERSITATIS BABEŞ-BOLYAI, CHEMIA, XLVI, 1-2, 2001

ZINCOPHOSPHATE CEMENTS – HARDENING MECHANISMS

ION TEOREANU[1] and CRISTINA DUMITRESCU[2]

[1] University "Politehnica" #1 sector Bucharest, #1 street Polizu
[2]National Institute for Cement – CEPROCIM S.A., #6 sector Bucharest #6 bd. Preciziei

ABSTRACT. Phosphate binders mostly, and zincophosphate dental cements especially, base their hardening on acid-base reactions, in which the liquid component is an aqueous phosphate solution and the solid component is usually an amphoteric, and only rarely basic one. In the present paper, investigations of the hardening mechanisms of zincophosphate cements were performed using X-ray diffraction analysis, IR spectroscopy, and scanning electron microscopy. The phase evolution of the hardening system and the microstructure of the hardenend binder were highlightened related to the specific mechanisms of the hardening process—specific to phosphate binders.

1. INTRODUCTION

The hardening of phosphate binders, mostly, and of zincophosphate dental binders, especially, takes place based on acid-base reactions between an acid liquid component and a usually amphoteric and seldow basic, solid component. The products in the forementioned chemical reactions undergo a structuring process, which determines the entire mechanical consolidation of the hardened system [1–5].

Dissimilarly from the hardening in the case of hydraulic binders—silicate binders (ordinary portland cement or portland cement with or without admixtures) or aluminate binders, including some phosphate binders with pre-established phosphate linkages within the used solid component—, the chemical reaction issuing zincophosphate binders—the subject of our paper—is not a hydrolysis reaction but—as shown before—an acid-base reaction in the presence of water. Similarly to the case of the hydraulic binders, the products are hydrocompounds with a further composition-structure development. The initially-formed hydrophosphates pass from coagulation structures to polycondensation-crystallisation structures, with corresponding changes of composition, which confer the hardened systems higher mechanical strengths depending on case. In developing hardened systems with adequate strengths, the kinetic conditioning of

The hardening process plays a special role. To this conditioning, not only the intrinsic parameters of the binding system, but also the processing parameters of the binding system are engaged.

The present paper deals with the investigations carried out on hardening mechanism of the zincophosphate cement in general, with particularisation to a zincophosphate cement of Romanian mark.

2. EXPERIMENTAL CONDITIONS AND PROCEDURES

In the our study was used, the zincophosphate cement ROMDENT of Romanian manufacture [6–8], with the chemical composition given in Table 1 and Table 2.

Table 1.

Oxide composition of the raw batch used in preparing the ROMDENT zincophosphate cement powder.

Oxide composition	ZnO	MgO	Al_2O_3	SiO_2
Proportion, %	85.5±1.0	8.5±1.0	2.0±0.5	1.5±0.5

Table 2.

Composition on the liquid component of ROMDENT zincophosphate cement

Liquid component composition	H_3PO_4	$Al(OH)_3$	ZnO	H_2O
Proportion, %	51.5±2.5	10.5±1.0	3.7±1.0	34.0±3.0

Figure 1 shows the X-ray diffraction pattern of ROMDENT cement powder illustrating its phase composition before casting.

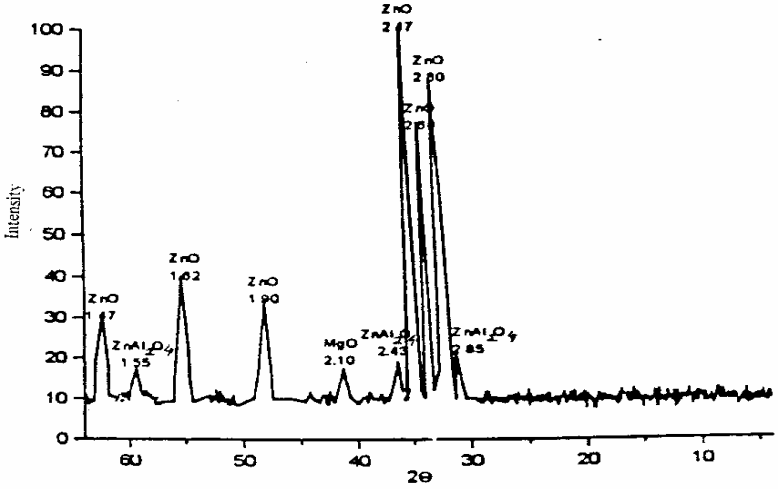

Figure 1. X-ray diffraction pattern of the solid component of ROMDENT zincophosphate Cement

On cement pastes as prepared there mere performed XRD, IR analysis and electron microscopy determinations, as well.

3. RESULTS AND INTERPRETATION

3.1. X-ray diffraction analyses, (XRD)

XRD analysis was performed on the cement pastes during the setting period (after 5 and 15 minutes) and on the cement hardened for 1 and 7 days. The obtained X-ray diffraction patterns are shown in Figures 2 and 3.

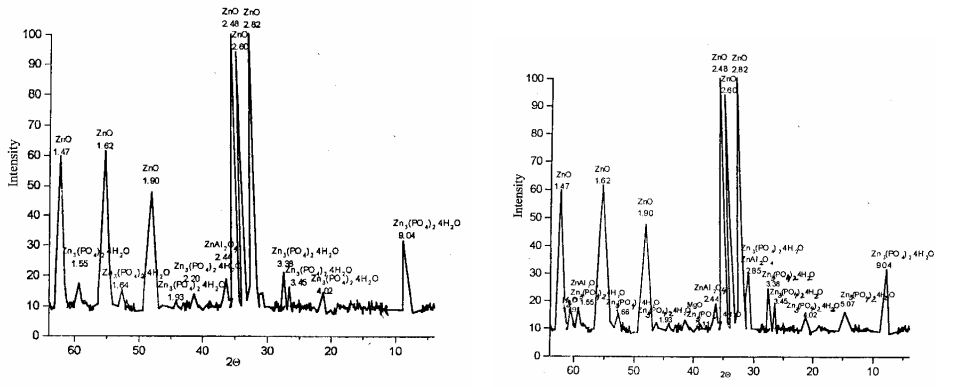

(a) (b)

Figure 2. X-ray diffraction patterns of the ROMDENT zincophosphate cement pastes cured (a) 5 minutes; (b) 15 minutes

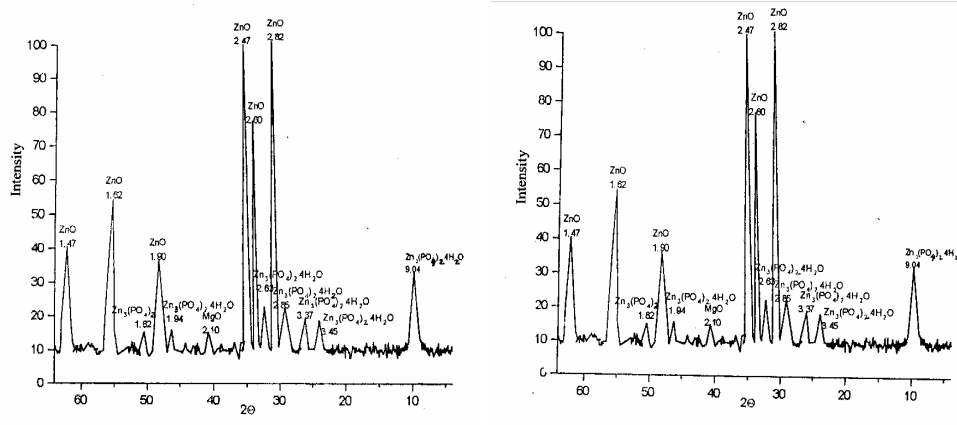

(a) (b)

Figure 3. X-ray diffraction patterns of the ROMDENT zincophosphate cements hardened—for (a) 1 day; (b) 7 days

Since from the setting period—even after the first 5 minutes from mixing of the two components of zincophosphate cement—it is emphasized the formation of the neutral zinc hydrophosphate $Zn_3(PO_4)_2 \cdot 4H_2O$, an insoluble compound. Its proportion does not change significantly further if compared with the zinc oxide remained unreacted.

Taking into consideration the relations of phase equilibrium in the ZnO-P_2O_5-H_2O system, the nature of the ternary phases in equilibrium with the corresponding saturated solutions, the features and the stability of the products, and the kinetics of the chemical reactions, it is very likely that the zinc hydrophosphate $Zn_3(PO_4)_2 \cdot 4H_2O$ should be the result of the conversion of

some unstable hydrophosphate phases initially, formed, such as the zinc hydrophosphate $Zn(H_2PO_4)_2 \cdot 2H_2O$ [1, 5, 9]. It is suggested a rapid chemical interaction on the surface of the particles of solid component of the zincophosphate cement. The hydrophosphates formed in the early stage of the process feature a higher rate of chemical conversion and transition from coagulation structures to crystallised structures, and constitute the matrix of a composite assemblage which hardens while including and binding the unreacted, anhydrous powder grains (mostly ZnO).

3.2. IR spectroscopy and scanning electron microscopy analyses

Also IR spectroscopy analysis was carried out on the ROMDENT zincophosphate cement pastes during setting and after 24 hours hardening in comparison with those of the two components befor mixing. The obtained results are shown in Figure 4.

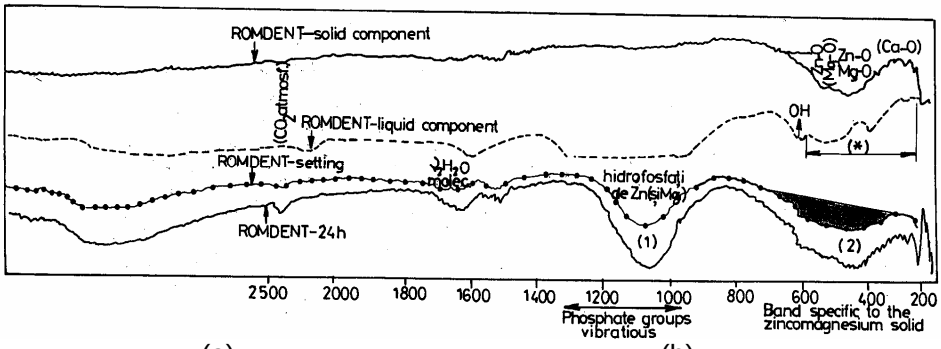

Figure 4. IR absorption spectra of the ROMDENT zincophosphate cements — (a) during setting; (b) hardened after 24 hours

The IR absorption spectra in Figure 4 emphasize two distinct domains: the domain 4000–1400 cm^{-1}—with relatively weaker absorption bands — and the domain 1400–200 cm^{-1}, respectively—with relatively strong, ample absorption bands alongside of weak and very weak peaks.

In the domain 4000–1400 cm^{-1} the following bands are observed —

(i) 3500–2900 cm^{-1}, corresponding to the vibrations of OH in the molecular water (the crystallisation water of the hydrated products, and the molecular water in the phosphate solution respectively—the liquid component of the cement);

(ii) 1650–1600 cm^{-1}, corresponding to the deformation vibrations of the molecular water;

(iii) round a maximum placed at ~2330 cm^{-1}, a meagre band corresponding to the CO_2 absorbed from the environment.

In the domain 1400–200 cm^{-1} the following bands are found:

(i) ~250–650 cm^{-1}, specific to the solid component of the ROMDENT cement and assigned to the Zn-O and Mg-O bondiugs; this band is also found in the hardened or during hardening cement. In the

anhydrous cement the band is centered at 460–465 cm^{-1} and exhibits also a maximum at 530 cm^{-1} (Zn-O). Besides, also weak and very weak peaks are visible in the domain of the Me-O vibrations, as follows: 470–480, 430, 405–410, 395–400, and 385 cm^{-1}, and 360, 335, 310, and 285–290 cm^{-1} respectively.

(ii) 800–1350 cm^{-1}, specific to the liquid component of the cement before casting and assingned to vibrations corresponding to the phosphate groups (of type PO_4^{3-}, HPO_4^{2-}, and $H_2PO_4^{-}$); these bands are also found in the hardened or during hardening cements as a result of hydrophosphates formation zinc especially.

(iii) 250–580 cm^{-1}, a band labeled with (x) in Figure 4 and which corresponds to the liquid component of the studied cement. The band is assigned to the neutralising agents of the H_3PO_4 solution, to the boudings of type Zn-O, Al-O respectively. Thus, the band superposes the band 250–650 cm^{-1} assigned to the solid component of the zincophosphate cement and is also further refound in the hardened or duringhardening cement pastes.

When compared, the IR spectra of the hardened cement and of the single components (liquid and solid) of the cement before hardening it is suggested the consumption of the phosphoric acid in its reaction with the solid component of the cement and the subsequent disappearance of the bands specific to the liquid component. A band specific to hydrophosphates appears within a frequency domain with a maximum at 1065–1070 cm^{-1}. The consumption of the solid component is supported particularly by the decreasing of the amplitude of its specific band, which is plating out.

The IR absorption spectra also suggest the composite character of the hardened zincophosphate cements, which is consistent with the XRD analysis. The binding matrix consists of the ready-formed hydrophosphates. It includes the unreacted particles of ZnO and other oxides, as well as the particles of the solid solutions of ZnO with other oxides.

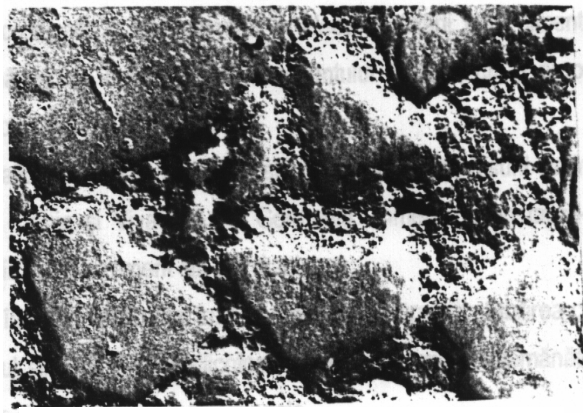

Figure 5. SEM image (x5000) of the ROMDENT zincophosphate cement hardened for 24 hours

The final structure of the zincophosphate cement is such as illustrated by the scanning electron microscopy image in Figure 5: a crystalline structure with a matrix growing from coagulation structures to crystallisation structures and forming interfaces consolidated with the included also crystalline grains.

4. CONCLUSIONS

The results obtained from the investigations carried out and their correlation together with their interpretation may suggest the following comprehensive description of the mechanisms in the processes taking place at hardening of the zincophosphate dental cements, namely: the succesion of processes, the nature of the products and their composition-structure development:

(a) In the early stage of hardening, just upon mixing the two components of the zincophosphate cements, rapid chemical interactions take place on the surface of solid particles, with formation of unstable acid hydrophosphates—such as $Zn(H_2PO_4)_2 \cdot 2H_2O$, in gelous state—, which develop coagulation structures, determining for the beginning of setting.

(b) With their coagulation structure, the acid hydrophosphates formed during the early stage of the hardening process feature a high rate of chemical and structural conversion. Thus, even after 5 minutes from the beginning of the process the integral conversion of the acid hydrophosphates into the stable neutral zinc hydrophosphate ($Zn_3(PO_4)_2 \cdot 4H_2O$) takes place, with transition from the coagulation structures to crystallisation structures.

(c) The phosphate constituent in the liquid component of the zincophosphate cement vanishes rapidly, with formation, upon its entire consumption, of neutral hydrophosphates, with progresive development from chemical and structural point of view. The neutral hydrophosphates evolve towards the anhydrous neutral phosphate, $Zn_3(PO_4)_2$, while the crystalline structure consolidates. The solid component is only partly consumed. The chemical interaction process between the two components of the cement ends up shortly, virtually in less than one day after mixing.

(d) The hardened zincophosphate cement shows itself as a composite material with a final structure of obvious crystalline nature and whose matrix (neutral hydrophosphates and phosphates formed during cement hardening) has evolved structurally up to crystallisation structures and formed interfaces consolidated with the enclosed grains, also crystalline.

LITERATURE

1. Teoreanu, I., *"Fundamentals of the inorganic binder technology" (in Romanian),* Editura Didactica si Pedagogica, Bucharest, 1993
2. Dumitrescu, C., *"Special binders with hardening based on acid-base reactions" (in Romanian), Ph D thesis (supervisor Prof. Dr. I. Teoreanu),* "Politehnica" University, Bucharest, 1998
3. Golînko-Volfson, S.L. et al., *"Himiceskie osnovi tehnologhii i primenenia fosfatnih sviazok i prokitii*", Himia Publishing House, Moskow, 1968
4. Skinner, E.W., Phillips, R.W., *"The science of dental materials",* 6th Edition, Philadelphia-London, 1967
5. Serwais, G.E. et al., J.Dent.Res. 50,613 (1971)
6. Romanian Patent no. 2030185/1978
7. Dumitrescu, C. et al., *"Zincophosphate dental cement",* 1987
8. Manufacture authorisation no. 459/1987 for the product "Zincophosphate dental cement ROMDENT"
9. Komrsko, J., Satava, V., *Silikaty,* 10 (3), 246 (1966)

STUDIA UNIVERSITATIS BABEŞ-BOLYAI, CHEMIA, XLVI, 1-2, 2001

ABOUT MESOPOROSITY CHARACTERISTICS OF IRON CONTAINING HYDROTALCITE-LIKE MATERIAL STUDIED BY USING N_2 ADSORPTION METHOD

GABRIELA CARJA [(a)], NECULAI AELENEI[(a)], CRETESCU IGOR[(c)], DOINA SIBIESCU[(b)]AND DANIEL MARECI[(a)]

[a] *Technical University "Ghe. Asachi", Faculty of Industrial Chemistry, Department of Physical Chemistry, Bd. D. Mangeron, RO- 6600, Iasi, ROMANIA*
[b] *Technical University "Ghe. Asachi", Faculty of Industrial Chemistry, Department of Inorganic Chemistry, Bd. D. Mangeron, RO- 6600, Iasi, ROMANIA*
[c] *Technical University "Ghe. Asachi", Faculty of Industrial Chemistry, Department of Environmental Chemistry, Bd. D. Mangeron, RO- 6600, Iasi, ROMANIA*

SUMMARY. *Layered double hydroxides in which iron was introduced in the hydrotalcite layer were synthesized by a coprecipitation method. X-ray diffraction (XRD) and N_2 adsorption were used like physical-chemical techniques to characterize the emerged materials. The treatment of the adsorption isotherms by different computation models show that nonuniformity and the constrictions of the mesoporous structure accentuated, BET surface area increased while pore volume decreased when iron was introduced in the hydrotalcite network.*

Keywords: hydrotalcite, layered double hydroxides, mesoporosity characteristics, BET surface area

INTRODUCTION

Hydrotalcite is a naturally occurring anionic clay with the formula $Mg_6Al_2(OH)_{16}CO_3 4H_2O$. It presents a positively charged brucite-like layers ($Mg(OH)_2$) in which some of Mg^{2+} are replaced by Al^{3+} in octahedral sites of the hydroxide sheets. Interstitial layers formed by CO_3^{2-} anions and water molecules compensate the excess of positive charge resulting from this substitution. Both magnesium and aluminum can be isomorphously substituted by other divalent or trivalent cations so a wide range of compositions containing various combinations of M(II), M(III) and different anions A^{n-} can be synthesized. The resulting materials, known as layered double hydroxides (LDHs) or hydrotalcite-like anionic clays, are layered mesoporous materials which have received considerable interests in recent years owing to their applications as catalysts, catalyst precursors, adsorbents and ion exchangers [1].

In defining or tailoring the catalytic and the adsorption properties of a material its crystallinity and textural characteristics are of particular importance. For example, the shape and the size of pores, associated with the uniformity of porous structure, can promote shape selectivity; a higher surface area will facilitate guest-host interactions; even mass transfer process depends on the porosity type. Despite this, many of the published studies concerning LDHs deal only briefly or not at all with their textural characteristics and with the possibility to tailor them for a required application [2,3].

In order to get new information about the possibility to tailor the mesoporous properties of LDHs, the aim of this study is to investigate by different physical-chemical techniques how these properties could be altered through direct synthesis when iron was introduced in LDH network.

EXPERIMENTAL

Synthesis of LDHs

All the samples were synthesized by a coprecipitation method in low supersaturation conditions [1], at 313 K, under a bubbling constant flow of nitrogen in the reaction medium and vigorous stirring. After an aging step, the obtained precipitates were separated by centrifugation, washed extensively with warm deionized water until sodium free and dried under vacuum at 338 K.

- hydrotalcite sample (MgAlLDH): 100 ml of an aqueous solution of $Mg(NO_3)_2 \cdot 6H_2O$ (0.03 mol) / $Al(NO_3)_3 \cdot 9H_2O$ (0.01mol) and an aqueous solution of NaOH / Na_2CO_3 ($CO_3^{2-}/Al^{3+}+Mg^{2+}=0.67$, $HO^-/Al^{3+}+Mg^{2+}=2.25$), were added dropwise together, in such a way that the pH remained at a constant value of 9.5. The resulting precipitate was aged at 338 K for 24 h under stirring.
- iron containing layered double hydroxide (FeLDH): an aqueous solution (85 ml) of $Mg(NO_3)_2 \cdot 6H_2O$ (0.03mol) / $FeSO_4$ (0.01mol) and an aqueous solution of Na_2CO_3 (1M, 30 ml) were added dropwise together over a period of 2 h at a constant pH value of 8.2. The resulting precipitate was aged at 305 K for 24 h under stirring.

Characterization

X-ray powder diffraction patterns were recorded on a Philips PW 1840 diffractometer using monochromatic CuKα radiation (λ=0.154 nm), operating at 40 kV and 30 mA over a 2θ range from 4 to 70 degree.

N_2 adsorption isotherms were measured on a Coulter SA 3100 automated gas adsorption system. Prior to the measurements the samples were heated for 5 h under vacuum at 383 K in order to expel the interlayer water molecules. The BET specific surface area (S_{BET}) was calculated by using the standard Brunauer, Emmett and Teller method on the basis of the adsorption data. Pore volume was determined by using the t-plot method of De Boer [4]. Pore size distributions were calculated from the desorption branches of the isotherms using the Barret, Joyner and Halenda method and the corrected Kelvin equation [4,5]. All these models are considered to be fully applicable to mesoporous materials. The IUPAC classification of pores and isotherms were used in this study.

RESULTS AND DISCUSSION

The XRD patterns of synthesized samples (not shown) exhibit sharp and symmetric reflections for the *(003)*, *(006)*, *(110)* and *(113)* planes and broad symmetric peaks for the *(102)*, *(105)* and *(108)* planes, which are characteristics of these materials [1]. The lattice parameters (see table I) are calculated by indexing the peaks under a hexagonal crystal system, using a least squared method.

The parameter ***a*** corresponds to the cation-cation distance within the brucite like layer while the parameter ***c*** is related to the total thickness of the brucite-like layer and the interlayer distance [1]. The decrease of the parameter ***a*** for the FeLDH sample clearly indicates the incorporation of iron into the brucite-like layer, as the ionic radius of Fe^{2+} hexacoordinate is 0.61 Å.(after Shanon [6]) which means smaller than the ionic radius of Mg^{2+} hexacoordinate (0.71 Å. after Shanon) The decrease of the parameter *c* and the d_{003} (basal spacing calculated from the 003 reflection position in the XRD pattern [1]) can be attributed to the modified electrostatic interactions between the layer and the interlayer network when another metal is introduced in the LDH layer.

Table I

The chemical composition and lattice parameters of MgAlLDH and FeLDH

Sample	Mg:Fe:Al	XRD phase	Lattice parameters (Å)		
			a	*c*	d_{003}
MgAl LDH	3: 0: 1	LDH	3.059	23.38	7.79
FeLDH	1: 2: 1	LDH	3.042	23.11	7.70

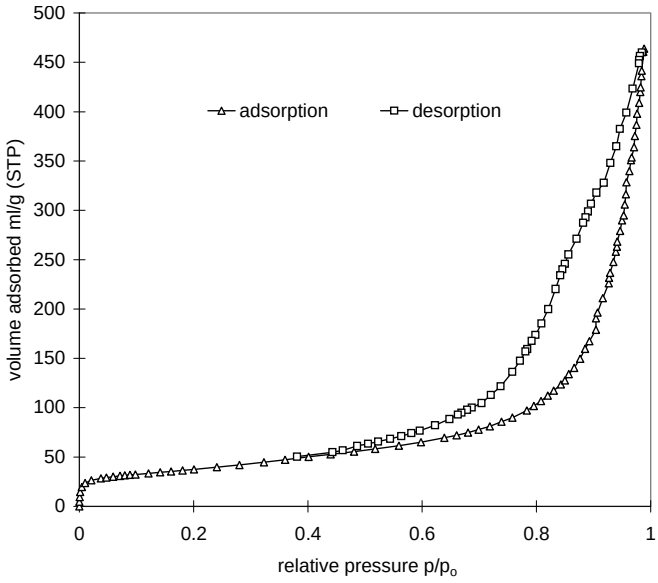

Figure 1. N_2 adsorption-desorption isotherms at 77 K of MgAlLDH

The nitrogen adsorption isotherms of MgAlLDH, and FeLDH are shown in figure 1 and figure 2, respectively. Their different appearances suggest the modifications of the porosity characteristics when iron substituted magnesium in the LDH network.

For MgAlLDH (figure 1) we observe a type IV isotherm with a broad type H_3 hysteresis loop, in the middle range of relative pressure. At low relative pressure the prevailing process is the formation of a monolayer while a multilayer adsorption takes place at a high relative pressure. For the values of relative pressure higher than 0.8 condensation takes place giving a sharp adsorption volume increase. This behavior indicates that this sample has a mesoporous character. Hysteresis loop type shows that aggregates of plate-like particles forming enough nonuniform slit shaped pores [5] are present in this sample. For FeLDH (figure 2) the adsorption isotherm changed its shape and the irregular form of type H_3 hysteresis loop indicates the presence of nonuniformity in pores size and/or shape. These characteristics allow us to conclude that for FeLDH the nonuniformity of the mesoporous structure accentuated.

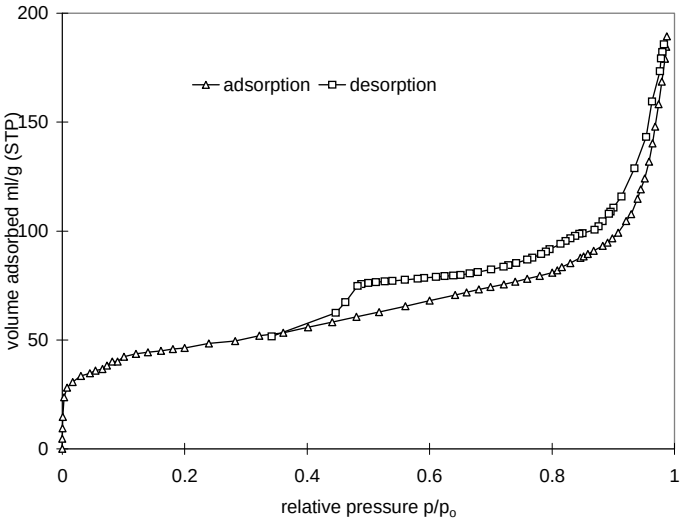

Figure 2. N_2 adsorption-desorption isotherms at 77 K of FeLDH

Pore size distribution (PSD), obtained from BJH method, is further used to check and to complete the previous results. The PSD curves, figure 3, points out important modifications in the pore size range of the samples. The PSD curve of MgAlLDH has two maximums at 9.5 and 12.6 nm. Pores with sizes belonging to the entire range characteristic for mesoporosity appear in this case. The PSD curve of FeLDH with two maximums at 27 and 37 nm shows clearly the enlargement of the pore size. All the pores are larger than 5 nm and we observe no mesopores with sizes larger than 45 nm. Moreover the PSD curve of FeLDH is broader showing also that nonuniformity of the porous structure accentuates when iron is introduced in the hydrotalcite network.

The values of BET surface area and pore volume (V_p) of synthesized samples are given in table II. It can be seen that the FeLDH develops lower BET surface area in comparison to MgAlLDH whereas the value of pore volume increases.

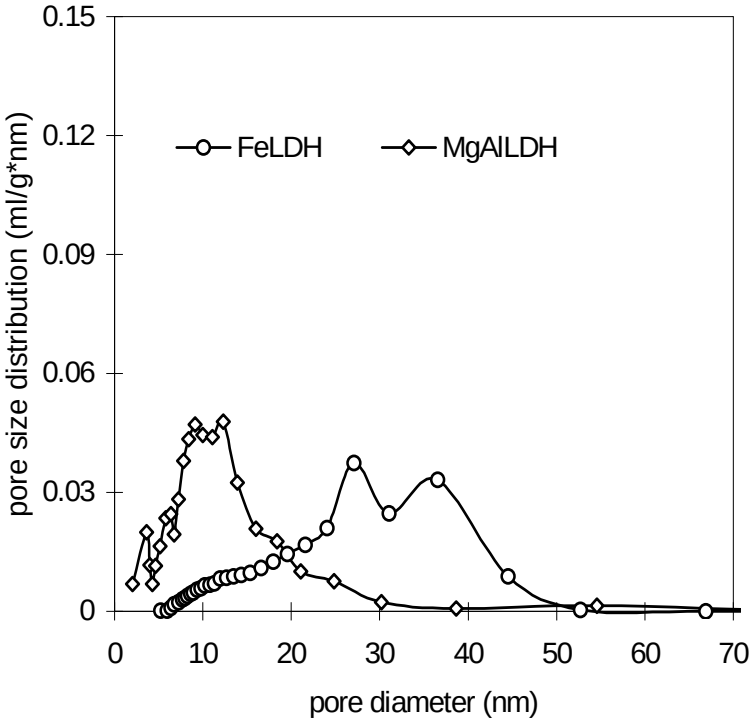

Figure 3. Pore size distribution calculated using BJH method from adsorption data

Table II.

The values of BET area and pore volume of synthesized samples

Sample	BET area (m^2/g)	V_p (ml/g)
MgAlLDH	132	0.640
FeLDH	107	0.680

CONCLUSIONS

The current study demonstrated that N_2 adsorption method proved to be a useful technique for studying the features of the porous structure of layered double hydroxides when vanadium is introduced in the LDH layer. As a general trend the iron containing layered double hydroxide presents a mesoporous structure with larger mesopores, lower BET surface area value

and a higher nonuniformity of the porous structure than MgAlLDH. The possibility of altering the textural properties of LDHs when a new metal is introduced in the layer may offer new perspectives in tailoring the textural characteristics of these materials for potential applications.

REFERENCES

1. F. Cavani, F. Trifiro, A. Vaccari, Catal. Today 11 (1991) 173 and references therein.
2. W. Jones, M. Chibwe, in: I.V. Mitchel (Ed.), Pillared Layer Structures Current Trends and Applications, Elsevier, London, 1991, p. 67.
3. S. Velu, N. Shah, T.M. Jyothi, S. Sivasanker, Microporous Mesoporous Mater. 33 (1999) 61.
4. S.J. Gregg, K.S.W. Sing, Adsorption, Surface Area and Porosity, 2nd ed., Academic Press, London, 1982.
5. M. Kruk, M. Jaroniek, A. Sayari, Microporous Mesoporous Mater. 27 (1999) 217.
6. R.D. Shanon, Acta Crystallogr. A, 32 (1976) 751.

STUDIA UNIVERSITATIS BABEŞ-BOLYAI, CHEMIA, XLVI, 1-2, 2001

SELECTIVE SEPARATION OF AMINO ACIDS BY REACTIVE EXTRACTION

CORNELIU ONISCU*, ANCA-IRINA GALACTION, DAN CASCAVAL***

** Technical University "Gh. Asachi" Iasi, Faculty of Industrial Chemistry, D. Mangeron 71, 6600, Iasi*
*** University of Medicine and Pharmacy "Gr.T. Popa" Iasi, Faculty of Medical Bioengineering, University 16, 6600, Iasi*

ABSTRACT. The method of reactive extraction with di-(2-ethylhexyl)phosphoric acid (D2EHPA) for the separation of a range of amino acids is studied. Amino acids are extracted by means of an interfacial reaction of ionic exchange type, if the amino acid exists as a cation in aqueous solution. The separation yield is controlled by the pH value of the aqueous phase, which is due to the acidic or basic character of each amino acid.

The results obtained on the individual reactive extraction indicated the possibility of the amino acids selective separation as a function of the pH value of aqueous solution and the acidic or basic character of each amino acid. Thus, an operation flow for selective separation has been elaborated and demonstrated experimentally. Using multistage extraction, the total separation of the following amino acids groups has been performed: neutral amino acids (l-glycine, l-alanine, l-tryptophan) at pH = 5 - 5.5 (nine extraction stages), basic amino acids (l-lysine, l-arginine) and l-cysteine at pH = 4 - 4.5 (ten extraction stages), l-histidine at pH = 3 - 3.5 (five extraction stages), and acidic amino acids (l-aspartic acid, l-glutamic acid) at pH = 2 - 2.5 (three extraction stages).

The proposed extraction method can be developed and used for the selective separation of amino acids from fermentation broths or protein hydrolysates.

INTRODUCTION

The amino acids can be obtained by biosynthesis or from protein hydrolysis, but their separation from fermentation broths or protein hydrolysates is rather difficult. Amino acids dissociate in aqueous solutions, forming characteristic ionic species as a function of the solution pH value. For this reason, their solubility in nonpolar solvents is very low. Generally, for the amino acids separation from fermentation broths or protein hydrolysates ionic exchange, crystallization at the isoelectric point or chromatography are used.

The liquid - liquid extraction of amino acids is only possible by adding into the organic phase extractants such as phosphoric acid derivatives [1,2], high molecular weight quaternary aliphatic amines [3-7] or crown-ethers [8-10]. In this article, the separation of some amino acids of acidic character (l-aspartic acid, l-glutamic acid), basic character (l-histidine, l-lysine, l-arginine) or neutral character (l-glycine, l-tryptophan, l-cysteine, l-alanine) by reactive extraction with di-(2-ethylhexyl) phosphoric acid (D2EHPA) is explored experimentally and the results discussed. Using the experimental data of the study on the individual reactive extraction, the selective separation of the considered amino acids from a mixture has been analyzed.

The results indicated the possibility of the selective separation by reactive extraction of individual amino acids or groups of amino acids as a function of the

solution pH value. This method is considered an efficient alternative for the fractionation of amino acids mixtures compared to existing techniques.

EXPERIMENTAL PART

The experiments have been carried out in two steps. In the first step, the individual reactive extraction of each amino acid has been analyzed. For this purpose, an extraction column with vibratory mixing has been used, this laboratory equipment being described in detail in previous papers [11,12]. The phase mixing was made by mean of a perforated disk with 45 mm diameter and 20% free section. The vibrations had a frequency of 50 s^{-1} and 4 mm amplitude. The mixer position was maintained at the initial contact interface between the aqueous and organic phases. The extraction time was of 1 minute. The resulted emulsion was evacuated at the base of the column and broken in a centrifugal separator at 5000 rpm.

The initial concentration in aqueous solutions and the pK values of the studied amino acids are given in Table 1 (α-NH_3^+ - the NH_3^+ group in (position from the COOH group, R - the amino acid radical, pH_i - the isoelectric point of the amino acid [13]).

Table 1.

The initial concentrations and the pK values of the extracted amino acids.

Amino acid	Initial concentration		pK_1	pK_2	pK_3	pH_i
	g/l	M	COOH	α NH_3^+	R	
l-aspartic acid	4.65	0.035	2.09	9.82	3.87	3.0
l-glutamic acid	5.14	0.035	2.19	9.66	4.28	3.2
l-cysteine	4.23	0.035	1.96	8.18	10.3	5.1
l-tryptophan	7.14	0.035	2.38	9.39	-	5.9
l-glycine	2.62	0.035	2.35	9.78	-	6.1
l-alanine	3.11	0.035	2.34	9.87	-	6.1
l-histidine	5.42	0.035	1.77	9.2	6.20	7.6
l-lysine	5.11	0.035	2.18	8.95	10.5	9.7
l-arginine	6.09	0.035	2.02	9.04	12.5	10.8

For extraction experiments a solution of 48.3 g/l (0,15 M) D2EHPA in butyl acetate has been used. The volume ratio between the aqueous solution and organic solvent was of 1, each phase volume being 50 ml.

The initial solution pH adjustement has been made with a solution of 4% w/w sulfuric acid, or 5% w/w sodium hydroxide, depending on the desired pH value (pH values were determined using a digital pH meter). The pH values have been recorded throughout each experiment and any pH change was noted.

In the second step of the experiments, the selective separation of amino acids from a mixture by reactive extraction has been studied. Each amino acid had an initial concentration in the mixture of 0,015 M. The extractions were carried out in the same laboratory equipment, similar experimental conditions being used.

The extraction degree has been calculated by means of the amino acid concentrations in the initial solution and in the raffinate. The amino acids

concentrations have been measured by high performance liquid chromatography (HPLC) (HP 1090 liquid chromatograph).

RESULTS AND DISCUSSION

The reactive extraction of individual amino acids

The reactive extraction of amino acids with D2EHPA occurs by means of an interfacial chemical reaction of the ion exchange type:

$$R\text{-}CH(NH_3^+)\text{-}COOH_{(aq)} + HP_{(o)} \rightleftharpoons R\text{-}CH(NH_3^+)\text{-}COOH.P^-_{(o)} + H^+_{(aq)}$$

where HP is the extractant. As it can be observed, the separation is possible if amino acids exist as cation in aqueous solution, as found at a low pH values. At the same time, if the solution pH is too low, then the extractant will become protonated and thus unable to extract the cations [1].

The effect of the pH value on the extraction degree is depicted in Figs. 1-3 for each class of amino acid.

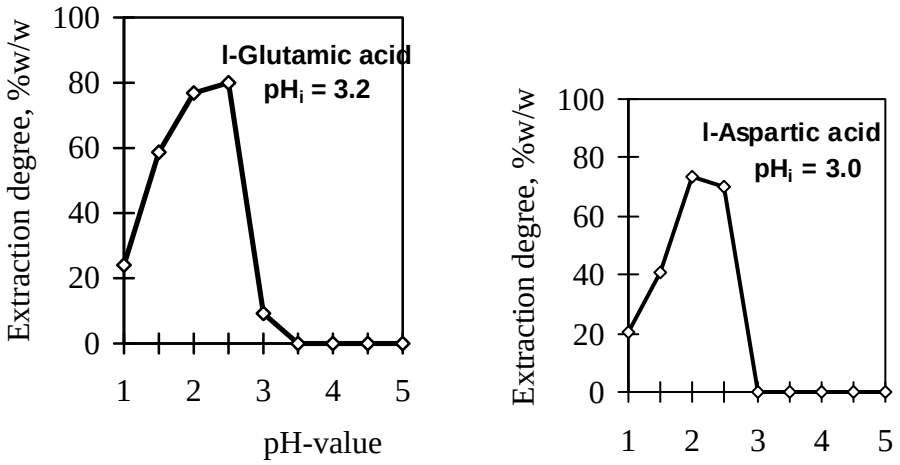

Figure 1. Effect of aqueous solution pH value on the reactive extraction degrees of acidic amino acids with D2EHPA dissolved in butyl acetate.

For all cases, the extraction degree reaches a maximum value as pH increases, corresponding to a maximum pH extraction domain of 2 - 3, followed by a strong decrease. The maximum is the result of the two opposite phenomena which occur as pH value increase: the increase of the concentration of extractant active form, which is able to react with the amino acid, and the decrease of the total amount of amino acid presenting a cationic form.

The reactive extraction of the amino acids with acidic character (l-aspartic acid, l-glutamic acid) occurs with maximum efficiency at pH 2.5, the extraction degree values being comparable (77% w/w for l-aspartic acid, 80% w/w for l-glutamic acid). Because of the increase of the zwitterion concentration in aqueous solution for both amino acids, any further increase of the pH value leads to the strong decrease of the extraction yield. At the isoelectric point of each amino acid the reactive extraction become impossible (i.e. yields $\cong$ 0).

In the case of neutral amino acids (l-glycine, l-alanine, l-tryptophan, l-cysteine), the maximum extraction yields are obtained at pH 3, these values varying between 78.4% w/w for l-glycine and 90% w/w for l-tryptophan as a function of the amino acid hydrophobicity. For higher pH values, the separation efficiency decreases, as a result of the amino acids COOH dissociation, and reaches zero at isoelectric point.

Figure 2. Effect of aqueous solution pH value on the reactive extraction degrees of neutral

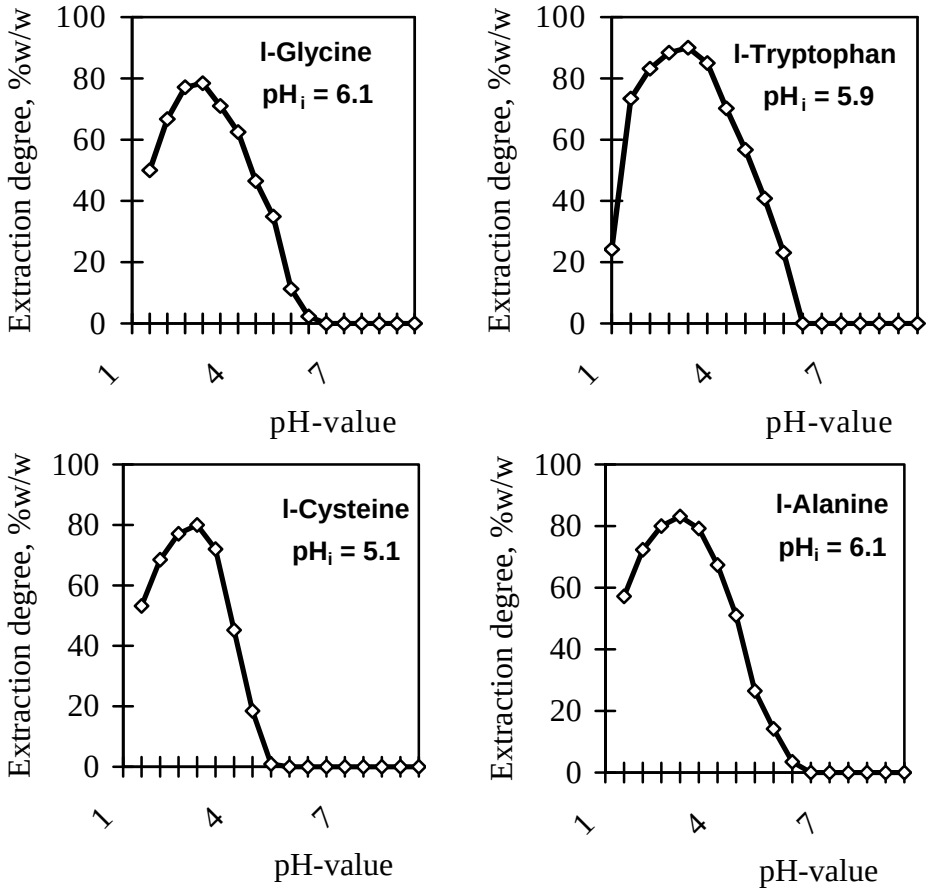

amino acids with D2EHPA dissolved in butyl acetate.

The amino acids with basic character exist as dianions at low pH values. For this reason, the mechanism of the reactive extraction with D2EHPA can be described using the following interfacial chemical reaction:

R_1^+-CH(NH_3^+)-$COOH_{(aq)}$ + $2HP_{(o)}$ ⟷ R_1^+-CH(NH_3^+)-$COOH.P^-_{2\,(o)}$ + $2H^+_{(aq)}$
(R_1^+ being the dissociated radical of amino acid).

The maximum separation yield for the basic amino acids studied (l-histidine, l-lysine, l-arginine) varies between 57.8% w/w for l-histidine and 68% w/w for l-lysine and l-arginine, being reached at pH value of 2.5 - 3. The difference is due to the more pronounced dissociation of l-histidine at this pH value and, thus, to the formation of dication - anionic species in aqueous solution. The increase of pH value leads to a significant decrease of the extraction degrees, which become zero at pH 4 for l-histidine, and pH 5 for the other two amino acids.

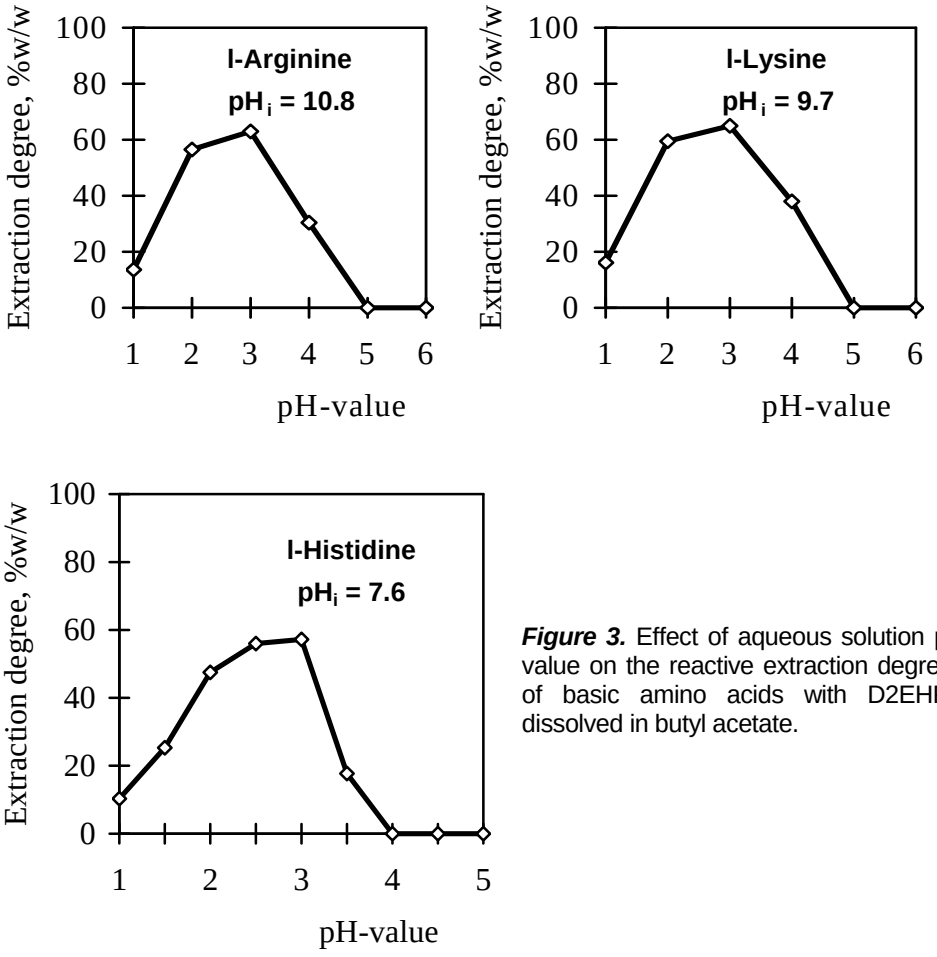

Figure 3. Effect of aqueous solution pH value on the reactive extraction degrees of basic amino acids with D2EHPA dissolved in butyl acetate.

Compared to the acidic and neutral amino acids, the reactive extraction of basic amino acids become impossible at pH values lower than the isoelectric point, as a result of the total dissociation of the -COOH group with formation of dication - anionic forms and a small amount of zwitterions.

The selective extraction of amino acids

The preliminary studies on the reactive extraction of individual amino acids indicated the possibility of the selective separation of different groups of amino acids with similar acidic properties as a function of aqueous solution pH value. In order to checking this hypotheses, the amino acids were extracted from a mixture with D2EHPA, at different pH values, the results being shown in Fig. 4.

In can be observed that all amino acids are extracted, with different yields, for a pH domain of 1.5 - 3. Over this interval, the extract contains only the amino acids with neutral and basic character. For pH 5 - 6, only the neutral amino acids are extracted, and for pH > 6 the extraction becomes impossible.

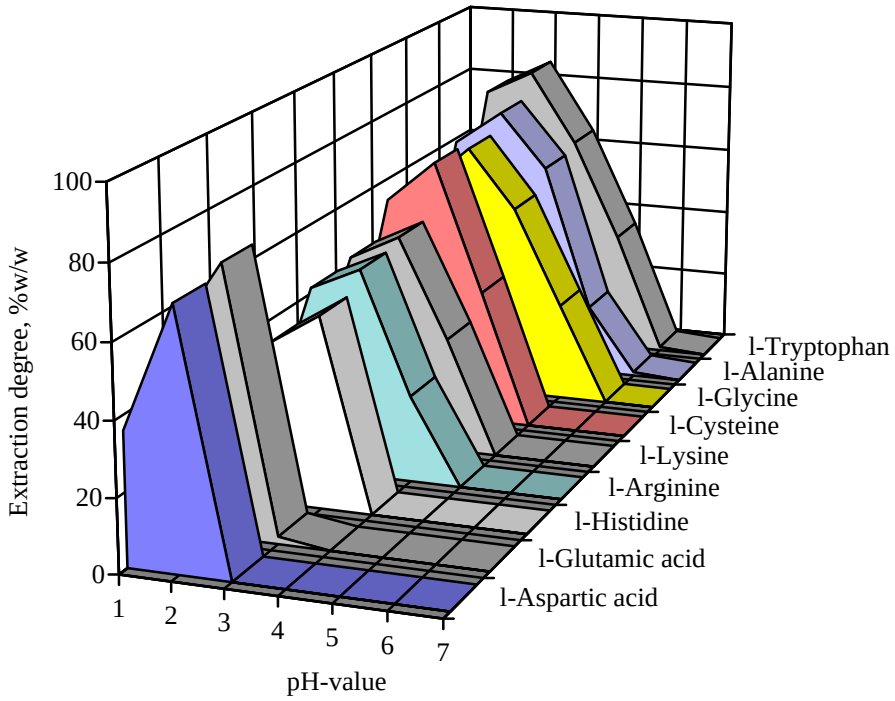

Figure 4. Effect of aqueous solution pH value on the reactive extraction degrees of amino acids from a mixture with D2EHPA dissolved in butyl acetate.

Using these data, a process flow sheet for the selective separation of the amino acids by reactive extraction with D2EHPA has been elaborated and applied (Fig. 5). Because the extraction degrees of each group of amino acids are rather low at the required pH values for selective separation, for total recovery of the considered amino a multistage extraction has been used. The extraction conditions are given in Table 2.

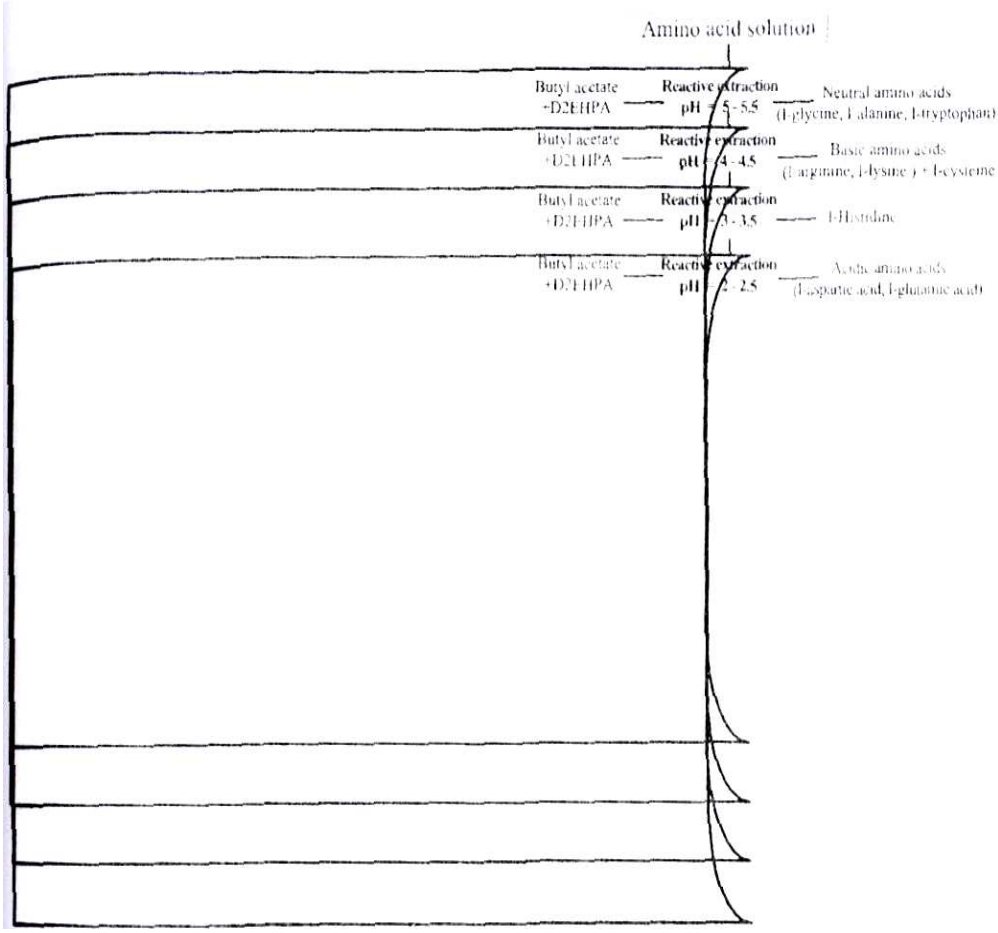

Figure 5. Operation chart for the selective extraction of amino acids with D2EHPA dissolved in butyl acetate.

Table 2.

The experimental conditions for the reactive extraction and separation of amino acids from a mixture.

Extracted amino acids	**pH domain**	**One stage extraction degree**, % w/w	**Number of extraction stages**
Neutral amino acids (- l-cysteine)	5 - 5.5	20 - 25	9
Basic amino acids (- l-histidine) + l-cysteine	4 - 4.5	18 - 25	10
l-Histidine	3 - 3.5	40	5
Acidic amino acids	2 - 2.5	60 - 63	3

CONCLUSIONS

Amino acids are extracted with D2EHPA by means of an interfacial reaction of ionic exchange type, if the amino acid exists as a cation in aqueous solution. The separation yield is controlled by the pH value of the aqueous phase, which is due to the acidic or basic character of each amino acid.

The individual extraction of amino acids indicated that the maximum yields are reached for a pH domain of 2 - 3, then strongly decreasing with the pH increase. Thus, for acidic and neutral amino acids, the extraction becomes impossible at the isolelectric point, and for basic amino acids at a pH value lower than pH_i, as a result of the carboxylic group dissociation.

By means of the pH influence on reactive extraction of the considered amino acids, an operation flow for selective separation has been elaborated and demonstrated experimentally. Using multistage extraction, the total separation of the following amino acids groups has been performed: neutral amino acids (l-glycine, l-alanine, l-tryptophan) at pH 5 - 5.5, basic amino acids (l-lysine, l-arginine) and l-cysteine at pH 4 - 4.5, l-histidine at pH 3 - 3.5, and acidic amino acids (l-aspartic acid, l-glutamic acid) at pH 2 - 2.5.

The proposed extraction method can be developed and used for the selective separation of amino acids from fermentation broths or protein hydrolysates.

REFERENCES

1. M. Itoh, M.P. Thien, T.A. Hatton, D.I.C. Wang - Biotechnol. Bioeng. 1990, 35, 853.
2. D. Cascaval, R.Z. Tudose - Roum. Chem. Quart. Rev., 1997, 5, 231.
3. H.J. Rehm, G. Reed (Eds.) -"Biotechnology", vol. 3, VCH, Weinheim, 1993, pp. 576.
4. K. Schuegerl - "Solvent Extraction in Biotechnology", Springer - Verlag, Berlin, 1994, pp. 111.
5. R. Hansel - Ph.D. Thesis, Hannover, 1984.
6. L. Handojo - Ph.D. Thesis, Hannover, 1988.
7. P. Deblay, M. Minier, H. Renon - Biotechnol. Bioeng., 1990, 35, 123.
8. C. Luca, L. Mutihac, T. Constantinescu - Rev. Roum. Chim. (Bucharest), 1990, 35, 467.
9. S. Shinkai, K. Inuzuka, K. Hara, T. Stone, O. Manabe - Bull. Chem. Soc. Jpn., 1984, 57, 2150.
10. S. Shinkai, T. Minami, Y. Araragi, O. Manabe - J. Chem. Perkin. Trans. II, 1985, 503.
11. D. Cascaval, R.Z. Tudose, C. Oniscu - Hung. J. Ind. Chem., 1997, 25, 245.
12. C. Oniscu, D. Cascaval - Roum. Biotechnol. Lett., 1996, 1, 23.
13. A.L. Lehninger - "Biochemistry" (2nd Ed.), Worth Publishers, Inc., New York, 1975, pp. 85.

STUDIA UNIVERSITATIS BABEŞ-BOLYAI, CHEMIA, XLVI, 1-2, 2001

PURE AND DOPED MESOPOROUS TiO_2 FILMS MADE FROM REVERSE MICELLES AND THEIR USE FOR THE PHOTOCATALYTIC DEGRADATION OF ADSORBED BASIC BLUE DYE

IOANA CARMEN LADIU[*], VIRGINIA DANCIU[*], VERONICA COSOVEANU[*], P. LIANOS[**]

***Faculty of Chemistry and Chemical Engineering, "Babes-Bolyai" University, 3400 Cluj-Napoca, Romania*

****Engineering Science Dept., University of Patras, 26500 Patras, Greece*

ABSTRACT. Films transparentes de TiO_2 ont été déposés sur des plâques de verre par une procedure sol-gel en présence de micelles inversées de Triton X-100 in cyclohexane. Solutions aqueuses de Basic Blue, (2- [[4- ethyl(2- hydroxyethyl)- amino)] phenyl]azo]- 5- metoxy-3-methyl (T-4)metoxysulfate), ont été absorbées sur ces films et leur photodégradation a été suivi par la spectrophotométry d'absoption. Pour obtenir le maximum du rendement de la photodégradation, la nanostructure du film a été optimisée en souivant le temps de géfication, la nature et la concentration du ion dopant et par l'irradiation du film avec des rayons UV. Les films qui ont incorporré, par micelles inversées, des ions d'argent et du chrôme sont plus efficaces que les films pures de TiO_2. Les films dopées avec Ag devient plus efficaces par irradiation UV. Les films dopées avec Au sont moins actifs, mais elles aussi devient plus éfficaces que les films pures de TiO_2 apres l'irradiation UV.

INTRODUCTION

Photodegradation catalyzed by TiO_2 particles provides a technological method for the treatment of air and water pollutant. This heterogeneous photocatalysis is an extensively studied process in the recent years[1-3]. In most of the applied technologies, TiO_2 aqueous suspensions have been employed[4,5]. Because the manipulation of TiO_2 powders and their removal is difficult, the most recent research is focused on the preparation of the immobilized catalysts, e.g. in the form of thin films on solid supports. These thin films are particularly interesting for applications to open-air purification panels[6,7]. The efficiency of thin films is lower than that of suspended powders[8]. For this reason, an intensive effort has been made to enrich titania with species that can enhance its photocatalytic capacity. Noble metals, in particular, silver have been used for this goal. Silver increases the photocatalytic capacity of titania by some different physical mechanisms that may act separately or simultaneously. Reduced silver particles of colloidal dimension (metallic silver) are considered to be electron scavengers. Thus, by trapping electrons produced in electron-hole pair after photons absorption, they prevent electron-hole recombination and liberate holes to participate in degradation reactions[9]. Plasmon resonance effects in metallic silver nanoparticles are also held responsible for local enhancement of the electric field, facilitating electron-hole pair production and separation[8,10,11]. Finally, silver is also reported to affect the structure of titania, leading to modification of its photocatalytic activity[12]. In the present work, we study the photocatalytic efficiency of transparent mesoporous titania thin films,

made by a sol-gel method involving reverse micellar templates[13-15]. Films are structured in nanoparticles of controlled and uniform size, both in pure form or doped with silver, chromium, gold and potassium. The metal ion is introduced in the films by initial solubilization in the reverse micellar solution. It has found that the presence of the impurity results in increasing photodegradation rate and it thus search for ways to optimize it.

The samples were tasted by monitoring rates of photodegradation of a model dye, Basic Blue (BB) absorbed on pure or doped titania mesoporous films. This choice was dictated by the following reasons: dye photodegradation on a transparent film can be easily monitored by absorption spectrophotometry; a large amount of water-borne pollutants is synthetic textile dyes and industrial dyes stuffs[16]; dye photodegradation can be carried out by visible light through photosensitization, i.e. by light absorption from the dye and subsequent electron separation by transfer to the semiconductor[16-18]; finally, TiO_2 photodegradation reactions in thin film configuration is a process acquiring increasing industrial interest since applications can be envisaged by deposition on large surfaces for both indoors and outdoors air-purifications system[1-3, 19].

EXPERIMENTAL

Materials. Titanium (IV) isopropoxide, polyoxiethilene(10)isooctyl- phenyl ether (triton X-100), $Ag(NO_3)$ hydrated, KNO_3, $NaAuCl_4xH_2O$, $Cr(NO_3)_3x9H_2O$ and benzothiazolium, (2-[[4-ethyl(2-hydroxyethyl)-amino)] phenyl]azo]-5-metoxy-3-methyl(T-4)-metoxysulfate) (Basic Blue, BB, cf. chemical structure from fig.1) were purchased from Aldrich and used as received. The rest of the reagents were from Merck, while millipore water was used in all experiments.

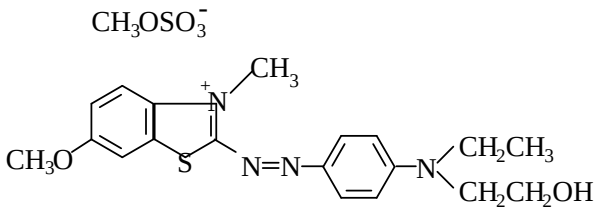

Fig.1. The chemical structure of Basic Blue.

Preparation of TiO_2 mesoporous films deposited on glass slides

Reverse micellar solutions of 0.2M Triton X-100 were prepared in cyclohexane. To each of these solutions it was added 0.2M titanium isopropoxide under vigorous stirring and at ambient conditions[13-15]. Hydrolysis and condensation of titanium isopropoxide begins as soon as it is introduced in the reverse micellar solution, but it may take more than one hour before the solution becomes a visible gel. This prepared composite material was deposited as thin film on a glass slide by dip-coating. The slide was previously sonicated for 20 min. in ethanol and was finally copiously washed with millipore water and dried in a stream of N_2. The thus prepared slide was dipped into the gelling solution and was fast withdrawn at a speed of 2cm/s. The composite of organic-inorganic film was

left to dry in air and then it was slowly heated in air, up to 450℃ at a rate of 3.5℃/min. The film was finally sintered at 450℃ f or about 15 more minutes. The procedure was repeated two additional times. Thicker films could be made by further successive coatings. However thickness grows at the expense of transparency. AFM and SEM images of the films prepared by the above method and published in previous publicati- ons[13-15] reveal a mesoporous structure that consists of TiO_2 nanoparticles of practi- cally monodisperse size with exceptional reproducibility. It was observed that choosing the water/surfactant ratio in the original solution easily controls the size of the nanoparticles[7]. Larger nanoparticles are made when more water exists in the solution. The advantage of the reverse micellar route in making TiO_2 particles, as compared with other methods, exactly lies on this capacity to control the mesoporous structure of the obtained films. The diameter of the nanoparticles employed in the present work, as estimated by using AFM images, was around 30 nm in the case of samples made with a water/surfactant ratio equal to two (0.2 M Triton X-100, 0.4M water). The TiO_2 films are too thin to give a detectable X-ray diffraction spectrum. The powder of TiO_2 obtained by the freeze drying procedure (in the same conditions) was study by X-ray diffraction. It gave a diffusion pattern, which corresponds to anatase nanocrystallites.

Incorporation of metal ions

Silver, chromium, gold and potassium ions were been directly incorporated in titania film by solubilization in the original reverse micellar solution, i.e. instead of pure water, it was used aqueous salt solution so that the final metal ion concentration is well defined. The rest of the procedure remained the same as above. The ions concentration was 0.005-0.05M, i.e. at 2.5-25% doping level with respect to titanium.

Adsorption of the dye on the films

Both pure titania and doped films adsorb a substantial amount of Basic Blue, when they are dipped in an aqueous solution of the dye. Adsorption is instantaneous and the films are immediately deeply colored (cf. figures 2 and 3). In typical preparations, dye concentration in solution was 10^{-2}M.

Methods

Absorption measurements were made with a Cary 1E spectrophotometer. UV-treatment of the films has been obtained by illumination with a mercury-containing 400W UV lamp. Illumination of the samples for dye photodegradation was achieved with a commercial 250W tungsten-halogen spotlight satisfactorily simulating solar radiation. The light intensity at the surface of the sample was 600 mW/cm^2. Measuring the absorbance of the dye at its maximum monitored photodegradation.

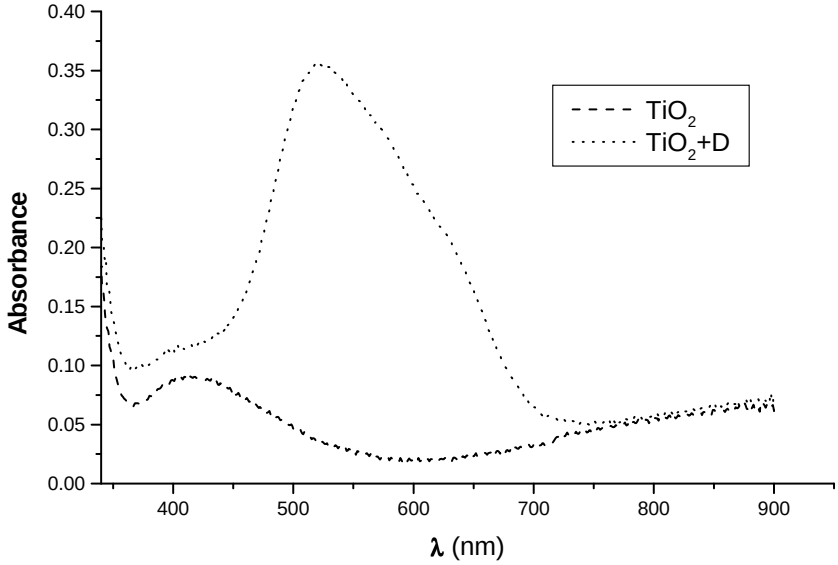

Fig.2. Absorbtion spectrum of pure titania film without and with adsorbed BB.

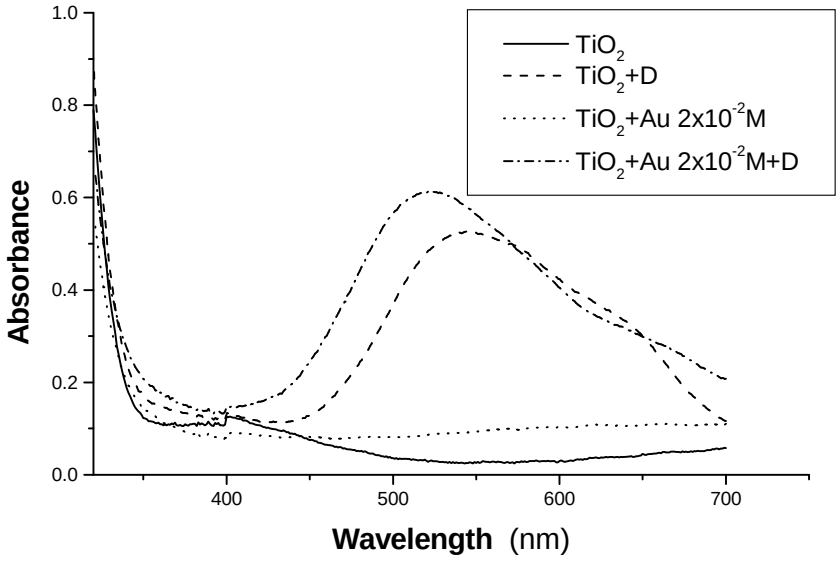

Fig.3. Absorption spectrum of a typical pure titania film (with and without adsorbed BB) and Au-doped titania film (with and without adsorbed BB).

RESULTS AND DISCUSSION

Figure 4 shows the variation of absorbance of pure titania films with adsorbed BB as a function of illumination time with visible light. The two curves correspond to two films made with the same reverse micellar solution but a different time of gelation. The chemical structure of BB is also presented in figures 1.

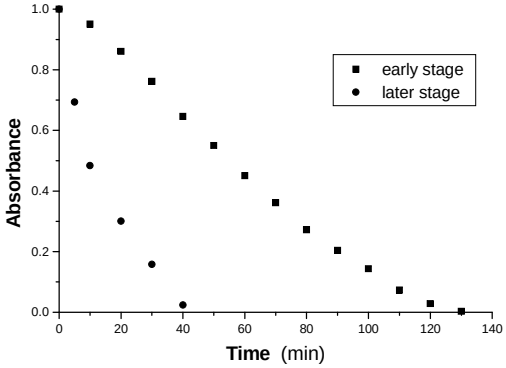

Fig.4. Variation of absorbance of pure titania films with adsorbed BB as a function of illumination time with visible light. The two curves correspond to two films made with the same reverse micellar solution but a different stage of gelation.

Fig. 5 shows the absorption spectrum of a representative titania film alone.

The oscillating part in the spectrum of titania is due to interference fringes. The photodegradation is realized by the photosensitizing procedure[16-18], i.e. light is almost exclusively absorbed by the dye. Then the excited electron is transferred into the conduction band of the semiconductor leaving behind a hole localized on the dye. The thus separated electron is scavenged by atmospheric molecular oxygen so that e^--h^+ recombination is prevented and the dye is destroyed by the remaining hole. Photodegradation by direct excitation of titania is not excluded but it is very limited. Indeed use of filters cutting off the Near UV radiation of the lamp (400nm cutoff filter) only slightly diminishes photodegradation rates. Hydrolysis of titanium isopropoxide and subsequent gelation by inorganic (i.e., -Ti-O-Ti-) polymerization, according to the sol-gel procedure, is very rapid for w/s $\geq$ 3. Fast gelation leads to very rough, light-scattering films that are not appropriate for the present studies. Thus the highest exploitable ratio was w/s = 2.5(0.2M Triton X-100 + 0.5M water). SEM, TEM and AFM9-11 have previously characterized titania films made by using different w/s ratios. As a general rule, later stage of gelation leads to mesoporous titania films composed of larger nanoparticles. The total active surface of the mesoporous structure is larger in smaller particles, i.e. in the case of early stage of gelation. Increase of time of gelation, i.e. increase of the nanoparticle size, makes rougher films with smaller active surface expansion. For this reason, it has found that films made after 1 h of gelation have smaller

capacity of BB absorption. It seems reasonable that no more than one BB molecule can be absorbed on a single titania nanoparticle. For this reason, smaller but more numerous nanoparticles can adsorb more dye than larger but less numerous nanoparticles. However, bigger particles are more effective in photodegradating BB than smaller particles, as can be seen in figure 4. It is obvious that photodegradation rates are much faster for later stage than for early stage of gelation. Even though more extensive studies are needed to explain this phenomenon, there may be plausible explanations. It is known, that according to Brus effective mass model for nanosize semiconductors[20], absorption occurs at longer wavelength for bigger particles due to the size effects on the electronic properties of the semiconductor. Indeed, as seen in fig. 5 showing absorption spectra of films made with different growth times, larger particles

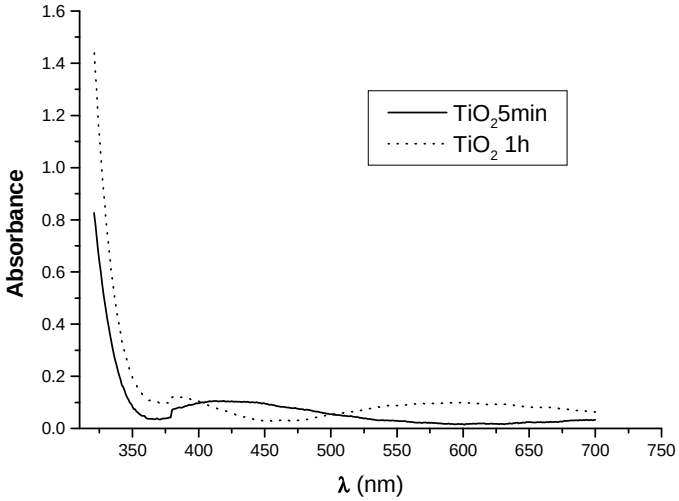

Fig.5. Absorption spectrum of a typical titania film made with the same reverse micellar solution but a different stage of gelation.

(longer growth) absorb light at longer wavelength than smaller particles (short times). One then possible reason for higher rates with later stage of gelation is the larger percentage of direct Near UV absorption of photons by the larger particles. However, this seems to us a rather weak argument since the direct participation of titania in photon absorption is, as already said, very limited. Meanwhile, smaller particles have a higher energy band-gap. It is then possible that the electron transfer from the dye to the higher - laying Conduction Band of the smaller-size semiconductor particles during photosensitization, is more difficult than in larger particles, which have a smaller band-gap. This can partly explain the smaller efficiency of smaller particles[21]. A second explanation is that in smaller particles it

is more probable to have extended surface defects that will quench the excited species by providing electron - hole recombination sites and thus give lower photodegradation rates. As a conclusion the above information indicated that more material is adsorbed on a film that has a finer mesoporous structure but it offers lower photodegradation rates. For this reason and in order to compensate the two opposing effects it has opted for 1h of gelation (0.2M Triton X-100 and 0.4 M water) as the best combination for both satisfactory adsorption capacity and photodegradation efficiency.

Photocatalytic degradation of BB has also been studied with doped TiO_2 films made by the above procedure, using a standard water/surfactant ratio w/s = 2. Four dopants were tried, Ag^+, Cr^{+3}, Au^{+3}, and K^+. Salts of these metals have been introduced at concentration 0.005 - 0.05M, i.e. at 2.5 - 25% doping level with respect to titanium, by solubilizing them in the water used to make Triton X-100 reverse micelles. Formation of films by dipping and subsequent heating up to 450℃ as well as BB adsorp tion for photodegradation experiments followed the same procedure as for pure titania films. The incorporation of dopants by the reverse micellar route introduces metal ions in titanium substitution sites in the nanocrystallite lattice. The present study is focused on the question of the photodegradation efficiency itself.

As a verification of the fact that smaller particles give lower photodegradation rates but higher dye adsorption capacity, it has produced films made with w/s = 2 and doped with Ag $2x10^{-2}$ F at two different stages of gelation, i.e. dipping in the solution was done 5 min and 15 min after component mixture. A longer waiting time means more extensive particle growth. In fact, approximately, the same effect is produced by using w/s = 2 and different concentrations of dopant ions and dipping a few minutes after preparation. Comparison of photodegradation rates between a film made at an early stage with a film made at a late stage of gelation is shown in fig. 6. Indeed the latter film adsorbs less dye but degrades it faster. The quantity of the adsorbed dye is not shown in fig. 6. Maximum absorbencies are normalized for the sake of comparison.

Two types of samples were examined. In the first type, immediately after the doped film was taken out of the furnace the absorption spectrum of the film was registered and then BB was adsorbed on the film by dipping. Finally, the film with adsorbed dye was illuminated with visible light and the photocatalytic degradation of the dye was monitored by absorption spectrophotometry. In the second type, after the films were taken out of the furnace, they were first subjected to UV treatment for about 15 min, and then the dye was adsorbed and finally was photodegradated by visible light illumination. UV treated doped films are much more efficient for dye photodegradation than untreated films. This can be seen in figures 7 and 8, where Ag-doped and Au-doped TiO_2 photocatalytic rates are, respectively, presented.

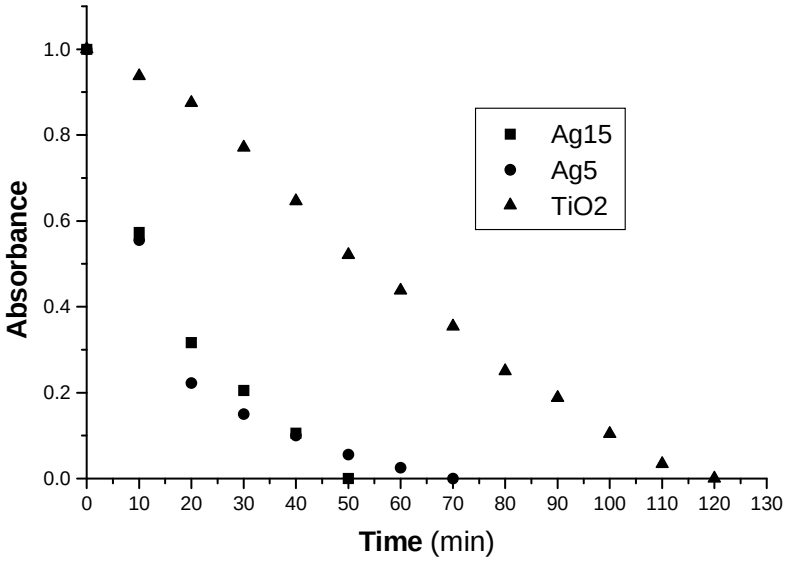

Fig.6. Variation of absorbance of pure titania film and Ag-doped titania films with adsorbed BB as a function of illumination time with visible light. The three curves correspond to three films: pure titania film, Ag-doped titania film after 5 min of gelation and Ag-doped titania film after 15 min of gelation

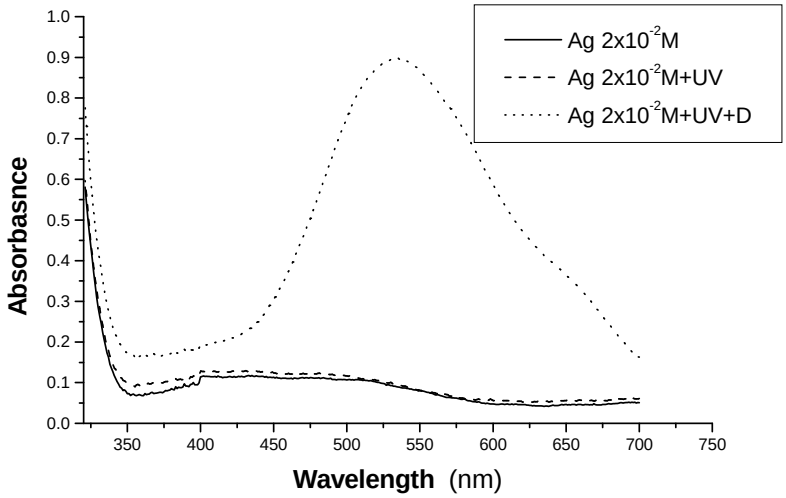

Fig.7a. Absorption spectrum of Ag-doped film. The three curves correspond to the same film before UV treatment, after UV treatment and after adsorption of BB

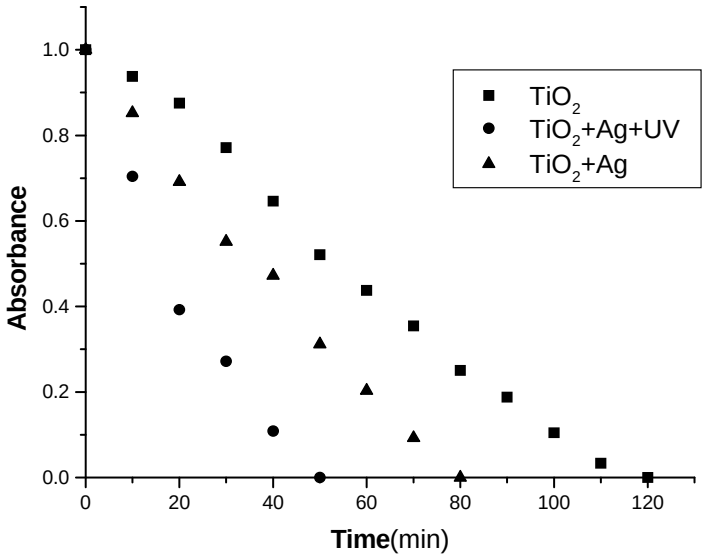

Fig.7b. Variation of absorbance of pure titania film, Ag-doped film with and without UV treatment.

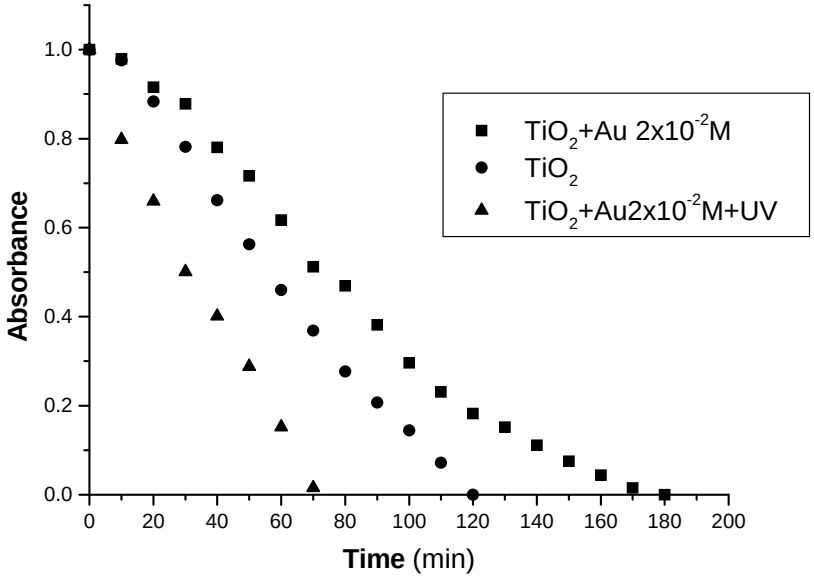

Fig.8. Variation of absorbance of pure titania film and Au-doped titania film with adsorbed BB as a function of illumination time with visible light. The three curves correspond

to three films: pure titania, Au-doped titania ($2x10^{-2}$M) with and without UV treatment.

Fig. 7 and 8 shows that it takes about two hours to photodegradate all adsorbed dye on pure TiO_2 films. Photodegradation diminishes with non-treated silver doped films and is limited to only 50 minutes when the films are previously treated with UV-radiation. The spectrum of this film can be seen in fig. 7a. In the case of Au, a markedly different behavior was observed. Non-treated Au-doped films decrease photodegradation efficiency, increasing photodegradation time from 2 hours, for pure TiO_2 films, to 3 hours, for untreated doped films. On the contrary, Au-doped films, previously treated with UV radiation decreased photodegradation time to 70 min. The Cr-doped films have a different comportment (cf. fig. 9). The spectrum of these films can be observed in fig.10.

Non treated Cr-doped films increase photodegradation efficiency, decreasing photodegradation time from 2 hours for pure titania films to 40 minutes for untreated doped films. On the contrary, Cr-doped films previously treated with UV radiation increase photodegradation time to 80 minutes.

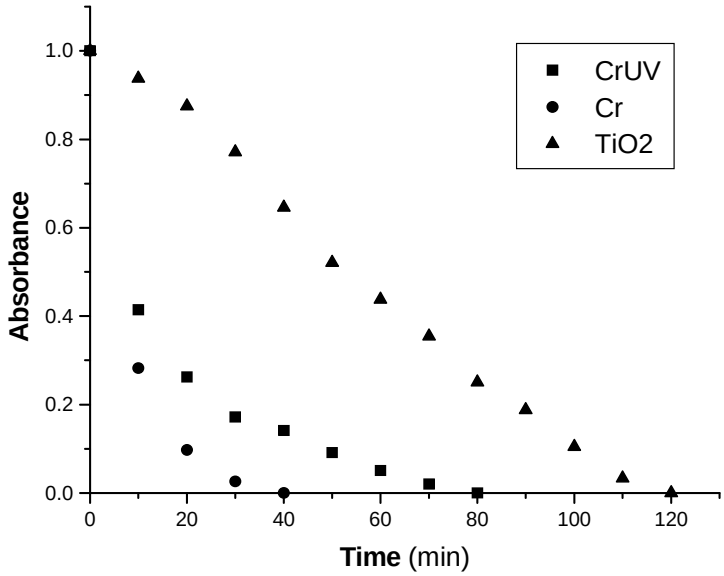

Fig.9. Variation of absorbance of pure titania film and Cr-doped titania films before and after UV treatment.

As already discussed in the introduction, silver doping of titania has beneficial effects on its photocatalytic activity owing to the existence of three mechanisms that may function separately or jointly. Metal particles created by silver ion reduction act as electron scavengers aiding electron-hole separation, dipole moment increase in the vicinity of metal particles also facilitates electron

excitation and e^- - h^+ separation and silver dopants may structurally modify titania increasing its photocatalytic activity[8-10]. The enhancement of photocatalytic

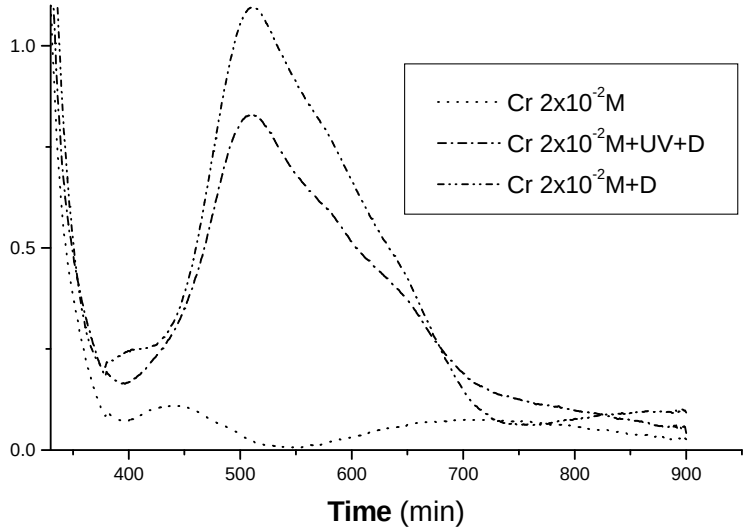

Fig.10. Absorbtion spectrum of Cr-doped titania film. The three curves correspond with the films made with the same reverse micellar solution doped with Cr^{+3} without the dye, with the dye and with UV treatment and after adsorbed the dye.

efficiency after UV irradiation is due to the creation of metal centers in the film, owing to reduction by electrons in the conduction band of the semiconductor. It was adopted the above model accepted for silver impurities. Titania absorbs UV-radiation, as can be seen fig. 5. Absorption of UV photons excites a large number of electrons, which can reduce Ag^+, Cr^{+3}, K^+ and Au^{+3}. Of course metal colloidal particle formation by reduction of the cationic species is easier in the case of the monovalent ions than in the case of the trivalent ions. For this reason only 15 minutes of UV-illumination are necessary to transform silver-doped films but it takes about 1 h in the case of trivalent ions-doped films. It is most probable that a large portion of silver ions are reduced during heating of the film, even before UV illumination, therefore the presence of silver always speeds up photodegradation. When silver or Au ions are incorporated into titania, they create traps, which aid electron-hole recombination and inhibit photodegradation[22]. This is obvious in the case of Au, the presence of which, before reduction by UV-treatment, largely decreases photodegradation rate (Fig. 8). This is not detected in Ag^+-doped films, since silver is easily reduced, so it acts to increase photodegradation rates even before UV-treatment (fig. 7). When the film was illuminated by UV-light, the electrons liberated by direct absorption of photons by titania eliminate these sites by reduction of silver ions. Whether silver metal particles are created is hard to say, since their density might be too small to be spectroscopically detected by plasmon resonance

absorbtion[15]. UV treatment of the Au containing films gives dramatic effects on photocatalytic efficiency.

The influence of dopant ion concentration can be observed for some films. For Ag-doped titania films the photodegradation time decrease with the increase of dopant ion concentration for the same conditions of preparation. The absorbance spectrum can be observed in fig. 11.

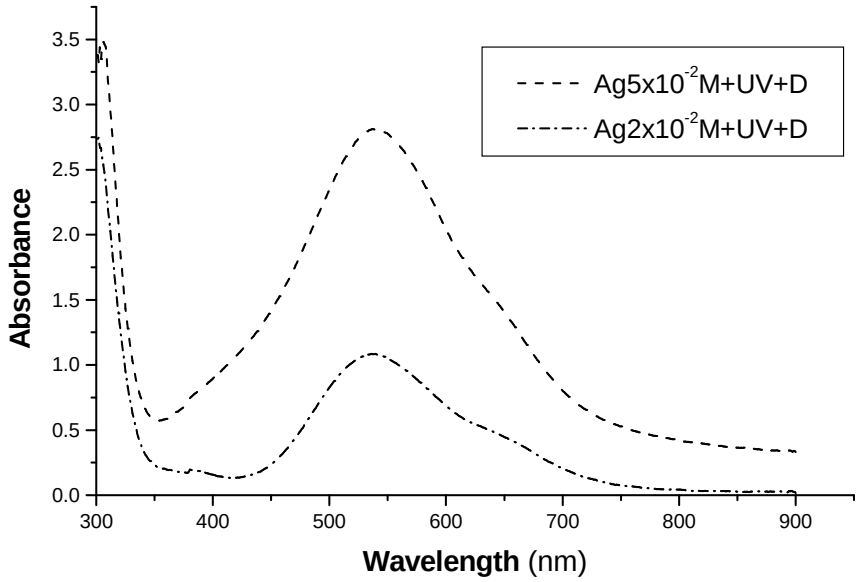

Fig.11. Absorption spectrum of Ag-doped films made at a different concentration of dopants on and after UV treatment.

The maximum of absorbance is three times greater for Ag $5x10^{-2}$M than for Ag $2x10^{-2}$M. The quantity of BB adsorbed on doped film with Ag $5x10^{-2}$ is high, thus the film are much more efficient for the dye photodegradation.

K-doped titania films have a different comportment and the spectrum can be seen in fig. 12. All the films are made in the same conditions. The nanoparticles' size is bigger for low K^+ concentration.

Conclusion

The above mesoporous films are efficient photocatalysts for the degradation of adsorbed BB. More dye is adsorbed on films made with smaller titania nanoparticles but faster photodegradation rates are obtained with larger nanoparticles. More dye is also adsorbed on thicker films but thickness grows at the ex- pense of transparency. The reverse micellar route in combination with the sol-gel procedure can be successfully employed to optimize the efficiency of

these films. Films doped with silver ions are very efficient photocatalysts when they are treated with UV radiation, i.e. when the ionic species are reduced. Films doped with silver and chromium ions, incorporated through the reverse micellar route, are more efficient photocatalysts than pure titania film. Films doped with gold ions are worse photocatalysts but when they are treated with UV-radiation, they also become more efficient photocatalysts than pure titania films.

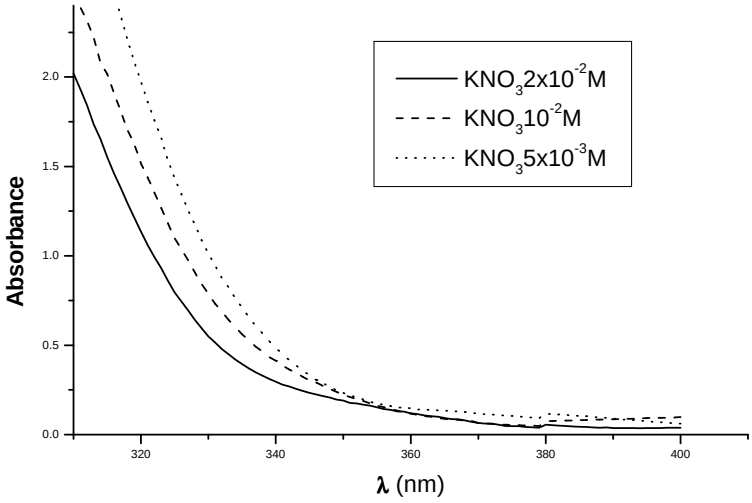

Fig.12. Absorption spectrum of three K-doped titania films made at different concentrations of dopant ion. The three curves correspond to three films prepared in the same conditions but at different concentrations of K-dopant: $5x10^{-3}$M, 10^{-2}M, and $2x10^{-2}$M.

REFERENCES

1. Fujishima, K.Hashimoto, T. Watanabe, *TiO_2 Photocatalysis. Fundamental and Applications.* BKC Inc., Tokyo, 1999, p.21.
2. N. Negishi, K.Takeuchi, T. Ibusuki, *J. Mater. Sci*., 1998, **33,** 5789.
3. I. Sopyan, M. Watanabe, S. Murasawa, K. Hashimoto, A. Fujishima, *J. Photochem. Photobiol. A: Chemistry,* 1996, **98**, 79.
4. J. Teurich, M. Lindner, D. W. Bahmemann, *Langmuir* 1996, **12**, 6368.
5. J.A. Navio, C. Cerillos, F.J. Marchena, F. Pablos, M.A. Pradera, *Langmuir* 1996, **12**, 2007.
6. J-M.Herrmann, H. Tahiri, Y. Ait-Ichou, G. Lassaletta, A.R. Gonzales-Elipe, A. Fernandez, *Appl. Catal. B: Enviromental*, 1997, **13**, 219.
7. I. Ilisz, A. Dombi*, Appl.Catal. A: General* 1999, **180,** 35.

8. G. Zhao, H. Kozuka, T.Yoko, *Thin Solid Films* 1996, **277**, 147.
9. G. Lassaletta, A.R. Gonzales-Elipe, A. Justo, A. Fernandez, F.T. Ager, M.A. Respaldiza, J.G. Soares, M.F. Da Silva, *J. Mater Sci.* 1996, **31**, 2325.
10. H. Tada, K .Tiranishi, Y-I. Inubushi, S. Ito*, Langmuir*, 2000, **16,** 3304.
11. E .Stathatos, D .Tsiourvas, P. Lianos, *Colloids and surfaces A: Phisicochem*. *Eng. Aspects* 1999, **149**, 49.
12. E. Stathatos, P. Lianos, F. Del Monte, D. Levy, D. Tsiourvas, *Langmuir***,** 1997, **13**, 4295.
13. E. Stathatos, P. Lianos, P. Falaras, A. Siokou, *Langmuir,* 2000, **16**, 2398.
14. K. Vinodgopal, D. E.Wynkoop, P.V. Kamat*, Environ Sci. Technol*, 1996, **30,** 1660.
15. K. Vinodgopal, P. V. Kamat*, Environ Sci. Technol.*, 1995, **29**, 841.
16. C. Nasr, K. Vinodgopal, L. Fisher, S. Hotchandani, A.K. Chattapadhyay, P.V. Kamat, *J. Phis. Chem*., 1996, **100**, 8436.
17. N. Neghishi, T. Iyoda, K. Hashimoto, A. Fujishima, *Chem. Letters,* 841, 1995
18. L. Brus, *J. Phis. Chem.,* 1986, **90**, 2555.
19. L. Kavan, T. Stoto, M. Gratzel, T. Fitzmaurice, V. Shklover, *J. Phys. Chem.,* 1993, **97**, 9492.
20. V. Brezova, A. Blazkova, E. Borosova, M. Ceppan, R. Fiala, *J. Molecular Catalysis A: Chemistry*, 1995, **98**, 109.
21. T. Ohno, T.F. Tanigawa, K. Fujihara, S. Izumi, M. Matsumura, *J. Photochem. Photobiol. A: Chemistry*, 1999, **127,** 107.
22. N. Serpone, D. Lawless, J. Disidier, J.-M. Herrmann, *Langmuir,* 1994, **10,** 643.

STUDIA UNIVERSITATIS BABEŞ-BOLYAI, CHEMIA, XLVI, 1-2, 2001

ULTRASOUND-ASSISTED CATHODIC REDUCTION OF 4,4' - DINITRODIBENZYLE

VIRGINIA DANCIU, VERONICA COSOVEANU, GABRIELA OPREA*, C. BERNARD**

Faculty of Chemistry and Chemical Engineering, "Babes-Bolyai" University, 3400 Cluj-Napoca, Romania
**Faculty of Science, North University, 4800 Baia-Mare, Romania*
***Organic Electrosynthesis Laboratory, Blaise Pascal University (CNRS URA 434), 63 177 Aubiere Cedex, France*

RESUMÉ. Reduction cathodique du 4,4'-dinitrodibenzyle assistee par ultrasons. Le travail présente la voltammétrie du 4,4'-dinitrodibenzyle en millieu alcoholique acide sur électrode-disque Pt/Hg, en absence et en présence des ultrasons produits d'une sonde ultrasonique (20 kHz) localisée à une courte distance de celle-ci, et directionés sur la surface d'électrode. On a étudié les effets de la distance entre l'extrémité de la sonde et la surface de l'électrode et de la vitesse de balayage sur le courant limite, et on les a comparé avec les mesures effectuées sur une électrode disque-tournante. Les conditions hydrodinamiques sont exprimées en termes de la vitesse de rotation necessaire dans la voltammétrie sur disque tournant pour obtenir des vitesses de transport de masse similaires.

1. Introduction

Mass transport is a very important aspect of electrochemical processes as well as of heterogeneous processes in general. Many heterogeneous reactions proceed under mass transport control and variation of the flux of material transported to and from the interface has been reported to cause in same cases a "switching" to a different reaction pathway [1]. In the literature there is widespread agreement on the dominant effect of ultrasound in electrochemistry being a strongly enhanced mass transport [2-24].

A macroscopic beam of liquid generated by ultrasonic horn ("acoustic streaming") [16, 25], a strong turbulent flow and microjets of liquid formed by transient cavitation [26, 27] close to the electrode surface may all contribute to this effect, and their relative contributions may be solvent and reactor geometry dependent. Furthermore, the intense soundfield causes changes at the electrode surface which have been described as cleaning [28, 29] or activation [30, 31].

The aim of this paper is to present experiments related to the ultrasound-assisted electroreduction of 4,4'-dinitrodibenzyle (DNDB) in ethanolic 2.5N H_2SO_4 solution. The role played by acoustic streaming and turbulence on one side, and microjetting on the other, in mass transfer enhancement will be shown.The effect of distance from sonicator tip to the electrode surface as well as the horn tip to the cell floor distance on limiting currents are considered and compared to measurements made at a rotating disk electrode. Hydrodynamic conditions are described in terms of the effective rotation rate which would be needed in rotating disk voltammetry to achieve similar transport rates.

2. Experimental

An ultrasonic cell disrupter (Sonics & Materials, CT) with an ultrasonic horn (titanium alloy, surface area 1cm^2) working at 20kHz frequency was used as the source of ultrasound. The output setting ca. 4 W, which correspond to an intensity of 4 W/cm^2 at the horn tip was found to be well adapted for sonication.

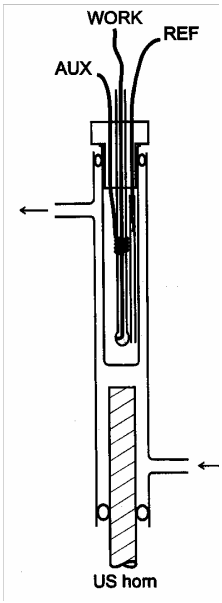

Figure 1. The sonoelectrochemical cell
working electrode: Pt/Hg
auxiliary electrode: Pt wire
refererence electrode: Ag wire

The electrochemical experiments were carried out with the help of the arrangement represented in Fig.1. An electrochemical cell of cylindrical shape (external diameter 16 mm) with a flat bottom was immersed in a larger glass tube (internal diameter 22 mm). The ultrasonic horn was situated at the bottom of this tube. Water flowing through this tube serves as a both a cooling agent and a coupling medium for transfer of ultrasound from the horn to the cell. An overpressure of 3 to 4 atm. was maintained inside the cooling water. In the absence of overpressure, an intense cavitation, *i.e.* formation of microbubbles, was observed near the horn tip inside the cooling water. It indicates that a large amount of ultrasonic energy was absorbed, and consequently only a low ultrasonic intensity was transferred to the vicinity of the electrode. With overpressure, the cavitation in the vicinity of the horn tip was much weaker, *i.e.* the transferred ultrasonic intensity was higher, and so formation of cavitating bubbles was observed in the vicinity of the electrode. Table 1 gives the values of the limiting reduction currents i_l of 4,4'-dinitrodibenzyle (DNDB) recorded at the stationary disc electrode under the following conditions of sonications: horn without and with overpressure. It indicates that the mass transfer coefficient $m = i_l / nFA$ [substrate] is ca **2.2 times higher** with overpressure than without. Table 1 also gives the rotation speeds, which would be obtained at a rotating electrode (Levich equation).

Table 1. Voltammetric data associated to the cathodic reduction of 4,4'-dinitrodibenzyle (2mM) in ethanolic 2.5 N H_2SO_4 solution under sonication on a stationary electrode, and under silent conditions at a rotating electrode; electrode / horn tip separation distance 5 mm and horn tip / cell floor separation distance 12 mm (scan rate 5 mVs^{-1}).

	Stationary electrode		Rotating electrode
	US horn with overpressure	US horn	No sonication
Limiting current [mA]	0.523	0.240	0.144
Rotation rate [rps]	659*	139*	50

* Equivalent rotation rate from the Levich equation (ν = 56.07 cm^2/s; D = $5 \cdot 10^{-6}$ cm^2/s; n = 12)

The main advantages result from this arrangement: (i) the horn is electrically isolated from the electrolyte and (ii) due to the cylindrical shape of the whole assembly all the acoustic energy is passing through a constant area of cca. 4 cm^2 and is not decreasing with the increasing distance from the horn.

The cell was equipped with three electrodes. A vertical position of the working electrode was used since it allows a free vertical movement of bubbles formed in the solution. A cylindrical Pt-net was used as an auxiliary electrode. An Ag wire quasi-reference electrode was placed near the surface of the solution where the intensity of ultrasound is low. A Pt/Hg-disc (ϕ = 1.5 mm) [32] was used as a working electrode. Voltammetric experiments were carried out using a PGSTAT 20, ECO CHEMIE potentiostat and for rde experiments a BAS-100 B/W electrochemical system was employed.

The cell without electrodes was filled with 10 ml ethyl alcoholic 2.5 N H_2SO_4 solution of DNDB and an aluminium kitchen foil was immersed. According to Pugin [33] the observation of the destruction of the foil by sonicaton allows the space in the cell with the most intense transient cavitation to be found, and the location of areas with and without transient cavitation to be discriminated. The foil was rapidly destroyed in the area at ca. 5 mm from the bottom of the cell, which proves an intense transient cavitation. Another area was observed where the destruction of the foil occurred (ca. 35 mm from the bottom of the cell). However, the destruction was much slower owing to weaker transient cavitation. Sporadic holes were sometime found on other parts of the foil but concentrated surface damage was located in only these two areas. These results show that the intensity of ultrasound varies with the distance from the horn being greatest near the bottom of the cell, and then decreases under the transient cavitations threshold and increases again above it after ca. 3.5 cm.

The cell was then washed, equipped with the three electrodes, the working electrode being positioned at 5 -12 mm from the bottom of the cell. It was filled with the electrolyte up to exactly the same level as previously in order to maintain the same distribution of ultrasonic energy, that is the volume of solution was ca. 8 ml.

Ethyl alcohol (Aldrich), sulfuric acid (Aldrich) and 4,4'-dinitrodibenzyle (Aldrich), recrystalised from toluene were used. The temperature was 20°C

without sonication, under sonication the temperature increased from 20°C up to ca.22°C.

3. Results and discussion

Voltammetric studies of 2 mM 4,4'-dinitrodibenzyle in ethyl alcoholic 2.5N H_2SO_4 solution on Pt/Hg electrode allow well-defined voltammograms to be recorded, both under silent conditions and under sonication, over a wide potential range. In Fig. 2 cyclic voltammogram (a) and sonovoltammogram (b) are shown.

Figure 2a illustrates that an irreversible $8e^-$ reduction (process 1) at $\varepsilon_{1/2}$ = - 0,55 V/Ag is followed by an irreversible $4e^-$ reduction (process 2) with a peak potential ε_{cp} = - 0,69 V/Ag.

$$O_2N–\phi–(CH_2)_2–\phi–NO_2 + 8e^- + 8H^+ \rightarrow HOHN–\phi–(CH_2)_2–\phi–NHOH \quad (1)$$

$$HOHN–\phi–(CH_2)_2–\phi–NHOH + 4e^- + 4H^+ \rightarrow H_2N–\phi–(CH_2)_2–\phi–NH_2 \quad (2)$$

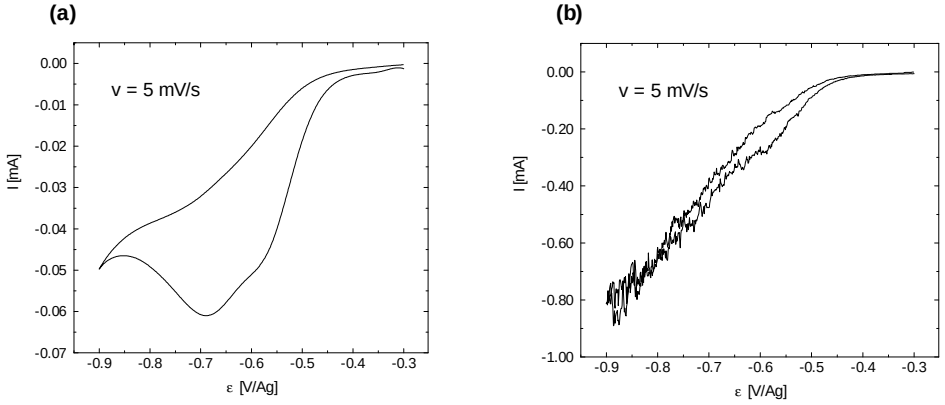

Figure 2. Cyclic voltammograms of 2 mM DNDB in the absence (a) and in the presence (b) of ultrasound

Figure 2b shows an analogous measurement except that 20 kHz ultrasound of intensity 2,8 W/cm^2 has been directed at the electrode surface, using the experimental arrangement described in figure 1 with a horn tip-electrode separation d = 5 mm. The average transport limited current is significantly enhanced as compared to the silent case, and the form of the voltammogram is qualitatively changed from that of a familiar cyclic voltammogram to a sigmoidal shape, indicative of a constant rate of transport of the electroactive species to the electrode surface so as to sustain an, in average, steady current. The magnitude of the current is considerably greater than that of the peak current seen under silent conditions.

In figure 3 two successive potential scans are shown. The limiting current decreases during the second potential scan, since it is as low as ca. 5-15 %

of its initial value. The same current is obtained after five successive scans as for the second scan.

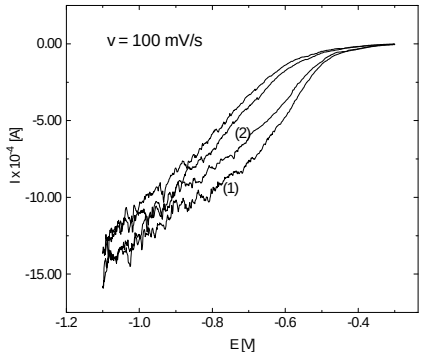

Figure 3. Succesive sonovoltammograms of 2 mM DNDB.

An important variable in sonoelectrochemical experiments is the distance between the electrode surface and the tip of the amplifying horn. Figure 4 confirms the expected current increase as the electrode is positioned closer to the region of highest cavitational intensity, near the tip of the amplifying horn. These experiments were performed maintaining a constant distance between the horn tip and the floor of the sonoelectrochemical cell.

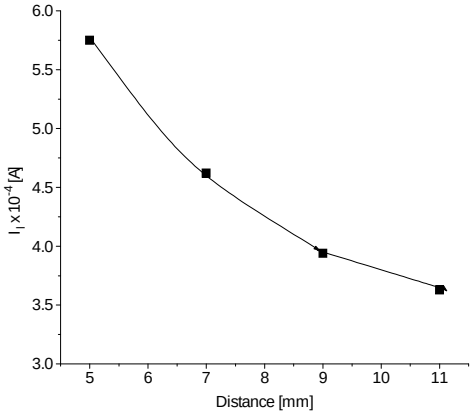

Figure 4. Limiting current *vs* separation distance between horn tip and electrode surface; horn tip/cell floor distance 12 mm, 2 mM DNDB in ethanolic 2.5 N H_2SO_4 solution.

Results presented in the table 2 indicate that scatter resulting from fluid profile changes at various horn tip/cell floor separation distances. It is minimized when small horn tip/electrode separation distances are employed. As is shown, if a distance of 5 mm is maintained between horn tip and electrode, a relative deviation of only 2 - 4% is found for limiting currents measured with horn tip/cell floor separation distances ranging from 1.5 to 12 mm.

Table 2.

Effect of distance from sonicator tip to cell floor on limiting current; 2 mM DNDB in ethanolic 2.5 N H_2SO_4 solution

Height above cell floor [mm]	$\mathbf{I_{ll} \cdot 10^{-4}}$ [A]	**Electrode / horn tip separation distance** [mm]
1.5	5.57	5
3	5.79	5
6	5.54	5
9	5.66	5
12	5.75	5

The mass transport limited current, I_{lim}, observed in sonovoltammetry may be described by the equation (3) [34,35]:

$$I_{lim} = n \cdot F \cdot A \cdot [substrate] \cdot m \qquad (3)$$

where [substrate] is the bulk concentration, $m = D/\delta$ is the average mass transport coefficient and the other symbols have their usual meanings.

Table 3 presents the limiting currents obtained from cyclic voltammetry, the equivalent rotation rates and the average mass transfer coefficients for the electroreduction of 2 mM DNDB in the presence of ultrasound.

Table 3

Limiting currents, equivalent rotation rate and average mass transfer coefficients for electroreduction of 2 mM DNDB in the presence of ultrasound; two successive potential scans.

v	$\mathbf{I_{lim} \cdot 10^{-4}}$ [A]		**rotation rate*** [rps]		$\mathbf{m \cdot 10^{-2}}$ [cm/s]	
[V/s]	1st cycle	2nd cycle	1st cycle	2nd cycle	1st cycle	2nd cycle
0.005	1.36	1.26	45	38	1.18	0.92

* Equivalent rotating rate - determinate from the equation:

$$I_l = 0{,}62 \cdot n \cdot F \cdot [substrate] \cdot A \cdot D^{2/3} \cdot \nu^{-1/6} \cdot \omega^{1/2}$$

By comparison, to duplicate the mass transport coefficient of 0.0273 cm/s calculated for the sonovoltammogram obtained at a scan rate of 0.010 V/s, a rotation rate of 75780 rpm would theoretically be necessary, an experimental improbability, as the onset of turbulence occurs rotation rates of > 10.000 rpm.

The significance of **m** obtained from sonovoltammetry is somewhat different from that for a rde. In the case of the rde, fluid velocity normal to the electrode surface remains constant from the bulk up to the outer edge of the hydrodynamic layer and is independent of the radial (r) and angular (φ) coordinates [34].

The mass transport coefficient then represents the volume flow per time per unit area ($cm^3/s \cdot cm^2$ = cm/s) [9]. In the cavitational environment of sonovoltammetry however, fluid velocity is expected to be highest at the sonicator tip,

to decrease normal to the tip, and then to increase again close to the electrode surface (due to the presence of fluid macrojets formed during interfacial bubble collapse), before finally dropping to zero at the solid/liquid interface. Furthermore, due to the turbulence nature of the flow patterns, the component of the fluid velocity normal to the electrode surface is not expected to be constant with respect to the radial or angular coordinates at a given distance from the electrode surface. For this reason, a mass transport coefficient measured in such an experiment represents a spatially average value over the electrode surface and is a time-varying quantity consisting of a steady-state component (m_{dc}) and a transient portion (m_{ac}) which sum to give the instantaneous value of the coefficient [34].

Characterization of the high rates of mass transport observed during sonovoltammetry, in terms of **m**, is useful due to the potential importance of these results in the areas of both sonochemistry[36] and industrial electrochemistry [37].

In table 4. are presented the mass transport coefficients determinated using a rotating-disk.

Table 4

Limiting currents and mass transport coefficients for electroreduction of 2 mM DNDB on Pt/Hg rotating disk electrode, in ethanolic 2,5 N H_2SO_4 solution; v = 0.005 V/s

ω [rps]	$I_{lim} \cdot 10^{-4}$ [A]	$m \cdot 10^{-2}$ [cm/s]
16.67	0.95	0.69
33.33	1.24	0.90
50	1.44	1.05
83.33	1.78	1.30

Using a comparison with a "classical" hydrodynamic technique, a rotating disk-electrode with a rotation speed of approximately 50 rps (3000 rpm) would be necessary to achieve an equivalent steady-state current as for cyclic voltammetry (at scan rate of 0,005 V/s) assisted by sonication (20 kHz, 4W/cm^2) (see also fig. 5).

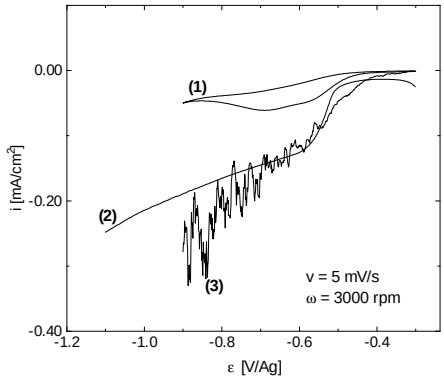

Figure 5. Voltammograms of 2 mM DNDB on stationary electrode, in absence (1), in presence (3) of ultrasound and on rotating disc electrode (2).

4. Conclusions

Examination of limiting currents obtained under a variety of sonochemical conditions yields information concerning the identity of the factors, which influence

the mass transport coefficient. Comparison of sonoelectrochemical experiments with rde measurements illustrates how acoustic cavitation and turbulence can influence steady-state currents. Minimisation of electrode-sonicator tip separation distance yields current values that are cell geometry independent.

REFERENCES

1. T. Ando, P. Bauchat, A. Foucaud, M. Fujita, T. Kimura, H. Sohmiya, *Tetrahedron Lett.,* 1991, **32**, 6371
2. V. Danciu, V. Co¿oveanu, E. Barabas, I.C. Ladiu, *Stud. Univ. Babes-Bolyai, Chem*., 1999, **44 1(2)**, 225
3. T. Ando, S. Sumi, T. Kawate, J. Ichihara, T. Hanafusa, *J. Chem. Soc. Chem. Commun.,* 1984, 439
4. a) C. Amatore, *Organic Electrochemistry,* (Ed. H. Lund, M.M. Baizer), Marcel Dekker, New York, 1991, b) C. Amatore, J.M. Saveant, *J. Electroanal. Chem.,* 1981, **123,** 189
5. P.H. Rieger, *Electrochemistry,* 2nd ed., Chapman & Hall, New York, 1994
6. R.G. Compton, J.C. Eklund, S.D. Page, T.J. Mason, D.J. Walton, *J. Appl. Electrochem.,* 1996, **26,** 775
7. F. Marken, J.C. Eklund, R.G. Compton, *J. Electroanal. Chem.,* 1995, **395**, 335
8. F. Marken, R.G. Compton, S.G. Davies, S.D. Bull, T. Thiemann, M. L. Melo, A.C. Neves, J. Castillo, C.G. Jung, A. Fontana, *J. Chem. Soc. Perkin Trans.,* 1997, **2,** 2055
9. A.J. Bard, L.R. Faulkner, *Electrochemical Methods*, J.W.Wiley & Sons, New York, 1980
10. R.G. Compton, J.C. Eklund, S.D. Page, *J. Phys. Chem.,* 1995, **99**, 4211
11. P.J. Daly, D.J. Page, R.G. Compton, *Anal. Chem*., 1983, 55, 1191
12. R.L. McCreery in A.J. Bard (Ed.), *Electroanalytical Chemistry*, Marcel Dekker, New York, 1991, vol. 17, p. 221
13. M.J. Weaver*, J. Phys. Chem.,* 1980, **84,** 568
14. R.G. Compton, J.C. Eklund, F. Marken, *Electroanalysis,* 1997, **9(7),** 509
15. V.G. Levich, *Physicochemical Hydrodynamics*, Prentice Hall, Englewood Cliffs, NJ, 1962
16. W. Le Mars Nyborg, *Physical Acoustics*, (Ed. W.P. Mason), Academic Press, New York, 1965, p. 265
17. H.A.O. Hill, Y. Nakagawa, F. Marken, R.G. Compton, *J.Phys. Chem*, 1996, **100,** 17395
18. C.M.A. Brett, A.M.O. Brett, *Electrochemstry*, Oxford University Press, Oxford, 1993, p. 93
19. F. Barz, C. Bernstein, W. Vielstich, *Adv. Electrochem. Electrochem. Engineer.* 1984, **13,** 261
20. S.A. Perusich, R.C. Alkire, *J. Electrochem. Soc.*, 1991,**138,** 700; 708
21. J. Reisse, H.H. Francois, J. Vandercammen, O. Fabre, A. Kirsch-de Mesmaeker, C. Maerschalk, J.L. Delplancke, *Electrochim. Acta*, 1994, **39,** 37
22. R.G. Compton, J.C. Eklund, F. Marken, D.N. Waller, *Electrochim. Acta*, 1996, **41,** 315
23. H. Huck, *Ber. Bunsenges. Phys. Chem.*, 1987, **91,** 648
24. C.R.S. Hagan, L.A. Coury Jr., *Anal. Chem.,* 1994, **66**, 599
25. J. Lighthill, *Wawes in Fluids,* Cambrige University Press, Cambrige, UK, 1978, p. 338
26. J. Klima, C. Bernard, C. Degrand, *J. Electroanal. Chem.,* 1995, **399,** 147
27. P.R. Bikin, S. Silva-Martinez, *J. Chem. Soc., Chem. Commun.,* 1995, 1807

28. A. Benahcene, C. Petrier, G. Reverdy, P. Labbe, *New J. Chem.,* 1995, **19,** 989
29. R.C. Alkire, S. Perusch, *Corros. Sci.,* 1983, **23,** 1121
30. H. Zhang, L.A. Coury, Jr., *Anal. Chem.,* 1993, **65,** 1552
31. J. O'M. Bockris, A.K.N. Reddy, *Modern Electrochemistry,* vol. 2, Plenum Press, New York, 1970, p. 1170
32. W.A. Koehler, *Application de l'Electrochimie,* Dunod, 1967
33. B. Pugin, *Ultrasonics,* 1987, **25,** 49
34. C.R.S. Hagan, L.A. Coury, Jr., *Anal. Chem.,* 1994, **66,** 399
35. R.G. Hickman, *Plating,* 1965, **52,** 407
36. J.A. Rooney, *Ultrasound: Its Chemical, Physical and Biological Effects,* K.S. Suslick Ed., New York, 1988, 65-96
37. J.R. Selman, C.W. Tobias, *Advances in Chemical Engineering,* T.B. Drew, G.R. Cokelet, J.W. Hoopes, T. Vermeulen Eds., New York, 1978, vol. 10, 211-318

STUDIA UNIVERSITATIS BABEŞ-BOLYAI, CHEMIA, XLVI, 1-2, 2001

ELECTROFILTRATION. THE INFLUENCE OF AN ELECTRICAL FIELD ON FILTRATION

A. GHIRISAN[*], K. WEBER[**] and W. STAHL[**]

[*]Faculty of Chemistry and Chemical Engineering, "Babes-Bolyai" University of Cluj-Napoca, Romania
[**]Institute of Mechanical Process Engineering and Applied Mechanics, University of Karlsruhe (TH), Germany

ABSTRACT. The combination of mechanical and electrical filtration was examined on a new laboratory filtration equipment (with a double-sided filtration cell) at the University of Karlsruhe, Germany. This method seems to lead to enhance of the filtration kinetics. The electrofiltration experiments with quartz sand (average particle size $d_{50\%}$ = 2 μm) in tap water of Karlsruhe (conductivity $\lambda \cong 700$ μS/cm) showed that the electrokinetic effects (electrophoresis and electroosmosis) accelerate the kinetic of the pressure filtration. However, on the residual moisture the electrical field has only a very small influence (the residual moisture remains as in the case of simple pressure filtration around 33-35%).

KEYWORDS: electrofiltration, electrokinetic effects, electroosmosis, electrophoresis, and pressure filtration.

INTRODUCTION

The separation of solids from liquids by filtration may be divided into three broad areas of interest:

1. *Surface filtration* of dilute suspensions where the liquid is usually the desired product.
2. *Depth filtration* in which small contaminants are retained in the filter medium itself.
3. *Cake filtration* where the solids quickly "take over" and act as the filter medium.

By the cake filtration, which was used in this work, the liquid flows through a filter medium, on which the solids deposited gradually increase in thickness. The particles form the cake, which then act themselves as a filter. It is generally accepted that the filtration resulting in a filter cake takes place by bridging mechanism over the surface pores within a filter medium. This helps to prevent the medium from clogging with fine particles.

The influence of electrical field on the solid-liquid separation of fine particles was in the attention of the researchers all over the world. The main research goal was usually the influence of the electrical field on the reduction of the moisture in the filter cakes, as an alternative to thermal procedures [1].

In the present work the main goal of our research was focused on the influence of an electrical field on the kinetic of the filtration. If an electrical field is applied on the cake-building filtration, an acceleration of filtration kinetics appears because of the electrokinetic effects [2]. Electrofiltration, the combination

of mechanical simple pressure filtration and electrical filtration, can be a useful technique for the filtration of fine suspensions to prevent usual problems like long filtration time or blocking of filter pores. The electrokinetic effects (electroosmosis and electrophoresis) were due to the developing of electrical double layer on the particle surface [3].

Formation of electrical double layer and the electrokinetic effects

If solid particles are in contact with electrolytic fluids, the dissociation of molecular groups and/or by specific adsorption of anions and cations cause a distribution of electric charge carriers at the phase boundary. The existing boundary charge attracts ions of opposite charge from the layer near the interface. Some of these dissolved ions are attracted so strongly to the surface that they can be regarded as fixed to the particle. The other ions form a diffusive layer around the particle (model of Stern [2]). The mostly negative boundary charge of the particles can be used to introduce a new force into the process by applying an electric field. According to the classical model [2] the wandering of the charged colloidal particles in the electric field is due to electrophoresis. Under electroosmosis take place the movement of the surrounding charged liquid of the diffusive double layer relative to the solid phase.

To describe the influence of the electroosmosis and electrophoresis on the electrofiltration process, Yukawa [4] based his model on Darcy's law:

$$\frac{dV_L}{dt} = \frac{\Delta p_H \cdot A}{\eta\left(r_C \cdot K \cdot \frac{V_L}{A} + R_m\right)} \tag{1}$$

where V_L is the volume of filtrate (m^3), Δp_H the pressure drops of the system (bar), A the area of the filter (m^2), η the liquid viscosity (kg/m.s), r_c the resistance of the cake (m^{-2}), R_m the resistance of the filter medium (m^{-1}) and K the concentration factor.

For constant pressure Equation (1) may be integrated under the form:

$$\frac{t}{V_L} = \frac{\eta \cdot r_C \cdot K}{2 \cdot \Delta p_H \cdot A^2} \cdot V_L + \frac{\eta \cdot R_m}{\Delta p_H \cdot A} \tag{2}$$

to give the resistance of the cake and the resistance of the filter medium R_m:

$$r_C = \frac{2\Delta p_H \cdot A^2 \cdot a}{K \cdot \eta} \qquad R_m = \frac{\Delta p_H \cdot A \cdot b}{\eta} \tag{3}$$

where a is the slope and b is the intercept of the linear correlation t/V_L *versus* V_L.

Yukawa considered electroosmosis as an additional pressure added to the applied hydraulic pressure. In this way, the entire filtration pressure results from the overlapping of the hydraulic pressure Δp_H and electroosmotic pressure Δp_E. Electrophoresis, in addition, reduces the filtration velocity of the

particles. If the electric field (E) reaches a critical value (E_{crit}), the electrophoretic velocity equals the filtration velocity, and the particles reach a stationary condition. The corresponding field strength is defined as the critical field strength (E_{crit}). The resulting velocity is zero, and there is no cake build up. Yukawa considered this effect using the electrophoretic coefficient (E_{crit}-E)/E_{crit}. This leads to a principal equation of pressure electrofiltration:

$$\frac{dV_L}{dt} = \frac{(\Delta p_H + \Delta p_E) \cdot A}{\eta \left(r_C \cdot K \cdot \left(\frac{E_{crit} - E}{E_{crit}} \right) \cdot \frac{V_L}{A} + R_m \right)} \tag{4}$$

The transformation and integration of this equation under the assumption that both the electroosmotic pressure as well the critical electrical field strength remain constant during the entire time of the experiment, provides the linear dependence of t/V_L to V_L:

$$\frac{t}{V_L} = \frac{\eta \cdot r_C \cdot K \cdot \left(\frac{E_{crit} - E}{E_{crit}} \right)}{2 \cdot (\Delta p_H + \Delta p_E) \cdot A^2} \cdot V_L + \frac{\eta \cdot R_m}{(\Delta p_H + \Delta p_E) \cdot A} \tag{5}$$

EXPERIMENTAL

The measurements were performed on new laboratory filtration equipment (Fig.1). The components of the laboratory equipment are: the computer with the EXCEL software tool, the power supply with the display control for the voltage, pressure manometer and pressure regular, the suspension container, the double-sided filtration cell and the balance. The laboratory filtration equipment from Karlsruhe offers a new possibility to analyse the filtration kinetics on the double-sided filtration simulating the filtration on a filter press.

The cumulative filtrate weight, the voltage and the current were recorded online by the computer and analysed by EXCEL software.

The main part of the equipment is the double-sided filtration cell (4 cm width), which consists of a middle part and two covers (Fig. 2). In both covers there is an electrode and a filter medium on a supporting lattice. On the specially designed pressure electrofiltration cell simulating the chamber of a filter press, the cake was built on two-sided. The filtrate flows from the middle part in two directions (to the left and to the right) similar to filter presses, through the filter medium and through the electrode, and then through the hoses onto the balance. At the beginning of each experiment the filter cell is filled with suspension and the covers are filled with water to ensure that the first drop of filtrate will be registered on the balance immediately. With this equipment, simple pressure filtration experiments (hydraulic pressure Δp_H = 4 bar) and electrofiltration experiments (Δp_H = 4 bar and the voltage between U = 20 V - 80 V) were performed. For the same experiment the equipment was operated at constant voltage and constant hydraulic pressure Δp_H = 4 bar.

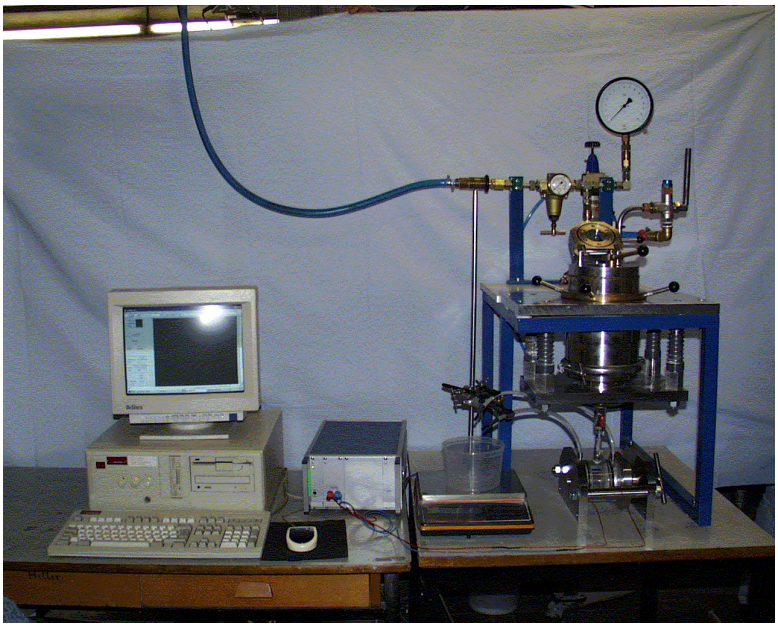

Fig. 1. Laboratory filtration equipment.

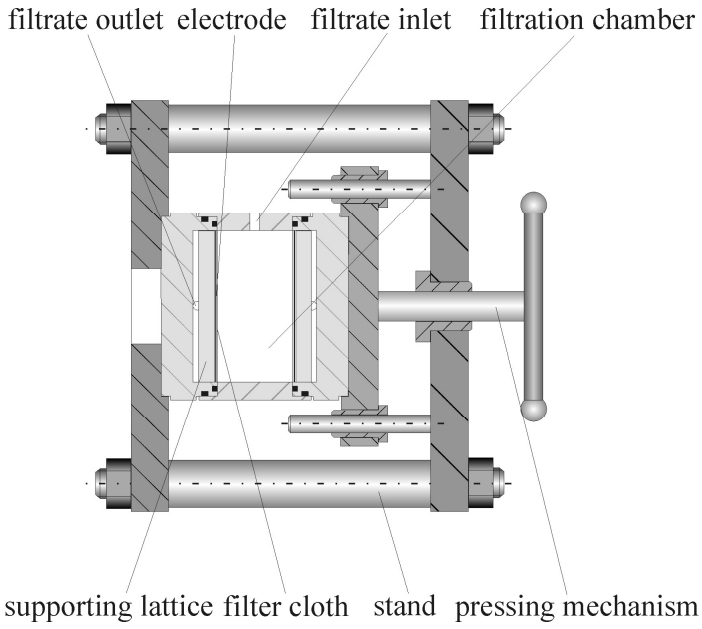

Fig. 2. The two-sided pressure electrofiltration cell.

Three to five replicate runs were carried out for each set of experimental conditions. The reproducibility of the experiments was for each case higher than 99.5 %. The surface of filtration totalises on both sided 51.5 cm^2.

Quartz sand SF 800 (density ρ_s = 2650 kg/m^3 and average particle size $d_{50\%}$ = 2 µm) from Quarzwerke (Frechen) was suspended in tap water of Karlsruhe (conductivity λ = 700 µS/cm) for the cake filtration experiments. The volume concentration of the solid was c_v = 20 % for all experiments.

A filter cloth of the company Sefar with the designation 03-5/1 made of polyamide PA 6.6 with mean mesh size of 5 µm and an open filter surface of 1 % was used.

RESULTS AND DISCUSSION

To analyse the filtration kinetics, the amount of filtrate volume accumulation was plotted over the filtration time (Fig. 3). The rapid increase of the filtrate volume at the beginning of each experiment can be explained by the redusing cake resistance. When the filtration cake reaches the maximale width the filtrate volume reaches the finally equilibrium value and the curve becomes flat.

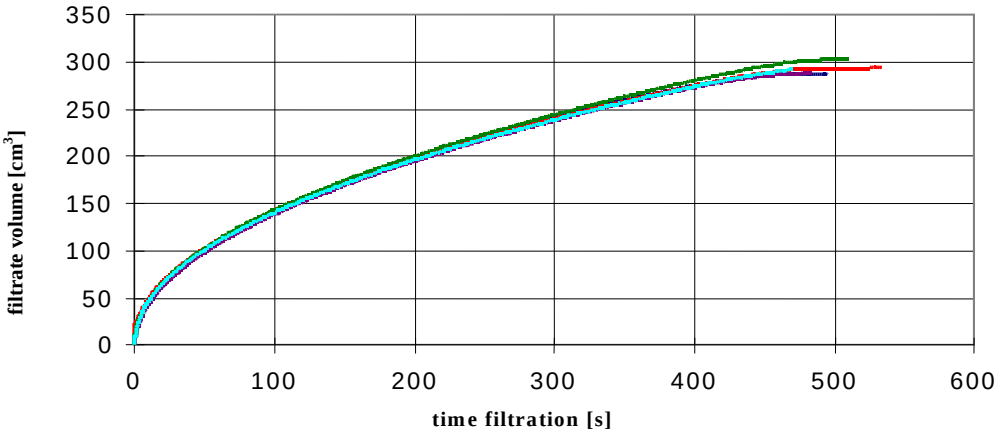

Fig.3. Filtrate volum *versus* time for filtration experiments with SF800, c_V = 20%, Δp_H = 4 bar and U = 80 V.

Five replicate runs of the experiments (carried out for electrofiltration with an electrical field of U = 80 V and the hydraulic pressure Δp_H = 4 bar) are shown in this diagramm. The reproductibility of the experiments was here and for each set of experimental conditions higher than 99.5%.

A direct comparison between simple pressure filtration and electrofiltration is shown in Figure 4 and 5. In Figure 4 the filtrate volume is plotted over the filtration time, in Figure 5 the time per filtrate volume is plotted over the filtrate volume. Figure 4 shows that the filtration kinetic was accelerated with increasing voltage. To reach for example, a filtrate volume of 250 g, it took 330 s without the use of an electric field. With an applied voltage of U = 40 V it lasted 295 s and 260 s with U = 80 V.

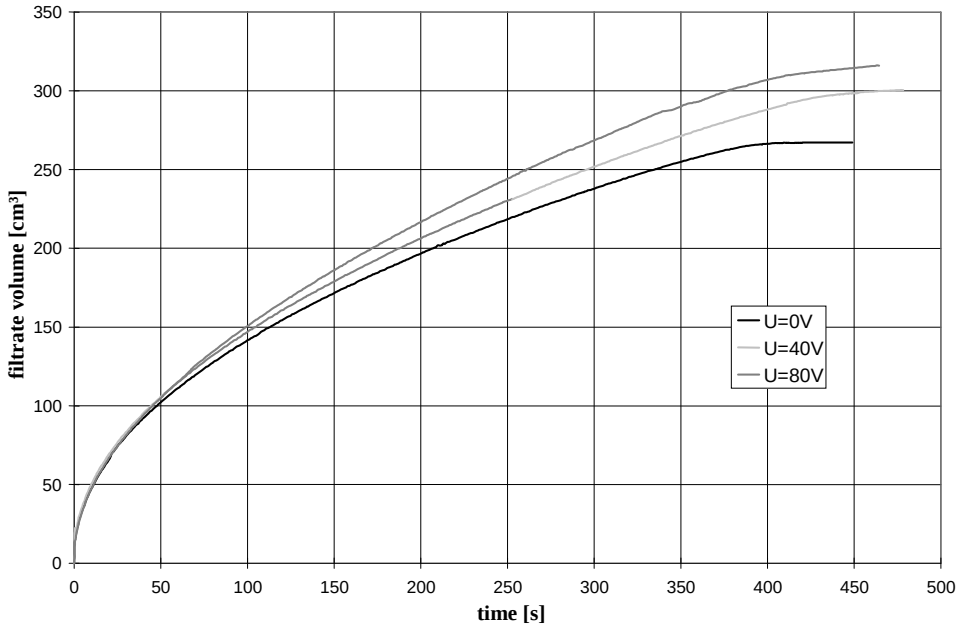

Figure 4. Comparison of three experiments for SF800, c_V=20%, Δp=4bar, b=4cm.

This kinetic acceleration can also be seen in the lower gradient of the plots with electric field in Figure 5. Based on equation (5) the specific filter cake resistance and the resistance of the filter medium can be determined by the gradient and the ordinate cut of the pressure filtration experiment with and without electric field. This calculation led to a specific filter cake resistance of $r_C = 5.3 \cdot 10^{14}$ m^{-2} and the resistance of the filter medium $R_m = 1.65 \cdot 10^{10}$ m^{-1} in the case of simple pressure experiment (U = 0 V). A value of the cake resistance $r_C = 4.35 \cdot 10^{14}$ m^{-2} was determined for the voltage of 40 V (E = 1000 V/m) and $r_C = 3.26 \cdot 10^{14}$ m^{-2} at 80 V (E = 2000 V/m). The gradient, and in this way the cake resistance, was reduced by using of the electric field.

For a two-sided cake building filtration electrophoresis reduces the cake build-up on the cathode side and increases it on the anode side [1]. In addition electroosmosis benefits the filtrate flow to the cathode, so that the bigger part of the total filtrate can be obtained on the cathode side. The results show that the negative effect on the anode side is covered by the positive effect of the cathode side. Thus the kinetic of electrofiltration has been accelerated.

The experiments with electric field showed that the electrolysis did not influence the results. The electrolytic gas did not penetrate the cake (the electrodes are situated outside of the cake) and so the electrolysis can be neglected. The influence of the electrolytic gas on the reducing of the moisture was also negligible (the residual moisture was around 34-35 % when the filtration was carried out with or without electric field, see Table 1). It turned out that the residual moisture could only be reduced minimally through the electric field [5].

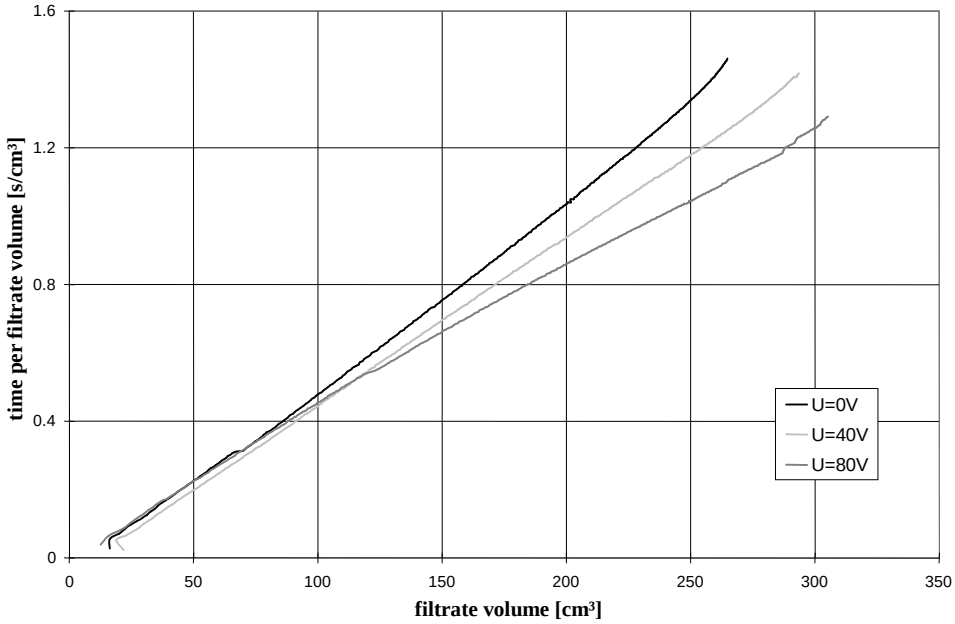

Figure 5. t/V_L vs. V_L for SF800, c_V=20%, Δp=4bar, b=4cm.

The separation of the thermal and the electrolytic processes showed that the electrokinetic effects represent the main influencing factors during the acceleration of the filtration kinetics [1]. From the same reason, the temperature is constant for a long time and only at the end of the experiment, when a very small volume of the filtrate flows trough the filtration chamber it increased slowly (2 - 5^{o} C). In this way the heating of the liquid during the filtration and the modification of the viscosity of the filtrate which can influence the flow of the filtrate can be negligible.

Table 1.

The residual moisture of the filtration cake with and without electric field.

Critical Number	Voltage of electric field (V)	Rest moisture
1.	0	0.323
2.	0	0.330
3.	20	0.333
4.	20	0.331
5.	40	0.332
6.	40	0.334
7.	50	0.345
8.	50	0.343
9.	60	0.350
10.	60	0.350
11.	80	0.350
12.	80	0.345

CONCLUSIONS

Based on an approch of Yukawa it was developed a model which could describe the two-sided pressure electrofiltration. In this way the combination of mechanical and electrical filtration is an effective method to enhance the filtration kinetics. With use of an electrical field the kinetics of cake building pressure of fine particles could be accelerated in a small laboratory filter cell with double-sided filtration surface. Due to the electrokinetic effects the filtration kinetic was inflenced strongly. The effect of the electrophoresis reduced the cake build-up on the cathode side and increases it on the anode side. In addition electroosmosis benefits the filtrate flow to the chatode. The positive effect on the cathode side covers the negative effect on the anode side.

REFERENCES

1. K. Weber and W. Stahl, *Filtrieren und Separieren*, 2000, **1**, 14
2. A. M. James, *Surface and Colloid Sience*, 1979, **11**, 121
3. H. J. Jacobasch, H. Kaden*, Z. Chem.,* 1983, **23**, 81
4. H. Yukawa, K. Kobayashi, Y. Tsukui, S. Yamano and M. Iwata, *J. Chem. Eng. Jap.,* 1976, **9**, 396
5. W. Bender*, Chem. Ing. Tech*., 1983, **55**, 823

STUDIA UNIVERSITATIS BABEŞ-BOLYAI, CHEMIA, XLVI, 1-2, 2001

PHOTOMETRIC DETERMINATION OF BIURET IN MELTED UREA USING FLOW INJECTION ANALYSIS

TIBERIU FRENTIU, MICHAELA PONTA, EUGEN DARVASI, LADISLAU NAGY-KEKEDY, IOAN MĂRGINEAN and EMIL A. CORDOŞ

University "Babeş-Bolyai", Dept. of Chemistry, 3400 Cluj-Napoca, Romania

ABSTRACT. A sensitive, rapid and automatable flow injection fotocolorimetric analysis is described for the determination of biuret in melted urea as blue-violet $[CuBt(OH)_2]^{2-}$ complex in strongly basic medium (pH>13). The automatic system consists of a refractometer and a double beam automated photometer equipped with a green filter (530-570 nm). The sample and reagents ($CuSO_4$ $5H_2O$ 15 g l^{-1} and an alkaline solution of tartrate 50 g l^{-1} in NaOH 40 g l^{-1}) are mixed in a 4:1:1 volumetric ratio. The kinetic study and the absorption spectra have shown the development of $[CuBt(OH)_2]^{2-}$ complex in the system urea-biuret-Cu-tartrate as a result of the decomposition of tartric complex according to a 1:1 stoechiometry. The experimental conditions were optimised at 555 nm where the best limit of detection, calibration and analytical sensitivities are obtained. For a detection limit of 0.05 % biuret in urea (m/m), the method allows the quantitation of biuret in the range 0.25-2.5% with an RSD lower than 10%. This approach offers significant advantages in terms of speed (5 samples/hour), automation and precision compared with existing manual procedures.

INTRODUCTION

Urea is the most important nitrogenous fertiliser with the best agrochemical properties. Urea losses are a real problem in the process of concentration of urea solution by evaporation. Ostrogovici *et all*. have studied the successive processes involved in the urea thermolysis and the mechanism of biuret development [1]. They indicated that the loss of urea by evaporation is due to both hydrolysis and formation of biuret from urea condensation (eqns. 1,2):

$$(NH_2)_2CO + H_2O = 2\ NH_3 + CO_2 \quad (1)$$

$$2(NH_2)_2CO = NH_2 - CO - NH - CO - NH_2 + NH_3 \quad (2)$$

While hydrolysis results in losses in urea quantity, the resulted biuret is an impurity in the final product and depreciates the fertiliser quality as it has a toxic action on plants and animals. The two $-NH_2$ groups in the molecule are responsible for the slightly basic character of the biuret whose corresponding stepwise dissociation constants are $K_1=10^{-9.2}$ and $K_2=10^{-12.15}$ [2]. Biuret is slightly soluble in water, but its solubility increases in basic media (NaOH, KOH, Na_2CO_3) [3] as well as in the presence of urea [4]. Generally, the biuret content in granulated urea is in the range of 0.4-2% and below 0.1% in crystallised urea. The biuret formation could be avoided if evaporation occurs at as low as possible temperature and pressure with short time maintenance in the evaporator.

In order to discourage the biuret formation it is necessarily to continuously determine the biuret content in melted urea. The knowledge of this content makes possible the intervention in the thermal stage of the urea concentration process.

Among the methods used to determine biuret, the most common are those based on the total nitrogen determination (Kjeldahl method) [5], the photocolorimetric determination of complex developed between biuret and different cations (Ni^{2+}, Cu^{2+}, Co^{2+}) [6-13], potentiometric titration with Cu^{2+} solution [14], amperometric titration [15] and polarographic determination [16].

The colorimetric method is best suited to be automatabled. Thus, an automated Technicon Autoanalyser was achieved [17]. An other automated apparatus based on a different photocolorimetric method was reported [18, 19].

This paper presents a sensitive and rapid flow injection photocolorimetric analysis for the determination of biuret as Cu-biuret complex in melted urea in the range 0.25-2.5%. The study and optimisation of the method in order to adapt it to flow injection analysis is presented. Thus the physical, chemical and time parameters of Cu-biuret complex development, the spectra of biuret-Cu-tartrate and urea-biuret-Cu-tartrate systems, the optimum experimental conditions using synthetic solution of urea-biuret were under study.

EXPERIMENTAL

Reagents. Biuret stock solution (2 g l^{-1}) was prepared by dissolving 2 g biuret and 4 g NaOH in 1 l solution. Urea stock solution (7.8 % m/v) was prepared by dissolving urea in distilled water. Copper sulphate (15 g $CuSO_4 \cdot 5H_2O$ g l^{-1}) solution and alkaline solution of sodium potassium tartrate tetrahidrate (50 g l^{-1} and 40 g l^{-1} NaOH) were also prepared. All reagents were of analytical grade (Flucka). At the same time, standard solutions of urea-biuret were prepared of 20 ml urea, 0…2 ml of biuret, 5 ml of tartrate and 5 ml of $CuSO_4$ stock solutions. All dilutions were made with distilled water to 50 ml. The standard solutions prepared as shown above have a biuret level in technical urea (urea+biuret) up to 2.5%. Standard solutions containing only biuret (without urea) were similarly prepared.

The absorption spectra for biuret-Cu-tartrate and urea-biuret-Cu-tartrate solutions were read against distilled water as blank. In the kinetic study and calibration curves construction, the blanks were Cu-tartrate and urea solution, respectively.

Instrumentation. The photocolorimetric measurements were carried out using the double beam photometer FEK-56M, the UV-VIS spectrometer M40 Karl Zeiss Jena (Germany) and the Automated Batchmeter of Biuret in Urea (ADAB-01, Research Institute for Analytical Instrumentation, Cluj-Napoca, Romania). The schematic diagram of the ADAB-01 is depicted in Fig. 1.

The ADAB-01 previously described is designed as a three-modular system consisting of a reagents and urea sample batchmeter, a refractometer and a double-beam automated photometer equipped with two photocells as

optical detectors [18,19]. The sample is continuously prepared from the melted urea resulted from the technological process further diluted to a concentration of 7-10%. The resulting solution passes through the refractometer in order to determine the accurate concentration in urea. The solution is then passed through an automated dosing system to the photometer for the determination of the biuret level. Than, the urea solution is mechanically mixed with reagents (copper sulphate and tartrate solutions) in a 3 cm-cell and after 10 min it is photometrated against urea solution as blank using a green-filter (530-570 nm). The mixing ratio urea sample: copper sulphate: tartrate is 4:1:1 (v/v/v). The controller sets out the biuret level in the original melted urea within an accuracy of ±5%. Five such determination sequences are possible in an hour.

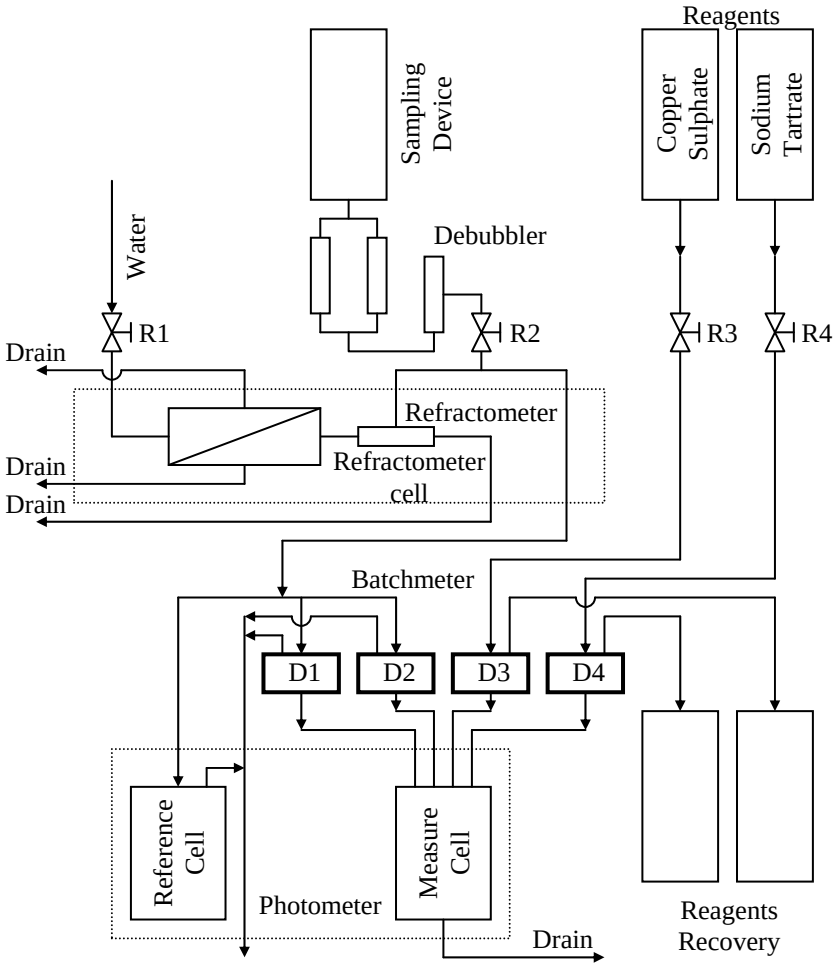

Fig.1. Bloc diagram for the Automated Batchmeter of Biuret in Urea ADAB 01

RESULTS AND DISCUSSION

Kinetic study. In the kinetic study of Cu-biuret complex development the absorbance change versus time for standard solutions of biuret-Cu-tartrate with constant content of reagents and different levels of biuret was followed. After adding the reagents, the absorbance was read at different times against the corresponding blank using a FEK-56M photocolorimeter, on the green filter (530-570 nm) in a 2-cm cell. The kinetic curves are presented in Fig. 2. As it can be seen, the absorbance changes significantly in the first two minutes after the addition of the reagents and remains almost constant after 8-12 minutes for all solutions under study. Consequently, all further measurements were performed 10 minutes after the addition of reagents.

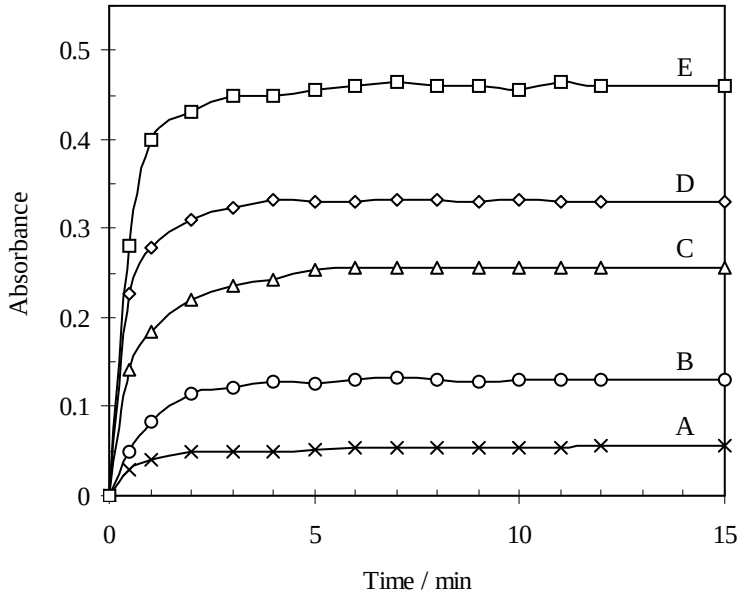

Fig. 2 Kinetic curves as absorbance-time variation for 0.006 (A); 0.02 (B); 0.03 (C); 0.04 (D) and 0.06 % (E) biuret in solution (m/v). Green filter (530-570 nm), 2-cm cell.

Absorption spectra and calibration curves. Copper ions develop differently co-ordinated complexes with biuret according to the pH range. Among these, the red-violet $[CuBt_2]^{2-}$ and the blue-violet $[CuBt(OH)_2]^{2-}$ intern complexes with maximum absorbances at 505 nm and 564 nm, respectively, are mentioned. The first complex develops generally in the range 10-12 pH, while the second at pH higher than 13. The structures of these complexes are presented in Fig. 3:

The recording of absorption spectra of Cu-biuret complexes was necessarily in order to study the mechanism of their development and the influence of urea on the complex absorbance. With this purpose, two sets of spectra of Cu-tartrate and Cu-biuret complexes developed both in the presence and in the absence of 3.12 % urea (m/v) and different biuret contents were

recorded. In both sets of solutions the biuret content was in the range 0.008-0.08 % (m/v) that corresponded to 0.25-2.5% biuret in solid urea. Spectra obtained with a Specord UV/VIS spectrophotometer in the range 450-800 nm are shown in Fig 4a,b. Unlike the Cu-biuret complexes, copper-tartrate complex exhibits a maximum absorption at 680 nm both in the presence and in the absence of urea and does not show a significant absorbance in the range 500-580 nm.The presence of urea in solution does not have an impact on the development of Cu-biuret complexes as it suggests the similitude of spectra presented in Fig. 4a,b. As the biuret is added in Cu-tartrate solution, the maximum absorbance moves from 680 nm to 580 nm, that indicates the formation of an other complex, Cu-biuret. The isosbestic point at 640 nm demonstrates the formation of Cu-biuret complex as a result of the decomposition of Cu-tartrate complex according to 1:1 stoechiometric equilibrium.

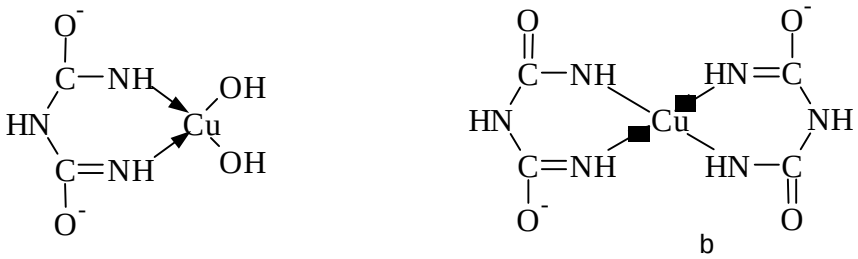

Fig. 3. a. Blue-violet $[CuBt(OH)_2]^{2-}$ complex (absorption maximum at 564 nm);
b. Structure of red-violet $[CuBt_2]^{2-}$ complex (absorption maximum at 505 nm)

On the basis of Cu-biuret-tartrate and Cu-urea-biuret-tartrate spectra, the chemical echilibria established in solution could be explained. In weakly alkaline medium, copper ion develops the $[Cu(OH)_4]^{2-}$ easily soluble complex with the stability constant of $1.3\ 10^{18}$ [20]. In strongly basic medium, copper ion could precipitate. To avoid this, a complexation reagent such as tartrate is added, which develops with copper ion mainly the $[CuT(OH)_2]^{2-}$ and $[CuT_2]^{2-}$ complexes with the stability constants of $1.4\ 10^{21}$ and $10^{5.4}$ [20, 21] (eqns. 3-6).

$$Cu^{2+} + 2OH^- \leftrightarrow Cu(OH)_2$$

$$Cu(OH)_2 + 2OH^- \leftrightarrow \left[Cu(OH)_4\right]^{2-} \tag{3}$$

$$\left[Cu(OH)_4\right]^{2-} + T^{2-} \leftrightarrow \left[CuT(OH)_2\right]^{2-} + 2OH^- \tag{4}$$

(5)

$$2Cu^{2+} + OH^- + 3T^{2-} \leftrightarrow \left[Cu_2T_3(OH)\right]^{3-} \leftrightarrow \left[CuT_2\right]^{2-} + Cu^{2+} + T^{2-} + OH^-$$

(6)

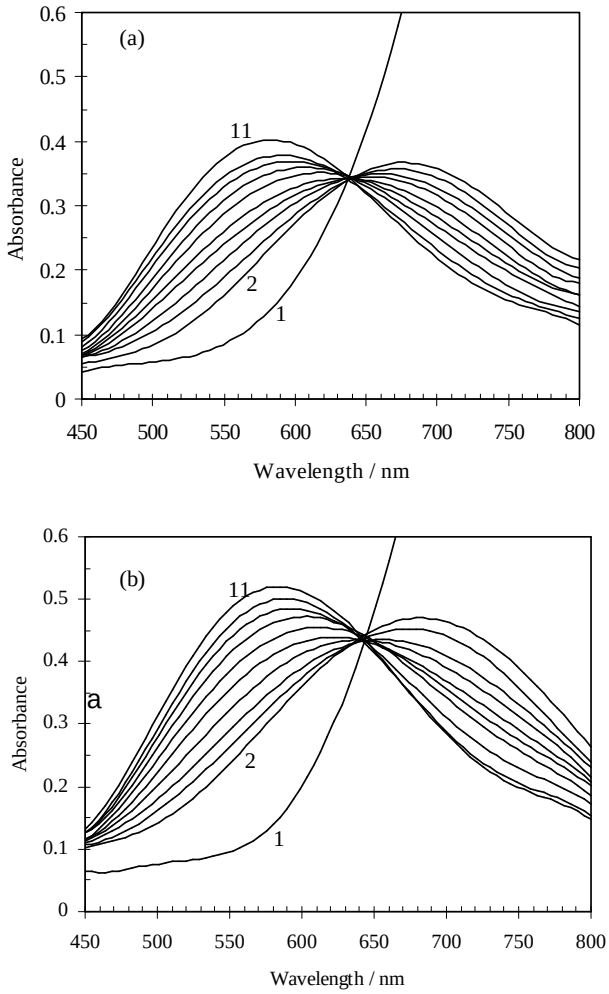

Fig. 4. Absorption spectra of copper-biuret and copper tartrate complexes (pH>13) in the absence (a) and in the presence of 3.12 % (m/v) urea content (b). Biuret content (m/v) in solutions: 0.008 % (curve 2) - 0.08% (curve 11). Curve (1): absorption spectra of copper-tartrate complex in the absence (a) and in the presence (b) of urea.

As biuret is added to the Cu-tartrate solution, the Cu-biuret complex develops as a result of the decomposition of tartric complexes according to a 1:1 stoechiometric equilibrium (eqns. 7-9).

$$\left[CuT(OH)_2\right]^{2-} + Bt^{2-} \leftrightarrow \left[CuBt(OH)_2\right]^{2-} + T^{2-} \quad (7)$$

$$\left[CuT_2\right]^{2-} + Bt^{2-} + 2OH^- \leftrightarrow \left[CuBt(OH)_2\right]^{2-} + 2T^{2-} \quad (8)$$

$$\left[CuT_2\right]^{2-} + 2Bt^{2-} \leftrightarrow \left[CuBt_2\right]^{2-} + 2T^{2-} \quad (9)$$

In the range of 10-12 pH the existence of the red-violet $[CuB_2]^{2-}$ complex with a maximum absorbance at 505 nm prevails, while in strongly basic medium (pH>13) the blue-violet $[CuBt(OH)_2]^{2-}$ complex with a maximum absorption at 564 nm is predominant. As compared with $[CuBt(OH)_2]^{2-}$, the $[CuBt_2]^{2-}$ complex is much more stable ($K= 10^{22.78}$) [21] but exhibits a lower molar extinction coefficient. At pH above 13, the development of the $[CuBt(OH)_2]^{2-}$ complex with a higher extinction coefficient is advantaged. Thus, to improve the sensitivity of the method as compared with other photometric procedures, the determination of biuret as $[CuBt(OH)_2]^{2-}$ at pH>13 was chosen.

In order to select the optimum wavelength for the photometric determination of biuret using ADAB-01, calibration curves in the range 0.25 – 2.5% biuret in urea at 500; 527; 555; 580 nm were constructed. The statistical data for the calibration curves of $[CuBt(OH)_2]^{2-}$ complex in urea-biuret-Cu-tartrate as well as the analytical performances are shown in Table 1.

Table 1.

Calibration results and analytical performances

	Wavelength (nm)			
Parameter	500	527	555	580
Linear range [a]/ %	0.25-2.5	0.25-2.5	0.25-2.5	0.25-2.5
R [b]	0.9991	0.9991	0.9992	0.9985
$(h\pm s_h)$ [c]	$3.2\ 10^{-4}\pm2.1\ 10^{-3}$	$2.7\ 10^{-4}\pm2.3\ 10^{-3}$	$4.6\ 10^{-4}\pm1.6\ 10^{-3}$	$1.0\ 10^{-3}\pm2.7\ 10^{-3}$
$(m\pm s_m)$ [d]	$76\ 10^{-3}\pm1.6\ 10^{-3}$	$103\ 10^{-3}\pm1.4\ 10^{-3}$	$114\ 10^{-3}\pm1.110^{-3}$	$98\ 10^{-3}\pm1.8\ 10^{-3}$
s_s [e]	$4.2\ 10^{-3}$	$3.6\ 10^{-3}$	$2.7\ 10^{-3}$	$4.8\ 10^{-3}$
γ [f], $\%^{-1}$	18	29	42	20
LOD [g], %	0.10	0.08	0.05	0.10
LOQ [h], %	0.50	0.40	0.25	0.50
m_c [i], %	0.06	0.04	0.04	0.05

[a] The number of data for each calibration curve corresponds to ten different biuret concentration (0.008…0.08% m/v); urea concentration: 3.12% m/v

[b] Correlation coefficient

[c] h and s_h - intercept and standard deviation, respectively

[d] m and s_m - slope and standard deviation, respectively. The slope of the calibration curve m is the calibration sensitivity according to IUPAC [22].

[e] s_s -standard deviation of the regression residual [23].

[f] Analytical sensitivity, $\gamma=m/s_s$ [22].

[g] Limit of detection calculated as percent biuret in urea; $(3/m)[s_b^2+s_h^2+(h/m)^2s_m^2]^{1/2}$ where s_b, s_h and s_m are the standard deviations of the blank, intercept and slope, respectively [24].

[h] Limit of quantitation calculated as five times limit of detection

[i] Characteristic mass calculated as percent biuret in urea; $m_c= 0.004343/m$ [22]

Statistical data from Table 1 show a good reproducibility in all measurements. The highest calibration and analytical sensitivity (m and γ) and the standard deviations of slope and intercept are the best at 555 nm. At this experimental wavelength the lowest limit of detection (0.05% biuret in urea) was obtained which allows a quantitation of five times the limit of detection

(0.25% m/m biuret in urea) with a relative standard deviation of 10%. Consequently, the green filter (530-570 nm) with the nominal wavelength at 555 nm was used as wavelength selector for ADAB-01. A simple formula allowed the percentage of biuret in urea to be calculated from the calibration curve. For a synthetic sample with 1% biuret in urea, the percentage standard deviation is up to 5% (5 successive measurements). Thus, for a real urea sample, the determined concentration level of biuret was 0.80±0.04 %.

CONCLUSIONS

This approach is designed for a near-continuous monitoring of biuret in urea (0.25-2.5% m/m) using a flow injection analysis system and offers significant advantages in terms of speed, automation and precision compared with existing manual procedures. The time sequence allows the analysis of five urea samples/hour. The method was satisfactorily applied to the quantitation of biuret in urea with a RSD_s down 10%.

REFERENCES

1. G. Ostrogovici, R. Bacaloglu, A. Nemes and M. Moraru, *Studii şi Cercetări Chimice, Timişoara,* 1961, **8**, 59.
2. M.B. Mishru and B.K. Bhupati, *Technology*, 1970, **7**, 15.
3. Ed. Schaer, *Z. Anal. Chem*., 1902, **42**, 1.
4. M. de Molde, *Chim. Ind. (Milano),* 1956, **38**, 571.
5. T. Takohasshi and D. Yosschida, *Soil and Plant. Food*, 1958, **3**, 142.
6. M.I. Plechan, *Jurn. Priklad. Himii*, 1940, **13**, 620.
7. G.E. Ellis and R.L. Fornurini, *J. Agric. Food Chem*., 1955, **3**, 615.
8. R.M. Sanyal and P.K. Pal, *Technology*, 1964, **1**, 62.
9. H.W. Robinson and C.G. Hogden, *J. Biol. Chem*., 1940, **135**, 707.
10. C. Shingal, R.C.P. Sinha and B. Bhupati, *Technology*, 1969, **6**, 35.
11. J. Guerts, J.E. van Stelle and E.G.Brinkman, *Anal. Chim. Acta*, 1969, **41**, 113.
12. V.M. Makarevici and A.E. Koiander, *Agrochimia,* 1970, **1**, 139.
13. G. Ostrogovici and R. Bacaloglu, *Studii şi Cercetări Chimice, Timişoara,* 1960, **7**, 277.
14. W.U. Malik and M.P.A. Rashid, *Proc. Natl. Acad. Sci. India A*, 1962, **32**, 123.
15. G.S. Deshmuch and R.K. Nandi, *Chem. Ind. (London),* 1969, **20**, 655.
16. R. Curti, V. Riganti and S. Locchi, *Chim. Ind. (Milano),* 1961, **43**, 782.
17. E.G. Beals, P.G. Garritsen and B. Meddings, *Technicon Symposia 1966 Automation in Analytical Chemistry, Mediad Incorporated, New York,* 1967, **1**, 187.
18. A. Fodor, A. Moraru, P. Dobra, A. Pop, T. Mureşan and E. Cordoş, *Rev. Chim.,* 1989, **40**, 525.
19. E. Darvasi, T. Mureşan, P. Dobra, A. Fodor, I. Gherheş and E. Cordoş, *Rev. Chim.*, 1989, **40**, 614.
20. K.B. Iatimirschi and V.P. Vasiliev, Izd. Akad. Nauk SSSR Moskva, 1959, p.94, 153.
21. L.G. Sillen, *Stability Constants of Metal-Ion Complexes, Burlington House, London,* 1964, p. 381, 413.
22. E. Cordoş, T. Frenţiu, A.M. Rusu, M. Ponta and A. Fodor, *Analiza prin Spectrometrie Atomică*, Institutul Naţional de Optoelectronică, Bucureşti, 1998, ISBN 973-98742-0-7, p. 266.
23. J.C. Miller and J.N. Miller, *Statistics for Analytical Chemistry*, Ellis Horwood Limited, Chichester, 2 nd edn., 1988, p. 110.
24. J.D. Winefordner and G. L. Long, *Anal. Chem*. 1983, **55**, 712.

STUDIA UNIVERSITATIS BABEŞ-BOLYAI, CHEMIA, XLVI, 1-2, 2001

SPECTROPHOTOMETRIC DETERMINATION OF TUNGSTEN(V) AS THIOCYANATE COMPLEX IN CERTIFIED STEEL MATERIALS

TIBERIU FRENTIU, MICHAELA PONTA, EMIL CORDOŞ

University "Babeş-Bolyai", Dept. of Chemistry, 3400 Cluj-Napoca, Romania

ABSTRACT. The method is based on the photometric determination of tungsten (V)-thiocyanate complex (420 nm, absorptivity coefficient 35 l g^{-1} cm^{-1}) after the reduction of W(VI) with $SnCl_2$ and $TiCl_3$. The method was applied to determine W in steel samples dissolved in Speacker reagent. The kinetics of the complex development and the interference of Mo on W determination were studied for ratios of Mo:W up to 2:1. The calibration curve was linear in the range 5-25 µg ml^{-1} W, with a correlation coefficient of 0.994 (n=5) and a detection limit of 1µg ml^{-1} W. For a certified content of 17.7% W in steel, the recovery was 99±2% and the relative standard deviation 2% (n=5). The method allows the determination of W in the presence of Mo up to a Mo/W ratio (m/m) of 1/2.

INTRODUCTION

Several spectrophotometric methods for W determination have been elaborated, but their use strongly depends on the nature and composition of the sample. As a refractory element, W is together with Mo a major constituent of rapid steel used in tool manufacturing. Molybdenum and tungsten have similar colorimetric properties and interferes with each other, which makes difficult the quantitation of W in the presence of Mo.

Feigl and Krumholz first determined tungsten with thiocyanate [1] based on the reduction of W(VI) to W(V) with $SnCl_2$ followed by the development of the photometrable yellow W(V)-thiocyanate complex. Within this procedure, the presence of Mo causes a severe interference.

Several modifications have been performed to simplify the determination of W in the presence of Mo in order to avoid the necessity of their separation. One of these procedures implies the use of $SnCl_2$ mixture with $TiCl_3$ [2] as reduction agent. The order of the reagents addition is of paramount importance. Thus, in the first stage Mo(VI) is reduced to Mo(V) and W(VI) to W(V) with $SnCl_2$ in HCl media. An excessive amount of $SnCl_2$ reduces the thiocyanate used subsequently as a complexation agent. As the thiocyanate is added, W(V) and Mo(V) form slight yellow complexes. The addition of titanium (III) chloride complete the reduction of W(VI) to W (V) and the initially yellow W-thiocyanate complex turns into an yellow-green one according to the remarks of Geld and Caroll [3]. They have pointed out that the yellow-green W(V)-SCN^- complex is obtained if thiocyanate is added before the reduction stage (with $TiCl_3$ in this case). The titanium (III) chloride destroys any residual colour due to Mo(V)-SCN^- since Mo(V) is reduced to Mo(III). This procedure could allow the determination of W in the presence of 1.5-4 % Mo, even at a Mo/W ratio of 6/1 [4].

Another method for the simultaneous determination of Mo(VI) and W(VI) without a previous separation is that based on their catalytic effect on the reaction between hydrogen peroxide and iodide and the spectrophotometric determination of iodine-starch complex.

$$H_2O_2 + 2\,KI + H_2SO_4 \rightarrow I_2 + K_2SO_4 + 2\,H_2O \qquad (1)$$

The amount of iodine produced in this reaction is proportional to the concentration of Mo(VI) and W(VI). When citric acid is added in the solution, the catalytic effect of Mo(VI) and W(VI) decreases differently as the catalytic effect of Mo(VI) decreases slightly and that of W(VI) decreases rapidly. The method has been employed in a flow injection system (FI) [5, 6]. The determination takes place in two steps. In the first stage the sum of Mo(VI) and W(VI) is determined in the absence of citric acid, by injecting the sample, H_2O_2, KI and starch into an aqueous carrier stream. In the second stage, in a subsequently injected sample, only Mo(VI) is determined in the presence of the citric acid, based on the same principle. Tungsten (VI) is found by difference. The method is rather complex while the correction for the decreasing catalytic effect of the Mo(VI) in the presence of citric acid is necessary.

Determination of the W(V)-thiocyanate complex after a previous separation by extraction was reported too. In this method, the complex is preconcentrated on column filled with Amberlite XAD-1180 resin [7], extracted with N-phenylacetamide in benzene [8] or as a mixed thiocyanate –propericiazine complex in chloroform [9]. In the determination of W (V) as blue W-toluene-3,4-dithiol complex extracted into heptane, the interference of Mo is inhibited but there is interference from Bi or Cu [10].

Spectrophotometric determination methods in which W(VI) developed complexes with rutin in the presence of hexadecyltrimethylammonium bromide [11] or with salicylfluorone [12] were also reported. Most of the interferences due to Al, Fe, Bi, Ti, Mo, Zr, Cr can be overcome by ion-exchange separation of W [11], extraction with dithiol or by masking with EDTA [12].

The determination of W by inductively coupled argon plasma atomic emission spectrometry (ICP-AES) [13 14], atomic absorption spectrometry with N_2O-C_2H_2 [15, 16] is less prone to interferences. Among electrochemical methods direct current polarography [17], differential pulse polarography [18] and stripping voltammetry [19] are used for the determination of W(VI). Another method used for the simultaneous determination of Mo(VI) and W(VI) in minerals and steel after chelatisation with tetracycline is reversed-phase high-performance liquid chromatography [20] and X-ray fluorescence spectrometry [21].

The aim of this paper was to evaluate a classical spectrophotometric method to determine W as W(V)-thiocyanate complex in steel with W in the presence of Mo. Thus, the kinetics of the W-thiocyanate complex development and the interference of Mo were studied. The dynamic range, the limit of detection and the characteristic mass of W as well as the maximum concentration of Mo, which allows the determination of W without interference, were established.

EXPERIMENTAL

Reagents and standard solutions

A 1000 μg ml^{-1} stock solution of tungsten was prepared by dissolving 0.1600 g Na_2WO_4 in 100 ml distilled water.

A 10000 μg ml^{-1} stock solution of molybdenum was prepared by dissolving 1.8400 g $(NH_4)_6Mo_7O_{24}\cdot 4H_2O$ in 100 ml distilled water.

A 0.5% solution of $SnCl_2$ (m/v) was obtained by dissolving 1 g $SnCl_2\cdot 2H_2O$ in 80 ml 32 % HCl and diluting to 200 ml with distilled water. This solution should be prepared fresh weekly.

A 25% (m/v) stock solution of KSCN was prepared by dissolving 25 g KSCN in 100 ml distilled water.

A $TiCl_3$ solution was prepared by dissolving 0.5 g Ti metallic powder in 30 ml 32 % HCl. The solution was filtrated and diluted to 50 ml with distilled water. This solution should be prepared fresh daily.

Speacker reagent was obtained by mixing 10 ml 85% H_3PO_4 (m/v), 10 ml 98% H_2SO_4 (m/v) and 10 ml distilled water.

In order to study the kinetics of the W(V)-SCN^- complex development, three standard solution with the concentrations of 5, 10 and 25 μg ml^{-1} W in the absence of Mo were prepared. In the optimum conditions for W determination, the chemical interference of Mo was studied, by preparing W solutions (10 μg ml^{-1}) in the presence of 0; 1; 5; 10; 20 μg ml^{-1} Mo. The influence of Mo on the kinetics of complex development was also studied. For this purpose, standard solutions of 10 μg ml^{-1} W in the presence of 0; 1 and 5 μg ml^{-1} Mo were necessary.

An amount of 0.1000 g certified steel sample (E114, C: 0.81%; Mn: 0.35%; Cr: 4.21%; Mo: 0.96%; Co: 4.71%; Si: 0.18%; S: 0.006%; V: 1.58%; W: 17.7%) was dissolved by carefully warming in 12 ml Speacker reagent. The solution was oxidised with concentrated HNO_3 added in drops until the liquid became clear and the present carbides were completely decomposed. The solution was cooled, filtered, then diluted to 50 ml with distilled water. In order to prepare the steel sample to be photometrated, 2 ml of the above solution, 4 ml 85% H_3PO_4 and 32 ml 0.5% $SnCl_2$ were mixed. After 10 minutes, 4 ml 25% KSCN and 2 ml $TiCl_3$ were added and the solution was diluted to 50 ml with 0.5% $SnCl_2$. After another 10 minutes, the sample was photometrated at 420 nm and the percentage of W in steel was calculated from the calibration curve using a simple formula. The calibration curve was obtained using five standard solutions containing W in the range 5-25 μg ml^{-1} in accordance with the following methodology. Appropriate aliquot volumes of tungsten stock solution, 4 ml 85% H_3PO_4 and 32 ml of 0.5% $SnCl_2$ solution were placed in 50 ml volumetric flasks. After 10 minutes, 4 ml of 25% KSCN and 2 ml of $TiCl_3$ stock solution were added to each flask. The solutions were diluted to 50 ml with 0.5% $SnCl_2$ and the green-yellow developed complex was photometrated after 10 minutes.

The blank solution was prepared of 2 ml of the solution obtained by dissolving steel and 4 ml 85% H_3PO_4 diluted to 50 ml with 0.5% $SnCl_2$.

All solutions were prepared using analytical-reagent grade chemicals (Flucka) and distilled water.

Instrumentation. The spectrophotometric measurements were carried out using the single-beam photometer Spekol 20 Karl Zeiss Jena (320-850 nm).

RESULTS AND DISCUSSION

Kinetics study of the complex development

The kinetics of the development of W(V)-SCN^- complex was studied in the absence and presence of different concentrations of Mo. Thus, the absorbance of the complex was measured at 420 nm and various times, respectively, for three solutions containing 5; 10; 25 μg ml^{-1} W. The kinetic curves are shown in Fig. 1.

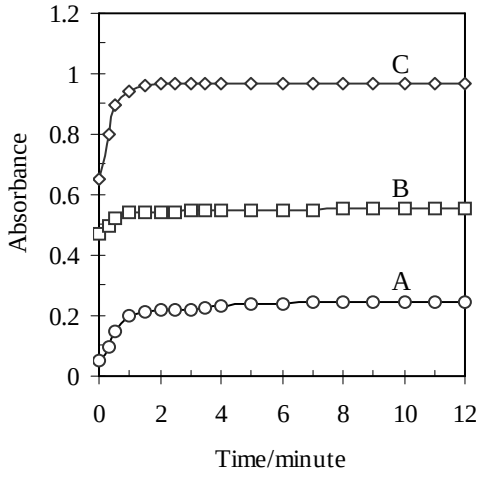

Fig. 1. Kinetic curves for the development of W(V)-SCN^- complex (absorbance measurement at 420 nm) in the absence of Mo for different concentrations of W. A - 5 μg ml^{-1} W; B - 10 μg ml^{-1} W; C - 25 μg ml^{-1} W.

After the prereduction of W(VI) to W(V) with 0.5% $SnCl_2$ in the presence of H_3PO_4 for 10 minutes, 4 ml of 25 % KSCN were added and immediately after that 2 ml of 1% $TiCl_3$. The development of a yellow-green complex was noticed. The solution was diluted to 50 ml and the change in absorbance versus time was immediately measured against blank. For the solution containing 10 μg ml^{-1} W it was studied the influence of Mo on the kinetics of the complex development in the presence of 0; 1 and 5 μg ml^{-1} Mo. The methodology to prepare the solutions was the same. After the prereduction of W(VI) and Mo(VI) to W(V) and Mo(V) with $SnCl_2$, it was added the 25 % KSCN solution. In the presence of Mo, the development of the Mo(V)-SCN^- brick-red complex was observed, which interfered with the complex W(V)-SCN^-. After the

addition of $TiCl_3$, the Mo(V)-SCN^- complex is decomposed in time, which was noticeable by the disappearance of the brick-red color and the development of the yellow-green complex of W(V). The decomposition of the Mo(V)-SCN^- complex is due to the fact that Mo(V) is reduced to Mo(III), which no more forms a complex with KSCN. As shown by the kinetic curves in Fig. 1, in the absence of Mo the absorbance remains constant after 6 minutes in a diluted W solution (curve A, 5 μg ml^{-1} W). For more concentrated W solutions (curve B- 10 μg ml^{-1} W and C- 25μg ml^{-1} W), the absorbance does not change any more after 2 - 4 minutes. In the presence of Mo (Fig. 2), the absorbance changes slowly during the time as the Mo concentration increases.

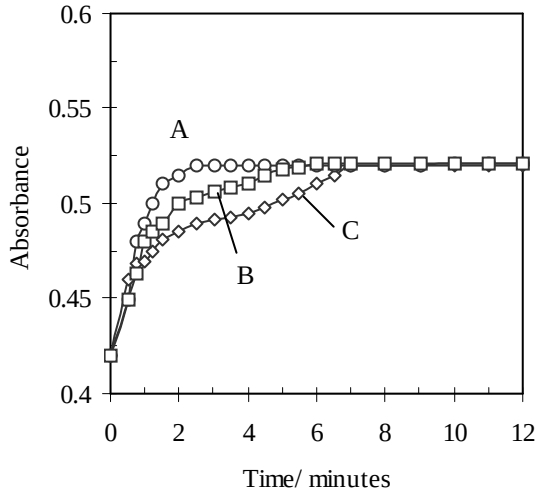

Fig. 2. Kinetic curves for the development of W(V)-SCN^- complex (absorbance measurement at 420 nm) in the presencence of Mo and the same W concentration (10 μg ml^{-1}). A - 0 μg ml^{-1} Mo; B - 1 μg ml^{-1} Mo; C - 5 μg ml^{-1} Mo.

Thus, in the absence of Mo the absorbance becomes constant after 3 minutes (curve A), while in the presence of 1 and 5 μg ml^{-1} Mo the absorbance remains unchanged after 5 and 7 minutes, respectively. After 8 minutes, the absorbance for a constant concentration of W in the presence of Mo in a Mo/W mass ratio in the range 0-0.5 reaches a constant level irrespective of the Mo concentration. The constant absorbance proves the lack of chemical interference of Mo on W determination up to a ratio Mo/W of 1/2. The kinetic study demonstrates that the absorbance of the complex could be measured 10 minutes after $TiCl_3$ is added, a sufficient time interval both for the development of the W-SCN^- complex and the diminishing of Mo(V) interference on W by reduction to Mo(III).

In order to study the interference of Mo on W determination over a wider concentration range, the absorbance of the developed complex was measured for three solutions having the same W concentration (10 μg ml^{-1})

and different Mo concentrations in the range 0-20 μg ml^{-1}.The determinations were carried out according to the following methodology. After the prereduction of samples with $SnCl_2$ for 10 minutes and the development of the W(V)-SCN^- complex subsequently reduced with $TiCl_3$, the absorbance was measured against the blank. The experimental results are presented in Fig. 3. They demonstrate the possibility to determine W in the presence of Mo without any chemical interference up to a mass ratio Mo/W of 1/2.

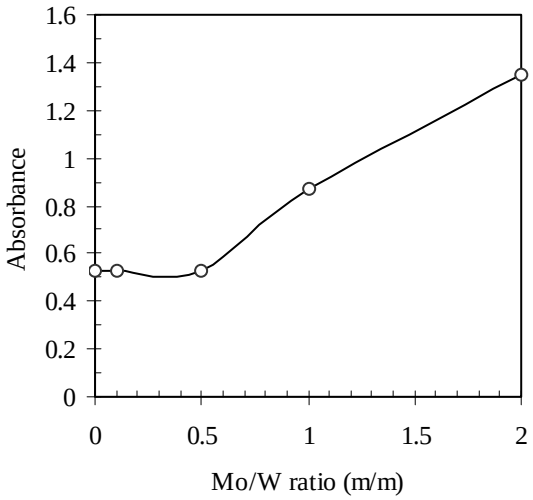

Fig. 3. Interference of Mo on W determination. W: 10 μg ml^{-1}; Mo in the range 0-20 μg ml^{-1}.

For ratios within 1/2 and 2/1 a linear increase of the chemical interference of Mo on W determination is observed. Results equally point out the possibility to eliminate the interference of Mo in W determination by the reduction with $TiCl_3$ to a Mo/W ratio (m/m) of 1/2. The method can not be applied for higher Mo/W ratios. Our results are significantly different from those mentioned in the literature [4], that reports the lack of interference up to a Mo/W ratio of de 6/1.

Analytical performance

In order to assess the analytical performance of the method, the E114 certified steel sample containing 17.7% W and 0.96% Mo was analyzed. The mass ratio Mo/W of 1/20 is within the range free of chemical interference. Our method allows the determination of W in steel up to a concentration of 20% in the presence of around 10% Mo.

The calibration of the spectrophotometer was carried out at 420 nm against the blank prepared as above. The statistical data for the calibration curve and the analytical performance is shown in Table 1.

Table 1.

Calibration results and analytical performance

Wavelength / nm	400
Calibration range [a]/ μg ml^{-1}	5 - 25
R [b]	0.994
(h±s_h) [c]	9 10^{-2}±3.6 10^{-2}
(m±s_m) [d]	3.5 10^{-2}±0.2 10^{-2}
s_s [e]	3.5 10^{-2}
γ [f], ml μg $^{-1}$	1
LOD [g], μg ml^{-1}	1
LOQ [h], μg ml^{-1}	5
m_c [i], μg ml^{-1}	0.12

[a] The number of data for the calibration curve corresponds to five different W concentration (5…25 μg ml^{-1})
[b] Correlation coefficient
[c] h and s_h - intercept and standard deviation, respectively
[d] m and s_m - slope and standard deviation, respectively. The slope of the calibration curve (m) is the calibration sensitivity according to IUPAC [22].
[e] s_s -standard deviation of the regression residual [23].
[f] Analytical sensitivity, $\gamma=m/s_s$ [22].
[g] Limit of detection calculated in μg ml^{-1}; $3/m[s_b^2+s_h^2+(h/m)^2s_m^2]^{1/2}$ where s_b, s_h and s_m are the standard deviations of the blank, intercept and slope, respectively [24].
[h] Limit of quantitation calculated in μg ml^{-1}as five times limit of detection
[i] Characteristic mass calculated as μg ml^{-1} W in solution; m_c= 0.004343/m [22]

Statistical data from Table 1 show a good reproducibility in all measurements. The limit of detection calculated according to the methodology presented in Table 1 is 1 μg ml^{-1} W that allows a calibration starting from 5 μg ml^{-1} W that corresponds to the limit of quantitation. Thus the method should allow the quantitation of at least 0.25% W in steel. The apparent absorptivity in respect with W calculated from the calibration curve for a 1-cm cell was 35 l g^{-1} cm^{-1}.

The proposed method was applied to the determination of tungsten in a steel reference material with a certified W content (17.7%). The obtained value was 17.5±0.4% which corresponded to a recovery of 99±2 % and a relative standard deviation (n=5) of 2 %. Adopting the null hypothesis, the two-tailed t-test showed that there was no systematic error between the certified and determined W concentration for a 95% confidence interval ($t_{calculated}=t_{critical}$, P=95%, ν=4, 1.11<2.78).

Conclusions

The possibility of the spectrophotometric determination of W as a complex with SCN^- in steel containing Mo was studied. The chemical interference of Mo was eliminated by adding $TiCl_3$. The method allows the determination of W without the interference of Mo up to a Mo/W ratio of 1/2. The limit of detection was 1 μg ml^{-1} W and the dynamic range was between 5 and 25 μg ml^{-1}. The relative standard deviation was 2 % and the recovery degree for a certified steel sample containing 17.7% W was within 97 and 101 %.

REFERENCES

1. F. Feigl and P. Krumholz, *Angew. Chem*., 1932, 45, 674. *Chem. Abst*. 1933, **27**, 243.
2. A.G. Fogg, D.R. Marriott and D.Thorburn Burns, *Analyst(London)*, 1970, **95**, 848.
3. I. Geld and J. Caroll, *Anal. Chem*., 1949, **21**, 1098.
4. British Iron and Steel Research Association Methods of Analysis Committee, J. Iron Steel Inst., 1952, 172, 413.
5. R. Liu, D. Liu, A. Sun and G. Liu, *Analyst(London)*, 1995, **120**, 565.
6. Z. Zhu, C. Han, Z. Gu and R. Chen, *Analyst(London)*, 1994, **119**, 2251.
7. M. Soylak, L. Elci and M. Dogan, *Talanta*, 1996, **43**, 391.
8. N. Mishra, S.K. Sinha, K.S. Patel and R.K. Mishra, *Analyst(London),* 1987, **112**, 1131.
9. A.T. Gowda and K.S. Rangappa, *Anal. Chem*., 1986, **58**, 827.
10. E.P. Welsch, *Talanta*, 1983, **30**, 876.
11. M. Xu and G.A. Parker, *Talanta*, 1987, **34**, 512.
12. V.A. Nazarenko, V.P. Antonovich and N.A. Veshchikova, *Talanta*, 1987, **34**, 215.
13. X. Luo, Z. Su, W. Gao, G. Zhan and X. Chang, *Analyst(London),* 1993, **117**, 145.
14. Z. Bae, S. Lee and S. Lee, *Talanta*, 1997, 4**4**, 47.
15. C. Chong and N. Meriam, *Analyst(London),* 1987, **112**, 627.
16. S. Raoot, S. Athavale and T. Rao, *Analyst(London),* 1986, **111**, 115.
17. S. Bhowal and M. Bhattacharyya, *Talanta*, 1989, **36**, 989.
18. P. Buldini, D. Ferri and D. Nobili, *Analyst(London),* 1988, **113**, 1319.
19. J. Wang and J. Lu, *Talanta*, 1992, **36**, 801.
20. X. Ding and C. Fu, *Talanta*, 1993, **40**, 641.
21. N. Sen, N. Roy and A. Das, *Talanta*, 1989, **36**, 697.
22. E. Cordoş, T. Frenţiu, A.M. Rusu, M. Ponta and A. Fodor, *Analiza prin Spectrometrie Atomică*, Institutul Naţional de Optoelectronică, Bucureşti, 1998, ISBN 973-98742-0-7, p. 266.
23. J.C. Miller and J.N. Miller, *Statistics for Analytical Chemistry*, Ellis Horwood Limited, Chichester, 2 nd edn., 1988, p. 110.
24. J.D. Winefordner and G. L. Long, *Anal. Chem*. 1983, **55**, 712.

STUDIA UNIVERSITATIS BABEŞ-BOLYAI, CHEMIA, XLVI, 1-2, 2001

BIOINDICATION OF ENVIRONMENTAL POLLUTION IN THE URBAN AND INDUSTRIAL AREAS

ANA-MARIA RUSU

Department of Chemistry, Babes-Bolyai University, Cluj-Napoca, Romania

ABSTRACT. Suitability of lichens mosses, fungi and tree leaves as accumulative indicators of trace element depositions in urban and industrial areas is discussed. The analysis of soils for the evaluation of the contamination level of an area is very important, but therefore the analysis of soils alone could be not sufficient. The use of different plant materials, due to their morphological characteristics, produces reliable results and can be done information about pollution at a very low cost comparatively to the traditional techniques. A short review of studies performed in the industrial area of Zlatna and Cluj-Napoca town with plant materials are given. The results obtained by plant materials and soil samples collected from the same areas provide a general overview on air pollution patterns within the investigated areas.

INTRODUCTION

The term “bioindicator” refer to the ability of an organism to indicate the presence/absence or high/low level of any factor in air pollution; where information is provided by the organism about pollutant gradients or changing pollution levels, the term “biomonitor” should be applied [1]. The terms are also used to differentiate between qualitative and quantitative, and further, monitoring can mean continuous observation, while indication can mean on-off measurements.

Vegetation may reveal the presence of man-made contaminated sites by measuring plant elemental contents. Source of contamination in which excessive concentrations of elements may be brought about are follows: 1. The exploration of mineral resources (mining activities, ore tailings, spoil tips; metal smelting, blast furnaces, smokes dusts); 2. Other industrial processes (electrolysis, cement, paint, tanning, plating, etc.); 3. Domestic and industrial waste disposal practices (landfills, sewage sludge, incinerators); 4. Energy supply (coal and petroleum burning, high tension lines, nuclear power plants); 5. Agriculture (Phosphate fertiliser, sewage sludge, pesticides); and 6. Traffic (leaded petrol, tyres, catalysts).

In general polluted air consist of a mixed gas-aerosol complex containing varying concentrations of SO_2, NO_x, O_3, and acid aerosols; notably in the vicinity of smelting operations, plants are subjected to fumes rich in SO_2 and other pollutants together with particulate matter.

The ideal accumulative bioindicator is a species, in which internal concentrations accurately reflect external concentrations, but in general it does not exist. Some demands must be fulfilled by an acceptable bioindicator. It should be:

- present in large amounts;
- widely distributed over the globe;
- easy to identify and to sample;
- analysable according to the standard analytical methods presently available.

The most widely used bioindicators of metal pollution in the industrial and urban areas are lichens, mosses, fungi and high plants. True mosses and lichens are useful indicators of pollution because not only are they long-lived and ubiquitous in all parts of the world from the tropics to the Arctic regions, but more importantly, they have no true root systems and obtain their nutrients (and pollutants) from the ambient air and water and not from the soil. It will be remembered that the fallout from recent Chernobyl disaster was measured largely by measuring the concentration of radionuclides in mosses and lichens from Fennoscardia and other parts of Europe [2.3]. Studies on lichens as biomonitors of metals and other elements were thoroughly reviewed by many authors [4-7]. As regards their suitability as bioindicators, and because there is a great similarity in many characteristics, mosses and lichens are often discussed together [8]. Because of the specific anatomical and physiological characteristics higher fungi are especially suitable for accumulating heavy metals from soil. In addition their intimate association with the soil and dead organic matter offer conditions for intensive exchange with the substrate [9]. Moreover it is very likely that heavy metal input to soil via deposition and litter fall is the main source of the heavy metal concentration found in fungi. In contrast to lichens, mosses and fungi, higher plants generally show a clear division into roots, shoots and leaves. The accumulation of heavy metals by higher plants represent both pathways of contamination, the accumulation of airborne heavy metals on the plant surfaces, and their uptake of heavy metal from soil [10-12]. Nevertheless it has been show in many studies that in polluted areas leaves can be regarded as accumulative monitors of many metal elements, because a great proportion of the elements deposited or intercepted is not imported into the leaf tissues but remains on the surface or in the wax cuticular.

This paper present a short review of studies performed in the industrial area of Zlatna and Cluj-Napoca town with plant materials. Moreover are presented the result of the deposition from atmosphere over industrial and urban areas, mainly due to the luck of suitable, sensitive and inexpensive techniques (using bioindicators) that permit simultaneous measurements usually at a large number of sampling sites. The present paper compares the contents of Cu, Pb and Zn in lichens, mosses, fungi, leaves and soils collected from two sampling sites from Zlatna (the lowest and the most polluted). Also, Cu, Pb and Zn concentrations determined in leaves collected from Zlatna and Cluj-Napoca are compared.

RESULTS AND DISCUSSION

Romania, like other countries in Europe and the World, is confronted with serious problems of environmental pollution as a consequence of intensive industrialisation. One ‘intensely polluted zone’ is the Zlatna region of central Transilvania. A cooper ore processing plant in the centre of Zlatna town produces

acidic emission and large amount of metal particulates, both causing extreme environmental degradation throughout the locality. Previous studies [13] have indicated that concentration of pollutant elements in soils (Pb – 1800 μg/g; Cu – 600 μg/g; Zn – 500 μg/g) greatly exceed current Romanian Standards [14] maximum acceptable levels (Pb - 20 μg/g; Cu - 20 μg/g; Zn - 100 μg/g).

The location of the 7 studied sample sites and also, plants and soils sampling and sample preparation for analysis were described in detail elsewhere [13,15,16]. Flame atomic absorption spectrometer was employed for the metal elements determination.

The Cu, Zn and Pb accumulation in lichens, mosses, fungi, leaves and soil at the two sites (Patringeni and Metes) from Zlatna town areas are shown in Fig. 1 and Fig. 2. In general, there are considerable differences in uptake and content of heavy metals between different plant materials. Considering the three elements Cu, Zn and Pb which were determined in all plant samples, the concentrations (μg/g d.w.) generally follow the order:

Cu - Patringeni: moss(2259)>lichen(1190)>leaf(761)>soil(687)>fungi(136)
- Metes: lichen(518)>moss(370)>leaf(349)>soil(106)>fungi(54)

Zn - Patringeni: leaf(1020)>moss(1019)>lichen(720)>soil(416)>fungi(143)
- Metes: leaf(638)>lichen(377)>moss(294)>soil(237)>fungi(120)

Pb - Patringeni : moss(3918)>lichen(2079)>soil(1833)>leaf(1679)>fungi(147)
- Metes: lichen(1087)>leaf(896)>moss(776)>soil(260)>fungi(73)

Cooper and Pb are higher in lichens and mosses, whereas Zn is higher in leaves. The soil and fungi samples have the lowest content of determined elements, except the very high Pb concentration measured in soil for the most polluted site investigated from Zlatna region. Also, the Cu, Zn and Pb concentration determined in all analysed samples decreases with distance from the pollutant source.

With regard to the present results no plant material can be considered to be an exact indicator of environmental heavy metal pollution. However, bioindicators could be useful for distinguishing between polluted and unpolluted areas and for determining sources of heavy metals emission. It may be concluded that many plants species can serve as indicator (accumulators), with different sensitivities to heavy metals and different abilities to accumulate them. Accumulation of heavy metals depends on the characteristics of the species in question as described above.

Undoubtedly urban pollution gives a serious contribution to global contamination of the environment. The extent and type and kind of this type of pollution depends on many factors among which are the number of inhabitants, their habits, types of energy sources, types and dimensions of the industrial zones, types and intensity of the motor-traffic and of course a lot of climatic factors.

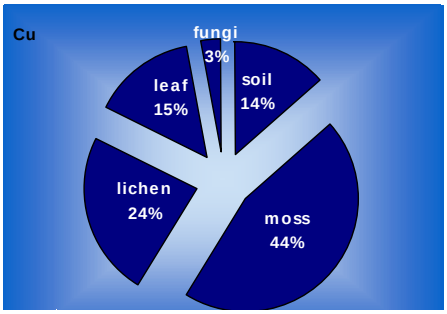

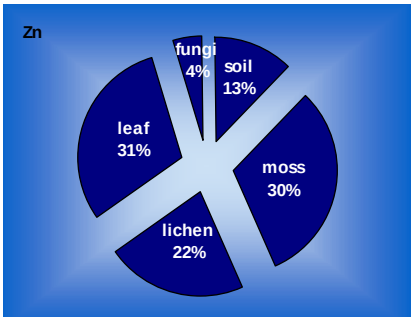

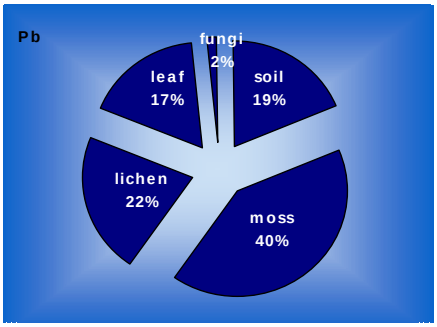

Fig. 1 Cu, Zn and Pb accumulation in lichens, mosses, fungi, leaves and soil in the most polluted site around Zlatna (Patringeni - 3.5 km SW close to the pollution sourse)

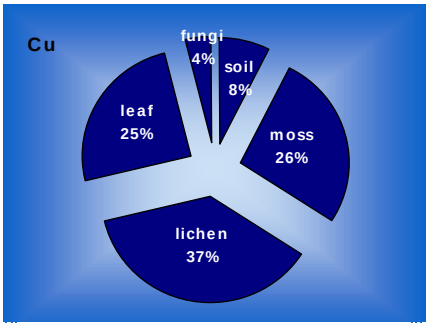

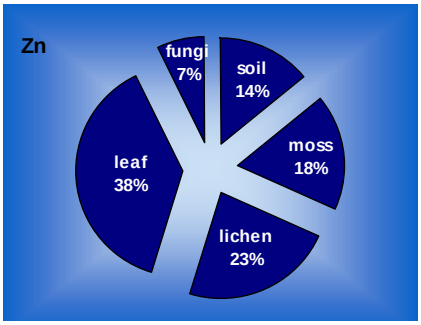

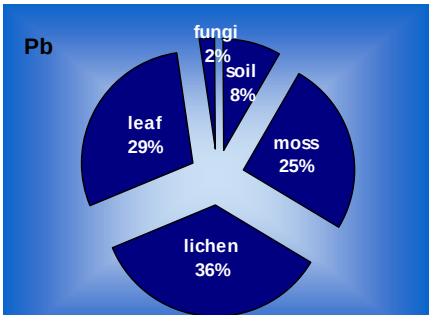

Fig. 2. Cu, Zn and Pb accumulation in lichens, mosses, fungi, leaves and soil collected in the most far studied site (Metes - 16 km WSW close to the pollution sourse).

Tilia cordata and *Acer Platanoides* leaves species has been used for passive monitoring of airborne heavy metal pollution in the urban area of Cluj-Napoca, Romania. By passive monitoring we have completed a general survey of the present heavy metal contamination within Cluj-Napoca in comparison with results from Zlatna (industrial) areas investigated in previous researches [15]. The metal concentrations in leaves samples show remarkable differences according to the different exposures to air pollution in Cluj-Napoca. Lead rises from 10 μg/g d.w. (dry weight) in slightly polluted areas, up to 104 μg/g d.w. next to main traffic roads. Cooper range from 7 μg/g d.w. up to 88 μg/g d.w., while Zn ranged from 31 μg/g d.w. to 154 μg/g d.w. For comparison has been analysed local control background leaf samples, collected from Botanical Garden, considered unpolluted area. The concentration of Pb, Cu and Zn were 2 μg/g d.w., 4 μg/g d.w., and 30μg/g d.w., respectively.

Comparative results of min. and max. Pb, Cu and Zn values measured in leaves collected from Zlatna industrial region and Cluj- Napoca urban areas are presented in Fig. 3. As show the fig. 3 the min. values for Pb, Cu and Zn measured in Zlatna are 90, 50 and 21 times higher than those determined in Cluj-Napoca; while the max. values measured in Zlatna are 16, 9 and 7 times higher than values determined in leaves collected in Cluj-Napoca for the same elements. Comparing the data for Pb, Cu and Zn found in the investigated industrial and urban areas with the control background leaf samples, collected from Botanical Garden, it is possible to draw conclusions about the pollution degree. In Zlatna the min. concentrations of Pb, Cu and Zn in leaves are approximately 450, 90 and 21 times higher than the control value; while in Cluj-Napoca the pollution degree for Pb and Cu is 5 and 2 times higher than in Botanical Garden, and the Zn concentration not exceed the control sample content. The max. values of Pb, Cu and Zn measured in leaves collected from Zlatna are 850, 192, and 34 times higher than those determined in Botanical Garden, while Pb, Cu and Zn max. concentration in leaves collected from Cluj-Napoca are 52, 22 and 5 times higher than in control samples.

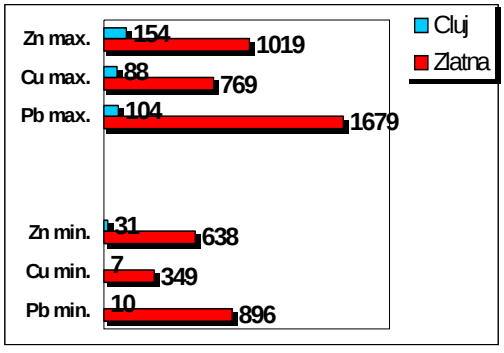

Fig. 3 Comparative results of min. and max. Pb, Cu and Zn values measured in leaf samples collected from Zlatna industrial region and Cluj- Napoca urban areas.

We concluded that Pb contamination in Zlatna is very high and in Cluj-Napoca relatively high. Also, Cu and Zn concentration exceed the normal admissible values in the main investigated areas.

REFERENCE

1. J.E. Sloof, M. De Bruin, H. Wolterbeek, in: *International Conference on Environmental Contamination, Venice Sept. 1988, Symposium proceedings:* Orio A.A. (ed.). Edinburgh, CEP Consultants Ltd.
2. J. Paatero, T. Jaakkola, A. Reponen, *Radiochim. Acta,* 1994, **64(2)**, 139-144.
3. I.G.Gokmen, M.Akgoz, A.Gokmen, *Fresenius'J.Anal.Chem.*, 1996, **355(5-6)**, 736-738.
4. P.W. James, in: *Air Pollution and Lichens*: B.W. Ferry, M.S. Baddeley, D.L Hawksworth, (eds.). London: The Athlone Press, 1973, 143-175.
5. Y. Tuominen, T. Jaakkola, in: *The Lichens:* V. Ahmadjian, M.E. Hale (eds.). New York: Academic Press, 1973, 185-223.
6. E. Niober, K.J. Puckett, D.H.S. Richardson, F.D. Tomassini, B. Grace, *International Conference of Heavy metals in the environment, Toronto, Ontario, Canada, Oct.1975, Symposium Proceedings,* Toronto, **Vol. 2**, 331-352.
7. E. Niober, D.H.S. Richardson, F.D. Tomassini, *The Bryologist,* 1978, **81**, 226-246.
8. K.J. Pucket, in: Lichens, Bryophytes and Air Quality. *Bibl. Lichenol* **30**, J. Cramer Verl., Berlin, 1988, 231-267.
9. A.R. Byrne, V.Ravnik, L.Kosta, *Sci.Total Environ.,* 1976, **6**, 65-78.
10. S. Halles, K. Debrock, J.M. Dumont, *Sci. Total Environ.,* 1979, **13**, 141-155.
11. R. Wittig, A. Terhorst, *Acta Biologica Benrodis,* 1988, **1** (2).
12. B. Mnkovska, *Biologia,* 1981, **36**, 489-496.
13. A.M. Rusu, W. Dubbin, N. Har, K. Bartok, W. O. Purvis, B. Williamson, *Studia Univ. Babes-Bolyai, Geologia,* 2000, **XLV (1)**, 105-113.
14. Monitorul Oficial al Romaniei (1997) IX, 303/I: 27.
15. A.M. Rusu, K. Bartok, W. Dubbin, W. O. Purvis, *Studia Univ. Babes-Bolyai, Chimia,* 2000, **XLV**, **1-2**, 241-250.
16. A.M. Rusu, K. Bartok, V. Din, W. O. Purvis, W. Dubbin, *Studia Univ. Babes-Bolyai, Chimia,* 2000, **XLV**, **1-2**, 251-259.

STUDIA UNIVERSITATIS BABEŞ-BOLYAI, CHEMIA, XLVI, 1-2, 2001

THE INCREASE OF THERMAL EFFICIENCY FOR THE HEATING FURNACE

IOAN LAZĂR, CĂLIN I. ANGHEL

Department of Chemical Engineering, Faculty of Chemistry and Chemical Engineering, University "Babeş-Bolyai" Cluj-Napoca, Str. Arany Janos No. 11

ABSTRACT. The purpose of this paper was to evaluate the general thermal efficiency for a heating furnace of phosphatic porcelain, materialized in two different structures. One is the classical structure of these furnaces and the second represent a modified type-obtained by plating the inner side with ceramic fibers. The analyze is based on the finite element method (FEM) for the unstable heat transfer stage, supported by a COSMOS/M Geostar professional software package. The analyses reveal a major isolating effect of ceramic fibers and a real increasing of thermal efficiency up to 30% compared to the classic type of furnace.

1. Introduction

The general structural constructions of heating chamber's furnaces are well known in engineering practice [1,2,3] from many years. In the last decades, since 1980, many investigations [4,5,6] were developed for the increasing of heating furnaces' thermal efficiency. One of the main trends consists in the increasing of the general thermal transfer from the inner heating side to the porcelain products. This modality must to consider the heating diagram of the porcelain products both the cumbersome process of the proper heating and structural, phisical and chemical, changes of the products. Another way of approach for the increasing of the thermal efficiency is the one, which consider the equivalent thermal yield to be the quantity of heat consumed for the same quantity of product. This type of analysis leads the study towards constructive modifications of the heating furnaces, with favorable technical and economical implications. On this direction evolves the present study, which proposes that by modifying the basic structure of the heating furnaces of phosphatic porcelain, will achieve a decrease of lost heat energy. One of the most appreciate construction alternative used on the previous direction consist in using ceramic fiber in the structure of the furnaces' walls.

Because the process of heating of these products is an intermittent one, for which the usual known analytical methods are practically inapplicable or leads to major complications and the heat transfer stage is one unstable we've been using for the comparative analysis the finite element method (FEM) supported by a COSMOS/M Geostar professional software package.

2. General analysis considerations

The main objective of this study is to analyze the efficiency of using ceramic fibers as a first inner layer of intermittent working heating furnaces. In this purpose it will be followed the temperatures, the heat transfer, thermal

heating flux, during heating and cooling down. All these were achieved considering the whole process in an unstationary process. Further through calculations based on achieved thermal fluxes, the quantity of heat energy inside the furnace's walls, the whole heat input and the exterior heat energy losses, it can be evaluated the quantity of real total heat energy used by the process and implicitly it can be determined the global thermal yield. The classic structure of these furnaces – chamber, sidewalls, back walls, arch, etc.- is one multilayer. It is made from a combination of masonry, which combines different types of refractory bricks and other different isolation materials (Table 1). From the multitude of situations of building furnace's walls it has been chosen one of the most common classical, respectively one modified type obtained by plating the inner side of the walls with ceramic fibers (Fig. 1).

Table 1.

Physical and thermal parameters of refractory brick, ceramic fibers and mineral wool

Parameters		Refractory bricks			Mineral wool	Ceramic fibers KVF 151
		I 35 A 06	I 62A 08C	I 62A 11C		
T_{max} [^{0}C]		1200	1300	1500	130	1500
Density [Kg/m^3]		600	800	1100	250	140
Thermal conductivity [W/m ^{0}C] $\lambda = f(T\ ^0C)$	200				0,06	0,066
	400	0,209	0,279	0,488		0,095
	600	0,233	0,314	0,488		0,12
	800	0,291	0,326	0,488		0,18
	1000	0,326		0,477		0,25
Specific heat [J/Kg ^{0}C] $c = f(T\ ^0C)$	200	900	900	900	753	932
	400	980	980	980		
	600	1030	1030	1030		1162
	800	1063	1063	1063		
	1000	1093	1093	1093		1297,66
	1200	1120	1120	1120		
	1400	1134	1134	1134		

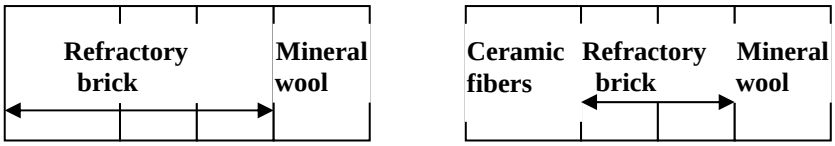

a. **b.**

Fig. 1. The equivalent structure for the walls of the furnace.
a. Equivalent structures for the walls of classic chamber furnace;
b. Equivalent structures for the walls of modified chamber furnace;

The following conditions are the most important from the heat transfer point of view:

- the heat transfer through the furnace's wall is determined by the unidirectional conduction in unstationary regime;
- relatively identical conditions for the convectiv and radiant heat transfer at the exterior of the wall for the classic type of furnace and as well as for the modifield type with ceramic fibers.

For really evaluating the impact of using ceramic fibers in the construction and upgrading the heating furnaces, we will consider the the analysis of heat transfer in real unstationary regime through the wall of a characteristic 4 m^3 chamber furnace in both constructive types: the classic one and the one upgraded with ceramic fibers (Fig. 2).

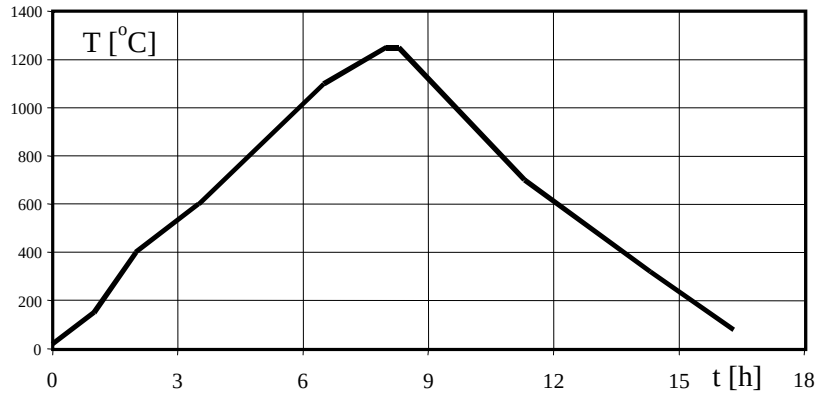

Fig. 2. Heating diagram for phosfathic porcelain.

We reduce the analysis to the conductive heat transfer through the furnace's walls because this is decisive for the global heat consumption of the furnace in both construtive types.

The main analysis assumptions:

- the temperature of all interior constructive elements of the furnace is known according to the heating diagram;

for the convectiv heat transfer between the outer sides' surface of the furnace and the environment it will be considered for partial coefficients of heat transfer the next general relations:

$\alpha \cong 7{,}1 + 0{,}057 \cdot T_e$ - transfer from plane wall to exterior environment;

$\alpha \cong 9{,}4 + 0{,}057 \cdot T_e$ - transfer from arch wall to exterior environment;

- heating cycle (Fig. 2) with a spread of 16 h 40', will be divided in 60" intervals resulting 500 steps until the end of the heating phase and 1000 steps until the end of the heating cycle;
- the MEF modeling and analysis will be achieved with square shapes (PLANE2D), 4 nodes and 0,025 m side bidimensional finite elements;
- because of the geometrical symmetry and the frontier conditions the MEF analyze model is considered only half of the transversal section of the furnace.

3. Numerical analysis

On the basic conditions and the previous presented context it has been achieved the unstationary regime heat transfer using MEF for two types of phosphatic porcelain chamber furnaces (Fig. 3):

- Type I (Fig. 1. a) classic solutions of the furnace;
- Type II (Fig. 1. b) a modified solution by which the interior walls and the arch are plated with a layer of type KVF 151 ceramic fiber with a thickness of 50 mm. Simultaneous complying the initial thickness of the fire place, under the plane fire place made by refractory bricks I 65 A 11C, a layer of 25 mm of ceramic fibers was introduced.

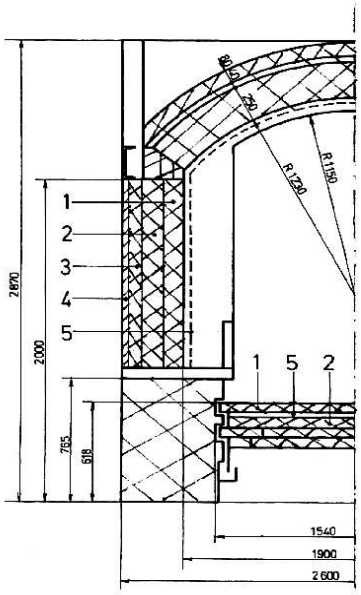

Fig. 3. The main constructive structure of heat furnace.
1-Refractory brick type I62A 11C;
2- Refractory brick type I35A 06;
3- Refractory brick type ID 06;
4- Refractory brick type I62A 11C;
5-Ceramic fibers layer ;

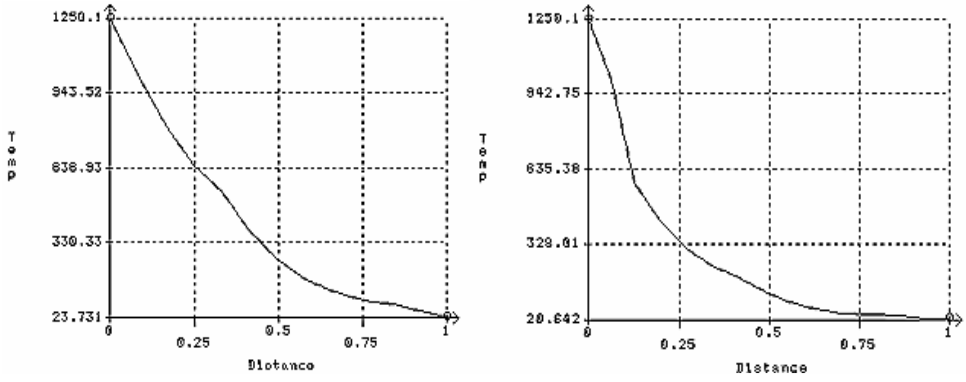

a. **b.**

Fig. 4. General temperature distribution through the plane wall of the furnace at the end of the heating phase only. **a.** Classic furnace; **b.** Modified furnace by ceramic fibers;

For a comparative and facial evaluation of the temperature variation through the thickness of side walls, at the end of the heating phase, on the base of MEF analyses are rendered the distributions for both types of analyzed furnaces (Fig. 4). From Figure 4 it comes out the favorable effect of the presence of ceramic fibers emphasized by the severe heat drop on the thickness of the fibers' layer thus the maximum temperature of the brick masonry doesn't exceeds 600 ^{0}C. The favorable isolating effect of the ceramic fibers is much more obvious from Figure 5, at the end of the whole heating cycle.

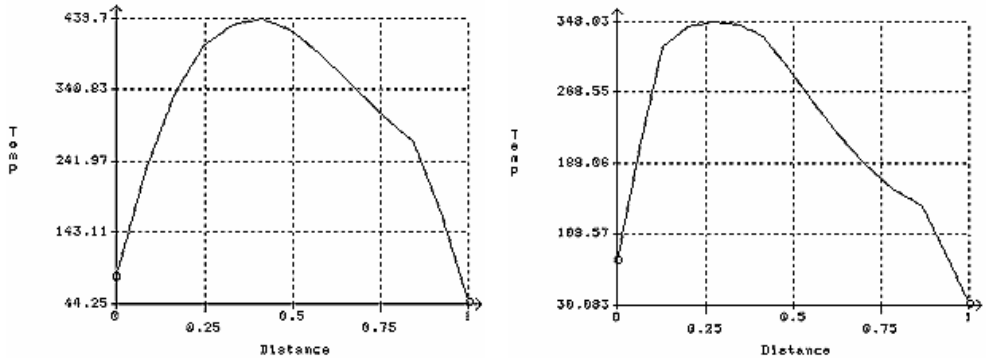

a. **b.**

Fig. 5. General temperature distribution through the plane wall of the furnace at the end of the whole heating cycle. **a.** For classic furnace; **b.** For modified furnace by ceramic fibers;

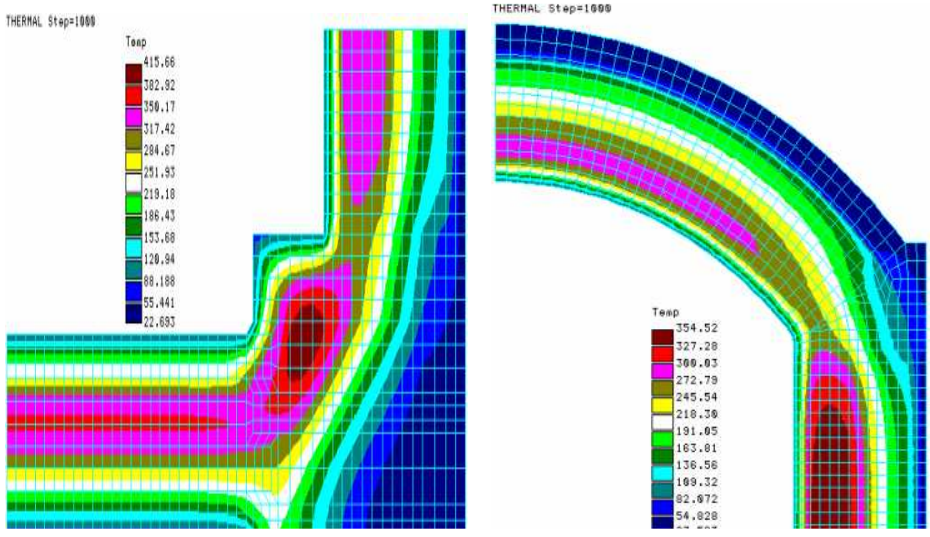

a. **b.**

Fig. 6. FE mesh and temperature distribution through the main parts of the heating furnace. **a.** Through the fireplace and sidewalls. **b.** Through the arch and sidewalls.

In fact, this favorable isolating effect of the presence of ceramic fibers can be appreciated more directively representing on the same diagram the maximum temperature distribution in assembly parts of the two types of furnaces.

Based on the previous diagrams (Fig. 4-7), derived by the FE analysis, it can be evaluated the conductive thermal flux throughout the main constructive elements of the furnace. In t he conductive thermal fluxes, also like in the case of temperatures distribution, it comes out that the maximum isolation effect of the presence of the ceramic fibers appears at the sidewalls and the arch of the furnace.

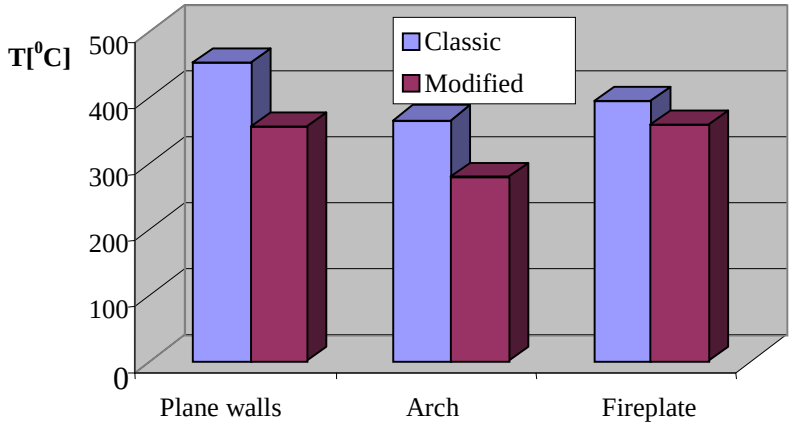

Fig. 7. Distribution of the maximum temperature in the two types of furnaces at the end of whole heating process.

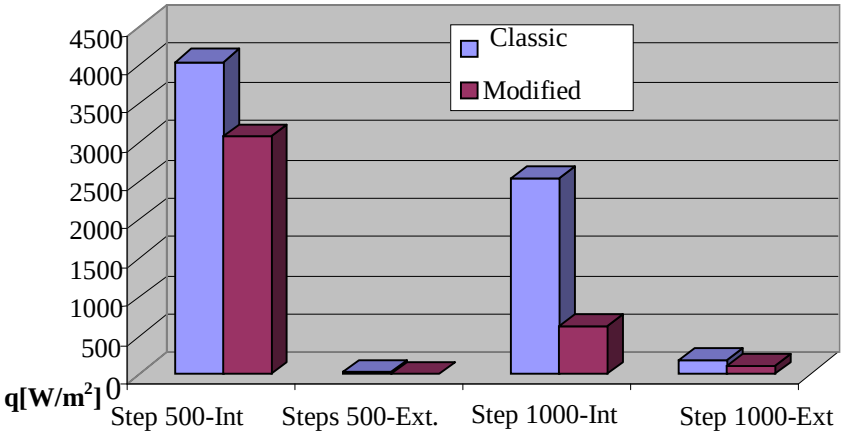

Fig. 8. Thermal flux throught the plane sidewalls.

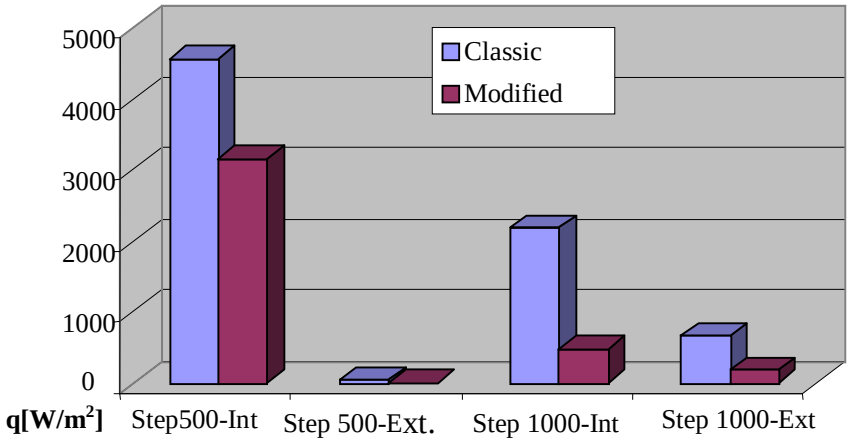

Fig. 9. Thermal flux throught the arch.

Based on modeled values by FE (Fig. 8-10) it can be specified that the presence of ceramic fiber leads to a smaller conductive flux up to 25% for the side walls and and 30% for the arch compared to the classic type of furnace. The great isolating effect of ceramic fibers is much more important for the cooling period (between step 500→1000) of the heating cycle because a conservation of heat accumulated in the furnace's structure is assured so at the beginning of a new heating cycle it will be needed a smaller quantity of heat for resuming the cycle.

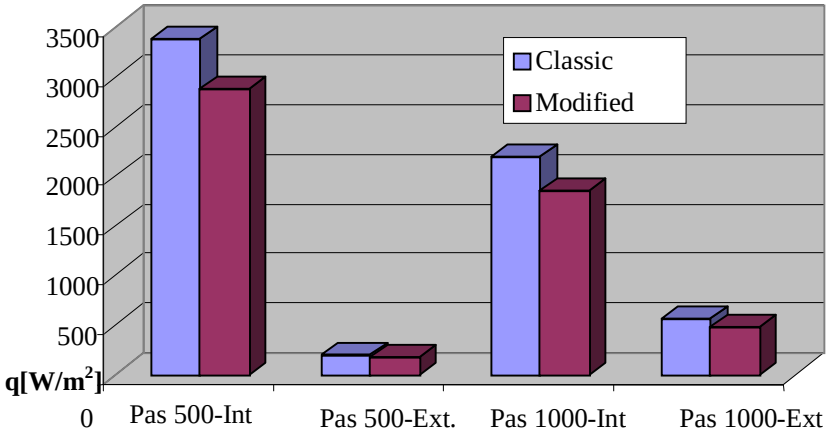

Fig. 10. Thermal flux throught the fireplate

For the particular considered furnace (Fig. 2) at the end of the whole heating cycle (step 1000) it cames out 75% less thermal fluxes on sidewalls and 78% for the arch. So it can be concluded that all the heat losses (towards outside and inside) from the accumulated in the furnace 's walls on the modified

type are much smaller than the classic type of furnace. This status determines a significant reduction of heat quantities consumed for heating the products in a new stage of resuming the porcelain heating process.

4. Conclusions

By using almost identical analysis models with real furnaces the study reveals the major advantages of usage of ceramic fibers for construction or for upgrading chambers furnaces of heating porcelain. Although the quantitative evaluations are obtained for a particular type of chamber furnace it can be highlighted the following general favorable effects:

- the decrease of temperature gradient on the thickness of the furnace's walls;
- the decrease of thermal conductive flux through the furnace walls;
- a very good conservation of accumulated heat;
- the increase of general thermal yield of the process.

The precision and the efficiency of the FE method justified this kind of approaches, which with relatively small efforts leads to spectacular economic and thermal results.

REFERENCES

1. J. H. B r u n k l a u s, *Cuptoare Industriale*, Editura Tehnică Bucureşti, 1977;
2. I. T e o r e a n u, D. B e c h e r e s c u, Em. B e i l i c h, H. R e h n e r, *Instalații Termotehnologice*, Editura Tehnică Bucureşti, 1979;
3. I. T e o r e a n u, H. R e h n e r, M. T h a l e r, D. R a d u, *Calcule de Operații, Utilaje şi Instalații termotehnologice din Industria Silicațiilor*, Editura Didactică şi Pedagogicăa Bucureşti 1983;
4. N. D e i c a, *Fibre Ceramice Refractare*, Editura Tehnică Bucureşti, 1988;
5. ***** R A T H – ceramic fibers, *Producer catalogue* 1998;
6. ***** R I E D H A M M E R – heating furnaces, *Producer catalogue* 1999;

STUDIA UNIVERSITATIS BABEŞ-BOLYAI, CHEMIA, XLVI, 1-2, 2001

SCREENING TECHNOLOGIES FOR AVIATION SECURITY

VICTOR BOCOŞ-BINȚINȚAN[*], AUREL-VASILE MARTINIUC[*], EMIL CORDOŞ[*,]**

[*] *Research Institute for Analytical Instrumentation, Cluj-Napoca, Romania*
[**] *"Babeş-Bolyai" University, Faculty of Chemistry and Chemical Engineering, Cluj-Napoca, Romania*

ABSTRACT. Ensuring the security of the air travel system is currently a monumental task. Air carriers are the first responsible for insuring and maintaining air travel security; a major part of this responsibility implies developing and using of a security program that includes screening all passengers and their baggages. Operationally speaking, it means that air carriers have to purchase the appropriate equipment, to design and setup checkpoints covering access to their flights, and to hire and train the personnel needed to operate these equipments and checkpoints. This paper's goal is to provide an overview to the technologies used for security screening in the civil aviation. Imaging technologies are best represented by X-ray methods, while most promising trace detection technology seems to be ion mobility spectrometry.

1. Introduction

Ensuring the safety of the air travel system is definitely a huge and challenging task. In USA only this involves the screening of more than 1.5 million passengers (with their luggage) every day, for the presence of metallic weapons and other dangerous materials **[1,2]**. As a response to these complex security requirements, the airport authorities have to examine the new technologies designed to improve the effectiveness of screening procedures and to implement other technologies able to detect not only metallic weapons but also other types of dangerous objects and substances (e.g. plastic explosives). There is a stringent need for the implementation of new, automated passenger screening methods, which are used to detect threats such as concealed weapons and explosives being carried by passengers **[1]**, but also for narcotics smuggling detection.

It is a well established fact that the level of tolerance demonstrated by the traveling public (concerning perceived health risk, lack of privacy, delays and so forth) is proportional to the perception of the threat's severity. From this point of view, more expensive screening equipment and more intrusive screening techniques will be accepted only at higher threat levels. It is interesting to note also at this point that screening technologies ensure detection of threat objects and materials, but they also function as deterrents (the effectiveness as a deterrent depends strongly on perceived, rather than real, reliability and fidelity of the system).

2. Passenger screening

There is a dilemma in passenger screening: how to provide an effective screening level at a reasonable cost and for all threat levels. Performances of the security systems used in commercial aviation security must be assessed to

determine both their effectiveness (the capability to detect threat objects, which in turn is dependent on the technology used) and suitability (the capability of a system to operate with fewest undesirable parameters, such as high radiation levels) **[3]**. These performances have to be evaluated continually, and this specific process should be designed to provide an effective feed-back that allow air carriers and instrument manufacturers to make the desired improvements of the system. Today the compliance of security systems with the standards set by the FAA (Federal Aviation Administration - USA) is considered the minimum acceptable level of performance.

This paper has the following goals:

- to review the potential automated instrumental methods currently under consideration for passenger screening applications
- to evaluate aspects of each method that may cause concerns over health risks, privacy and traveler comfort
- to consider ways in which the above mentioned methods can be implemented to maintain a high level of effectiveness, together with minimizing health risks and increasing of public acceptance
- to examine the key factors that could affect airport implementation of such technologies
- to suggest some alternate screening methods for those passengers who wish or need to avoid the automated systems.

The ideal passenger screening technology should require the following specifications **[3]**:

- detection of both metallic and non-metallic threat items in real time (less than 10 seconds)
- a high degree of accuracy – including a high detection rate together with a low false-alarm rate
- giving the operator a significant amount of information, in an appropriate format, to allow for the speedy and accurate resolution alarms.

It must be emphasized here that current passenger security screening requirements and procedures were developed in response to the increase in airplane hijackings prior to 1972 **[2]**. However, because of increasing attractiveness of aircraft as terrorist targets, the need to improve the capabilities of existing airport security screening systems and processes was recognized. These improvements include:

- enhancing the ability of metal-detection portals to operate effectively in an electrical noisy environment
- providing better information to security personnel on the type and location of potential weapons/threats on individuals
- increasing the detection capabilities of existing systems, by adding the ability to detect a broader spectrum of metals, alloys, plastic explosives, and any other threat materials.

It was found that trace detection technologies, which detect the explosives by interaction with their vapors (or particles), can be used to supplement metal detection technologies to build more comprehensive security systems. By this way metal-detection portals could be replaced by improved systems that reveal the objects concealed under clothings and enable both metallic and non-metallic threat objects identification. The conclusion is that these new detection technologies have technical and analytical features that strengthen their detection capabilities.

However, the acceptance or the rejection of a given technology both by the people who use it (e.g., air carriers companies and airport operators) and the people affected by it (e.g., passengers and aircraft crews) is clearly as important as its performances. For instance, air carriers will manifest strong opposition to the implementation of any technology, no matter how perfect it is, if this technology is unacceptable to the traveling people for various reasons: health reasons, legal and privacy reasons, operational problems and convenience.

The key issues in the passenger screening requirements are:

- ability to find passengers carrying metallic weapons
- detection of explosives, plastic explosives and any other threat materials
- reliability of the system, which is related to consistency in the performances of that system
- fidelity of the system (how accurately the output from the system represents the item to be examined)
- reliability issues regarding operating personnel.

In Table 1 the responsibilities of all factors involved in passenger screening are described, as in the American FAA (Federal Aviation Administration) specifications **[2,3]**.

Table 1.

Responsibilities for passenger screening

Entity	*Responsibility*	*Action*
Air carriers	Provide secure travel	- maintain security program - screen passengers and carry-on baggage - secure baggages/cargo - protect/secure aircraft
Airports	Provide secure operating environment	- maintain security program - protect operations area - provide law enforcement support
Civil aviation authority	Provide the administrative & procedural guidance	- identify/analyze threats - establish requirements/procedures - coordinate crisis situations - provide technical assistance - enforce regulations
Passengers	Cooperate	- fund carrier & airport security via travel tickets purchase

3. Technological improvements

The biggest problem concerning the current passenger screening technologies and procedures is that they don't provide the operator with specific and clear information about the nature and location of the potential threat items, so all the new technologies used in aviation security have to identify and locate this kind of dangerous objects by addressing in the same time the following concerns:

- Convenience (manifested by the smallest possible delay possible for the passengers).
- Respect of the passengers' privacy.
- Legal aspects (for example, the information about non-threat items can be minimized by simply limiting the search area; on the same time, there is a stringent need to discover some non-threat but illegal items, such as narcotics carried by a passenger).

The advanced technologies used in the future for the passenger screening can be classified in two large categories:

1. *Imaging technologies* – which can "see through" clothes and consequently produce an image of the human body plus the objects carried on. It must be emphasized here that all these images yield various amounts of details (depending on the technology used to generate it), but none of them is of photographic quality; as a matter of fact, operators are always needed to view and interpret the images. Imaging technologies can be further classified as well in *active* and *passive* technologies. In the passive screening technologies, the natural radiation emitted by the human body is detected and analyzed, so this type of technology minimize the risks due to the radiations. Active imaging technologies suppose the irradiation of an individual with radiation (either X-rays or microwaves) and then the radiation scattered from the body is analyzed. In both imaging procedures, objects (e.g., metallic weapons or explosives) that emit or scatter radiation differently from the human body will appear different from the background on the image. It was concluded that the images produced by using these techniques are of sufficient high quality to be effective in passenger screening. Another issue is the possible health effects due to the radiation used in active imaging technologies, but we have to specify that these levels of radiation exposure used for screening are by far insignificant when compared with those experienced during many other common activities.
2. *Trace-Detection Technologies*, which physically collect samples of air or material (small particles) from the clothes, bodies or baggage of a passenger and use these samples to detect the presence of a dangerous material. Sample collection is here the key step of an analysis, and it supposes either sampling the air around a person, or touching/swapping the individuals to remove the particles of materials (e.g., plastic explosives) from them or their hand-carried baggages, electronic devices and boarding cards. Unlike the imaging technologies,

where the technologies themselves are already quite mature and the specific equipment is consolidated, accepted and commercially available, many trace-detection techniques are still in a development and assessment phase.

3.1. Imaging technologies

These technologies can detect metallic and nonmetallic weapons, explosives and other contraband material concealed under multiple layers of clothing, by creating images that can be examined to discern these items. Basically, there is not involved any physical contact with the passenger **[3,4]**.

Imaging methods are well established and already used for a wide variety of security applications, such as screening of visitors in prisons or screening the employees at shops' exit to deter thefts. In Table 2 the ways of implementation of imaging technologies in commercial aviation security are described.

Table 2.

Screening technologies based on imaging

Detection technology	*Uses*	*Comments*
Millimeter waves	Portals	- Requires more than a single view
	Wall units	- Requires more than a single view
	Enclosed spaces	- Could provide a 360º view
X-Rays	Portals	- Requires more than a single view
	Enclosed spaces	- Could provide a 360º view

These screening systems generate television-like digital images that can be evaluated by image processing and analysis methods. Images are viewed by an operator trained to identify potential threat objects in these images. Sometimes it is used a special image enhancing software that highlights some unusual features; advanced computed tomography (CT) X-ray systems are good examples for this kind of investigation.

Neutron technologies are also considered for the detection of explosives; thermal neutron analysis and fast (or pulsed fast) neutron analysis are the best known.

Although these techniques cannot detect objects concealed inside the human body or in skin flaps, they are widely considered and used for airport passenger screening because their capability to allow the screening of a wide variety of materials.

3.1.1. Passive and active millimeter-wave imaging

This technology operates in the millimeter-wave range (near 100 GHz) of the electromagnetic spectrum. Passive millimeter-wave imaging is based on the principle that any object (which has not 0 K) emits electromagnetic radiation at all wavelengths. By using an appropriate receiver, this radiation can be detected to produce an image. An important advantage of passive millimeter-wave imaging technique is exactly its ability to provide the image by simply gathering only the radiation emitted naturally from the human body,

without using any artificial radiation; thus, practically no health risks are associated to this technology.

The display methods of the passive millimeter-wave imaging technique are similar to those used for X-ray methods.

Passive millimeter-wave imaging produces screening images of various items carried by passengers: wallets, keys, belts, pocket knives, other common and non-threatening items, but also hidden weapons. An image-analysis software was developed to facilitate interpretation of the images, but finally current technology requires a decision from the human operator **[3,4]**.

Active millimeter-wave imaging systems work as short-range radar devices that project a narrow beam against the target (traveler's body) then detect the reflected radiation. This beam is scanned from head to toes to produce a complete image of that person.

However, the popular perception of the dangers of microwave radiation may cause concerns about this technique.

3.1.2. Active X-ray imaging

This technology uses low-energy, low-intensity X-rays reflected from the subject scanned to create an image. These images are then interpreted to detect the presence of metallic and non-metallic weapons and explosives concealed under multiple layers of clothing or in baggage **[3,5]**.

As in passive imaging systems, the presence of non-threat items complicate the images produced by X-ray imaging systems, making them difficult to analyze and interpret.

Concerning the possible health effects due to the ionizing radiation used in screening systems, it should be pointed out that these effects are negligible (0.003 mrem per exposure at X-ray security screening) comparing with, for example, 5 mrem for a transcontinental air travel (one way trip), 50...200 mrem for annual radon exposure and also some medical X-ray exposures, 5,000 mrem which is the maximum allowable annual radiation exposure to workers and the huge amount of 500,000 for the acute radiation effects or even 5,000,000 for radiation therapy (total treatment) for cancer **[6,7]**. The effects of ionizing radiation on the pregnancy are significant (developmental anomalies and mental retardation) only when the radiation dose exceeds 10,000...20,000 mrem. Also, the passengers who wear pacemakers are not affected by the radiation exposure in passenger screening systems, because pacemaker malfunction occurs only when radiation doses exceed 1,000,000 mrem.

3.1.3. Evaluation of imaging technologies

Factors that influence the usefulness of these technologies are:

- the effectiveness of imaging systems depends on how clear is the image produced; in other words, on how distinct can be made the threat items (such as metallic weapons) on the body background
- although the imaging technologies cannot create a photographic image, they can produce images that can be interpreted by trained operators

- all current imaging techniques require human operators to view, analyze and interpret the complex images produced and to identify the anomalous (threat) items more efficiently than any available software; as a matter of fact, the great variety of human body shapes and sizes complicates the automated image interpretation
- the amount of time necessary to obtain enough information to make a decision affects also the effectiveness of imaging technologies: in screening passengers, the processing time for one person is about 6 seconds
- there are situations when two-sides (front and back) images are taken, to provide a 360° view.

3.2. Trace-detection technologies

As it was already highlighted above, trace-detection technologies are based on the direct chemical identification of either particles of explosive materials or vapor-containing explosive materials. Thus, the presence or the absence of a bomb is confirmed by the presence/absence of explosives' particulate matter or explosives' vapors **[5]**.

One may observe that the fundamental difference between trace-detection, imaging and electromagnetic techniques is that in trace-detection we must have a physical transport of a sample containing explosive (of course in concentrations exceeding the detection limit) to the instrument.

Trace-detection techniques cannot be used to detect the presence of metallic weapons, as imaging technologies currently do.

The two distinct steps occurring in trace-detection are *sample collection* and *chemical identification*. Obviously, to enable identification of explosives both steps have to function well simultaneously. We can observe also that the sample collection phase is the main procedural point of contact between this technology and the passengers to be screened. Potential applications of trace-detection equipment in airports were summarized in Table 3.

Table 3.

Applications of the screening technologies based on trace-detection

Implemented as...	*Comments*
Portal screening - noncontact	Involves high-volume air flows to gather vapors or to dislodge particles from surfaces.
Portal screening - contact	Passenger opens the portal's doors with hands. Passenger passes through a portal lined with brushes.
Hand-wand device - noncontact	Involves high-volume air flows to gather vapors or to dislodge particles adhering to surfaces.
Canine screening - noncontact	Technology currently in use.
Boarding card scanner - contact	Boarding card is scanned for particles of explosive materials, after handling by passenger.

Concerning the possible health effects, it must be kept in the mind that trace-detection technologies for passenger screening may involve person to

person contact or direct contact between an individual and the detection equipment. Of course, these personal contacts could be a vehicle for transmitting various microbial diseases (bacterial, fungal, and viral) from one individual to another, through inhalation or ingestion of disease-causing microorganisms, direct contact with individuals, through wounds and cuts. However, the probability of transmitting diseases as a direct consequence of using trace-detection systems appears to be insignificant in comparison to other more common disease transmission scenarios (like using public washroom facilities). Equipment should be designed to allow frequent cleaning to minimize passenger to passenger disease transmission **[3]**.

3.2.1. Sample collection

Explosives can be transported from the passenger screened to the trace-detection equipment as vapors or as solid microparticles. We shall remind here that the initial efforts in the development stages of trace-detection techniques were focused toward collection and preconcentration of vapors around a person or a baggage. However, because most modern explosives (especially plastic high explosive materials) have extremely low vapor pressures and consequently they don't emit practically vapors at room temperature, the focus has expanded toward the detection of particulates of explosives, on the skin and other surfaces (such as clothes, baggages).

So, if one has to detect traces of explosives material these traces must be concentrated from the air sample (vapor technologies) or dislodged from a substrate (particulate technologies). The result is that in vapor technologies we have to collect very large amounts of air, and in particle technologies the microparticles of explosives must be removed from the surfaces to which are adhering.

Both approaches have their strengths and weaknesses, which in turn depend on the type of explosive screened **[3,5]**. From this specific point of view, vapor technologies are much more effective for detecting those explosives that possess high vapor pressures, while particulate technologies are used for explosives with low and very low vapor pressures (for instance, military plastic high explosives).

Samples can be taken by using 2 methods:

- by passing the subject (the passenger) through a portal
- by passing a hand-wand device over the subject.

Each method can be implemented as a contact or non-contact technique (see Table 3 above):

- In contact portal sampling, the passenger walks through the portal by rubbing against brushes and paddles; generally speaking, contact methods' goal is to gather particles of explosive material from the hands/clothing of a subject.
- In non-contact portal systems, an air flow passes over the passenger when he walks through the portal; these systems can use the air stream either to dislodge particles or to collect a sample of vapors.

It is obvious that even if the use of a hand-wand device is an efficient sample collection technique, it is also much more labor intensive and time consuming than collecting the same samples using an automated portal, which is very similar with common portals used to detect metals.

A conclusion which is arising from the ideas stated above is the following: due to the difficulties encountered in extracting explosive vapors from large volumes of air or to gather particles of explosives from a huge variety of materials, it is not surprising that we don't have yet currently an universal adopted sampling technique **[5]**. For example, there are many companies which develop such systems used to dislodge the material mechanically either with air flows (air brushes) or air vacuum devices, but we must underline that none of the sampling techniques was universally effective under all conditions. As a consequence, this lack of a specific sampling approach generates difficulties in discussing about a generic trace method, and also creates serious problems in designing a standard protocol (for testing and certification) which could be used to compare and assess the effectiveness of various technological approaches.

Another serious problem which should be discussed here for all the trace detection techniques is the clearing of vapors/particles of explosive material from the sample collection device, so that the next readings will be not influenced by any previous traces of explosive materials (memory effects that result in false positive alarms). Therefore, the equipment should give an alarm when a high level of contamination was reached.

3.2.2. Identification of explosive materials

There are currently a variety of commercially available chemical identification technologies that could be used to see if the sample collected previously contains any explosive materials.

It must emphasize here that the limits of detection of most techniques used in the aviation security field are generally sufficient to allow the identification of explosives in a sample. However, some technologies (such as mass spectrometry) that are able to identify and measure ultra-trace amounts of relevant chemicals (like explosives and illicit drugs) are too complex in utilization, because for instance they need highly trained operators to use the instrumentation and subsequently to maintain their high level of performance (detection capability) **[3]**.

The chemical identification/detection part of the trace detection system is smaller than the portal sample collection part of that system, so the sample collection system is determinant for the space and size needed in an airport.

Also, a series of trace chemical detection technologies are small enough to be incorporated into hand-held instruments, having the potential to use them in wand-type portable devices. The techniques under consideration here are:

- ion mobility spectrometry **[8]**
- mass spectrometry
- gas chromatography

- thermo-redox
- chemiluminescence.

The above mentioned technologies should be combined with a sample collection stage, because of the very low vapor pressure of explosives/drugs and their low concentrations. For instance, if the detection limits for IMS are on the low ppb range, by using preconcentration these limits were pushed toward low-ppt domain (3 ppt for TNT!) **[8]**. However, this need to collect a sample by moving very large amounts of air could be a drawback which may limit the application of these technologies as methods used in hand-wand devices.

One of the most promising and proven trace detection technique, which was implemented on a large number of airports, is Ion Mobility Spectrometry.

3.3. Nonimaging electromagnetic technologies

These technologies are used for continuous screening in various public places, such as clothing stores, sport stadiums, schools, libraries, court houses and so on. There are mature techniques, which function basically as metal detectors that detect thefts and for safety insurance. For airport security use, the improvements of nonimaging techniques should make them sensitive specifically to weapons. These systems are pre-programmed to recognize false alarms due to common nonthreat metallic objects (like belt buckles). Other improvements include making these metal detectors: more versatile in detecting a broad spectrum of metal alloys, more specific in locating the suspected threat items (like weapons) and more tolerant to any electrical noise generated by nearest sources (such as terminals, fluorescent lights, video displays).

The American civil aviation authority (FAA) is considering a nonimaging dielectric portal system which uses the microwave radiation and a pair transmitter/receiver to determine the complex dielectric constant of the objects that are screened, then the measured dielectric constant is compared to known responses for humans and threat objects. The levels of microwave power used for weapons' discovery are extremely low - less that 0.1% of the levels established for microwave energy safety regulations. A single 360° scan is completed in about 5 seconds.

The hand-wand electromagnetic screening devices are used for locating specific items and have already a widespread use in the airports. However, they are slower than portals. We have to underline an important disadvantage of the nonimaging electromagnetic screening techniques: these technologies are unfortunately unable to detect nonmetallic threat objects/materials. Microwave-based systems are capable to detect both metallic and non-metallic threat objects.

Compared with ionizing radiation, the possible health effects associated with non-ionizing fields (such as extremely low-frequency electric and magnetic fields) are even smaller **[9,10]**. Although some laboratory medical studies have confirmed that low levels of electromagnetic radiation may cause biochemical and physiological changes in human cells, they don't appear to damage the

DNA directly, and consequently they would be unlikely to initiate cancer. Also, these technologies are not expected to cause adverse effects on health of developing embryos and fetuses. A large number of epidemiological studies have already been conducted on reproductive and teratogenic effects (e.g., birth defects or spontaneous abortions) in human groups exposed to electromagnetic and magnetic fields from video display terminals (VDTs), power lines, and household appliances **[10]**; the results of these studies strongly suggest that the radiation and field exposures at the levels associated with passenger screening devices do not have reproductive or teratogenic effects. For instance, the exposure given by a VDT is a magnetic field of max. 2 milligauss (mG) at 30 cm from the screen, which is comparable to magnetic fields found near home television apparatus. A magnetic field strength of 2 mG will produce an electric field (at 16 kHz) of about 1 mV/m in the abdomen of the operator; for comparison, flying in an airplane through the magnetic field of the Earth produces a uniform static electric field of about 10 mV/m through the entire human body.

3.4. Clearing an alarm

The concept of "clearing an alarm" is related to the return of the instrument to its initial, pre-examination state.

As a matter of fact, only trace-detection technologies are expected to be affected by possible problems due to clearing an alarm (such as the memory effects). Neither imaging technologies, nor nonimaging electromagnetic technologies present a memory effect, which is a serious advantage.

In contrast to imaging technologies and nonimaging electromagnetic technologies, trace-detection equipments are interacting directly with the vapors/particulates of the materials of interest and indicate the presence of these substances if the concentration is above a threshold level. Ideally, the instrument signal should return automatically to its baseline (initial) value once the detection was completed; however, if the area close to sampling inlet is still contaminated or if the compounds of interest remain somewhere in the instrument then the equipment will be obviously unable to return automatically to its baseline level, and this is the phenomenon known as "memory effect". The contamination who generates memory effects will generate also persistent elevated signals without analyte in the sample, and may even trigger the alarm without a real cause (false positive alarms) **[3,8]**.

Contamination of the internal parts of the system may occur if:

- the vapors have high affinity for the materials which compose the sample collection part of the trace-detection instrument
- the particulate trace is dislodged from the subject screened by using mechanical means (e.g., air brushing), has high affinity for sample collection stage materials or remains stuck in the sample collection mechanism.

The memory effects could be minimized by a judicious choice of the materials used to build up the sample collection devices, so by using materials which do have a low free energy of adsorption for the molecules of explosives

materials. As an additional feature, the instrument should have a mechanism for by-passing the sample collection inlet, just to verify (with uncontaminated air) the presence or absence of any memory effects.

Another serious issue refers to the tendency of most trace-detection systems to react to the presence of non-threating interferents (substances that are chemically similar to explosive materials, like some drugs used in medications). This would lead to false positive alarms.

3.5. Problems related to health and privacy

The health effects concerning trace-detection, imaging and nonimaging technologies used in the security screening systems were already discussed earlier.

At this point, however, it would be more than useful to present a summary of the basic problems associated with health and privacy. The conclusions that could be drawn are as follows:

- four categories of issues seem to be most relevant to public acceptance of passenger screening technologies: health, privacy, convenience, and comfort
- health concerns are more a risk perception problem, because in fact these technologies do not pose any significant health hazards; this problem could be effectively dealt with good communication and public education
- privacy concerns about displaying images of bodies and initiating physical contacts may be significant drawbacks to implementation of screening techniques
- convenience and comfort, in the form of avoiding time delays, appear to be also a highly important factor in public acceptance; technologies that require more than 6 seconds to screen each person are prone to be banned by the public.

4. Conclusions

Ensuring the security of the air travel system is definitely a monumental task, involving screening of millions of passengers (plus their baggage) every day for the presence of metallic weapons or dangerous materials. For this reason, the civil aviation authorities are looking for technologies that can address anticipated changes in security screening requirements, by expanding the ability to detect the presence of dangerous materials on a person. The increased probability of terrorist threats in the future will conduct to the higher acceptance and use of more invasive technologies.

Improvements to the current screening systems are of paramount importance; however, these improvements have to increase overall screening efficiency by simultaneously decreasing the number of false alarms and also by allowing the screening operators to solve more quickly these alarms by providing

information about the specific type and location of the object that triggered the alarm. Although a series of screening technologies are already mature and ubiquitous, they could suffer further improvements to make them more effective for aviation security; for example, the metal detection portals can be improved by using parallel algorithms to detect simultaneously different metals, alloys, and structures, and detector arrays can be used to localize threat posing items much more specifically.

Technologies used and developed in the commercial aviation security screening can be broadly divided into imaging technologies or trace detection technologies, with their specific advantages and drawbacks. As for imaging technologies, in the current state of technology development human operators are required to interpret the images resulted, because they are familiar with various human and objects form and its variation. Trace-detection technologies, on the other hand, rely on the collection of samples (vapors and/or particles) of explosive materials to identify the presence of a threat; this collection can imply sampling the air around a person or touching the individual to remove the particles of explosive from the body, clothing or baggage. Of course, non-contact methods of sample collection (such as using an air shower or a vacuum device) are more acceptable to passengers' convenience, but they may be also less efective than contact sampling.

BIBLIOGRAPHY

[1] ATA (Air Transport Association), *ATA Annual Report of the U.S. Scheduled Airline Industry* (1994).

[2] FAA (Federal Aviation Administration), *FAA Report "Criminal acts against civil aviation"*, Washington, DC (1993).

[3] National Research Council (NRC), *"New Technologies for Airline Passenger Security Screening: Implementation Issues"*, National Academy Press, Washington, DC (1996).

[4] National Research Council (NRC), *"Detection of explosives for commercial aviation security"*, Report 471, Washington, DC (1993).

[5] Jankowski, P., FAA DOT/FAA/CT-TN95/05, *"Trace explosives portal workshop"*, Washington, DC (1995).

[6] National Research Council (NRC), *"Health effects of exposure to low levels of ionizing radiation"*, National Academy Press, Washington, DC (1990).

[7] National Council on Radiation Protection and Measurements (NRCP), *"Ionizing radiation exposure of the population of the United States"*, NRCP Report No. 93, Bethesda, Maryland (1987).

[8] Bocos-Bintintan, V., *"Spectrometria de mobilitate ionică"*, Editura Presa Universitară Clujeană, Cluj-Napoca (1998).

[9] National Radiological Protection Board (NRPB), *"Electromagnetic fields and the risk of cancer"*, Documents of NRPB, 3(1) (1992).

[10] Oak Ridge Associated Universities (ORAU), *"Health effects of low-frequency electric and magnetic fields"*, ORAU 92/F8, Springfield, Virginia, National Technical Information Service (1992).

STUDIA UNIVERSITATIS BABEŞ-BOLYAI, CHEMIA, XLVI, 1-2, 2001

INFLUENCE OF SPECIFIC SURFACE AREA ON THE REACTION OF LIME WITH SO_2. I.EXPERIMENTAL DATA

S.DRAGAN[*] and I.SIMINICEANU[**]

**University "Babes-Bolyai" of Cluj-Napoca, Faculty of Chemistry and Chemical Engineering, Str.Arany Janos 11, Romania, e-mail:sdragan@che.ubbcluj.ro*
***Technical University of Iasi, Faculty of Industrial Chemistry, 71 Bd.Mangeron, Romania, e-mail:isiminic@ch.tuiasi.ro*

ABSTRACT. Experimental measurements concerning the influence of calcinated and particles size on the specific surface area and reactivity CaO in the capture of SO_2 were performed. The paper presents data about the study of the SO_2/CaO reaction which includes specific surface area as an experimental variable. The obtained values of specific surface area are in the range of 19 – 55 m^2/g coresponding to particles size of 25 to 900μm. The CaO-reactivity increases significantly with the specific surface area, calcinated temperature and SO_2 concentration in the gas mixture.

INTRODUCTION

Reactions of acidic gases with calcined limestone have received much experimental study due to their industrial importance. They have also received extensive theoretical analysis as a class of gas-solid reaction because of the fact that the high porosity of the CaO (54%) makes them well suited for tests of the numerous grain – and pore – reaction models that have been formulated during the past decade.

A particular case is the reaction CaO-SO_2. The porous solid CaO, produced by calcining limestone:

$$CaCO_3 = CaO + CO_2 \quad (1)$$

can then react with SO_2 in the presence of oxygen to give calcium sulphat:

$$CaO + SO_2 + ½\ O_2 = CaSO_4 \quad (2)$$

A lot of experimental data have been achieved in modeling, but the rate-limiting step are still not understood [1].

The high temperature sensitivity of reaction (2) to has led some researchers to conclude that chemical reaction is rate controlling [2,3], while different features of the same data have been interpreted by others as evidence that the process is controlled by either:

- diffusion of the reactive gas through the product layer on the CaO grains that comprise the interior of the particles [4], or
- combinations of diffusion and chemical reaction on the grains.

Maybe for these reasons the process has been extensively studied both by scientists involved in the environmental protection [5 -6] and by academics interested in solid-gas reactions [7-9].

The aim of the present paper is to present data about the study of the SO_2/CaO reaction which included specific surface area as an experimental variable. Because of the importance of such data to an elucidation of the rate

controlling mechanism of the process, this study was carried out with the objective of quantifying the surface area effect using the experimental techniques recently developed for producing CaO *in situ*.

EXPERIMENTAL

The experimental equipment used in our kinetic measurements was a CAHN TG-121 system (Figure 1).

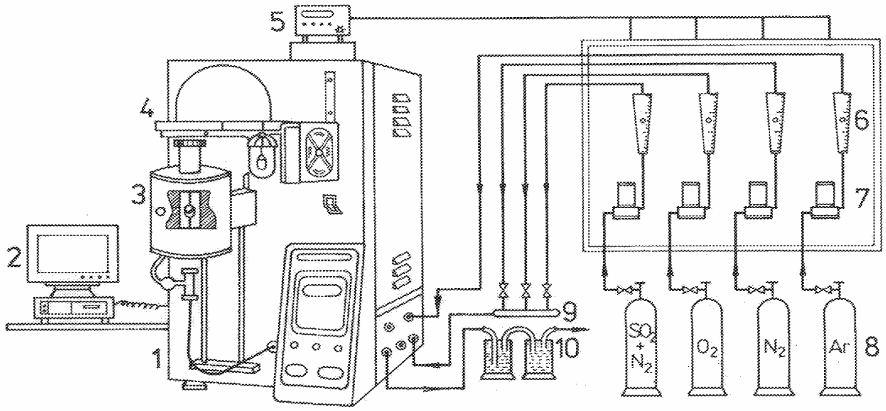

Figure 1. Experimental equipment: 1.Main frame; 2.Data Acquisition Control Station (DACS);3.Electric Furnace; 4. Microbalance and cooling fan; 5.Flow-gas-regulator; 6.Gasrotameter; 7.Massflowcontroller; 8. Gas cylinders; 9.Gas-mixture room; 10.Absorbing vessel for unreacted gas.

It consisted of two main sections: the main frame and the Data Acquisition and Control Station (DACS) which controlled the system. The microbalance, the furnace, the cooling fan, the thermocouple, the gas and vacuum ports were the components of the main frame. The CAHN microbalance included in the TG- 121 system is considered the finest apparatus available today for this application. Its sensitivity is of 0.1µg and the maximum capacity of 1.5 g. Each sample of limestone has been primarily calcinated for 40 minutes at 973 K;1023 K; 1123 K; 1173 K; 1273K and 0.3403 bar. The thirty probes belonged to one of the following average particle diameter: 25µm, 90µm,180µm and 900µm. After the complete calcination, each sample has been sulfated in a gas mixture containing 0,3 % and 0,9% (vol.) SO_2, 20 % (vol.) O_2, and nitrogen for the balance. The gas mixture was prepared from pure gases measured with rotameters.

The temperature in the sulfation process was kept constant at 973K, and 1173K. The solid weight has been continuously registered. Specific surface areas were measured by nitrogen adsorbtion at –195 ˚C using the BET method.

RESULTS AND DISCUSSION

The principal variables that are expected to determine the rate of SO_2 capture by a given limestone are reaction temperature, specific surface area of

the CaO and the SO_2 concentration in the gas mixture. The results of experimental evaluation of these variables are shown in Figure 2-7.

The effect of particles size and calcination temperature on the specific surface area is shown in Figure 2 and Figure 3.

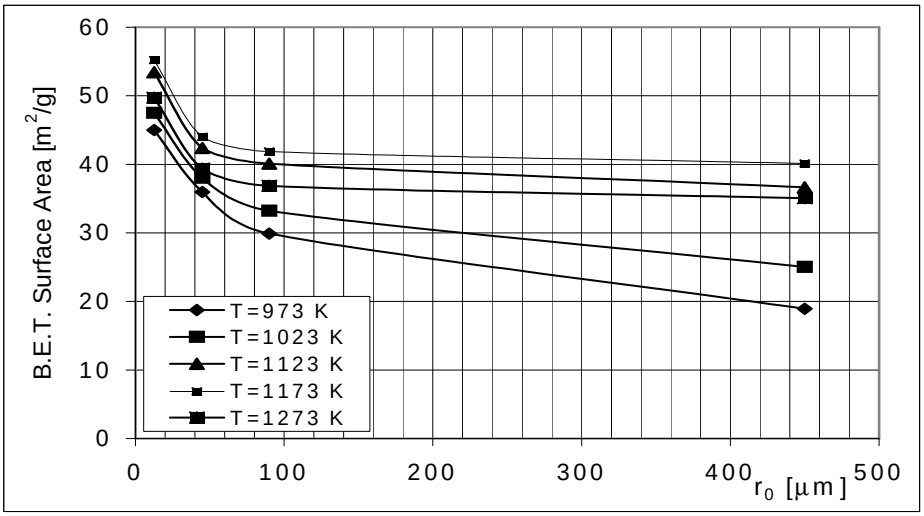

Figure 2. Effect of particles size on the specific surface area of CaO

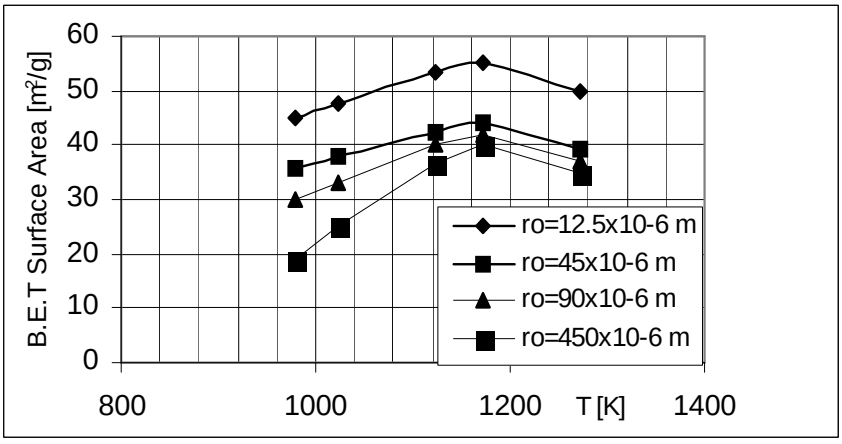

Figure 3. Effect of calcination temperature on the specific surface area of CaO

Figure 2 shows that the higer BET surface area belonged to smaller particles of CaO at 1173 K. For our limestone particles calcined in the TGA reactor at temperatures of 973 K-1273 K these are in the range of 19 to 55 m^2/g and this range is also similar to the CaO surface area found by Beruto et.al. [10].

Figure 3 shows that the surface area for constant particles size increases with the calcination temperature.The highest surface area was obtained by calcination in situ at 1173 K, and the lowest was obtained at 973 K.

At temperatures above 1173 K, while the sintering process begins the specific surface area decrease continuosly.

The effect of specific surface area on the reaction rate was determined at a constant temperature of 973 K and 1173 K with the results shown in Figure 4 and Figure 5. The reaction (2) is accompanied by an important solid weight increase, and the effects of side reactions are negligible. On the basis of materials balance equations (3):

$$\begin{aligned} m_{Cao} &= m^0{}_{CaO} - m^0{}_{CaO}.\eta_{CaO} \\ m_{CaSO_4} &= \frac{136}{56} m^0{}_{CaO}.\eta_{CaO} \\ m_{A''} &= m^0{}_{A''} \\ m_S &= m^0{}_S (1 + \frac{80}{56} \bar{x}_{CaO}.\eta_{CaO}) \end{aligned} \qquad (3)$$

the relation between the solid mass increase (Δm_S) and the fractional conversion of lime (η_{CaO}) can be derived:

$$\eta_{CaO} = \frac{56}{80} \frac{\Delta m_S}{x^0{}_{CaO}.m^0{}_S} \qquad (4)$$

According to the equation (4), at an average conversion of 50 %, a sample of 100 mg pure lime increase in weight with 71.42 mg because of sulfation reaction (2).

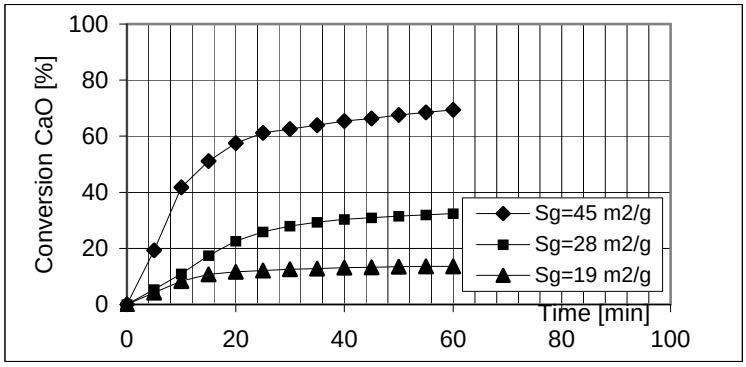

Figure 4. Reactivity of CaO as a function of its specific surface area T=973 K; C_{SO2}=0,9% vol ;Gv=50 cm^3/min

Figures 4 and 5 shown that the reactivity of CaO is strongly influenced by the specific surface area. The highest reactivity was obtained for the greatest specific surface area either at the reaction temperature of 973 K or 1173 K.

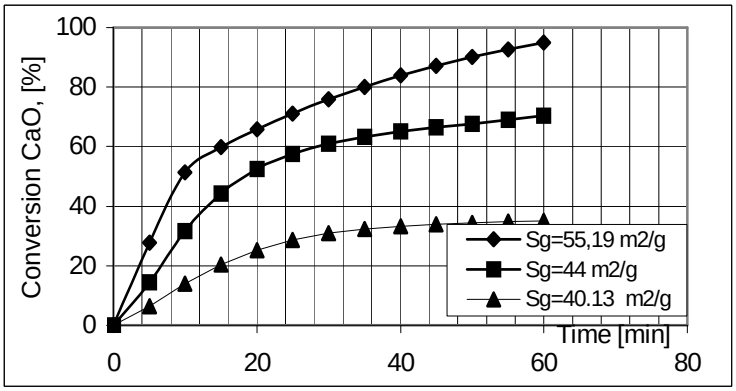

Figure 5. Reactivity of CaO as a function of its specific surface area T=1173 K; C_{SO_2}=0,9% vol;Gv=50 cm^3/min

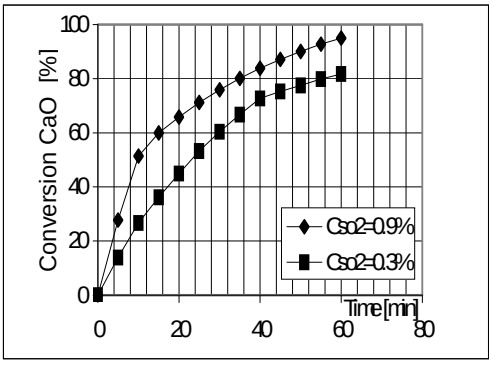

Figure 6. Effect of SO_2 concentration on CaO reactivity at T=1173 K; S_g=55 m^2/g

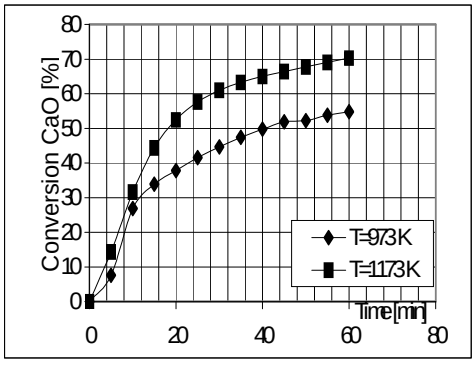

Figure 7. Effect of temperature on CaO reactivity at C_{SO_2}=0,9%; S_g=36 m^2/g

Figures 6 and 7 illustrates a significant influence of SO_2-concentration on the CaO reactivity at constant temperature (1173 K) and specific surface area respectively at constant sulfure dioxide concentration in the gas mixture and two different temperatures. Higher reactivities were obtained for greater sulfure dioxide concentrations at constant temperatures (fig. 6) and for greater temperature at constant sulfure dioxide concentration.

When the SO_2-concentration is uniform within the pore structure, which can be assumed to particles of low surface area, the reactivity versus time will be expected to follow one of five possible responses depending on the rate-controlling processes at the grain surfaces. These influences as described [11], can be written for constant temperature and constant grain size as follows:

- if chemical reaction controls at the surface of a shrinking core of unreacted CaO within the grain:

$$1-(1-\eta_{CaO})^{1/n} = k_c \cdot t \qquad n = 1,2,3 \qquad (5)$$

- if homogeneous first-order reaction occurs within the grains:

$$-\ln(1-\eta_{CaO}) = k_h \cdot t \tag{6}$$

- for power law reaction within the grains:

$$(1-\eta_{CaO})^{-n} = k_p \cdot t \qquad n>0 \tag{7}$$

- for product nucleation and growth on grain surfaces:

$$[-\ln(1-\eta_{CaO})]^{1/n} = k_g \cdot t \qquad n = 1,2,3,4 \tag{8}$$

- for diffusion through the product layer surrounding unreacted cores of (spherical) grains:

$$1-3(1-\eta_{CaO})^{2/3} + 2(1-\eta_{CaO}) = k_d \cdot t \tag{9}$$

Using the above equations, in the second part of the paper it should be presented the results for the establishment of the rate – controlling processes.

CONCLUSIONS

The limestone is quickly converted to lime which further reacts with sulfur dioxide. New studies have been carried out on the sulfation reaction using a CAHN TG –121 system for experimental measurements.

The experimental data shown that the reactivity of CaO are strongly influenced by three factors: calcined temperature, specific surface area and SO_2 concentration in the gas mixture.

Higher reactivities were obtained for greater sulfure dioxide concentrations at constant temperatures (fig. 6) and for greater temperature at constant sulfure dioxide concentration.

When the SO_2-concentration is uniform within the pore structure, which can be assumed to particles of low surface area, the reactivity versus time will be expected to follow one of five possible responses depending on the rate-controlling processes at the grain surfaces.

NOTATIONS

A'' – inert substances in the solid, - ;

m_i - mass of component , kg ;

P – pressure, Pa ;

S_g– specific surface area, m^2/g ;

T – temperature, K;

k_c, k_h, k_p, k_g, k_d – Constants defined by equations (5-9) for a given temperature, grain size, and SO_2-concentration relating conversion and time for grain reactions controlled, respectively by: c-chemical reaction; h-homogeneous reaction; p-power law reaction; g- product nucleation; d- product layer diffusion;

$\overline{x_{CaO}}^{0}$ - mass fraction of CaO in the lime, -;

Δm_s - thermogravimetric mass increase, kg ;

η_{caO} - fractional conversion of CaO.

REFERENCES

1.Borgwardt, R.H., Roache, N.F., Bruce, K.R., *Ind. Eng. Chem. Fundam*., (1985) **25**, 156

2. Borgwardt, R.H., *Environ. Sci. Technol*., (1970) **4**, 59.

3. Pigford, R.L., Sliger, G., *Ind. Eng. Chem. Process Des. Dev*., (1973) **12**, 85.

4. Hartman, M., Trnka,O., *Chem. Eng. Sci*., (1980) **35**, 1189.

5. Bjerle, J., Ye, Z., Wang, W., *Limits and potentials of the dry injection process, 1993 SO_2 Control Symposium,* 1993 **vol. 1**, EPRI, Boston.

6. Dunderdale, J. (Editor), *Energy and the Environment,* Royal. Soc .1990 Cambridge.

7. Fields, R.B., Burdett, N.A., Davidson, J.F., *Trans. Instn. Chem. Engrs*., (1979) **57**,276.

8. Hartman, M., Colln. *Czech Chem. Commun*., (1975) **40**, 1466.

9. Borgwardt, R.H*., 2nd Joint Symposium on Dry SO_2 and Simultaneous SO_2/NO_x Control Technologies*, San Diego, California, 1984.

10. Beruto, D. *Am. Ceram.Soc.* 1979, **62**, 580 – 584.

11. Szekeky, J.J. *Gas – Solid Reactions,* Acadenic Press, New York, (1976).

STUDIA UNIVERSITATIS BABEŞ-BOLYAI, CHEMIA, XLVI, 1-2, 2001

MULTIVARIABLE FUZZY LOGIC CONTROL OF THE HEXAMETHYLENE TETRAMINE REACTOR

M.V. CRISTEA, M. BALDEA, P.S. AGACHI

"Babes-Bolyai" University of Cluj-Napoca, Faculty of Chemistry and Chemical Engineering, 11, Arany Janos St. 3400 Cluj-Napoca, Romania, mcristea@chem.ubbcluj.ro

ABSTRACT. The paper presents the simulation results of the Fuzzy Logic Control (FLC) of the hexamethylene tetramine reactor. Fuzzy Logic has become a valuable control strategy for chemical processes, due to its natural and intuitive way of representing information. Simulation results reveal its efficiency in terms of the main control performance indexes. The control difficulties generated by the multivariable approach and non-linear process behavior have been overcome by this control technique, with real possibility for industrial implementation.

INTRODUCTION

Fuzzy Logic control is obviously one of the most important control approaches developed during the last two decades. In the past few years, it has become a widely accepted control method in process industry plants, consecutive to the practical validation of the theoretical concepts. The possibility of creating software products that embed the simple *if...then* clauses used in natural language has been a major contributor to the success of fuzzy logic control. Indeed, fuzzy logic controllers can be designed to benefit of the knowledge accumulated by highly trained process operators, by directly transforming it into fuzzy inference rules. This often regularly creates more robust controllers, able to deal with process uncertainties and complex dynamic behavior (difficult to describe by first-principle models).

MODEL DESCRIPTION

The fuzzy logic approach has been tested for the control of the hexamethylene tetramine reactor (Ungureanu [1]). The stoechiometry of the reaction is described by:

$$4NH_3 + 6CH_2O \rightarrow N_4(CH_2)_6 + 6H_2O \quad (1)$$

A number of simplifying assumptions have been considered for modeling the reactor: the process is assumed to take place in a Continuous Stir Tank Reactor (CSTR), with no heat loss to the environment, irreversible third-order reaction mechanism and an Arrhenius type rate constant. The simplified mathematical model was experimentally validated and consists of a set of differential equations describing the main mass and energy balance:

$$\frac{dC_A}{dt} = \frac{q_A}{V} C_{A_i} - \frac{q_A + q_F}{V} C_A - r \tag{2}$$

$$\frac{dC_F}{dt} = \frac{q_F}{V} C_{F_i} - \frac{q_A + q_F}{V} C_F - 1.5 \cdot r \tag{3}$$

$$\frac{dT}{dt} = \frac{q_A}{V} T_{A_i} + \frac{q_F}{V} T_{F_i} - \frac{q_A + q_F}{V} T + \frac{(-\Delta H)}{\rho\, C_p} r - \frac{K\ A \Delta T_m}{V \rho C_p} \tag{4}$$

where

$$r = k_0 C_A C_F^2 \exp\left(-\frac{E}{RT}\right) \tag{5}$$

$$(-\Delta H) = -78.968 \cdot 10^6 + 0.50645 \cdot 10^6 \cdot T \tag{6}$$

$$\Delta T_m = \frac{T_{r_0} - T_{r_i}}{\ln\left(\frac{T - T_{r_i}}{T - T_{r_0}}\right)} \tag{7}$$

$$\frac{K\ A \Delta T_m}{V \rho C_p} = \frac{\rho_r C_r}{\rho C_p} \frac{q_r}{V} (T - T_{r_i}) \cdot \left[1 - \exp\left(-\frac{K A}{\rho_r C_r q_r}\right)\right] \tag{8}$$

The main process variables taken into consideration are the outlet concentrations of ammonia and formaldehyde and the outlet temperature (as outputs), and the inlet flows of ammonia, formaldehyde and cooling agent (as inputs).

In despite of its fairly basic structure, the model is able to describe the dynamic features of the process that are used for control purposes.

RESULTS AND DISCUSSION

A fuzzy inference system is made of several rules using the same output variables. The inference procedure defines the way the conclusions are to be inferred using this set of rules. Output variables can be discrete ('crisp') or continuous, the inference system being called, respectively, a Sugeno or a Mamdani system.

Fuzzy reasoning works just like any other logical reasoning: a fuzzy conditional rule is made up of a *premise* and a *conclusion*

if premise ***then*** conclusion (9)

The premise may contain a number of predicates P_i, also called antecedents. The antecedents can be negated or combined by operators like AND, OR (computed with t-norms, or t-conorms). Based on the concepts introduced, a fuzzy conditional rule would be or the following form (M. Russo[2]):

if P_1 ***and*** P_2 ***or*** P_3 ***then*** P_4 (10)

where P_4 is referred to as the *consequent*.

Any process controller's mission is to receive a number of inputs and compute the appropriate outputs in order to eliminate a possible error. The fuzzy controller is no exception: it receives a measured value from the system (which is the universe of discourse), if fuzzyfies it, applies the conditional rules, computes an overall result of all the rules and then converts the result into a number which is an appropriate command for the system it controls. (Em. Sofron et. al.[3])

A multivariable controller has been used to control the three considered outputs. The parameters of the FL controller have been adjusted to account for the nonlinear features of the process and the interactions between the target variables.

First, the setpoint tracking capabilities of the FLC have been investigated using a step increase of the setpoint. The evolution of the three controlled outputs in case of a step increase of the setpoint (+0.4 kmol/m^3 at t=2000 s) of the ammonia outlet concentration is presented in Fig. 1.

Simulation results reveal the good performance of the FL controller. The controller is capable of leading the system to the new ammonia concentration setpoint value in a short time and with minimum overshoot. Also, no important deviation is induced on the evolution of the other controlled outputs of the system.

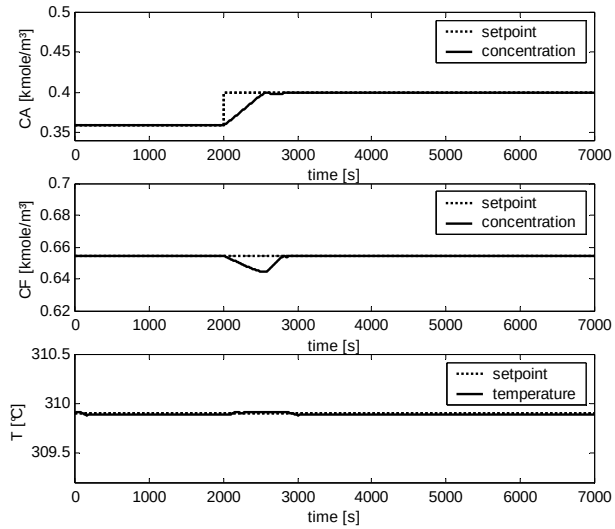

Fig. 1: Fuzzy Logic Control for the case of a step change in the setpoint of the ammonia concentration

The evolution of the controlled outputs in case of a step decrease in the setpoint (-5℃, at t=2000s) of the outlet temperat ure is presented in Fig. 2.

Again, a good setpoint tracking performance was obtained, accompanied by an efficient reduction of the interaction effect between the controlled outputs.

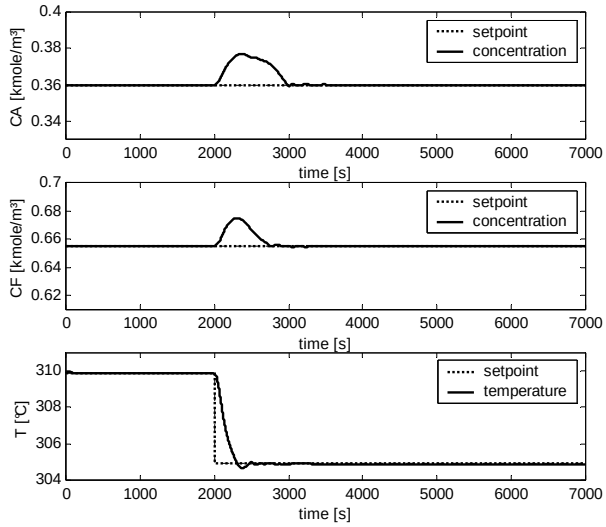

Fig. 2: Fuzzy Logic Control for the case of a step change in the setpoint of the outlet temperature

Second, the disturbance rejection ability of the controller has been tested. The results are presented in figures 3 and 4.

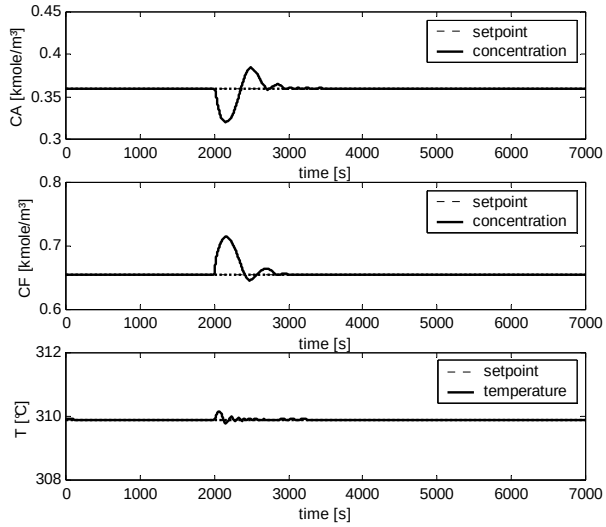

Fig. 3: Fuzzy Logic control for the case of a formaldehyde inlet concentration disturbance

Three typical disturbances have been considered: concentration of the inlet ammonia flow, concentration of the inlet formaldehyde flow and the inlet

temperature of the cooling liquid. Simulation were carried out for the case of an increase (+0.6 kmol/m^3 at t=2000s) in formaldehyde concentration and for an increase (+6.8 ℃, at t=2000) in cooling liquid tem perature.

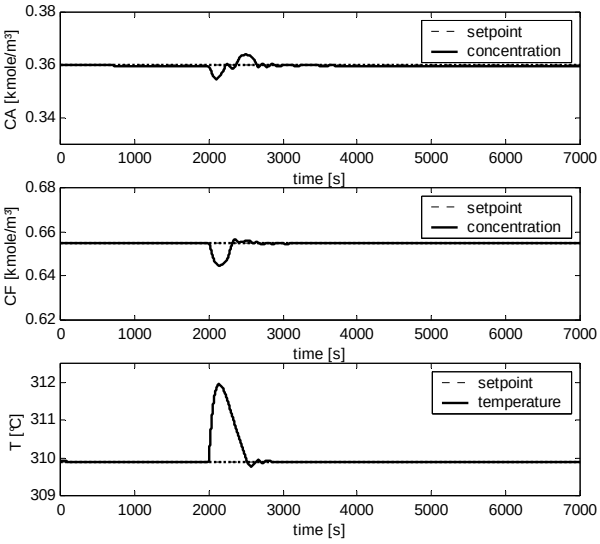

Fig. 4: Fuzzy Logic Control for the case of a cooling agent temperature disturbance

The controller performs very well in rejecting the tested disturbances. Low overshoot and minimum settling time are to be noticed. This good performance is due to the particular design of the fuzzy inference system: detailed fuzzification and defuzzification of the controlled systems inputs and outputs, each input and output using five membership functions (MF) and an asymmetrical membership function structure. This setup uses a total of fifteen fuzzy rules. MFs are of triangular shape. Their asymmetrical setup assists the controller in dealing with the difficulties induced by the non-linear system. A sample asymmetrical MF structure is depicted in Fig. 5.

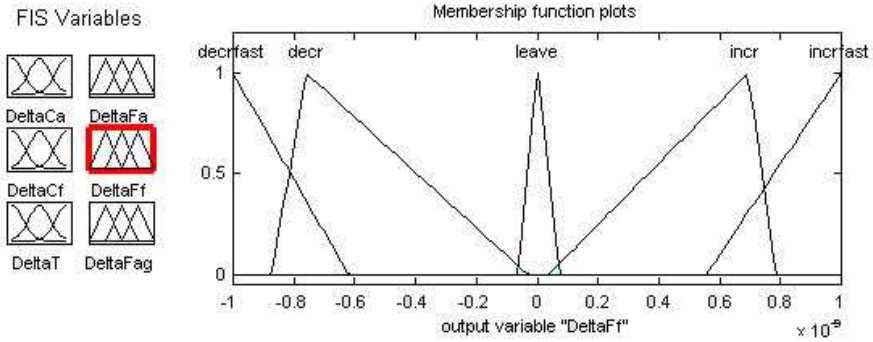

Fig. 5: Membership function structure for the defuzzification of formaldehyde flow rate

The model was coded as a Matlab S-function (Matlab [4]) and simulations were carried out using the Matlab extension, Simulink, in association with other dedicated Matlab toolboxes.

CONCLUSIONS

The present work investigates the possibility of implementing a fuzzy logic algorithm for controlling the hexamine CSTR. A multivariable (three-input and three-output) fuzzy-logic controller is developed and tested. The asymmetrical membership function definitions and fifteen rules are found to be capable of countering the system's nonlinear features, with minimal overshoot and short settling time. The controller exhibits good setpoint tracking performance and efficiency in rejecting disturbances. The controller is designed to minimize the interaction between the controlled variables.

All these features indicate that fuzzy logic control is a feasible approach to the control of process plants, for both large-scale and pilot-sized units.

NOMENCLATURE

C_P = mean heat capacity [J/kg K]
E = activation energy [J/kmol]
K = heat transfer coefficient [W/m^2 K]
k_0= frequency factor [$(kmole/m^3)^{-2}$ s^{-1}]
q = flow rate [m^3/s]
R= gas constant [J/kmol K]
r = reaction rate [$kmol/m^3$ s]
T= temperature [K]
V= reactor volume [m^3]
ΔH= reaction enthalpy [kJ/kmol]
ΔT_m= logarithmic mean temperature difference

Indices:
A= ammonia
F= formaldehyde
i= input
m= mean
r= cooling agent

REFERENCES

1. St.Ungureanu, *Sensibilitatea sistemelor dinamice*, Ed. Tehnica, Bucuresti, 1988
2. M. Russo, *IEEE Trans. Fuzzy Systems,* 6(3), 1998, pp.373-389
3. Em. Sofron, N. Bizon, S. Ionita, R. Raducu, *Sisteme de control Fuzzy*, Ed. All, Bucuresti, 1998
4. *** *Matlab User's Guide*, The MathWorks, Inc., Natick, Mass., 1999

SIMULATION OF THE DOLOMITE THERMAL DECOMPOSITION BASED ON THE GRANULE MODEL

ANA-MARIA CORMOS, MIRCEA CRISTEA, GABRIELA ZAHA, SERBAN AGACHI, ALEXANDRU POP

"Babes-Bolyai" University of Cluj-Napoca, Faculty of Chemistry and Chemical Engineering, Arany Janos 11, 3400 Cluj-Napoca, e-mail: cani@chem.ubbcluj.ro,

ABSTRACT. In this paper the mathematical model of thermal decomposition for a dolomite granule has been developed and studied. The model offers the possibility to estimate the distribution of the over heated oxide obtained from dolomite and unreacted dolomite core for given operating conditions of the kiln. The mathematical equations of the model are presented and the simulator is implemented using MATLAB and FEMLAB software package.

Mathematical Model

The mathematical model, as basis for the dynamic simulator development, aims at studying different possibilities of reducing the fuel consumption of the kiln. According to data reported in literature, the dolomite decomposition process was considered and implemented on the assumption of the unreacted core model, firstly developed by Kunii. The model for the dolomite thermal decomposition was chosen in order to reflect the real process behaviour, in a better way. In order to define the mathematical equations, the geometrical shape of the dolomite granule has to be specified. Spherical dolomite granules [1] with initial radius R have been considered, figure 1. The decomposition process begins on the dolomite surface. The reaction takes place on the interface surface situated at a distance r_m from the centre. The solid reactant is assumed to lie within the r_m radius sphere. The reaction zone moves toward the centre of the granule. During the decomposition process the unreacted core (dolomite) decreases with time changing velocity.

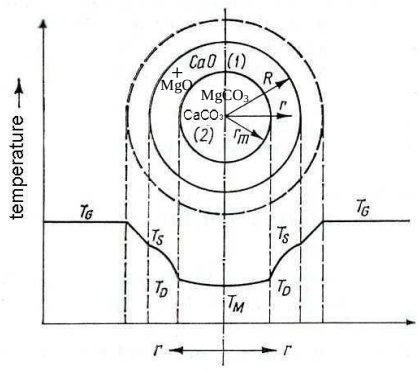

Fig. 1 The unreacted core model for dolomite granule

The mathematical model of the dolomite granule decomposition is built considering the following assumptions [1, 2]:

- dolomite granules are spherical and present initial homogeneous properties: equal diameter, uniform temperature on the external surface and radial propagation of the reaction in each granule;
- gaseous phase properties have been considered constant.

Thermal decomposition of dolomite considers the following phenomena:

- heat transfer from the gaseous phase to the solid surface;

- heat transfer through the reacted product;
- reaction on the surface;
- diffusion of the carbon dioxide from the solid phase to the gaseous phase;
- heating the dolomite unreacted core up to the reaction temperature;
- heating the resulted layer.

The mathematical equations for thermal the decomposition of dolomite are [1,3,4]:

- heating the granule core by conduction

$$\frac{\partial T_2}{\partial t} = a_2 \cdot \left(\frac{\partial^2 T_2}{\partial r^2} + \frac{2}{r} \cdot \frac{\partial T_2}{\partial r}\right)$$

- heating the reacted layer

$$\frac{\partial T_1}{\partial t} = a_1 \cdot \left(\frac{\partial^2 T_1}{\partial r^2} + \frac{2}{r} \cdot \frac{\partial T_1}{\partial r}\right) + \frac{M_{CO2} \cdot Cp_{CO2} \cdot \rho_2}{M_{dolomite} \cdot Cp_m \cdot \rho_1} \cdot \frac{r_m^2}{r^2} \cdot \frac{dr_m}{dt} \cdot \frac{dT_1}{dr}$$

- the heat transferred between gaseous phase and the solid surface:

$$\frac{\partial T_G}{\partial t} = k_T \cdot S_v \cdot \rho \, (v_S / W_G) \cdot (T_G - T_{sp})$$

The initial and boundary conditions taken into consideration are:

$t = 0, \quad 0 \le r \le R; \quad T_1 = T_2 = T_0$

$t > 0; \quad r = R, \; T_1 = T_s \quad \lambda_1 \frac{\partial T_1}{\partial r} = k_T (T_G - T_{sp})$

$r = r_m; \quad T_1 = T_2 = T_d$

$$\lambda_1 \frac{\partial T_1}{\partial r} + \Delta H_R \cdot \rho_2 \cdot \frac{dr_m}{dt} = \lambda_2 \cdot \frac{\partial T_2}{\partial r}$$

The mathematical model of the process was implemented using FEMLAB software package [5]. A special developed application opens up possibilities of approaching the moving boundary problem and solving the involved PDEs.

Simulation Results

Diagrams have been obtained for a dolomite granule of 16-mm diameter at 1000 ^oC gaseous phase temperature.

As it can be noticed from the above figures the granule surface reaches the decomposition in approximate 17-20 min. Heat exchange between the dolomite granule surface and gaseous phase depends on the partial heat transfer coefficients and the temperature gradient.

Profiles of the temperature versus time and radius of the granule at different moments of time, t=3 and t=7 min, are presented in figures 2 and 3.

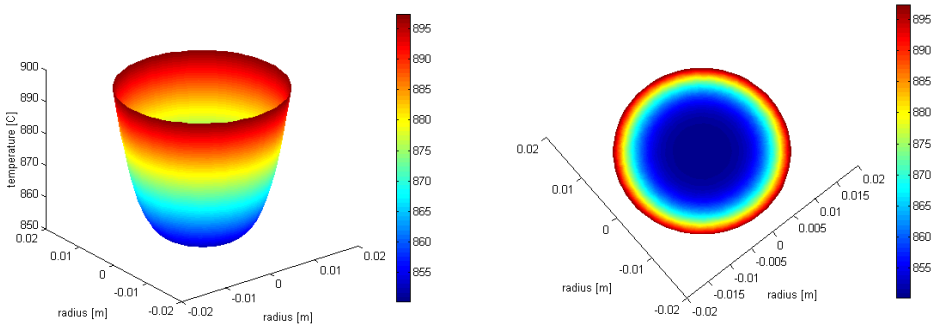

Fig 2. a) Representation of the temperature profile in a granule section, after 3 min (3-D), b) Temperature profile in a granule section, after 3 min (2-D).

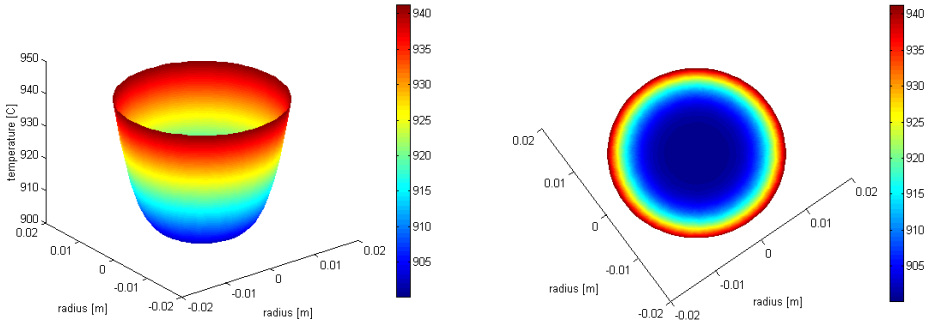

Fig 3. a) Representation of the temperature profile in a granule section, after 7 min (3-D), Temperature profile in a granule section, after 7 min (2-D).

A good agreement between the process simulation results and the experimental data results may be noticed. The decomposition time is of about 17-20 min, both for the simulation of dolomite decomposition and for the experimental data. The temperature evolutions on the solid surface and the temperature in the core (experimental data results) are presented in figure 4.

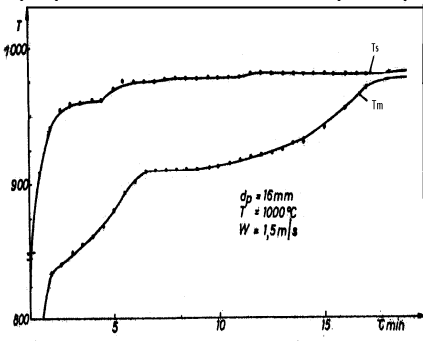

Fig. 4 Time dependence of the temperature on solid surface and in the core (experimental data results) [2]

The dolomite decomposition rate decreases progressively after the oxide layer formation because of the increased heat transfer resistance through the already formed calcium and magnesium oxide layer. The time evolutions for the reaction front velocity and dolomite granule radius are shown in figure 5 and figure 6.

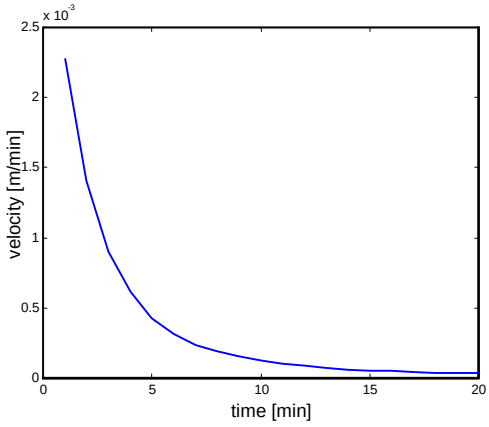

Fig. 5 Dolomite reaction front velocity vs time

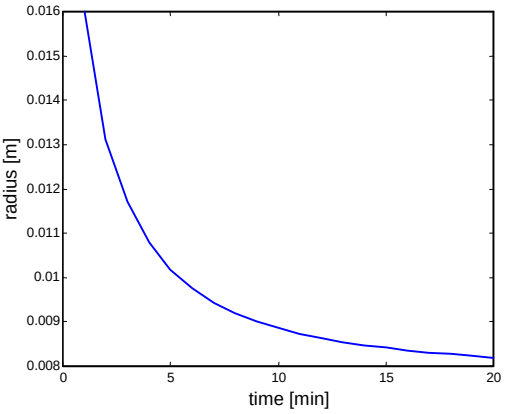

Fig. 6 Dolomite granule radius vs time

The good agreement between the process simulation results and the experimental data results is pointing out that the unreacted core model for dolomite thermal decomposition may be successfully used to describe the dolomite thermal decomposition and to investigate the decomposition process at temperatures between 900 – 1200^{o}C.

Conclusions

The paper presents the modelling and simulation results of the dolomite thermal decomposition. The model offers the possibility to estimate the time and space distribution of the obtained over heated oxide and the unreacted dolomite core, under different conditions of the granule size and temperature of the gaseous phase.

The involved PDEs have been solved using a special developed recursive algorithm based on the parabolic equation solver of FEMLAB, working with the Finite Element Method.

The mathematical model of the dolomite thermal decomposition may be also used to study the behaviour of the process in changing operating conditions and the influence of different impurities on the thermal decomposition of dolomite.

The process simulation results are useful to establish the optimal operation conditions but also for the control system design of the commercial plant.

The dynamic simulations of the dolomite granule with moving boundary reaction geometry allows the investigation of the dolomite decomposition process offering, at the same time, a general framework for the study of gas-solid reaction systems fitted to the unreacted core model description.

Nomenclature

a - thermal diffusion (m^2/h)
T - temperature (^oC)
r - distance from the centre of the granule (m)
t - time (h)
λ - thermal conductivity (W/m ^oC)
c_p - heat capacity (J/kg ^oC)
M - molecular mass (kg/kmol)
ρ - density (kg/m^3)
T_G - gaseous phase temperature (^oC)
K_T - heat transfer coefficient (W/m^2 h grd)
V_S - dolomite granules velocity (m/h)
S_v - specific surface (m^2/m^3)
W_G - thermal capacity of the gaseous stream (W/m^2 h grd)
T_{sp} - temperature on the external surface (^oC)

Indices:
1 - porous oxide product from product zone
2 - dolomite (unreacted zone)
m - core
d - decomposition

Acknowledgements

This research was performed with the support of the World Bank Grant "Informatics of Chemical Systems (ICS)", contract Nr. 46174/27.11.97, Theme Nr.70.

REFERENCES

1. R.Mihail, *Modeling of Chemical Reactor*, Ed. Tehnica, Bucuresti, 1976
2. Al. Pop, *Contribution at the Modelling of Dolomite Thermal Decomposition Process,* PhD. Thesis, 1983
3. A.M. Cormos, M. Cristea, G. Zaha, S. Agachi, *SICHEM 2000*, 3-6 October, 2000, Bucuresti, Paper of Chemical Engineering Symposium, p. 256
4. G. D. Le Blanc, D.E. Seborg, K.L. Holman, *AIChE Annual Meeting,* Los Angeles, November 18, 1997
5. Femlab, Version 2.0, User's Guide, Model Library, GUI Reference and Function Reference, by CONSOLAB 2000

STUDIA UNIVERSITATIS BABEŞ-BOLYAI, CHEMIA, XLVI, 1-2, 2001

THE HYDRODINAMIC OF THREE-PHASE FLUIDIZED BED WITH LOW DENSITY SOLIDS

POP AL., DRAGAN S., BOTAR-JID C, BĂTINAŞ A.

University "Babes-Bolyai" of Cluj-Napoca, Faculty of Chemistry and Chemical Engineering, Arany Janos street No. 11, 3400 Cluj-Napoca, Romania, Tel.: 0040-64-193833, Fax: 0040-64-190818; E-mail: cbotar@personal.ro

ABSTRACT. In this paper are presented the experimental data concerned minimum fluidization velocity and pressure fall in fluidized bed with low density solids (ρ=179 ÷ 312 kg/m^3) and high diameter (d=19 ÷ 38 mm) with pellicular two and three-phases flow of fluid on fluidized solid surface.

New relations are propoused for minimum fluidization velocity and pressure fall determination on base of obtained experimental data.

Minimum fluidization velocity has been corelate with solid specific features and sprinkling density form which column is getting drown.

Low pressure falling and fluidization velocity (2 ÷ 5 m/s) gives the utilization possibility of three-phases fluidized bed, with small density solids, in purification of high fluid debits through absorption and chemosorption processes in low dimension and compact instalation unit.

Introduction

The depollution of gas emanations represents one of the most fundamental problems of humanity. Through industrial activities in many times, big volumes of gas who contain noxes are ousted in atmosphere. This emanation have an important impact on environment. The quantities of noxes, in continous development, had imposed the elaboration of new tehnologies for purification of gas emanations before remission in atmosphere.

The essential characteristics of those emanations are higher debits of gas and small concentrations of noxes in the gas mass. This determine a lower efficienty of gas purification proccess.

The classic methods as absorbtion in columns, sparkling beds and pulverisation has been inefficient because of higher power consuption (big drop pressure) and small rates of mass transfer. All this determine the necessity of big dimentions for industrial units. Also cannot be neglected the drowned phenomenon in packed towers then when gas debit excel a certain value.

Those are the resons who had determine the conception of new methods of phase contact in gas-liqiud system.

This paper has the role to drow up a new method of phase contact in gas-liqiud system. This method is three phase fluidised bed. In this method is much lessened the drowned phenomenon of column simullation with achivement of higher coefficient of transfer.

The use of fluidized bed in chemosorbtion proccess is limitated by big drop pressure because of high density particules, even at small hights of beds. This was the reason who lead to attempts of use of certain beds particles with d_p>10^{-2} m and small densities.

Because specialty literature contain a few dates for hydrodynamics of three-phase fluidized beds, for filling corps with big dimentions (d_p>10^{-2}-$7\cdot10^{-2}$) and low density (50-350 kg/m^3), this study have the purpose to determine the hydrodynamics in this new conditions.

In specialty literature [1,3,4,5,6,7] are suggested many ecuations for establish minimum fluidization velocity. Critical analysis of those ecuations with a view to applying for this new conditions (d_p ↑, ρ_p ↓) had showned that this cannot be used (table 1).

Comparing the obtained experimental results with those determined by specialty literature ecuations porpoused, it's fending out that in all cases there are big difference. In all cases minimum fluidization velocity, determined experimental, is much smaller than that determined with existing ecuations. Result the elaboration necessity of new relations as for two-phase fluidization as three-phase in conditions when liqiud flowing on bed surfaces is filming and fluidized bed isn't drowned.

Table 1.

Analysis of speciality literarure ecuations for minimum fluidization velocity.

Ecuation	Type of filling				
	d_p=0,01m ρ_p=337,5kg/m^3 ε_0=0,45	d_p=0,0194m ρ_p=312kg/m^3 ε_0=0,33	d_p=0,0191m ρ_p=210kg/m^3 ε_0=0,33	d_p=0,038m ρ_p=94 kg/m^3 ε_0=0,30	d_p=0,074m ρ_p=48 kg/m^3 ε_0=0,50
1. **Lewa** $w = 9{,}35\cdot10^{-3}\cdot\frac{d_p^{1,8824}}{\nu_f^{0.8824}}\cdot\left(\frac{\rho_p-\rho_f}{\rho_f}\right)^{0,9421}$	5,81	18,8	12,55	21,36	39,28
2. **Levis** $w=\frac{1}{200}\cdot\frac{\varepsilon_0^3}{1-\varepsilon_0}\cdot\varphi^2\cdot\frac{d_p^{\,2}\cdot\rho_p\cdot g}{\eta_f}$	15,23	17,16	11,19	14,26	179,06
3. **Rowe** $w=0{,}00081\cdot\left(\rho_p-\rho_f\right)\cdot\frac{g\cdot d_p^{\,2}}{\eta}$	14,84	51,62	33,61	59,09	112,9
4. **Gupalo** $\mathrm{Re}=\frac{Ar\cdot\varepsilon_0^{4,75}}{18-10{,}6\cdot\sqrt{Ar\cdot\varepsilon_0^{4,75}}};$ $\mathrm{Re}=\frac{w\cdot d_p\cdot\rho_f}{\eta_f}.$	25,15	19,08	12,42	13,77	324,64
5. **Experimental results**	2,44	2,45	2,44	3,15	2,99

Experimental development

For hydrodynamic study of fluidized bed in this conditions has been used the next installation (figure1).

1-fluidization column;
2-air pump;
3-liquid pump;
4-liquid tank;
5-air rotameter;
6-liquid rotameter;
7-pressure gauge.

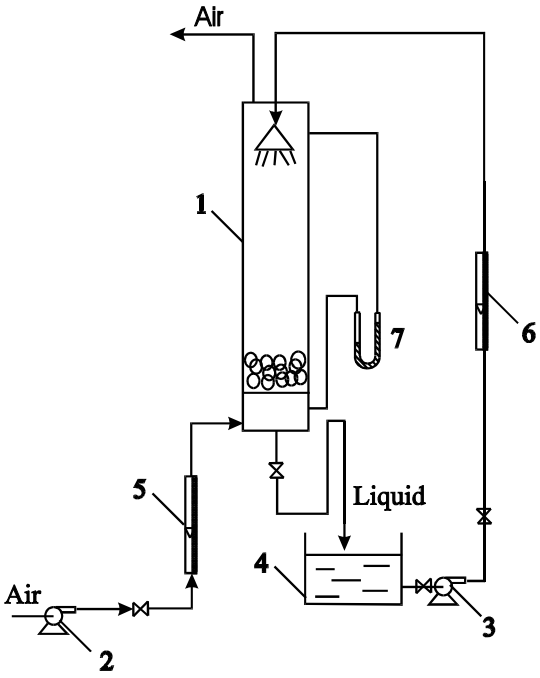

Fig.1. Installation for hydrodynamic study of fluidized bed

The gas and liquid flows is measured with liquid manometer.

The drop pressure on the bed was measured with a gas manometer.

It was measured the drop pressure, at flowing in column without filling and at different hights of filling (h_0). It was used two columns for determination of optimum h_0/D ratio at what fluidization has no secondary effects.

The quality of fluidization was the best than when h_0/D=0,5-0,8.

Experimental was determined that ratio D/d_p must be biger than 8 for a good fluidization.

At ratio h_0/D biger than 0,8 begin to show secondary phenomenon as pistonation and canalisation.

For once establish the conditions for a good homogenous fluidization has past away to determination on experimental way to minimumfluidization velocity. In this purpose has been followed the variation of drop pressure as a function of velocity. Has been seen the phenomenon who take place in filling bed.

In first phase it was studied the two-phase fluidized bed. The obtaining results for different work conditions can be seen in figure 2.

The results obtained in conditions of three-phase fluidized bed can be seen in figures 3,4,5 for different tipes of fillings.

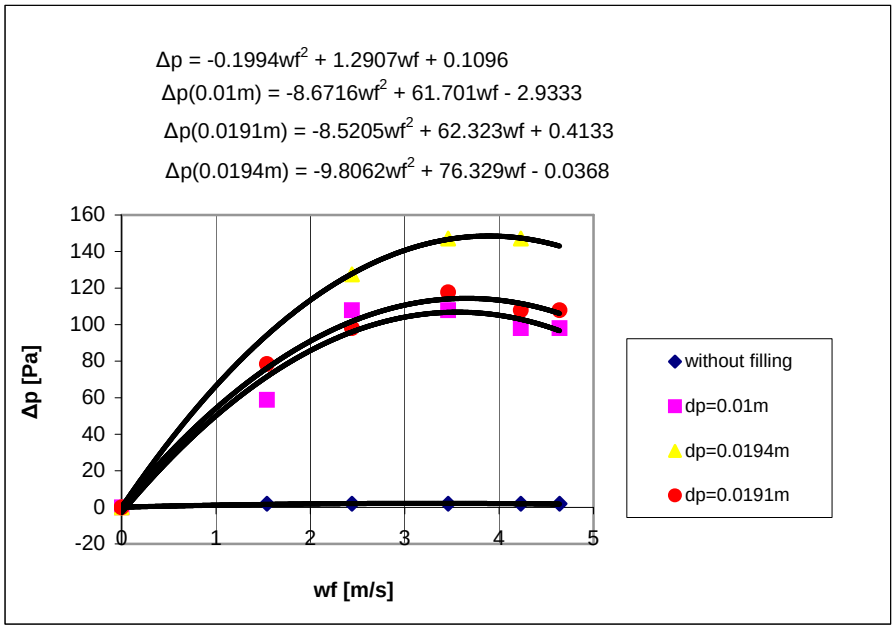

Fig.2. Pressure drop on different types of fillings

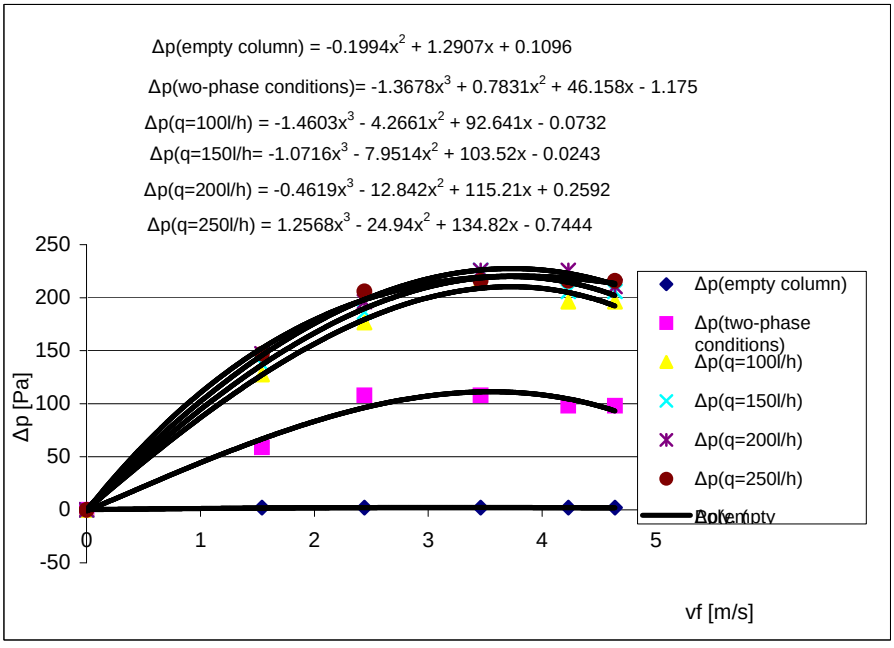

Fig.3. Pressure drop on the filling with particles diameter d_p = 0,01 m

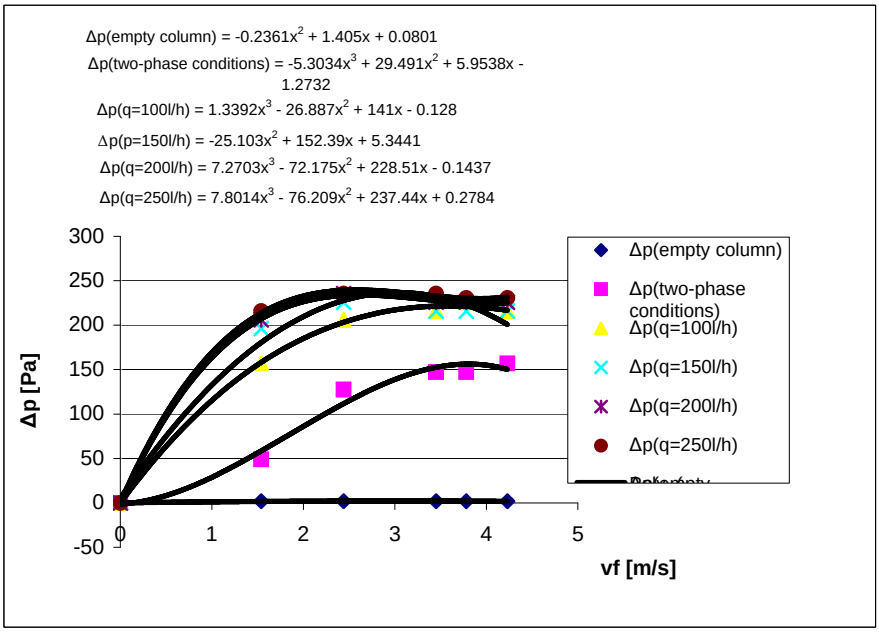

Fig.4. Pressure drop on the filling with particles diameter d_p = 0,0194 m

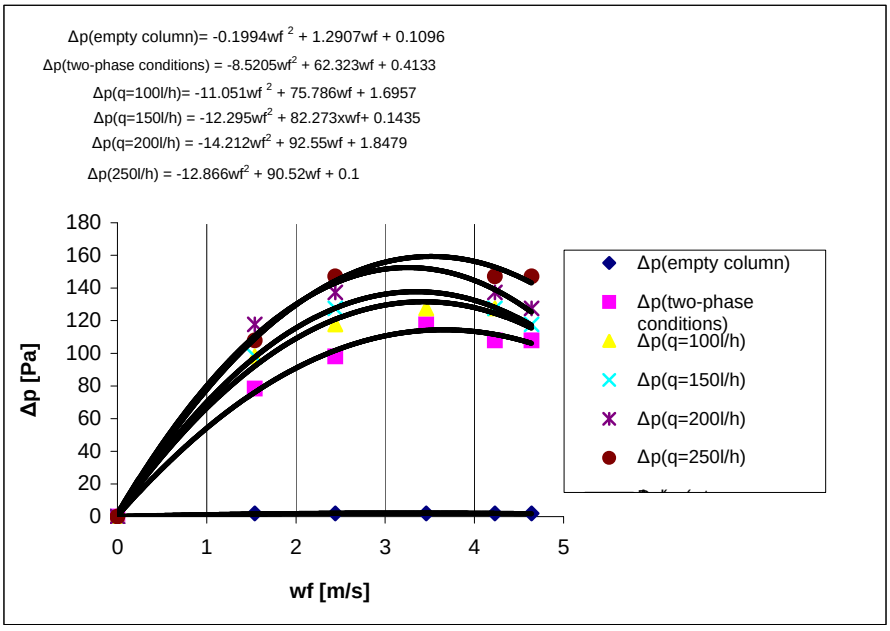

Fig 5. Pressure drop filling with particles diameter d_p = 0,0191 m

In all cases has been observed an improving of fluidization quality in condition of three-phase fluidization.

The fluid film formed on filling surface had replaced the gas-solid friction with the gas-liquid friction. Also was observed that the pressure drop is bringing up a little with sprinkling density.

Analysis of experimental results

The analysis of experimental results suggest that minimum fluidization velocity is bringing up in limits of (10-20%) once with growing of sprinkling density.

For establish a calculation relation for minimum fluidization velocity in three-phase fluidization conditions it was necessary to establish a new relation for minimum fluidization velocity in two-phase conditions.

In this purpose it was been made the diagram $\varepsilon_0 \cdot Ar = f(Re)$, figure 6.

In the second phase it was corelate the minimum fluidization velocity, determined experimental, with sprinkling density.

$$\varepsilon_0 Ar = \left(\mathrm{Re}_p\right)^x \tag{1}$$

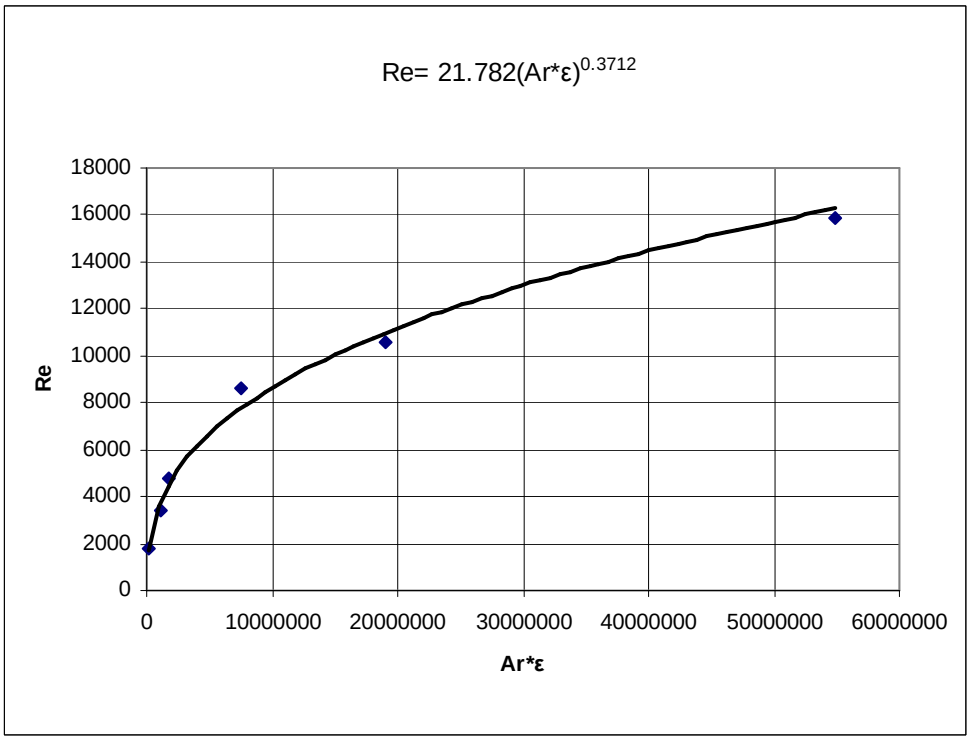

Fig.6. Dependence of Reynolds number of $\varepsilon_0 \cdot Ar$

The results are presented in table 2 and figure 7.

The relation who was determined for minimum fluidization velocity is:

$$w_f = \frac{(\varepsilon_0 Ar)^x \cdot \eta_f}{0{,}001 \cdot d_p \cdot \rho_f}. \tag{2}$$

Table 2.

Minimum fluidization velocity

dp [m]	$\varepsilon_0 \cdot Ar$	q [l/m²h]	x	wf [m/s]	x = f(q)
0,1	131622,2	6,49 9,74 12,99 16,24	9,827 9,372 9,033 8,756	4,24 4,5 4,7 4,9	$x = 10{,}526 \cdot e^{-0{,}0118 \cdot q}$
0,0191	1087409	6,49 9,74 12,99 16,24	12,016 11,603 11,308 11,079	2,317 2,41 2,49 2,55	$x = 12{,}632 \cdot e^{-0{,}0083 \cdot q}$
0,0194	1722981	6,49 9,74 12,99 16,24	12,471 12,056 11,758 11,526	2,27 2,36 2,43 2,62	$x = 13{,}091 \cdot e^{-0{,}008 \cdot q}$

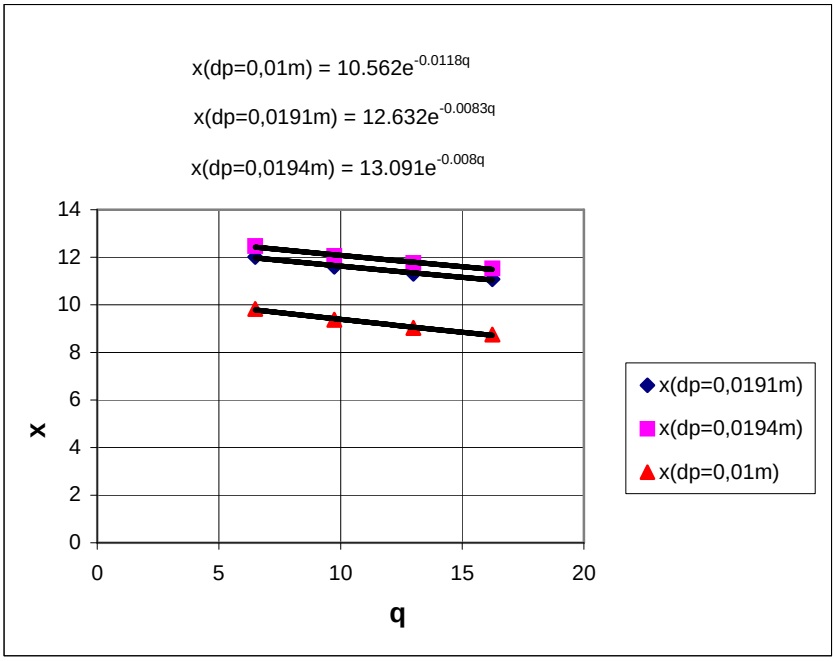

Fig.7. Dependence of x by sprinkling density

The pressure drop on fluidized bed is infuenced by d_p, ρ_p, q. The dependence is presented in figures 8 and 9.

It can be observed that Δp it is minimum at ratio h_0/D = 0,5-0,7. In this conditions the fluidization quality it is better too.

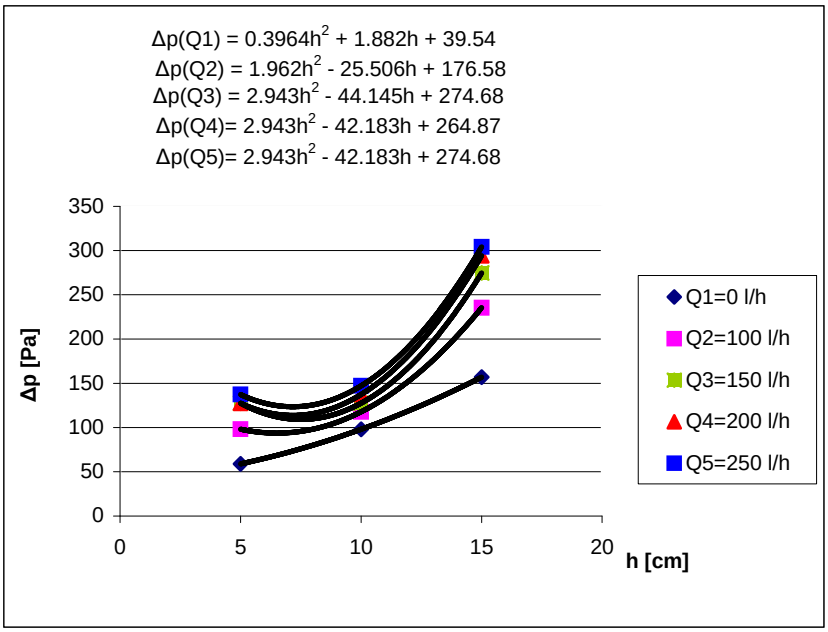

Fig.8. Dependence of pressure drop by sprinkling density

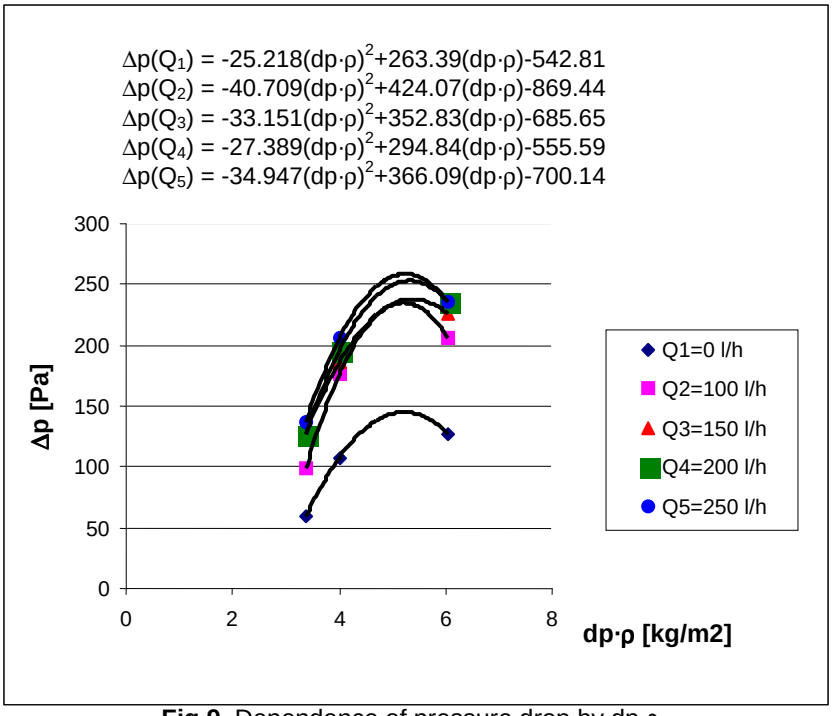

Fig.9. Dependence of pressure drop by dp·ρ

Conclusions

It was establish a new calculation relation for minimum fluidization velocity in condition of two-phase fluidization for filling corps with high diameter and small density.

The experimental data have been corelated in a new calculation relation for minimum fluidization velocity in three-phase fluidization case and it was establish the relation between minimum fluidization velocity and sprinkling density.

It was determined the relation between pressure drop and sprinkling density I three-phase conditions, establishing the ratio h_0/D = 0,5-0,7 for minimum drop pressure on the filling bed.

It is necessary the research continuation for establish the corelation between pressure drop and sprinkling density as well as determination of minimum fluidization velocity for more different filling corps.

Symbols

Ar = Arhimedes number;
Re = Reynolds number;
d_p = particles diameter;
ρ = particles density;
wf = minimum fluidizaton velocity;
h_0 = filling hight
D = column diameter
Δp = pressure drop.
ε_0 = goals ratio of filling

REFERENCES

[1] Floarea, O., Jinescu, G., Procedee intensive în operații unitarea de transfer, Editura Tehnică, Bucureşti, 1975.
[2] Billet, R., Packed towers in processing and environmental tehnology, VCH Verlagsgesellschaft, Wienheim, 1995.
[3] Lewa, M., Takassi, S., Wen, C.Y., Genie Chim.,**75**, 33, 1956.
[4] Lewis, W.K., Gilliland, E.R., Bauer, W.C., Ind. Eng. Chem., **41**, 1104, 1949.
[5] Rowe, P.N., Trans. Inst. Chem. Eng., **39**, 175, 1961.
[6] Gupalo, Yu.P., Ing Fiz.Jurn., **5,** 96, 1962.
[7] Ivanuş, Gh., Todea, I., Pop, Al., Nicola, S., Damian, Gh., Ingineria fluidizării, Editura Tehnică, Bucureşti.

STUDIA UNIVERSITATIS BABEŞ-BOLYAI, CHEMIA, XLVI, 1-2, 2001

SAMPLE HANDLING. CHROMATOGRAPHIC ANALYSIS OF TRIFLURALIN FROM ENVIRONMENTAL SAMPLE. I. WATER SAMPLE

S.COBZAC, M.C.BACIU, A.MOCANU*, I.HAIDUC

Faculty of Chemistry and Chemical Engineering, Babes-Bolyai University, 11 Arany Janos Street, Cluj-Napoca
**Institute for Public Health, 6 Pasteur Street, Cluj-Napoca*

ABSTRACT. Trifluralin is a preemergent herbicide with little postemergent activity. When incorporated in the soil it is effective for the control of annual grasses and broad–leaved weeds in beans, soyabeans, sugar beet, sunflower, and tomatoes. That is why trifluralin can be found in small quantities in the soil and accidentally, in greater concentrations in soil and water as a consequence of other human activities in the field.

In the analytical chain, sample handling is very important for the accuracy and the precision of the analysis. This pesticide is extracted from environmental water sample using liquid-liquid extraction and solid phase extraction.

The present paper deals with SPE of trifluralin on C18 cartridge. The efficiency of the sample treatment was evaluated by the recovery degree of the pesticide from spiked water samples.

When methanol was used as a conditioning and elution solvent, the recovery was higher than 90% and the reproductibility was better.

INTRODUCTION

2,6- dinitro-N,N-dipropyl-4-trifluoromethylaniline or trifluralin (fig 1.) is an orange crystalline solid, melting point 48,5 – 49^{o}C, small solubility in water 1mg/mL, maximum solubility in xilen 580g/mL.

Trifluralin

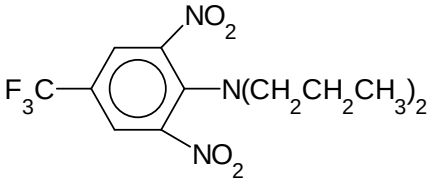

Figure 1. Trifluralin structure.

In a study [1] for the determination of trifluralin from water, Colina used the solid phase extraction on C18 cartridge. The sorbent conditioning was achieved with 5 mL isooctane, ethyl acetate, methanol and water passed successively through the cartridge. After analyt retention achieved at a flow rate 10-15 mL/min. the sorbent was washed with water and dried with air. The elution was achieved with a solvent mixture consisting in ethyl acetate – isooctane (1:1, v/v). The elution solvent evaporated and the residuum was dissolved in 1 mL methanol. This procedure provides a 96% recovery. The same procedure applied on river water provides a 85% recovery.

Senseman [2] used Empore C18 discs in order to concentrate trifluralin from water. When the ethyl acetate was used as elution solvent, the recovery was 72,3%.

Triska [3] used a mixture of dichlormethan-acetone (1:1, v/v) as eluent. Generally, in order to isolate the trifluralin from water, C18-sorbent and ethyl acetate or ethyl ether [4] as elution solvent were used, the recovery being 65%-96%.

Because of the high volatility of these solvents and because they are not mixable with water, in this paper we try to use methanol either as conditioning and elution solvent. As the solid phase for the extraction three different sorbents synthesized by three different procedures were used.

As analytical procedure in order to determine trifluralin gas chromatography was used. [5 - 7]. In this study we have analyzed trifluralin also using liquid-chromatography.

CHEMICALS AND STANDARD SOLUTION

Solvents from Chimopar (Bucuresti, Romania), trifluralin – technical grade from CIG –Turda (Romania), solid phase cartridge SepPack C18, Merck (Darmstadt, Germany) were used and a methanol solution containing 10,85 μg trifluralin / mL for gas-chromatography and another one containing 100μg trifluralin / mL for liquid chromatography analysis were prepared.

PROCEDURE

I. Water Sample Analysis by Liquid-Chromatography

a) Sample preparation using SPE

The extraction cartridge containing 300 mg sorbent was prepared. The characteristics of this sorbent are presented in Table 1.

Table 1.

The characteristics of the three different sorbents used in the SPE procedure

Sorbent	Sil C18 (I)	Sil C18(II)	Sil C18(III)
SiOH residual (%)	28,73	22,06	8,91
pH	3,9	4,5	4,8
Hydrophobic parameter - % methyl red remain in the solution	62,19	68,998	73,53
Carbon content (%)	7,63	11,4	7,57
IR analysis (Absorbtivity at 2950cm^{-1})	0,0714	0,0766	0,0235
Thermogravimetric analysis (weight losses – mg)	7,4	12	8
Ligand density (μmol/g)	1,581	2,56	---

The sorbent conditioning was achieved in two ways:

a) 5 mL methanol

b) 5 mL acetone followed by 5 mL methanol.

The solvent excess was removed with 5-mL water. The trifluralin retention from the synthetic sample (100mL water spiked with 1 mL stock solution - 100μg trifluralin / mL) was achieved by passing it through the cartridge at a flow rate 10 mL/min. The cartridge was then washed with 5-mL water, air- dried and the analyt eluted in two ways:

a) 3 mL methanol
b) 3 mL acetone.

The organic solvent evaporated and the solid residuum was dissolved into 1 mL methanol. The symbols for this sample are given in Table 2.

b). Chromatographic analysis

The determination was achieved on a Hewlett Packard 1100 liquid-chromatograph, with manual injection (20 μm microcolumn), operated at 25^{o}C. A Lichrosphere RP 60 Select B , 250mmx4mm column was used. The mobile phase was an acetonitrile – water (85:15, v/v) mixture, at a 1 mL/min flow rate. The detection was achieved in UV at 275nm, where the trifluralin has a maximum absorbance spectrum (fig.2)

Table 2.

The symbol for each sample obtained after the SPE procedure

Sorbent	Conditioning and elution type	Nr. of extraction	Symbol
Sil C 18 I	A	1 ; 2 ; 3	Ia_1 ; Ia_2 ; Ia_3
	B	1 ; 2 ; 3	Ib_1 ; Ib_2 ; Ib_3
Sil C 18 II	A	1 ; 2 ; 3	IIa_1 ; IIa_2 ; IIa_3
	B	1 ; 2 ; 3	IIb_1 ; IIb_2 ; IIb_3
Sil C 18 III	A	1 ; 2 ; 3	$IIIa_1$; $IIIa_2$; $IIIa_3$
	B	1 ; 2 ; 3	$IIIb_1$; $IIIb_2$; $IIIb_3$
Sil C18 IV (Sep Pack C18)	A	1 ; 2 ; 3	IVa_1 ; IVa_2 ; IVa_3
	B	1 ; 2 ; 3	IVb_1 ; IVb_2 ; IVb_3

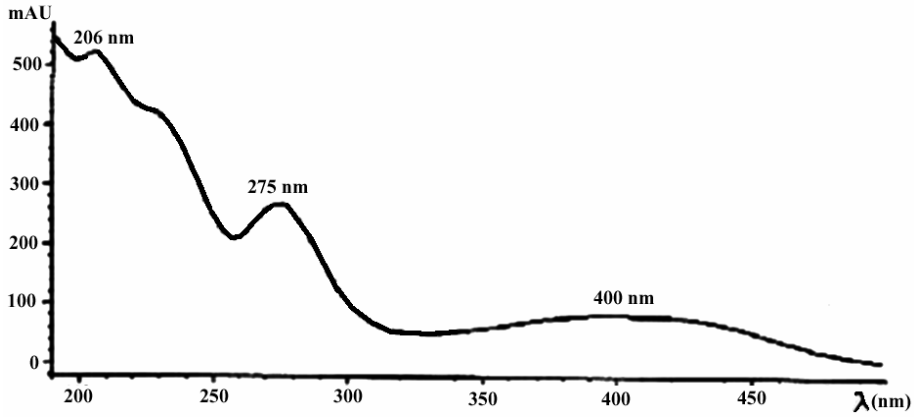

Figure 2. Absorbance spectrum.

RESULTS AND DISCUSSION

In Figures 3 and 4 the bi- and tri-dimensional chromatograms for trifluralin in stock solution are presented. The chromatographic peak of trifluralin was observed at 3.89 min retention time. The recovery was calculated by dividing the peak area of trifluralin from the processed sample by the peak area of trifluralin from the stock solution. Table 3 presents the recoveries after the SPE procedures presented above.

Table 3.

The recoveries of trifluralin when using different sorbents and elution solvents.

Sample	Recovery (GR%)			Average
	Extr.1	Extr.2	Extr.3	$GR_{\%} \pm RSD_{\%}$
Ia	52,51	54,75	53,29	53,52 ± 2,124
Ib	45,50	43,25	44,45	44,4 ± 2,536
IIa	52,62	48,43	48,26	49,77 ± 5,00
IIb	49,92	43,52	45,92	46,45 ± 6,96
IIIa	60,80	54,60	58,54	57,98 ± 1,961
IIIb	51,66	54,74	53,49	53,30 ± 2,908
IVa	54,77	57,55	56,39	56,24 ± 2,489
IVb	41,96	45,93	40,88	42,92 ± 6,198

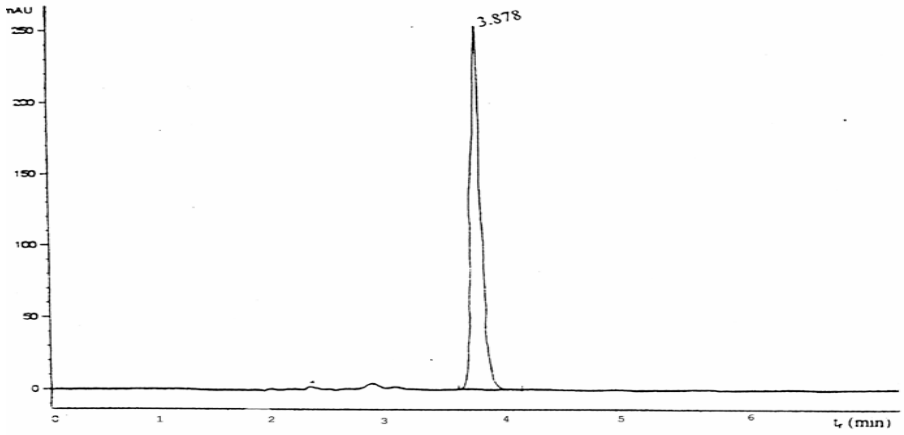

Figure 3. The trifluralin chromatogram (λ= 275).

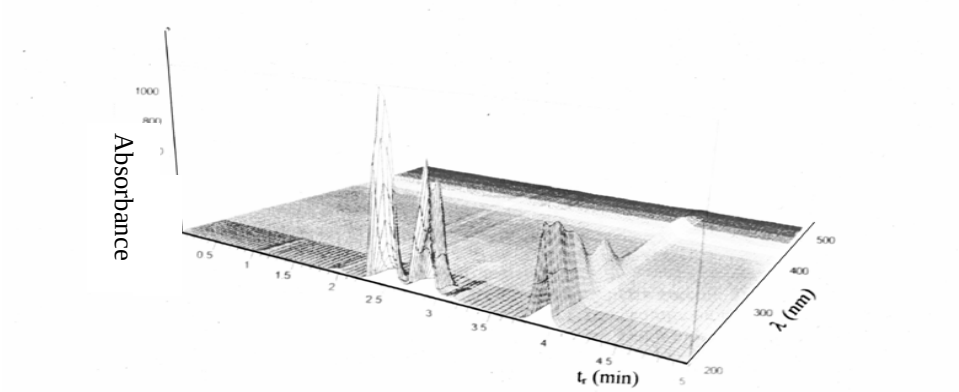

Figure 4. The tridimensional chromatogram for trifluralin.

In Figure 5 there is the recovery as the chart of the sorbent and elution solvent type.

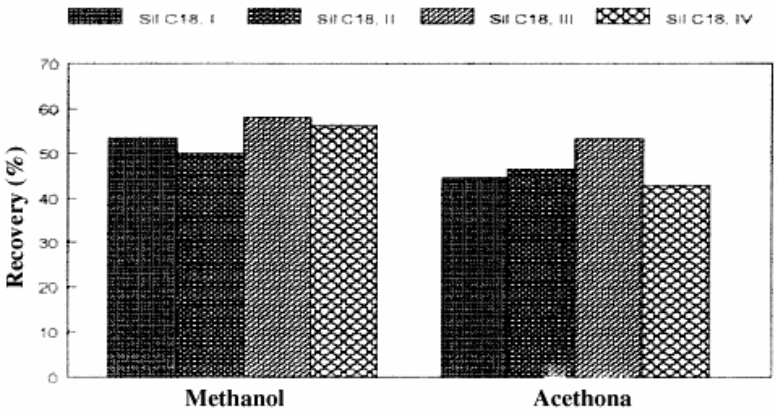

Figure 5. The sorbent and the eluent influence on the recovery.

The small recovery values can be explained only by analyt losses in the evaporation phase, when variable quantities of trifluralin also evaporated.

II.Water Sample Analysis by Gas-Chromatography

a). *Sample preparation using SPE*

After cartridge preparation the sorbent was conditioned in two ways:

a) 5 ml methanol

b) 5 ml ethyl acetate followed by 5 mL methanol.

The conditioning solvent was then removed with 5 mL water. The trifluralin retention from the synthetic sample (100 mL water spiked with 1 mL stock solution 10,85μg/mL) was achieved at a 10 mL/min flow rate. After the sorbent was dried, trifluralin was eluted in two ways:

a) 1 mL methanol

b) 1 mL ethyl acetate.

The volume of the sample was then adjusted to 1 mL with methanol, respectively with ethyl acetate.

b) Chromatographic analysis

The determination was achieved on a Fractovap 2450, Karlo Erba gas chromatograph equipped with capture electron detector. The stainless steel column filed with OV 17 (methylfenil silicon), 3% on a Gas-Chrom support, was operated at 170^{o}C. As eluent was used nitrogen at 15mL/min flow rate.

Results and discussions

In these condition the peak of trifluraline was observe at 7.4 min. retention time. In Table 4 are given the recoveries calculated in the same manner like presented before.

In Figure 6 there is the recovery as the chart of the sorbent and elution solvent type.

Table 4.

The recoveries of trifluralin when using different sorbents and elution solvents.

Sorbent	Recovery (%)						Average GR±RSD (%)
	Solvent						
	Ethyl Acetate	Methanol					
		Extra. 1	Extr. 2	Extr. 3	Extr. 4	Extr. 5	
Sil C18 I	107,5	98,35	103,75	107,25	81,75	81,00	94,42±12,33
Sil C18 II	83,14	107,25	99,38	99,14	78,87	80,62	93,05±12,59
Sil C18 III	87,43	99,00	105,00	102,00	86,25	80,25	94,50±10,7
Sil C18 IV	92,57	95,14	96,75	94,50	99,75	96,00	96,43±2,04

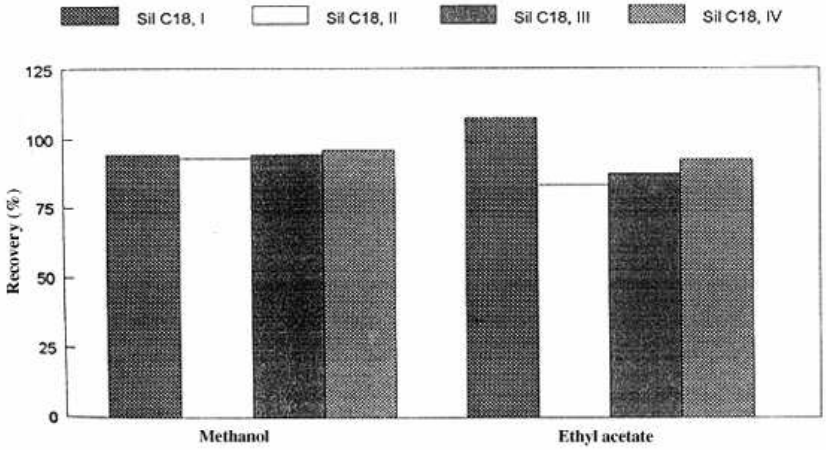

Figure 6. The sorbent and the eluent influence on the recovery

In this experiment, it can be observe that the recovery values are higher as first attempt. These can be explained by avoiding the evaporation phase. So, the recovery increased from 50% at 90%.

CONCLUSIONS

It is clear that the preparation step is very important in obtaining accurate results. So, when evaporation step is eliminated the recovery increased from 50% to 90%. Better reproductibility were achieved when a polar organic solvent, like methanol, mixable with water was used.

REFERENCES

1. C.de la Colina, F.S.Rosero, G.D.Cancela, E.R.Taboada, A.Pena, *Analyst,* **120**(1995), 1723
2. S.A.Senseman, T.L.Lavy, J.D.Matice, *Anal.Chem.,* **67**(1995), 3064.
3. J.Triska. *Chromatographia,* **40**(1995), 712.
4. P.Cabras, M.Melis, L.Spaneda, C.Tuberosa, *J.Chromatogr.,* **585**(1991), 164.
5. A.J.Cesena, L.A.Kerr, E.Patey, T.Zhu, R.L.Desjardins, *J.Chromatogr.,* **710**(1995), 251.
6. Z.Liu, S.R.Sirimane, D.G.Patterson, L.L.Needham, J.B.Phillips, *Anal.Chem.,* **66**(1994), 3086.
7.R.C.Worthing, D.Phil, *The Pesticide Manual,* 1987, The Lavenham Press Limited, Suffol, 832.